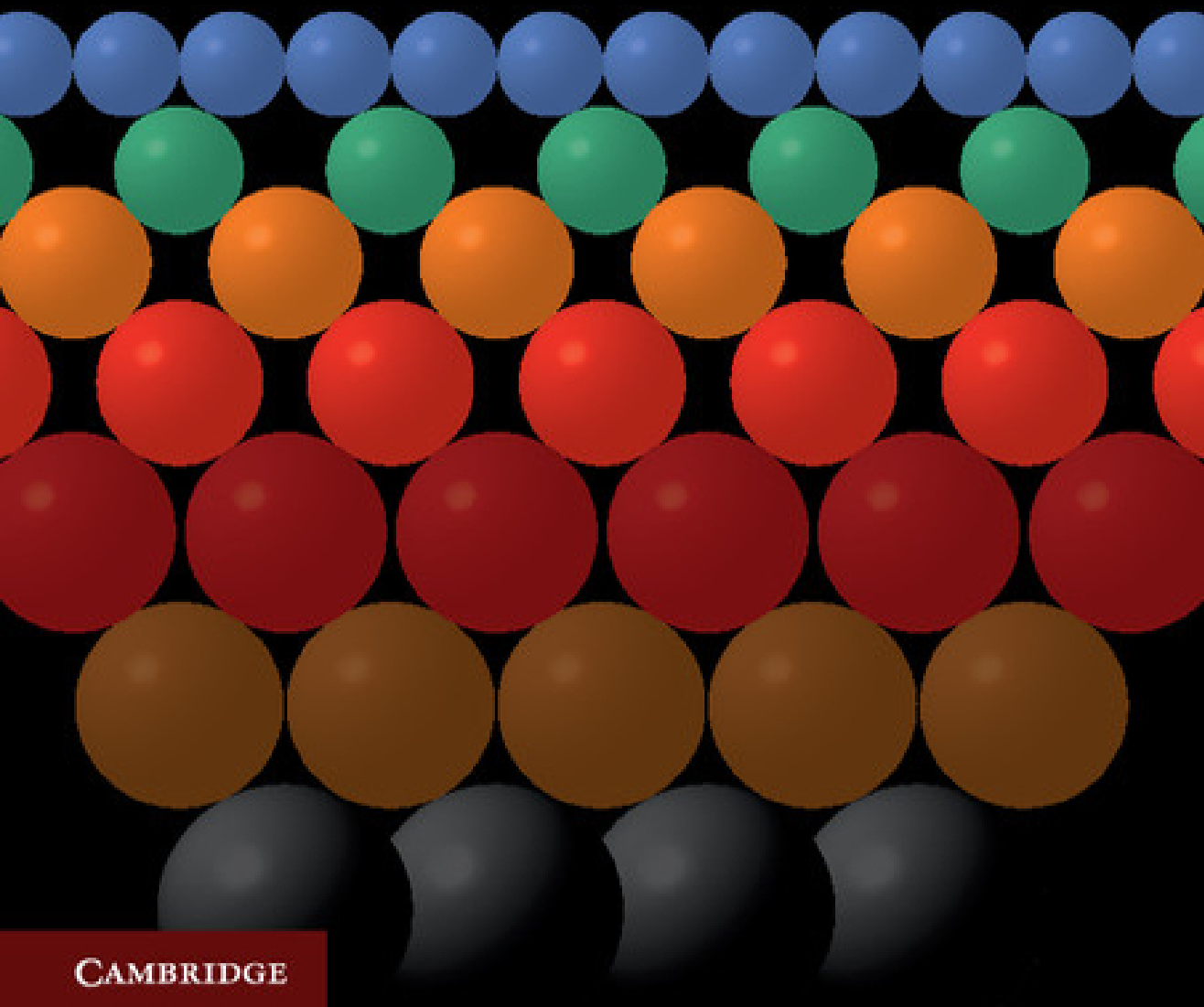
Colloidal Quantum Dot Optoelectronics and Photovoltaics

Edited by Gerasimos Konstantatos
and Edward H. Sargent



CAMBRIDGE

Colloidal Quantum Dot Optoelectronics and Photovoltaics

Capturing the most up-to-date research in colloidal quantum dot (CQD) devices, this book is written in an accessible style by the world's leading experts. The application of CQDs in solar cells, photodetectors, and light-emitting diodes (LEDs) has developed rapidly over recent years, promising to transform the future of clean energy, communications, and displays. This complete guide to the field provides researchers, students, and practitioners alike with everything they need to understand these developments and begin contributing to future applications.

Introductory chapters summarize the fundamental physics and chemistry, whilst later chapters review the developments that have propelled the field forwards, systematically working through key device advances. The science of CQD films is explained through the latest physical models of semiconductor transport, trapping, and recombination, whilst the engineering of organic and inorganic multilayered materials is shown to have enabled major advances in the brightness and efficiency of CQD LEDs.

Gerasimos Konstantatos is an Assistant Professor at the Institut de Ciències Fotòniques (ICFO) in Barcelona. His research interests lie in the area of nanomaterials and nanostructures for optoelectronics and solar cell applications. His expertise is in the field of colloidal quantum dots, and he was awarded the TR35 Spain Prize 2012 and the 2013 Fresnel Prize for Applied Aspects for his salient contributions in the field of colloidal quantum dot optoelectronics.

Edward H. Sargent is a Professor in the Department of Electrical and Computer Engineering at the University of Toronto, where he holds the Canada Research Chair in Nanotechnology. His book *The Dance of Molecules: How Nanotechnology is Changing Our Lives* (2005) has been translated into French, Spanish, Italian, Korean, and Arabic. He is a Founder and CTO of InVisage Technologies, Inc.

Colloidal Quantum Dot Optoelectronics and Photovoltaics

Edited by

GERASIMOS KONSTANTATOS

ICFO – The Institute of Photonic Sciences, Barcelona

EDWARD H. SARGENT

University of Toronto

CAMBRIDGE
UNIVERSITY PRESS

CAMBRIDGE
UNIVERSITY PRESS

University Printing House, Cambridge CB2 8BS, United Kingdom

Published in the United States of America by Cambridge University Press, New York

Cambridge University Press is part of the University of Cambridge.

It furthers the University's mission by disseminating knowledge in the pursuit of education, learning and research at the highest international levels of excellence.

www.cambridge.org
Information on this title: www.cambridge.org/9780521198264

© Cambridge University Press 2013

This publication is in copyright. Subject to statutory exception and to the provisions of relevant collective licensing agreements, no reproduction of any part may take place without the written permission of Cambridge University Press.

First published 2013

Printed in the United Kingdom by TJ International Ltd. Padstow Cornwall

A catalogue record for this publication is available from the British Library

Library of Congress Cataloguing in Publication data
Colloidal quantum dot optoelectronics and photovoltaics / [edited by] Gerasimos Konstantatos, Edward H. Sargent.
pages cm
Includes bibliographical references and index.
ISBN 978-0-521-19826-4 (hardback)
1. Quantum electronics. 2. Quantum dots. 3. Photovoltaic cells. I. Konstantatos, Gerasimos, 1979– editor of compilation.
[DNLM: 1. Colloids.]
TK7874.88.C65 2013
537.5 – dc23 2013013116

ISBN 978-0-521-19826-4 Hardback

Cambridge University Press has no responsibility for the persistence or accuracy of URLs for external or third-party internet websites referred to in this publication, and does not guarantee that any content on such websites is, or will remain, accurate or appropriate.

Contents

List of contributors *page* xi
Preface xiii

1 Engineering colloidal quantum dots: synthesis, surface chemistry, and self-assembly 1
Maryna I. Bodnarchuk and Maksym V. Kovalenko

1.1 Colloidal synthesis of inorganic nanocrystals and quantum dots 1
1.1.1 Introductory remarks: history and terminology 1
1.1.2 Basics of the surfactant-assisted colloidal synthesis of NC quantum dots 2
1.2 Long-range ordered NC solids 7
1.2.1 Single-component NC superlattices 7
1.2.2 Multicomponent NC superlattices 9
1.2.3 Shape-directed self-assembly of NCs 13
1.3 Surface chemistry – a gateway to applications of NCs 16
1.3.1 Organic capping ligands 16
1.3.2 Complete removal of organic ligands and inorganic surface functionalization 19
References 20

2 Aqueous based colloidal quantum dots for optoelectronics 30
Vladimir Lesnyak and Nikolai Gaponik

2.1 Introduction 30
2.2 Aqueous colloidal synthesis of semiconductor NCs 32
2.2.1 ZnX NCs 32
2.2.2 Alloyed ZnSe based NCs 34
2.2.3 CdX NCs 35
2.2.4 Core/shell CdTe based NCs 36
2.2.5 Alloyed CdTe based NCs 37
2.2.6 CdSe, CdSe/CdS NCs 39
2.2.7 HgX and PbX NCs 39

2.2.7.1 HgX NCs 40
2.2.7.2 PbX NCs 40
2.3 Assemblies and functional architectures of NCs 41
2.3.1 LbL assembly technique 43
2.3.2 Assembly of NCs on micro- and nano-beads 46
2.3.3 Covalent coupling of NCs 47
2.3.4 Controllable aggregation 48
2.3.5 Nanowires and nanosheets 49
2.3.6 Nanocrystal based gels and aerogels 49
2.4 Conclusions and outlook 50
References 51

3 Electronic structure and optical transitions in colloidal semiconductor nanocrystals 59
Todd D. Krauss and Jeffrey J. Peterson

3.1 Introduction 59
3.2 Foundational concepts 60
3.3 A simple model 65
3.4 Experimental evidence for quantum confinement 67
3.5 Engineered quantum dot structures 71
3.6 Advanced theoretical treatments 73
3.7 Atomistic approaches 76
3.8 Current challenges and future outlook 80
References 81

4 Charge and energy transfer in polymer/nanocrystal blends: physics and devices 87
Kevin M. Noone and David S. Ginger

4.1 Introduction 87
4.2 A brief history of QD/polymer optoelectronics 88
4.2.1 Quantum dot light emitting diodes (QD-LEDs) – size-tunable emission across the spectrum 88
4.2.2 Quantum dot photovoltaics (QD-PV) and photodetectors – converting photons to electrons 90
4.2.2.1 QD-PVs 90
4.2.2.2 Quantum dot photodetectors 93
4.3 The QD–organic interface – ligands and more 96
4.3.1 Ligands 96
4.3.2 Energetics 98
4.3.2.1 Charge transfer and Förster resonance energy transfer (FRET) in QD-LEDs 99
4.3.2.2 Type II heterojunctions and charge transfer in QD-PVs 99
4.4 Conclusion and future outlook 104
References 105

5 Multiple exciton generation in semiconductor quantum dots and electronically coupled quantum dot arrays for application to third-generation photovoltaic solar cells 112
Matthew C. Beard, Joey M. Luther, and Arthur J. Nozik

5.1 Introduction 112
5.2 Relaxation dynamics of photogenerated electron–hole pairs in QDs 115
5.2.1 Transient absorption spectroscopy (TA) 117
5.3 Multiple exciton generation (MEG) 121
5.3.1 MEG in QDs 121
5.3.2 MEG controversy and role of photocharging 125
5.3.3 MEG efficiency and comparison to impact ionization in bulk semiconductors 128
5.4 QD solar cells 131
5.4.1 MEG photocurrent and determination of the internal quantum efficiency (IQE) in QD solar cells 133
5.5 QD arrays 136
5.5.1 MEG in PbSe QD arrays 137
5.6 Conclusions 140
References 141

6 Colloidal quantum dot light emitting devices 148
Vanessa Wood, Matthew Panzer, Seth-Coe Sullivan, and Vladimir Bulovic

6.1 Introduction 148
6.2 Why QDs for LEDs? 148
6.2.1 Saturated colors 148
6.2.2 Solution processable 150
6.2.3 Stability 150
6.3 QD and device physics influencing LED performance 151
6.3.1 Quantifying the luminescence efficiency 151
6.3.2 QD surface states 152
6.3.3 QD charging 153
6.3.4 Charge transport in QD films 154
6.3.5 Field driven luminescence quenching 154
6.3.6 Isolating the effects of charge and field 155
6.4 Characterizing QD-LEDs 157
6.5 QD-LEDs based on optical downconversion 160
6.6 QD-LEDs based on organic charge transport layers 161
6.6.1 Deposition of QDs: spin casting, phase separation, and microcontact printing 161
6.6.2 Operation of colloidal QD-LEDs 163
6.7 QD-LEDs with inorganic charge transport layers 165
6.7.1 Reasons for inorganic charge transport layers 165

6.7.2 Fabrication of all inorganic QD-LEDs 165
6.7.3 Operation of QD-LED with inorganic charge transport layers 166
6.7.4 Improving the efficiency of QD-LEDs with inorganic charge transport layers 167
6.8 Future work 167
References 168

7 Colloidal quantum dot photodetectors 173
Gerasimos Konstantatos

7.1 Introduction 173
7.1.1 Applications of top-surface photodetectors 173
7.1.2 Colloidal quantum dots (CQDs) for light detection 174
7.2 Fundamentals of photodetectors 175
7.2.1 Types of photodetectors 175
7.2.2 Figures of merit 176
7.3 Prior art in solution-processed photodetectors 177
7.4 Solution-processed QD photoconductors 179
7.4.1 Photoconductive gain and noise in PbS QD photodetectors 179
7.4.2 Visible-wavelength and multispectral photodetection 183
7.4.3 Control of temporal response in photoconductive detectors via trap state engineering 185
7.5 CQD based phototransistors 187
7.6 CQD photodiodes 190
7.7 Conclusions – summary 193
References 195

8 Optical gain and lasing in colloidal quantum dots 199
Sjoerd Hoogland

8.1 Introduction 199
8.2 Optical properties of colloidal nanocrystal quantum dots 200
8.3 Carrier dynamics in colloidal quantum dots 202
8.3.1 Auger recombination 205
8.3.2 Poisson statistics and state filling 206
8.4 Gain in solid state nanocrystal quantum dot films 207
8.4.1 Amplified spontaneous emission (ASE) 208
8.4.2 Variable strip length (VSL) for optical gain measurements 209
8.4.3 Experimental techniques for waveguide loss measurement in colloidal quantum dot films 209
8.4.4 Modal gain in visible colloidal quantum dots based on cadmium chalcogenides 211
8.4.5 Modal gain in infrared colloidal quantum dots based on lead chalcogenides 213

8.5 Spectral and temporal characteristics of optical gain in nanocrystal quantum dots 214
8.5.1 Visible colloidal quantum dots based on cadmium chalcogenides 214
8.5.2 Infrared colloidal quantum dots based on lead chalcogenides 218
8.6 Colloidal nanocrystal lasers 221
8.6.1 Microcapillary resonators 223
8.6.2 Microsphere resonators 224
8.6.3 Distributed feedback resonators 225
8.6.4 Microtoroid resonators 225
8.6.5 Other resonators 226
8.7 Future prospects 226
8.7.1 Single exciton gain 226
References 229

9 Heterojunction solar cells based on colloidal quantum dots 233
Jeffrey J. Urban and Delia J. Milliron

9.1 Introduction 233
9.2 Chemistry of CQDs for solar cells 234
9.3 Physics of CQDs for solar cells 238
9.3.1 Electronic structure evolution in low dimensional systems 238
9.3.2 Fundamentals of light–matter interactions in QDs 240
9.3.3 Selection rules and the complications of H 241
9.4 Optical and electronic properties of CQD films for solar cells 241
9.5 Device physics and design of CQD heterojunction solar cells 246
9.6 Technology and scientific outlook 250
References 251

10 Solution-processed infrared quantum dot solar cells 256
Jiang Tang and Edward H. Sargent

10.1 Introduction 256
10.2 Infrared CQDs for the full absorption of solar spectrum 257
10.2.1 Bandgap engineering for the broadband solar spectrum match 257
10.2.2 Light absorption in CQD film 260
10.3 Semiconductor solar cell fundamentals 260
10.3.1 Fundamentals of p–n junction 260
10.3.2 Fundamentals of solar cells 263
10.3.3 Implications for CQD solar cell optimization 264
10.4 Electrical properties of CQD films 265
10.4.1 Measurements of electrical properties of CQD films 265
10.4.2 Transport in CQD film 269
10.4.3 CQD passivation 272
10.4.4 CQD film doping 275
10.4.5 Dielectric constant of CQD film 276

10.5 Progress in CQD solar cell performance 276
10.5.1 Schottky solar cells 276
10.5.2 Heterojunction solar cells 279
10.6 Device stability 283
10.7 Perspectives and conclusions 285
References 286

11 Semiconductor quantum dot sensitized TiO_2 mesoporous solar cells 292
Lioz Etgar, Hyo Joong Lee, Sang Il Seok, Md. K. Nazeeruddin, and Michael Grätzel

11.1 Introduction 292
11.2 Mesoscopic PbS quantum dot/TiO_2 heterojunction solar cells 294
11.2.1 Solid-state PbS/TiO_2 heterojunction solar cell 299
11.3 QD/TiO_2 mesoporous solar cell using the SILAR process 301
11.4 Cobalt complex-based redox couples in CQD-TiO_2 mesoporous solar cells 305
References 308

Index 310

Contributors

Matthew C. Beard
The National Renewable Energy Laboratory, USA

Maryna Bodnarchuk
ETH Zurich

Vladimir Bulovic
Massachusetts Institute of Technology

Nikolai Gaponik
Technical University of Dresden

David S. Ginger
University of Washington

Sjoerd Hoogland
University of Toronto

Gerasimos Konstantatos
The Institute of Photonic Sciences (ICFO), Barcelona

Maksym V. Kovalenko
EMPA – Swiss Federal Laboratories for Materials Science and Technology

Todd D. Krauss
University of Rochester

Hyo Joong Lee
Chonbuk National University, South Korea

Vladimir Lesnyak
Technical University of Dresden

Lioz Etgar
Ecole Polytechnique Fédérale de Lausanne (EPFL)

Joey M. Luther
The National Renewable Energy Laboratory, USA

Michael Grätzel
Ecole Polytechnique Fédérale de Lausanne (EPFL)

Delia J. Milliron
Lawrence Berkeley National Laboratory

Md. K. Nazeeruddin
Ecole Polytechnique Fédérale de Lausanne (EPFL)

Kevin M. Noone
University of Washington

Arthur J. Nozik
University of Colorado, Boulder

Matt Panzer
Tufts University

Jeffrey J. Peterson
State University of New York, Geneseo

Edward H. Sargent
University of Toronto

Sang Il Seok
Korea Research Institute of Chemical Technology

Seth-Coe Sullivan
QD Vision, Inc., USA

Jiang Tang
University of Toronto

Jeffrey J. Urban
Lawrence Berkeley National Laboratory

Vanessa Wood
Integrated Systems Laboratory, ETH Zurich

Preface

2013 is a landmark year for the field of colloidal quantum dot (CQD) optoelectronics. Nearly three decades have passed since the pioneering syntheses of CQDs; since then countless innovations in synthesis and processing of quantum dots have led to multifunctional colloidal nanoparticles and nanomaterials, achieved via advanced control over particle size, shape, and composition. A deeper understanding has been gained of the physical chemistry of these materials, with electronic and optical properties increasingly elaborated and traced to detailed atomic-scale composition. Excitingly, the first products based on this new class of materials have been announced and will revolutionalize optoelectronics. No longer will high-efficiency and high-performance devices be limited to the realm of single-crystal epitaxy. Companies large and small will deploy CQDs in their next-generation displays to improve the efficiency and quality of the displays. Quantum dots will feature in high-efficiency light-emitting diodes, enabling vastly improved color rendering in displays and lighting alike. The first quantum-dot-based cameras will soon be shipped to customers, offering high-fidelity imaging and professional camera features in a mobile platform. Impacting the economically vast and societally important field of solar energy harvesting is within sight as photovoltaic devices leverage CQDs' spectral tunability for more spectrally efficient harvesting via multijunction architectures or multiexciton processes now demonstrated in devices.

This book aims to provide an updated snapshot of this fast-moving field. It is intended for both new researchers in the CQD dot field, and also experts seeking to gain an up-to-date view of CQD domains adjacent their own.

The book has three main sections: chemistry and synthesis of CQDs and their assembly; the physics and optoelectronic properties of these materials; and optoelectronic devices including lasers, light-emitting diodes, photodetectors, and solar cells.

In Chapters 1 and 2 we present advances in the synthesis and self-assembly of CQDs into solids. Chapter 1 focuses on the organometallic synthesis of CQDs and nanocrystals, and presents the innovative synthetic schemes that have enabled enhanced control over size, shape, and composition. It devotes considerable attention to the organic and the new inorganic ligands that are used to control the properties of the quantum dots and reviews the self-assembly of quantum dots into supra-nanocrystalline solids. Chapter 2 presents aqueous-based synthesis of CQDs and their self-assembly into functional thin films. Aqueous-based CQDs have enabled biological applications and may offer a less materials- and energy-consuming route to CQD optoelectronics.

The second section of the book examines the physical properties of CQDs and quantum dot nanocomposites. Chapter 3 presents the fundamental physical processes that describe how photons and charge carriers interact inside quantum dots. It lays out the theoretical framework within which to understand the quantum size effect, a distinguishing feature of quantum dots that sets them apart from bulk materials and has earned them the name artificial atoms. Chapter 4 explores the optoelectronic properties of hybrid nanocomposites of quantum dots and polymers that have been exploited in light emission, detection, and solar harvesting. It offers a fundamental picture of charge transfer dynamics and energy transfer in quantum dot polymer composites and their applications to devices. Chapter 5 focuses on multiple exciton generation, a phenomenon at play in colloidal quantum dots that enhances their potential in third-generation photovoltaics. The chapter reviews how the Shockley–Quiesser limit can be overcome, looking at both basic physics and applications.

The third section shines a light on optoelectronic devices made using CQDs. Chapter 6 presents the development of light-emitting diodes based on CQDs for display and lighting applications. After consideration of the fundamental mechanisms at play in CQD electroluminescent devices, the chapter presents different architectures and reviews metrology and characterization techniques of CQD light-emitting diodes. Chapter 7 lays out the ideas that have enabled sensitive, rapid, and convenient photodetection using CQD solids, beginning with the first observations of photoconduction and proceeding to advanced photodetector architectures including photoconductors, photodiodes, and phototransistors. The last chapter of this section reviews lasing from quantum dots with emphasis on optically pumped laser cavities and the physics of optical gain and lasing in CQD materials.

The last three chapters of the book are dedicated to the timely and fast-growing field of CQD solar cells: Chapter 9 introduces and elaborates on polymer–nanocrystal hybrid solar cells and the key achievements in the synthesis of quantum dots, rods, and tetrapods that brought about a significant boost in performance in these solar cell architectures. Chapter 10 discusses the solar cells that have led to the highest certified CQD photovoltaic performance reported, architectures that employ a dense and crosslinked quantum dot solid from which electrons and holes are extracted using selective solid-state contacts. Chapter 11 deals with the evolution of dye-sensitized solar cells via the employment of inorganic sensitizers comprising CQDs. It considers the physics involved and the deployment of CQDs on the surface of mesoporous nanostructured electrodes.

1 Engineering colloidal quantum dots

Synthesis, surface chemistry, and self-assembly

Maryna I. Bodnarchuk and Maksym V. Kovalenko

1.1 Colloidal synthesis of inorganic nanocrystals and quantum dots

1.1.1 Introductory remarks: history and terminology

Historically, one of the most accomplished nanoscale building blocks is the quantum dot, also known as a semiconductor nanocrystal (NC). Since the early 1980s, the chemistry of colloidal nanostructures has been almost exclusively concentrated on colloidal semiconductors such as CdS and TiO_2. Those early efforts rose from the oil crisis in the late 1970s, and semiconductor NCs with enhanced surface chemistry were considered highly important for efficient harvesting of solar energy via photoelectrochemistry [1] and later using dye-sensitized solar cells [2]. The interest in quantum dots was further triggered by the discovery of quantum-size effects in the optical spectra of nanometer-sized semiconductors, by the teams of A. Ekimov and A. Efros in the USSR [3, 4], and by L. Brus at Bell Laboratories in the USA [5]. The first observations were collected from optical measurements on the semiconductor dots dispersed in glass matrices [3] or aqueous semiconductor sols [5]. Until the mid-1990s, a major challenge was to master the production of quantum dots in the form of uniform, size-tunable and isolable NCs, with adjustable physical and chemical properties. This goal was largely accomplished only in 1993 when the hot-injection technique was introduced by Murray, Norris, and Bawendi, enabling synthesis of highly monodisperse Cd chalcogenide NCs [6]. Surfactant-assisted nucleation and growth in organic solvents, initiated by hot-injection [6] or by heating [7] the reaction mixture became standard for growing monodisperse colloidal NCs of metals, metal oxides, and other classes of inorganic compounds. Even water was demonstrated as a suitable synthesis medium for certain compounds, such as thiol-capped II–VI semiconductor NCs [8] with bright and stable photoluminescence.

The multitude of methods for producing nanosize particles and crystals is truly impressive (Figure 1.1). The top-down approaches for the formation of engineered nanomaterials include fragmentation and structuring of macroscopic solids, either mechanically (e.g., ball-milling) or chemically (lithography, exfoliation, etching, etc.). The bottom-up assembly starts with molecules, atoms, and ions and proceeds via gas-phase or liquid-phase chemical reactions, aggregation, and crystallization. Liquid-phase synthesis in aqueous or non-aqueous solvents turned out to be particularly convenient and successful.

Colloidal Quantum Dot Optoelectronics and Photovoltaics, eds. G. Konstantatos and E. H. Sargent.
Published by Cambridge University Press. © Cambridge University Press, 2013.

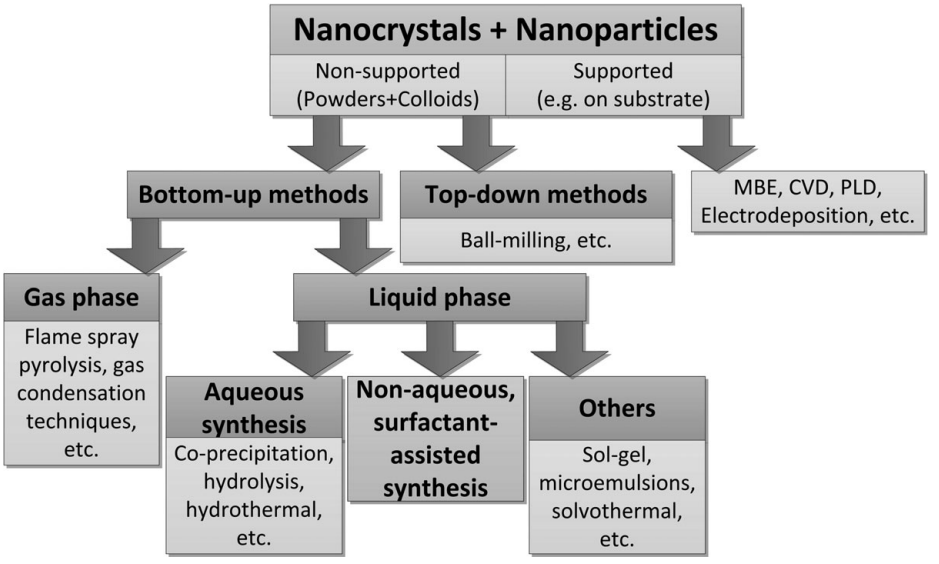


Figure 1.1 An overview of various methods for fabrication of inorganic nanoparticles and nanocrystals. Non-aqueous surfactant-assisted synthesis is colloidal synthesis in organic solvents – the key methodology for all NC quantum dots discussed in this book. Color version of this figure is available online at www.cambridge.org/9780521198264.

Surfactant-assisted, colloidal synthesis in organic solvents earned the highest appreciation and will be discussed here in detail. Physical and chemical methods of growth on planar supports constitute a separate and broad field of science and technology, outside the scope of this book.

While the general term "nanoparticle" refers to the characteristic size (usually 1–100 nm), a *crystalline* nanoparticle is often called a "nanocrystal" (Figure 1.2(a), (b)). The quantum-mechanical definition of "quantum dot" refers to the peculiar electronic structure – the piece of matter (typically a semiconductor) having electrons and holes confined in all three dimensions. When this property is found in a NC, that entity is often called a "NC quantum dot". For simplicity, the terms "semiconductor NC" and "quantum dot" are used interchangeably, a legitimate assumption for most of 2–20 nm NCs. Finally, the phrases "colloidal NCs" or "colloidal quantum dots" indicate the colloidal method of synthesis and colloidal state of dispersion (Figure 1.2(c)).

1.1.2 Basics of the surfactant-assisted colloidal synthesis of NC quantum dots

In a typical NC synthesis (Figure 1.2(c), (d) and Figure 1.3), suitable molecular precursors are introduced into a reaction mixture, where they undergo a chemical reaction supplying "monomers" (reaction I) for the homogeneous nucleation of NCs (reaction II). The further growth occurs due to continuous flux of monomers onto the NC surface (reaction III). Upon depletion of the monomer concentration, further growth may occur through the Ostwald ripening process (also known as Lifshitz–Slyozov–Wagner growth) [10, 11], i.e., growth of larger dots by dissolving smaller ones. All these consecutive stages can be significantly altered by the presence of surface capping molecules, also

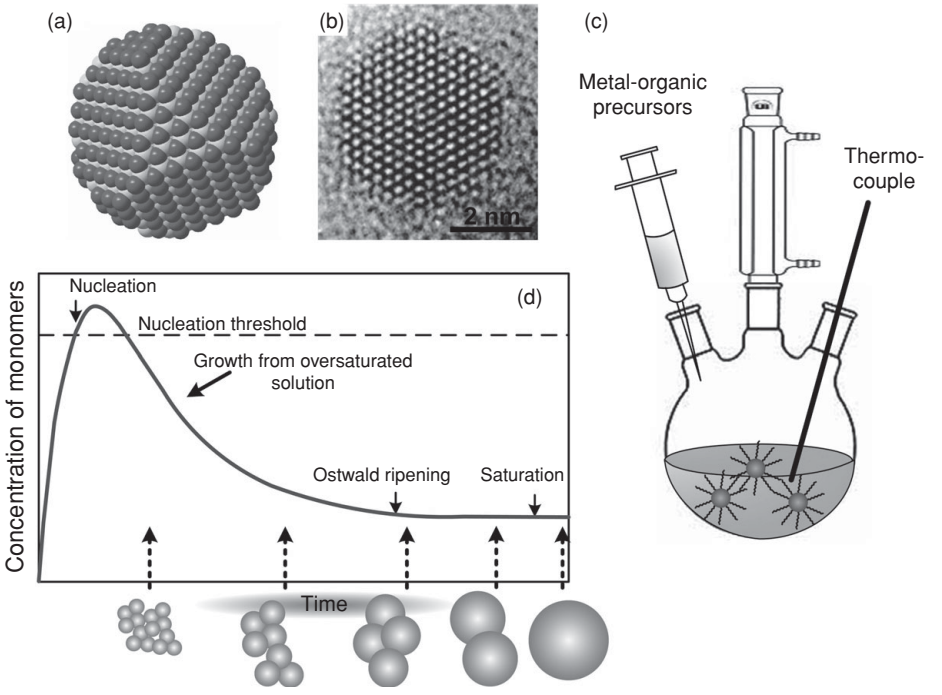


Figure 1.2 Colloidal NC quantum dots. (a) Crystallographic model and (b) high-resolution TEM image of a single CdSe NC. Reproduced with permission from [9]. (c) Illustration of a typical setup used in the chemical synthesis of colloidal NCs. (d) Schematics of the main stages in the synthesis of colloidal NCs in relation to the concentration of the monomers. Color version of this figure is available online at www.cambridge.org/9780521198264. Adapted from [9].

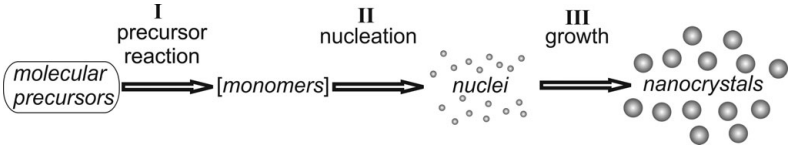


Figure 1.3 Illustration of the three key steps in the synthesis of colloidal NCs: precursor-to-monomer conversion, homogeneous nucleation, and heterogeneous growth.

known as surfactants or stabilizers. These molecules dynamically adhere to the NC surface during NC nucleation and growth, and provide chemical and colloidal stability of the final product. It is generally accepted that temporal separation of the nucleation and growth is required for growing monodisperse NCs [6, 12]. The concept of the nucleation "burst" relates to the fast nucleation that occurs after the monomer concentration surpasses a certain threshold, as originally proposed by La Mer and others (Figure 1.2(d)) [12, 13]. Fast nucleation is best implemented using the so-called *hot-injection technique*, in which the precursors are rapidly injected into a hot solvent to induce their fast conversion into monomers (Figure 1.2(c)) [6, 14]. Alternatively, the separation of nucleation and growth stages can be achieved upon steady heating of the reaction mixture if the initial accumulation of monomers is sufficiently slow [15]. High-boiling solvents are typically used to provide a wide reaction temperature window of 25–350 °C.

Studies have demonstrated the great importance of the optimal precursor chemistry. High reactivity of precursors is the basis of the hot-injection technique. In the framework of the classical nucleation theory the nucleation rate *dN/dt* is expressed as [16]:

$$\frac{dN}{dt} = A \exp\left(-\frac{\Delta G^N}{RT}\right),$$

where $\Delta G^N = 16\pi\gamma^3 V_m^2/3(RT \ln S)^2$ is the activation free energy, γ is the specific surface energy, V_m is the molar volume, and S is the supersaturation. The last is defined as the ratio between the monomer concentration and the solubility of the bulk material: $S = [\text{Monomer}]/C^o_{bulk}$. Hence the decomposition of precursors must generate a large concentration of monomers in a short period of time (typically during the first 0.1–10 s) at a given reaction temperature. Excellent examples of highly reactive precursors are metal amides which show excellent results in the synthesis of metallic Co [17], Fe [18], FeCo [19] NCs and metal compound NCs such as SnTe [20], SnS [21], SnSe [22], PbSnTe [23], $Fe_{1-y}O$ [24], and γ-Fe_2O_3 [25] NCs. Much safer, cheaper, and less air-sensitive are metal carboxylates, which are routinely used in the preparation of Pb chalcogenide [26, 27], Cd chalcogenide [28, 29], and many other NCs. Schemes (1)–(8) below illustrate various chemical reactions underlying the synthesis of inorganic NCs. Trimethysilyl-, alkyl-, and trialkylphosphine-based derivatives are often used as non-metal precursors. At the same time, the procedures developed more recently involve simple, inexpensive, and safe inorganic precursors such as metal chlorides and elemental substances (schemes (4) and (6)), providing NCs of comparable quality. Typical stabiliziers (surfactants or capping ligands) include long-chain carboxylic and phosphonic acids (e.g., oleic acid, OA, myristic acid, MA, and n-octadecylphosphonic acid, ODPA), alkylthiols (e.g., dodecanethiol), alkyl phosphines and alkylphosphine oxides (typically trioctylphosphine, TOP, and trioctylphosphine oxide, TOPO), and alkylamines such as hexadecylmine (HDA). If the stabilizer can act as a solvent, such as HDA or TOPO, it is called a coordinating solvent. Alternatively, a chemically inert, non-coordinating solvent is used (e.g., octadecene, ODE).

$$Bi[N(SiMe_3)_2]_3 \xrightarrow{140\,^\circ C,\ HDA,\ LiBH(Et)_2} Bi\ NCs,\ [30] \tag{1}$$

$$Sn[N(SiMe_3)_2]_2 + (C_8H_{17})_2Te \xrightarrow{140\,^\circ C,\ TOP-HDA} SnTe\ NCs,\ [20] \tag{2}$$

$$Pb(CH_3COO)_2 + [Me_3Si]_2S \xrightarrow{180\,^\circ C,\ oleic\ acid} PbS\ NCs,\ [27] \tag{3}$$

$$PbCl_2 + S \xrightarrow{150\,^\circ C,\ OLA} PbS\ NCs,\ [27, 31] \tag{4}$$

$$Cd(CH_3)_2 + (C_8H_{17})_3PSe \xrightarrow{300\,^\circ C,\ HDA-TOPO-TOP} CdSe\ NCs,\ [32] \tag{5}$$

$$Cd(C_{13}H_{27}COO)_2 + Se \xrightarrow{260\,^\circ C,\ TOP} CdSe\ NCs,\ [29] \tag{6}$$

$$InCl_3 + [Me_3Si]_3P \xrightarrow{260\,^\circ C,\ TOP} InP\ NCs,\ [33] \tag{7}$$

$$In(CH_3COO)_3 + PH_3 \xrightarrow{260\,^\circ C,\ ODE-MA} InP\ NCs,\ [34] \tag{8}$$

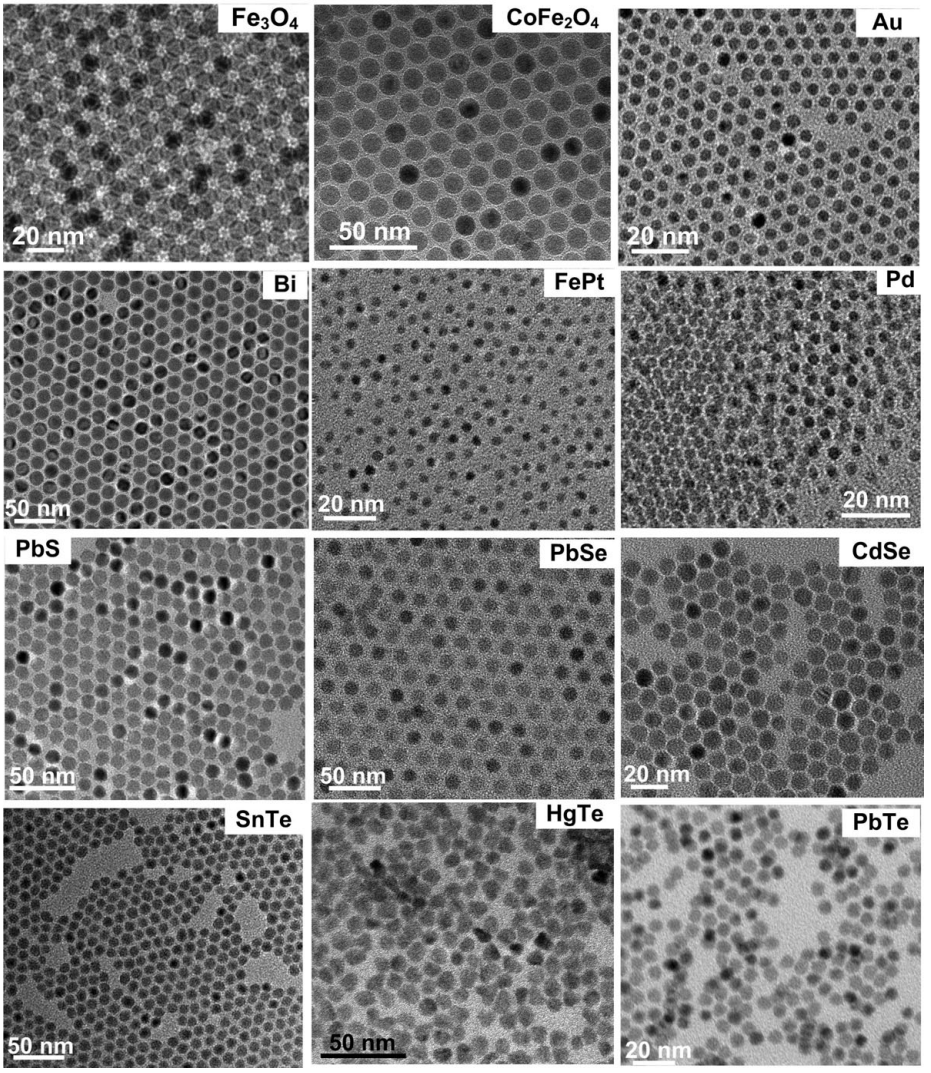


Figure 1.4 Typical examples of monodisperse, colloidally synthesized inorganic NCs.

The synthesis of monodisperse NCs has been developed for II–VI (CdSe, CdTe, CdS) [6, 28, 32], III–V (InP, InAs) [33, 35] and IV–VI (PbS, PbSe, PbTe) [26, 27, 31, 36] NCs. A comprehensive overview of various kinds of colloidal quantum dots, synthesized primarily as sub-20 nm spherical NCs, can be found in selected review articles [9, 12, 29, 37, 38]. Typical transmission electron microscopy (TEM) images of monodisperse, single-phase NCs are illustrated in Figure 1.4.

The success of the colloidal synthesis is mainly derived from (i) the virtually unlimited combinations of solvents–precursors–surfactants and (ii) the low temperature of the reactions and crystal growth, typically ranging from the room temperature to 350 °C. The low-temperature chemistry allows access to many far-from-equilibrium

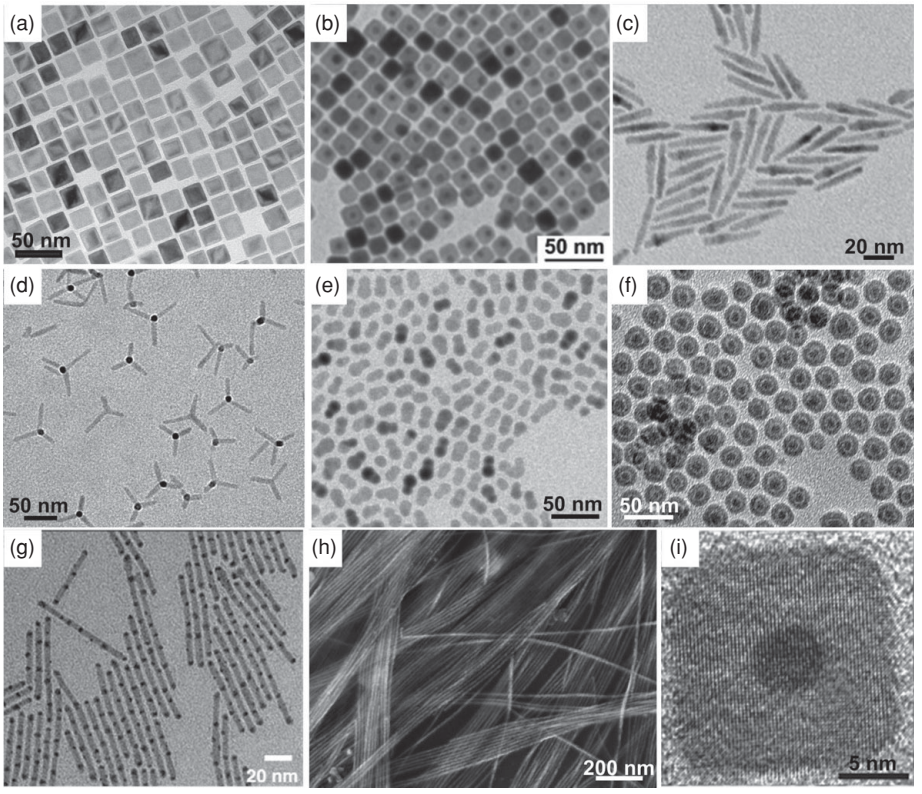


Figure 1.5 TEM images of: (a) 25 nm $Fe_xO/ZnFe_2O_4$ NCs; used with permission from [46]; (b) cubic Au/PbS NCs; used with permission from [47]; (c) CdSe/CdS nanorods; used with permission from [48]; (d) CdSe/CdS nanotetrapods; (e)$CoPt_3$/Au dumbbells; (f) gold/iron oxide (core/hollow-shell) NCs; (g) CdS/Ag_2S nanorods; used with permission from [49]. (h) SEM image of PbSe nanowires. (i) A high-resolution TEM image of FePt/PbS cubical core-shell NCs; used with permission from [50].

and metastable compositions and morphologies. Furthermore, the sought-after characteristics achievable with this method include precisely controlled size, size distribution, shape, and composition. Chemical methods opened access to an entirely new and previously inaccessible family of nanomaterials characterized by their complex shapes [39–42], compositional gradients, multicomponent architectures, and core–shell morphologies [37, 41, 43, 44]. Examples of multicomponent and shape-controlled NCs are shown in Figure 1.5. Importantly, colloidal methods are becoming increasingly inexpensive and robust. The synthetic equipment used is identical to the typical infrastructure for molecular chemistry, while inexpensive and simple precursors are converted into colloidal NCs with high atomic economy in just one or two steps. Furthermore, preparation and handling of nanoparticles in liquid phases is of paramount importance for occupational and environmental safety. Thermodynamically stable, clean and easy to handle colloidal solutions are ideal for low-temperature solution-based processes such as spin- and spray-coating, inkjet and screen printing [45].

The shape of the NC is determined by the interplay between the underlying crystal structure and the growth conditions. Thus, many different anisotropic shapes are found even in materials with highly symmetric crystal structures such as cubic rock-salt (e.g., IV–VI compounds), zinc-blende (most of the II–VI and III–V compounds) or face-centered cubic (fcc, many metals) lattices. In practice, efficient shape control is usually achieved through the selective adhesion of capping molecules to tune the crystal growth kinetics of different facets, leading to various faceted and anisotropic NCs (cubes, rods, wires, etc.) [39]. As an example, synthesis in a mixture of TOPO and alkylphosphonic acids (with varying length of alkyl chain) allows selective growth of the rod-, arrow-, rice-, teardrop-, and tetrapod-shaped CdSe NCs [42, 51]. There are multiple other phenomena that can be used to deliberately control the NC shape. The formation of single- and five-fold twin planes in fcc lattice of noble metal particles (Au, Ag) gives rise to nanorods and nanowires [52]. The observation of rod- and tetrapod-shaped Cd chalcogenide NCs is attributed to the polymorphism of the initial seeds – wurzite or zinc-blende [51]. Long and uniform colloidal nanowires can be synthesized by the oriented attachment and fusion of individual NCs [53] or via solution–liquid–solid [54] growth catalyzed by droplets of molten metallic nanoparticles (Au, Bi). Since the NC dimensions are comparable to the typical width of the reaction zone in solid-state reactions a number of unique growth modes have been found. The formation of hollow NCs was explained by the nanoscale Kirkendall effect – faster outward diffusion of atoms during the interfacial chemical reaction leading to the accumulation of vacancies [55]. In a confined space such as an NC, aggregation of vacancies forms a single hole, as observed during oxidation or sulfidation of Fe and Co NCs [56]. The cation exchange reactions were found to occur nearly instantly with the full preservation of the NC shape and size, allowing conversion of Cd-chalcogenide NCs to Pb- or Ag-chalcogenide NCs and vice-versa [57]. Similar hollow structures form with galvanic displacement reactions of Ag nanocubes with Au^{3+} ions [58, 59]. In this case, the void is formed because each Au^{3+} ion requires the oxidative dissolution of three silver atoms from the NC core.

The steep learning curve in the synthetic art and the rapid progress in atomic-level characterization techniques (e.g., aberration-corrected electron microscopy) lead one to expect further improvements of NC building blocks, and extension to previously inaccessible, yet highly technologically important, colloidal nanomaterials such as GaAs, many metallic alloys, and complex metal oxides.

1.2 Long-range ordered NC solids

1.2.1 Single-component NC superlattices

The great uniformity of sizes and shapes obtained has led to one of the most fascinating directions in NC research – the assembly of NCs into long-range ordered structures (superlattices, supercrystals). NC superlattices can spontaneously form upon the evaporation of the solvent. Just like atoms, monodisperse spherical particles pack into

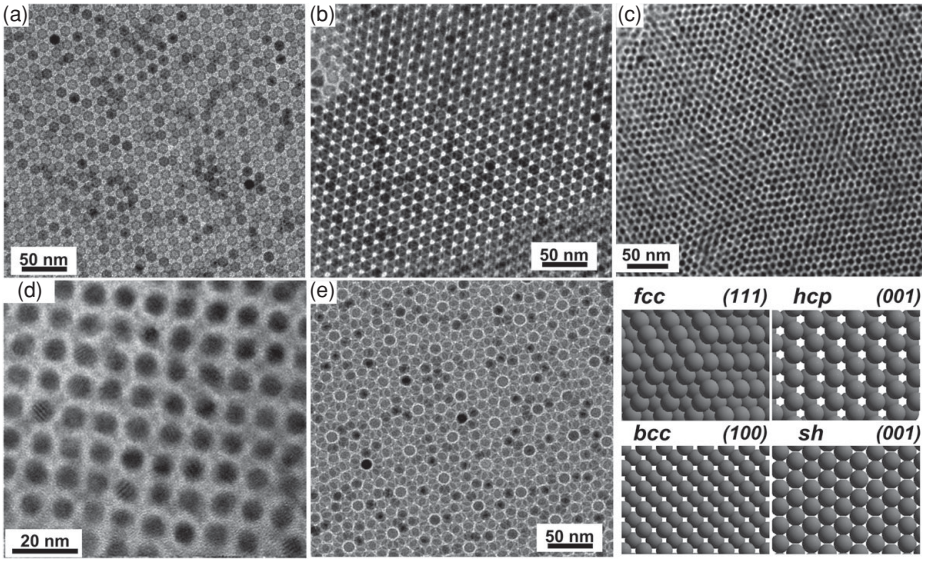


Figure 1.6 TEM images of (a) face-centered cubic and (b) hexagonal close-packed lattices formed by 11 nm $Fe_xO/CoFe_2O_4$ NCs. (c) The simple hexagonal lattice self-assembled from 7.2 nm PbSe NCs. Used with permission from [70]. (d) Body-centered cubic lattice self-assembled from 9 nm PbSe NCs. Used with permission from [71]. (e) Non-close-packed structures self-assembled from solution of 11 nm $Fe_xO/CoFe_2O_4$ NCs. Used with permission from [102].

dense crystalline structures, leading to a new class of materials – metamaterials or "artificial solids".

The packing of objects is one of the most ubiquitous phenomena and challenging problems in the materials world. Packing density in ordered structures is a central principle in the field of intermetallic compounds [60], liquid crystals [61], gem opals [62, 63], and also NCs [64]. NCs can arrange into two- and three-dimensional superlattices (Figures 1.6, 1.7). Very often they behave as hard (non-interacting) spheres, similarly to micron-sized silica or latex spheres [65, 66]. The hard-sphere approximation predicts the formation of ordered assemblies with the highest entropy. For example, monodisperse NCs typically pack into hexagonal close-packed (hcp) and fcc superlattices, which are known as the structures with the highest packing density of 0.74 for single-sized spherical particles. Entropy can favor the ordered state because of the increased local free space available for each sphere in the fcc lattice compared with the disordered state [67]. Theoretical calculations suggest that the fcc structure is slightly more stable than the hcp structure [68, 69], although the free energy difference is just $\sim 10^{-3} k_B T$ per particle. These structures differ only in how the hexagonal two-dimensional sheets of NCs stack on top of each other (Figure 1.6). Furthermore, there are many non-close-packed structures observed in NC superlattices (Figures 1.6(c)–(e)), which can only be explained as a result of strong interparticle interactions.

The self-assembly of NCs can occur both on solid substrates and at liquid surfaces and interfaces. The approaches to growing NC superlattices can be divided into two

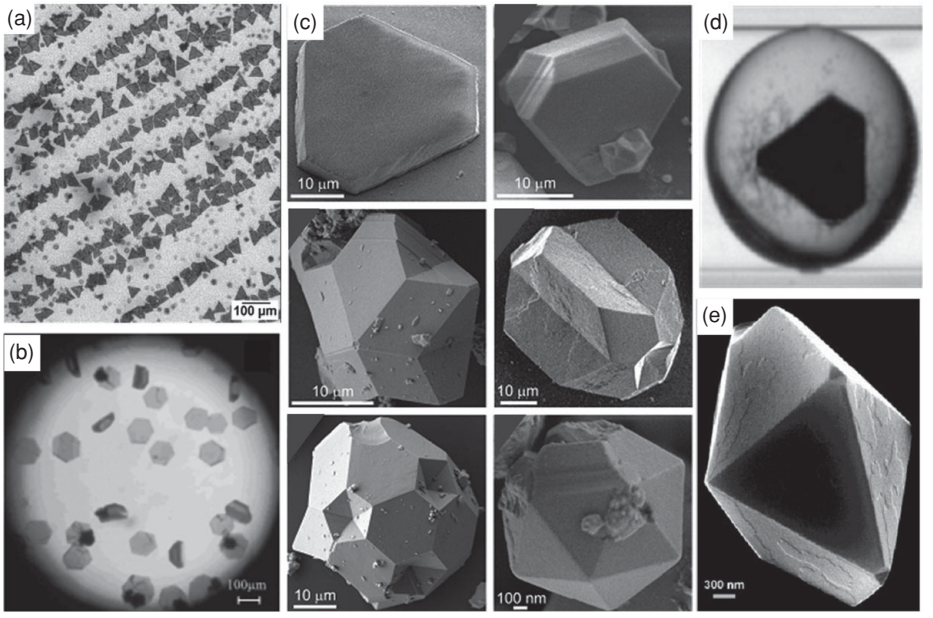


Figure 1.7 (a) Optical micrograph of three-dimensional colloidal crystals of 5.7 nm CdSe NCs. Used with permission from [9]. (b) Optical micrographs of colloidal crystals of CdSe NCs. Used with permission from [72]. (c) Scanning electron microscope (SEM) images showing the characteristic morphologies for superlattices self-assembled from PbS NCs of different sizes. Used with permission from [73]. (d) Optical image of the plug containing faceted superlattice of 11 nm $CoFe_2O_4$ NCs grown in nanoliter microfluidic plugs. Used with permission from [74]. (e) SEM image of faceted superlattice assembled from $CoPt_3$ NCs by the technique of controlled oversaturation. Used with permission from [75]. Color version of this figure is available online at www.cambridge.org/9780521198264.

categories. In "evaporation-driven" methods, the carrier solvent is slowly evaporated from a colloidal solution of NCs. When the NC volume fraction reaches a certain threshold, the system undergoes a transition from a disordered state to an ordered one, followed by the complete evaporation of the solvent. In contrast, "destabilization-driven" approaches use slow destabilization of a colloidal solution, typically achieved by layering the NC solution with a precipitant that slowly diffuses into the NC solution. It allows the growth of large three-dimensional faceted crystals (supercrystals, colloidal crystals) of long-range-ordered NCs. This approach is similar to the technique of free interface diffusion employed in protein crystallization [76] and has been successfully used for growing faceted three-dimensional superlattices of CdSe [9, 72], PbS [73, 77], FePt [78], $CoPt_3$ [75], Bi [30], and many other NCs.

1.2.2 Multicomponent NC superlattices

Binary NC superlattices (BNSLs)

The formation of binary crystals through self-assembly of larger and smaller particles (such as silica and latex spheres) has led to much interest in materials science since

the early 1980s [62, 63, 79, 80]. In 1990, this research was extended to nanomaterials: BNSLs were first observed for Au and Ag NCs of two different sizes [81, 82]. In 2002, small regions with AB_5 arrangement were found by Shevchenko *et al.* using mixtures of smaller and larger $CoPt_3$NCs [83]. Redl *et al.* extended this approach to NCs of two different compositions – binary NC superlattices isostructural with AB_2, AB_5 or AB_{13} compounds were formed from mixtures of semiconducting PbSe NCs and magnetic γ-Fe_2O_3NCs [84]. Shevchenko and coworkers have demonstrated the formation of BNSLs with AB, AB_2, AB_3, AB_4, AB_5, AB_6, and AB_{13} compositions, which are nanosize analogues of known ionic, atomic, and intermetallic phases (NaCl, CuAu, AlB_2, $MgZn_2$, $MgNi_2$, Cu_3Au, Fe_4C, $CaCu_5$, CaB_6, and $NaZn_{13}$) [85, 86]. Typical TEM images of such superlattices grown as thin films on carbon substrates are shown in Figure 1.8.

The details of the crystallography [87–89], thermodynamics [90], and kinetics [91] of NC assembly have attracted broad interest in the scientific community. Many key features of conventional atomic and molecular crystals, such as faceting, twinning, polymorphism, etc. have been observed in NC superlattices [73, 92–94]. Major efforts are focused on understanding the self-organization of NCs [89, 95, 96] and developing robust methods for large-area self-assembly. Centimeter-scale, uniform membranes of BNSLs that can readily be transferred to arbitrary substrates have been prepared by the liquid–air interfacial assembly of NCs [97].

Studies of binary NC superlattices have shown that entropy often dominates the assembly of sterically stabilized NCs [64, 95]. The gain in free volume entropy upon ordering of hard spheres is greater than the decrease in configurational entropy, thus providing a net positive change in the system's entropy. This purely entropic effect favors the formation of highly dense NC superlattices with AlB_2, $NaZn_{13}$, and NaCl structure, whose packing densities can be higher than single-component lattices (fcc or hcp). The packing density (ρ) in the BNSL is a function of the effective size ratio (γ_{eff}) between smaller and larger NCs, as illustrated by so-called space-filling curves (Figure 1.8). This implies that the size ratio is an important consideration for obtaining BNSL with a certain structure. Densely packed AlB_2- and $NaZn_{13}$-type lattices are found in natural as well as artificial opals built of (sub)micrometer spheres [79]. However, other BNSLs form at packing densities much lower than single-component fcc or hcp structures, yet they are stable against phase separation into individual lattices. The stability of these BNSLs can be explained by the contribution from the entropy of mixing and additional configurational entropy. In addition, contributions from particle–particle and particle–substrate interactions such as Coulombic, van der Waals, charge–dipole, dipole–dipole, entropic, capillary, convective, shear, and other forces have been widely discussed [98]. Finally, van der Waals ligand–ligand interactions between long hydrocarbon ligands are also important [70, 99]. At the nanoscale, the magnitudes of all these interactions are often comparable to each other, providing flexibility to the interparticle potentials [100]. Assuming near-equilibrium conditions for NC self-assembly, the change in the Gibbs free energy can be generally expressed as $dG = dH - TdS$ [101]. All specific interparticle interactions can be grouped into the enthalpy term dH, whereas packing principles contribute to the entropic term TdS. Accordingly, temperature can determine

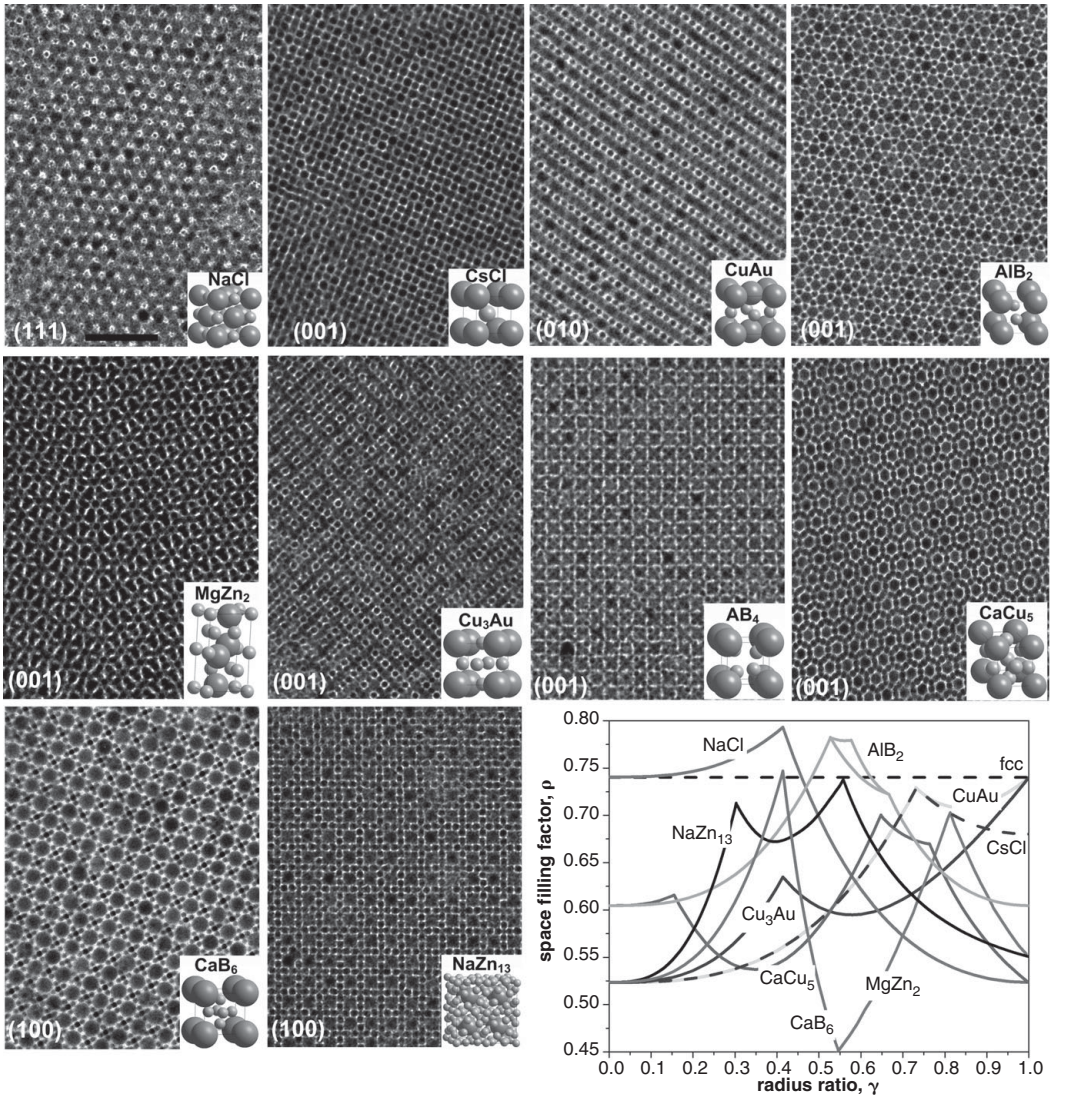


Figure 1.8 Diversity of multicomponent superlattices prepared by the slow evaporation method observed with TEM and space-filling curves of various binary structures that have been observed in BNSLs. Color version of this figure is available online at www.cambridge.org/9780521198264.

the relative contribution of the entropic factor. Assembly experiments in a given binary mixture at different temperatures (from −60 °C to 120 °C) indeed showed that structures with the highest density form at higher temperatures [95].

Ternary and quasi-ternary NC superlattices (TNSLs and quasi-TNSLs)

Shevchenko *et al.* showed a straightforward approach for obtaining periodic structures of three different materials using multicomponent NCs [102]. Such quasi-TNSLs are, in fact, BNSLs of NaCl, NiAs, AlB_2, and $NaZn_{13}$ types (Figures 1.9(a), (b)), obtained by

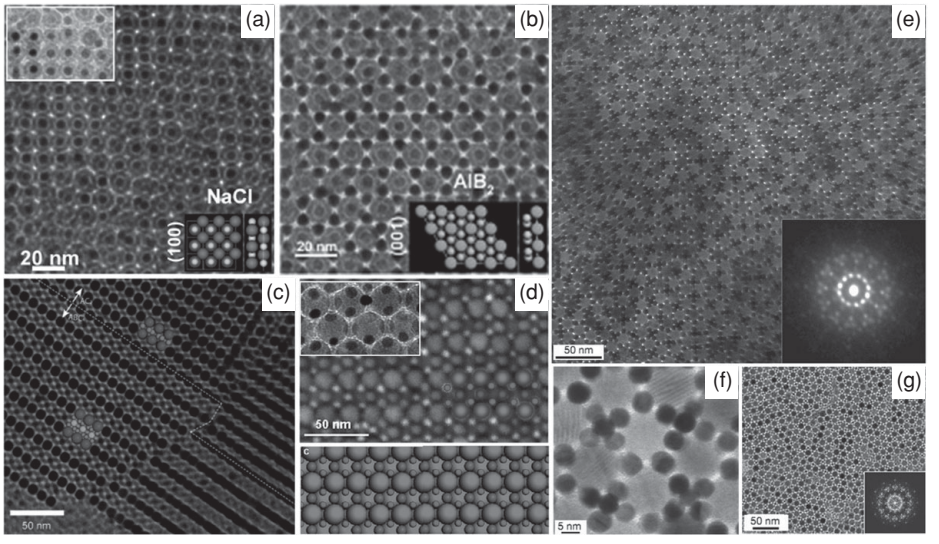


Figure 1.9 TNSLs, quasi-TNSLs, and quasicrystalline BNSLs. TEM micrographs of two quasi-TNSLs formed by (a) 11.7 nm iron/(iron oxide) core/(hollow shell) NCs and (b) 4.5 nm Au NCs and isostructural with NaCl and AlB_2 lattice. Used with permission from [102]. (c) TEM projection of the ternary ABC_4-type TNSL assembled from 12.1 nm PbSe, 7.9 nm PbSe, and 5.8 nm CdSe NCs. Used with permission from [104]. (d) High-resolution SEM image of the ABC_2-type TNSL self-assembled from 16.5 nm Fe_3O_4, 7.0 nm Fe_3O_4, and 5.0 nm FePt NCs. The inset in (d) shows the high-resolution TEM image of superlattice. Used with permission from [103]. (e) TEM image of a quasicrystalline superlattice self-assembled from 13.4 nm Fe_2O_3 and 5 nm Au NCs. The inset in (e) shows the selected-area electron diffraction pattern with non-crystallographic 12-fold rotational symmetry. (f) Magnified view of a dodecagonal nanoparticle quasicrystal. (g) Dodecagonal quasicrystalline superlattice self-assembled from 9 nm PbS and 3 nm Pd NCs with a fast Fourier transform pattern. Used with permission from [105]. Color version of this figure is available online at www.cambridge.org/9780521198264.

co-crystallization of iron/(iron oxide) core/(hollow shell) NCs and Au NCs. Compared with the growth of BNSLs (and quasi-TNSLs), the formation of true TNSLs is much less understood and requires more rigorous control of the NC sizes; there have been only two TNSL structures reported in literature [103, 104]. The first TNSL isostructural with $AlMgB_4$ was observed upon evaporation of the solvent from a solution containing 12.1 nm PbSe, 7.9 nm PbSe, and 5.8 nm CdSe NCs (Figure 1.9(c) [104]. Co-assembly of 16.5 nm Fe_3O_4, 7.0 nm Fe_3O_4, and 5.0 nm FePt NCs at the liquid–air interface yielded an ABC_2-type TNSLs with micron-large domains (Figure 1.9(d)) [103].

Quasicrystalline BNSLs

It has been shown that colloidal inorganic NCs can be packed into aperiodic superlattices, also known as quasicrystals [105]. The formation of dodecagonal quasicrystalline (DDQC) and Archimedean tilings was observed in three binary nanoparticle crystal systems: 13.4 nm Fe_2O_3–5 nm Au NCs, 12.6 nm Fe_3O_4–4.7 nm Au NCs, and 9 nm PbS–3 nm Pd NCs (Figures 1.9(e), (f), and (g)). Such compositional flexibility indicates that the formation of quasicrystalline BNSLs does not require a unique combination

of interparticle interactions, but is a general sphere-packing phenomenon governed by the entropy and simple interparticle potentials [105]. However, the striking coincidence of size ratios in all three systems (~0.43) suggests that particle size has an important role. Furthermore, the DDQC phase and Archimedean tilings were observed at a crossing point of the space-filling curves for the AlB_2 and CaB_6 phases, at a packing density of 0.70. At the crossing point, the translational entropies of the AlB_2, CaB_6, and DDQC phases and Archimedean tilings are very similar [105]. The quasi-periodicity is a result of maximizing the entropy of arrangement of square and triangular "tiles" – many degenerate ways of packing contribute to the configurational entropy and cause the quasicrystalline state to be more stable than crystalline BNSL states [105].

Multicomponent superlattices open new opportunities in materials design. The first demonstrations of novel properties of BNSLs came from assemblies of magnetic NCs. Zeng *et al.* prepared a novel exchange-coupled spring magnet from assembly of FePt and Fe_3O_4NCs [106]. Upon annealing, the BNSL was sintered to produce a fine-grained nanocomposite of magnetically hard FePt and soft Fe_3Pt domains. Cheon *et al.* demonstrated the fabrication of binary magnetic superlattices of Fe_2O_3 and Co NCs, which showed an interesting annealing-induced transformation into a $Fe_3O_4/CoFe_2O_4$ nanoalloy system with magnetically soft–hard inhomogeneities [107]. Magneto-transport measurements on BNSLs have shown that their magnetoresistance is dependent on the structure (stoichiometry) of the BNSLs [107]. Interparticle dipole–dipole interactions in high-quality magnetic BNSL membranes grown by the liquid–air interfacial assembly approach have been studied by Murray and co-workers [108].

Although aesthetically beautiful, the multicomponent NC superlattices assembled from spherical NCs are presently of very little practical use in electronic and optoelectronic applications. It is anticipated that the integration of two or more kinds of NCs with intrinsically different functionalities into a single crystal could introduce new concepts for engineering semiconductor properties such as p- and n-type doping, carrier concentrations, bandgap tuning, or heat transport. For example, Urban *et al.* demonstrated that binary superlattices of PbTe and Ag_2Te NCs exhibit strong synergistic effects in electronic transport, resembling the behavior of bulk Ag-doped PbTe crystals [109]. A unique combination of stoichiometry and symmetry, along with structural diversity, may provide many possibilities for designing novel materials for electronic, optoelectronic, luminescent, catalytic, and other applications. The major challenge is to engineer efficient electronic communication, heat transport, and magnetic coupling between adjacent NCs. This requires a dedicated effort to control the NC surface chemistry and surface properties, as discussed in Section 1.3.

1.2.3 Shape-directed self-assembly of NCs

Self-organization of NCs with non-spherical shapes is of rapidly increasing interest. Progress in the synthesis of NCs has made it possible to fabricate nanocubes, nanooctahedra, nanorods, and nanoplates of a multitude of inorganic materials. Compared with spherically isotropic NCs with random crystallographic orientations, the non-spherical NCs do not behave as "artificial atoms" and may form crystalline phases not found in atomic crystals, which have long-range translational and orientational (rotational) order.

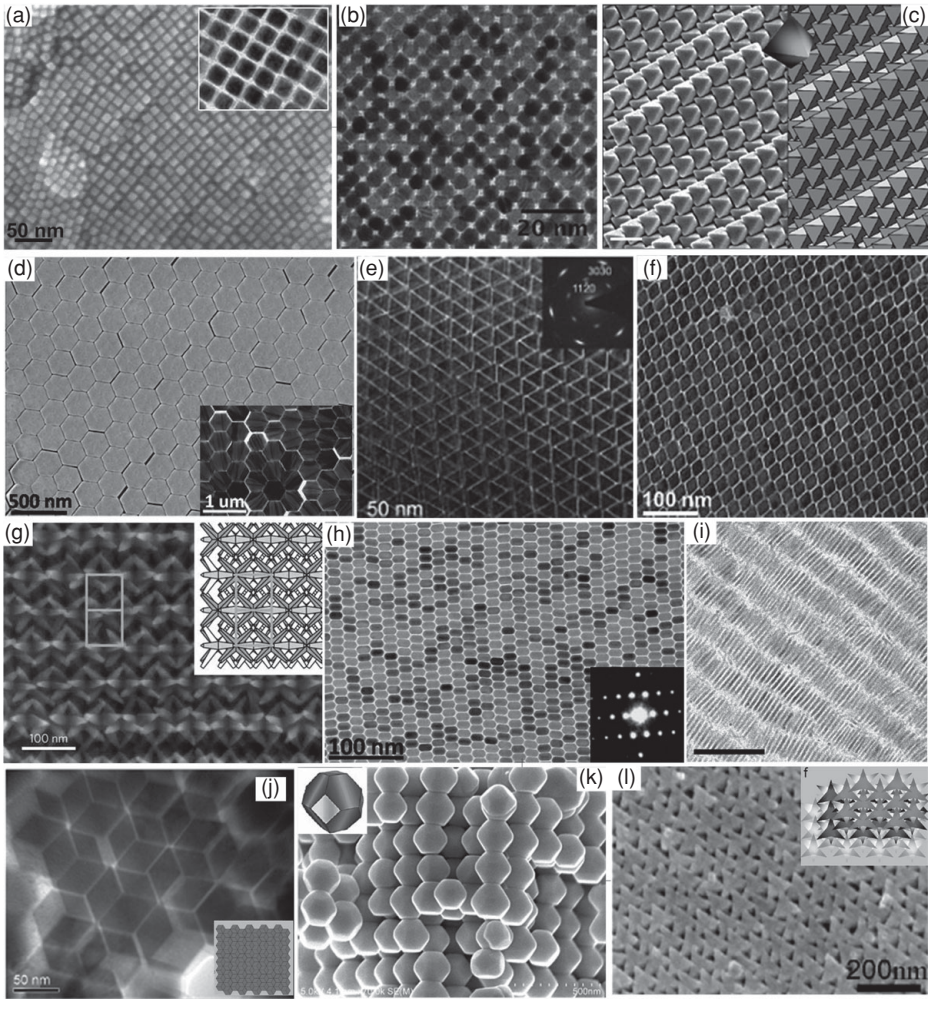


Figure 1.10 (a) SEM and TEM (inset) images of ordered structure from $Fe_xO/CoFe_2O_4$ cubical NCs. (b) TEM image of superlattice from truncated cubic Pt NCs. Used with permission from [130]. (c) SEM micrographs of the colloidal lattices from Ag octahedral NCs and the corresponding diagrams of lattice packing; shading is used to indicate different layers. Used with permission from [115]. (d) SEM and TEM (inset) images of the self-assembled superlattice of $NaYF_4$: Yb/Er hexagonal nanoplates. Used with permission from [118]. (e) TEM images of the edge-to-edge superlattices of LaF_3 trigonal nanoplates. The inset is the selective area electron diffraction (SAED) pattern. Used with permission from [119]. (f) TEM image of rhombic GdF_3 nanoplates assembled into columnar liquid crystalline superlattices. Used with permission from [120]. (g) SEM image of a three-dimensional superlattice from CdSe/CdS octapod-shaped NCs. Used with permission from [131]. (h) TEM image of a monolayer superlattice of $NaYF_4$ nanorods that are oriented parallel to the substrate. the inset is the corresponding SAED pattern. Used with permission from [118]. (i) TEM image of smectic ordered CdS nanorods. (j) TEM image of [111]-oriented assemblies of Cu_2O rhombic dodecahedra. Used with permission from [132]. (k) SEM image of ordered truncated octahedron PbS NCs with schematic illustration of the truncated octahedron. Used with permission from [117]. (l) SEM image of three-dimensional hcp assemblies of PbS six-horn nanostars. Used with permission from [133]. Color version of this figure is available online at www.cambridge.org/9780521198264.

Nanocubes are usually close-packed into square arrays and are commonly attached face-to-face, presumably minimizing their surface energy and maximizing ligand–ligand interactions. For the multilayer (three-dimensional) assemblies, two types of ordering can be observed: a simple cubic superlattice in which two-dimensional rectangular layers are stacked on top of each other and distorted superlattice in which layers are shifted horizontally with respect to each other. The maximum contact of two (100) surfaces corresponds to a simple cubic superlattice, as found in many NC systems such as $Fe_xO/CoFe_2O_4$ (Figure 1.10(a)) [46], PbTe [110], and Fe_xO_y [111]. The shifted version is typically represented by the body-centered cubic (bcc) structure. In this lattice, all nanocubes are aligned with their crystallographic axes [18].

A number of studies have dealt with three-dimensional assembly of high-quality NCs with an octahedral shape. Monodisperse In_2O_3 [112], MnO [113], Fe_3O_4 [114], Ag [115], and Au [116] octahedral NCs can spontaneously pack into long-range ordered structures. For octahedra, the densest packing is known as the Minkowski lattice, which has been found in the sediments of colloidal Ag NCs (Figure 1.10(c), the Minkowski lattice is illustrated in the right hand part of Figure 1.10(c)) [115]. Unlike cubes and truncated octahedra, the densest lattice packing of octahedra contains incomplete face-to-face contacts, where equivalent faces of neighboring octahedra do not lie in a common plane, but the number of neighbors in face-to-face contact is maximized. As a result the free volume is extremely reduced, leading to the very high packing density of $18/19 = 0.947$. In the same system of Ag octahedra, the assembly motifs were driven towards less dense structures by modulating the interparticle interactions with adsorbing polymers [115]. Truncated octahedra such as PbS NCs [117] often tend to rectangluar packing by sharing their square faces (Figure 1.10(k)).

Superstructures of uniformly sized nanoplates of different materials such as $NaYF_4$:Yb/Er (Figure 1.10(d)) [118], LaF_3 (Figure 1.10(e)) [119], GdF_3 (Figure 1.10(f)) [120], Gd_2O_3 [121], CuS (Cu_2S) [122], Eu_2O_3 [123], Co[124] have also been demonstrated. Edge-to-edge assembly can be illustrated by trigonal LaF_3 (Figure 1.10(e)) [119] and hexagonal $NaYF_4$:Yb/Er nanoplates (Figure 1.10(d)) [118], which assemble into hexagonally ordered monolayers, consistent with the six-fold symmetry of the plates. Rhombic GdF_3 (Figure 1.10(f)) nanopates form columnar assemblies with both edge-to-edge and face-to-face periodic arrangements (out-of-plane oriented, densely packed columns) [120].

Nanorods are well-known anisotropic building blocks which form oriented liquid crystalline superlattices (nematic and smectic, Figure 1.10(i)) [125], previously fabricated by drying mediated self-assembly [126], electric-field-assisted assembly [127], depletion attraction [128], and by slow destabilization with non-solvent [125]. Nanorod superlattices are common for CdS and CdSe/CdS [125, 126, 128], Cu_2S [129], and many metallic and metal oxide NCs. In the case of small aspect ratio nanorods such as $NaYF_4$, they preferentially align with their *c*-axis parallel to the substrate, exhibiting both positional and orientation order on the scale of tens of micrometers [118].

Strongly branched NCs may provide new packing motifs, due to the strong van der Waals interactions and the further increased number of possible arrangement of nearest neighbors. Manna and coworkers showed that octapod-shaped CdSe/CdS NCs can

spontaneously interlock into chains, which self-assemble into three-dimensional crystals with a trigonal unit cell. The observed hierarchical self-assembly can be explained by the octapod's shape and the solvent-tunable van der Waals interactions. In contrast, six-horn nanostars of PbS NCs pack into conventional hcp lattice (Figure 1.10(l)).

1.3 Surface chemistry – a gateway to applications of NCs

In a non-vacuum environment, metal ions do not exist in a completely isolable form but in a solvated or ligand-coordinated state. Similarly, inorganic NCs require a shell of capping and stabilizing molecules when placed in an organic solvent host. Thus, the capping molecules are a vital and integral part of NCs. The importance of surface ligands can hardly be overemphasized. These molecules are not only critically important for the NC nucleation and growth, but they also remain adhered to the surface providing chemical and colloidal stability. Capping ligands can influence the predominant type of interparticle interaction (steric or electrostatic repulsion, van der Waals attraction), solubility in certain solvents, and mixibility with other materials. Because of inherently high surface-to-volume ratios, the surface chemistry has a strong influence on the physical properties of NCs, including optics [134, 135], charge transport [136, 137], catalysis [138], and magnetism [139].

Proper surface engineering is considered a major challenge for making efficient NC-based photodetectors [140], solar cells [141], transistors [36], and light-emitting devices [142]. This is mainly due to the critical effect of capping molecules on the electronic coupling and transport in the NC solids. The most common ligands used in the synthesis of NCs are based on long-chain organic hydrocarbon molecules with anchoring end groups. These molecules offer the highest chemical flexibility, but act as bulky insulating barriers between NCs, hindering charge transport [143]. Typical electrical conductivities do not exceed $\sigma \approx 10^{-11}-10^{-14}$ S cm^{-1}. At the same time, the complete removal of organic surface ligands has proven to be very difficult. It often generates multiple surface dangling bonds which act as carrier traps in semiconductor NCs [134]. Annealing of NC samples can only partially remove the organic ligands and often leaves undesirable carbonaceous products of pyrolysis [144] or leads to sintering of NCs [145]. Therefore, nearly all adjustments of the surface chemistry are accomplished using mild chemical removal of ligands and ligand-exchange reactions, i.e., replacement of initial capping molecules with more suitable, typically smaller, ligands. Figure 1.11 captures major types of surface chemistries, including not only standard organic ligands, but also increasingly popular inorganic ions and "bare" NC surfaces.

1.3.1 Organic capping ligands

Initial capping molecules (surfactants, stabilizers)

Typically used molecules contain a single anchoring group (thio-, amino-, carboxylic-, phopshonato-, sulfonato-, etc.) and an alkyl (typically C_{12}–C_{18}) or aromatic tail group

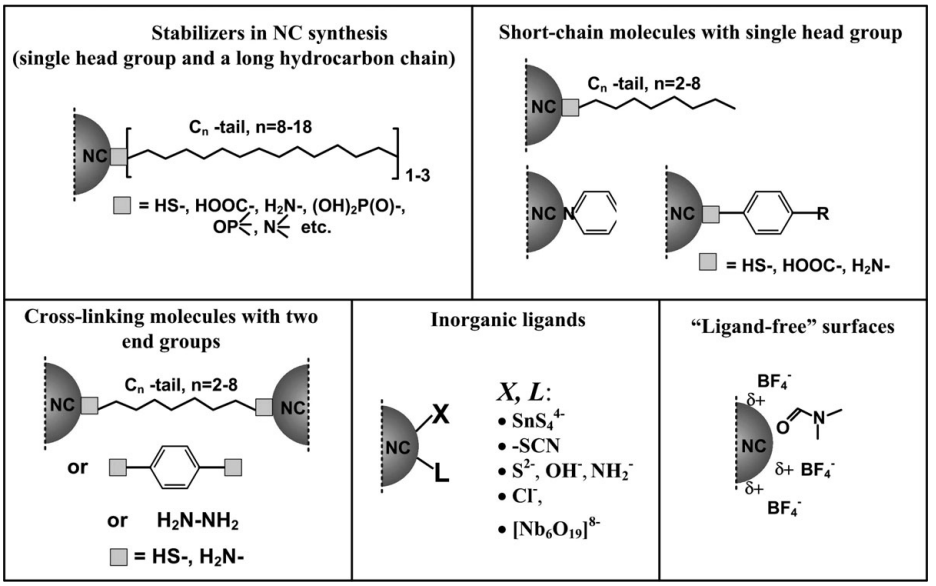


Figure 1.11 An overview of commonly used surface chemistries, including organic and inorganic ligands, and "bare" NC surfaces. Color version of this figure is available online at www.cambridge.org/9780521198264.

which provides steric stabilization of a colloidal solution in non-polar solvents [146]. Alternatively, the surface of II–VI semiconductor NCs (CdS, CdTe, CdSe, HgTe) can be functionalized with small molecules containing both a thiol group (attached to the NC surface) and charged group (e.g., R-COO^- or R-NH_3^+), providing the electrostatic mechanism for colloidal stabilization [8]. Unfortunately, the direct synthesis of such charge-stabilized NC quantum dots has so far mainly been limited to highly-luminescent, thiol-capped II–VI colloidal quantum dots such as CdTe NCs capped with thioglycolic acid [147] and thioglycerol-stabilized HgTe NCs [148].

The current understanding of the binding modes at the NC–ligand interface is rather incomplete, owing to the lack of the analytical tools to determine directly the surface atomic structure of NCs. Thus, in most cases the binding modes typically found in metal–ligand complexes and salts are assumed. For instance, TOPO binds datively, as neutral, L-type ligand (via the oxygen atom), whereas oleate and phosphonate anionic species (X-type ligands) bind the cationic surface sites such as Cd^{2+} [149].

Ligand-exchange with smaller capping molecules and with cross-linking molecules

There are generally two strategies for the replacement of initial, long-chain capping molecules – solution-exchange with retention of colloidal stability and solid-state exchange. The solid-state exchange entails a two-step procedure – first assembling the NCs into a densely packed thin film, followed by soaking in a solution containing the new molecules. A typical limitation of the solution-phase exchange of larger ligands

by smaller ones is the decrease of colloidal stability which often leads to nanoparticle aggregation. Hence solid-state exchange is typically combined with convenient fabrication of high-quality NC films using colloidal solutions. Typical examples include soaking of CdSe or PbSe NC films in solutions of methylamine, ethylamine, butylamine, ethanethiol, sodium hydroxide, or pyridine [150–152]. The resulting solids exhibit drastically improved electrical characteristics, including high photoconductivity in the range of $\sim 10^{12}$–10^{13} Jones in photodetectors made of PbS NCs treated with butylamine [153] and electrical conductivities up to 10^{-1} S cm^{-1} in arrays of thiol-capped metallic NCs [143]. The electronic conductivity can be improved not only by decreasing the inter-NC spacing, but also by using electrically conjugated polymers and oligomers, such as end-functional polythiophenes [154] or poly (para-n-phenylene vinylene) [155], as capping ligands.

The incoming ligand may have lower chemical affinity than the original capping molecules, and may also have the same (e.g., thiol-for-thiol exchange) [156] or a different anchoring functional group. Partial or complete ligand exchange usually requires that the NC surface is exposed to the large excess of competing ligand [6, 9, 134]. At ambient temperature or with moderate heating ($\leq$100 °C), the surface reactions can take from several seconds for strongly binding ligands such as thiols [148] to several days for weakly coordinating species such as pyridine [6]. The solution-phase exchange is often facilitated by the phase separation of the NCs and by-products by using, for example, two-phase mixtures of polar and non-polar solvents [157]. A well-known example of such phase-transfer reactions is replacement of hydrophilic thiols by hydrophobic alkylthiols [157] and vice versa [158].

Cross-linking surface ligands

This strategy has enabled considerable progress in preparing electrically conductive NC solids using short-chain molecules with the same head groups or cross-linking molecules such as hydrazine [36] and phenylenediamine [136]. The highest electron mobilities, up to 2 cm^2 V^{-1} s^{-1}, have been reported for N_2H_4-treated PbSe NC solids [36]. Zabet-Khosousi *et al.* showed metal-to-insulator transition in arrays of sub-10 nm Au NCs linked with dithiol $HS(CH_2)_nSH$ molecules at $n = 5$ [159]. Sequential linking of NC monolayers was developed as a powerful methodology for making densely-packed, multilayer NC films. In such layer-by-layer processes, the substrate is alternately dipped into NC solution to adsorb the NC layer and into the bi-functional linker solution. The dips are interspersed with short immersions in clean solvent to wash off the unbound NC and linker residues. Cross-linking with dithiols was first demonstrated using Au NCs and $HS(CH_2)_nSH$ ($n = 6$–12) as a linker [160] and has helped to improve the photoconductive properties of PbS and PbSe NC solids (e.g., ethylenedithiol and benzendithiol) [161–163].

In summary, the use of smaller organic molecules increases the electronic coupling in the solids of colloidal NCs. However, such small molecules are volatile and are prone to be oxidizable, leading to continuous degradation and instabilities of device characteristics.

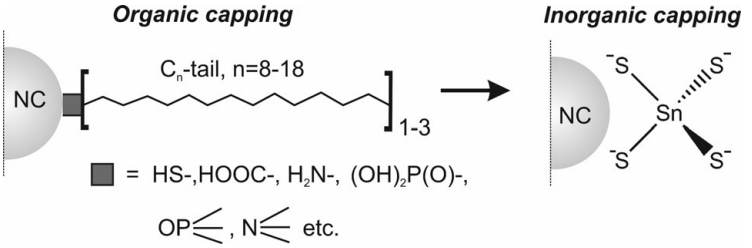


Figure 1.12 Schematic of the ligand exchange process used for the preparation of all-inorganic NCs. Used with permission from [164].

1.3.2 Complete removal of organic ligands and inorganic surface functionalization

Inorganic capping ligands

Semiconductor technology is primarily based on inorganic and crystalline materials with high stability and superior electronic characteristics. New and exciting opportunities for nanomaterial-based photovoltaics, thermoelectrics, and catalytic and electrochemical applications have been opened by novel, all-inorganic design of NC surfaces.

In 2009, the traditional "inorganic core–organic shell" was revised by demonstrating that various metal chalcogenide complexes ("MCCs," e.g., SnS_4^{4-}, $Sn_2S_6^{4-}$, $SnTe_4^{4-}$, $In_2Se_4^{2-}$, $SbSe_4^{3-}$, MoS_4^{4-}, and similar species) can replace organic molecules, and act as NC surface capping ligands (Figure 1.12) [164–168]. Through ligand-exchange reactions MCCs can be attached to nearly all known NCs synthesized with conventional organic ligands, maintaining colloidal stability, size, shape, and composition. Milliron and co-workers proposed an alternative method of anchoring MCCs to NC surface in a solid-state exchange in the films of organically-functionalized NCs [169]. The terminal chalcogenide atoms are highly nucleophilic and exhibit high chemical affinity to the undercoordinated, electron-deficient metallic atoms on the surface of NCs. Fourier tranform infrared (FTIR), nuclear magnetic resonance (NMR), and elemental analysis showed quantitative replacement of the original capping ligands. High colloidal stability and solubility in common polar solvents with a high dielectric constant (water, hydrazine, formamide, dimethylsulfoxide) was found for virtually limitless numbers of MCC–NC pairs. Finally, NCs retain not only their morphology but also basic photophysical properties such as size-tunable optical absorption and efficient luminescence.

The success of MCCs as capping ligands suggested that many other nucleophilic inorganic species can act as capping ligands and stabilizers. Thus, surface functionalization with simple and metal-free ions such as S^{2-}, OH^-, NH^{2-}, TeS_3^{2-} [168], and thiocyanate (CNS^-) [170] have been demonstrated to yield stable, organic-free colloidal NCs. Milliron and co-workers demonstrated on all-oxidic design by using polyniobates and vanadates as capping ligands for Sn-doped In_2O_3 (ITO) nanocrystals leading to Nb_2O_5–ITO, V_2O_5–ITO and VO_2–ITO nanocomposite films [171].

Surface passivation with monovalent, X-type halide (Cl^-, Br^-, I^-) ligands allows further reduction of the shell thickness down to 0.1 nm and can be achieved via either

solution-phase or solid-state exchange. Sargent and co-workers showed that halide passivation of alkylphosphonate-capped PbS/CdS NCs can be conveniently obtained by treating thin NC films with alkylamonium halides [172]. Owen *et al.* [149] showed that alkylphosphonate ligands can also be removed using reagents with reactive silicon–chalcogenide and silicon–chloride bonds. In the latter case, the resulting NCs terminated with chloride ions form stable colloidal solutions in toluene in the presence of tridecylammonium cations.

In summary, comparison of organic and inorganic capping ligands shows that the latter allow superior (opto)electronic characteristics to be achieved: band-like transport and electron mobilities up to 20 cm^2/Vs [173], photon detectivities up to 10^{13} Jones [173], photovoltaic efficiencies of at least 5% [172], and enhanced thermoelectric characteristics [166].

Ligand-free NC surfaces

A bare NC surface is an optimal solution for many applications. As mentioned earlier, such a surface is hard to achieve without undesirable consequences such as NC aggregation, sintering or contamination. $NOBF_4$ has been proposed as efficient remover of capping ligands [174]. The resulting stable dispersions contain positively charged NCs (Figure 1.11). BF_4^- may act as a hard, weakly nucleophilic anion that easily dissociates in polar solvents leaving a cationic NC surface behind. Unfortunately, due to oxidative properties and Lewis acidity of nitrosonium ions, $NOBF_4$ treatments are applicable only to certain metal oxide and fluoride NCs. The acids HBF_4 and HPF_6 are equally efficient ligand removers, confirming that the key step in the removal of the native ligand is its protonation [168]. Such strong acids are, however, prone to etch many inorganic compounds. Therefore, non-oxidizing and non-acidic reagents have been developed based on trialkyloxonium tetrafluoroborates such as Meerwein's salt (Et_3OBF_4) [175]. In this case, the stripping of the ligands occurs due to their alkylation instead of protonation.

References

1 A. J. Nozik, Photoelectrochemistry – applications to solar energy conversion. *Annual Review of Physical Chemistry*, **29** (1978), 189–222.
2 S. Y. Huang, G. Schlichthorl, A. J. Nozik, M. Gratzel, A. J. Frank, Charge recombination in dye-sensitized nanocrystalline TiO_2 solar cells. *Journal of Physical Chemistry B*, **101** (1997), 2576–2582.
3 A. I. Ekimov, A. A. Onushchenko, Quantum size effects in 3-dimensional microscopic semiconductor crystals. *JETP Lett.*, **34** (1981), 345–349.
4 A. L. Efros, Interband absorption of light in a semiconductor sphere. *Soviet Physics Semiconductors*, **16** (1982), 772–775.
5 L. Brus, Electronic wave functions in semiconductor clusters: experiment and theory. *Journal of Physical Chemistry*, **90** (1986), 2555–2560.
6 C. B. Murray, D. J. Norris, M. G. Bawendi, Synthesis and characterization of nearly monodisperse CdE (E = sulfur, selenium, tellurium) semiconductor nanocrystallites. *Journal of the American Chemical Society*, **115** (1993), 8706–8715.

7 J. Park, K. An, Y. Hwang, *et al.*, Ultra-large-scale syntheses of monodisperse nanocrystals. *Nature Materials*, **3** (2004), 891–895.

8 N. Gaponik, D. V. Talapin, A. L. Rogach, *et al.*, Thiol-capping of CdTe nanocrystals: an alternative to organometallic synthetic routes. *Journal of Physical Chemistry B*, **106** (2002), 7177–7185.

9 C. B. Murray, C. R. Kagan, M. G. Bawendi, Synthesis and characterization of monodisperse nanocrystals and close-packed nanocrystal assemblies. *Annual Review of Materials Science*, **30** (2000), 545–610.

10 I. M. Lifshitz, V. V. Slyozov, The kinetics of precipitation from supersaturated solid solutions. *Journal of Physics and Chemistry of Solids*, **19** (1961), 35–50.

11 C. Wagner, Theorie der Alterung von Niederschlagen durch Umlosen (Ostwald Reifung). *Zeitschrift Fur Elektrochemie*, **65** (1961), 581–591.

12 J. Park, J. Joo, C. G. Kwon, Y. Jang, T. Hyeon, Synthesis of monodisperse spherical nanocrystals. *Angewandte Chemie International Edition*, **46** (2007), 4630–4660.

13 V. K. La Mer, R. H. Dinegar, Theory, production, and mechanism of formation of monodisperse hydrosols. *Journal of the American Chemical Society*, **72** (1950), 4847–4854.

14 C. de Mello Donega, P. Liljeroth, D. Vanmaekelbergh, Physicochemical evaluation of the hot-injection method, a synthesis route for monodisperse nanocrystals. *Small*, **1** (2005), 1152–1162.

15 S. G. Kwon, Y. Piao, J. Park, *et al.*, Kinetics of monodisperse iron oxide nanocrystal formation by "heating-up" process. *Journal of the American Chemical Society*, **129** (2007), 12571–12584.

16 J. W. Mullin. *Crystallization*. Oxford: Oxford University Press, 1997, third edition.

17 O. Margeat, C. Amiens, B. Chaudret, P. Lecante, R. E. Benfield, Chemical control of structural and magnetic properties of cobalt nanoparticles. *Chemistry of Materials*, **17** (2005), 107–111.

18 F. Dumestre, B. Chaudret, C. Amiens, P. Renaud, P. Fejes, Superlattices of iron nanocubes synthesized from Fe[N(SiMe3)2]2. *Science*, **303** (2004), 821–823.

19 C. Desvaux, C. Amiens, P. Fejes, *et al.*, Multimillimetre-large superlattices of air-stable iron–cobalt nanoparticles. *Nature Materials*, **4** (2005), 750–753.

20 M. V. Kovalenko, W. Heiss, E. V. Shevchenko, *et al.*, SnTe nanocrystals: a new example of narrow-gap semiconductor quantum dots. *Journal of the American Chemical Society*, **129** (2007), 11354–11355.

21 S. G. Hickey, C. Waurisch, B. Rellinghaus, A. Eychmuller, Size and shape control of colloidally synthesized IV–VI nanoparticulate tin(II) sulfide. *Journal of the American Chemical Society*, **130** (2008), 14978–14980.

22 W. J. Baumgardner, J. J. Choi, Y. F. Lim, T. Hanrath, SnSe nanocrystals: synthesis, structure, optical properties, and surface chemistry. *Journal of the American Chemical Society*, **132** (2010), 9519–9521.

23 I. U. Arachchige, M. G. Kanatzidis, Anomalous bandgap evolution from band inversion in PbSnTe nanocrystals. *Nano Letters*, **9** (2009), 1583–1587.

24 A. Glaria, M. L. Kahn, P. Lecante, B. Barbara, B. Chaudret, $Fe_{1-y}O$ nanoparticles: organometallic synthesis and magnetic properties. *Chemphyschem*, **9** (2008), 776–780.

25 A. Glaria, M. L. Kahn, A. Falqui, *et al.*, An organometallic approach for very small maghemite nanoparticles: synthesis, characterization, and magnetic properties. *Chemphyschem*, **9** (2008), 2035–2041.

26 J. J. Urban, D. V. Talapin, E. V. Shevchenko, C. B. Murray, Self-assembly of PbTe quantum dots into nanocrystal superlattices and glassy films. *Journal of the American Chemical Society*, **128** (2006), 3248–3255.
27 M. A. Hines, G. D. Scholes, Colloidal PbS nanocrystals with size-tunable near-infrared emission: observation of post-synthesis self-narrowing of the particle size distribution. *Advanced Materials*, **15** (2003), 1844–1849.
28 Z. A. Peng, X. Peng, Nearly monodisperse and shape-controlled CdSe nanocrystals via alternative routes: nucleation and growth. *Journal of the American Chemical Society*, **124** (2002), 3343–3353.
29 P. Reiss, M. Protiere, L. Li, Core/shell semiconductor nanocrystals. *Small*, **5** (2009), 154–168.
30 M. Yarema, M. V. Kovalenko, G. Hesser, D. V. Talapin, W. Heiss, Highly monodisperse bismuth nanoparticles and their three-dimensional superlattices. *Journal of the American Chemical Society*, **132** (2010), 15158–15159.
31 L. Cademartiri, J. Bertolotti, R. Sapienza, *et al.*, Multigram scale, solventless, and diffusion-controlled route to highly monodisperse PbS nanocrystals. *Journal of Physical Chemistry B*, **110** (2006), 671–673.
32 D. V. Talapin, A. L. Rogach, A. Kornowski, M. Haase, H. Weller, Highly luminescent monodisperse CdSe and CdSe/ZnS nanocrystals synthesized in a hexadecylamine-trioctylphosphine oxide-trioctylphospine mixture. *Nano Letters*, **1** (2001), 207–211.
33 O. I. Micic, C. J. Curtis, K. M. Jones, J. R. Sprague, A. J. Nozik, Synthesis and characterization of InP quantum dots. *Journal of Physical Chemistry*, **98** (1994), 4966–4969.
34 L. Li, P. Reiss, One-pot synthesis of highly luminescent InP/ZnS nanocrystals without precursor injection. *Journal of the American Chemical Society*, **130** (2008), 11588–11589.
35 D. Battaglia, X. Peng, Formation of high quality InP and InAs nanocrystals in a noncoordinating solvent. *Nano Lett*, **2** (2002), 1027–1030.
36 D. V. Talapin, C. B. Murray, PbSe nanocrystal solids for n- and p-channel thin film field-effect transistors. *Science*, **310** (2005), 86–89.
37 P. D. Cozzoli, T. Pellegrino, L. Manna, Synthesis, properties and perspectives of hybrid nanocrystal structures. *Chemical Society Reviews*, **35** (2006), 1195–1208.
38 A. M. Smith, S. M. Nie, Semiconductor nanocrystals: structure, properties, and band gap engineering. *Accounts of Chemical Research*, **43** (2010), 190–200.
39 Y. Yin, A. P. Alivisatos, Colloidal nanocrystal synthesis and the organic–inorganic interface. *Nature*, **437** (2005), 664–670.
40 K. S. Cho, D. V. Talapin, W. Gaschler, C. B. Murray, Designing PbSe nanowires and nanorings through oriented attachment of nanoparticles. *Journal of the American Chemical Society*, **127** (2005), 7140–7147.
41 D. V. Talapin, J. H. Nelson, E. V. Shevchenko, *et al.*, Seeded growth of highly luminescent CdSe/CdS nanoheterostructures with rod and tetrapod morphologies. *Nano Letters*, **7** (2007), 2951–2959.
42 D. J. Milliron, S. M. Hughes, Y. Cui, *et al.*, Colloidal nanocrystal heterostructures with linear and branched topology. *Nature*, **430** (2004), 190–195.
43 E. V. Shevchenko, M. I. Bodnarchuk, M. V. Kovalenko, *et al.*, Gold/iron oxide core/hollow-shell nanoparticles. *Advanced Materials*, **20** (2008), 4323–4329.
44 M. A. Hines, P. Guyot-Sionnest, Synthesis and characterization of strongly luminescing ZnS-capped CdSe nanocrystals. *Journal of Physical Chemistry*, **100** (1996), 468–471.
45 D. V. Talapin, J.-S. Lee, M. V. Kovalenko, E. V. Shevchenko, Prospects of colloidal nanocrystals for electronic and optoelectronic applications. *Chemical Reviews*, **110** (2009), 389–458.

46 M. I. Bodnarchuk, M. V. Kovalenko, H. Groiss, *et al.*, Exchange-coupled bimagnetic wustite/metal ferrite core/shell nanocrystals: size, shape, and compositional control. *Small*, **5** (2009), 2247–2252.
47 J.-S. Lee, E. V. Shevchenko, D. V. Talapin, Au−PbS core−shell nanocrystals: plasmonic absorption enhancement and electrical doping via intra-particle charge transfer. *Journal of the American Chemical Society*, **130** (2008), 9673–9675.
48 D. V. Talapin, J. H. Nelson, E. V. Shevchenko, *et al.*, Seeded growth of highly luminescent CdSe/CdS nanoheterostructures with rod and tetrapod morphologies. *Nano Letters*, **7** (2007), 2951–2959.
49 R. D. Robinson, B. Sadtler, D. O. Demchenko, *et al.*, Spontaneous superlattice formation in nanorods through partial cation exchange. *Science*, **317** (2007), 355–358.
50 J.-S. Lee, M. I. Bodnarchuk, E. V. Shevchenko, D. V. Talapin, "Magnet-in-the-semiconductor" FePt−PbS and FePt−PbSe nanostructures: magnetic properties, charge transport, and magnetoresistance. *Journal of the American Chemical Society*, **132** (2010), 6382–6391.
51 L. Manna, D. J. Milliron, A. Meisel, E. C. Scher, A. P. Alivisatos, Controlled growth of tetrapod-branched inorganic nanocrystals. *Nature Materials*, **2** (2003), 382–385.
52 C. Lofton, W. Sigmund, Mechanisms controlling crystal habits of gold and silver colloids. *Advanced Functional Materials*, **15** (2005), 1197–1208.
53 Z. Tang, N. A. Kotov, M. Giersig, Spontaneous organization of single CdTe nanoparticles into luminescent nanowires. *Science*, **297** (2002), 237–240.
54 T. J. Trentler, K. M. Hickman, S. C. Goel, *et al.*, Solution-liquid-solid growth of crystalline III–V Semiconductors: an analogy to apor-liquid-solid growth. *Science*, **270** (1995), 1791–1794.
55 A. D. Smigelskas, E. O. Kirkendall, Zinc diffusion in alpha-brass. *Transactions of the American Institute of Mining and Metallurgical Engineers*, **171** (1947), 130–142.
56 Y. D. Yin, R. M. Rioux, C. K. Erdonmez, *et al.*, Formation of hollow nanocrystals through the nanoscale Kirkendall effect. *Science*, **304** (2004), 711–714.
57 D. H. Son, S. M. Hughes, Y. D. Yin, A. P. Alivisatos, Cation exchange reactions-in ionic nanocrystals. *Science*, **306** (2004), 1009–1012.
58 Y. Sun, B. T. Mayers, Y. Xia, Template-engaged replacement reaction: a one-step approach to the large-scale synthesis of metal nanostructures with hollow interiors. *Nano Letters*, **2** (2002), 481–485.
59 Y. Yin, C. Erdonmez, S. Aloni, A. P. Alivisatos, Faceting of nanocrystals during chemical transformation: from solid silver spheres to hollow gold octahedra. *Journal of the American Chemical Society*, **128** (2006), 12671–12673.
60 W. Paszkowicz, Stoichiometries of compounds in Ho–Si and Y–Ni–Si systems– a study with hard sphere packing model. *Philosophical Magazine B*, **59** (1989), 451–462.
61 D. Frenkel, B. M. Mulder, J. P. McTague, Phase-diagram of a system of hard ellipsoids. *Physical Review Letters*, **52** (1984), 287–290.
62 M. J. Murray, J. V. Sanders, Close-packed structures of spheres of two different sizes. II The packing densities of likely arrangements. *Philosophical Magazine A*, **42** (1980), 721–720.
63 J. V. Sanders, Close-packed structures of spheres of two different sizes. I Observations on natural opal. *Philosophical Magazine A*, **42** (1980), 705–720.
64 Z. Chen, S. O'Brien, Structure direction of II–VI semiconductor quantum dot binary nanoparticle superlattices by tuning radius ratio. *ACS Nano*, **2** (2008), 1219–1229.
65 D. J. Norris, E. G. Arlinghaus, L. L. Meng, R. Heiny, L. E. Scriven, Opaline photonic crystals: How does self-assembly work? *Advanced Materials*, **16** (2004), 1393–1399.

66 A. P. Hynninen, M. Dijkstra, Phase diagram of dipolar hard and soft spheres: Manipulation of colloidal crystal structures by an external field. *Physical Review Letters*, **94** (2005), 138303.
67 B. J. Alder, W. G. Hoover, D. A. Young, Studies in molecular dynamics. V High-density equation of state and entropy for hard disks and spheres. *Journal of Chemical Physics*, **49** (1968), 3688–3696.
68 P. G. Bolhuis, D. Frenkel, S.-C. Mau, D. A. Huse, Entropy difference between crystal phases. *Nature*, **388** (1997), 235–236
69 B. J. Alder, B. P. Carter, D. A. Young, Crystal transformation for hard spheres. *Physical Review*, **183** (1969), 831–833.
70 D. V. Talapin, E. V. Shevchenko, C. B. Murray, A. V. Titov, P. Kral, Dipole–dipole interactions in nanoparticle superlattices. *Nano Letters*, **7** (2007), 1213–1219.
71 B. W. Goodfellow, R. N. Patel, M. G. Panthani, D.-M. Smilgies, B. A. Korgel, Melting and sintering of a body-centered cubic superlattice of PbSe nanocrystals followed by small angle X-ray scattering. *The Journal of Physical Chemistry C*, **115** (2011), 6397–6404.
72 D. V. Talapin, E. V. Shevchenko, A. Kornowski, *et al.*, A new approach to crystallization of CdSe nanoparticles into ordered three-dimensional superlattices. *Advanced Materials*, **13** (2001), 1868–1871.
73 S. M. Rupich, E. V. Shevchenko, M. I. Bodnarchuk, B. Lee, D. V. Talapin, Size-dependent multiple twinning in nanocrystal superlattices. *Journal of the American Chemical Society*, **132** (2009), 289–296.
74 M. I. Bodnarchuk, L. Li, A. Fok, *et al.*, Three-dimensional nanocrystal superlattices grown in nanoliter microfluidic plugs. *Journal of the American Chemical Society*, **133** (2011), 8956–8960.
75 D. V. Talapin, E. V. Shevchenko, N. Gaponik, *et al.*, Reply: Self-assembly of monodisperse nanocrystals into faceted crystal superlattices. *Advanced Materials*, **17** (2005), 1325–1329.
76 L. Li, R. F. Ismagilov, Protein crystallization using microfluidic technologies based on valves, droplets and SlipChip. *Annual Peview of Biophysics*, **39** (2010), 139–158.
77 M. Nagel, S. G. Hickey, A. Fromsdorf, A. Kornowski, H. Weller, Synthesis of monodisperse PbS nanoparticles and their assembly into highly ordered 3D colloidal crystals. *Zeitschrift fur Physikalische Chemie*, **221** (2007), 427–437.
78 E. Shevchenko, D. Talapin, A. Kornowski, *et al.*, Colloidal crystals of monodisperse FePt nanoparticles grown by a three-layer technique of controlled oversaturation. *Advanced Materials*, **14** (2002), 287–290.
79 J. V. Sanders, M. J. Murray, Ordered arrangements of spheres of two different sizes in opal. *Nature*, **275** (1978), 201–203.
80 S. Hachisu, S. Yoshimura, Optical demonstration of crystalline superstructures in binary mixtures of latex globules. *Nature*, **283** (1980), 188–189.
81 C. J. Kiely, J. Fink, M. Brust, D. Bethell, D. J. Schiffrin, Spontaneous ordering of bimodal ensembles of nanoscopic gold clusters. *Nature*, **396** (1998), 444–446.
82 C. J. Kiely, J. Fink, J. G. Zheng, *et al.*, Ordered colloidal nanoalloys. *Advanced Materials*, **12** (2000), 640–643.
83 E. V. Shevchenko, D. V. Talapin, A. L. Rogach, *et al.*, Colloidal synthesis and self-assembly of $CoPt_3$ nanocrystals. *Journal of the American Chemical Society*, **124** (2002), 11480–11485.
84 F. X. Redl, K. S. Cho, C. B. Murray, S. O'Brien, Three-dimensional binary superlattices of magnetic nanocrystals and semiconductor quantum dots. *Nature*, **423** (2003), 968–971.
85 E. V. Shevchenko, D. V. Talapin, N. A. Kotov, S. O'Brien, C. B. Murray, Structural diversity in binary nanoparticle superlattices. *Nature*, **439** (2006), 55–59.

86 E. V. Shevchenko, D. V. Talapin, C. B. Murray, S. O'Brien, Structural characterization of self-assembled multifunctional binary nanoparticle superlattices. *Journal of the American Chemical Society*, **128** (2006), 3620–3637.

87 J. Chen, X. Ye, C. B. Murray, Systematic electron crystallographic studies of self-assembled binary nanocrystal superlattices. *ACS Nano*, **4** (2010), 2374–2381.

88 D. K. Smith, B. Goodfellow, D.-M. Smilgies, B. A. Korgel, Self-assembled simple hexagonal AB2 binary nanocrystal superlattices: SEM, GISAXS, and defects. *Journal of the American Chemical Society*, **131** (2009), 3281–3290.

89 H. Friedrich, C. J. Gommes, K. Overgaag, *et al.*, Quantitative structural analysis of binary nanocrystal superlattices by electron tomography. *Nano Letters*, **9** (2009), 2719–2724.

90 D. B. Mitzi, M. Copel, S. J. Chey, Low-voltage transistor employing a high-mobility spin-coated chalcogenide semiconductor. *Advanced Materials*, **17** (2005), 1285–1289.

91 T. P. Bigioni, X. M. Lin, T. T. Nguyen, *et al.*, Kinetically driven self assembly of highly ordered nanoparticle monolayers. *Nature Materials*, **5** (2006), 265–270.

92 R. L. Whetten, M. N. Shafigullin, J. T. Khoury, *et al.*, Crystal structures of molecular gold nanocrystal arrays. *Accounts of Chemical Research*, **32** (1999), 397–406.

93 C. B. Murray, C. R. Kagan, M. G. Bawendi, Self-organization of CdSe nanocrystallites into three-dimensional quantum dot superlattices. *Science*, **270** (1995), 1335–1338.

94 K. J. M. Bishop, C. E. Wilmer, S. Soh, B. A. Grzybowski, Nanoscale forces and their uses in self-assembly. *Small*, **5** (2009), 1600–1630.

95 M. I. Bodnarchuk, M. V. Kovalenko, W. Heiss, D. V. Talapin, Energetic and entropic contributions to self-assembly of binary nanocrystal superlattices: temperature as the structure-directing factor. *Journal of the American Chemical Society*, **132** (2010), 11967–11977.

96 W. H. Evers, B. De Nijs, L. Filion, *et al.*, Entropy-driven formation of binary semiconductor-nanocrystal superlattices. *Nano Letters*, **10** (2010), 4235–4241.

97 A. Dong, J. Chen, P. M. Vora, J. M. Kikkawa, C. B. Murray, Binary nanocrystal superlattice membranes self-assembled at the liquid–air interface. *Nature*, **466** (2010), 474–477.

98 Y. Min, M. Akbulut, K. Kristiansen, Y. Golan, J. Israelachvili, The role of interparticle and external forces in nanoparticle assembly. *Nature Materials*, **7** (2008), 527–538.

99 Z. Chen, J. Moore, G. Radtke, H. Sirringhaus, S. O'Brien, Binary nanoparticle superlattices in the semiconductor-semiconductor system: CdTe and CdSe. *Journal of the American Chemical Society*, **129** (2007), 15702–15709.

100 D. V. Talapin, LEGO materials. *ACS Nano*, **2** (2008), 1097–1100.

101 S. L. Tripp, S. V. Pusztay, A. E. Ribbe, A. Wei, Self-assembly of cobalt nanoparticle rings. *Journal of the American Chemical Society*, **124** (2002), 7914–7915.

102 E. V. Shevchenko, J. B. Kortright, D. V. Talapin, S. Aloni, A. P. Alivisatos, Quasi-ternary nanoparticle superlattices through nanoparticle design. *Advanced Materials*, **19** (2007), 4183–4188.

103 A. Dong, X. Ye, J. Chen, C. B. Murray, Two-dimensional binary and ternary nanocrystal superlattices: the case of monolayers and bilayers. *Nano Letters*, **11** (2011), 1804–1809.

104 W. H. Evers, H. Friedrich, L. Filion, M. Dijkstra, D. Vanmaekelbergh, Observation of a ternary nanocrystal superlattice and its structural characterization by electron tomography. *Angewandte Chemie-International Edition*, **48** (2009), 9655–9657.

105 D. V. Talapin, E. V. Shevchenko, M. I. Bodnarchuk, *et al.*, Quasicrystalline order in self-assembled binary nanoparticle superlattices. *Nature*, **461** (2009), 964–967.

106 H. Zeng, J. Li, J. P. Liu, Z. L. Wang, S. H. Sun, Exchange-coupled nanocomposite magnets by nanoparticle self-assembly. *Nature*, **420** (2002), 395–398.

107 J. Cheon, J. I. Park, J. S. Choi, *et al.*, Magnetic superlattices and their nanoscale phase transition effects. *Proceedings of the National Academy of Sciences*, **103** (2006), 3023–3027.

108 J. Chen, A. Dong, J. Cai, *et al.*, Collective dipolar interactions in self-assembled magnetic binary nanocrystal superlattice membranes. *Nano Letters*, **10** (2010), 5103–5108.

109 J. J. Urban, D. V. Talapin, E. V. Shevchenko, C. R. Kagan, C. B. Murray, Synergism in binary nanocrystal superlattices leads to enhanced p-type conductivity in self-assembled PbTe/Ag_2Te thin films. *Nature Materials*, **6** (2007), 115–121.

110 J. Zhang, A. Kumbhar, J. He, *et al.*, Simple cubic super crystals containing PbTe nanocubes and their core-shell building blocks. *Journal of the American Chemical Society*, **130** (2008), 15203–15209.

111 F. X. Redl, C. T. Black, G. C. Papaefthymiou, *et al.*, Magnetic, electronic, and structural characterization of nonstoichiometric iron oxides at the nanoscale. *Journal of the American Chemical Society*, **126** (2004), 14583–14599.

112 W. Lu, Q. Liu, Z. Sun, *et al.*, Super crystal structures of octahedral c-$_2O_3$ nanocrystals. *Journal of the American Chemical Society*, **130** (2008), 6983–6991.

113 S. Xie, X. Zhou, X. Han, *et al.*, Supercrystals from crystallization of octahedral MnO nanocrystals. *Journal of Physical Chemistry C*, **113** (2009), 19107–19111.

114 L. Li, Y. Yang, J. Ding, J. Xue, Synthesis of magnetite nanooctahedra and their magnetic field-induced two-/three-dimensional superstructure. *Chemistry of Materials*, **22** (2010), 3183–3191.

115 J. Henzie, M. Grünwald, A. Widmer-Cooper, P. L. Geissler, P. Yang, Self-assembly of uniform polyhedral silver nanocrystals into densest packings and exoticsuperlattices. *Nature Materials*, **11** (2012), 131–137.

116 C.-C. Chang, H.-L. Wu, C.-H. Kuo, M. H. Huang, Hydrothermal synthesis of monodispersed octahedral gold nanocrystals with five different size ranges and their self-assembled structures. *Chemistry of Materials*, **20** (2008), 7570–7574.

117 N. Wang, X. Cao, L. Guo, S. Yang, Z. Wu, Facile synthesis of PbS truncated octahedron crystals with high symmetry and their large-scale assembly into regular patterns by a simple solution route. *ACS Nano*, **2** (2008), 184–190.

118 X. Ye, J. E. Collins, Y. Kang, *et al.*, Morphologically controlled synthesis of colloidal upconversion nanophosphors and their shape-directed self-assembly. *Proceedings of the National Academy of Sciences of the United States of America*, **107** (2010), 22430–22435.

119 Y. W. Zhang, X. Sun, R. Si, L. P. You, C. H. Yan, Single-crystalline and monodisperse LaF_3 triangular nanoplates from a single-source precursor. *Journal of the American Chemical Society*, **127** (2005), 3260–3261.

120 T. Paik, D.-K. Ko, T. R. Gordon, V. Doan-Nguyen, C. B. Murray, Studies of liquid crystalline self-assembly of GdF_3 nanoplates by in-plane, out-of-plane SAXS. *ACS Nano*, **5** (2011), 8322–8330.

121 Y. C. Cao, Synthesis of square gadolinium-oxide nanoplates. *Journal of the American Chemical Society*, **126** (2004), 7456–7457.

122 A. E. Saunders, A. Ghezelbash, D.-M. Smilgies, M. B. Sigman, B. A. Korgel, Columnar self-assembly of colloidal nanodisks. *Nano Letters*, **6** (2006), 2959–2963.

123 R. Si, Y.-W. Zhang, L.-P. You, C.-H. Yan, Rare-earth oxide nanopolyhedra, nanoplates, and nanodisks. *Angewandte Chemie International Edition*, **44** (2005), 3256–3260.

124 V. F. Puntes, D. Zanchet, C. K. Erdonmez, A. P. Alivisatos, Synthesis of hcp-Co nanodisks. *Journal of the American Chemical Society*, **124** (2002), 12874–12880.

125 D. V. Talapin, E. V. Shevchenko, C. B. Murray, *et al.*, CdSe and CdSe/CdS nanorod solids. *Journal of the American Chemical Society*, **126** (2004), 12984–12988.
126 J. L. Baker, A. Widmer-Cooper, M. F. Toney, P. L. Geissler, A. P. Alivisatos, Device-scale perpendicular alignment of colloidal nanorods. *Nano Letters*, **10** (2009), 195–201.
127 K. M. Ryan, A. Mastroianni, K. A. Stancil, H. Liu, A. P. Alivisatos, Electric-field-assisted assembly of perpendicularly oriented nanorod superlattices. *Nano Letters*, **6** (2006), 1479–1482.
128 D. Baranov, A. Fiore, M. van Huis, *et al.* Assembly of colloidal semiconductor nanorods in solution by depletion attraction. *Nano Letters*, **10** (2010), 743–749.
129 T. H. Larsen, M. Sigman, A. Ghezelbash, R. C. Doty, B. A. Korgel, Solventless synthesis of copper sulfide nanorods by thermolysis of a single source thiolate-derived precursor. *Journal of the American Chemical Society*, **125** (2003), 5638–5639.
130 A. Demortiere, P. Launois, N. Goubet, P. A. Albouy, C. Petit, Shape-controlled platinum nanocubes and their assembly into two-dimensional and three-dimensional superlattices. *Journal of Physical Chemistry B*, **112** (2008), 14583–14592.
131 K. Miszta, J. de Graaf, G. Bertoni, *et al.*, Hierarchical self-assembly of suspended branched colloidal nanocrystals into superlattice structures. *Nat Mater*, **10** (2011), 872–876.
132 K. X. Yao, X. M. Yin, T. H. Wang, H. C. Zeng, Synthesis, self-assembly, disassembly, and reassembly of two types of Cu_2O nanocrystals unifaceted with {001} or {110} planes. *Journal of the American Chemical Society*, **132** (2010), 6131–6144.
133 T. Huang, Q. Zhao, J. Xiao, L. Qi, Controllable self-assembly of PbS nanostars into ordered structures: close-packed arrays and patterned arrays. *ACS Nano*, **4** (2010), 4707–4716.
134 M. Kuno, J. K. Lee, B. O. Dabbousi, F. V. Mikulec, M. G. Bawendi, The band edge luminescence of surface modified CdSe nanocrystallites: probing the luminescing state. *The Journal of Chemical Physics*, **106** (1997), 9869–9882.
135 A. Pandey, P. Guyot-Sionnest, Slow electron cooling in colloidal quantum dots. *Science*, **322** (2008), 929–932.
136 D. Yu, C. Wang, P. Guyot-Sionnest, n-Type conducting CdSe nanocrystal solids. *Science*, **300** (2003), 1277–1280.
137 N. Y. Morgan, C. A. Leatherdale, M. Drndic, *et al.*, Electronic transport in films of colloidal CdSe nanocrystals. *Physical Review B*, **66** (2002), 075339.
138 H. Lee, S. E. Habas, S. Kweskin, *et al.*, Morphological control of catalytically active platinum nanocrystals. *Angewandte Chemie-International Edition*, **45** (2006), 7824–7828.
139 C. B. Murray, S. H. Sun, H. Doyle, T. Betley, Monodisperse 3d transition-metal (Co, Ni, Fe) nanoparticles and their assembly into nanoparticle superlattices. *MRS Bulletin*, **26** (2001), 985–991.
140 G. Konstantatos, I. Howard, A. Fischer, *et al.*, Ultrasensitive solution-cast quantum dot photodetectors. *Nature*, **442** (2006), 180–183.
141 I. Gur, N. A. Fromer, M. L. Geier, A. P. Alivisatos, Air-stable all-inorganic nanocrystal solar cells processed from solution. *Science*, **310** (2005), 462–465.
142 J. M. Caruge, J. E. Halpert, V. Wood, V. Bulovic, M. G. Bawendi, Colloidal quantum-dot light-emitting diodes with metal-oxide charge transport layers. *Nature Photonics*, **2** (2008), 247–250.
143 A. Zabet-Khosousi, A. A. Dhirani, Charge transport in nanoparticle assemblies. *Chemical Reviews*, **108** (2008), 4072–4124.

144 M. Drndic, M. V. Jarosz, N. Y. Morgan, M. A. Kastner, M. G. Bawendi, Transport properties of annealed CdSe colloidal nanocrystal solids. *Journal of Applied Physics*, **92** (2002), 7498–7503.

145 B. A. Ridley, B. Nivi, J. M. Jacobson, All-inorganic field effect transistors fabricated by printing. *Science*, **286** (1999), 746–749.

146 J. A. Dahl, B. L. S. Maddux, J. E. Hutchison, Toward greener nanosynthesis. *Chemical Reviews*, **107** (2007), 2228–2269.

147 M. Y. Gao, C. Lesser, S. Kirstein, *et al.*, Electroluminescence of different colors from polycation/CdTe nanocrystal self-assembled films. *Journal of Applied Physics*, **87** (2000), 2297–2302.

148 M. V. Kovalenko, E. Kaufmann, D. Pachinger, *et al.*, Colloidal HgTe nanocrystals with widely tunable narrow band gap energies: from telecommunications to molecular vibrations. *Journal of the American Chemical Society*, **128** (2006), 3516–3517.

149 J. S. Owen, J. Park, P.-E. Trudeau, A. P. Alivisatos, Reaction chemistry and ligand exchange at cadmium selenide nanocrystal surfaces. *Journal of the American Chemical Society*, **130** (2008), 12279–12281.

150 M. V. Jarosz, V. J. Porter, B. R. Fisher, M. A. Kastner, M. G. Bawendi, Photoconductivity studies of treated CdSe quantum dot films exhibiting increased exciton ionization efficiency. *Physical Review B*, **70** (2004), 195327.

151 D. C. Oertel, M. G. Bawendi, A. C. Arango, V. Bulovic, Photodetectors based on treated CdSe quantum-dot films. *Applied Physics Letters*, **87** (2005), 213505–213503.

152 M. Law, J. M. Luther, Q. Song, *et al.*, Structural, optical, and electrical properties of PbSe nanocrystal solids treated thermally or with simple amines. *Journal of the American Chemical Society*, **130** (2008), 5974–5985.

153 E. H. Sargent, Solar cells, photodetectors, and optical sources from infrared colloidal quantum dots. *Advanced Materials*, **20** (2008), 3958–3964.

154 J. S. Liu, T. Tanaka, K. Sivula, A. P. Alivisatos, J. M. J. Frechet, Employing end-functional polythiophene to control the morphology of nanocrystal-polymer composites in hybrid solar cells. *Journal of the American Chemical Society*, **126** (2004), 6550–6551.

155 H. Skaff, K. Sill, T. Emrick, Quantum dots tailored with poly(para-phenylene vinylene). *Journal of the American Chemical Society*, **126** (2004), 11322–11325.

156 M. J. Hostetler, A. C. Templeton, R. W. Murray, Dynamics of place-exchange reactions on monolayer-protected gold cluster molecules. *Langmuir*, **15** (1999), 3782–3789.

157 N. Gaponik, D. V. Talapin, A. L. Rogach, A. Eychmuller, H. Weller, Efficient phase transfer of luminescent thiol-capped nanocrystals: from water to nonpolar organic solvents. *Nano Letters*, **2** (2002), 803–806.

158 E. E. Foos, A. W. Snow, M. E. Twigg, M. G. Ancona, Thiol-terminated di-, tri-, and tetraethylene oxide functionalized gold nanoparticles: a water-soluble, charge-neutral cluster. *Chemistry of Materials*, **14** (2002), 2401–2408.

159 A. Zabet-Khosousi, P. E. Trudeau, Y. Suganuma, A. A. Dhirani, B. Statt, Metal to insulator transition in films of molecularly linked gold nanoparticles. *Physical Review Letters*, **96** (2006), 156403.

160 M. Brust, D. Bethell, C. J. Kiely, D. J. Schiffrin, Self-assembled gold nanoparticle thin films with nonmetallic optical and electronic properties. *Langmuir*, **14** (1998), 5425–5429.

161 E. J. D. Klem, D. D. MacNeil, P. W. Cyr, L. Levina, E. H. Sargenta, Efficient solution-processed infrared photovoltaic cells: planarized all-inorganic bulk heterojunction devices

via inter-quantum-dot bridging during growth from solution. *Applied Physics Letters*, **90** (2007), 151115.

162 J. M. Luther, M. Law, M. C. Beard, *et al.*, Schottky solar cells based on colloidal nanocrystal films. *Nano Letters*, **8** (2008), 3488–3492.

163 G. I. Koleilat, L. Levina, H. Shukla, *et al.*, Efficient, stable infrared photovoltaics based on solution-cast colloidal quantum dots. *ACS Nano*, **2** (2008), 833–840.

164 M. V. Kovalenko, M. I. Bodnarchuk, J. Zaumseil, J.-S. Lee, D. V. Talapin, Expanding the chemical versatility of colloidal nanocrystals capped with molecular metal chalcogenide ligands. *Journal of the American Chemical Society*, **132** (2010), 10085–10092.

165 M. V. Kovalenko, M. Scheele, D. V. Talapin, Colloidal nanocrystals with molecular metal chalcogenide surface ligands. *Science*, **324** (2009), 1417–1420.

166 M. V. Kovalenko, B. Spokoyny, J. S. Lee, *et al.*, Semiconductor nanocrystals functionalized with antimony telluride Zintl ions for nanostructured thermoelectrics. *Journal of the American Chemical Society*, **132** (2010), 6686–6695.

167 M. V. Kovalenko, M. I. Bodnarchuk, D. V. Talapin, Nanocrystal superlattices with thermally degradable hybrid inorganic−organic capping ligands. *Journal of the American Chemical Society*, **132** (2010), 15124–15126.

168 A. Nag, M. V. Kovalenko, J.-S. Lee, *et al.*, Metal-free inorganic ligands for colloidal nanocrystals: S_2-, HS-, Se_2-, HSe-, Te_2-, HTe-, TeS_{32}-, OH-, and NH_2- as surface ligands. *Journal of the American Chemical Society*, **133** (2011), 10612–10620.

169 R. Tangirala, J. L. Baker, A. P. Alivisatos, D. J. Milliron, Modular inorganic nanocomposites by conversion of nanocrystal superlattices. *Angewandte Chemie-International Edition*, **49** (2010), 2878–2882.

170 A. T. Fafarman, W.-K. Koh, B. T. Diroll, *et al.*, Thiocyanate-capped nanocrystal colloids: vibrational reporter of surface chemistry and solution-based route to enhanced coupling in nanocrystal solids. *Journal of the American Chemical Society*, **133** (2011), 15753–15761.

171 A. Llordes, A. T. Hammack, R. Buonsanti, *et al*., Polyoxometalates and colloidal nanocrystals as building blocks for metal oxide nanocomposite films. *Journal of Materials Chemistry*, **21** (2011), 11631–11638.

172 J. Tang, K. W. Kemp, S. Hoogland, *et al.*, Colloidal-quantum-dot photovoltaics using atomic-ligand passivation. *Nature Materials*, **10** (2011), 765–771.

173 J.-S. Lee, M. V. Kovalenko, J. Huang, D. S. Chung, D. V. Talapin, Band-like transport, high electron mobility and high photoconductivity in all-inorganic nanocrystal arrays. *Nature Nanotechnology*, **6** (2011), 348–352.

174 A. G. Dong, X. C. Ye, J. Chen, *et al.*, A generalized ligand-exchange strategy enabling sequential surface functionalization of colloidal nanocrystals. *Journal of the American Chemical Society*, **133** (2011), 998–1006.

175 E. L. Rosen, R. Buonsanti, A. Llordes, *et al.*, Exceptionally mild reactive stripping of native ligands from nanocrystal surfaces by using Meerwein's salt. *Angewandte Chemie International Edition*, **51** (2011), 684–689.

2 Aqueous based colloidal quantum dots for optoelectronics

Vladimir Lesnyak and Nikolai Gaponik

2.1 Introduction

Colloidal aqueous synthesis of semiconductor nanocrystals (NCs), otherwise known as quantum dots (QDs), is an advantageous alternative to the widely used organometallic route [1]. In comparison to the latter, the aqueous method employs the most widespread and biocompatible solvent, is not restricted to an inert atmosphere, is easily up-scalable, and provides various functionalizations of NCs by applying an appropriate capping ligand [2]. In general, an aqueous synthetic protocol consists of the reaction between metal ions or their complexes and chalcogen containing precursors in the presence of an appropriate stabilizer with subsequent nucleation and growth of NCs, typically controlled by heating. The history of this method began in the 1980s starting from an early work of Henglein's group [3]. Comprehensive historical overviews of progress made in the field during this time may be found in the literature [4–6]. The aqueous approach has already yielded stable binary II–VI and IV–VI compounds, such as CdS [7], CdTe [1, 8–10], CdSe [11–13], ZnSe [14, 15], HgTe [16], PbS [17–19], as well as some alloyed structures, such as CdSeTe [20], CdHgTe [21, 22], ZnSeS [15], ZnCdSe [14, 23, 24], ZnHgSe [25], and ZnSeTe [26]. Most of these materials possess strong photoluminescence (PL) (Figure 2.1) whose efficiency is substantially determined by a proper choice of a stabilizer [27]. In the case of aqueous synthesis, short chain thiols are undoubtedly the most used ligands for the stabilization of various semiconductor materials. The tunable luminescence and the high extinction coefficients of NCs determine their potential applicability in the fields of light emitting diodes (LEDs) [28], color conversion [29], energy scavenging [30], optical sensing [31], and bioimaging [32].

The mild synthetic conditions used in aqueous syntheses often prevent perfect arrangements of atoms in the crystal lattice of nanoparticles, which are normally achievable by synthesis in high boiling organic solvents. In order to improve the crystal structure, size distribution, and the corresponding optical properties of QDs the use of microwave irradiation [34] and synthesis in autoclaves [35] have been reported as applied to CdTe NCs. Microwave-assisted synthesis has resulted also in obtaining alloyed ZnSeS NCs [36] and even core/shell/shell CdTe/CdS/ZnS [37], which, to the best of our

Colloidal Quantum Dot Optoelectronics and Photovoltaics, eds. G. Konstantatos and E. H. Sargent.
Published by Cambridge University Press. © Cambridge University Press, 2013.

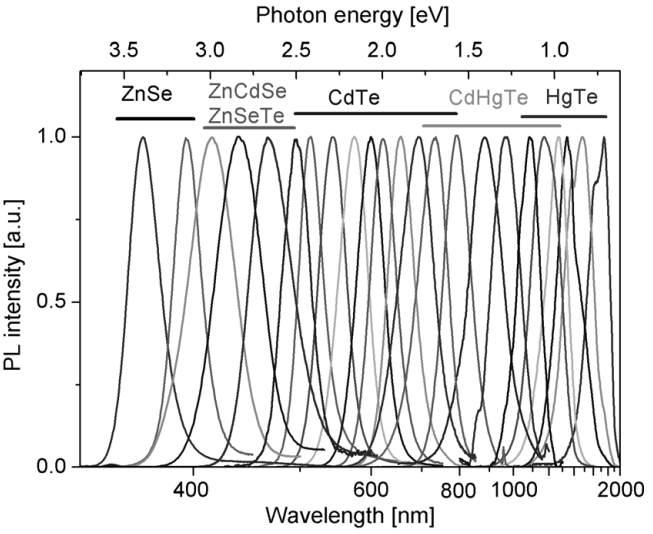


Figure 2.1 Representative normalized photoluminescence spectra of a series of aqueous NCs. Reproduced from [33] by permission of The Royal Society of Chemistry.

knowledge, was the first example of this type of sophisticated structure that was prepared by the aqueous method. Different core/shell semiconductor nanoparticles are achievable by a common aqueous synthetic protocol, e.g., ZnSe/ZnS [38], CdSe/CdS [39, 40], CdTe/CdS [41], CdHgTe/CdS [42], and HgTe/CdS [43]. Obtaining different core/shell and core/shell/shell structures directly in water as has been reported since 2000 is a great step forward towards obtaining superior quality of NCs previously accessible solely from the organometallic synthetic route.

Interesting hybrid approaches for the synthesis of core/shell NCs combining aqueous and organic phase techniques have been developed. Depending on the accessibility of the corresponding core and shell materials, cores being synthesized in water (organics) have been transferred into organics (water) for subsequent shell formation [44, 45]. One advance has lead to a facile synthesis of one-dimensional structures such as CdTe [46] and CdHgTe [47] nanorods, allowing control of their sizes and aspect ratios. Nevertheless, it is accepted that the aqueous method usually does not permit direct efficient shape control of nanoparticles during their growth and the NCs synthesized have been mainly spherical or quasi-spherical, since this shape is thermodynamically the most stable [48].

In the following sections we will review in more detail some results of the aqueous synthesis of various semiconductor materials, arranging them in decreasing order of their band gap, i.e., beginning from wide band gap compounds emitting in the ultraviolet (UV) region (ZnSe) through visible (CdTe) to near-infrared (NIR) and infrared (IR) emitters possessing narrow energy gaps (HgTe, PbS). This will be followed by the overview of assembly approaches and their optoelectronic application perspectives.

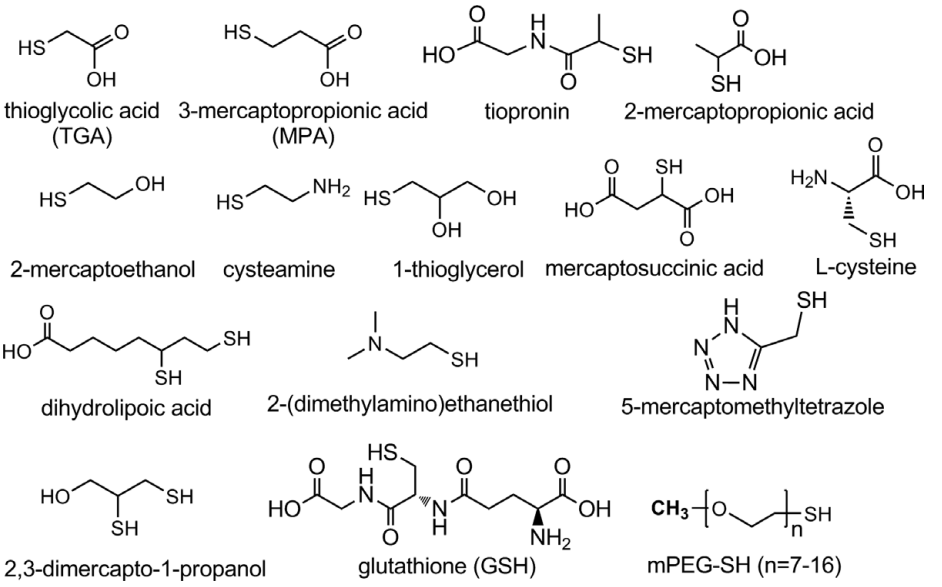


Figure 2.2 Chemical structures of typical thiol capping ligands employed in the aqueous synthesis of NCs.

2.2 Aqueous colloidal synthesis of semiconductor NCs

2.2.1 ZnX NCs

Zn chalcogenides attract scientific interest due to the demand for non- or low-toxic nanoparticulate semiconductor materials, which would reduce the amount of pollutants such as Cd, Hg, Pb released into the environment. The most developed materials produced by an aqueous approach are ZnSe NCs. ZnS, which has the wide bulk band gap of 3.54 eV (cf. 2.58 eV for ZnSe and 2.26 eV for ZnTe) [49], is commonly used as a shell material for the creation of core/shell structures. The synthesis of ZnTe NCs, although reported [50], has not yielded high quality light emitting colloids, probably due to high reactivity of ZnTe towards oxygen and water and its instability under ambient conditions.

Nanostructured ZnSe exhibiting luminescence in the near-UV and blue spectral region is a promising candidate for the fabrication of blue emitting LEDs and laser diodes [51], and also as a potentially non-toxic material is very appropriate for biolabelling. The first successful aqueous colloidal synthesis of strongly emitting ZnSe NCs was reported by Shavel *et al.* [15]. A typical procedure comprised reacting Zn ions with H_2Se gas in the presence of thiol-stabilizers (thioglycolic acid (TGA), 3-mercaptopropionic acid (MPA) or 1-thioglycerol (TG) (Figure 2.2)), followed by growing NCs under reflux. We note that the pH value of the reaction mixture plays a very important role in the aqueous synthesis of NCs, ensuring their stability and providing control of their growth. Since the as-prepared ZnSe NC colloids exhibited negligible photoluminescence quantum yield (PLQY) ($\leq$0.1%), they underwent photochemical treatment consisting of illumination with white light in the presence of Zn salt and thiol-stabilizer. The latter was decomposed

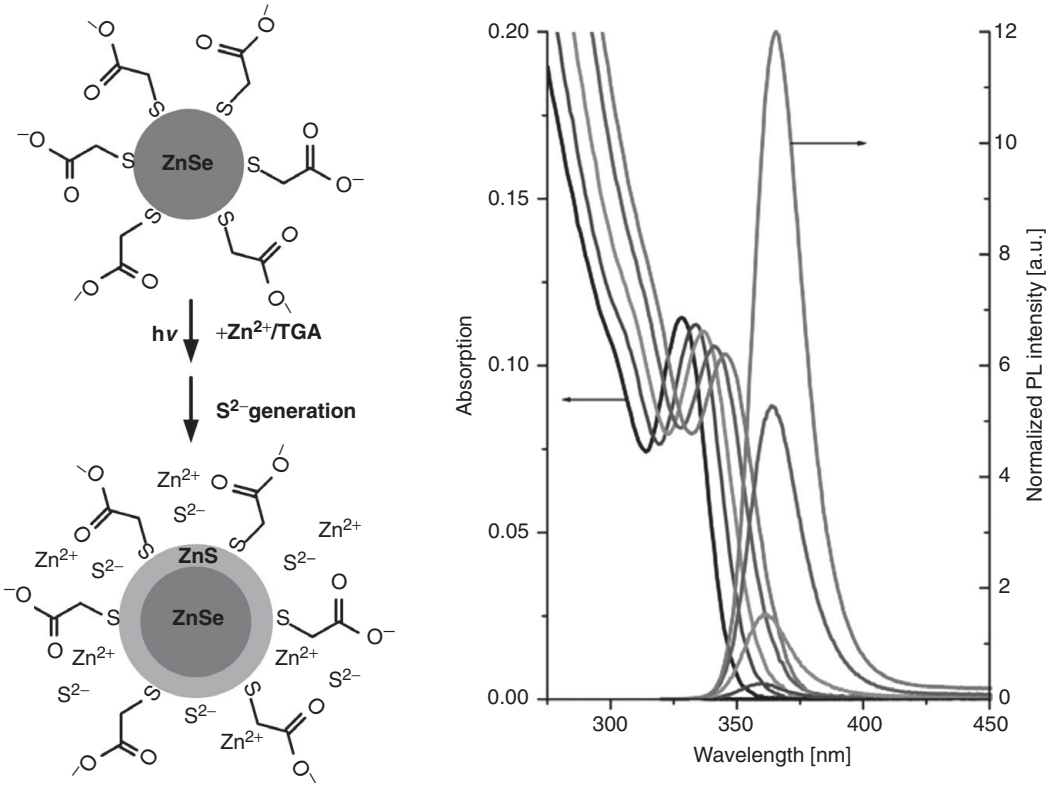


Figure 2.3 Schematic of ZnS layer formation on the surface of ZnSe NCs upon irradiation (left). Changes in the absorption and PL of ZnSe NCs during irradiation with white light (right). Reproduced with permission from [15]. Copyright 2004, American Chemical Society.

under irradiation releasing S ions which subsequently reacted with Zn ions, forming a ZnS or mixed ZnSSe shell on the surface of the ZnSe NCs (Figure 2.3) [52]. This photochemical treatment enhances the PLQY by up to 30% [15]. The layer of wider band gap material covering the particle prevents the escape of excitons or their nonradiative recombination in traps. Application of microwave irradiation in the synthesis of ZnSe NCs leads to a simplification of the procedure, enabling the fast preparation of an emitting colloid in one stage [36].

L-glutathione (GSH) capping allows preparation of readily luminescing ZnSe NCs without additional post-preparative treatment, probably due to the quite labile ZnS–C bond which decomposes by heating during particle growth forming a ZnS shell layer. Thus prepared NCs have an average size of 2.7nm, emission with a maximum at approx. 370 nm and a PLQY reaching 20% [14, 38]. An additional reaction stage consisting of the heat treatment of the synthesized QDs in the presence of Zn ions, GSH, and thiourea leads to improvement of the ZnS shell and a corresponding quantum yield (QY) enhancement of up to 65% [38]. Nevertheless, in spite of the high QYs achieved in the synthesis of ZnSe and ZnSeS NCs, they demonstrate a PL only at the edge of

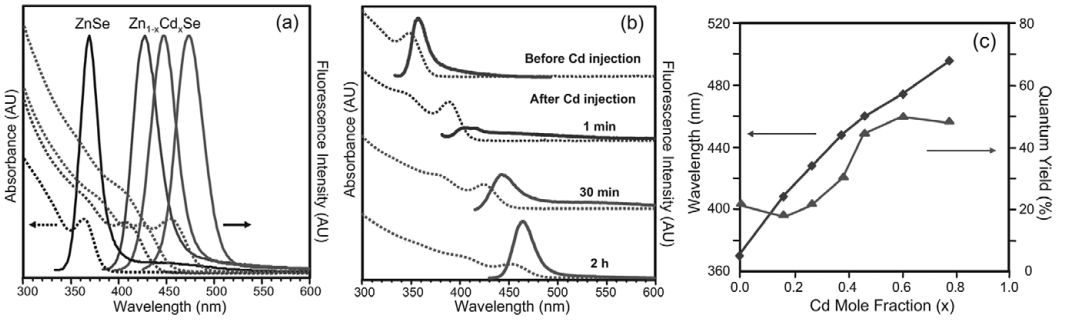


Figure 2.4 (a) Absorption (···) and PL (–) spectra of pure ZnSe and $Zn_{0.75}Cd_{0.25}Se$, $Zn_{0.62}Cd_{0.38}Se$ and $Zn_{0.4}Cd_{0.6}Se$ alloyed QDs, respectively. (b) Evolution of the absorption (···) and PL (–) spectra of $Zn_{1-x}Cd_xSe$ QDs with time. (c) QYs and PL maxima of $Zn_{1-x}Cd_xSe$ QDs as a function of Cd molar fraction. Adapted with permission from [14]. Copyright 2007, WILEY VCH Verlag GmbH & Co. KGaA.

the visible region. Apparently, the conditions of aqueous synthesis do not permit size tuning of ZnSe QDs over a wide range, thereby restricting their luminescence to around 350–400 nm. In this case the formation of alloyed structures provides an additional opportunity for controlling the material properties by changing their composition and consequently their band gaps. In order to shift the emission of ZnSe to longer wavelengths, incorporation of a narrower band gap material is necessary.

2.2.2 Alloyed ZnSe based NCs

Although, in principle, the aforesaid synthesis of ZnSe NCs accompanied by the incorporation of a thin layer of ZnS may be considered as a method of alloying, the composition of the resulting particles is not fully controlled by the process conditions. The incorporation of Cd atoms into a ZnSe matrix has been carried out in a more controllable way. Two basic strategies have been developed for the synthesis of alloyed $Zn_xCd_{1-x}Se$ NCs: incorporation of Cd ions into already synthesized ZnSe QDs [14], and direct synthesis of an alloyed structure by means of partial replacement of a Zn precursor by a Cd salt in the reaction mixture [23, 24]. Incorporation of Cd into GSH capped ZnSe NCs enabled variation of the alloy composition up to a molar ratio of Zn/Cd = 0.4/0.6, shifting the PL to longer wavelengths, from 360 nm (for initial pure ZnSe) to 500 nm (Figure 2.4). This approach has yielded alloyed ZnCdSe NCs with a tunable composition in the size range of about 3–4 nm and possessing strong fluorescence with a PLQY of up to 50% [14].

The other strategy, i.e., the direct synthesis of alloyed ZnCdSe NCs, ensures a decrease of Cd content providing the same PL shift [23, 24]. The composition of the alloyed crystals thus obtained depends mainly on the initial ratio of the metal precursors and their intrinsic reactivities towards the chalcogen source. The same method of photochemical treatment as described for pure ZnSe has been applied to alloyed particles in order to enhance their emission by means of ZnS enriched layer formation, leading to PLQYs

of 20–30% [23, 24]. Obtaining alloyed GSH capped $Zn_xHg_{1-x}Se$ QDs by a one-pot synthesis provides further narrowing of the band gap and yields colloids emitting in the range of 550–620 nm [25]. X-ray diffraction (XRD) analysis shows a zinc blende cubic crystal structure for all aqueous ZnSe NCs and their alloys.

An alternative way of changing the band gap energies is to prepare alloyed materials based on a ZnSe matrix by means of a partial replacement of Se atoms by, for example, Te, with the aim of obtaining, material with a smaller band gap. This approach has been realized in a facile one-step protocol, providing Cd-free QDs blue emitting in the 370–430 nm region with QYs of up to 20% [26]. Therefore, the chemical and physical properties of semiconductor NCs can be varied by changing particle size as well as by changing their composition. Alloying paves the way for designing materials with electronic and optical properties different from their corresponding constituent parts.

2.2.3 CdX NCs

Although the first colloidal material synthesized via an aqueous approach and thoroughly investigated was CdS, the most successful example of the cadmium chalcogenides is CdTe owing to its unique optical properties, in particular its strong and tuneable PL in the visible region. For an overview of the work on CdS colloidal synthesis we refer the reader to the corresponding chapters in [4, 6]. CdTe NCs were first obtained directly in water by Rajh *et al.* [10], who employed a mixed stabilizer system containing hexametaphosphate and 3-mercapto-l,2-propanediol. Later optimization by Rogach *et al.* led to a synthesis of stable NCs with sizes from 1.3 to 2.4 nm solely in the presence of thiols [9]. State-of-the-art preparation techniques enable facile aqueous synthesis of CdTe NCs capped by mercaptoacids, mercaptoamines, or mercaptoaminoacids (Figure 2.2). The NCs have diameters of up to 6 nm and a PL covering most of the visible region and extending to the near IR (NIR) with a QY of up to 70–80%, which can compete with the best organometallically prepared materials [8]. For instance, NCs prepared by the microwave irradiation approach were reported to have a PLQY up to 82% and a narrow size distribution [34]. Here we would like to note that the very high QYs reported in the literature should be considered with care, since the QY value is very dependent on the method of determination, standards used, instrumental conditions, etc. [53].

Thiols determine the chemical functionality and the charge of the NC surface. This opens the possibility of manipulating these NCs, e.g., by the layer-by-layer (LbL) assembly technique, oriented attachment, electrostatic assembly, or electrophoresis. Specific chemical functionality (e.g., amino- or carboxylic groups) is attractive for the covalent linking to macrosurfaces, to the surfaces of other NCs as well as to biomolecules. This correct thiol capping may be considered as a key factor in the successful fabrication, assembly, and application of the aqueous NCs. In addition to common carboxylic- and amino- surface functionalities a variety of more specific capping thiol molecules have been used. For example, 5-mercaptomethyltetrazole is a thiol-containing stabilizer that enables reversible three-dimensional assembly of CdTe NCs [54]. The chiral structure of the CdX surface was imparted by application of enantiomeric thiols, L- and D-cysteinemethylester hydrochloride, bidentate R- and S-α-lipoic acids in the synthesis

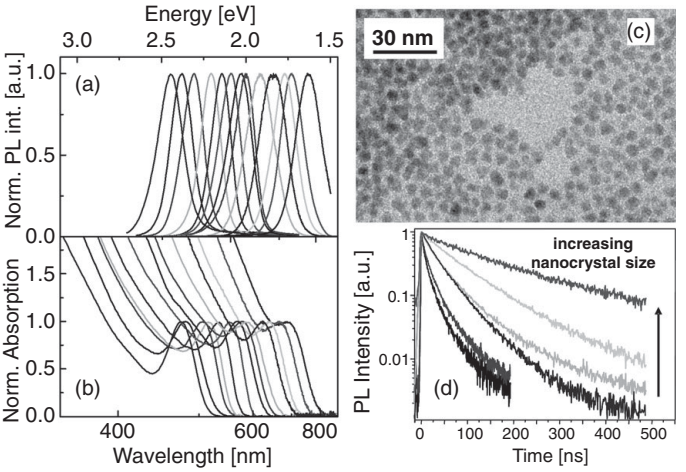


Figure 2.5 (a) PL and (b) absorption spectra of TGA- and MPA-capped CdTe NCs. (c) TEM image of MPA-capped CdTe NCs. (d) PL decays of MPA-capped CdTe NCs of increasing sizes. Adapted with permission from [8]. Copyright 2007, American Chemical Society.

[55, 56]. These NCs keep their optical activity even after ligand exchange (so called chiral memory).

Figure 2.5 shows typical PL and absorbance spectra of TGA and MPA capped CdTe QDs together with the evolution of the PL lifetime of CdTe/MPA NCs during their growth and the transmission electron microscopy (TEM) image of a CdTe/MPA sample emitting with a maximum at 780 nm. We note that MPA stabilization ensures very fast growth of the largest achievable NCs with an emission peak of 840 nm [22], which is quite close to the bulk band gap of CdTe (1.56 eV at 300 K [10]). As in the case of ZnSe and its alloys, aqueous CdTe NCs have, as a rule, the zinc blende cubic crystal structure. In certain cases the quality of the resulting NCs has not been satisfactory. In order to improve the quality of the as-synthesized particles one applies a post-preparative treatment. Some of the main post-preparative treatments are: size selection [1, 57], surface modification by means of Cd-thiol complex formation [58], photoetching [1, 59, 60].

The solubility of thiol-capped NCs is not limited to aqueous solutions. NCs synthesized in water can be transferred into nonpolar organic solvents, such as toluene and chloroform, via an exchange of stabilizer to long-chain thiols [61], by utilizing polymerizable surfactants [62] or by employing amphiphilic molecules for the stabilization [63]. Having being transferred to organic solutions the NCs may be used for the fabrication of functional polymer–NC composites [62] or thin film hybrid LEDs [64].

2.2.4 Core/shell CdTe based NCs

Microwave irradiation has been revealed as an advantageous technique for core/shell particle synthesis. This method was used in the first synthesis in water of core/shell/shell MPA-capped CdTe/CdS/ZnS NCs (Figure 2.6) [37]. The resulting QDs were found

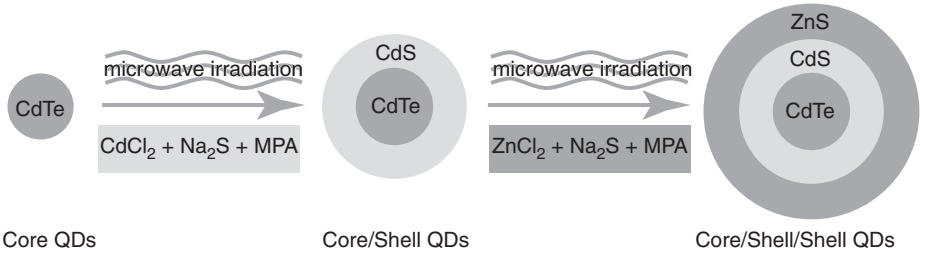


Figure 2.6 Schematic illustration of the microwave-assisted three-step synthesis of aqueous CdTe/CdS/ZnS core/shell/shell QDs. Reproduced with permission from [37]. Copyright 2008, WILEY VCH Verlag GmbH & Co. KGaA.

to be very stable in biological media and noncytotoxic, which makes them promising candidates for biolabelling.

Another material for bioimaging applications, namely type II CdTe/CdSe core/shell QDs with NIR fluorescence, was prepared by applying a successive ion-layer adsorption and reaction (SILAR) technique [65]. In this method, L-cysteine-stabilized CdTe cores are covered with 1–6 CdSe layers by sequential injection of Cd^{2+}/cysteine and KHSe solutions. The SILAR technique ensures very efficient control of the shell thickness, tuning the behavior of core/shell CdTe/CdS QDs from type I to type II structure by gradual deposition of several shell layers [35]. In addition to microwave irradiation and SILAR, ultrasonic treatment has been used for CdS shell formation on CdTe NCs [66]. In this case, acoustic cavitation facilitates the decomposition of thiourea which releases S^{2-} to react with Cd^{2+} present in solution with the subsequent creation of a gradated shell.

We have to admit that, unfortunately, the formation of core/shell structures is often not unambiguously proven. In our opinion, some reports, especially those claiming a one-pot aqueous synthesis of core/shell NCs, in which the precursors for both the core and shell are added and react simultaneously, give rise to logical criticism, since in this case the formation of an alloyed structure rather than a classical core/shell is much more probable. One such example is the one-pot synthesis of CdTe/ZnTe NCs [67], a system which is particularly doubtful taking into account the already mentioned instability of ZnTe.

2.2.5 Alloyed CdTe based NCs

All the above-mentioned approaches ensure the synthesis of NCs emitting mainly in the visible region. In order to extend the emission of CdTe to longer wavelengths one alloys the NCs with materials which have narrower band gaps and which have quite similar lattice parameters to CdTe. An appropriate candidate for alloying with CdTe is HgTe, which has a very similar lattice constant (cf. 6.477 and 6.462Å for bulk zinc blende CdTe and HgTe, respectively [49]). The aqueous synthesis of NIR emitting alloyed CdHgTe and core/shell CdHgTe/CdS along with pure HgTe NCs was first reported by Harrison, Rogach and others (Figure 2.7) [21, 68]. A similar Hg incorporation approach has been

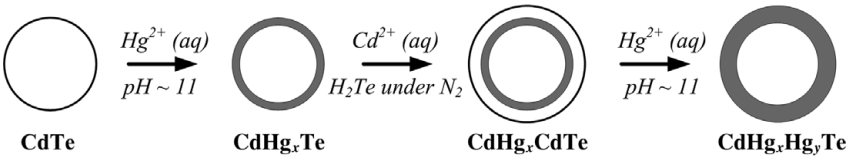


Figure 2.7 Schematic of the idealized synthetic route for obtaining $Cd_xHg_{1-x}Te$ NCs. Reproduced with permission from [69]. Copyright 2000, Elsevier.

applied in the preparation of CdHgTe nanorods using CdTe nanorods as a template [47]. It was assumed that the redistribution of mercury and cadmium ions in the growing QDs leads to the formation of $Cd_xHg_{1-x}Te$ alloys rather than to discretely layered NCs. The shell formation is more obvious in the hybrid approach, when CdTe or CdHgTe particles were transferred from water to organics with the subsequent coating with an ZnS shell employing an organometallic route yielding small-diameter, highly NIR-luminescent NCs [44]. It should be noted that water strongly absorbs in the NIR and IR spectral region starting from approx. 1150 nm, obscuring the luminescence of the samples [22]. Therefore, solvents with lower absorption have to be used to acquire PL spectra (e.g., D_2O) or alternatively measurements have to be performed on dried NC films.

The incorporation method is limited in terms of the achievable spectral position of the PL maximum, i.e., the tuneability of the PL band. The ultimate value achievable with this synthesis is 1100 nm for the PL maximum and 40% for the PLQY of the corresponding NCs. The newly developed facile one-pot synthesis provides a wide range of alloyed TGA stabilized $Cd_xHg_{1-x}Te$ NC batches having a strong PL, in the spectral range 640–1600 nm with a PLQY of up to 60% [22]. The recipe is very similar to that for the synthesis of pure CdTe and includes partial replacement of the Cd salt by an Hg precursor. In contrast to the incorporation technique, the nucleation and growth of alloyed NCs using the addition of only a small concentration of the Hg precursor leads to a significant decrease of the band gap and correspondingly to a shift of the PL to longer wavelengths. Here we would like to bring the attention of the reader to the necessity of reconsidering the PLQYs of NIR-emitting samples measured using IR-26 as the standard dye. Its QY has been re-examined and revealed to be 0.05% (in 1,2-dichloroethane), which is an order of magnitude lower than the previously reported value [70]. Therefore, PLQYs may have been previously overestimated by a factor of ~10.

Alloying via the replacement of Te ions in the CdTe crystal lattice by another anion is another method of band gap engineering. Analogous to the CdHgTe NC preparation, the incorporation technique has been applied for the synthesis of alloyed L-cysteine capped CdSeTe and CdSeTe/ZnS particles using CdTe as the initial material [71, 72]. Although CdSe possesses a wider band gap than CdTe (1.74 eV for the wurtzite structure [49]), the alloyed QDs demonstrate a nonlinear dependence of the band gap on their composition, called the optical bowing effect, with the optical band gap decreasing in alloyed particles compared with CdTe NCs of the same size, enabling a shift the PL up to 814 nm [71]. ZnS shell coating ensures a high PLQY (70%) of the resulting core/shell particles [72]. Piven *et al.* developed a one-pot synthesis for alloyed CdSeTe/TGA and CdSTe NCs using

simultaneous injection of precursor solutions [20]. In this case the emission efficiency is approximately one order of magnitude lower than that for thiol-capped CdTe NCs, this is determined by the different energetics of the thiol-related trap surface states for CdTe and CdSe serving as nonradiative channels (see below).

2.2.6 CdSe, CdSe/CdS NCs

Another member of the Cd chalcogenide group is CdSe. Whereas the organometallic synthesis of this material in nanoparticulate form is very well developed, there are only a few examples of CdSe NCs obtained by the aqueous approach. The main reason is that CdSe capped with various thiols usually possesses only weak trap related emission [13]. As was explained by Wuister *et al.*, hole trapping on a thiol molecule is responsible for exciton emission quenching [73]. This process is enabled by a favorable position of the thiol redox energy level within the CdSe band gap, i.e., it is situated at a higher energy than the top of the valence band of CdSe, unlike CdTe, which has a valence band above the redox energy of most thiols. Nevertheless, successful aqueous synthesis of highly luminescent CdSe NCs has been reported [11, 12]. A PLQY of 40% was achieved in the synthesis of CdSe NCs employing MPA as a stabilizer and a hydrazine hydrate–Se complex as a Se source, providing size control of the particles in the range 1.6–3.4 nm and emission covering a wide range from blue to red [12].

Analogously to the photoactivation of the PL of ZnSe and CdTe by their post-preparative treatment, results were obtained using citrate capped CdSe NCs. Ambient light treatment of CdSe/CdS core/shell NCs synthesized under microwave irradiation either in solution or in solid multilayer films over several days resulted in drastic QY enhancement from 0.5–2% up to 25–45% [74]. Application of laser illumination along with a common heat treatment in the synthesis of citrate capped CdSe and CdSe/CdS instead of microwave irradiation has resulted in stable particles in the size range 3.7–6.3 nm, emitting from 560 to 615 nm with an ultimate QY of 60% [40].

2.2.7 HgX and PbX NCs

To the best of our knowledge, HgTe and PbS are the only narrow band gap semiconductor materials successfully prepared in nanoparticulate form by the aqueous approach thus far. Here we note that bulk Hg chalcogenides are often ascribed to semimetals since they exhibit zero band gaps. High reactivity of metal ions towards their chalcogen counterparts is the main reason for their poor colloidal stability, which strongly affects application of these materials. Typically, the aqueous synthesis of both HgTe and PbS NCs is carried out at room temperature by the simple mixing of metal salts with the corresponding chalcogen sources ($H_2Te(Se)$ or $NaHTe(Se)$, Na_2S) in the presence of thiols. Particles obtained in such a fashion proceed to grow and coalesce when stored even at quite low temperatures and after purification.

NIR and IR emitting aqueous semiconductor NCs have great potential for application as optical amplifiers for telecommunication systems based on silica fibre technology. Conventional silica fibres possess optimal low-loss transmission windows (so called

telecommunication windows) at around 1.3 and 1.55 μm [68]. Other applications are biolabelling [42, 75], electronics [76, 77] and optoelectronics [64], photovoltaics [76, 78], and nanophotonics [79].

2.2.7.1 HgX NCs

Aqueous synthesis is the only successful colloidal approach for HgTe preparation, since the organometallic method suffers from either high toxicity of the mercury precursors (e.g., dimethylmercury) or severe difficulty in controlling the growth, especially at higher temperatures [44]. As was mentioned in the previous subsection, the first reports of a synthesis of HgTe NCs were published by Rogach, Harrison and co-workers, who employed $Hg(ClO_4)_2$and H_2Te as initial precursors in the presence of TG, which acts as a stabilizer [16, 43]. The particles obtained had a broad size distribution which could be narrowed by size-selective precipitation; their PL covered a wide spectral region, from approx. 900 nm to 2000 nm [21]. HgTe NCs with a mean particle size of 3.5 nm show an exceptionally high QY of around 50%. HgS and HgSe colloids prepared using the same synthesis method exhibited even lower thermostability than HgTe, with the PL centered at 1 μm and a PLQY of 0.5% [80]. To increase the stability of these materials, protection and passivation of the mercury chalcogenide core with a CdS layer were proposed [43, 80].

Another strategy to improve stability is encapsulation into some inert matrix, e.g., a polymer. Thus, LbL assembly of HgTe QDs with a polyelectrolyte allowed the fabrication of a thin-film hybrid polymer/NC LED [68]. A composite polydiallyldimethylammonium chloride (PDDA)/HgTe NC film deposited on indium tin oxide (ITO) coated glass employed as a substrate/bottom electrode with an evaporated aluminum top electrode above the LbL film emits IR light when pumped electrically, albeit with rather low quantum efficiency (~0.001%). This low quantum efficiency is attributed largely to the poor carrier-transport properties of the insulating PDDA. Koktysh *et al.* proposed the device architecture shown in Figure 2.8, which employs methyl-substituted ladder-type poly(paraphenylene) (MeLPPP) as a host matrix and HgTe NCs transferred from water into toluene which formed a homogeneous coating with a thickness of 100–150 nm on ITO glass [64].

Aqueous HgTe synthesis was further improved by Kovalenko and co-workers, who extended the size range of the NCs up to 12 nm and the corresponding PL up to 4 μm (Figure 2.9) [81]. Their technique consisted of a two-step growth of the particles: first, reaction and nucleation with growth at room temperature leading to 3–4 nm NCs; second, heating at 75–80 °C yielding larger particles with controllable sizes in the range of 4–12 nm with subsequent transfer of the obtained HgTe from water to nonpolar organic solvents using dodecanethiol for ligand exchange. It is significant that the PLQY of these NCs gradually decreased with increasing size.

2.2.7.2 PbX NCs

As in the case of HgTe, thiols were successfully used for stabilization of PbS NCs [17–19]. The best results in terms of stability of particles and their optical properties were achieved employing a mixture of two ligands: TG and dithioglycerol (DTG) [18, 19].

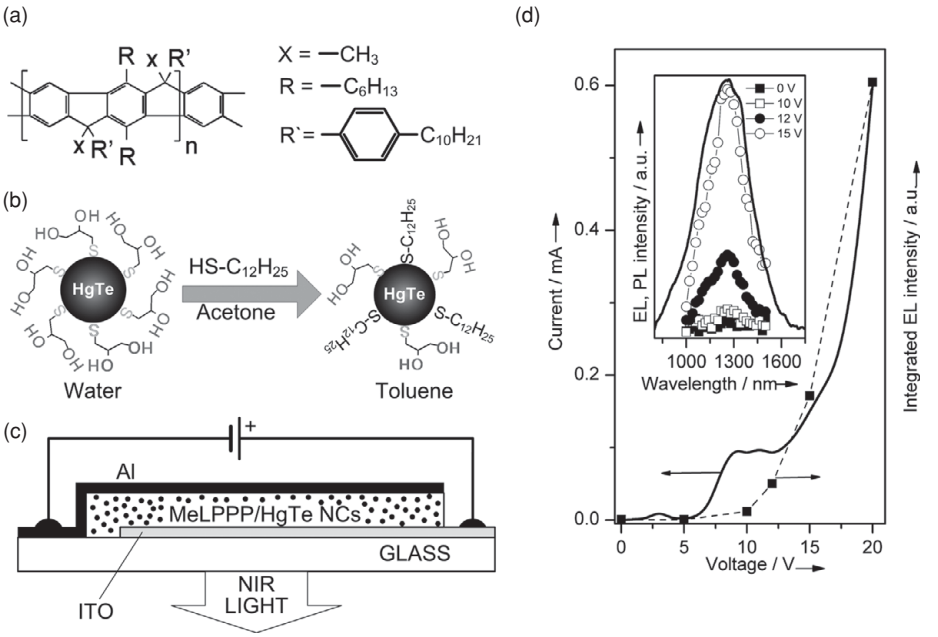


Figure 2.8 (a) Structural formula of MeLPPP. (b) Transfer of aqueous TG-capped HgTe NCs to toluene. (c) Representation of the MeLPPP/HgTe NC device. (d) Current–voltage (—) and integrated electroluminescence (EL) intensity–voltage (- -■- -) traces of the MeLPPP/HgTe NC device. The inset in (d) shows EL spectra of the MeLPPP/HgTe NC device taken at different voltages in comparison with a PL spectrum of HgTe NCs in a composite MeLPPP/HgTe film. Reproduced with permission from [64]. Copyright 2004, WILEY VCH Verlag GmbH & Co. KGaA.

Variation of the Pb^{2+}/S^{2-}/TG/DTG molar ratio provides an opportunity for controlling the NCs' properties, e.g., decreasing the Pb^{2+}/S^{2-} initial ratio allows the PL maxima to be tuned from approx. 1050 nm to 1350 nm (Figure 2.10). The optimized procedure yields PbS colloids stable to aggregation for 2–3 months, with an average size of 4±1 nm and a PLQY of 7–10% [18]. It should be noted that using neither TG nor DTG as a sole ligand leads to sufficient stability of the NCs. The same tendency was observed in the synthesis of a PbTe NC colloid employing TG as a stabilizer [80]. However, dihydrolipoic acid, which is a bidentate ligand, provides quite stable PbS colloids [17]. As an example of a possible application, an NIR emitting LED with a turn-on voltage of 4–5 V was fabricated on the basis of the conducting polymer poly(p-phenylenevinylene) and PbS NCs [19].

2.3 Assemblies and functional architectures of NCs

Assemblies and functional architectures of nanocrystalline materials have been receiving increased interest. Colloidal semiconductor and metal NCs are used to build artificial

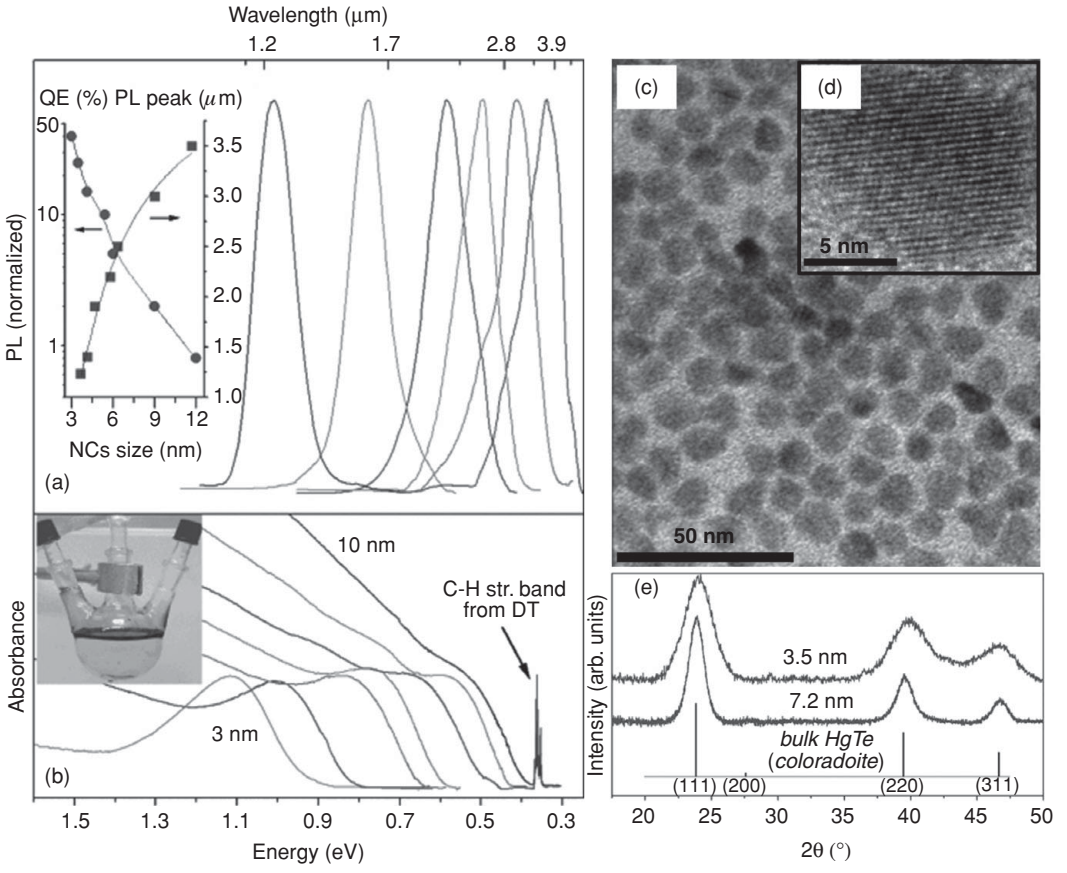


Figure 2.9 (a) PL and (b) absorption spectra of dodecanethiol-capped HgTe NCs. The insets in (a) shows the size dependence of the PL peaks with the corresponding quantum efficiencies and that in (b) illustrates the phase transfer completeness. (c) TEM and (d) high-resolution TEM images of HgTe NCs emitting at 3 μm. (e) XRD patterns of 3.5 and 7.2 nm HgTe NCs. Adapted with permission from [81]. Copyright 2006, American Chemical Society.

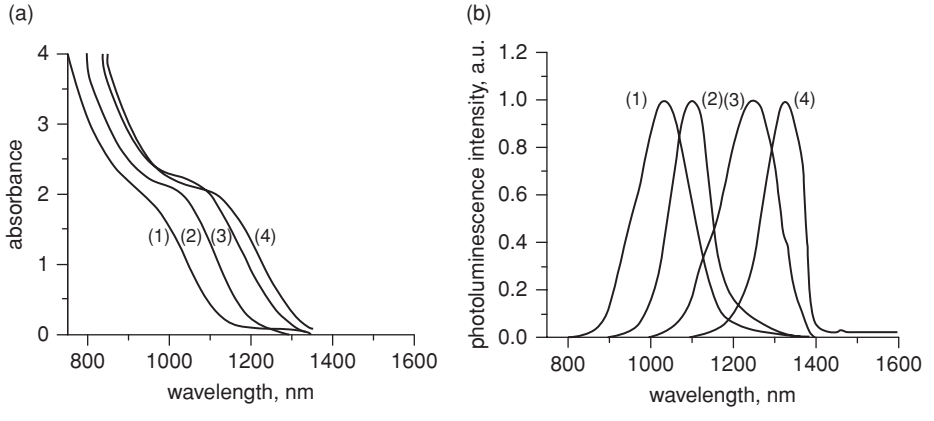


Figure 2.10 (a) Absorbance and (b) PL spectra of PbS NCs of different sizes, obtained by changing the Pb/S molar ratio: (1) 1/0.3, (2) 1/0.4, (3) 1/0.5, (4) 1/0.7. Molar ratio of Pb/TG/DTG = 1/6/2. Reproduced with permission from [19]. Copyright 2004, WILEY VCH Verlag GmbH & Co. KGaA.

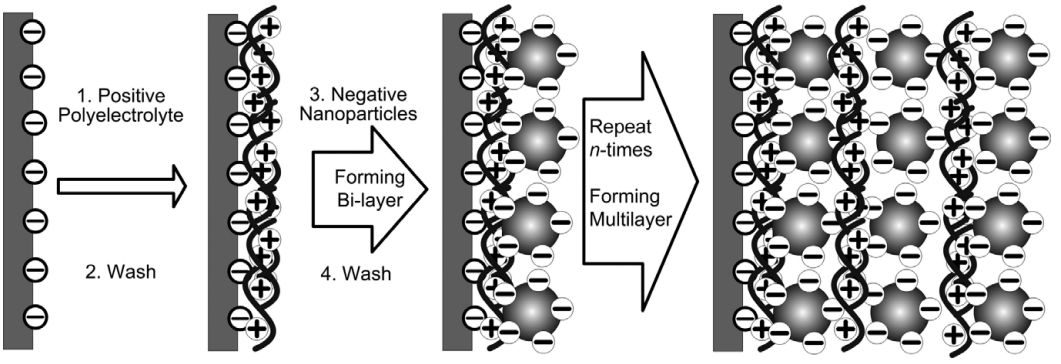


Figure 2.11 Schematic of the LbL technique as applied to assembling positively charged polyelectrolyte with negatively charged NCs.

molecules and solids [82]. These arrays and superlattices offer new perspectives for the application of nanoparticles, e.g., in optoelectronic devices. Various approaches towards assembling NCs are known. One-dimensional oriented attachment results in the formation of necklace-like nanowire structures [83]. Three-dimensional nanostructures of semiconductor nanoparticles have been built up via self organization [84], gelation [85], and crystallization [86, 87]. Other main routes towards ordered structures of NCs include their covalent binding with and without linker molecules [88] and electric field-directed [89] and electrostatic assemblies [90]. These efforts have a direct correlation to investigations in the fields of the covalent coupling of nanoparticles to biomolecules and surface functionalization of NCs [91]. In this section advances in assembling the colloidal thiol-capped NCs for possible applications in nanophotonics and optoelectronics are discussed.

2.3.1 LbL assembly technique

Multicomponent thin films consisting of functional molecules and/or NCs may be formed by applying the LbL technique, which was originally introduced for the assembly of polymer electrolytes [92] and small particles [93] and which was later adapted for the deposition of charged NCs on both flat [94] and curved surfaces [95, 96]. The formation of monolayers of deposited materials is based on the electrostatic interaction between the NCs and the surface (Figure 2.11). Alternating the sign of the charges of the species to be deposited allows the growth of thick (up to hundreds of nanometers) multilayers, while the introduction of new components in one of the layers yields the opportunity of virtually unlimited but controllable variations of multistructure compositions [97, 98]. The application of this method to the modification of artificial opals resulted in intrinsically light emitting photonic crystals which have been successfully used for the investigation of photonic confinement phenomena [99–101]. The thickness of the LbL film depends linearly on the number of deposited NC/polyelectrolyte “bilayers”.

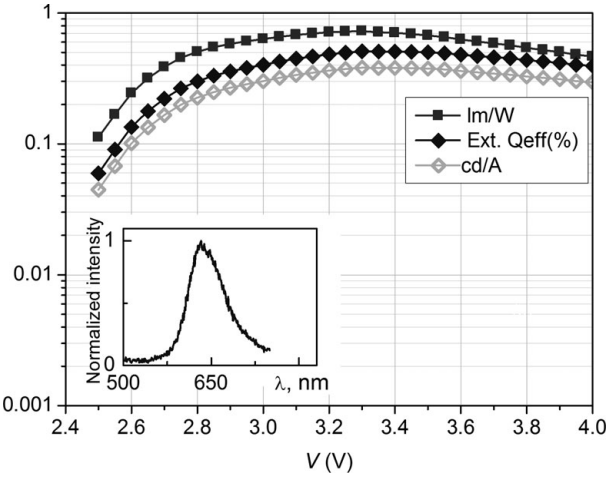


Figure 2.12 Efficiency values for the CdTe/PDDA LED. The inset shows the emission spectrum of the device. Reproduced with permission from [108]. Copyright 2007, American Institute of Physics.

Consequently, a linear dependence of the optical absorption on the number of bilayers was observed [15, 102]. Quick nonlinear formation of relatively less uniform films may be achieved by the so-called exponential LbL assembly, which has been successfully demonstrated for various organic species [103] and inorganic nanosheets [104]. Despite its promise this approach has still not been realized for semiconductor NCs. LbL-like assembly may also be implemented without utilization of polyelectrolyte, as was demonstrated for cysteamine (CA) (positively charged) and TGA (negatively charged) stabilized CdTe NCs. However, it has been shown that the formation of only one bilayer of oppositely charged NCs is achievable without using polyelectrolytes [105]. This method, which is also called direct electrostatic assembly of nanoparticles, was also successfully utilized for the fabrication of photodetectors [106].

Probably, the most impressive example of the application of the LbL technique is the fabrication of LEDs as has been successfully demonstrated by several groups [94, 107, 108] and reviewed in [28]. In a typical device, made of alternating layers of CdTe NCs and PDDA, electroluminescence started at 2.5 V and reached a maximum at 3.3 V, with a peak radiated power of 141 nW corresponding to an external quantum efficiency of 0.51%. The luminous efficiencies of the red-emitting LED shown in Figure 2.12 reached 0.4 cd A^{-1} and 0.81 Lm W^{-1} [108]. In the case of patterned conducting substrates the application of an electric field enables the acceleration or, if necessary, inhibition of the LbL assembly [109]; this has been successfully utilized for the selective fabrication of green and red emitting micro-LEDs with 50 μm spatial resolution [89].

A similar technique has also been applied to the fabrication of all-inorganic LEDs based on CdTe NCs assembled with layered double hydroxide (LDH), a hydrotalcite-like material (Figure 2.13) [110]. The LED was fabricated at room temperature in ambient conditions and possessed high thermal stability, operating continuously up to 90 °C. A

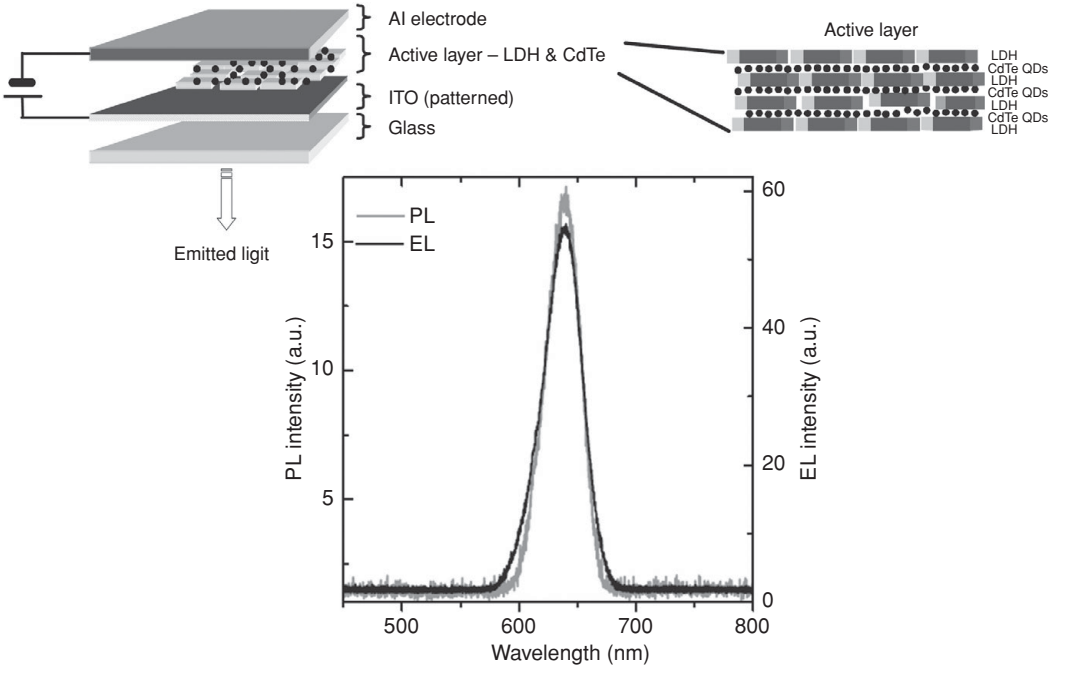


Figure 2.13 Schematic of the architecture of the all-inorganic LED made by alternating inorganic nanosheets and CdTe NCs (top); PL peak of aqueous CdTe NCs compared to the electroluminescence peak of the device (bottom). Adapted with permission from [110]. Copyright 2010, WILEY VCH Verlag GmbH & Co. KGaA.

maximum efficiency of 0.031%, with respect to the theoretical maximum of 683.002 Lm W^{-1} at 0.12 A cm^{-2} (6.44 V) was obtained, which corresponds to a luminance of 232.7 Cd m^{-2}. The device was targeted at the automotive industry, where relatively rigid operating conditions limit the applicability of organic or hybrid LEDs.

The building of LbL films from NCs of two different sizes allows controllable design of Förster resonance energy transfer (FRET) based devices. FRET rates as high as 4 ns^{-1} were observed between NCs separated by one polyelectrolyte monolayer [111]. By utilizing direct electrostatic assembly (without polyelectrolyte) the strong electrostatic interaction between oppositely charged donor and acceptor NCs allows the observation of an increase in the FRET rates of up to 14 ns^{-1} [105]. The phenomenon of FRET in layered NC structures has been utilized for the optimization of energy scavenging systems [30] as well as for the fine tuning of the chromacity coordinates of NC composites [29]. As shown in Figure 2.14 varying the distance between layers of differently sized NCs influences the relative intensity of corresponding emission bands and results in controllable tuning of chromacity coordinates. The use of the LbL technique for the formation of semiconductor and noble metal nanoparticle layers with controllable interlayer distance allowed the observation of off-resonance surface plasmon enhancement of the band-gap fluorescence of NCs [112].

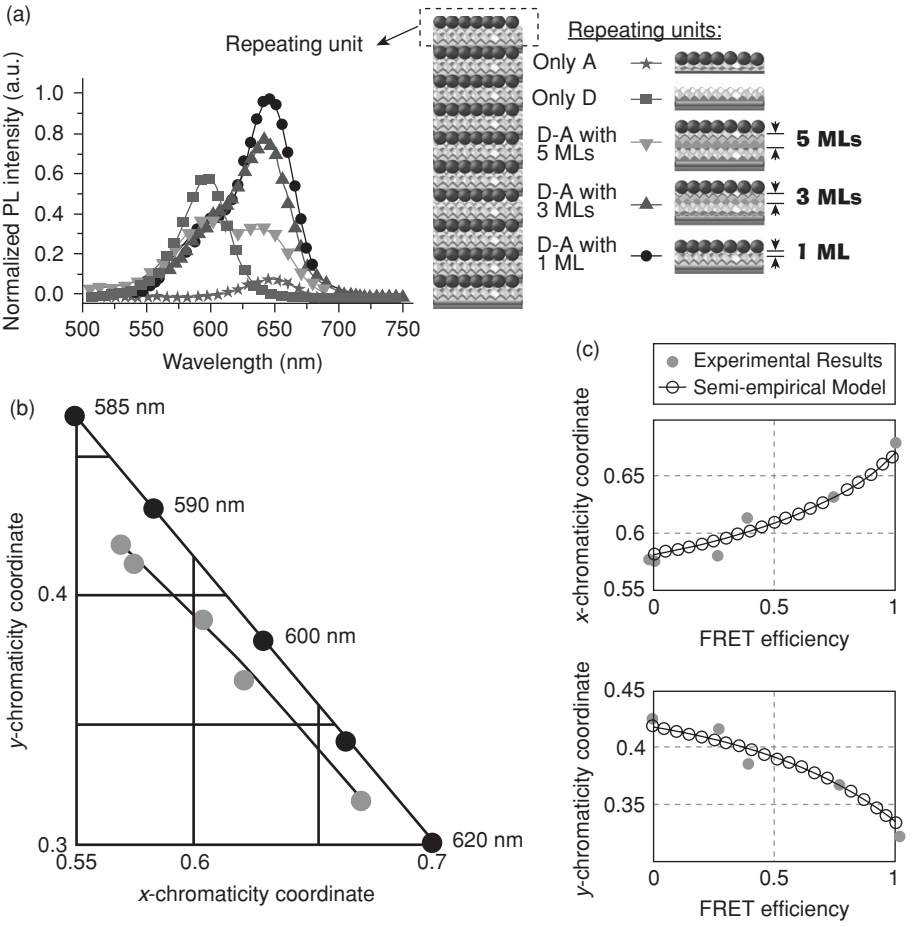


Figure 2.14 (a) PL spectra of donor, acceptor, and controllably spaced (1 monolayer (ML) polyelectrolyte = 1.0 nm, 3 ML = 2.2 nm, and 5 ML = 3.4 nm) donor–acceptor samples. (b) CIE chromaticity diagram for the LbL spaced nanocrystal samples. (c) Comparison of semiempirical analytical model simulation and experimental results for color tuning based on FRET efficiency. Adapted with permission from [29]. Copyright 2009, American Institute of Physics.

2.3.2 Assembly of NCs on micro- and nano-beads

The LbL assembly of NCs on the surface of polymer (polystyrene (PS), polymethylmetacrylate (PMMA), melamine formaldehyde (MF), etc.) or silica beads opens up an opportunity to create submicrometer-sized objects exhibiting the properties of their nano-sized components [113, 114]. In this case the LbL assembly can be done by suspending the beads in solutions of the corresponding layer component and subsequent centrifugation. The compositions of the polyelectrolyte and NC solutions are generally the same as for the procedures described above. Repetitive centrifugation from pure water suspensions is used to wash the beads and remove excessive reactants. The modified beads retain the PL properties of the NCs used with a slight red shift of the PL

maximum due to energy transfer from the smaller to the larger NCs in the assembled surface film [96, 115]. The comparatively large size of the beads allows their manipulation by optical tweezers or their use when mounted on the tip at the end of an optical fibre. Thus, the beads can be used as subwavelength-sized light sources for photonic applications [79] or for the selective amplification of a signal in scanning near-field optical microscopy (SNOM)[116].

Larger LbL modified beads (> 2 μm) show an efficient coupling of the light emitted by the NCs with the whispering gallery modes (WGM) of spherical microresonators [117, 118]. Moreover, optical coupling between two adjacent microresonators modified with light emitting NCs allowed observation of photonic molecule phenomena, i.e., transition from individual (atom-like) to collective (molecule-like) photonic states [118, 119].

The use of beads made from materials which can be dissolved after LbL deposition of the polyelectrolytes (such as MF, $MnCO_3$, etc.) allows the formation of hollow polyelectrolyte/NCs shells [75, 120, 121]. By proper choice of assembled NCs the shells may be coded by different emission colors and color combinations, or may be simultaneously magnetic (due to assembled Fe_3O_4 NCs) and light emitting (due to CdTe NCs) [121]. The shells are promising as microcapsules for drug delivery systems where the PL and magnetic properties of inserted NCs can be used for the coding and monitoring of the delivery process [122].

Alternatively, the coating of microspheres can be performed through the solvent controlled precipitation of NCs [123]. The aggregation of NCs onto colloidal beads is induced by the solvent–nonsolvent pair precipitation technique which is normally successfully used to separate semiconductor NCs by size. Relatively large (from several tens of nanometers to several tens of micrometers) colloidal beads statistically harvest aggregated NCs, which consequently leads to the formation of a shell of NCs on a bead. Moreover, the thickness of the shell can be to some extent controlled through the proper choice of the concentration ratio of the beads and the NC species. This method, in comparison to the LbL technique, has the advantage of being a quick one-step procedure for the formation of relatively thick shells.

2.3.3 Covalent coupling of NCs

While covalent coupling between thiol-capped NCs aimed at creating molecular like NC species (NCs dimers, trimers, etc.) is still in its infancy, carbodiimide chemistry may well be applied to the coupling of NCs to pre-treated macrosurfaces. Accordingly, appropriate fractions of CdTe NCs have been used for conjugation with various substrates, such as glass, silica, and silicon, with different surface shapes [124]. The method is based on the binding of acid-stabilized NCs to aminated surfaces with the aid of carbodiimide as a mediator and is not limited to bulk substrates but is of more generality as can be seen from successful attempts to coat glass spheres or silica beads with CdTe NCs [124].

An approach for immobilizing CdTe NCs on thin, fluid films using poly(acrylic acid) (PAA) polymer chains tethered by one end to an underlying substrate in a polymer brush configuration has been demonstrated [125]. The protocol involves covalent bonding similar to that described above, but between amino groups present on the surface of

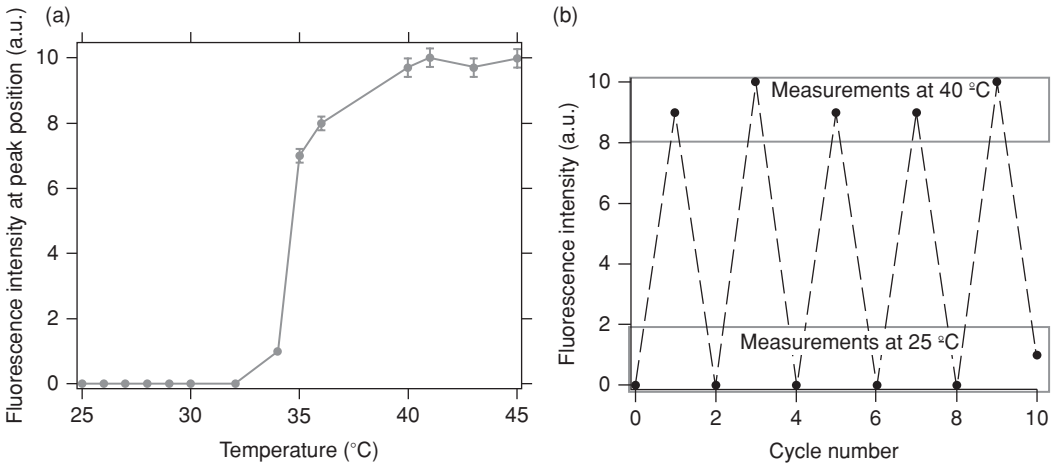


Figure 2.15 (a) PL intensity of the PNIPAM–CdTe microgels at 620 nm as a function of temperature. (b) PL intensity measured during repeated heating (40 °C) and cooling (25 °C) cycles of the microgels. Adapted with permission from [127]. Copyright 2008, American Chemical Society.

the CdTe NCs (stabilized by cysteamine (CA)) and the carboxylic groups of PAA polymer chains. The thickness of the PAA polymer brush employed (ca. 4.5 nm) was comparable to the nanoparticle size. Exploitation of such a thin polymer brush was found to suppress nanoparticle aggregation and facilitate complete surface coverage [125, 126]. As a fine example of the practical application of covalently bound assemblies, the thermosensitive poly(N-isopropyl acrylamide) (PNIPAM) microgel linked to CA-capped CdTe NCs should be mentioned. Due to the temperature dependent transition between collapsed and swollen stages of the microgel (ca. 35 °C) the composite shows pronounced and reversible quenching/antiquenching fluorescence behavior (Figure 2.15) [127]. Such optical microsensors may be utilized for the monitoring of temperature changes in biological systems or in microfluidics.

2.3.4 Controllable aggregation

Electrostatic interactions as well as covalent linking between positively charged CA stabilized NCs and negatively charged TGA stabilized CdTe NCs have been utilized for the formation of closely packed solids [128, 129]. The CdTe(CA)–CdTe(TGA) coupling was dictated by the surfactant spacer, ranging between 0.93 and 1.14 nm, and by electrostatic and covalent interactions, enabling a FRET process among the NCs. It was demonstrated that covalent bonding allows a closer surface-to-surface distance and thus quicker energy transport (in the region of 1 ns^{-1}) from smaller (donors) to larger (acceptors) NCs in assemblies [128].

Divalent positively charged Ca^{2+} ions can act as electrostatic chelating linkers able to induce clustering of CdTe NCs through coordination to the negatively charged carboxylic groups of TGA or MPA ligands [130]. Moreover, the addition of sodium carbonate,

which binds Ca^{2+}, reverses the clustering process. An efficient FRET was found to be responsible for changes in the emission spectra and the luminescence decay times of binary- and ternary-sized CdTe NC clusters bound by Ca^{2+} ions.

2.3.5 Nanowires and nanosheets

As has been shown by several groups, the gentle removal of thiol surfactant [131] or the partial destabilization of a colloidal solution by the addition of phosphate buffer at physiological concentrations [132] causes a spontaneous assembly of CdTe NCs into brightly emitting nanowires. Moreover, the latter method allowed the in-situ observation of the process of nanowire formation under a confocal microscope. Due to this observation the proper conditions for a quick and controllable assembly were established [132]. The PL maximum of the CdTe nanowires is red-shifted by 10 nm in comparison to the initial NC colloid, which points towards a decrease of the electronic confinement in these one-dimensional objects [132]. The wires were also found as a by-product of ageing CdTe NC solutions. This wire formation can be the result of slow degradation of the stabilizing thiols. Alternatively, strongly emitting branched one-dimensional assemblies of CdTe NCs were also prepared by utilizing the Langmuir–Blodgett technique in combination with a soft templating method using amphiphilic molecules [133]. Self-assembled CdTe nanowires were further decorated with SiO_2, resulting in complex nanostructures named "nanocentipedes" [134]. When similar "nanocentipedes" were formed from CdTe NCs bioconjugated to CdTe nanowires and conditions of optimal distances and spectral matching were achieved, an efficient cascade energy transfer resembling the principles of biological photosynthetic systems was observed [135]. A prototype of logical nanocircuitry formed from the triangular arrangement of bioconjugated nanowires has also been demonstrated [136]. Not only wires, but also strongly emitting nanotubes may be formed if CdTe NCs are assembled on the surface of Cd-thiolate nanowires [137].

An interesting example of NC assembly is the spontaneous formation of free-floating sheets which occurs when 2-(dimethylamino)ethanethiol (DMAET) is used as the capping agent [137]. Comparative analysis of the self-assembly behavior of TGA- and DMAET-capped CdTe NCs, which form nanowires and nanosheets respectively, showed that NC shape, directional attraction, and electrostatic interactions are key parameters responsible for the anisotropy of the NC–NC interaction and the final self-assembled architectures. Surprisingly, these data show the resemblance of NC assemblies to self-ordering biological systems, such as S-layer-forming proteins [138].

2.3.6 Nanocrystal based gels and aerogels

In spite of the fact that the fabrication of aerogels, highly porous materials whose properties bridge the macro and nano dimensions,[139] has been known for metal oxides since 1931 [140], the first demonstrations of aerogels built solely from colloidal semiconductor NCs appeared only in 2005 [85, 141, 142]. In the case of thiol-capped NCs it has been shown that controllable ageing and chemical and photochemical treatment may lead to

the formation of three-dimensional networks (gelation). Photochemical treatment and metal assisted assembly have been shown to be the most controllable and reproducible methods of gel formation, allowing the pristine emission of the NCs to be preserved also in the gels [54, 142]. The formation of highly porous strongly emitting aerogels as well as their hybridization with polymers has been demonstrated [142]. A pore surface of ca. 210 m^2/g and a monolith density of less than 1/500th of corresponding bulk material have been achieved. The hybrids of the aerogels with polymers are processable using common casting or thermoplating techniques. The utilization of conducting polymers for the gel infiltration will open new possibilities for fabrication, depending on design, of highly efficient hybrid LEDs or energy harvesting systems. In such composites percolated polymer and nanocrystalline phases may allow efficient separated charge carrier transport, while a huge interfacial area may ideally serve for carrier separation or recombination, depending on design. The high porosity of the light-emitting aerogels may be utilized for optical sensing and photocatalysis.

2.4 Conclusions and outlook

Aqueous colloidal synthesis has yielded various nanoparticulate semiconductor II–VI and IV–VI materials, whose main representatives were reviewed in the first part of this chapter. The synthetic methods developed so far allow the fine tuning of band gap energies of resulting nanoparticles via size and composition control, thus providing a wide variety of electronic and optical properties. Strongly emitting thiol-capped NCs with a flexible surface chemistry that is determined by the choice of functional ligands can be processed by various techniques based on compounding with polymers, self-organization, electrostatic interactions, covalent linking, etc.

In spite of this, most of the examples of application by means of assembly and design of functional architectures reported in literature and discussed in the second part of the chapter have been obtained by using CdTe NCs. Thus, potential applications in optoelectronics cover LEDs, microarrays of light-emitting pixels, energy harvesting nanostructures and photosensitive films. This is closely connected to photonic applications in which these assemblies play the role of subwavelength emitters, tunable light sources coupled to optical modes of photonic crystals and heterocrystals, spherical microresonators, photonic molecules, and waveguides. Biology related applications include temperature sensitive nanoassemblies, conjugates with “smart” polymers, luminescent coding of multifunctional microbeads, and microcapsules suitable for drug delivery systems. The ability of NCs to interact with neighboring nanoentities gives rise to the assembly of FRET based and nanoplasmonic devices as well as various sensors.

Indeed CdTe NCs are the most successful and prominent members of thiol-capped family. Nevertheless, it is very important to stress that the developed assembly methods are versatile and are also applicable to other types of thiol-capped NCs. Moreover, most of the NCs synthesized in organic media (e.g., CdSe NCs and nanorods, their core/shell combinations, lead chalcogenides, etc.) may undergo surface exchange of the capping agent to short chain thiols. As our experience shows, such “secondary” thiol-capped

NCs are compatible with most of the assembly methods described above. Taking into account the variety of materials available from both aqueous and organic syntheses, each of which has unique physico-chemical properties, the methods described above have literally unlimited applicability in nanotechnology.

References

1 N. Gaponik, D. V. Talapin, A. L. Rogach, *et al.*, Thiol-capping of CdTe nanocrystals: an alternative to organometallic synthetic routes. *Journal of Physical Chemistry B*, **106** (2002), 7177–7185.

2 N. Gaponik, A. L. Rogach, Thiol-capped CdTe nanocrystals: progress and perspectives of the related research fields. *Physical Chemistry Chemical Physics*, **12** (2010), 8685–8693.

3 A. Henglein, Small-particle research – physicochemical properties of extremely small colloidal metal and semiconductor particles. *Chemical Reviews*, **89** (1989), 1861–73.

4 A. Eychmüller, Synthesis and characterization of II–VI nanoparticles. In *Nanoparticles: From Theory to Application*, ed. G. Schmid, pp. 50–79. Weinheim: WILEY-VCH Verlag GmbH & Co. KGaA, 2004.

5 N. Gaponik, S. G. Hickey, D. Dorfs, A. L. Rogach, A. Eychmüller, Progress in the light emission of colloidal semiconductor nanocrystals. *Small*, **6** (2010), 1364–78.

6 N. Gaponik, A. L. Rogach, Aqueous synthesis of semiconductor nanocrystals. In *Semiconductor Nanocrystal Quantum Dots: Synthesis, Assembly, Spectroscopy and Applications*, ed. A. L. Rogach, pp. 73–100. Vienna: Springer, 2008.

7 H. Weller. Colloidal semiconductor Q-particles: chemistry in the transition region between solid state and molecules. *Angewandte Chemie International Edition*, **32** (1993), 41–53.

8 A. L. Rogach, T. Franzl, T. A. Klar, *et al.*, Aqueous synthesis of thiol-capped CdTe nanocrystals: state-of-the-art. *Journal of Physical Chemistry C*, **111** (2007), 14628–14637.

9 A. L. Rogach, L. Katsikas, A. Kornowski, *et al.*, Synthesis and characterization of thiol-stabilized CdTe nanocrystals. *Berichte der Bunsengesellschaft für Physikalische Chemie*, **100** (1996), 1772–1778.

10 T. Rajh, O. I. Mićić, A. J. Nozik, Synthesis and characterization of surface-modified colloidal cadmium telluride quantum dots. *Journal of Physical Chemistry*, **97** (1993), 11999–12003.

11 M. Bäumle, D. Stamou, J.-M. Segura, R. Hovius, H. Vogel, Highly fluorescent streptavidin-coated CdSe nanoparticles: preparation in water, characterization, and micropatterning. *Langmuir*, **20** (2004), 3828–31.

12 M. N. Kalasad, M. K. Rabinal, B. G. Mulimani, Ambient synthesis and characterization of high-quality CdSe quantum dots by an aqueous route. *Langmuir*, **25** (2009), 12729–35.

13 A. L. Rogach, A. Kornowski, M. Gao, A. Eychmüller, H. Weller, Synthesis and characterization of a size series of extremely small thiol-stabilized CdSe nanocrystals. *Journal of Physical Chemistry B*, **103** (1999), 3065–3069.

14 Y. Zheng, Z. Yang, J. Y. Ying, Aqueous synthesis of glutathione-capped ZnSe and $Zn_{1-x}Cd_xSe$ alloyed quantum dots. *Advanced Materials*, **19** (2007), 1475–1479.

15 A. Shavel, N. Gaponik, A. Eychmüller, Efficient UV-blue photoluminescing thiol-stabilized water-soluble alloyed ZnSe(S) nanocrystals. *Journal of Physical Chemistry B*, **108** (2004), 5905–5908.

16 A. Rogach, S. Kershaw, M. Burt, *et al.*, Colloidally prepared HgTe nanocrystals with strong room-temperature infrared luminescence. *Advanced Materials*, **11** (1999), 552–555.
17 D. Deng, W. Zhang, X. Chen, *et al.*, Facile synthesis of high-quality, water-soluble, near-infrared-emitting PbS quantum dots. *European Journal of Inorganic Chemistry*, **23** (2009), 3440–3446.
18 X. S. Zhao, I. Gorelikov, S. Musikhin, *et al.*, Synthesis and optical properties of thiol-stabilized PbS nanocrystals. *Langmuir*, **21** (2005), 1086–1090.
19 L. Bakueva, I. Gorelikov, S. Musikhin, *et al.*, PbS quantum dots with stable efficient luminescence in the near-IR spectral range. *Advanced Materials*, **16** (2004), 926–929.
20 N. Piven, A. S. Susha, M. Döblinger, A. L. Rogach, Aqueous synthesis of alloyed $CdSe_xTe_{1-x}$ nanocrystals. *Journal of Physical Chemistry C*, **112** (2008), 15253–15259.
21 A. L. Rogach, M. T. Harrison, S. V. Kershaw, *et al.*, Colloidally prepared CdHgTe and HgTe quantum dots with strong near-infrared luminescence. *Physica Status Solidi B*, **224** (2001), 153–158.
22 V. Lesnyak, A. Lutich, N. Gaponik, *et al.*, One-pot aqueous synthesis of high quality near infrared emitting $Cd_{1-x}Hg_xTe$ nanocrystals. *Journal of Materials Chemistry*, **19** (2009), 9147–9152.
23 V. Lesnyak, A. Plotnikov, N. Gaponik, A. Eychmüller, Toward efficient blue-emitting thiol-capped $Zn_{1-x}Cd_xSe$ nanocrystals. *Journal of Materials Chemistry*, **18** (2008), 5142–5146.
24 F.-C. Liu, T.-L. Cheng, C.-C. Shen, W.-L. Tseng, M. Y. Chiang, Synthesis of cysteine-capped $Zn_xCd_{1-x}Se$ alloyed quantum dots emitting in the blue-green spectral range. *Langmuir*, **24** (2008), 2162–2167.
25 F.-C. Liu, Y.-M. Chen, J.-H. Lin, W.-L. Tseng, Synthesis of highly fluorescent glutathione-capped $Zn_xHg_{1-x}Se$ quantum dot and its application for sensing copper ion. *J. Colloid and Interface Science*, **337** (2009), 414–419.
26 V. Lesnyak, A. Dubavik, A. Plotnikov, N. Gaponik, A. Eychmüller, One-step aqueous synthesis of blue-emitting glutathione-capped $ZnSe_{1-x}Te_x$ alloyed nanocrystals. *Chemical Communications*, **46** (2010), 886–888.
27 M. Green. The nature of quantum dot capping ligands. *Journal of Materials Chemistry*, **20** (2010), 5797–5809.
28 A. L. Rogach, N. Gaponik, J. M. Lupton, *et al.*, Light-emitting diodes with semiconductor nanocrystals. *Angewandte Chemie International Edition*, **47** (2008), 6538–6549.
29 N. Cicek, S. Nizamoglu, T. Ozel, *et al.*, Structural tuning of color chromaticity through nonradiative energy transfer by interspacing CdTe nanocrystal monolayers. *Applied Physics Letters*, **94** (2009), 061105.
30 T. Franzl, T. A. Klar, S. Schietinger, A. L. Rogach, J. Feldmann, Exciton recycling in graded gap nanocrystal structures. *Nano Letters*, **4** (2004), 1599–1603.
31 A. S. Susha, A. M. Javier, W. J. Parak, A. L. Rogach, Luminescent CdTe nanocrystals as ion probes and pH sensors in aqueous solutions *Colloids and Surfaces A*, **281** (2006), 40–43.
32 I. Nabiev, S. Mitchell, A. Davies, *et al.*, Nonfunctionalized nanocrystals can exploit a cell's active transport machinery delivering them to specific nuclear and cytoplasmic compartments. *Nano Letters*, **7** (2007), 3452–3461.
33 N. Gaponik. Assemblies of thiol-capped nanocrystals as building blocks for use in nanotechnology. *Journal of Materials Chemistry*, **20** (2010), 5174–5181.
34 Y. He, L. M. Sai, H. T. Lu, *et al.*, Microwave-assisted synthesis of water-dispersed CdTe nanocrystals with high luminescent efficiency and narrow size distribution. *Chemistry of Materials*, **19** (2007), 359–365.

35 Q. Zeng, X. Kong, Y. Sun, *et al.*, Synthesis and optical properties of type II CdTe/CdS core/shell quantum dots in aqueous solution via successive ion layer adsorption and reaction. *Journal of Physical Chemistry C*, **112** (2008), 8587–8593.
36 H. Qian, X. Qiu, L. Li, J. Ren, Microwave-assisted aqueous synthesis: a rapid approach to prepare highly luminescent ZnSe(S) alloyed quantum dots. *Journal of Physical Chemistry B*, **110** (2006), 9034–9040.
37 Y. He, H. T. Lu, L. M. Sai, *et al.*, Microwave synthesis of water-dispersed CdTe/CdS/ZnS core–shell–shell quantum dots with excellent photostability and biocompatibility. *Advanced Materials*, **20** (2008), 3416–3421.
38 Z. Fang, Y. Li, H. Zhang, X. Zhong, L. Zhu, Facile synthesis of highly luminescent UV-blue-emitting ZnSe/ZnS core/shell nanocrystals in aqueous media. *Journal of Physical Chemistry C*, **113** (2009), 14145–14150.
39 Y. Wang, Z. Y. Tang, M. A. Correa-Duarte, *et al.*, Mechanism of strong luminescence photoactivation of citrate-stabilized water-soluble nanoparticles with CdSe cores. *Journal of Physical Chemistry B*, **108** (2004), 15461–15469.
40 Y.-W. Lin, M.-M. Hsieh, C.-P. Liu, H.-T. Chang, Photoassisted synthesis of CdSe and core−shell CdSe/CdS quantum dots. *Langmuir*, **21** (2005), 728–734.
41 D. Zhao, Z. He, W. H. Chan, M. M. F. Choi. Synthesis and characterization of high-quality water-soluble near-infrared-emitting CdTe/CdS quantum dots capped by N-acetyl-l-cysteine via hydrothermal method. *Journal of Physical Chemistry C*, **113** (2008), 1293–1300.
42 H. Qian, C. Dong, J. Peng, *et al.*, High-quality and water-soluble near-infrared photoluminescent CdHgTe/CdS quantum dots prepared by adjusting size and composition. *Journal of Physical Chemistry C*, **111** (2007), 16852–16857.
43 M. T. Harrison, S. V. Kershaw, A. L. Rogach, *et al.*, Wet chemical synthesis of highly luminescent HgTe/CdS core/shell nanocrystals. *Advanced Materials*, **12** (2000), 123–125.
44 J. M. Tsay, M. Pflughoefft, L. A. Bentolila, S. Weiss, Hybrid approach to the synthesis of highly luminescent CdTe/ZnS and CdHgTe/ZnS nanocrystals. *Journal of the American Chemical Society*, **126** (2004), 1926–1927.
45 C. Li, M. Ando, H. Enomoto, N. Murase, Highly luminescent water-soluble InP/ZnS nanocrystals prepared via reactive phase transfer and photochemical processing. *Journal of Physical Chemistry C*, **112** (2008), 20190–20199.
46 H. Zhang, D. Wang, H. Möhwald, Ligand-selective aqueous synthesis of one-dimensional CdTe nanostructures. *Angewandte Chemie International Edition*, **45** (2006), 748–751.
47 B. Tang, F. Yang, Y. Lin, *et al.*, Synthesis and characterization of wavelength-tunable, water-soluble, and near-infrared-emitting CdHgTe nanorods. *Chemistry of Materials*, **19** (2007), 1212–1214.
48 A. M. Smith, S. Nie, Semiconductor nanocrystals: structure, properties, and band gap engineering. *Accounts of Chemical Research*, **43** (2010), 190–200.
49 D. R. Lide, ed. *CRC Handbook of Chemistry and Physics*, 84th edn Boca Raton, FL: CRC Press, 2004.
50 U. Resch, H. Weller, A. Henglein, Photochemistry and radiation chemistry of colloidal semiconductors. 33. Chemical changes and fluorescence in CdTe and ZnTe. *Langmuir*, **5** (1989), 1015–1020.
51 P. Reiss, ZnSe based colloidal nanocrystals: synthesis, shape control, core/shell, alloy and doped systems. *New Journal of Chemistry*, **31** (2007), 1843–1852.

52 N. P. Osipovich, A. Shavel, S. K. Poznyak, N. Gaponik, A. Eychmüller, Electrochemical observation of the photoinduced formation of alloyed ZnSe(S) nanocrystals. *Journal of Physical Chemistry B*, **110** (2006), 19233–19237.
53 M. Grabolle, M. Spieles, V. Lesnyak, *et al.*, Determination of the fluorescence quantum yield of quantum dots: suitable procedures and achievable uncertainties. *Analytical Chemistry*, **81** (2009), 6285–6294.
54 V. Lesnyak, S. V. Voitekhovich, P. N. Gaponik, N. Gaponik, A. Eychmüller, CdTe nanocrystals capped with a tetrazolyl analogue of thioglycolic acid: aqueous synthesis, characterization, and metal-assisted assembly. *ACS Nano*, **4** (2010), 4090–4096.
55 Y. Zhou, M. Yang, K. Sun, Z. Tang, N. A. Kotov, Similar topological origin of chiral centers in organic and nanoscale inorganic structures: effect of stabilizer chirality on optical isomerism and growth of CdTe nanocrystals. *Journal of the American Chemical Society*, **132** (2010), 6006–6013.
56 T. Nakashima, Y. Kobayashi, T. Kawai, Optical activity and chiral memory of thiol-capped CdTe nanocrystals. *Journal of the American Chemical Society*, **131** (2009), 10342–10343.
57 S. Ho, K. Critchley, G. D. Lilly, B. Shim, N. A. Kotov, Free flow electrophoresis for the separation of CdTe nanoparticles. *Journal of Materials Chemistry*, **19** (2009), 1390–1394.
58 H. Zhang, Z. Zhou, B. Yang, M. Gao, The influence of carboxyl groups on the photoluminescence of mercaptocarboxylic acid-stabilized CdTe nanoparticles. *Journal of Physical Chemistry B*, **107** (2003), 8–13.
59 H. Bao, Y. Gong, Z. Li, M. Gao, Enhancement effect of illumination on the photoluminescence of water-soluble CdTe nanocrystals: toward highly fluorescent CdTe/CdS core-shell structure. *Chemistry of Materials*, **16** (2004), 3853–3859.
60 H. Borchert, D. V. Talapin, N. Gaponik, *et al.*, Relations between the photoluminescence efficiency of CdTe nanocrystals and their surface properties revealed by synchrotron XPS. *Journal of Physical Chemistry B*, **107** (2003), 9662–9668.
61 N. Gaponik, D. V. Talapin, A. L. Rogach, A. Eychmüller, H. Weller, Efficient phase transfer of luminescent thiol-capped nanocrystals: from water to nonpolar organic solvents. *Nano Letters*, **2** (2002), 803–806.
62 H. Zhang, C. Wang, M. Li, *et al.*, Fluorescent nanocrystal-polymer composites from aqueous nanocrystals: methods without ligand exchange. *Chemistry of Materials*, **17** (2005), 4783–4788.
63 A. Dubavik, V. Lesnyak, W. Thiessen, *et al.*, Synthesis of amphiphilic CdTe nanocrystals. *Journal of Physical Chemistry C*, **113** (2009), 4748–4750.
64 D. S. Koktysh, N. Gaponik, M. Reufer, *et al.*, Near-infrared electroluminescence from HgTe nanocrystals. *ChemPhysChem*, **5** (2004), 1435–1438.
65. Y. Zhang, Y. Li, X. P. Yan, Aqueous layer-by-layer epitaxy of type-II CdTe/CdSe quantum dots with near-infrared fluorescence for bioimaging applications. *Small*, **5** (2009), 185–189.
66 C. Wang, H. Zhang, J. Zhang, *et al.*, Application of ultrasonic irradiation in aqueous synthesis of highly fluorescent CdTe/CdS core–shell nanocrystals. *Journal of Physical Chemistry C*, **111** (2007), 2465–2469.
67 W. C. Law, K. T. Yong, I. Roy, *et al.*, Aqueous-phase synthesis of highly luminescent CdTe/ZnTe core/shell quantum dots optimized for targeted bioimaging. *Small*, **5** (2009), 1302–1310.
68 A. L. Rogach, A. Eychmüller, S. G. Hickey, S. V. Kershaw, Infrared-emitting colloidal nanocrystals: synthesis, assembly, spectroscopy, and applications. *Small*, **3** (2007), 536–557.

69 M. T. Harrison, S. V. Kershaw, M. G. Burt, *et al.*, Wet chemical synthesis and spectroscopic study of CdHgTe nanocrystals with strong near-infrared luminescence. *Materials Science and Engineering B*, **69** (2000), 355–360.
70 O. E. Semonin, J. C. Johnson, J. M. Luther, *et al.*, Absolute photoluminescence quantum yields of IR-26 dye, PbS, and PbSe quantum dots. *Journal of Physical Chemistry Letters*, **1** (2010), 2445–2450.
71 G.-X. Liang, M.-M. Gu, J.-R. Zhang, J.-J. Zhu, Preparation and bioapplication of high-quality, water-soluble, biocompatible, and near-infrared-emitting CdSeTe alloyed quantum dots. *Nanotechnology*, **20** (2009), 415103.
72 G.-X. Liang, L.-L. Li, H.-Y. Liu, *et al.*, Fabrication of near-infrared-emitting CdSeTe/ZnS core/shell quantum dots and their electrogenerated chemiluminescence. *Chemical Communications*, **46** (2010), 2974–2976.
73 S. F. Wuister, C. de Mello Donega, A. Meijerink, Influence of thiol capping on the exciton luminescence and decay kinetics of CdTe and CdSe quantum dots. *Journal of Physical Chemistry B*, **108** (2004), 17393–17397.
74 Y. Wang, Z. Tang, M. A. Correa-Duarte, L. M. Liz-Marzan, N. A. Kotov, Multicolor luminescence patterning by photoactivation of semiconductor nanoparticle films. *Journal of the American Chemical Society*, **125** (2003), 2830–2831.
75 N. Gaponik, I. L. Radtchenko, M. R. Gerstenberger, *et al.*, Labeling of biocompatible polymer microcapsules with near-infrared emitting nanocrystals. *Nano Letters*, **3** (2003), 369–372.
76 E. H. Sargent, Infrared quantum dots. *Advanced Materials*, **17** (2005), 515–522.
77 J. Jang, K. Cho, H. S. Lee, S. Kim, Transparent and flexible thin-film transistors with channel layers composed of sintered HgTe nanocrystals. *Nanotechnology*, **19** (2008), 015204.
78 S. Günes, H. Neugebauer, N. S. Sariciftci, *et al.*, Hybrid solar cells using HgTe nanocrystals and nanoporous TiO_2 electrodes. *Advanced Functional Materials*, **16** (2006), 1095–1099.
79 P. Olk, B. C. Buchler, V. Sandoghdar, *et al.*, Subwavelength emitters in the near-infrared based on mercury telluride nanocrystals. *Applied Physics Letters*, **84** (2004), 4732–4734.
80 S. V. Kershaw, M. Harrison, A. L. Rogach, A. Kornowski, Development of IR-emitting colloidal II–VI quantum-dot materials. *IEEE Journal of Selected Topics in Quantum Electronics*, **6** (2000), 534–543.
81 M. V. Kovalenko, E. Kaufmann, D. Pachinger, *et al.*, Colloidal HgTe nanocrystals with widely tunable narrow band gap energies: From telecommunications to molecular vibrations. *Journal of the American Chemical Society*, **128** (2006), 3516–3517.
82 C. P. Collier, T. Vossmeyer, J. R. Heath, Nanocrystal superlattices. *Annual Review of Physical Chemistry*, **49** (1998), 371–404.
83 Z. Tang, N. A. Kotov, One-dimensional assemblies of nanoparticles: preparation, properties, and promise. *Advanced Materials*, **17** (2005), 951–962.
84 C. B. Murray, C. R. Kagan, M. G. Bawendi, Synthesis and characterization of monodisperse nanocrystals and close-packed nanocrystal assemblies. *Annual Review of Materials Science*, **30** (2000), 545–610.
85 I. U. Arachchige, S. L. Brock, Sol–gel methods for the assembly of metal chalcogenide quantum dots. *Accounts of Chemical Research*, **40** (2007), 801–809.
86 D. V. Talapin, E. V. Shevchenko, A. Kornowski, *et al.*, A new approach to crystallization of CdSe nanoparticles into ordered three-dimensional superlattices. *Advanced Materials*, **13** (2001), 1868–1871.

87 A. L. Rogach, D. V. Talapin, E. V. Shevchenko, *et al.*, Organization of matter on different size scales: monodisperse nanocrystals and their superstructures. *Advanced Functional Materials*, **12** (2002), 653–664.
88 A. N. Shipway, E. Katz, I. Willner, Nanoparticle arrays on surfaces for electronic, optical, and sensor applications. *ChemPhysChem*, **1** (2000), 18–52.
89 M. Gao, J. Sun, E. Dulkeith, *et al.*, Lateral patterning of CdTe nanocrystal films by the electric field directed layer-by-layer assembly method. *Langmuir*, **18** (2002), 4098–4102.
90 N. A. Kotov, Layer-by-layer assembly of nanoparticles and nanocolloids: intermolecular interactions, structure and materials perspective. In *Multilayer Thin Films: Sequential Assembly Of Nanocomposite Materials*, G. Decher and J. B. Schlenoff, eds., pp. 207–70, Weinheim: Wiley-VCH, 2003.
91 X. Michalet, F. F. Pinaud, L. A. Bentolila, *et al.*, Quantum dots for live cells, in vivo imaging, and diagnostics. *Science*, **307** (2005), 538–544.
92 G. Decher, Fuzzy nanoassemblies: toward layered polymeric multicomposites. *Science*, **277** (1997), 1232–1237.
93 R. K. Iler, Multilayers of colloidal particles. *Journal of Colloid and Interface Science*, **21** (1966), 569–594.
94 M. Gao, C. Lesser, S. Kirstein, *et al.*, Electroluminescence of different colors from polycation/CdTe nanocrystal self-assembled films. *Journal of Applied Physics*, **87** (2000), 2297–2302.
95 M. T. Crisp, N. A. Kotov, Preparation of nanoparticle coatings on surfaces of complex geometry. *Nano Letters*, **3** (2003), 173–177.
96 A. S. Susha, F. Caruso, A. L. Rogach, *et al.*, Formation of luminescent spherical core–shell particles by the consecutive adsorption of polyelectrolyte and CdTe(S) nanocrystals on latex colloids. *Colloids and Surfaces A*, **163** (2000), 39–44.
97 T. A. Klar, T. Franzl, A. L. Rogach, J. Feldmann, Super-efficient exciton funneling in layer-by-layer semiconductor nanocrystal structures. *Advanced Materials*, **17** (2005), 769–773.
98 A. A. Mamedov, A. Belov, M. Giersig, N. N. Mamedova, N. A. Kotov, Nanorainbows: graded semiconductor films from quantum dots. *Journal of the American Chemical Society*, **123** (2001), 7738–7739.
99 S. G. Romanov, D. N. Chigrin, V. G. Solovyev, *et al.*, Light emission in a directional photonic bandgap. *Physica Status Solidi A*, **197** (2003), 662–672.
100 N. Gaponik, A. Eychmüller, A. L. Rogach, *et al.*, Structure-related optical properties of luminescent hetero-opals. *Journal of Applied Physics*, **95** (2004), 1029–1035.
101 S. G. Romanov, D. N. Chigrin, C. M. Sotomayor Torres, *et al.*, Emission stimulation in a directional band gap of a CdTe-loaded opal photonic crystal. *Physical Review E*, **69** (2004,) 046606/1-/4.
102 J. W. Ostrander, A. A. Mamedov, N. A. Kotov, Two modes of linear layer-by-layer growth of nanoparticle–polyelectrolyte multilayers and different interactions in the layer-by-layer deposition. *Journal of the American Chemical Society*, **123** (2001), 1101–1110.
103 E. Hübsch, G. Fleith, J. Fatisson, *et al.*, Multivalent ion/polyelectrolyte exchange processes in exponentially growing multilayers. *Langmuir*, **21** (2005), 3664–3669.
104 P. Podsiadlo, M. Michel, J. Lee, *et al.*, Exponential growth of LBL films with incorporated inorganic sheets. *Nano Letters*, **8** (2008), 1762–1770.
105 T. Franzl, A. Shavel, A. L. Rogach, *et al.*, High-rate unidirectional energy transfer in directly assembled CdTe nanocrystal bilayers. *Small*, **1** (2005), 392–395.

106 C.-C. Tu, L. Y. Lin, High efficiency photodetectors fabricated by electrostatic layer-by-layer self-assembly of CdTe quantum dots. *Applied Physics Letters*, **93** (2008), 163107/1-/3.
107 D. E. Gallardo, C. Bertoni, S. Dunn, N. Gaponik, A. Eychmüller, Cathodic and anodic material diffusion in polymer/semiconductor-nanocrystal composite devices. *Advanced Materials*, **19** (2007), 3364–3367.
108 C. Bertoni, D. Gallardo, S. Dunn, N. Gaponik, A. Eychmüller, Fabrication and characterization of red-emitting electroluminescent devices based on thiol-stabilized semiconductor nanocrystals. *Applied Physics Letters*, **90** (2007), 034107.
109 A. Shavel, N. Gaponik, A. Eychmüller, The assembling of semiconductor nanocrystals. *European Journal of Inorganic Chemistry*, **18** (2005), 3613–3623.
110 J. S. Bendall, M. Paderi, F. Ghigliotti, *et al.*, Layer-by-layer all-inorganic quantum-dot-based LEDs: a simple procedure with robust performance. *Advanced Functional Materials*, **20** (2010), 3298–3302.
111 T. Franzl, D. S. Koktysh, T. A. Klar, *et al.*, Fast energy transfer in layer-by-layer assembled CdTe nanocrystal bilayers. *Applied Physics Letters*, **84** (2004), 2904–2906.
112 V. K. Komarala, Y. P. Rakovich, A. L. Bradley, *et al.*, Off-resonance surface plasmon enhanced spontaneous emission from CdTe quantum dots. *Applied Physics Letters*, **89** (2006), 253118/1–3.
113 F. Caruso, R. A. Caruso, H. Möhwald, Nanoengineering of inorganic and hybrid hollow spheres by colloidal templating. *Science*, **282** (1998), 1111–1114.
114 F. Caruso, Nanoengineering of particle surfaces. *Advanced Materials*, **13** (2001), 11–22.
115 C. R. Kagan, C. B. Murray, M. Nirmal, M. G. Bawendi, Electronic energy transfer in CdSe quantum dot solids. *Physical Review Letters*, **76** (1996), 1517–1520.
116 F. Müller, S. Götzinger, N. Gaponik, *et al.*, Investigation of energy transfer between CdTe nanocrystals on polystyrene beads and dye molecules for FRET-SNOM applications. *Journal of Physical Chemistry B.*, **108** (2004), 14527–14534.
117 Y. P. Rakovich, J. F. Donegan, N. Gaponik, A. L. Rogach, Raman scattering and anti-Stokes emission from a single spherical microcavity with a CdTe quantum dot monolayer. *Applied Physics Letters*, **83** (2003), 2539–2541.
118 Y. P. Rakovich, J. F. Donegan, M. Gerlach, *et al.*, Fine structure of coupled optical modes in photonic molecules. *Physical Review A*, **70** (2004), 051801.
119 Y. P. Rakovich, M. Gerlach, A. L. Bradley, *et al.*, Confined optical modes in small photonic molecules with semiconductor nanocrystals. *Journal of Applied Physics*, **96** (2004), 6761–6765.
120 N. Gaponik, I. L. Radtchenko, G. B. Sukhorukov, H. Weller, A. L. Rogach, Toward encoding combinatorial libraries: charge-driven microencapsulation of semiconductor nanocrystals luminescing in the visible and near IR. *Advanced Materials*, **14** (2002), 879–882.
121 N. Gaponik, I. L. Radtchenko, G. B. Sukhorukov, A. L. Rogach, Luminescent polymer microcapsules addressable by a magnetic field. *Langmuir*, **20** (2004), 1449–1452.
122 G. B. Sukhorukov, A. L. Rogach, B. Zebli, *et al.*, Nanoengineered polymer capsules: tools for detection, controlled delivery, and site-specific manipulation. *Small*, **1** (2005), 194–200.
123 I. L. Radtchenko, G. B. Sukhorukov, N. Gaponik, *et al.*, Core–shell structures formed by the solvent-controlled precipitation of luminescent CdTe nanocrystals on latex spheres. *Advanced Materials*, **13** (2001), 1684–1687.
124 A. Shavel, N. Gaponik, A. Eychmüller, Covalent linking of CdTe nanocrystals to amino-functionalized surfaces. *ChemPhysChem*, **6** (2005), 449–451.

125 S. Gupta, P. Uhlmann, M. Agrawal, *et al.*, Covalent immobilization of quantum dots on macroscopic surfaces using poly(acrylic acid) brushes. *Journal of Materials Chemistry*, **18** (2008), 214–220.
126 L. Ionov, S. Sapra, A. Synytska, *et al.*, Fast and spatially resolved environmental probing using stimuli-responsive polymer layers and fluorescent nanocrystals. *Advanced Materials*, **18** (2006), 1453–1457.
127 M. Agrawal, J. Rubio-Retama, N. E. Zafeiropoulos, *et al.*, Switchable photoluminescence of CdTe nanocrystals by temperature-responsive microgels. *Langmuir*, **24** (2008), 9820–9824.
128 R. Osovsky, A. Shavel, N. Gaponik, *et al.*, Electrostatic and covalent interactions in CdTe nanocrystalline assemblies. *Journal of Physical Chemistry B*, **109** (2005), 20244–20250.
129 K. Hoppe, E. Geidel, H. Weller, A. Eychmüller, Covalently bound CdTe nanocrystals. *Physical Chemistry Chemical Physics*, **4** (2002), 1704–1706.
130 S. Mayilo, J. Hilhorst, A. S. Susha, *et al.*, Energy transfer in solution-based clusters of CdTe nanocrystals electrostatically bound by calcium ions. *Journal of Physical Chemistry C*, **112** (2008), 14589–14594.
131 Z. Tang, N. A. Kotov, M. Giersig, Spontaneous organization of single CdTe nanoparticles into luminescent nanowires. *Science*, **297** (2002), 237–240.
132 Y. Volkov, S. Mitchell, N. Gaponik, *et al.*, In-situ observation of nanowire growth from luminescent CdTe nanocrystals in a phosphate buffer solution. *ChemPhysChem*, **5** (2004), 1600–1602.
133 L. Zhang, N. Gaponik, J. Müller, *et al.*, Branched wires of CdTe nanocrystals using amphiphilic molecules as templates. *Small*, **1** (2005), 524–527.
134 Y. Wang, Z. Tang, X. Liang, L. M. Liz-Marzan, N. A. Kotov, SiO_2-coated CdTe nanowires: bristled nano centipedes. *Nano Letters*, **4** (2004), 225–231.
135 J. Lee, A. O. Govorov, N. A. Kotov, Bioconjugated superstructures of CdTe nanowires and nanoparticles: multistep cascade Förster resonance energy transfer and energy channeling. *Nano Letters*, **5** (2005), 2063–2069.
136 Y. Wang, Z. Tang, S. Tan, N. A. Kotov, Biological assembly of nanocircuit prototypes from protein-modified CdTe nanowires. *Nano Letters*, **5** (2005), 243–248.
137 H. Niu, M. Gao, Diameter-tunable CdTe nanotubes templated by 1D nanowires of cadmium thiolate polymer. *Angewandte Chemie International Edition*, **45** (2006), 6462–6466.
138 Z. Zhang, Z. Tang, N. A. Kotov, S. C. Glotzer, Simulations and analysis of self-assembly of CdTe nanoparticles into wires and sheets. *Nano Letters*, **7** (2007), 1670–1675.
139 N. Hüsing, U. Schubert. Aerogels – airy materials: chemistry, structure, and properties. *Angewandte Chemie International Edition*, **37** (1998), 22–45.
140 S. S. Kistler. Coherent expanded aerogels and jellies. *Nature*, **127** (1931), 741.
141 J. L. Mohanan, I. U. Arachchige, S. L. Brock, Porous semiconductor chalcogenide aerogels. *Science*, **307** (2005), 397–400.
142 N. Gaponik, A. Wolf, R. Marx, *et al.*, Three-dimensional self-assembly of thiol-capped CdTe nanocrystals: gels and aerogels as building blocks for nanotechnology. *Advanced Materials*, **20** (2008), 4257–4262.

3 Electronic structure and optical transitions in colloidal semiconductor nanocrystals

Todd D. Krauss and Jeffrey J. Peterson

3.1 Introduction

This chapter discusses the electronic structure of colloidal semiconductor nanocrystals, commonly referred to as quantum dots (QDs), with special emphasis on their allowed optical transitions from a theoretical and an experimental perspective. The motivation to explore this subject is two-fold. First, and especially germane to the topic of this book, is that successful use of QDs in technological applications is predicated upon an accurate and detailed knowledge of QDs' photophysical properties, of which energy states are paramount. For example, the ability of QDs to create multiple electron–hole pairs from the absorption of a single photon (i.e., multiexciton generation, MEG) has generated significant interest in their potential use as photosensitizers in inexpensive but highly efficient solar cells [1, 2]. In order to fully understand the MEG effect and whether or not QDs will ultimately prove useful in technologies exploiting this phenomenon, a detailed knowledge of both the band edge and higher lying energy states, as well as the relaxation pathways that connect them, is required. A second motivation to understand QDs' energy states is that they provide exemplary illustrations of a number of basic quantum mechanical phenomena, and consequently have substantial didactic value. For example, a "ladder" of QD absorption spectra demonstrates how QDs' lowest energy transition evolves as a function of particle size (Figure 3.1), and is a striking illustration of the "particle in a box" model commonly taught in introductory quantum mechanics. One should not infer from this statement that QDs are simplistic and well-understood systems. In contrast, understanding the nature of QD energy states is a complex and rich subject that has motivated scientists since the early days of nanoscience research and continues to be an active area of study today.

In this chapter, we provide the reader with a basic framework to understand the relevant photophysics that is referenced throughout this book. Attention is given to a broad range of semiconductor materials (e.g., II–VI, and IV–VI semiconductors) and theoretical models (e.g., effective mass, tight binding (TB), and pseudopotential), which we expect will complement other texts and reviews on the subject [3–17]. We begin by introducing material properties, terminology, and basic concepts related to nanocrystalline QDs and the phenomenon of quantum confinement in zero-dimensional materials. A simple

Colloidal Quantum Dot Optoelectronics and Photovoltaics, eds. G. Konstantatos and E. H. Sargent.
Published by Cambridge University Press. © Cambridge University Press, 2013.

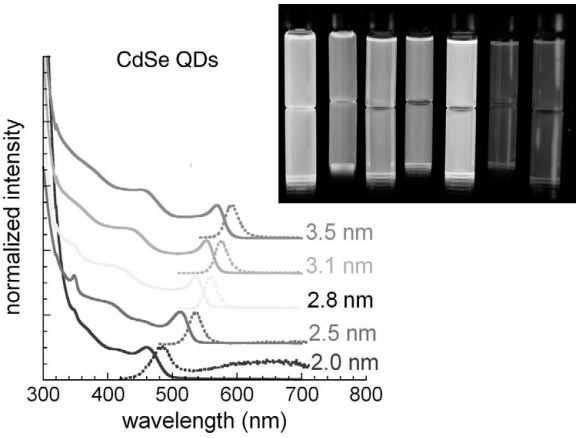


Figure 3.1 "Ladder" of absorption and emission spectra for a series of different-sized CdSe QDs. Spectra are offset for clarity and the average diameter of each sample is listed on the right hand side of the plot. The inset shows a digital picture of photoluminescence (PL) of the different sized CdSe QDs under ultraviolet illumination.

"particle in a sphere" model provides important first-order expectations and is shown to describe surprisingly well the basic photophysics of QDs. We continue with more advanced treatments, specifically comparing the theoretical predictions derived from effective mass and TB calculations of QD optical properties with experimental data of CdSe and PbSe QD optical transitions. We conclude with some current challenges for the field and provide an outlook for future progress.

3.2 Foundational concepts

QDs are crystalline inorganic particles that are spherically shaped and have diameters between 2 and 50 nm (corresponding to hundreds to thousands of atoms) (Figure 3.2). From the perspective of a chemist, QDs would be regarded as a rather large molecule; from the perspective of a solid state physicist, they would be regarded as a small semiconductor crystal. In fact, QDs fall in a mesoscopic size regime between molecular and bulk crystal counterparts and have physical characteristics reminiscent of both extremes. For example, similar to bulk semiconductor crystals, QDs exhibit broad absorption spectra and robust photostability; similar to molecular dyes, QDs can exhibit spectrally narrow and efficient fluorescence (Figure 3.1). Furthermore, QDs' optical properties are exquisitely sensitive to the precise size of the particle, and thus, allow one to tune them simply by controlling their size. The energy level spacing increases as the diameter of the QD decreases, and the emission wavelength can be tuned by on the order of 1 eV, and thus across large regions of the electromagnetic spectrum in a material of a single chemical composition. This unique property of size-tunability in the electronic and optical properties is unprecedented in traditional materials and has spurred much of the interest in QDs' potential use in optoelectronic technologies.

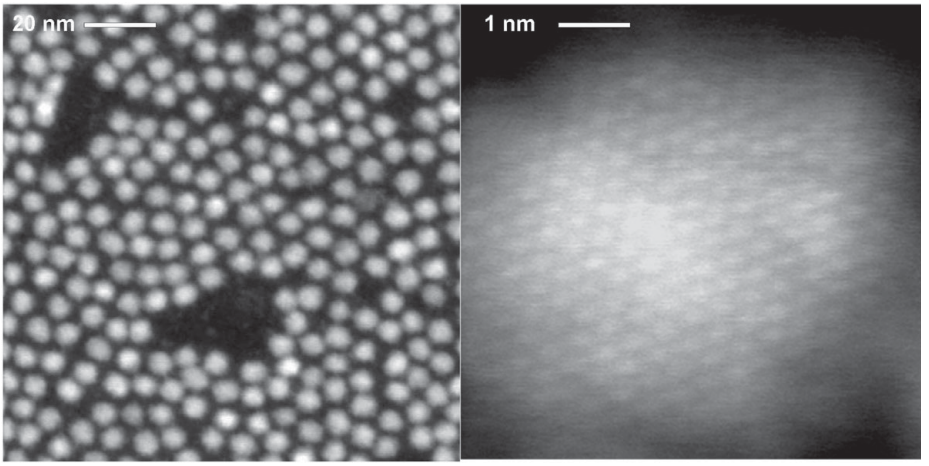


Figure 3.2 Transmission electron micrographs of (a) PbSe QDs at low 500 000× magnification and (b) an individual PbSe QD at high 10 000 000× magnification. At low magnification, the shape and size uniformity is apparent; at high magnification, the columns of individual Pb atoms are apparent. Image acquired in the laboratory of John Silcox, Cornell University.

The molecule-like and bulk-crystal-like perspectives of QDs have guided differing theoretical approaches to understanding QD energy states. In one approach, researchers have taken a "bottom-up" perspective in which the properties of the larger QD are built up from the sequential addition of individual atoms to a core particle. Historically restricted to QDs of very small size, this approach gained increasing importance with the surge in available computational power allowing calculations on QDs comprising hundreds of atoms [18]. Alternatively, one can take a "top-down" approach, in which the properties of the larger crystal are modified by the finite size of the QD. The latter approach has proven especially useful due to the analogies one can draw with familiar quantum mechanical models (i.e., particle in a box) and provides a convenient starting point for a basic understanding of QD photophysics.

In the "top-down" perspective, the electronic structure of QDs is modeled as arising from a simple modification of the bulk crystal properties. It is helpful, therefore, to briefly review the optical properties of bulk crystals. In a macroscopic crystal, the combination of the large number of atomic orbitals in the crystal (effectively infinite) gives rise to a continuous distribution of energy states, known as energy bands (Figure 3.3). The lowest unoccupied and highest occupied energy levels in the molecule evolve in the crystal to form the conduction band and the valence band, respectively, which are separated by a characteristic gap in which there are no allowed energy states, known as the band gap E_g. In the ground state the valence band of the pure semiconductor is filled with electrons, and upon absorbing a photon of energy greater than or equal to the band gap, an electron is promoted from the valence band to the conduction band, producing two effective charge carriers: a negatively charged electron in the conduction band (e^-) and a positively charged hole in the valence band (h^+). Electrons and holes

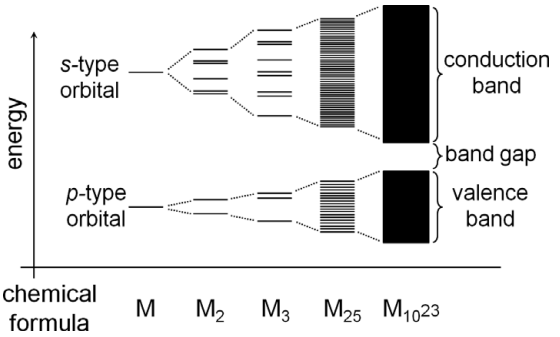


Figure 3.3 Schematic illustrating the formation of energy bands from atomic orbitals for a hypothetical element M. As the number of atoms in the species grows, the spacing between energy levels decreases. In a macroscopic crystal, containing $\sim 10^{23}$ atoms, the spacing is sufficiently small that the energy levels may be treated as a continuous energy band, rather than a discrete energy level.

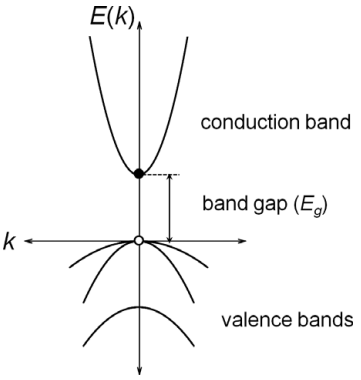


Figure 3.4 Dispersion curve for a prototypical bulk semiconductor near $k = 0$. The energy bands scale as k^2 and the curvature of the bands is characteristic of the effective mass of the electron or hole. A gap exists between the bands where no energy states exist (the band gap E_g), and upon absorbing a photon of energy greater than or equal to E_g, an electron is promoted from the valence band to the conduction band.

are free to move through the crystal in the periodic potential defined by the crystal lattice, and are characterized by an energy and wave vector – a measure of electron (or hole) quantum mechanical momentum $p = \hbar k$ (where p is momentum, $\hbar$ is the reduced Plank's constant, and k is wave vector). These effects are summarized in the energy band *dispersion curve* (Figure 3.4), which plots allowed energy levels E as a function of allowed wavevectors k. Given the classical expression for the energy of a free particle $E = p^2/2m$, where m is particle mass, the dispersion of the bands can be approximated as

$$E_c = \frac{\hbar^2 k^2}{2m_c^*} + E_g. \tag{3.1}$$

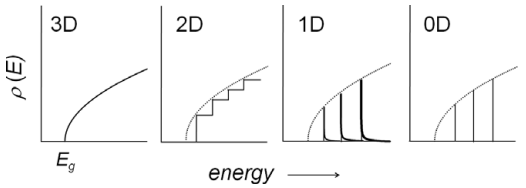


Figure 3.5 Density of energy states ρ for bulk crystals and structures of reduced dimensionality. The dotted line in the two-, one-, and zero-dimensional structures indicates the corresponding density of states from a macroscopic crystal. In zero-dimensional nanocrystal QDs, the density of states reduces to a set of delta functions.

The subscript c refers to the conduction band. There is a continuous distribution of allowed energy levels in a bulk crystal, the bands scale as k^2, and the curvature of the bands is characteristic of the "effective mass" of the electronically excited electron and hole.

The major consequence of the QD's physical boundary is that it imparts a rigid boundary condition on the electron and hole wavefunctions: the wavefunctions must drop to zero at the QD edge. In analogy to the wavefunctions found by solving the canonical "particle in an infinite potential well" problem of introductory quantum mechanics, this rigid boundary condition on the electron and hole wavefunctions results in a quantization of their allowed energy levels (and wavevectors). Thus, in contrast to the continuous distribution of allowed energy levels in a bulk crystal, near the band edge the reduced dimensions of the QD result in *discrete* energy levels. More generally, this quantization effect in the QD is simply the zero-dimensional analog of the same quantum confinement phenomenon that defines the electronic energy levels of semiconductor quantum wells and quantum wires. As depicted in Figure 3.5, the density of energy states ρ scales with dimensionality d as

$$\rho(E) \propto E^{(d-2)/2}, \qquad d = 1, 2, 3, \tag{3.2}$$

where E is energy. For zero-dimensional quantum dots, the resulting density of states is described by a set of delta functions, closely resembling the density of states of a small molecule.

Quantum confinement effects are not equally important for all semiconductor nanocrystals, but become significant when the size of the nanocrystal approaches the natural length scale of the electron and hole. This length scale, known as the Bohr radius a_B, is defined in analogy to the electron Bohr radius in a hydrogen atom, and can be calculated by scaling the hydrogen atom Bohr radius a_0 by the ratio of the semiconductor dielectric constant ε and carrier effective mass m^*:

$$a_B = \varepsilon \frac{m_0}{m^*} a_0. \tag{3.3}$$

Furthermore, when the electron and hole are confined together, e.g., by a Coulombic attraction in a bulk crystal or by the physical boundary of a QD, they can form a quasi-particle known as an exciton. The Bohr radius of the exciton is calculated from its reduced mass ($m_{exc}^{*-1} = m_e^{*-1} + m_h^{*-1}$) and defines the length scale at which quantum

Table 3.1. Material properties and Bohr radii a_B of various bulk semiconductors [19]

		E_g (eV)	m_e^*/m_0	m_h^*/m_0		Electron a_B (nm)	Hole a_B (nm)	Exciton a_B (nm)
II–VI	CdS	2.48	0.25	0.6	5	1	<1	2
	CdSe	1.73	0.12	0.9[a]	6	3	1[a]	4
	CdTe	1.48	0.09	0.8[a]	7	4	1[a]	5
III–V	InP	1.34	0.073	0.45[a]	11	7	1	8
	InAs	0.35	0.023	0.57[a]	12	27	2	29
	InSb	0.17	0.012	0.44[a]	16	59	2	61
IV–VI	PbS[c]	0.42	0.087[b]	0.083[b]	17	10	11	21
	PbSe[c]	0.28	0.047[b]	0.041[b]	23	26	29	55
	PbTe[c]	0.31	0.034[b]	0.032[b]	33	56	48	104

[a] m_h^* listed for heavy hole.
[b] All data at 4 K and $m_{e,h}$ are calculated as $3\bar{m}^{1} = m_{//}^{-1} + 2m_{\perp}^{-1}$.

confinement effects start to become significant. Simply stated, the exciton Bohr radius defines the length scale at which an electron or hole "feels" the walls of the QD as the nanoparticle size is decreased. Table 3.1 lists characteristic material properties and Bohr radii for the electron, hole, and exciton of various bulk semiconductors.

A few conclusions are apparent from browsing Table 3.1. First, the minimum QD size required to observe quantum confinement effects on the semiconductor energy levels varies significantly, from 2 nm in CdS to 100 nm in PbTe. The confinement energy, the energy of an electron or hole in addition to the bulk band gap that originates from the finite size of the QD, scales approximately with the inverse of the carrier effective mass, and the larger the exciton a_B, the greater the degree of quantum confinement a fixed size QD will experience. For example, electrons and holes in a 3-nm diameter PbSe QD would experience a confinement energy two times greater than that experienced in a 3-nm diameter CdSe QD. A second observation is that in most semiconductors electrons have a larger Bohr radius than holes. Consequently, quantum confinement effects are more significant in the conduction band than in the valence band. In fact, given that typical QD diameters are rarely less than ~2 nm, one expects that it is extremely difficult to confine the holes in any material except QDs made from IV–VI lead salts.

The Bohr radii of the electron, hole, and exciton naturally define three quantum confinement regimes for QDs: a weak confinement regime, in which the QD radius a is greater than both the electron and hole Bohr radii (i.e., $a_{B,e}$, $a_{B,h} < a$), an intermediate confinement regime, in which the QD radius is less than the Bohr radius of one charge carrier, but greater than that of the other (e.g., $a_{B,h} < a < a_{B,e}$), and a strong confinement regime, in which the QD radius is less than both the electron and hole Bohr radii (i.e., $a < a_{B,e}, a_{B,h}$). Semiconductor QDs in each regime have unique photophysical characteristics and have been extensively investigated [10]. In the remainder of this chapter, we focus on two technologically relevant materials in the strong confinement regime, specifically CdSe and PbSe QDs.

Table 3.2. Roots of the spherical Bessel function

l	$n = 1$	$n = 2$	$n = 3$
0	3.142 (π)	6.283 (2π)	9.425 (3π)
1	4.493	7.725	10.904
2	5.764	9.095	12.323
3	6.988	10.417	

3.3 A simple model

A simple model originally used to describe the energy levels of a QD is a "particle in a sphere" model [20, 21]. In this model a charge carrier of mass m is confined in a spherically symmetric potential V, defined by

$$V(r) = \begin{cases} 0 & r < a, \\ \infty & r \geq a, \end{cases} \tag{3.4}$$

where a is the sphere radius. For this potential function, the Schrödinger equation is separable into radial and angular functions and the resulting solutions are the product of radial and angular eigenfuntions. Specifically, the total wavefunction Ψ is given by

$$\Psi(r, \theta, \phi) = C j_l(kr)\, Y_l^m(\theta, \phi), \tag{3.5}$$

where C is a normalization constant, $j_l(kr)$ s an lth-order spherical Bessel function, and $Y_l^m(\theta, \phi)$ s a spherical harmonic. The boundary condition that the wavefunction must be zero at the QD edge is satisfied by requiring $k = \beta_{nl}/a$, where β_{nl} is the nth zero of j_l (Table 3.2).

Allowed energy levels for the particle in a spherical potential are indexed by quantum numbers n and l and are given by

$$E_{n,l} = \frac{\hbar^2 k^2}{2m} = \frac{\hbar^2 \beta_{n,l}^2}{2ma^2}. \tag{3.6}$$

Although simple, this model accounts for a number of important fundamental expectations regarding the optical transitions of QDs. First, the model predicts that the confinement energy scales as $1/d^2$ (where d is QD diameter), in analogy to the energy of a free electron in a one-dimensional infinite square well potential. Second, because the Coulomb attraction between the electron and hole scales as $1/d$, the confinement energy is expected to be the significant additional contribution to the energy gap for QDs in the strong confinement regime (Equation (3.1)), with Coulomb effects acting as a small perturbation to these energy states. Third, QD wavefunctions are labeled by the quantum numbers n, l, and m, analogously to the familiar hydrogen-atom wavefunctions, and can be characterized as s-, p-, and d-type wavefunctions with appropriate optical transition selection rules based on the orbital angular momentum associated with these symmetries.

These basic results are preserved if one considers a more realistic model in which the electron or hole in the QD is placed in a periodic potential defined by the QD lattice

[20, 22, 23]. The central approximation in this model is that the periodic crystalline potential in the QD is the same as it is in the bulk crystal or, equivalently, that the effective mass is the same in the QD as it is in the bulk crystal. In a macroscopic crystal, Bloch's theorem states that the wavefunction of a free carrier (i.e., an electron or hole) is the product of two functions: one that has the periodicity of the lattice $u_{nk}(\vec{r})$ (the periodic Bloch function) and a plane wave:

$$\Psi_{nk}(\vec{r}) = u_{nk}(\vec{r})\, e^{i\vec{k}\bullet\vec{r}}, \tag{3.7}$$

where the index n labels different energy bands and k is an index corresponding to the wave vector of the particle [24]. Here, the plane wave can be regarded as the backbone of the wavefunction and the periodic Bloch function corresponds to the atomic-like portion of the wavefunction. The periodic Bloch function can be thought of as arising from a linear combination of the atomic orbitals within the unit cell, and the index k is explicitly included to emphasize that a given wavefunction is uniquely defined at each point in k-space. In a QD, one assumes that the atomic-like portion of the wavefunction is the same as that of the bulk crystal at $k = 0$, but due to the lack of translational symmetry, the backbone portion now consists of a linear combination of plane waves that form an envelope function satisfying the spherical boundary condition. The wavefunction is then given by

$$\Psi_n(\vec{r}) = u_{n0}(\vec{r}) \sum_k C_{nk} e^{i\vec{k}\bullet\vec{r}} = u_{n0}(\vec{r}) f(\vec{r}), \tag{3.8}$$

where C_{nk} are expansion coefficients and f is the envelope function. The problem of determining the envelope function f is the same problem solved in the particle in a sphere model and its solutions are given by (3.5). Thus, the electron and hole wavefunctions in QDs are a product of three components: one that originates from the unit cell of the crystal (u), the second, a spherical Bessel function that satisfies the boundary condition at the edge of the QD (j), and the third, a spherical harmonic (Y). The total wavefunction for the photoexcited QD includes contributions from electrons and holes and can be written as:

$$\begin{aligned}\Psi_{exc}(\vec{r}_e, \vec{r}_h) &= \Psi_e(\vec{r}_e)\, \Psi_h(\vec{r}_h) \\ &= u_c f(\vec{r}_e)\, u_v f(\vec{r}_h) = C\left(u_c j_{L_e}(kr_e)\, Y_{L_e}^m\right)\left(u_h j_{L_h}(kr_h)\, Y_{L_h}^m\right),\end{aligned} \tag{3.9}$$

where the subscripts c and v refer to the conduction and valence bands, respectively. The subscript L labels the spherical harmonic angular momentum quantum number and QD energy states can be labeled as $n_e L_e$ and $n_h L_h$ for the electron and hole, respectively. Thus, allowed energy levels are predicted to occur at energies

$$E = E_g + \frac{\hbar^2 \beta_{n_e,L_e}^2}{2m_e^* a^2} + \frac{\hbar^2 \beta_{n_h,L_h}^2}{2m_h^* a^2} - E_C, \tag{3.10}$$

where E_C is a first-order correction due to the Coulombic attraction between electrons and holes. E_C can be calculated from perturbation theory and is equal to $1.8e^2/4\pi\varepsilon a$, where e is the elementary charge and ε is the dielectric permittivity [21].

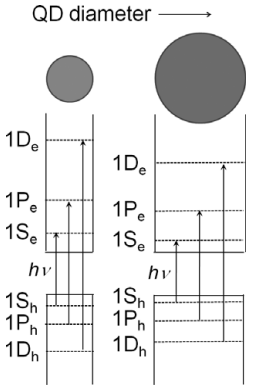


Figure 3.6 Size-dependent energy level diagram and allowed optical transitions in nanocrystal QDs predicted from a particle in a sphere model.

The probability P of making an optical transition between valence and conduction band states is given by

$$P = |\Psi_e \, |\vec{e} \bullet \hat{p}| \, \Psi_h|^2 \,, \tag{3.11}$$

where $\vec{e}$ is the polarization vector of the light and $\hat{p}$ is the momentum operator. Because the envelope function is considered to be constant within a unit cell of the crystal, it is assumed that $\hat{p}$ only operates on the atomic-like portion of the wavefunction, giving

$$P = |u_c \, |\vec{e} \bullet \hat{p}| \, u_v|^2 \, |f_c| f_v|^2 \,. \tag{3.12}$$

The first term corresponds to the standard transition dipole matrix element that characterizes the optical transition between two atomic or molecular orbitals. The envelope functions calculated in the particle in a sphere model are orthonormal eigenfunctions of a Hermitian operator, therefore,

$$P = |u_c \, |\vec{e} \bullet \hat{p}| \, u_v|^2 \, \delta_{n_e,n_h} \delta_{L_e,L_h} \,, \tag{3.13}$$

where $\delta_{e,h}$ are Dirac delta functions. Thus, the simple dipole allowed optical transition selection rules $\Delta n = 0$ and $\Delta L = 0$ are obtained. In summary, one expects allowed optical transitions between matching nL-states of the electron and hole which occur at an energy predicted by (3.10) (Figure 3.6).

3.4 Experimental evidence for quantum confinement

Absorption spectroscopy is a simple experimental technique that can elucidate the strong size dependence of the energy gap of semiconductor QDs and reveal their underlying electronic structure. Linear absorption spectra for a series of different sized CdSe and PbSe QDs are shown in Figure 3.7. Average QD diameters can be accurately determined by combining QD absorption spectra with an analysis of QD sizes obtained from transmission electron microscopy images. The resulting "sizing curves" (i.e., absorbance peak wavelength versus average QD diameter) have been reported for a number of

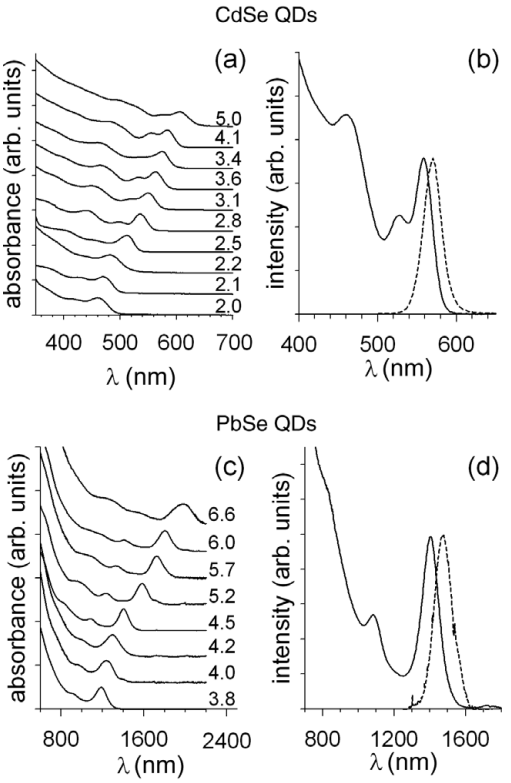


Figure 3.7 Absorbance spectra for a series of different sized (a) CdSe and (c) PbSe QDs; and absorbance (solid line) and photoluminescence emission (dashed line) spectra for (b) CdSe and (d) PbSe QDs. Absorbance spectra in (a) and (c) are offset for clarity. Average QD diameters (in units of nanometers) are listed on the right hand side of each plot and are taken from [26] and [30] for CdSe and PbSe QDs, respectively.

different materials, such as CdSe, PbSe, and InAs QDs [25–32]. From a qualitative perspective, the QD energy gap does decrease with increasing particle size as theoretically expected. Further, given the advances in QD synthesis that now routinely produces highly monodisperse samples with well-defined structure in their absorbance spectra [33–37], it is possible to identify not only the first optical transition, but higher energy absorption transitions as well. PL emission spectra are spectrally narrow (full width at half maximum ≈ 30 meV, approximately 20 nm in the case of CdSe QDs), with band-edge emission (Stokes shift ≈ 10–30 meV), and (for high quality samples) with little evidence of emission from low-energy surface trap states. PL quantum yields (QYs) for core QDs are routinely 10–50%, but several post-synthetic modifications to QDs are capable of further increasing this efficiency (see Section 3.5).

From a more quantitative perspective, several issues are apparent. First, although the energy gap for a core QD does scale as approximately $1/d^2$ as expected from the simple particle in a sphere model (Figure 3.8), the predicted transition energies (both the lowest as well as higher energy transitions) deviate significantly from this model. In the case of CdSe QDs, the relative error between the observed confinement energy and the value

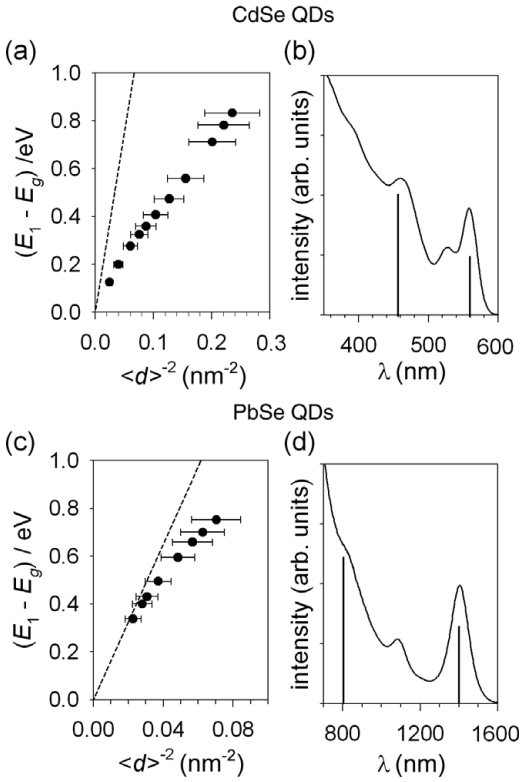


Figure 3.8 Comparisons of the quantum confinement energies ($E_1 - E_g$) predicted from the particle in a sphere model (dashed lines) with experimentally determined values for different sized (a) CdSe and (c) PbSe QDs. Plots (b) and (d) compare higher energy optical transitions predicted from a particle in a sphere model with the experimentally measured absorbance spectra for (b) CdSe and (d) PbSe QDs. For the theoretical predictions, effective masses of electrons and holes were taken from [19], and average QD diameters were taken from [26] and [30] for CdSe and PbSe QDs, respectively. In (b) and (d), the theoretically predicted lowest transition energy has been selected to match the first absorbance peak to enable meaningful comparisons of the higher order transitions to be made.

predicted from a particle in a sphere model can be as much as 100%. Second, additional absorption peaks which are totally unexpected from the particle in a sphere model are observed (Figure 3.8(b) and (d)). These results suggest that although the particle in a sphere model describes the basic photophysics of QDs, more advanced treatments are necessary to quantitatively understand QD energy states and allowed optical transitions.

From an experimental perspective, absorbance spectroscopy is a limited tool because even the smallest distribution of QD sizes in an ensemble prevents the identification of multiple transitions that are similar in energy, due to the strong dependence of a QD's energy gap on diameter. Two relatively simple techniques that circumvent this problem are photoluminescence excitation (PLE) and fluorescence line narrowing (FLN) spectroscopy [38, 39]. Both techniques function by only sampling QDs which are optically active in a narrow spectral range. PLE scans the excitation wavelength while monitoring the emission at a fixed, spectrally narrow wavelength; FLN uses a fixed

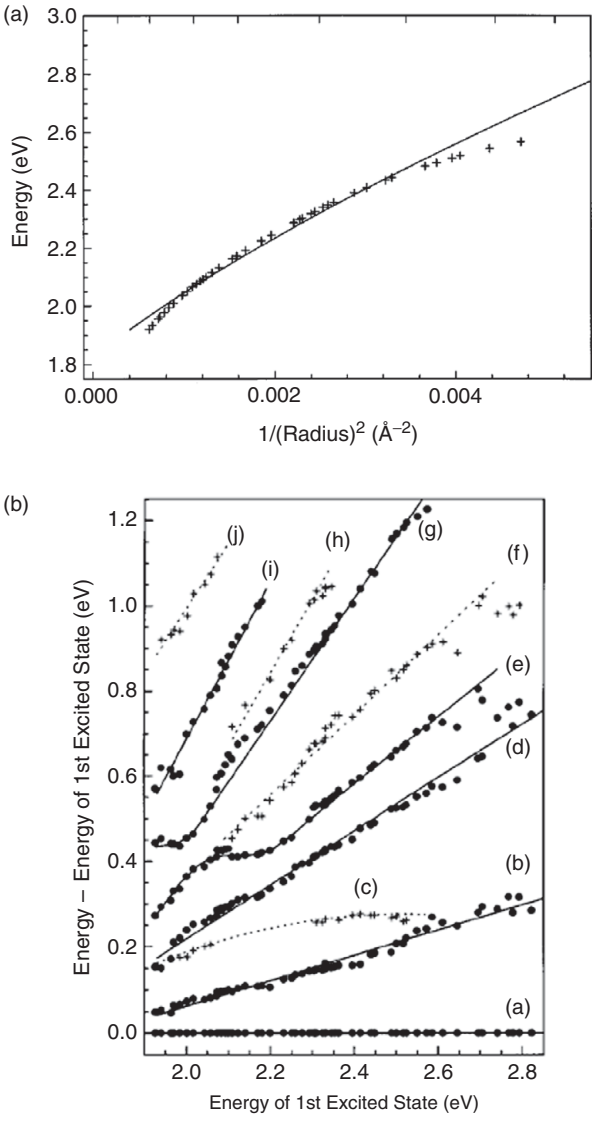


Figure 3.9 Comparison of (a) the first transition energy and (b) higher energy optical transitions predicted from a multiband effective mass treatment of CdSe QD energy states with experimentally observed values from PLE spectroscopy experiments performed by Norris and Bawendi [39]. In part (b) lines are shown as guides for the eye. Plots are used with permission from [39].

excitation wavelength that it is selected on the low energy side of the ensemble absorption peak so that only the smallest sized QDs in the sample are excited. Both techniques dramatically improve spectral resolution. Whereas an absorbance measurement may exhibit 3–4 distinct optical transitions, a PLE measurement with ~0.5 nm spectral resolution can reveal as many as eight well-resolved transitions (Figure 3.9) [39].

3.5 Engineered quantum dot structures

Following synthesis of a colloidal QD sample, a variety of post-synthetic modifications are available to further optimize the QD's optical properties or to engineer entirely new types of heterostructures with their own unique photophysics. These modifications generally involve the epitaxial growth of a second semiconductor material ("the shell") on top of the existing "core" particle and are commonly referred to as "core/shell" nanostructures. The motivation for shelling is to passivate the surface atoms of the QD with an inorganic layer, which is necessitated by the fact that core QDs have a very high ratio of surface atoms to core atoms. For example, for a 5-nm diameter PbSe QD, approximately 40% of the atoms are on the surface. Thus, in the core QD the delocalized electron and hole will sample many surface atoms, which are all potential places to energetically trap charge carriers due to incomplete passivation by organic molecules.

Core/shell nanostructures can be classified according to the relative offsets between the conduction and valence bands in the core and shell materials. In "type I" structures the energy of the conduction (valence) band is lower (greater) in the shell than in the core (sometimes called a "straddling gap"); in "type II" structures the energy of the conduction (or valence) band is greater in the shell, while the energy of the valence (or conduction, respectively) band is greater in the core (sometimes called a "staggered gap") (Figure 3.10). The relative alignment between the valence and conduction bands of the core and shell is important because it impacts the spatial distribution of photoexcited electrons and holes within the core/shell QD. Photoexcited electrons quickly relax to the global minimum in the manifold of conduction band states; photoexcited holes relax to the global maximum in the manifold of valence band states (note that the energy of hole states increases in the opposite direction to that of electron states; e.g., the energy of hole states increases in the downward direction in Figure 3.10). In the case of type I structures, the photoexcited electron and hole remain in relatively close proximity – both remain within either the core *or* shell material. In the case of type II structures, the charge carriers become separated – one carrier is localized in the core and the other carrier is localized in the shell.

A common example of a type I structure is a CdSe/ZnS core/shell QD, formed by growing a thin layer of ZnS (typically 3–6 monolayers) on the outside of a traditional CdSe core particle [40, 41]. ZnS has a bulk band gap of 3.6 eV [19] and forms a type I structure with CdSe. Upon absorption of a photon, electrons and holes in CdSe/ZnS core/shell QDs remain confined within the core CdSe particle. The finite potential defined by the energy difference between core and shell materials is sufficiently large ($\sim$1 eV) that tunneling of the exciton wavefunction into the shell material is minimal. Furthermore, the ZnS shell passivates trap states that exist at the surface of the core particle and are believed to quench the QD emission. Since the addition of a few monolayers of ZnS is effectively making a slightly bigger "box" for the electron and hole, the peak absorption and emission wavelengths of a CdSe/ZnS core/shell QD shows only a slight red shift compared with a traditional CdSe QD (Figure 3.10), while the increased surface passivation causes the emission intensity to increase (5–10)-fold [40, 41]. In commercially available core/shell/shell QDs composed of CdSe/CdS/ZnS, QYs

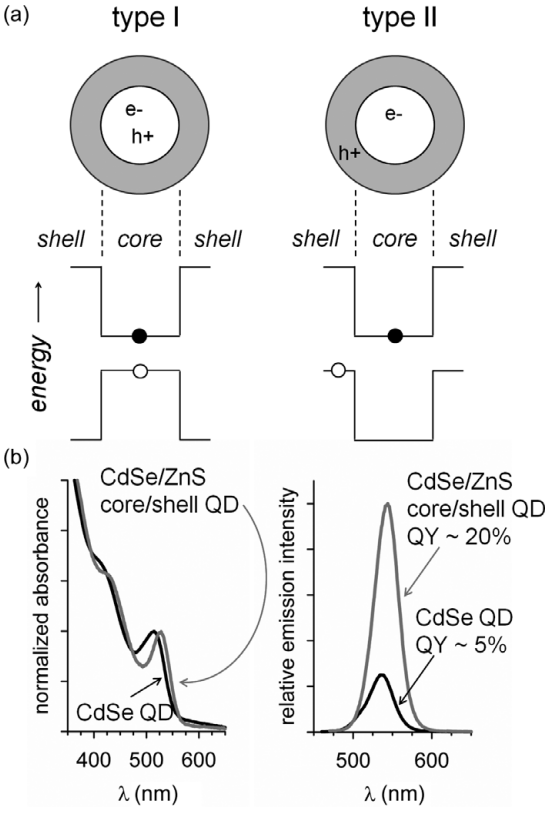


Figure 3.10 (a) Cartoon of band alignment in type I and type II core/shell QD heterostructures. In a type I system, *both* the electron and hole remain confined within the core QD; in a type II system, one carrier becomes localized in the shell and one carrier remains in the core. (b) Comparison of absorbance and emission spectra (left and right panels, respectively) from CdSe QDs and type I CdSe/ZnS core/shell QDs. The absorbance maximum of the core/shell QD is slightly red-shifted in comparison to the core QD due to penetration of the exciton wavefunction into the shell material. The emission intensity of the core/shell QD is approximately 4× greater than the core QD, consistent with expectations due to the passivation of trap states at the surface of the core QD.

as high 80% have been reported [42, 43]. The added brightness and greater surface protection provided by a shell material make core/shell QDs ideal for biological imaging applications in aqueous media [44–46].

Common examples of type-II core/shell QD structures are CdTe/CdSe, CdSe/ZnTe, and CdS/ZnSe combinations [47–49]. Although type II core/shell QDs generally do not have high fluorescence efficiency, they are very efficient at intraparticle charge separation due to the localization of charge carriers that occurs in different portions of the core/shell QD [50, 51]. Several novel technological applications that can exploit this efficient charge separation, such as high efficiency photovoltaics and single exciton lasers, have been reported utilizing type-II core/shell structures [52–54]. Type II structures have also found

important use in deep-tissue biological imaging experiments that occur in water's near infrared transparency window [55].

3.6 Advanced theoretical treatments

The logical improvement to the particle in a sphere model is to consider a more realistic semiconductor band structure than just two energy bands. In the multiband "effective mass" treatment of III–V and II–VI semiconductor band structures, the single valence band of the particle in sphere model is replaced by three valence bands, termed the "heavy hole," "light hole," and "split-off" bands, respectively, near the band extremum at $k = 0$. Using CdSe as an example, these three bands are derived from linear combinations of the Se 4*p* atomic orbitals and give rise to valence band energy states which are six-fold degenerate (including spin) at $k = 0$. The conduction band is derived from the Cd 5*s* atomic orbitals and can be accurately described by a single band near $k = 0$. The valence bands are labeled by their total angular momentum J, given by $J = l + \mathrm{s}$, where l is the orbital angular momentum and s is the spin angular momentum. The energies of the valence bands, as well as the conduction band, are calculated by "$k \bullet p$" theory [24]. For a detailed account, we point the reader to the reviews by Gaponenko [8] and Norris [12]. In summary, "$k \bullet p$" accounts for coupling between bands by diagonalizing the $N \times N$ Hamiltonian matrix which expresses interaction between bands in terms of various momenta operators. The Hamiltonian matrix takes different forms depending upon the level of theory one wishes to include. In the case of III–V and II–VI semiconductors, two important forms are the Luttinger Hamiltonian and the Kane Hamiltonian. The Luttinger Hamiltonian is a 6×6 matrix that describes intra-valence-band coupling for terms of spherical symmetry in diamond-like semiconductors [56, 57]. The Kane Hamiltonian is an 8×8 matrix that extends the Luttinger Hamiltonian to include inter-band coupling between valence and conduction bands [58, 59].

Given an accurate description of the band structure, the simplest extension would treat each valence band as independent and "particle-in-a-sphere-like," giving rise to a series of hole energy states and producing a ladder of optical transitions. However, when the Hamiltonian is modified to include the QD spherical potential, mixing occurs between the valence bands of the bulk semiconductor. Furthermore, the QD envelope function (f) and underlying unit cell function (u) mix as well, an effect termed *S–D* mixing. The net result is that the complex valence band structure produces a dense manifold of QD hole energy states. In theory, this treatment would be exact if all energy bands of the semiconductor could be included in the model. In practice, a small subset of valence and conduction bands are included that have energies closest to the semiconductor energy gap. A full theoretical description of CdSe QD energy states has been developed by Efros and coworkers in the context of degenerate "$k \bullet p$" perturbation formalism [60, 61]. It describes the CdSe hole energy states using the Luttinger Hamiltonian and the electron energy states with the Kane Hamiltonian. One important result from this model is that due to the *S–D* mixing, the QD angular momentum has contributions from the underlying atomic orbitals which form the bulk valence bands (J) and its envelope function (L)

[23, 62, 60, 61]. Thus, neither L nor J are good quantum numbers and only the total angular momentum F, given by $F = J + L$, and parity are conserved [63]. Consequently, the strict $\Delta n = 0$and $\Delta L = 0$ selection rules are relaxed. Energy states are labeled nL_F and transitions are labeled with the corresponding electron and hole pair. For example, the lowest energy electron and hole states are labeled $1S_e$ and $1S_{3/2}$, respectively, and the lowest energy transition is labeled $1S_{3/2}1S_e$.

The multiband envelope function theoretical formalism gives good agreement with experimental data of the size dependence of CdSe QDs' lowest energy optical transition (Figure 3.9) [39]. Confinement energies are predicted within approximately 10% of the experimentally observed values, compared to ~100% relative error predicted from the simple particle in a sphere model. Notably, the model predicts very well the energy of higher excited state transitions relative to the energy of the first excited state and as many as ten transitions in CdSe QDs have been assigned [39]. One interesting prediction of this model is the existence of a "dark exciton." The dark exciton refers to fine structure splitting of the lowest excited state due to electron–hole exchange interactions, the prolate shape of the QD, and the anisotropy of the CdSe wurtzite crystal lattice [64–66]. The eight-fold degenerate ground state (six valence band states plus two conduction band states, including spin) are split into five energy states based on the projection of their total angular momentum ($F_e + F_h$) along the unique crystal axis. Notably, the lowest energy exciton state contains two quanta of angular momentum and is split ~10–15 meV lower in energy than the next highest energy state with one quantum of angular momentum. Given the electric dipole approximation, which requires that absorption or emission of a photon couple energy states that differ by one unit of angular momentum [67], optical transitions from the lowest energy excited state to the ground state are formally forbidden. Thus, the multiband envelope function prediction of a dark exciton state can explain the Stokes shift observed in CdSe QD emission spectra, as well as their anomalously long fluorescence lifetimes (~30 ns) [68, 69].

The optical transitions of IV–VI semiconductors (e.g., PbSe and PbS) have been modeled within an effective mass framework as well [70]. In comparison to II–VI and III–V semiconductors, the bulk band structure of IV–VI QDs is relatively simple, which in principle leads to a simple manifold of electronic states in the QD as well. Specifically, the lead salts contain one conduction band and *one* valence band near their band edge, with highly symmetric dispersions, as suggested by the equivalent electron and hole effectives masses. Thus, the relatively few and symmetric energy bands in the crystal give rise to relatively sparse and symmetric QD energy states, which are further widely separated in energy due to their strongly confined character (i.e., large Bohr radius in lead salts). Especially unique are the hole states, which in this simple picture remain uncongested and well separated (Figure 3.11), in contrast to QDs from II–VI materials.

The unique character of the lead chalcogenides' band structure can be traced to the fact that their band gap occurs at the L-edge of the Brillouin zone ($k = \pi/a$, (111) direction, where k is the wave vector and a is the bulk lattice constant), whereas most semiconductors have their band gap at the Γ-point ($k = 0$). The origin of the difference is hinted at by the anomalous bonding in IV–VI materials. As described by Zunger and

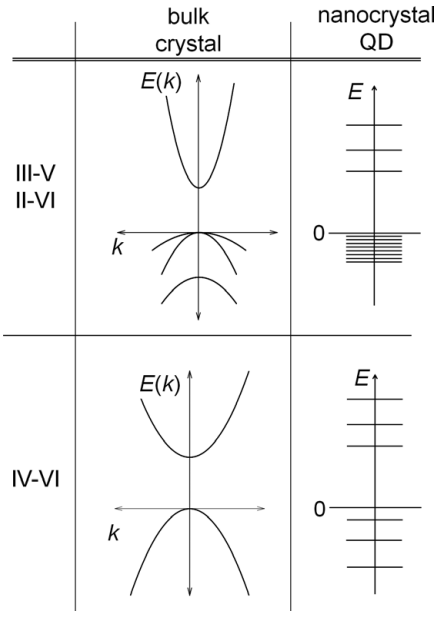


Figure 3.11 Illustration of proptypical II–VI (top) and IV–VI (bottom) semiconductor bulk band structures (left) and nanocrystal energy states (right). In IV–VI materials, the presence of only one valence band and large electron and hole Bohr radii lead to nanocrystal energy states that are widely spaced and uncongested for both the electron and hole.

coworkers [71, 72], although Pb is a s^2p^2 group IV cation, the Pb *6s* orbital (normally the highest occupied atomic orbital) is significantly lowered in energy due to strong spin-orbit coupling, creating a pseudo-divalent group II cation (like Cd or Zn) that bonds with group VI elements. In the bulk crystal, the Pb *6s* band (normally the conduction band minimum) is pulled below the manifold of valence band states, leaving the *p*-states, specifically those involved in *p–p* σ bonding, to produce a direct band gap at the L-edge of the Brillouin zone [73]. One important consequence of the occurrence of the band gap at the edge of the Brillouin zone is that conduction and valence bands are both four-fold degenerate (eight-fold including spin), which leads to an $(8 \times 8 = 64)$-fold, highly degenerate lowest electronic transition transition.

Kang and Wise have calculated the energy states of PbS and PbSe QDs using a four-band effective mass treatment [74]. Energy states are labeled *nL*, where *n* is the primary quantum number and *L* is the angular momentum of the envelope function, and one-photon transitions follow the selection rule $\Delta L = 0$. Their model predicts lowest transition energies ~30% larger than the experimentally observed value for QDs that are optically active in the 1200–1600 nm range (Figure 3.11). Scaling from the energy of the lowest transition, the four-band effective mass approximation (EMA) approach predicts energies of several higher excited states with a high level of precision, although this model cannot explain some prominent features found in the absorption spectra of PbS and PbSe QDs (see next section) [74, 75].

3.7 Atomistic approaches

Whereas the effective mass approach starts from the crystalline nature of semiconductors with a periodic potential to begin describing the wavefunctions and energies of the QD, atomistic approaches build up the larger band structure starting from the atomic orbitals of a single atom. Atomistic approaches to calculate QD energy states have taken several major forms: including empirical TB, empirical psuedopotential, and time domain ab initio calculations. In the following, we briefly outline the major features of these approaches and direct the reader to the excellent reviews, for example, by Delerue and Lannoo [13], for further details.

The basic premise of the TB approach is that the wavefunction of any N-atom system can be built up from a linear combination of atomic orbitals

$$\psi = \sum_{i,a} \varphi_{i,a}, \tag{3.14}$$

where $\phi_{i,a}$ is ath atomic orbital of atom i. Given the wavefunction defined by (3.14), the energy levels ε of the system satisfy

$$\det |H - \varepsilon S| = 0, \tag{3.15}$$

where H is the Hamiltonian matrix and S is the overlap integral defined by $S = \varphi_{i,a}|\varphi_{j,b}$. A variety of approaches exist to solve (3.14) for real systems. In the empirical TB approach, one typically makes several simplifying assumptions for the forms of H and S such that the solution to (3.15) produces a relatively simple equation with several independent, adjustable parameters. For example, one typically limits the summation in (3.14) to include only valence atomic orbitals, interatomic overlap integrals are neglected, and only Hamiltonian matrix elements of σ- and π-type atomic orbital interactions (e.g., s–s, and p–p, respectively) that occur between first and second neighbors are considered. These adjustable parameters are then fit so that the predicted energies match known values of the energy bands of the bulk crystal near some point in k-space. Once the Hamiltonian is solved for the bulk crystal, it can be applied to calculate the energy (and wavefunctions) of excitons in nanocrystal QDs by diagonalizing the $N \times N$ matrix defined by (3.15) (where N is the number of atoms in the QD). For systems containing more than ~1000 atoms (i.e., QDs with diameters greater than 2 nm), explicitly diagonalizing the $N \times N$ matrix is computationally intensive and a variety of simplifying algorithms that exploit the QD's spherical symmetry are used to enable calculation of energy states in QDs with diameters as large as 10 nm [13].

Whereas TB calculations assume a wavefunction formed by a linear combination of atomic orbitals, pseudopotential calculations take the approach of defining a self-consistent atomic potential (the pseudopotential) which yields the bulk band structure for a macroscopic-sized crystal [76]. This pseudopotential is determined from ab initio local density approximation calculations and can be written with the functional form

$$V(r) = \sum_{n} \sum_{\alpha} v_{\alpha}(r - R_n - d_{\alpha}), \tag{3.16}$$

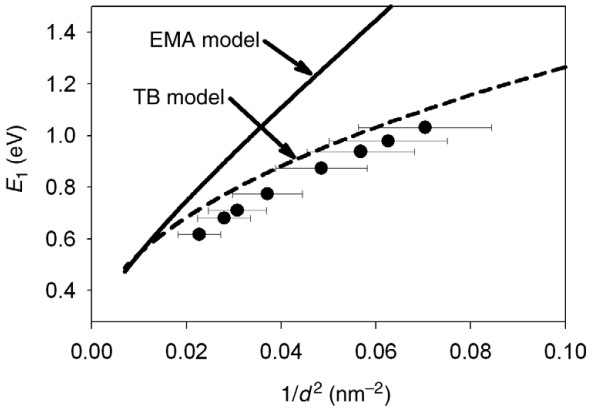


Figure 3.12 Comparison of the experimentally observed lowest transition energy in PbSe QDs with the theoretical predictions from a four-band EMA (solid line) and TB (dashed line) models [73, 74].

where the index n runs over all unit cells in the crystal positioned at R_n and the index α runs over all atoms in the unit cell positioned at $\boldsymbol{d}_\alpha$ [13]. Once known, this same potential is used to define the nanocrystal QD potential and the Schrödinger equation is solved explicitly for the N-atom system by a direct diagonalization approach. The primary advantage of the pseudopotential technique is that it provides an accurate description of the bulk crystal energy band dispersion in reciprocal space throughout the entire Brillouin zone (i.e., the full range of possible k values). Consequently, the pseudopotential approach is capable of describing the effect of coupling between bands with large wavevectors and those at the band edge on QD energy states [77, 78].

TB and pseudopotential approaches have been used to calculate allowed energy states in a variety QDs: InAs, CdSe, PbSe, PbS [79–82, 73, 83–86, 72]. In contrast to the EMA approach, in which one typically assumes an infinite spherical well potential and which leads to a general overestimation of energy states, TB and pseudopotential approaches allow one to incorporate a more realistic potential energy function. Consequently, atomistic approaches tend to predict transition energies 10–100 meV lower than EMA approaches, and are generally within 10% of the experimentally observed values. Comparison of the lowest predicted transition energies calculated with a TB approach for PbSe QDs is shown in Figure 3.12.

While the EMA, TB, and pseudopotential methods all exhibit good agreement with the lowest energy transition in a variety materials, they do make different predictions about the nature of higher energy transitions [87]. One of the most prominent examples concerns the nature of the second absorption peak in the absorption spectrum of PbSe QDs. According to predictions from both EMA and TB calculations [73, 74], the first and third absorption peaks should be assigned as $1S_h1S_e$ and $1P_h1P_e$, respectively, the two lowest one-photon allowed transitions [75, 88]. The second absorption peak is consistent with an assignment as an S–P transition. However, such a transition is formally one-photon forbidden and, as a first-order expectation, would not be expected in the linear

absorption spectrum. In contrast, pseudopotential calculations assign the second peak as the one-photon allowed $1P_h1P_e$ transition [72]. The difference originates from the treatment of coupling between remote bands and those at the band edge: in EMA and TB these are neglected or treated as a perturbation, in pseudopotential calculations they are explicitly included in the calculation. Indeed, strong experimental evidence supports the pseudopotential assignment of the second absorption peak as the one-photon allowed $1P_h1P_e$ transition [89, 90]. However, there has also been some experimental support for the assignment as the forbidden *S*–*P* transition [91, 92], although there is no quantitative theoretical explanation for the strength of the peak in the one-photon spectrum.

Finally, we briefly mention ab initio approaches to modeling QD energy states, such as the Hartree–Fock and density functional theory (DFT) methods, that complement earlier atomistic approaches. An advantage of ab initio approaches is that effects of the QD surface, ligands, and electron–electron correlations are naturally included in the theory and do not have to be artificially accounted for in the model. Time domain ab initio studies combine DFT with nonadiabatic molecular dynamics, and are especially useful for calculating optically active states of small diameter QDs and for real time modeling of photoexcitation dynamics [93–95]. The details of this model are described in [18, 95–98]. One of the important insights from time domain ab initio approaches is that only near the band edge are the QD energy states really sparse. At energies above the QD bandgap the density of states is predicted to be quasi-continuous. Consequently, discrete energy states exist only for the electron; for the hole states even those near the band edge are near continuous. Thus, the simple "particle in a box" picture of QD energy states is only a basic picture. In fact, the optical density of states is quite congested even for small QDs of the most strongly confined systems, such as PbSe QDs.

Predictions from time-domain ab initio methods have solved longstanding puzzles in QD photophysics [18]. For example, the sparse energy levels of semiconductor QDs as predicted by EMA approaches, especially for PbS and PbSe QDs, would lead to the conclusion that relaxation of highly photoexcited electrons would be slower than in the bulk crystal, since the spacing between energy states is much greater than a phonon frequency. This expected slowing of electron and hole cooling times in QDs is termed the "phonon bottleneck." However, the phonon bottleneck has not generally been observed in QDs. On the other hand, ab initio methods explain why the "phonon bottleneck" has been so hard to find in QDs: the QD excited energy states are indeed not discrete and thus relaxation through vibrational coupling is quick and efficient. Further, QDs actually can exhibit significantly faster vibrational dephasing (and thus larger absorption and emission linewidths) than bulk semiconductor crystals (a counterintuitive conclusion based on quantum confinement considerations) because the ab initio methods show directly that electron–photon coupling increases as the molecule size decreases [99].

At present, the computational cost of pseudopotential and time domain ab initio methods makes them best suited for QDs containing ~1000 atoms or less, whereas TB and EMA approaches are better suited for larger QDs. One area in which the computational capabilities of the atomistic approaches are converging with the experimental ability to grow small QDs is in the field of semiconductor "magic-sized clusters" (MSCs)

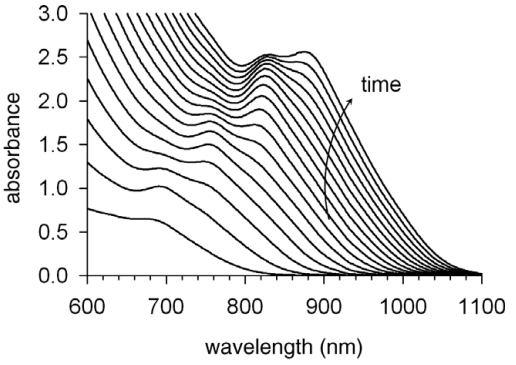


Figure 3.13 The evolution of PbSe MSCs' absorbance spectra. The in situ measurements were taken every 10 min, beginning at 30 min growth time, as MSCs grew in a cuvette at room temperature.

[100]. MSCs are small semiconductor particles, containing tens to hundreds of atoms that are bonded in a well-defined geometry that may or may not match the bulk crystal, but yet nonetheless exhibit extraordinary stability. The stability of MSCs is believed to arise from the existence of "closed shell" structures, in which the energetic penalty for addition of a single atom to the cluster is unusually large. Different sized particles in a family of MSCs can be thought of as sequential additions of whole monolayer units to the basic unit cell. Consequently, whereas traditional semiconductor QDs exhibit absorption peaks that are continuously tunable with QD size, MSCs exhibit absorption spectra that only exist at discrete wavelengths (Figure 3.13).

Given their small size, MSCs exhibit optical transitions that occur at energies significantly greater than their QD counterparts. MSCs were first reported for CdSe semiconductors and identified through optical transitions that occurred in the ultraviolet region of the electromagnetic spectrum [100]. MSCs composed of PbSe have also been reported [101]. Surprisingly, these PbSe MSCs exhibit band-edge emission with PL QYs greater than 50%, whereas MSCs composed of other materials typically have QYs on the order of 1% due to a relatively high number of surface trap quenching sites resulting from their large surface to volume ratio. Furthermore, given that typical PbSe QDs are near infrared (NIR) emitters in the range of 1200–2000 nm, PbSe MSCs emit in the biological transparency window near ~900 nm, where scattering and absorption of NIR light are minimized. Originally prepared in organic solvents, PbSe MSCs can be transferred to aqueous media using a simple ligand exchange [102], are stable over a period of weeks, and thus may someday be ideal fluorophores for NIR biological imaging. From a theoretical perspective, PbSe MSCs can help elucidate the evolution of QD optical properties as they grow from molecular clusters, well-suited for atomistic theoretical approaches, to traditional QD materials, with developed EMA and TB models. Results have demonstrated MSCs' usefulness in developing a detailed understanding of PbSe QDs' controversial second absorption peak [92], and continued insights are expected in the future as more semiconductor nanomaterials in the MSC-size regime are synthesized.

3.8 Current challenges and future outlook

We conclude this chapter with a brief look at challenges in the area of QD energy states and allowed optical transitions. From an experimental perspective, the necessary techniques to characterize QD energy states are well established and have been demonstrated in a variety of model systems. As new material systems and new types of QDs, such as band gap engineered QDs and crystal-confined structures [47, 51, 52, 103–105], are continually developed, these techniques will continue to be important to elucidate details of their electronic structure. The most prominent of these techniques, namely PLE and FLN spectroscopies, rely on selecting a subset of QDs that are optically active in a narrow spectral range in order to minimize the inhomogeneous broadening that is present in ensemble samples due to the distribution of QD sizes. With the advent of single molecule spectroscopy in 1990 [106], in which molecules are interrogated one at a time and average properties are built up by the sequential addition of hundreds of individuals, the traditional size-selection process can be pushed to its fundamental limit. Indeed, fluorescence spectroscopy of single QDs has revealed a wealth of new phenomena that are only evident at the single molecule level, enabling new insights into QD photophysics and opening entirely new fields of study, such as QDs' homogeneous lineshape and the origin of fluorescence intermittency [107–109]. However, the complement of single QD fluorescence spectroscopy, single QD PLE spectroscopy, has only been reported in one or two incidences and has not yet found widespread use [110]. This relative absence of single QD PLE spectra exists for a variety of reasons, perhaps most notably because of the dynamic processes that result in random shifts in single QD's emission maxima and fluorescence intensity, making data acquisition and interpretation extremely difficult. Nonetheless, one of the notable challenges is to develop robust techniques that are capable of measuring *excitation* spectra of individual QDs.

The understanding of core QD energy states and allowed optical transitions is now well established by a variety of theoretical approaches. Future efforts will continue to develop new techniques to apply atomistic theoretical models to larger and larger systems. A major challenge is to understand the effect of the QD surface on its energy states and thus its photophysics. How specific details of a QD's surface properties affect both core and surface electronic states is largely unknown, but under-addressed in current experimental and theoretical studies. For example, we have only just begun to understand how lattice strain [111], organic capping ligands [112, 113], and solvent environment [114, 115] influence the photophysics of QDs. While not of significance for simple optical absorption, the surface can have a huge effect on radiative and nonradiative pathways in QDs. For example, the precise nature of carrier multiplication in QDs, whereby a single, high energy photoexcited electron nonradiatively relaxes to produces two or more excitons, is a matter of intense investigation and discussion in the literature [116–119]. It is increasingly clear that the exact nature of the QD surface is intimately related to the apparent efficiency of the carrier multiplication process [117].

In summary, since the 1990s a basic understanding of the fascinating size dependence of the electronic states of semiconductor QDs has been well established. Several

theoretical methods have been developed with varying degrees of refinement that predict the basic photophysics of QDs. However, in many respects the study of the electronic states in QDs is still in its infancy. Even something as fundamental as a true single particle absorption spectrum, free from averaging over the ensemble, has remained elusive. The chemistry and physics of the surface atoms, which given the large percentage of surface atoms would seem to fundamentally be important, are largely ignored. With regard to developing new experimental and theoretical methods to study the electronic states of QDs, which will naturally lead to the use of QDs in new technologies, it is clear that the future is very bright indeed.

References

1 R. D. Schaller, V. I. Klimov, High efficiency carrier multiplication in PbSe nanocrystals: implications for solar energy conversion. *Physical Review Letters*, **92** (2004), 186601.
2 R. J. Ellingson, M. C. Beard, J. C. Johnson, *et al*., Highly efficient multiple exciton generation in colloidal PbSe and PbS quantum dots. *Nano Letters*, **5** (2005), 865–871.
3 L. Brus, Electronic wave functions in semiconductor clusters: experiment and theory. *Journal of Physical Chemistry*, **90** (1986), 2555–2560.
4 L. Bányai, S. W. Koch, *Semiconductor Quantum Dots*. River Edge, NJ: World Scientific Publishing Company, 1993.
5 H. Weller, Colloidal semiconductor Q-particles: chemistry in the transition region between solid state and molecules. *Angewandte Chemie International Edition*, **32** (1993), 41–53.
6 U. Woggon, *Optical Properties of Semiconductor Quantum Dots*. Berlin: Springer, 1996.
7 A. P. Alivisatos, Semiconductor clusters, nanocrystals, and quantum dots. *Science*, **271** (1996), 933–937.
8 S. V. Gaponenko, *Optical Properties of Semiconductor Nanocrystals*. Cambridge: Cambridge University Press, 1998.
9 M. Nirmal, L. Brus, Luminescence photophysics in semiconductor nanocrystals. *Accounts of Chemical Research*, **32** (1999), 407–414.
10 A. L. Efros, M. Rosen, Electronic structure of semiconductor nanocrystals. *Annual Review of Materials Science*, **30** (2000), 475–521.
11 A. Eychmuller, Structure and photophysics of semiconductor nanocrystals. *Journal of Physical Chemistry B*, **104** (2000), 6514–6528.
12 D. Norris, Electronic structure in semiconductor nanocrystals. In *Semiconductor and Metal Nanocrystals: Synthesis and Electronic and Optical Properties*, V. I. Klimov, ed., pp. 65–102. New York, NY: Marcel Dekker, 2003.
13 C. Delerue, M. Lannoo, *Nanostructures: Theory and Modeling*. Berlin, Heidelberg: Springer-Verlag, 2004.
14 C. Burda, X. Chen, R. Narayanan, M. A. El-Sayed, Chemistry and properties of nanocrystals of different shapes. *Chemical Reviews*, **105** (2005), 1025–1102.
15 E. H. Sargent, Infrared quantum dots. *Advanced Materials*, **17** (2005), 515–522.
16 Y. Masumoto, T. Takagahara, *Semiconductor Quantum Dots: Physics, Spectroscopy, and Applications*. Berlin, Heidelberg: Springer, 2010.
17 D. E. Gómez, M. Califano, P. Mulvaney, Optical properties of single semiconductor nanocrystals. *Physical Chemistry Chemical Physics*, **8** (2006), 4989–5011.

18 O. V. Prezhdo, Photoinduced dynamics in semiconductor quantum dots: insights from time-domain ab initio studies. *Accounts of Chemical Research*, **42** (2009), 2005–2016.
19 O. Madelung, *Semiconductors: Data Handbook*. Berlin: Springer-Verlag, 2004.
20 A. L. Efros, A. L. Efros, Interband absorption of light in a semiconductor sphere. *Soviet Physics Semiconductors*, **16** (1982), 772–775.
21 L. E. Brus, A simple model for the ionization potential, electron affinity, and aqueous redox potentials of small semiconductor crystallites. *Journal of Chemical Physics*, **79** (1983), 5566–5571.
22 L. E. Brus, Electron–electron and electron–hole interactions in small semiconductor crystallites: the size dependence of the lowest excited electronic state. *Journal of Chemical Physics*, **80** (1984), 4403–4409.
23 P. C. Sercel, K. J. Vahala, Analytical formalism for determining quantum-wire and quantum-dot band structure in the multiband envelope-function approximation. *Physical Review B*, **42** (1990), 3690–3710.
24 N. Ashcroft, N. D. Mermin, *Solid State Physics*. Fort Worth, TX: Saunders College Publishing, 1976.
25 O. I. Mićić, H. M. Cheong, H. Fu, *et al*., Size-dependent spectroscopy of InP quantum dots. *Journal of Physical Chemistry B*, **101** (1997), 4904–4912.
26 W. W. Yu, L. Qu, W. Guo, X. Peng, Experimental determination of the extinction coefficient of CdTe, CdSe, and CdS nanocrystals. *Chemistry of Materials*, **15** (2003), 2854–2860.
27 C. D. M. Donegá, R. Koole, Size dependence of the spontaneous emission rate and absorption cross section of CdSe and CdTe quantum dots. *Journal of Physical Chemistry C*, **113** (2009), 6511–6520.
28 I. Moreels, K. Lambert, D. Smeets, *et al*., Size-dependent optical properties of colloidal PbS quantum dots. *ACS Nano*, **3** (2009), 3023–3030.
29 L. Cademartiri, E. Montanari, G. Calestani, *et al*., Size-dependent extinction coefficients of PbS quantum dots. *Journal of the American Chemical Society*, **128** (2006), 10337–10346.
30 I. Moreels, K. Lambert, D. De Muynck, *et al*., Composition and size-dependent extinction coefficient of colloidal PbSe quantum dots. *Chemistry of Materials*, **19** (2007), 6101–6106.
31 Q. Dai, Y. Wang, X. Li, *et al*., Size-dependent composition and molar extinction coefficient of PbSe semiconductor nanocrystals. *ACS Nano*, **3** (2009), 1518–1524.
32 P. Yu, M. C. Beard, R. J. Ellingson, *et al*., Absorption cross-section and related optical properties of colloidal InAs quantum dots. *Journal of Physical Chemistry B*, **109** (2005), 7084–7087.
33 C. B. Murray, D. J. Norris, M. G. Bawendi, Synthesis and characterization of nearly monodisperse CdE (E = S, Se, Te) semiconductor nanocrystallites. *Journal of the American Chemical Society*, **115** (1993), 8706–8715.
34 L. Qu, Z. A. Peng, X. Peng, Alternative routes toward high quality CdSe nanocrystals. *Nano Letters*, **1** (2001), 333–337.
35 C. B. Murray, S. Sun, W. Gaschler, *et al*., Colloidal synthesis of nanocrystals and nanocrystal superlattices. *IBM Journal of Research and Development*, **45** (2001), 47–56.
36 D. V. Talapin, A. L. Rogach, A. Kornowski, M. Haase, H. Weller, Highly luminescent monodisperse CdSe and CdSe/ZnS nanocrystals synthesized in a hexadecylamine-trioctylphosphine oxide-trioctylphospine mixture. *Nano Letters*, **1** (2001), 207–211.
37 C. B. Murray, C. R. Kagan, M. G. Bawendi, Synthesis and characterization of monodisperse nanocrystals and close-packed nanocrystal assemblies. *Annual Review of Materials Science*, **30** (2000), 545–610.

38 M. Nirmal, C. B. Murray, M. G. Bawendi, Fluorescence-line narrowing in CdSe quantum dots: surface localization of the photogenerated exciton. *Physical Review B*, **50** (1994), 2293.
39 D. J. Norris, M. G. Bawendi, Measurement and assignment of the size-dependent optical spectrum in CdSe quantum dots. *Physical Review B*, **53** (1996), 16338–16346.
40 M. A. Hines, P. Guyot-Sionnest, Synthesis and characterization of strongly luminescing ZnS-capped CdSe nanocrystals. *Journal of Physical Chemistry*, **100** (1996), 468–471.
41 B. O. Dabbousi, J. Rodriguez-Viejo, F. V. Mikulec, *et al*., (CdSe)ZnS core-shell quantum dots: synthesis and characterization of a size series of highly luminescent nanocrystallites. *Journal of Physical Chemistry B*, **101** (1997), 9463–9475.
42 Invitrogen Corporation, "QDot Nanocrystal Technology". www.invitrogen.com (accessed December 1, 2010).
43 J. Yao, D. R. Larson, H. D. Vishwasrao, *et al*., Blinking and nonradiant dark fraction of water-soluble quantum dots in aqueous solution. *Proceedings of the National Academy of Sciences USA*, **102** (2005), 14284–14289.
44 M. Bruchez Jr, M. Moronne, P. Gin, S. Weiss, A. P. Alivisatos, Semiconductor nanocrystals as fluorescent biological labels. *Science*, **281** (1998), 2013–2016.
45 W. C. W. Chan, S. Nie, Quantum dot bioconjugates for ultrasensitive nonisotopic detection. *Science*, **281** (1998), 2016–2018.
46 B. Dubertret, P. Skourides, D. J. Norris, *et al*., In vivo imaging of quantum dots encapsulated in phospholipid micelles. *Science*, **298** (2002), 1759–1762.
47 S. Kim, B. Fisher, H.-J. Eisler, M. Bawendi, Type-II quantum dots: CdTe/CdSe(core/shell) and CdSe/ZnTe(core/shell) heterostructures. *Journal of the American Chemical Society*, **125** (2003), 11466–11467.
48 R. Xie, X. Zhong, T. Basche, Synthesis, characterization, and spectroscopy of type-II core/shell semiconductor nanocrystals with ZnTe Cores. *Advanced Materials*, **17** (2005), 2741–2745.
49 S. A. Ivanov, A. Piryatinski, J. Nanda, *et al*., Type-II core/shell CdS/ZnSe nanocrystals: synthesis, electronic structures, and spectroscopic properties. *Journal of the American Chemical Society*, **129** (2007), 11708–11719.
50 G. D. Scholes, Controlling the optical properties of inorganic nanoparticles. *Advanced Functional Materials*, **18** (2008), 1157–1172.
51 S. S. Lo, T. Mirkovic, C. H. Chuang, C. Burda, G. D. Scholes, Emergent properties resulting from type-II band alignment in semiconductor nanoheterostructures. *Advanced Materials*, **23** (2011), 180–197.
52 V. I. Klimov, S. A. Ivanov, J. Nanda, *et al*., Single-exciton optical gain in semiconductor nanocrystals. *Nature*, **447** (2007), 441–446.
53 P. Peng, D. J. Milliron, S. M. Hughes, *et al*., Femtosecond spectroscopy of carrier relaxation dynamics in type II CdSe/CdTe tetrapod heteronanostructures. *Nano Letters*, **5** (2005), 1809–1813.
54 H. Zhong, Y. Zhou, Y. Yang, C. Yang, Y. Li, Synthesis of type II CdTe-CdSe nanocrystal heterostructured multiple-branched rods and their photovoltaic applications. *Journal of Physical Chemistry C*, **111** (2007), 6538–6543.
55 S. Kim, Y. T. Lim, E. G. Soltesz, *et al*., Near-infrared fluorescent type II quantum dots for sentinel lymph node mapping. *Nature Biotechnology*, **22** (2004), 93–97.
56 J. M. Luttinger, W. Kohn, Motion of electrons and holes in perturbed periodic fields. *Physical Review*, **97** (1955), 869–883.
57 J. M. Luttinger, Quantum theory of cyclotron resonance in semiconductors: general theory. *Physical Review*, **102** (1956), 1030–1041.

58 E. O. Kane, Band structure of indium antimonide. *Journal of Physics and Chemistry of Solids*, **1** (1957), 249–261.
59 C. R. Pidgeon, R. N. Brown, Interband magneto-absorption and Faraday rotation in InSb. *Physical Review*, **146** (1966), 575.
60 A. I. Ekimov, F. Hache, M. C. Schanne-Klein, *et al*., Absorption and intensity-dependent photoluminescence measurements on CdSe quantum dots: assignment of the first electronic transitions. *Journal of the Optical Society of America B*, **10** (1993), 100–107.
61 G. B. Grigoryan, E. M. Kazaryan, A. L. Efros, T. V. Yazeva, Quantized holes and the absorption edge in spherical semiconductor microcrystals with a complex valence band structure *Sov*. *Physics of the Solid State*, **32** (1990), 1031.
62 J. B. Xia, Electronic structures of zero-dimensional quantum wells. *Physical Review B*, **40** (1989), 8500–8507.
63 K. J. Vahala, P. C. Sercel, Application of a total-angular-momentum basis to quantum-dot band structure. *Physical Review Letters*, **65** (1990), 239–242.
64 A. L. Efros, A. V. Rodina, Band-edge absorption and luminescence of nonspherical nanometer-size crystals. *Physical Review B*, **47** (1993), 10005–10007.
65 T. Takagahara, Effects of dielectric confinement and electron–hole exchange interaction on excitonic states in semiconductor quantum dots. *Physical Review B*, **47** (1993), 4569–4584.
66 M. Nirmal, D. J. Norris, M. Kuno, *et al*., Observation of the "dark exciton" in CdSe quantum dots. *Physical Review Letters*, **75** (1995), 3728–3731.
67 C. Cohen-Tannoudji, B. Diu, F. Laloë, *Quantum Mechanics*. Paris: Wiley & Sons, 1977.
68 D. J. Norris, A. L. Efros, M. Rosen, M. G. Bawendi, Size dependence of exciton fine structure in CdSe quantum dots. *Physical Review B*, **53** (1996), 16347–16354.
69 M. G. Bawendi, W. L. Wilson, L. Rothberg, *et al*., Electronic structure and photoexcited-carrier dynamics in nanometer-size CdSe clusters. *Physical Review Letters*, **65** (1990), 1623–1626.
70 F. W. Wise, Lead salt quantum dots: the limit of strong quantum confinement. *Accounts of Chemical Research*, **33** (2000), 773–780.
71 S. H. Wei, A. Zunger, Electronic and structural anomalies in lead chalcogenides. *Physical Review B*, **55** (1997), 13605–13610.
72 J. M. An, A. Franceschetti, S. V. Dudiy, A. Zunger, The peculiar electronic structure of PbSe quantum dots. *Nano Letters*, **6** (2006), 2728–2735.
73 G. Allan, C. Delerue, Confinement effects in PbSe quantum wells and nanocrystals. *Physical Review B*, **70** (2004), 245321.
74 I. Kang, F. W. Wise, Electronic structure and optical properties of PbS and PbSe quantum dots. *Journal of the Optical Society of America B*, **14** (1997), 1632–1646.
75 H. Du, C. Chen, R. Krishnan, *et al*., Optical properties of colloidal PbSe nanocrystals. *Nano Letters*, **2** (2002), 1321–1324.
76 D. R. Hamann, Semiconductor charge densities with hard-core and soft-core pseudopotentials. *Physical Review Letters*, **42** (1979), 662–665.
77 L. W. Wang, A. Zunger, Local-density-derived semiempirical pseudopotentials. *Physical Review B*, **51** (1995), 17398–17416.
78 A. Zunger, Pseudopotential theory of semiconductor quantum dots. *Physica Status Solidi B*, **224** (2001), 727–734.
79 L. M. Ramaniah, S. V. Nair, Optical absorption in semiconductor quantum dots: a tight-binding approach. *Physical Review B*, **47** (1993), 7132.
80 R. S. Kane, R. E. Cohen, R. Silbey, Theoretical study of the electronic structure of PbS nanoclusters. *Journal of Physical Chemistry*, **100** (1996), 7928–7932.

81 S. Pokrant, K. B. Whaley, Tight-binding studies of surface effects on electronic structure of CdSe nanocrystals: the role of organic ligands, surface reconstruction, and inorganic capping shells. *European Physical Journal D*, **6** (1999), 255–267.
82 G. Allan, Y. M. Niquet, C. Delerue, Quantum confinement energies in zinc-blende III–V and group IV semiconductors. *Applied Physics Letters*, **77** (2000), 639–641.
83 L. W. Wang, A. Zunger, Electronic structure pseudopotential calculations of large (approx.1000 atoms) Si quantum dots. *Journal of Physical Chemistry*, **98** (1994), 2158–2165.
84 L. W. Wang, A. Zunger, Pseudopotential calculations of nanoscale CdSe quantum dots. *Physical Review B*, **53** (1996), 9579–9582.
85 H. Fu, A. Zunger, Local-density-derived semiempirical nonlocal pseudopotentials for InP with applications to large quantum dots. *Physical Review B*, **55** (1997), 1642–1653.
86 E. Rabani, B. Hetényi, B. J. Berne, L. E. Brus, Electronic properties of CdSe nanocrystals in the absence and presence of a dielectric medium. *Journal of Chemical Physics*, **110** (1999), 5355–5369.
87 S. L. Sewall, R. R. Cooney, P. Kambhampati, Experimental tests of effective mass and atomistic approaches to quantum dot electronic structure: ordering of electronic states. *Applied Physics Letters*, **94** (2009), 243116.
88 B. L. Wehrenberg, C. Wang, P. Guyot-Sionnest, Interband and intraband optical studies of PbSe colloidal quantum dots. *Journal of Physical Chemistry B*, **106** (2002), 10634–10640.
89 P. Liljeroth, P. A. Z. Van Emmichoven, S. G. Hickey, *et al*., Density of states measured by scanning-tunneling spectroscopy sheds new light on the optical transitions in PbSe nanocrystals. *Physical Review Letters*, **95** (2005), 086801.
90 M. T. Trinh, A. J. Houtepen, J. M. Schins, J. Piris, L. D. A. Siebbeles, Nature of the second optical transition in PbSe nanocrystals. *Nano Letters*, **8** (2008), 2112–2117.
91 J. J. Peterson, L. Huang, C. Delerue, G. Allan, T. D. Krauss, Uncovering forbidden optical transitions in PbSe nanocrystals. *Nano Letters*, **7** (2007), 3827–3831.
92 G. Nootz, L. A. Padilha, P. D. Olszak, *et al*., Role of symmetry breaking on the optical transitions in lead-salt quantum dots. *Nano Letters*, **10** (2010), 3577–3582.
93 E. Runge, E. K. U. Gross, Density-functional theory for time-dependent systems. *Physical Review Letters*, **52** (1984), 997–1000.
94 E. K. U. Gross, W. Kohn, Local density-functional theory of frequency-dependent linear response. *Physical Review Letters*, **55** (1985), 2850–2852.
95 O. V. Prezhdo, Multiple excitons and the electron–phonon bottleneck in semiconductor quantum dots: an *ab initio* perspective. *Chemical Physics Letters*, **460** (2008), 1–9.
96 C. F. Craig, W. R. Duncan, O. V. Prezhdo, Trajectory surface hopping in the time-dependent Kohn–Sham approach for electron-nuclear dynamics. *Physical Review Letters*, **95** (2005), 163001.
97 B. F. Habenicht, C. F. Craig, O. V. Prezhdo, Time-domain ab initio simulation of electron and hole relaxation dynamics in a single-wall semiconducting carbon nanotube. *Physical Review Letters*, **96** (2006), 187401.
98 S. V. Kilina, C. F. Craig, D. S. Kilin, O. V. Prezhdo, Ab initio time-domain study of phonon-assisted relaxation of charge carriers in a PbSe quantum dot. *Journal of Physical Chemistry C*, **111** (2007), 4871–4878.
99 H. Kamisaka, S. V. Kilina, K. Yamashita, O. V. Prezhdo, Ultrafast vibrationally-induced dephasing of electronic excitations in PbSe quantum dots. *Nano Letters*, **6** (2006), 2295–2300.

100 S. Kudera, M. Zanella, C. Giannini, *et al*., Sequential growth of magic-size CdSe nanocrystals. *Advanced Materials*, **19** (2007), 548–552.
101 C. M. Evans, L. Guo, J. J. Peterson, S. Maccagnano-Zacher, T. D. Krauss, Ultrabright PbSe magic-sized clusters. *Nano Letters*, **8** (2008), 2896–2899.
102 S. Hinds, S. Myrskog, L. Levina, *et al*., NIR-emitting colloidal quantum dots having 26% luminescence quantum yield in buffer solution. *Journal of the American Chemical Society*, **129** (2007), 7218–7219.
103 X. Wang, X. Ren, K. Kahen, *et al*., Non-blinking semiconductor nanocrystals. *Nature*, **459** (2009), 686–689.
104 N. Akopian, G. Patriarche, L. Liu, J. C. Harmand, V. Zwiller, Crystal phase quantum dots. *Nano Letters*, **10** (2010), 1198–1201.
105 A. M. Smith, S. Nie, Semiconductor nanocrystals: structure, properties, and band gap engineering. *Accounts of Chemical Research*, **43** (2010), 190–200.
106 W. E. Moerner, M. Orrit, Illuminating single molecules in condensed matter. *Science*, **283** (1999), 1670–1676.
107 M. Nirmal, B. O. Dabbousi, M. G. Bawendi, *et al*., Fluorescence intermittency in single cadmium selenide nanocrystals. *Nature*, **383** (1996), 802–804.
108 S. A. Empedocles, D. J. Norris, M. G. Bawendi, Photoluminescence spectroscopy of single CdSe nanocrystallite quantum dots. *Physical Review Letters*, **77** (1996), 3873–3876.
109 S. Empedocles, M. Bawendi, Spectroscopy of single CdSe nanocrystallites. *Accounts of Chemical Research*, **32** (1999), 389–396.
110 H. Htoon, P. J. Cox, V. I. Klimov, Structure of excited-state transitions of individual semiconductor nanocrystals probed by photoluminescence excitation spectroscopy. *Physical Review Letters*, **93** (2004), 187402.
111 A. M. Smith, A. M. Mohs, S. Nie, Tuning the optical and electronic properties of colloidal nanocrystals by lattice strain. *Nature Nanotechnology*, **4** (2009), 56–63.
112 A. Pandey, P. Guyot-Sionnest, Slow electron cooling in colloidal quantum dots. *Science*, **322** (2008), 929–932.
113 H. Liu, P. Guyot-Sionnest, Photoluminescence lifetime of lead selenide colloidal quantum dots. *Journal of Physical Chemistry C*, **114** (2010), 14860–14863.
114 C. A. Leatherdale, M. G. Bawendi, Observation of solvatochromism in CdSe colloidal quantum dots. *Physical Review B*, **63** (2001), 1653151–1653156.
115 M. Jones, S. S. Lo, G. D. Scholes, Quantitative modeling of the role of surface traps in CdSe/CdS/ZnS nanocrystal photoluminescence decay dynamics. *Proceedings of the National Academy of Sciences USA*, **106** (2009), 3011–3016.
116 A. Franceschetti, J. M. An, A. Zunger, Impact ionization can explain carrier multiplication in PbSe quantum dots. *Nano Letters*, **6** (2006), 2191–2195.
117 J. A. McGuire, J. Joo, J. M. Pietryga, R. D. Schaller, V. I. Klimov, New aspects of carrier multiplication in semiconductor nanocrystals. *Accounts of Chemical Research*, **41** (2008), 1810–1819.
118 A. J. Nozik, M. C. Beard, J. M. Luther, *et al*., Semiconductor quantum dots and quantum dot arrays and applications of multiple exciton generation to third-generation photovoltaic solar cells. *Chemical Reviews*, **110** (2010), 6873–6890.
119 C. Delerue, G. Allan, J. J. H. Pijpers, M. Bonn, Carrier multiplication in bulk and nanocrystalline semiconductors: mechanism, efficiency, and interest for solar cells. *Physical Review B*, **81** (2010), 125306.

4 Charge and energy transfer in polymer/nanocrystal blends

Physics and devices

Kevin M. Noone and David S. Ginger

4.1 Introduction

The vision of consumer semiconductor devices manufactured by inexpensive roll-to-roll printing techniques is one that has driven research in many fields, including solution-processable polymers [1] and colloidal inorganic semiconductors such as quantum dots (QDs) [2]. Blends of conjugated polymers and inorganic QDs in principle allow scientists to obtain the best properties of both organic and colloidal inorganic materials in a single system, and a broad range of hybrid polymer/quantum dot devices – including light emitting diodes (LEDs), photodetectors, and photovoltaics (PVs) – have been reported.

QDs initially drew the interest of researchers because of their size dependent electronic structure, which arises from the strong quantum confinement of charge carriers inside semiconductor particles with dimensions smaller than the exciton Bohr radius [3–6]. CdSe nanocrystals are the archetypal colloidal QD material and can be synthesized in the 2–5 nm diameter range with bandgaps covering almost the entire visible spectrum. Early pioneering work on colloidal quantum dots was done by Brus [7, 8], Efros [9], Weller [10, 11], and others in the 1980s and 1990s, however, the field entered an exciting new phase with the development of the hot-injection synthesis of monodisperse nanocrystalline CdSe [12], which initiated a wave of interest that has grown continuously since the 1990s and has expanded to include a variety of QD materials with bandgaps ranging from the ultraviolet through the infrared.

The driving factors behind the growing research into colloidal QDs have been solution processability, the broad range of wavelengths that can be accessed with different QD sizes and materials, their inherent size-tailorable absorption and emission spectra, and the search for properties not exhibited by bulk semiconductors. Bright, narrow-band emission from visible-bandgap QDs, such as cadmium (II) selenide (CdSe) could potentially be used in LEDs to create more efficient displays [13]. Highly emissive CdSe QDs are already being used as down converting phosphors to improve the color rendering index of inorganic solid state lighting and displays [14]. Likewise, emission from infrared bandgap QDs, such as lead (II) sulfide (PbS) holds promise for telecommunications applications [2, 15–17]. New physics in quantum confined systems, such as slow carrier cooling via the long sought "phonon bottleneck" [18, 19], could possibly allow the use of

Colloidal Quantum Dot Optoelectronics and Photovoltaics, eds. G. Konstantatos and E. H. Sargent.
Published by Cambridge University Press. © Cambridge University Press, 2013.

hot carrier effects in various applications such as solar PVs that circumvent the Schottky–Quiesser limit, though many challenges remain [20]. Even without new physics like multiexciton generation or hot carrier effects, the combined advantages of large extinction coefficients, broad-band absorption, size-tailorable bandgaps, and solution processability make QDs appealing for both photodetectors [16, 21, 22] and solar cells [16, 22, 23].

Many of these devices can be made by incorporating both QDs and organic semiconductors into the same structure, typically in intimate physical and electrical contact with each other. If such devices are to be deployed in commercial products, it will be important to understand the physics and chemistry of the interactions between these materials, as well as the factors that dictate the behavior of charge carriers and excitons within hybrid structures. In this chapter we provide a selective overview of work aimed at understanding and improving LEDs, photodetectors, and solar cells containing colloidal QDs. In particular we emphasize hybrid materials and devices containing both organic semiconductors and inorganic QDs.

4.2 A brief history of QD/polymer optoelectronics

4.2.1 Quantum dot light emitting diodes (QD-LEDs) – size-tunable emission across the spectrum

Size-tunable bandgaps and superior color purity (from highly monochromatic emission with bands as narrow as 30 meV exhibited by the best QDs) make colloidal monodisperse QDs attractive candidates as emitters in LEDs for display, solid state lighting, and telecommunication applications. Furthermore, since well-coated QDs have been shown to possess greater photostability than organic emitters, QD-LEDs have the potential to exhibit longer operation lifetimes than their purely organic LED (OLED) counterparts [24, 25]. At the time of writing, the state of the art in QD-LEDs has advanced to the verge of commercialization. One issue, of course, is the use of toxic heavy metals such as Cd and Pb, but energy efficiency and alternative emitters may offer the potential to overcome these concerns [26].

While classic inorganic LEDs containing QDs and quantum wells made by molecular beam epitaxy have a long history [3, 27, 28], among the earliest LEDs containing colloidal QDs were those reported as QD/polymer bilayers in 1994 by Colvin *et al.* [29] and as QD/polymer blends in 1995 by Dabbousi *et al.* [30]. These early devices had relatively low external quantum efficiencies (EQEs, defined for LEDs as the number of photons out of the device per injected electron) of 0.01% and 0.0005%, respectively. Furthermore, they exhibited electroluminescence from both the QDs and the organic semiconductors, which compromised their color purity. Since then, devices have improved dramatically, and can now exhibit narrow-band electroluminescence originating from the QDs alone [24, 25, 31, 32], with commercial start ups reporting EQEs as high as 7%, and brightnesses of up to 41 000 cd/m^2 [33]. To achieve this performance, most of the QD-LEDs being investigated at the time of writing consist of a layer of QDs sandwiched between organic hole and electron transport layers (Figure 4.1(a)). This multilayer architecture has been used to fabricate LEDs that emit white light [34, 35], as well as colors across

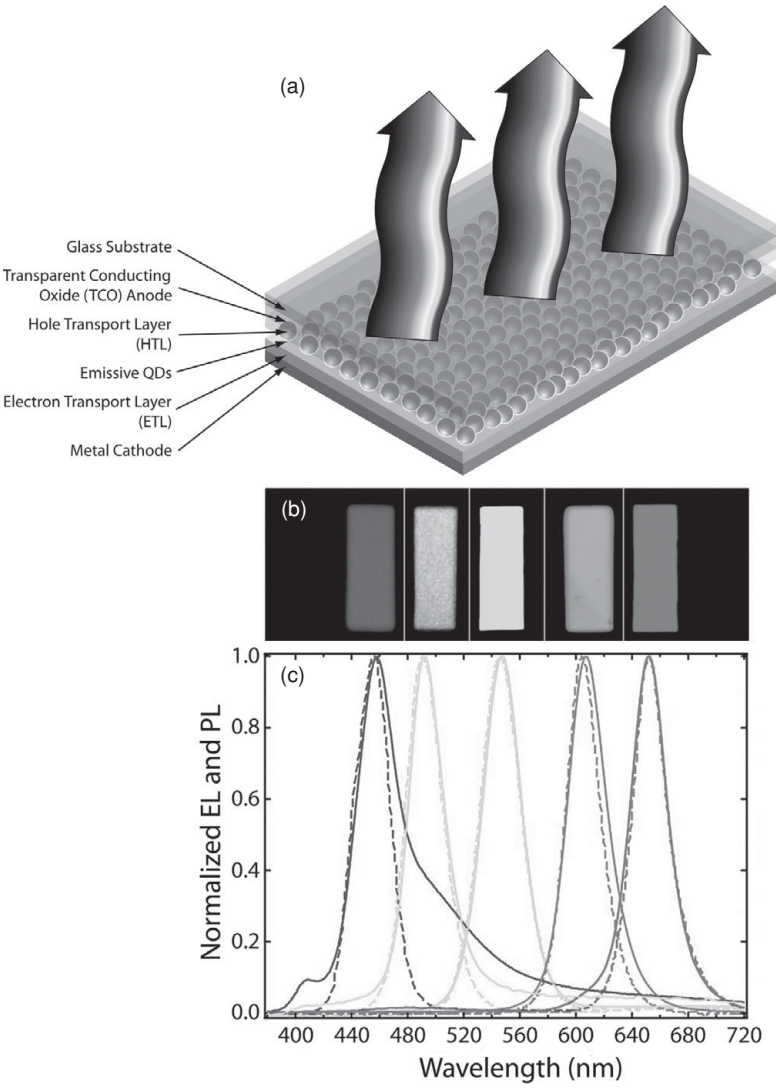


Figure 4.1 (a) Cartoon schematic depicting a typical QD-LED device structure. (b) Photographs of pixels from CdSe QD-LED devices spanning the visible spectrum (in color in the electronic version). (c) Measured electroluminescence (EL, solid lines) and photoluminescence (PL, dashed lines) of the CdSe quantum dots used in the LEDs. Color version of this figure is available online at www.cambridge.org/9780521198264. Printed with permission from [35].

the visible spectrum (Figures 4.1(b) and (c)) [36], and even into the infrared [15, 17, 37, 38]. While the QD layer is often represented as a monolayer (as in Figure 4.1(a)), the layer is probably imperfect. LEDs with emissive QD layers slightly greater than a monolayer have been shown to exhibit better performance in some cases [32] and others have reported that QDs can be partially buried in the organic matrix, even when deposited by soft lithography, a result which has important implications for understanding device operation and efficiency [39].

Understandably, the exact operating mechanism of QD-LEDs has been a major area of study. Two theories exist to describe exactly how excitons are generated in the QD layer of the device. In the first, electrons and holes are injected directly into the QDs from the n- and p-type transport layers, respectively. However, the band alignments are such that there is typically a large barrier to hole injection from most organic semiconductor materials into most QD materials. A second possible method for exciton formation is to first form the excitons on one of the organic materials and then Förster transfer them to the QDs. Work done on LEDs with inorganic charge transport layers suggests that these all-inorganic devices operate primarily by means of the direct charge injection mechanism [40, 41], however, evidence from hybrid organic/inorganic devices (discussed in more detail in Section 4.3.2.1) could be interpreted as supporting either of the proposed mechanisms. The function of QD-LEDs may, in fact, rely on some combination from each of them, depending on the bandgap of the QDs and the choice of electron and hole transport layers [36, 42]. However, it appears that the method of operation is dominated by the Förster transfer mechanism in most of the best devices [36].

There are compelling reasons to study QD-LEDs. While they still (at the time of writing) lagged behind their solution-processable OLED counterparts in terms of efficiency and brightness, the gap is closing [13]. Furthermore, the color purity of QD-LEDs is exceptional, and can be used to produce displays with superior color rendering. Regardless, the fact that some of the fundamental questions about QD-LED device operation remain open suggests that plenty of room for improvement remains.

4.2.2 Quantum dot photovoltaics (QD-PV) and photodetectors – converting photons to electrons

With bandgaps ranging from the visible into the near-infrared, and absorbance over broad spectral ranges, colloidal QDs are promising candidates for use as light harvesting materials in both PVs and photodetectors. In the early 1990s, Wang and Herron reported photoconductivity from a blend of colloidal CdS QDs with the conjugated polymer, N-polyvinylcarbazole (PVK) [43]. This early work opened the door for QD/polymer blends to be used for both solar power conversion and optical sensing. While both solar cells and photodetectors made from QD/polymer blends convert absorbed light into electrical current, and can do so through similar mechanisms, there are significant differences between the two in terms of their ultimate applications. A solar cell must produce electrical power under incident radiation, while a photodetector can consume power to exhibit gain and generate a larger signal. As such, it is useful to discuss the two classes of devices separately before exploring the similarities in the physics that drive them.

4.2.2.1 QD-PVs

Figure 4.2(a) shows the general sandwich photodiode architecture typical of solution-processed PVs. Active layers are cast on top of a transparent conducting layer, often

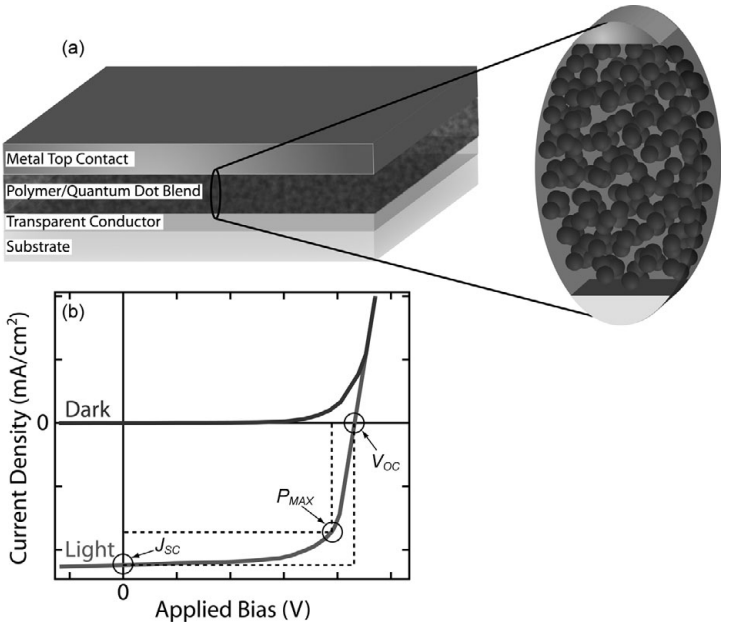


Figure 4.2 (a) Schematic of a typical bulk heterojunction blend photodiode containing inorganic, colloidal QDs embedded in an organic semiconductor film. (b) Standard light and dark *J–V* curves. Labeled on the light *J–V* curve are the short circuit current (J_{SC}), the open circuit voltage (V_{OC}), and the maximum power point (P_{max}) used to calculate fill factor (*FF*).

indium tin oxide (ITO), and metal top contacts are deposited via thermal evaporation through a shadow mask. In principle, the top contacts can also be deposited by printing, which would enable the realization of an entirely solution-processed device [44]. To generate electrical power under illumination, solar cells must produce both a photovoltage and a photocurrent. The photocurrent for a solar cell is often reported as the EQE (defined for a solar cell as the number of collected electrons per incident photon). A solar cell's performance is measured by its total power conversion efficiency (PCE). The total PCE is calculated by measuring the short circuit current density (J_{SC}), open circuit voltage (V_{OC}), and fill factor (*FF*) under illumination and using the following relation:

$$PCE = \frac{J_{SC} \times V_{OC} \times FF}{P_{opt}}.$$

These values (except for the incident optical power, P_{opt}) are extracted from current–voltage (*J–V*) curves taken from a device under illumination (see Figure 4.2(b)). J_{SC} and V_{OC} are taken directly from the *J–V* curves, while the *FF* is calculated by dividing the ratio of the maximum power point (P_{MAX}) by the product of the J_{SC} and the V_{OC}.

Some researchers have focused on "all-inorganic" QD-PVs utilizing QDs as both the electron donor (p-type) and electron acceptor (n-type). Such devices include: (1) the QD/QD bilayer devices reported by Gur *et al.* [45] and Sholin *et al.*, [46]; (2) dye-sensitized solar cells (DSSCs) that utilize QD sensitizers adsorbed on TiO_2 [47]; and (3) solution-processed bilayers that utilize a layer of infrared absorbing QDs as the

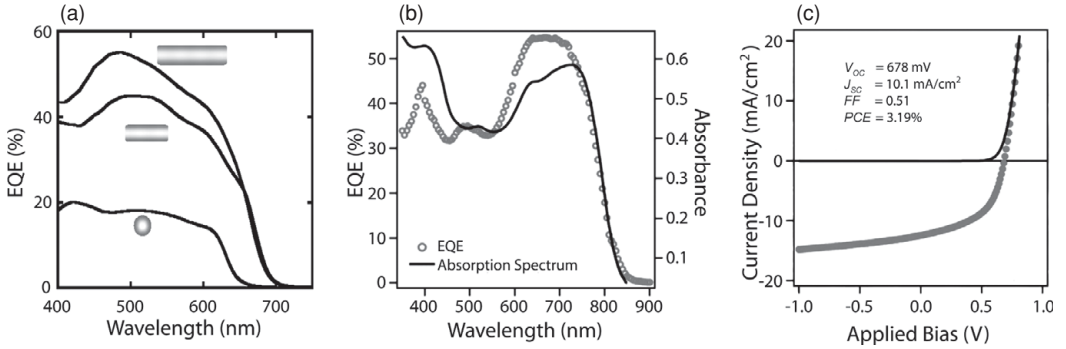


Figure 4.3 (a) The EQEs of CdSe/P3HT BHJ blend devices improve when quasi-spherical particles are replaced with nanorods. Printed with permission from [52]. (b) Further improvements in device performance were realized for blends of CdSe tetrapods with the low bandgap polymer PCPDTBT giving (c) a PCE of a polymer/quantum dot bulk heterojunction blend solar cell exceeding 3% under AM1.5 radiation. Printed with permission from [55].

p-type layer and solution-processed metal oxide nanoparticles as n-type layers, such as PbSe/ZnO [48] and PbS/TiO_2 [49] PVs, with the latter operating with PCEs as high as 5%, which at the time of writing was the record for QD-PVs. However, it is also common to combine QDs with organic semiconductors, such as conjugated polymers, in bulk heterojunction (BHJ) blend thin films. Many semiconducting polymers are easily cast from solution into thin solid films, and these polymers can improve the film-forming properties of the colloidal QD suspensions, making them attractive hosts for nanocrystalline inorganic semiconductor materials.

One early QD/polymer blend to show promise in a PV device structure was that of CdSe QDs blended with poly(2-methoxy,5-(2'-ethyl)hexyloxy–*p*–phenylenevinylene) (MEH-PPV). These devices, reported by Greenham *et al.*, exhibited maximum EQEs of 12% and PCEs of less than 1% [50]. Efficiencies improved as better polymers, such as poly-3-hexylthiophene (P3HT), were used and when the quasi-spherical QDs were replaced by nanorods [51–53], tetrapods [54, 55] (Figure 4.3), and hyperbranched structures [56], all of which provide more contiguous charge conduction pathways, enhancing charge collection efficiency. At the time of writing, the best reported hybrid organic–inorganic PVs employ bulk heterojunction blends of CdSe tetrapods with a low bandgap polymer, poly[2,6-(4,4-bis-(2-ethylhexyl)-4*H*-cyclopenta[2,1-b;3,4-b′]dithiophene)-*alt*-4,7-(2,1,3-benzothiadiazole)] (PCP-DTBT), exhibited a PCE of more than 3% under simulated solar illumination [55]. Though this is lower than the PCEs of the best all-organic (polymer/fullerene) solid state PVs, it is reasonable to believe QD blend PVs could one day surpass their all-organic counterparts. Potential advantages of colloidal QDs include better photostability, the potential for absorption spectra more suitable to solar energy collection, and higher dielectric constants. Since charge carrier generation and recombination in organic PV devices is sensitive to the Coulombic attraction between the electron and hole, we speculate that the theoretical performance limit for hybrid devices incorporating higher dielectric constant inorganic acceptors could be higher than that for an all-organic device.

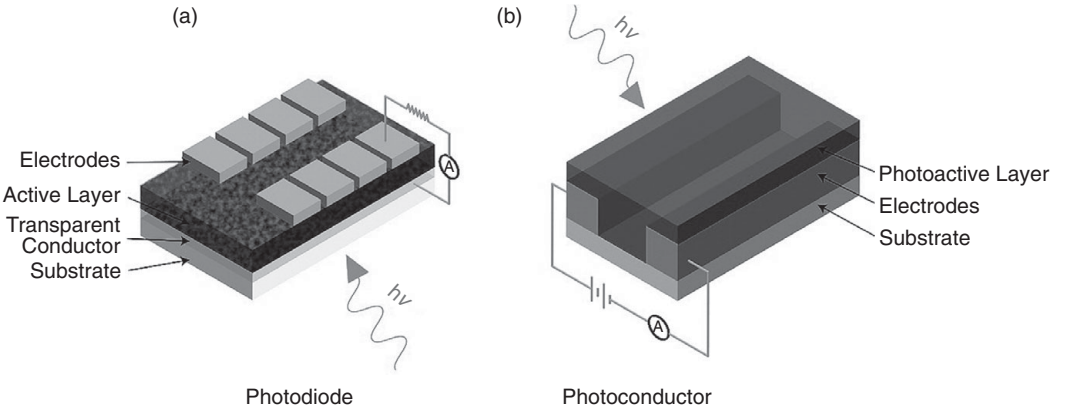


Figure 4.4 Cartoon schematics of the device structure of (a) a typical photodiode and (b) a typical photoconductor.

4.2.2.2 Quantum dot photodetectors

There are two main device architectures used to construct photodetectors with QDs: (1) photodiodes, like those used for the PVs discussed above; and (2) photoconductors, which utilize a horizontal device architecture with a photoactive layer deposited between contacts, often of the same metal (see Figure 4.4) [57]. Blends of QDs with organics have been employed in both architectures; however, the most sensitive QD photodetectors reported to date are photoconductors made with active layers comprising treated nanocrystalline solids [21].

Because photodetectors are not used to generate power, but to sense an optical signal with as little noise as possible, the metrics used to quantify their performance differ from those used for PVs. EQE, defined identically for photodetectors and solar cells, does appear in the photodetector literature and can still be used to gauge performance. However, because photodetectors are often measured under bias with appreciable dark currents, which are not accounted for in EQE measurements, normalized detectivity (D^*) is a more appropriate and more commonly used measure of photodetector sensitivity. D^* is defined as the inverse of the noise equivalent power, normalized for device active area and bandwidth to allow comparison between photodetectors of different device architectures and geometries, and is measured in the unit of Jones (cm $\sqrt{\text{Hz}}$ /W). Typical inorganic crystalline infrared photodetectors have D^*s in the range of 10^{10}–10^{13} Jones [58] and several reports of solution-processed QD photodetectors have comparable detectivities [59–61]. Another important performance parameter for photodetectors is the frequency range over which they can operate, reported either as a device bandwidth or response time, though several reports of QD photodetectors fail to report either.

In the realm of photodetectors, QD based devices have generated the most interest as infrared sensors. Visible photodetectors, typically utilizing silicon as the active layer, are already well established and widespread. However, silicon, is limited to the visible and near-infrared by its relatively large bandgap (~1.1 eV). QDs with size-tunable infrared bandgaps – such as PbS [62], PbSe [63], InAs [64], and others [15] – are easily

synthesized, making them attractive candidates for use in optical signal transduction at wavelengths suitable for applications where detection further into the infrared is necessary, for example, night vision and telecommunications [2, 15]. In these applications, the ability to tailor the bandgap can be especially advantageous as it can help balance the working wavelength range with noise parameters.

Though much of the work on QD based photodetectors has focused on devices that use treated nanocrystalline solids as the photoactive layer [21], this architecture has been demonstrated for hybrid organic–inorganic devices as well. In 2006, Biebersdorf *et al.* demonstrated that CdTe, CdSe, and InP QDs could be used to photosensitize needle-like C_{60} crystals that had been grown across parallel electrodes, producing photodetectors with EQEs up to 10% and photoresponse that tracked with the quantum dot absorption spectra [65]. Later, infrared-sensitive photoconductors made by spin-coating blends of PbS QDs with (6,6)-phenyl-C61-butyric acid methyl ester (PCBM) were reported. These devices exhibited gain, with "EQEs" that were reported to be as high as 400% under 15 V bias, and with normalized detectivities as high as 2.5×10^{10} Jones, comparable to some lower-end commercially available infrared photodetectors [59].

Photodiodes incorporating both QDs and organic semiconductors, similar to the solar cells discussed above, can also be utilized as photodetectors. Photodiodes can exhibit faster response times than photoconductors, making them suitable for a broader range of applications, particularly those that require high refresh rates, such as video recording. Though typically less sensitive than photoconductors that take advantage of large photoconductive gain, careful engineering of device architecture and chemical manipulation of QD films has produced QD photodiodes with normalized detectivities greater than 10^{11} Jones, making them sufficiently sensitive to compete with commercially available infrared photodetectors [66]. In 2004, McDonald and coworkers reported on a photodiode that utilized PbS QDs as infrared sensitizers incorporated into a thin film of MEH-PPV [67]. These devices were among the first QD based photodetectors to demonstrate sensitivity in the infrared. Later, it was shown that the photoresponse of these devices could be tuned by changing the size of the PbS quantum dots, and that they exhibited a small but measurable PV response [68]. Other early photodiodes that blended PbSe QDs with PVK [69] and pentacene [70] exhibited photoresponses in the infrared, but had to be driven at high voltages, and only achieved EQEs of less than 10%.

One notable report of a photodiode made with infrared bandgap QDs used PbS nanocrystals (NCs) as infrared sensitizers blended in a P3HT/PCBM blend device. It was reported that the presence of all three materials was required for the devices to generate a photoresponse in the infrared. The PbS QDs absorb infrared light and the ternary structure must somehow transfer holes to P3HT and electrons to PCBM. The resulting devices, when deposited onto amorphous silicon active matrix backplanes, were capable of imaging in the near-infrared (1310 nm) with response times fast enough to record video. This work represented an important step toward the engineering of solution-processed infrared photodetectors incorporating QDs as it demonstrates that QDs can be integrated into a fully functional imaging device. Figure 4.5 shows the device architecture as well as an image of a monarch butterfly taken under infrared illumination [71].

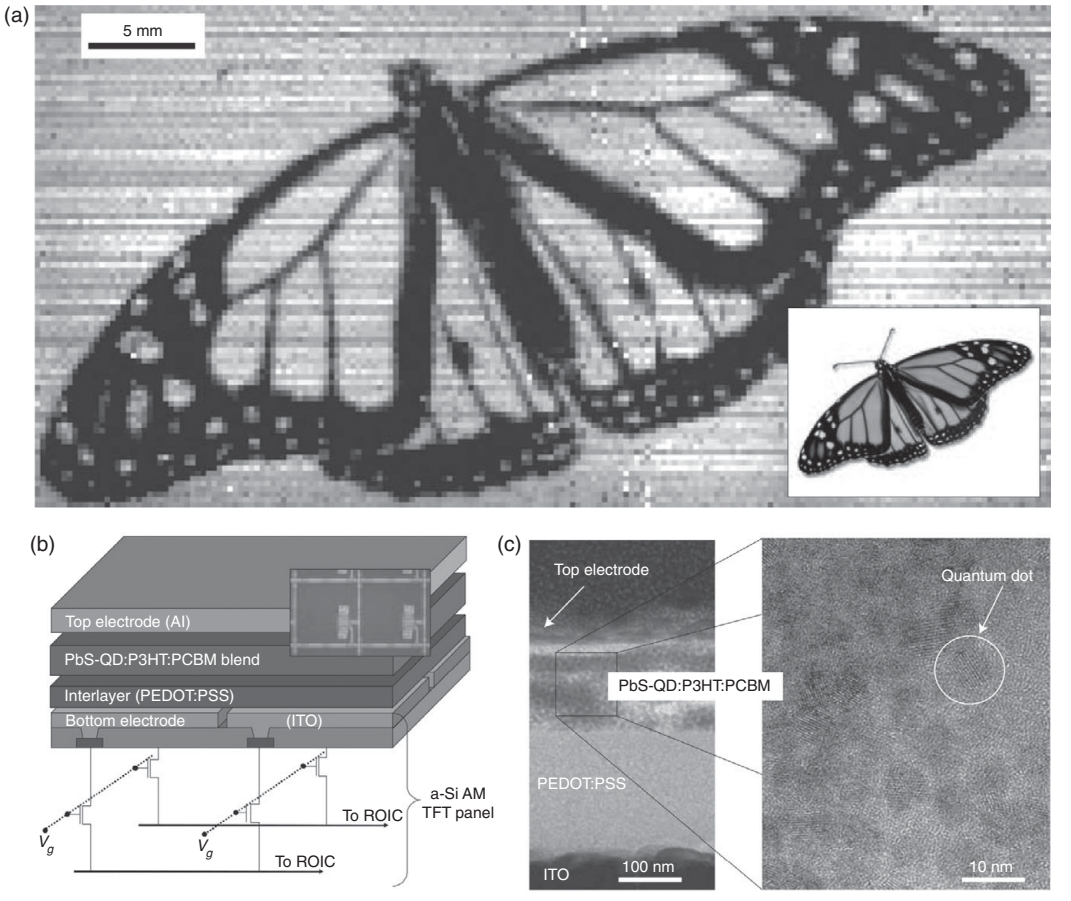


Figure 4.5 (a) An image of the transmission of 1310 nm light through a monarch butterfly on a microscope slide captured by a PbS:P3HT:PCBM hybrid photodiode with the device architecture shown in (b). (c) Cross-sectional transmission electron microscopy (TEM) image of the hybrid photodiode alongside a TEM image of the PbS QDs used in these devices. Printed with permission from [71].

Finally, researchers have also exploited QDs in photodetectors to enhance sensitivity by using them to introduce pathways facilitating efficient photoconductive gain. Photoconductive gain occurs when photogenerated charge carriers fall into deep traps, which extends their lifetimes. If the trapped carrier lifetimes are longer than their transit time through the device under the applied bias, then they can essentially be collected more than once before they recombine, leading to gain and EQEs greater than 100% [72]. Qi *et al*. reported on a blend of PbSe/MEH-PPV that did not exhibit a photoresponse in the infrared, but did produce EQEs in the visible spectrum that exceeded 100%, originally attributing the high sensitivity to charge multiplication in the PbSe QDs upon absorption of photons larger than their bandgap [73]. Later, it was demonstrated that similar blends exhibit bulk photoconductive gain, where some fraction of the excitons generated upon photoexcitation dissociated to produce trapped electrons on PbSe [72]. This strategy

of introducing charge traps with QDs has been utilized by Chen *et al.* to make highly sensitive visible photodetectors by blending CdTe QDs into thin films with P3HT/PCBM [74]. The CdTe QDs acted as deep electron traps in films facilitating photoconductive gain and the resulting photodiodes exhibited EQEs as high as 8000% with less than 5 V applied bias; however, the authors did not report either a bandwidth or a detectivity.

While they serve different applications, LEDs, photodetectors, and PVs all share the common function of interconverting optical and electrical energy. In just two decades, quantum dots devices have already made significant gains in performance, however, efficiencies and stability need further improvement before such applications can be realized outside of the laboratory. For hybrid QD/organic devices, strong electronic coupling between organic and inorganic materials is crucial to facilitate the charge transport and interfacial charge transfer integral to their operation. Optimizing these organic–inorganic interactions will require an intimate understanding of the physics and chemistry that dictate the processes that occur at the interfaces between materials.

4.3 The QD–organic interface – ligands and more

4.3.1 Ligands

One of the most important factors influencing these interfacial processes is the layer of organic molecules that coat the surfaces of QDs [24]. Colloidal QDs are often stabilized by a layer of organic surfactant molecules, or surface ligands, which serve the dual role of passivating dangling bonds on the QD surfaces and rendering the dots soluble in a variety of solvents. Because QDs, and nanoscale materials in general, possess large surface-area-to-volume ratios, their surface chemistry can have tremendous influence on many of their physical properties. Though the chemistry of the interactions between QDs and their surface ligands is not within the scope of this chapter, it has an important impact on the efficiency and operation of optoelectronic devices containing QDs. For example, though almost all of the donor–acceptor PVs discussed above utilize p-type organics as electron donors with n-type QDs as electron acceptors, it should be noted that QDs can be switched between p- and n-type simply by exposing them to different surface treatments [75, 76]. Additionally, the chemistry of the QD surface can influence many of the properties important to optoelectronic device operation, such as photoluminescence quantum efficiency, the efficiency of charge injection or extraction, and QD processability [2, 24, 77, 78]. The right ligands can even alter the quantum confinement of the electronic states of the QD core, thus altering their energy levels [79].

Because ligands coat the surfaces of QDs, they also determine how the particles chemically interact with their surroundings; ligands can dictate if a QD is hydrophobic or hydrophilic [63] or whether QDs will disperse or aggregate in a given polymer matrix [79]. Coating QDs with ligands that have nonpolar tails renders them soluble in many of the same solvents as conjugated polymers, which facilitates solution processing of QD/polymer blend films. However, the chemical interactions between a QD's ligands

and the surrounding polymer matrix also influence important device parameters like blend morphology (or phase segregation). The length scale of the phase segregation in donor–acceptor blend films, like those utilized in polymer/QD BHJ solar cells, is critical to device performance. To prevent losses stemming from the decay of excitons before they can dissociate at a donor–acceptor heterojunction (described in more detail below, see Section 4.3.2.2), the donor and acceptor materials in a BHJ blend solar cell must be finely blended on the nanoscale [80–83]. Although some QD aggregation is often beneficial in a hybrid PV, for some QD/polymer blends, such as pyridine-capped CdSe blended with some alkoxy-PPVs [84] or with P3HT [85], the interactions between the polymers and ligands can cause phase segregation on length scales much larger than what is ideal for solar cell performance. In some cases, this can be overcome with a careful choice of solvents, or post-deposition processing steps, such as thermal annealing [85].

The ligands employed in QD synthesis are typically long chain aliphatic molecules, like oleic acid and stearic acid. Because the saturated hydrocarbon tails of these molecules are electronically insulating and quite long, they present a significant barrier to electron tunneling. Replacement of these molecules with shorter chain ligands was shown to be necessary for interfacial charge transfer in blends of CdSe QDs and MEH-PPV [50, 84]. In QD solids, shorter ligands result in tighter packing of adjacent nanoparticles. Liu *et al.* reported that using progressively shorter and shorter thiols as ligands in thin films of PbSe QDs resulted in progressively higher field effect mobilities of both holes and electrons as the interparticle spacing decreased [86]. Closer packed nanoparticles experience stronger coupling with their neighbors, facilitating charge transfer, a result that has important implications for devices that require the movement of charge carriers, including both PVs and photodetectors, as well as transistors [75].

One of the challenges facing the field of QD optoelectronics is the development of ligands that facilitate the processing of QDs into QD solids or into blends with polymers but do not present a significant barrier to the movement of charge. This might be accomplished by using ligands with conjugated tails [87, 88] or made from molecules, such as metal chalcogenide complexes, that can be thermally decomposed under relatively gentle heating ($<200\,^{\circ}C$) either completely or into very short, conductive ligands that no longer impede charge transport [89].

While the presence of ligands typically represents a disadvantage facing colloidal QD optoelectronics, one example of ligands being used for good instead of evil was reported by Tessler and coworkers in 2008 [64]. They showed that ligands with various dipole moments can be used to shift highest occupied molecular orbital (HOMO) and lowest unoccupied molecular orbital (LUMO) levels of InAs QDs. In that work, electrochemical studies and scanning tunneling microscopy (STM) was used to measure energy level shifts as large as 200 meV. In addition, they were able to demonstrate that one of their polar ligands, 4-methylthiophenol (MTP), could be used to tune the energy levels of InAs QDs into and out of a type II heterojunction (see below, Figure 4.6 and Section 4.3.2) with the semiconducting polymer, yellow-PPV, resulting in more than an order of magnitude improvement of photosensitivity of a photodiode made from a blend of yellow-PPV with MTP-coated InAs [64]. More recently, Munro *et al.* have reported

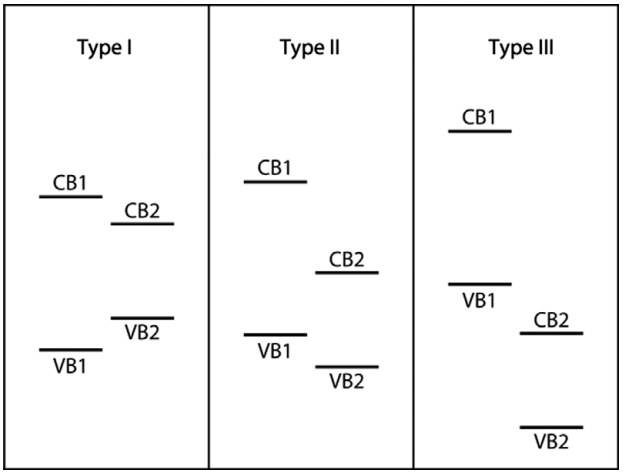


Figure 4.6 Illustration of the three possible alignments of semiconductor CB and VB edges at a heterojunction interface. VB and CB can be thought of as the HOMO and LUMO, respectively, for organic semiconductors.

similar shifts in the QD energy levels from ligand dipoles measured with ultraviolet photoelectron spectroscopy (UPS) [90].

The complexity of the interactions between QDs and their ligands represents both a challenge and an opportunity to realizing highly efficient QD optoelectronic devices. Ligands are essential to the solution processability of quantum dots (and the passivation of surface defects which can trap carriers or promote non-radiative recombination), yet their presence can also present a barrier to charge and energy transfer processes that are at the heart of many optoelectronic devices. The imaginative scientist should see opportunity here: because so many of the properties of colloidal QDs can be influenced by their surfaces, ligands can provide a powerful handle to tailor not just solubility, but trap and carrier densities, interfacial energy level offsets, and even bandgaps.

4.3.2 Energetics

The interface between two different semiconductors is called a ”heterojunction”. The valence band (VB) and conduction band (CB) edges of adjacent semiconductors (or HOMO and LUMO levels of organic semiconductors) can align in one of three ways, depicted graphically in Figure 4.6. In a type I, or straddling-gap, heterojunction, the VB and CB edges of one material both lie within the bandgap of the second. In a type II, or staggered-gap, heterojunction, the levels of the two materials are offset such that either the VB or the CB of one material lies within the bandgap of the second, but not both. In a type III, or broken-gap, heterojunction, the CB and VB levels of the two semiconductors are offset such that there is no overlap between their bandgaps [91]. The exact energetic overlap between the energy levels of a given combination of semiconductor materials has important implications for how that combination will function in an optoelectronic device. Of course, because energy levels of QDs depend on their size and surface

chemistry, whether they form type I, II, or III heterojunctions with other materials can be altered by changing the dot size, or altering the ligand chemistry.

4.3.2.1 Charge transfer and Förster resonance energy transfer (FRET) in QD-LEDs

Much of the early research toward improving QD-LEDs was carried out under the assumption that they operated by way of the direct charge injection mechanism described above in Section 4.2.1 [29, 30]; however, the importance of energy transfer to device performance was soon realized [92]. More recently, the direct charge injection mechanism has been demonstrated to apply for QD-LEDs that utilize inorganic metal-oxide charge transport layers, which exhibit longer devices lifetimes than their hybrid organic/inorganic counterparts, but thus far operate with lower efficiencies [40, 41].

Typically, however, it remains challenging to balance the carrier concentration in the emissive QD layer. This is because the barrier to hole injection in QD-LEDs is typically larger than that to electron injection for the materials that have been studied as charge transport layers to date. This difference in injection barriers can contribute to an accumulation of electrons in the QD layer. Charging of the QDs might increase the likelihood of non-radiative recombination via Auger processes and has been identified as a dominant loss mechanism in CdSe QD-LEDs that contain organic charge transport layers [42]. In that same work, devices were engineered that intentionally blocked the direct injection of electrons into the CdSe QDs by embedding the CdSe in the hole transport layer (HTL). This device structure encouraged the formation of excitons on the organic electron transport layer (ETL), in this case tri-(8-hydroxyquinoline) (Alq_3), which could then undergo Förster transfer to the CdSe QDs, resulting in more efficient devices [42]. FRET is a non-radiative dipole–dipole interaction by which one material can give its energy to another. The strength of this interaction, which influences the energy transfer rate and the distance over which it can occur, depends on the strength of the emitter's dipole (its fluorescence quantum efficiency) as well as the overlap between the acceptor's absorption spectrum with the donor's emission spectrum [93]. Optimizing devices to operate via the FRET mechanism resulted in the most efficient red, orange, green, and blue emitting QD-LEDs to date. The large performance gains (particularly in green and red QD-LEDs) were attributed to the presence of wide-gap transport layers that were selected to maximize the efficiency of the energy transfer. Likewise, the relatively smaller improvement observed for blue QD-LEDs was attributed to inefficient energy transfer from the ETL to the larger bandgap QDs being used as blue emitters [36].

4.3.2.2 Type II heterojunctions and charge transfer in QD-PVs

One of the major motivating factors behind the research into QDs as light harvesters in PVs is the need for solution-processable materials that absorb a larger fraction of the infrared portion of the solar spectrum. Currently, Schottky diode PVs made from infrared bandgap colloidal QDs are more efficient than blends of infrared-absorbing QDs with polymers. Schottky diode device structures utilize ligand-treated NC films ("QD solids") as the active layer and rely on a metal–semiconductor Schottky barrier

across which charge carriers move to equilibrate the Fermi levels of the two materials. This redistribution of charge results in a depletion region within the semiconductor layer, where band-bending creates an electric field that can drive photogenerated carriers to the collecting electrodes. The best PCE measured for such devices at the time of writing was ~4% under simulated AM 1.5G solar radiation, which was only a factor of about 2 lower than the best current all organic BHJ blend solar cells [94, 95]. While the Schottky diode structure and polymer/QD BHJ blend structures both enable beautiful science and producing good performance, it is not clear which will ultimately prove more desirable in applications.

The upper limit of the *Voc* of a Schottky cell is approximately one half of the bandgap of the semiconductor [96]. On the other hand, the empirically determined upper limit for all-organic BHJ blend PVs is approximately E_g/q – 0.6 eV [97], so for infrared absorbing PVs (i.e., for cells with E_g less than 1 eV), the Schottky cell limit may not be a significant disadvantage. However, the layer-by-layer (LbL) processing commonly used to deposit the active layers of Schottky cells involves several (sometimes several dozen) sequential deposition and surface treatment steps. The numerous processing steps required to deposit LbL films can be time consuming, sacrificing some of the ease of fabrication that motivated the use of solution-processable materials in the first place.

The final consideration concerns how Schottky and BHJ cells generate and collect charge. In typical QD-Schottky cells, depletion regions have been measured to be on the order of 100 nm [22, 98, 99]. The rest of the semiconductor layer is called the "quasi-neutral region" and experiences relatively little band bending, so carriers generated in this region must diffuse to the depletion region to be collected. Since the extinction coefficient of infrared-bandgap QD films is commonly ~10^4 cm^{-1} at the first exciton transition [100], Schottky devices will have to employ QD layers ~1 μm thick to absorb the majority of the incident solar light with energy in the infrared, near the bandgap. For current QD Schottky devices with active layers that thick, the quasi-neutral region would comprise the majority of the semiconductor active layer. To achieve high internal quantum efficiencies (IQE, defined for solar cells as electrons collected per photon *absorbed*), the minority carrier diffusion length must be increased to be on the order of several hundred nanometers as carriers photogenerated in the quasi-neutral region of the films must diffuse through this region to be collected. In 2013, The largest reported diffusion lengths in Schottky cells have been on the order of 100 nm [98, 99], so an improvement of a little bit less than an order of magnitude is required for Schottky cells to absorb a significant fraction of the light and still retain high photon-to-electron conversion efficiencies [22]. The diffusion length of carriers depends on both carrier mobility (μ) and carrier lifetime (τ) by [101]:

$$l_{diff} = (\mu \tau kT/q)^{1/2}.$$

Perhaps significant improvements to either or both of these factors will one day result in the required larger diffusion lengths, possibly by means of ligand manipulation [99]. Barring such improvements, however, photodiode architectures employing either p–n bilayers or BHJ donor/acceptor blends would be needed for efficient solar energy conversion.

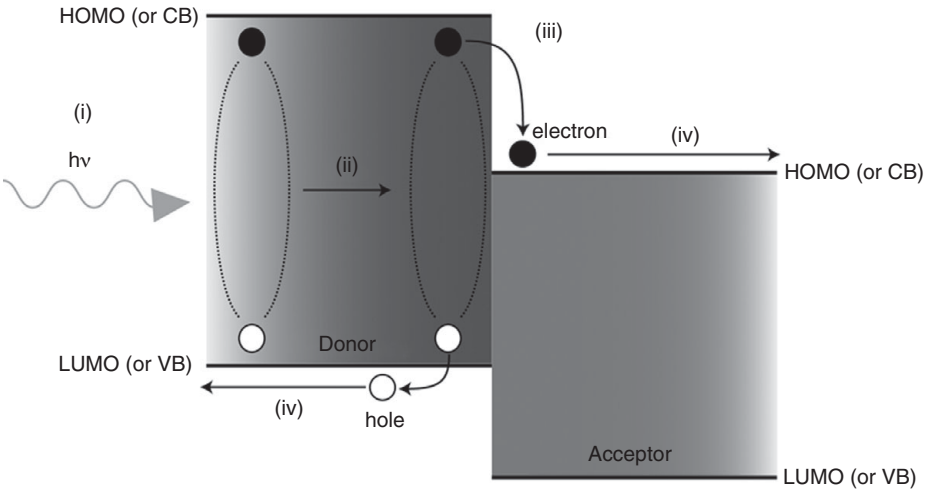
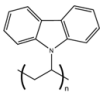
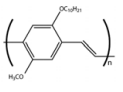
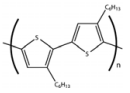
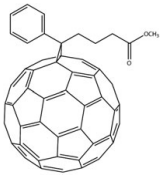
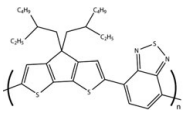
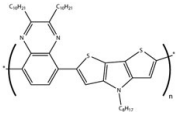


Figure 4.7 Mechanism of photoinduced charge generation in an excitonic solar cell. (i) Absorption of a photon creates an exciton, which (ii) diffuses to an interface between the donor and the acceptor. (iii) Exciton dissociation at the donor–acceptor interface results in free charge carriers which can then (iv) be transported out of the device.

However, BHJ devices are not exempt from the thickness constraints imposed by the light absorption depth in low-gap materials either. Because of constraints imposed by relatively low charge mobilities in semiconducting polymers, the IQE of BHJs decreases with film thickness [102], a problem exacerbated in low-bandgap materials that often have smaller extinction coefficients than their visible-bandgap counterparts [103]. Because of the constraints of light absorption, both Schottky diode cells and BHJ blends are good candidates for the use of nonplanar device structures [104] or light-trapping strategies such as plasmonic nanostructures [105–109].

Like most PVs using organic semiconductors, the hybrid polymer/QD solar cells are "excitonic" in nature. This is because absorption of photons by organic semiconductors generates excitons, which are Coulombically-bound electron–hole pairs (Figure 4.7(i)). Excitonic solar cells rely on the energy levels of the donor and acceptor materials to align in a "type II" heterojunction, as in Figure 4.7. In order to generate free charge, excitons must be able to diffuse to a donor–acceptor (polymer–QD) interface (Figure 4.7(ii)), where they can dissociate into separated electrons and holes (Figure 4.7(iii)) that are then conducted through their respective transport layers to the electrodes, resulting in a measured photocurrent (Figure 4.7(iv)) [80, 110]. The exciton diffusion length of most organic molecules is on the order of 10 nm, but organic films typically need to be ~100 nm thick to absorb an appreciable amount of incident solar light. As a result, only photons that are absorbed near (within ~10 nm) donor–acceptor interfaces result in excitons that can reach an interfaces. In polymer PVs, this problem is often alleviated by spin-coating the donor and the acceptor together into a BHJ blend film, thereby increasing the interfacial surface area in the bulk of the film and providing for the dissociation of a majority of the photogenerated excitons. Of course, excitons in inorganic semiconductors

Table 4.1. Organic materials, widely employed in hybrid polymer-QD optoelectronics, that are discussed in this chapter

Abbreviation	Full chemical name	Chemical structure	Energy levels	Book section
PVK	N-polyvinylcarbazole		HOMO: –5.9 eV LUMO: –1.2 eV [115, 116]	4.2.2
MDMO-PPV*	poly[2-methoxy-5-(3',7'-dimethyloctyl-oxy)-1,4-phenylene vinylene]		HOMO: –5.4 eV LUMO: –2.9 eV [117]	4.2.2 4.3.1
P3HT	poly-3-hexyl-thiophene		HOMO: –5.1 eV LUMO: –3.0 eV [118]	4.2.2 4.3.1 4.3.2
PCBM	(6,6)-phenyl-C-61-butyric acid methyl ester		HOMO: –4.3 eV LUMO: –6.3 eV [118, 119]	4.2.2 4.3.2
PCPDTBT	poly[2,6-(4,4-bis-(2-ethylhexyl)-4H-cyclo-penta [2,1-b;3,4-b′]dithiophene)-alt-4,7-(2,1,3-benzothiadiazole)]		HOMO: –5.3 eV LUMO: –3.5 eV [119]	4.2.2
PDTPQx	poly(2,3-didecyl-quinoxaline-5,8-diyl-alt-N-octyldithieno [3,2-b:2′,3′-d]pyrrole)		HOMO: –4.6 eV LUMO: –2.6 eV [23]	4.3.2

are less strongly bound due to the higher dielectric constants of crystalline inorganic materials, and may not need a strong a driving force to be dissociated. In theory, this could mean that BHJ blend devices containing higher dielectric materials like QDs could have a higher limit to their V_{OC}. Additionally, the high dielectric constants could enhance photocurrent generation efficiency by screening charge carriers from each other, reducing recombination losses.

In the polymer/CdSe PVs described in Section 4.2.2.1, the polymer is the electron donor and the CdSe is the electron acceptor (in Table 4.1 we summarize the organic materials considered in this chapter). Photoinduced electron transfer from alkoxy-PPVs to CdSe QDs has been explored by Ginger and Greenham using quasi-steady state photoinduced absorption spectroscopy (PIA) [84]. PIA is a pump–probe spectroscopic technique that monitors the change in transmission of a probe beam due to the presence of long-lived photogenerated species, such as polarons. Polarons are created in polymer/QD blends when the polymer becomes charged as a result of photoinduced electron transfer upon excitation by pump photons. The positive charge on the polymer backbone induces a structural reorganization of the bonds around it, resulting in a corresponding localized

change in the electronic structure. Together, the charge and the associated structural distortion around it are called a polaron. Positive polarons on P3HT and alkoxy-PPVs have new subbandgap, optically-allowed transitions that can absorb probe beam, creating a spectral signature of photogenerated charge in a blend, detectable with PIA [23, 84, 111].

After the initial success of solar cells made from blends of alkoxy-PPVs or P3HT with CdSe QDs, several groups tried similar blends with infrared-bandgap QDs, like PbS and PbSe, but experienced little success [112–114]. These low efficiencies caused research into BHJ devices containing blends of polymers with infrared-bandgap QDs to stagnate, even while research into CdSe/polymer blend BHJ devices blossomed. Our group used quasi-steady state PIA to show that blends of PbSe QDs with MDMO-PPV or P3HT do not generate long-lived photoinduced charge, explaining the low efficiencies of devices made from them [111]. Under the assumption that the reason for the lack of charge transfer was unfavorable band alignment or electronic coupling between the QDs and those polymers, PIA was used to screen a number of new polymers for their viability as electron donors in blends with PbS QDs. One of the polymers tested, poly(2,3-didecyl-quinoxaline-5,8-diyl-alt-N-octyldithieno[3, 2-b:2′, 3′-d]pyrrole) (PDT-PQx), yielded far more photoinduced charge transfer than the others and could be made into BHJ blend devices with PbS QDs that exhibited PCEs of 0.5%. While these efficiencies are modest compared with the best QD/polymer blend devices described above, they are still ~20× larger than any other BHJ PVs made with IR-bandgap QDs up to that point [23].

Though hybrid organic/inorganic blend devices that utilize infrared-absorbing quantum dots as n-type electron *acceptors* still lag behind their visible bandgap counterparts, some groups have been successful incorporating both PbSe and PbS as a p-type electron *donor* into devices with n-type organic molecules like C_{60} and PCBM [120–122]. The rationale for this stems from the fact that deposited PbSe QDs exhibit p-type transistor behavior, and must be treated with a strong reducing agent, such as hydrazine, to be made n-type [75]. Additionally, the majority carrier in the Schottky diode PVs made by LbL processed films of PbS and PbSe is holes [94, 98]. The best organic/inorganic hybrid devices that use infrared-bandgap QDs as the p-type electron donor are made with a quasi-bilayer architecture by first depositing and immobilizing a film of PbS QDs using a LbL process of successive spin-coating and post-deposition ligand treatments. An n-type PCBM layer is then spin-coated on top of this and a metal top-contact is thermally deposited. These devices achieved PCEs as high as 2.4% [122]. An all-inorganic analog of these device structures made from bilayers of p-type PbS QDs on top of TiO_2 electron acceptors has also been demonstrated, yielding a PCE of more than 5% at just under 1sun illumination, which represented champion device performance for PVs made with quantum dots at the time [49]. It must be noted, however, that the QD layers in all of these devices are fabricating using LbL deposition techniques, which require several fabrication steps, including multiple post-deposition ligand treatments, similar to those performed on QD based Schottky devices. Depositing QD active layers in a single step is most readily accomplished when the fabrication is facilitated by soluble, semiconducting polymers [123]. Nevertheless, the rapid progress in this area shows that

there are still many ideas to be explored, and considerable room for improving both hybrid organic/inorganic and all-inorganic PV devices incorporating colloidal QDs.

4.4 Conclusion and future outlook

Solution-processed materials have tremendous potential to make manufacturing optoelectronic devices such as LEDs, photodetectors, and PV cells less expensive by enabling the use of roll-to-roll printing techniques in their fabrication. Colloidal QDs combine solution processability with some of the advantages of bulk semiconductors, such as superior thermal and photostability and higher charge mobility. Additionally, colloidal QDs have many properties not exhibited by bulk semiconductors, such as size-tailorable energy levels and bandgaps, and bright, narrow-band luminescence. Many devices under investigation employ both organic semiconductors and colloidal QDs, and as the physics and chemistry of these materials and their interactions become better understood, they may one day be used to fabricate devices that are both inexpensive and highly efficient.

However, scientific challenges remain to be addressed. Research into QD-LEDs must continue to close the gaps in brightness, EQE, and stability that still separate them from their all-organic (OLED) counterparts. Considering that QDs can be synthesized with near-unity photoluminescence quantum yield and with superior color purity, it does not take a significant stretch of one's imagination to envision that they will one day exceed organic emitters in LEDs used for display applications.

Another area where QDs may make an impact is as absorbers in infrared photodetectors, with potential applications ranging from spectroscopy to night vision. Indeed, QD photodetectors already exhibit efficiencies high enough to make them competitive with some kinds of commercially available devices. Solar energy harvesting is also attractive, but PV cells containing colloidal QDs are still only about half as efficient as all-organic cells and the efficiency gap between them and cells containing bulk semiconductors is even greater. Again, however, the combination of solution processability with so many other potential advantages possessed by QDs, including broad-band absorption, high material stability, synthetic shape control, and size-tunable electronic structure sets them apart from any other class of material, including both organic and bulk inorganic semiconductors. Given the prospect that processes like multiple exciton generation or hot carrier extraction may occur with greater efficiency in nanocrystals, they remain extremely intriguing for applications in both inexpensive and efficient solar energy conversion (see Chapter 5).

Looking to the future of optoelectronic devices containing colloidal QDs, it seems that one of the major hurdles standing in their way is that many of the most commonly studied materials contain toxic heavy metals such as lead and cadmium. Though it is feasible to include these undesirable materials in consumer products (many rechargeable batteries contain cadmium, for example), the stigma of such toxic elements might make it difficult for them to realize broad consumer use. With this in mind, the transition to materials that contain more benign elements like iron and copper has already begun. The development of syntheses of highly luminescent colloidal QDs like InP/ZnS

core-shell QDs, may help move the field of QD-LEDs away from Cd containing materials [26]. Meanwhile, in the field of PVs, the impetus to utilize nontoxic materials may be even greater, as semiconductors such as iron pyrite (FeS_2) and copper sulfide (Cu_2S) have been identified as having superior power generation potential to silicon, the material that currently dominates the PV market. If facile syntheses of colloidal QDs of these or other, abundant and nontoxic materials can be developed, they could lead to next-generation solution-processed solar cells that are better than silicon in terms of both of performance and cost [124].

References

1 A. C. Arias, J. D. MacKenzie, I. McCulloch, J. Rivnay, A. Salleo, Materials and applications for large area electronics: solution-based approaches. *Chemical Reviews*, **110**:1 (2010), 3–24.

2 D. V. Talapin, J.-S. Lee, M. V. Kovalenko, E. V. Shevchenko, Prospects of colloidal nanocrystals for electronic and optoelectronic applications. *Chemical Reviews*, **110**:1 (2009), 389–458.

3 A. D. Yoffe, Semiconductor quantum dots and related systems: Electronic, optical, luminescence and related properties of low dimensional systems. *Advances in Physics*, **50**:1 (2001), 1–208.

4 F. W. Wise, Lead salt quantum dots: the limit of strong quantum confinement. *Accounts of Chemical Research*, **33**:11 (2000), 773–780.

5 A. M. Smith, S. Nie, Semiconductor nanocrystals: structure, properties, and band gap engineering. *Accounts of Chemical Research*, **43**:2 (2009), 190–200.

6 C. Burda, X. Chen, R. Narayanan, M. A. El-Sayed, Chemistry and properties of nanocrystals of different shapes. *Chemical Reviews*, **105**:4 (2005), 1025–1102.

7 L. E. Brus, Electron–electron and electron–hole interactions in small semiconductor cystallites – the size dependence of the lowest excited electronic state. *Journal of Chemical Physics*, **80**:9 (1984), 4403–4409.

8 L. E. Brus, A simple model for the ionization-potential, electron-affinity, and aqueous redox potentials of small semiconductor crystallites. *Journal of Chemical Physics*, **79**:11 (1983), 5566–5571.

9 A. I. Ekimov, A. L. Efros, A. A. Onushchenko, Quantum size effect in semiconductor microcrystals. *Solid State Communications*, **56**:11 (1985), 921–924.

10 H. Weller, Quantized semiconductor particles: A novel state of matter for materials science. *Advanced Materials*, **5**:2 (1993), 88–95.

11 H. Weller, H. M. Schmidt, U. Koch, *et al.*, Photochemistry of colloidal semiconductors. Onset of light absorption as a function of size of extremely small CdS particles. *Chemical Physics Letters*, **124**:6 (1986), 557–560.

12 C. B. Murray, D. J. Norris, M. G. Bawendi, Synthesis and characterization of nearly monodisperse CdE (E = sulfur, selenium, tellurium) semiconductor nanocrystallites. *Journal of the American Chemical Society*, **115**:19 (1993), 8706–8715.

13 S. Coe-Sullivan, Optoelectronics: Quantum dot developments. *Nature Photon*, **3**:6 (2009) 315–316.

14 QDVision. Quantum Light™ Optic. Watertown, MA: QD Vision; 2010 [cited 2010 Oct 15]; Available from: http://www.qdvision.com/quantum-light-optic.

15 A. L. Rogach, A. Eychmüller, S. G. Hickey, S. V. Kershaw, Infrared-emitting colloidal nanocrystals: synthesis, assembly, spectroscopy, and applications. *Small*, **3**:4 (2007), 536–557.
16 E. H. Sargent, Solar cells, photodetectors, and optical sources from infrared colloidal quantum dots. *Advanced Materials*, **20**:20 (2008), 3958–3964.
17 K. N. Bourdakos, D. Dissanayake, T. Lutz, S. R. P. Silva, R. J. Curry, Highly efficient near-infrared hybrid organic-inorganic nanocrystal electroluminescence device. *Applied Physics Letters*, **92**:15 (2008), 15331.
18 B. L. Wehrenberg, C. J. Wang, P. Guyot-Sionnest, Interband and intraband optical studies of PbSe colloidal quantum dots. *Journal of Physical Chemistry B*, **106**:41 (2002), 10634–10640.
19 A. Pandey, P. Guyot-Sionnest, Slow electron cooling in colloidal quantum dots. *Science*, **322**:5903 (2008) 929–932.
20 W. A. Tisdale, K. J. Williams, B. A. Timp, *et al.*, Hot-electron transfer from semiconductor nanocrystals. *Science*, **328**:5985 (2010), 1543–1547.
21 G. Konstantatos, E. H. Sargent, Nanostructured materials for photon detection. *Nature Nanotechnology*, **5**:6 (2010), 391–400.
22 E. H. Sargent, Infrared photovoltaics made by solution processing. *Nat Photon*, **3**:6 (2009), 325–331.
23 K. M. Noone, E. Strein, N. C. Anderson, *et al.*, Broadband absorbing bulk heterojunction photovoltaics using low-bandgap solution-processed quantum dots. *Nano Letters*, **10**:7 (2010), 2635–2639.
24 A. M. Munro, J. A. Bardecker, M. S. Liu, *et al.*, Colloidal CdSe quantum dot electroluminescence: ligands and light-emitting diodes. *Microchimica Acta*, **160**:3 (2008), 345–350.
25 Y. H. Niu, A. M. Munro, Y. J. Cheng, *et al.*, Improved performance light-emitting diodes quantum dot layer. *Advanced Materials*, **19**:20 (2007), 3371–3376.
26 P. Reiss, M. Protière, L. Li, Core/shell semiconductor nanocrystals. *Small*, **5**:2 (2009), 154–168.
27 H. Morkoc, S. Strite, G. B. Gao, *et al.*, Large band gap SiC, III-V nitride, and II-VI ZnSe-based semiconductor device technologies. *Journal of Applied Physics*, **76**:3 (1994), 1363–1398.
28 S. Nakamura, M. Senoh, N. Iwasa, *et al.*, Superbright green ingan single quantum well structure light emitting diodes. *Japanese Journal of Applied Physics Part 2–Letters*, **34**:10B (1995), L1332–L1335.
29 V. L. Colvin, M. C. Schlamp, A. P. Alivisatos, Light-emitting diodes made from cadmium selenide nanocrystals and a semiconducting polymer. *Nature*, **370**:6488 (1994), 354–357.
30 B. O. Dabbousi, M. G. Bawendi, O. Onitsuka, M. F. Rubner, Electroluminescence from CdSe quantum-dot polymer composites. *Applied Physics Letters*, **66**:11 (1995), 1316–1318.
31 S. Coe, W. K. Woo, M. Bawendi, V. Bulovic, Electroluminescence from single monolayers of nanocrystals in molecular organic devices. *Nature*, **420**:6917 (2002), 800–803.
32 J. Zhao, J. A. Bardecker, A. M. Munro, *et al.*, Efficient CdSe/CdS quantum dot light-emitting diodes using a thermally polymerized hole transport layer. *Nano Letters*, **6**:3 (2006), 463–467.
33 QDVision. QDVision's Quantum Light™ Platform Surpasses Brightness, Efficiency and Lifetime Performance Thresholds. Watertown, MA: QD Vision; 2009 [cited 2010 November 10]; Available from: http://www.qdvision.com/release-02062009.
34 Y. Li, A. Rizzo, M. Mazzeo, *et al.*, White organic light-emitting devices with CdSe/ZnS quantum dots as a red emitter. *Journal of Applied Physics*, **97**:11 (2005), 113501–113504.

35 P. O. Anikeeva, J. E. Halpert, M. G. Bawendi, V. Bulović, Electroluminescence from a mixed red−green−blue colloidal quantum dot monolayer. *Nano Letters*, **7**:8 (2007), 2196–2200.
36 P. O. Anikeeva, J. E. Halpert, M. G. Bawendi, V. Bulović, Quantum dot light-emitting devices with electroluminescence tunable over the entire visible spectrum. *Nano Letters*, **9**:7 (2009), 2532–2536.
37 N. Tessler, V. Medvedev, M. Kazes, S. Kan, U. Banin, Efficient near-infrared polymer nanocrystal light-emitting diodes. *Science*, **295**:5559 (2002), 1506–1508.
38 J. S. Steckel, S. Coe-Sullivan, V. Bulović, M. G. Bawendi, 1.3 μm to 1.55 μm tunable electroluminescence from PbSe quantum dots embedded within an organic device. *Advanced Materials*, **15**:21 (2003), 1862–1866.
39 M. J. Panzer, K. E. Aidala, P. O. Anikeeva, *et al.*, Nanoscale morphology revealed at the interface between colloidal quantum dots and organic semiconductor films. *Nano Letters*, **10**:7 (2010), 2421–2426.
40 V. Wood, M. J. Panzer, J. E. Halpert, *et al.*, Selection of metal oxide charge transport layers for colloidal quantum dot LEDs. *ACS Nano*, **3**:11 (2009), 3581–3586.
41 J. M. Caruge, J. E. Halpert, V. Wood, V. Bulovic, M. G. Bawendi, Colloidal quantum-dot light-emitting diodes with metal-oxide charge transport layers. *Nature Photonics*, **2**:4 (2008), 247–250.
42 P. O. Anikeeva, C. F. Madigan, J. E. Halpert, M. G. Bawendi, V. Bulovic, Electronic and excitonic processes in light-emitting devices based on organic materials and colloidal quantum dots. *Physical Review B*, **78**:8 (2008), 085434.
43 Y. Wang, N. Herron, Photoconductivity of CdS nanocluster-doped polymers. *Chemical Physics Letters*, **200**:1–2 (1992), 71–75.
44 C. Girotto, B. P. Rand, S. Steudel, J. Genoe, P. Heremans, Nanoparticle-based, spray-coated silver top contacts for efficient polymer solar cells. *Organic Electronics*, **10**:4 (2009), 735–740.
45 I. Gur, N. A. Fromer, M. L. Geier, A. P. Alivisatos, Air-stable all-inorganic nanocrystal solar cells processed from solution. *Science*, **310**:5747 (2005), 462–465.
46 V. Sholin, A. J. Breeze, I. E. Anderson, *et al.*, All-inorganic CdSe/PbSe nanoparticle solar cells. *Solar Energy Materials and Solar Cells*, **92**:12 (2008), 1706–1711.
47 P. V. Kamat, Quantum dot solar cells. Semiconductor nanocrystals as light harvesters. *The Journal of Physical Chemistry C*, **112**:48 (2008), 18737–18753.
48 J. J. Choi, Y.-F. Lim, M. E. B. Santiago-Berrios, *et al.*, PbSe nanocrystal excitonic solar cells. *Nano Letters*, **9**:11 (2009), 3749–3755.
49 A. G. Pattantyus-Abraham, I. J. Kramer, A. R. Barkhouse, *et al.*, Depleted-heterojunction colloidal quantum dot solar cells. *ACS Nano*, **4**:6 (2010), 3374–3380.
50 N. C. Greenham, X. G. Peng, A. P. Alivisatos, Charge separation and transport in conjugated-polymer/semiconductor-nanocrystal composites studied by photoluminescence quenching and photoconductivity. *Physical Review B*, **54**:24 (1996), 17628–17637.
51 W. U. Huynh, J. J. Dittmer, N. Teclemariam, *et al.*, Charge transport in hybrid nanorod-polymer composite photovoltaic cells. *Physical Review B*, **67**:11 (2003), 115326.
52 W. U. Huynh, J. J. Dittmer, A. P. Alivisatos, Hybrid nanorod-polymer solar cells. *Science*, **295**:5564 (2002), 2425–2427.
53 B. Sun, N. C. Greenham, Improved efficiency of photovoltaics based on CdSe nanorods and poly(3-hexylthiophene) nanofibers. *Physical Chemistry Chemical Physics*, **8**:30 (2006), 3557–3560.

54 D. J. Milliron, I. Gur, A. P. Alivisatos, Hybrid organic–nanocrystal solar cells. *Mrs Bulletin*, **30**:1 (2005), 41–44.

55 S. Dayal, N. Kopidakis, D. C. Olson, D. S. Ginley, G. Rumbles, Photovoltaic devices with a low band gap polymer and cdse nanostructures exceeding 3% efficiency. *Nano Letters*, **10**:1 (2009), 239–242.

56 I. Gur, N. A. Fromer, C. P. Chen, A. G. Kanaras, A. P. Alivisatos, Hybrid solar cells with prescribed nanoscale morphologies based on hyperbranched semiconductor nanocrystals. *Nano Letters*, **7**:2 (2007), 409–414.

57 K. M. Noone, D. S. Ginger, Doping for speed: colloidal nanoparticles for thin-film optoelectronics. *ACS Nano*, **3**:2 (2009), 261–265.

58 S. M. Sze, *Physics of Semiconductor Devices*, pp. 742–748. New York, NY: Wiley, 1981.

59 K. Szendrei, F. Cordella, M. V. Kovalenko, *et al.*, Solution-processable near-IR photodetectors based on electron transfer from PbS nanocrystals to fullerene derivatives. *Advanced Materials*, **21**:6 (2009), 683–687.

60 G. Konstantatos, J. Clifford, L. Levina, E. H. Sargent, Sensitive solution-processed visible-wavelength photodetectors. *Nature Photonics*, **1**:9 (2007), 531–534.

61 G. Konstantatos, I. Howard, A. Fischer, *et al.*, Ultrasensitive solution-cast quantum dot photodetectors. *Nature*, **442**:7099 (2006), 180–183.

62 M. A. Hines, G. D. Scholes, Colloidal PbS nanocrystals with size-tunable near-infrared emission: observation of post-synthesis self-narrowing of the particle size distribution. *Advanced Materials*, **15**:21 (2003), 1844–1849.

63 W. W. Yu, J. C. Falkner, B. S. Shih, V. L. Colvin, Preparation and characterization of monodisperse pbse semiconductor nanocrystals in a noncoordinating solvent. *Chemistry of Materials*, **16**:17 (2004), 3318–3322.

64 M. Soreni-Harari, N. Yaacobi-Gross, D. Steiner, *et al.*, Tuning energetic levels in nanocrystal quantum dots through surface manipulations. *Nano Letters*, **8**:2 (2008), 678–684.

65 A. Biebersdorf, R. Dietmuller, A. S. Susha, *et al.*, Semiconductor nanocrystals photosensitize C60 crystals. *Nano Letters*, **6**:7 (2006), 1559–1563.

66 J. P. Clifford, G. Konstantatos, K. W. Johnston, *et al.*, Fast, sensitive and spectrally tuneable colloidal-quantum-dot photodetectors. *Nature Nanotechnology*, **4**:1 (2009), 40–44.

67 S. A. McDonald, P. W. Cyr, L. Levina, E. H. Sargent, Photoconductivity from PbS-nanocrystal/semiconducting polymer composites for solution-processible, quantum-size tunable infrared photodetectors. *Applied Physics Letters*, **85**:11 (2004), 2089–2091.

68 S. A. McDonald, G. Konstantatos, S. G. Zhang, *et al.*, Solution-processed PbS quantum dot infrared photodetectors and photovoltaics. *Nature Materials*, **4**:2 (2005), 138–142.

69 K. R. Choudhury, Y. Sahoo, T. Y. Ohulchanskyy, P. N. Prasad, Efficient photoconductive devices at infrared wavelengths using quantum dot-polymer nanocomposites. *Applied Physics Letters*, **87**:7 (2005), 073110.

70 K. R. Choudhury, W. J. Kim, Y. Sahoo, K. S. Lee, P. N. Prasad, Solution-processed pentacene quantum-dot polymeric nanocomposite for infrared photodetection. *Applied Physics Letters*, **89**:5 (2006), 051109.

71 T. Rauch, M. Boberl, S. F. Tedde, *et al.*, Near-infrared imaging with quantum-dot-sensitized organic photodiodes. *Nat Photon*, **3**:6 (2009), 332–336.

72 I. H. Campbell, B. K. Crone, Bulk photoconductive gain in poly(phenylene vinylene) based diodes. *Journal of Applied Physics*, **101**:2 (2007), 024502.

73 D. Qi, M. Fischbein, M. Drndic, S. Selmic, Efficient polymer-nanocrystal quantum-dot photodetectors. *Applied Physics Letters*, **86**:9 (2005), 093103.

74 H.-Y. Chen, K. F. LoMichael, G. Yang, H. G. Monbouquette, Y. Yang, Nanoparticle-assisted high photoconductive gain in composites of polymer and fullerene. *Nature Nanotechnology*, **3**:9 (2008), 543–547.
75 D. V. Talapin, C. B. Murray, PbSe nanocrystal solids for n- and p-channel thin film field-effect transistors. *Science*, **310**:5745 (2005), 86–89.
76 M. Law, J. M. Luther, Q. Song, *et al.*, Structural, optical, and electrical properties of PbSe nanocrystal solids treated thermally or with simple amines. *Journal of the American Chemical Society*, **130**:18 (2008), 5974–5985.
77 A. M. Munro, D. S. Ginger, Photoluminescence quenching of single CdSe nanocrystals by ligand adsorption. *Nano Letters*, **8**:8 (2008), 2585–2590.
78 A. M. Munro, I. Jen-La Plante, M. S. Ng, D. S. Ginger, Quantitative study of the effects of surface ligand concentration on CdSe nanocrystal photoluminescence. *Journal of Physical Chemistry C*, **111**:17 (2007), 6220–6227.
79 M. T. Frederick, E. A. Weiss, Relaxation of exciton confinement in cdse quantum dots by modification with a conjugated dithiocarbamate ligand. *ACS Nano*, **4**:6 (2010), 3195–3200.
80 C. Groves, O. G. Reid, D. S. Ginger, Heterogeneity in polymer solar cells: local morphology and performance in organic photovoltaics studied with scanning probe microscopy. *Accounts of Chemical Research*, **43**:5 (2010), 612–620.
81 L. S. C. Pingree, O. G. Reid, D. S. Ginger, Electrical scanning probe microscopy on active organic electronic devices. *Advanced Materials*, **21**:1 (2009), 19–28.
82 D. C. Coffey, D. S. Ginger, Time-resolved electrostatic force microscopy of polymer solar cells. *Nature Materials*, **5**:9 (2006), 735–740.
83 D. C. Coffey, O. G. Reid, D. B. Rodovsky, G. P. Bartholomew, D. S. Ginger, Mapping local photocurrents in polymer/fullerene solar cells with photoconductive atomic force microscopy. *Nano Letters*, **7**:3 (2007), 738–744.
84 D. S. Ginger, N. C. Greenham, Photoinduced electron transfer from conjugated polymers to CdSe nanocrystals. *Physical Review B*, **59**:16 (1999), 10622–10629.
85 W. U. Huynh, J. J. Dittmer, W. C. Libby, G. L. Whiting, A. P. Alivisatos, Controlling the morphology of nanocrystal–polymer composites for solar cells. *Advanced Functional Materials*, **13**:1 (2003), 73–79.
86 Y. Liu, M. Gibbs, J. Puthussery, *et al.*, Dependence of carrier mobility on nanocrystal size and ligand length in PbSe nanocrystal solids. *Nano Letters*, **10**:5 (2010), 1960–1969.
87 D. J. Milliron, A. P. Alivisatos, C. Pitois, C. Edder, J. M. J. Fréchet, Electroactive surfactant designed to mediate electron transfer between CdSe nanocrystals and organic semiconductors. *Advanced Materials*, **15**:1 (2003), 58–61.
88 H. Skaff, K. Sill, T. Emrick, Quantum dots tailored with poly(para-phenylene vinylene). *Journal of the American Chemical Society*, **126**:36 (2004), 11322–11325.
89 M. V. Kovalenko, M. I. Bodnarchuk, J. Zaumseil, J.-S. Lee, D. V. Talapin, Expanding the chemical versatility of colloidal nanocrystals capped with molecular metal chalcogenide ligands. *Journal of the American Chemical Society*, **132**:29 (2010), 10085–10092.
90 A. M. Munro, B. Zacher, A. Graham, N. R. Armstrong, Photoemission spectroscopy of tethered CdSe nanocrystals: shifts in ionization potential and local vacuum level as a function of nanocrystal capping ligand. *ACS Applied Materials & Interfaces*, **2**:3 (2010), 863–869.
91 C. Kittel, *Introduction to Solid State Physics*, seventh edition. New York, NY: John Wiley & Sons Inc., 1996.
92 S. Coe, W.-K. Woo, M. Bawendi, V. Bulovic, Electroluminescence from single monolayers of nanocrystals in molecular organic devices. *Nature*, **420**:6917 (2002), 800–803.

93 M. Pope, C. E. Swenberg, *Electronic Process in Organic Crystals and Polymers*, second edition, pp. 96–101. New York, NY: Oxford University Press, 1999.

94 R. Debnath, J. Tang, D. A. Barkhouse, *et al.*, Ambient-processed colloidal quantum dot solar cells via individual pre-encapsulation of nanoparticles. *Journal of the American Chemical Society*, **132**:17 (2010), 5952–5953.

95 K. Szendrei, W. Gomulya, M. Yarema, W. Heiss, M. A. Loi, PbS nanocrystal solar cells with high efficiency and fill factor. *Applied Physics Letters*, **97**:20 (2010), 203501.

96 J. Nelson, *The Physics of Solar Cells*. London: Imperial College Press, 2003.

97 D. Veldman, S. C. J. Meskers, R. A. J. Janssen, The energy of charge-transfer states in electron donor-acceptor blends: insight into the energy losses in organic solar cells. *Advanced Functional Materials*, **19**:12 (2009), 1939–1948.

98 G. I. Koleilat, L. Levina, H. Shukla, *et al.*, Efficient, stable infrared photovoltaics based on solution-cast colloidal quantum dots. *ACS Nano*, **2**:5 (2008), 833–840.

99 D. A. R. Barkhouse, A. G. Pattantyus-Abraham, L. Levina, E. H. Sargent, Thiols passivate recombination centers in colloidal quantum dots leading to enhanced photovoltaic device efficiency. *ACS Nano*, **2**:11 (2008), 2356–2362.

100 L. Cademartiri, E. Montanari, G. Calestani, *et al.*, Size-dependent extinction coefficients of PbS quantum dots. *Journal of the American Chemical Society*, **128**:31 (2006), 10337–10346.

101 K. W. Johnston, A. G. Pattantyus-Abraham, J. P. Clifford, *et al.*, Efficient Schottky-quantum-dot photovoltaics: The roles of depletion, drift, and diffusion. *Applied Physics Letters*, **92**:12 (2008), 122111.

102 G. Dennler, M. C. Scharber, C. J. Brabec, Polymer-fullerene bulk-heterojunction solar cells. *Advanced Materials*, **21**:13 (2009), 1323–1338.

103 S. Hellstrom, F. L. Zhang, O. Inganas, M. R. Andersson, Structure–property relationships of small bandgap conjugated polymers for solar cells. *Dalton Transactions*, **45** (2009), 10032–10039.

104 O. Inganas, F. Zhang, M. R. Andersson, Alternating polyfluorenes collect solar light in polymer photovoltaics. *Accounts of Chemical Research*, **42**:11 (2009), 1731–1739.

105 A. P. Kulkarni, K. M. Noone, K. Munechika, S. R. Guyer, D. S. Ginger, Plasmon-enhanced charge carrier generation in organic photovoltaic films using silver nanoprisms. *Nano Letters*, **10**:4 (2010), 1501–1505.

106 M. Niggemann, M. Riede, A. Gombert, K. Leo, Light trapping in organic solar cells. *Physica Status Solidi a–Applications and Materials Science*, **205**:12 (2008), 2862–2874.

107 M. Agrawal, P. Peumans, Broadband optical absorption enhancement through coherent light trapping in thin-film photovoltaic cells. *Optics Express*, **16**:8 (2008), 5385–5396.

108 B. P. Rand, P. Peumans, S. R. Forrest, Long-range absorption enhancement in organic tandem thin-film solar cells containing silver nanoclusters. *Journal of Applied Physics*, **96**:12 (2004), 7519–7526.

109 A. J. Morfa, K. L. Rowlen, T. H. Reilly, M. J. Romero, J. van de Lagemaat, Plasmon-enhanced solar energy conversion in organic bulk heterojunction photovoltaics. *Applied Physics Letters*, **92**:1 (2008), 013504.

110 B. A. Gregg, The photoconversion mechanism of excitonic solar cells. *MRS Bulletin*, **30**:1 (2005), 20–22.

111 K. M. Noone, N. C. Anderson, N. E. Horwitz, *et al.*, Absence of photoinduced charge transfer in blends of PbSe quantum dots and conjugated polymers. *ACS Nano*, **3**:6 (2009), 1345–1352.

112 J. Seo, S. J. Kim, W. J. Kim, *et al.*, Enhancement of the photovoltaic performance in PbS nanocrystal:P3HT hybrid composite devices by post-treatment-driven ligand exchange. *Nanotechnology*, **20**:9 (2009), 095202.
113 W. Y. Wong, X. Z. Wang, Z. He, *et al.*, Metallated conjugated polymers as a new avenue towards high-efficiency polymer solar cells. *Nature Materials*, **6**:7 (2007), 521–527.
114 X. Zhang, T. T. Steckler, R. R. Dasari, *et al.*, Dithienopyrrole-based donor–acceptor copolymers: low band-gap materials for charge transport, photovoltaics and electrochromism. *Journal of Materials Chemistry*, **20**:1 (2010), 123–134.
115 T. K. Daubler, I. Glowacki, U. Scherf, *et al.*, Photogeneration and transport of charge carriers in hybrid materials of conjugated polymers and dye-sensitized. TiO_2. *Journal of Applied Physics*, **86**:12 (1999), 6915–6923.
116 A. van Dijken, J. J. A. M. Bastiaansen, N. M. M. Kiggen, *et al.*, Carbazole compounds as host materials for triplet emitters in organic light-emitting diodes: polymer hosts for high-efficiency light-emitting diodes. *Journal of the American Chemical Society*, **126**:24 (2004), 7718–7727.
117 I. H. Campbell, T. W. Hagler, D. L. Smith, J. P. Ferraris, Direct measurement of conjugated polymer electronic excitation energies using metal/polymer/metal structures. *Physical Review Letters*, **76**:11 (1996), 1900–1903.
118 M. C. Scharber, D. Mühlbacher, M. Koppe, Design rules for donors in bulk-heterojunction solar cells – towards 10% energy-conversion efficiency. *Advanced Materials*, **18**:6 (2006), 789–794.
119 M. Morana, M. Wegscheider, A. Bonanni, *et al.*, Bipolar charge transport in PCPDTBT-PCBM bulk-heterojunctions for photovoltaic applications. *Advanced Functional Materials*, **18**:12 (2008), 1757–1766.
120 D. M. N. M. Dissanayake, R. A. Hatton, T. Lutz, R. J. Curry, S. R. P. Silva, The fabrication and analysis of a PbS nanocrystal:C-60 bilayer hybrid photovoltaic system. *Nanotechnology*, **20**:24 (2009), 25202.
121 D. M. N. M. Dissanayake, R. A. Hatton, T. Lutz, *et al.*, A PbS nanocrystal-C-60 photovoltaic device for infrared light harvesting. *Applied Physics Letters*, **91**:13 (2007), 133506.
122 N. Zhao, T. P. Osedach, L.-Y. Chang, *et al.*, Colloidal PbS quantum dot solar cells with high fill factor. *ACS Nano*, **4**:7 (2010), 3743–3752.
123 D. Yang, Semiconductor nanocrystal–polymer composites: using polymers for nanocrystal processing. In: A. L. Rogach, editor. *Semiconductor Nanocrystal Quantum Dots*, first edition, pp. 171–196. Vienna: Springer, 2008.
124 C. Wadia, A. P. Alivisatos, D. M. Kammen, Materials availability expands the opportunity for large-scale photovoltaics deployment. *Environmental Science and Technology*, **43**:6 (2009), 2072–2077.

5 Multiple exciton generation in semiconductor quantum dots and electronically coupled quantum dot arrays for application to third-generation photovoltaic solar cells

Matthew C. Beard, Joey M. Luther, and Arthur J. Nozik

5.1 Introduction

Power conversion efficiency (PCE) is one of the most important parameters that can directly affect the overall cost of a photovoltaic (PV) installation. Current solar cell technology based on a single light-absorbing layer is limited in its PCE of unconcentrated solar irradiance into electrical or chemical free energy to 33% as determined in 1961 by Shockley and Queisser (termed the Shockley–Queisser (SQ) limit) [1]. The first Si based solar cell was introduced in 1941 by Russell Ohl, and advances in material processing, material quality, and device configurations have resulted in increasing PCEs which have reached 80% of the SQ limit for Si or GaAs [2]. However, the maximum thermodynamic limit for solar photon conversion to free energy without solar concentration can reach 66%, and can be achieved in a tandem device with many semiconductor absorbers or with hot carrier solar cells that do not permit relaxation of supra-bandedge photogenerated carrier through electron–phonon scattering [3, 4]. In order to bypass the SQ limit we need to understand where the energy losses occur. The origin of this energy loss that ultimately determines the SQ limit is excess photon energy. This photon energy, which is greater than the semiconductor bandgap, is converted very efficiently to heat through electron–phonon coupling and subsequent phonon relaxation and energy dissipation. The most successful approach to overcoming the SQ limit is to use a stack of cascaded multiple p–n junctions with successively reduced band gaps. In this approach, the higher energy photons are absorbed in the larger band-gap semiconductors and lower energy photons in the smaller band-gap semiconductors, thus reducing the overall heat loss and increasing the amount of free energy available for useful work. In the limit of an infinite stack of band gaps perfectly matched to the solar spectrum, the conversion efficiency can reach about 66% [3] for unconcentrated light, with current efforts

Colloidal Quantum Dot Optoelectronics and Photovoltaics, eds. G. Konstantatos and E. H. Sargent.
Published by Cambridge University Press. © Cambridge University Press, 2013.

obtaining 32% for a three-stack device consisting of GaInP/GaAs/Ge [2]. However, the high cost of such approaches limits their commercial viability to either high end space applications or to terrestrial concentrator systems (under concentration the PCE increases) [5]. Approaches that overcome the hot-carrier relaxation in a single absorber layer and achieve low manufacturing costs are typically termed third-generation approaches [4] and include hot-carrier solar cells [3, 6], solar cells producing multiple electron–hole pairs per photon through impact ionization [7–9], multiband and impurity solar cells [4, 10], and thermophotovoltaic/thermophotonic cells [4]. For many of the above applications semiconductor nanostructures are being actively pursued to achieve the required effects due to their ability to modify electrooptical properties such as the radiative and non-radiative relaxation rates, interfacial electron-transfer kinetics, band gap, carrier generation rates, effective dielectric constant, and Fermi-level positions. Considerable interest has been generated by the observation that quantum dots (QDs) can enhance the efficiency of the electron–hole pair multiplication process (EHPM) [7, 11, 12]. In this process, excess photon energy can be used to produce additional electron–hole pairs rather than that energy dissipating to wasteful heat generation.

The creation of more than one electron–hole pair per absorbed photon has been studied for over 50 years in bulk semiconductors; for example, it has been observed in the photocurrent of bulk Si, Ge, PbS, PbSe, PbTe, and InSb [8, 13–21], and in these systems is termed *impact ionization*. Impact ionization (II) has not contributed to improved PCEs in present solar cells because it is too inefficient. For semiconductors such as Si where the band gap is near optimal for PV conversion, II does not produce additional carriers until the absorbed photon energies reach into the ultraviolet region of the spectrum where few solar photons exists. While for small band-gap semiconductors, such as PbSe, PbS, PbTe, and InSb where additional carriers are produced within the solar spectrum, the number of additional carriers per absorbed photon is too small to overcome the low inherent photovoltages that result from small band gaps [12]. The possibility of enhanced II in quantum confined nanostructures was first proposed by Nozik [7, 22] (the original concept is shown in Figure 5.1). Nozik realized that while for bulk semiconductors II must conserve both energy and crystal momentum (**k**), the conservation of crystal momentum is relaxed in QDs. Therefore, the threshold photon energy for the EHPM process (II in bulk semiconductors and multiple exciton generation (MEG) in QDs) in QDs can approach values as low as twice the threshold energy for absorption because only energy conservation needs to be satisfied. Lowering the threshold energy allows better utilization of the available solar spectrum resulting in a higher photocurrent, and, as was later realized, lowering the threshold also increases the efficiency of the EHPM process [12]. Auger processes, including the inverse of Auger recombination – EHPM, are enhanced in QDs [23] because the electron–hole pairs remain correlated even at room temperature due to the spatial confinement of the QD and therefore they interact strongly with one another through the Coulomb potential. Since the electron–hole pairs interact in QDs they remain as excitons and not free-carriers. For these reasons we have labeled the formation of multiple excitons in quantum dots *MEG* to distinguish the unique physics that occurs in QDs from impact ionization [24]; furthermore, free carriers can only form upon dissociation of the excitons.

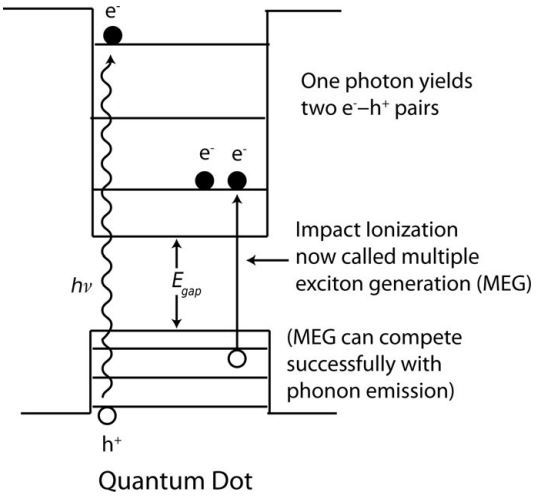


Figure 5.1 Proposed concept of enhanced electron–hole pair multiplication in QDs. A high energy photon is absorbed within a QD. The excess energy can be efficiently converted to multiple electron–hole pairs. Reproduced with permission from Elsevier from [7].

The first account of exciton multiplication presented by Schaller and Klimov [11] for PbSe QDs reported an excitation energy threshold for the efficient formation of two excitons per photon at $3E_g$. This onset is already lower than what is required by momentum conservation considerations in bulk PbSe ($\sim 4E_{\downarrow g}$) and approximately two times lower than what was reported for impact ionization in bulk PbSe [26]. Reports confirming efficient MEG in PbSe QDs quickly followed [27] and MEG was also reported in PbS [27] and PbTe QDs [28]. Additional experiments observing MEG have been reported for PbSe [29, 30], CdSe [31, 32], InAs [33, 34], Si [35], InP [36], CdTe [37], (6,5) single wall carbon nanotubes (SWCNTs) [38], and CdSe/CdTe core/shell QDs [39]. After the initial reports of MEG in QDs, intense interest in producing solar cells that incorporated QDs followed [40–45]. The goal of that effort is to incorporate QDs in a PV cell such that multiple excitons can be separated and collected as photocurrent [46]. Rapid progress saw QD solar cells, where the QDs retain their useful quantum size properties, achieve PCEs above 5% [47] and with internal quantum efficiencies approaching 90% [46] in a short period of time. However, following the discovery of MEG along with the optical measurements of this phenomenon in a wide variety of QD material systems, there were several groups who reported lower quantum yields (QYs) in PbS and PbSe [48] and no multiplication in CdSe [49] and InAs QDs [50]. Researchers also questioned the notion that MEG in QDs was actually enhanced over II in bulk semiconductors: the argument of an enhanced Coulomb interaction in QDs may be offset by a lower density of final states in QDs relative to bulk semiconductors [26, 48]. One group reported that they could not reproduce their previous positive results on InAs QDs [51]. Because of the discrepancies and various negative reports, doubts arose surrounding all of the MEG measurements. Therefore, efforts were directed towards understanding the variations in the reported QYs. Subsequently, McGuire and

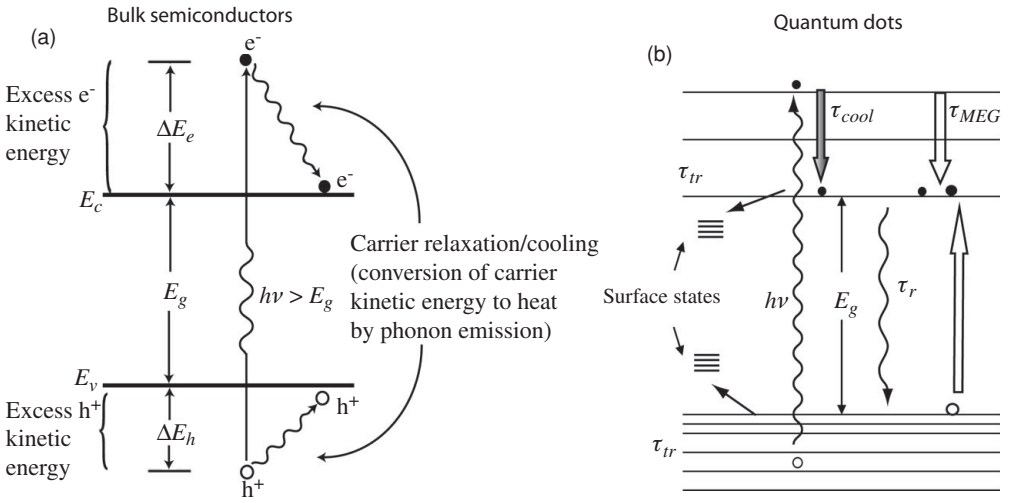


Figure 5.2 Carrier dynamics in (a) bulk semiconductors and (b) QDs can be quite different due to the discrete nature of the electronic states in QDs, the increased Coulomb interaction between the electron and hole, surface states, and ligand or solvent molecules near the surface. Adapted with permission from *Annual Review of Physical Chemistry* from [22].

coworkers [52, 53] reported that one source of the discrepancies in the reported QYs could be traced to extraneous effects of photocharging. Photocharging occurs when a high energy photon ionizes the QD leaving a charged QD. McGuire and coworkers found that the photoionization event must have a very low probability and that the ionized QD lifetime must be very long. Beard *et al*. [54] and Midgett *et al*. [55] reported that some of the variations in the QYs could be traced to different surface conditions of the QDs. Differences in the surface chemistry could affect either the competition between cooling and MEG or the degree of photocharging. Midgett *et al*. further analyzed the photocharging in PbSe QDs and found that the photocharging occurred with a probability of 1×10^{-5} for absorption of photons with $\sim 4E_g$ of energy but that once photocharged its lifetime could be between 10 and 30 s [55]. Whether photocharging plays a role in other QD systems such as Si, CdSe, InAs, and InP remains an open question.

5.2 Relaxation dynamics of photogenerated electron–hole pairs in QDs

Hot carriers are produced when the energy of a photon absorbed in semiconductor QDs is greater than that of the lowest energy excitonic transition. The excess energy is partitioned between the valence (hole states) and conduction (electron states) band such that $h\nu = E_g + \Delta E_e + \Delta E_h$, where ΔE_e and ΔE_h are the excess energies in the conduction and valence bands, and E_g is the band-gap energy (see Figure 5.2). Several things can happen to this excess energy: (1) it can be dissipated as heat through electron–phonon interactions, energy transfer to ligand or solvent vibrational modes [56–58], or various Auger relaxation processes [23] as the carriers relax to their lowest state; (2) if

$\Delta E_e \geq E_g$, a second electron–hole pair can be created as depicted in Figure 5.1; and (3) the electrons and holes can separate and the excess energy can be converted to increased electrical free energy via a PV effect or stored as additional chemical free energy [22]. The efficiency of photon conversion devices can be enhanced if paths (2) or (3) dominate over path (1). In bulk semiconductors, electron–phonon coupling is efficient and path (1) dominates resulting in cooling in a few picoseconds or less for photogenerated carrier densities less than $\sim 5 \times 10^{17}$ cm^{-3} [59–61]. The cooling time can be increased in bulk semiconductors by two orders of magnitude when the photogenerated carrier density increases above $\sim 5 \times 10^{18}$ cm^{-3} by a process termed a "hot phonon bottleneck" [59, 61, 62] and occurs due to the slow relaxation of phonons, which can then reheat the electron population. But this requires a photon flux much greater than the solar irradiance. In QDs, the electron–phonon coupling can be reduced such that slow cooling of energetic electrons and/or holes can occur at low photogenerated carrier densities [6, 63–66], specifically at light intensities corresponding to the solar insolation on earth. Boudreaux *et al*. [6] made the first prediction of slowed cooling at low light intensities in quantized structures. They expected slowed cooling due to decreased electron–phonon coupling arising from the quantized energy levels in the conduction and/or valence band (see Figure 5.2(b)). If the energy separation, ΔE, exceeds that of the LO-phonon energy, then a multiphonon process would be required to dissipate the excess energy. Because of the lower probability of such multiphonon processes this slowed cooling is termed a "phonon bottleneck". They analyzed highly doped n-type TiO_2 semiconductors where high doping levels ($>1 \times 10^{19}$ cm^{-3}) produce narrow space charge layers (200 Å) with a $\sim$1 eV barrier depth. Within the space charge region, quantized energy levels arise with an estimated energy separation of $\Delta E > 0.2$ eV. The hot carrier cooling time, τ_c, would be $\tau_c \sim \omega^{-1}\exp(\Delta E/kT)$, where ω is the phonon frequency, and could reach >100 ps. However, this system is analogous to a quantum film, where confinement occurs in one dimension, and the resulting quantized energy states have dispersion in k-space so that hot carriers can cool by undergoing inter-state transitions that require only one emitted phonon followed by a cascade of single phonon intra-state transitions.

In QDs, confinement occurs in all three dimensions so the phonon bottleneck should be enhanced. If cooling is governed only by phonon emission, a slower cooling rate is expected in smaller QDs due to the increased spacing of electronic levels. However, the opposite trend is observed experimentally – the cooling rate increases as the size of the QDs decreases for InP [67, 68] and CdSe [69] QDs. Theoretical models for slowed cooling in QDs have been proposed by Bockelmann and coworkers [66, 70] and Benisty and co-workers [65, 71]. The Benisty mechanism [65, 71] requires that cooling only occurs via LO phonon emission. However, when the phonon relaxation channel is impeded there are other mechanisms by which hot electrons can cool in QDs. Most prominent among these is an Auger-like mechanism [72], the excess energy of the electron/hole is transferred to the hole/electron, which can then relax rapidly due its higher density of states, thereby, breaking the phonon bottleneck [72]. Since the electron–hole interaction increases with smaller QDs an increase in the cooling rate is expected, as observed experimentally. Other mechanisms for bypassing any phonon bottleneck include electron–hole scattering [73], deep level trapping [74], and acoustical–optical

phonon interactions [75, 76]. The capping ligands may also provide a way to dissipate the excess energy via excitation of their vibrations [57]. Because of the various ways in which carriers may relax the occurrence of a true phonon bottleneck is controversial with many experimental results showing large variations in cooling dynamics, some that support and others that contradict a phonon bottleneck. Accounting for and then reducing various alternative relaxation channels, Pandey and Guyot-Sionnest showed that a phonon bottleneck exists for carefully constructed CdSe core/shell QDs [58].

5.2.1 Transient absorption spectroscopy (TA)

To measure the carrier dynamics in QDs there are several experimental techniques that are based on time-resolved spectroscopy. The most common is femtosecond TA which monitors the change in transmission of a weak probe beam in response to an intense photoexcitation event. Here we give a brief overview of TA measurements in QDs because this is the most common method used in determining MEG; however, transient photoluminescence [48, 49, 52, 53] and transient THz spectroscopy [26, 33] are the other commonly employed experimental probes of carrier dynamics. A typical TA apparatus (Figure 5.3(a)) consists of an amplified Ti:sapphire laser that produces ~30–100 fs FWHM pulses with a 1 kHz repetition rate. The laser pulse train is typically split into two independent beams: a pump and a probe beam. In the most versatile version each arm can contain independently tunable optical parametric amplifiers (OPAs) to produce visible and near-infrared pulses. A synchronous chopper phase-locked to the laser pulse train modulates the pump beam so that the transmitted probe pulse with and without the pump pulse is recorded using either lock-in amplifiers or box-car integrators. Comparison of the transmitted probe pulse energy with and without the pump permits calculation of the differential transmission, $\Delta T/T_0 = [T_{pump-on}(\tau) - T_0]/T_0$. For small values of $\Delta T/T_0$, and uniform excitation, we can relate this quantity to the change of the absorption coefficient, $\Delta\alpha - l = -\ln(\Delta T/T_{0+1}) \approx \Delta T/T_0$, where l is the pathlength. Figure 5.3(b) is a schematic of a typical TA experiment, where the two pulses are delayed by a pump–probe delay time, τ. Each point in a typical TA scan (Figure 5.3(c)) consists of averaging many laser pulses for a given τ. Typically ~900–3000 laser shots are averaged per delay and consist of ~1–3 s of averaging, each TA trace contains ~100 different pump–probe delays.

Following photon absorption, the resulting electronic excitation consists of an electron in the conduction band and a hole in the valence band (see inset in Figure 5.3(d)). Immediately after excitation the electron and hole have excess energy and lose that energy as they relax to the bottom of the conduction band, or the lowest unoccupied molecular orbital (LUMO), and the top of the valence-band, or highest occupied molecular orbital (HOMO), in a few picoseconds. Once carriers have relaxed to the lowest exciton state then there are two measurable effects in the absorption spectra and these are illustrated in Figure 5.3(d). The linear (no photoexcitation) absorption spectrum is shown as the black line with a peak at the first exciton transition ($E_g = 0.94$ eV), while the absorption spectrum taken at a delay of 100 ps is overlaid (gray line). First, the lowest-energy exciton transition is bleached (α decreases so that more light is transmitted), and also

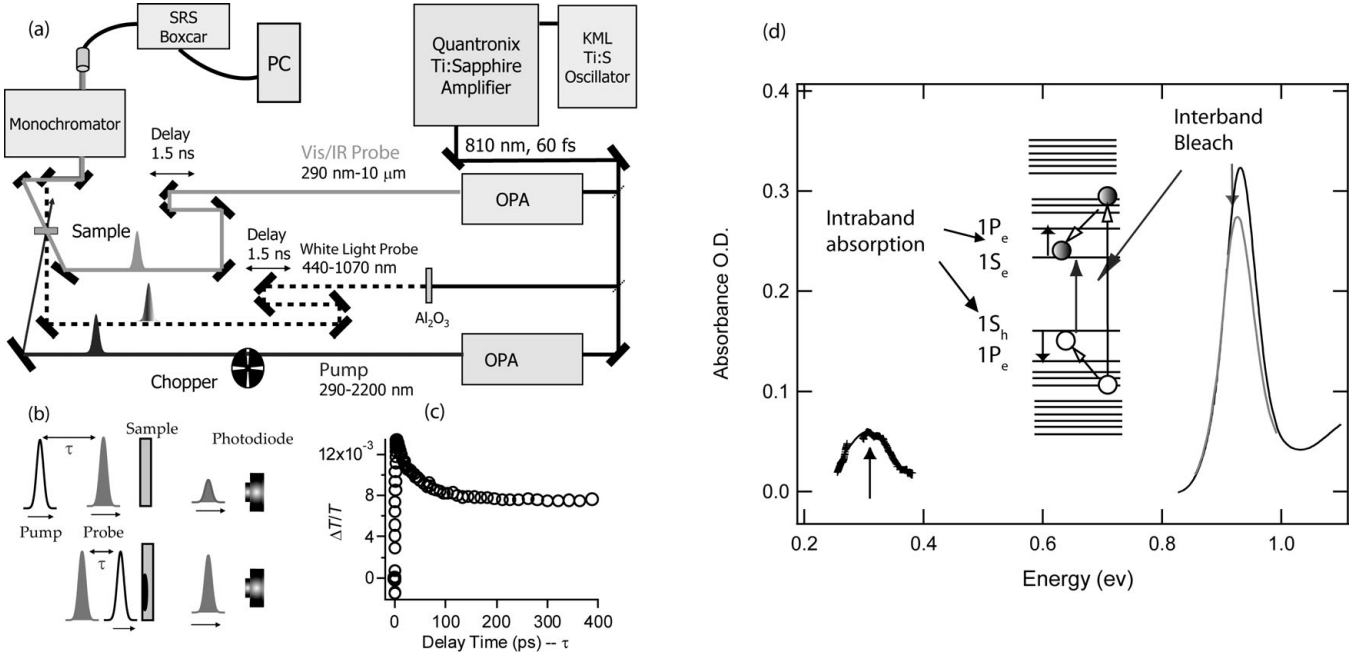


Figure 5.3 (a) A schematic of a typical TA spectrometer. There are two arms that produce independent tunable pump and probe pulses of light. (b) A schematic representation of a pump–probe experiment. There is a delay of τ between the pump and probe pulses. The delay is accomplished by varying the pathlength of the pump pulse relative to the probe pulse (see (a)). If the pump pulse arrives before the probe pulse the transmission of the probe pulse increases due to a bleaching of the excitonic transition. (c) The differential transmission of the probe pulse for a variety of pump–probe delays. (d) The absorption spectrum of a representative QD sample. The peak is the first exciton transition. The gray overlaid line displays the absorption spectrum at 100 ps delay time. An induced absorption also appears that is an intra-band absorption.

red-shifts slightly; second, a new absorption band appears in the infrared – for this sample the intra-band absorption appears at ~0.3 eV, which is equal to the difference between the $1S_e$ and $1P_e$ levels. The photoinduced bleach arises from state filling, or Pauli blocking and is proportional to the average occupation level. Beer's law states that the change in the light transmitted through a slab dz is linearly proportional to the intensity of the light, J, the absorption cross section, σ_{probe}, of the sample and the density of available states, $dJ = -\sigma_{probe} J\,[n_0 - n_{ex}\,(z, \tau)]\,dz$, where $n_{ex}(z, \tau)$ is the density of excited states produced by the pump pulse at position z and pump–probe delay τ. Shifts in absorption may also occur due to Stark effects, photoionization, and carrier trapping. PbSe QDs have an eight-fold degenerate first exciton transition, and for low excitation intensities where the average number of absorbed photons per QD is less than ~2, the measured $\Delta T/T_0$ is linear in pump intensity for both inter-band bleaching and intra-band absorption. Monitoring the recovery of the absorption as a function of pump–probe delay time is therefore directly proportional to the population carrier dynamics. A detailed discussion of TA measurements in QDs can be found in [69, 77]. Here we only discuss the aspects that are relevant for MEG measurements.

For MEG measurements it is important to know how the carrier dynamics is modified by the presence of two or more excitons per QD. It is assumed that the probability that a QD will absorb a photon is independent of whether it has already absorbed a photon. Then pulsed laser excitation of a solution of QDs with pulses of sufficiently short duration follows Poisson statistics, such that the fraction, P_m, of QDs within the excitation volume with m photogenerated excitons is

$$P_m = \frac{\langle N_0 \rangle^m}{m\,!} \exp\left[-\langle N_0 \rangle\right], \tag{5.1}$$

where $\langle N_0 \rangle$ is the average number of photons absorbed per QD per pulse, given by $\langle N_0 \rangle = \sigma_a \cdot j_p$, with a per-QD absorption cross section of σ_a (cm^2) and a photon pump fluence (photons cm^{-2} $pulse^{-1}$) [78]. The per-dot absorption cross section is measured in a separate experiment using inductively coupled plasma mass spectrometry (ICP-MS) [79] or other analytical analysis [80], and has been measured and tabulated for a variety of QD materials [79–83]. By careful control of the laser beam spot size, photon energy, and pulse fluence, one can control the excitation level for a sample of QDs to produce populations of photoexcited QDs weighted toward $m = 1$, for example, when $\langle N_0 \rangle = 0.25$ an average excitation level with ~90% of the excited QDs having $m = 1$ is produced, while $\langle N_0 \rangle = 2$ produces an average occupation level with ~68% of the excited QDs with $m > 1$.

In Figure 5.4, TA traces for a colloidal solution of PbSe QDs with $E_g = 0.83$ eV and an excitation photon energy of 1.5 eV, corresponding to $1.8E_g$ (so the total excess energy is $0.8E_g$) are displayed. The average occupation level was increased from $\langle N_0 \rangle = 0.19$ to $\langle N_0 \rangle = 1.14$ and there are two noticeable trends in the data: (1) the $\Delta T/T_0$ signal increases as the total number of photoexcited QDs increases; and (2) a fast component grows with increasing occupation level. At $\langle N_0 \rangle = 0.19$ about 90% of the signal is due to QDs with only one exciton, while for $\langle N_0 \rangle = 1.14$ about 46% of the signal is due to QDs with more than one exciton. Single exciton lifetimes depend much more on

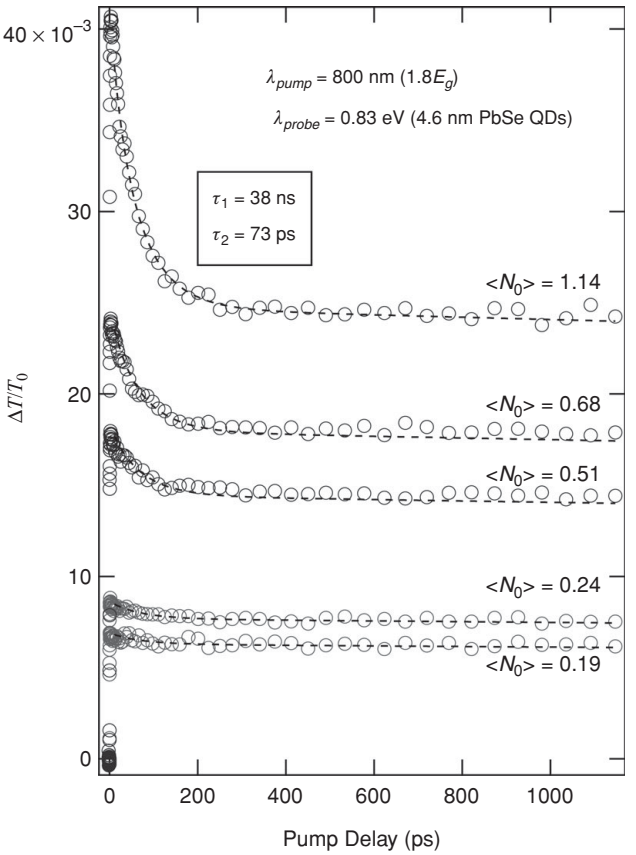


Figure 5.4 TA spectra of a 4.6 nm PbSe QD colloidal sample ($E_g = 0.83$ eV). The photoexcitation energy was $1.8E_g$ and the photon fluence was adjusted to produce $\langle N_0 \rangle$s between 0.19 and 1.14. A non-linear least squares fitting routine is used to globally model the data (dashed lines) and finds the single exciton lifetime $\tau_1 = 38$ ns, while the biexciton lifetime is $\tau_2 = 73$ ps.

the dipole transition strength and the QD surface properties, and range from ~20 ns for CdSe QDs to ~2 μs for PbSe or PbS QDs. However, when QDs have more than one exciton, the relaxation dynamics are governed by non-radiative Auger recombination. Auger recombination describes a multiparticle interaction; the excitons interact so that the energy of one of the excitons is given up to the other one and limits the lifetime of the two-exciton state for typically-sized QDs to the range ~10–100 ps. In the case where MEG is not energetically allowed, the time-dependent population of the first exciton level is to a very good approximation given by $n_{1s}(\tau_p) = n_0 \sum_i^A \exp(-\tau_p/\tau_i)$, where $A_i = \sum_{m=i}^{\infty} P_m$ and P_m is the mth term of the Poisson distribution (Equation (5.1)). The lifetimes of the higher multiplicities ($m > 2$) are related to the biexciton lifetime by $\tau_m = 4\tau_2/m^2$.

A non-linear least squares global fitting function is employed to model all of the transients simultaneously, where τ_1 and τ_2 (single-exciton and bi-exciton lifetimes) are varied globally, while $\langle N_0 \rangle$ is independently varied for each transient. This global

fitting approach returns consistent values for τ_1 and τ_2 with small uncertainties. This analysis has been done for a variety of PbSe QD sizes and the biexciton lifetime varies approximately linearly with the volume of the QDs [25]. In a study of Ge QDs, Robel *et al*. [84] found that for PbSe, Ge, and CdSe the Auger recombination rates varied only weakly with the material and effective bandgap while being mainly governed by the volume of the QDs.

5.3 Multiple exciton generation (MEG)

5.3.1 MEG in QDs

In 2004, Schaller and Klimov [11] noticed that when photoexciting a colloidal suspension of PbSe QDs at high photon energies a fast component persisted in the TA dynamics even when the laser fluence was adjusted so that $\langle N_0 \rangle$ was very small (<0.1). They analyzed the fast component and found that it had the same characteristics of the biexciton lifetime, τ_2, described above. Furthermore, the amplitude corresponding to the fast component increased with increasing photon energy after exceeding a photon energy threshold. Upon investigating QDs with different band gaps, the fast component tracked the expected linear dependence of the biexciton lifetime and was identical to the value found by photoexciting with lower photon energies but high photon fluences. They also reported that when plotting their data with normalized band gap (plotted as $h\nu/E_g$) the data from various sized PbSe samples collapsed onto a single line. The appearance of the fast component was ascribed to efficient multiexciton generation with threshold energy of $3E_g$. The evidence that multiple excitons were produced per absorbed photon, therefore, is the appearance of the fast multiexciton decay component with the identical time constant as τ_2 when photoexciting above the energy conservation threshold ($>2E_g$) and at low intensity so that each photoexcited QD absorbs at most one photon.

We now describe the analysis of the TA data to extrapolate QYs >1. As we saw in the preceding section, a set of intensity-dependent TA traces in the absence of MEG could all be described by $n_{1s}(\tau_p) = n_0 \sum_i^A \exp(-\tau_p/\tau_i)$, where the A_is are related to the initial populations determined from Poisson statistics. When MEG does occur, this relationship no longer holds because there are additional contributions to the A_is for $i > 1$. By analyzing these additional contributions, the QY (number of excitons produced per absorbed photon) is determined. We first determine the A_is and τ_is under sub-threshold conditions where MEG *cannot occur* (e.g., $h\nu < 2E_g$), i.e., the case for which the A_is depend solely on the photon fluence and the per-QD absorption cross section as shown in Figure 5.4. For our MEG analysis, we assume that each absorbed photon creates one or more excitons, excluding other possible processes such as QD photoionization (we show how photoionization contributes to the TA and MEG analysis in the next section), and we treat the MEG event as instantaneous. For photoexcitation in the range where $2E_g < h\nu < 3E_g$, energy conservation permits a QY of at most 2. There are two possible scenarios: no MEG occurs with a probability of $1 - \eta$, or MEG does occur with a

probability of η. For a QD absorbing two photons there are four possible scenarios and so forth. The modified A_is (for the first three terms) were determined to be;

$$A_1 = \sum_{m=1}^{\infty} P_m$$

and does not change from the no MEG scenario;

$$A_2 = \sum_{m=2}^{\infty} P_m + P_1\eta,$$

$$A_3 = \sum_{m=3}^{\infty} P_m + P_2[2\eta(1-\eta) + \eta^2],$$

where P_m accounts for directly generated excitons. In the region where the photon energy satisfies $3E_g < h\nu < 4E_g$, energy conservation permits a QY = 3; i.e., one exciton can produce two additional excitons. η is the probability of an exciton succeeding to produce an additional exciton, and the probability that an exciton fails to produce an additional pair is $(1 - \eta)$. The probability of producing two additional pairs is then η^2. The A_is can be suitably modified as above and the interested reader can find the exact modifications elsewhere [27].

Experimentally, transients are collected for a variety of pump photon energies maintaining a constant $\langle N_0 \rangle$ at the front of the sample. Figure 5.5 shows a typical experiment to determine MEG in this fashion. Figure 5.5(a) is the linear absorption spectrum and we have overlaid arrows indicating the different pump wavelengths employed for the transients as symbols in Figure 5.5(b). The solid lines are a result of a global non-linear least squares fit of a model to the data set. The τ_is are held fixed in the model and the extracted QYs (related to η) are shown in the inset. Note that the transients are all normalized at pump–probe delays longer than the Auger recombination (AR) time where only single excitons remain.

The analysis described above requires knowledge of the absorption cross section at all excitation wavelengths and the exact determination of the photon fluence for each excitation energy. Since some experimental error occurs for each of these determinations, a more reliable method has been developed in order to improve upon the errors in the reported QYs. Here a series of transients is collected, one transient at each of the desired pump photon energies with decreasing photon fluence to determine the amplitude in the limit of $\langle N_0 \rangle \to 0$. The fluence is decreased until the transients no longer show a change in their dynamics. Then a point at early delays $(\Delta T/T)_{\tau=0}$ is extracted from each transient and divided by a point at long pump delay times $(\Delta T/T)_{\tau>3\tau_2}$. The long delay time data point is chosen so that it is $>3\tau_2$ so that it represents the point where only single excitons remain. The carrier population ratio, $R_{pop} = (\Delta T/T)_{\tau=0}/(\Delta T/T)_{\tau>3\tau_2}$, is then plotted vs. the input photon fluence, J_0, in photons cm^{-2} pulse^{-1}. To analyze R_{pop} vs. J_0 we need to know how the population of excited carries behaves at $\tau = 0$ and $\tau > 3\tau_2$. The differential transmission for photoinduced bleach of absorption is $\Delta T/T = \exp(\sigma_{probe}N_{ex}l) - 1 \approx \sigma_{probe}N_{ex}l$, where we have introduced the absorption cross section at the probe wavelength, σ_{probe}, and N_{ex}

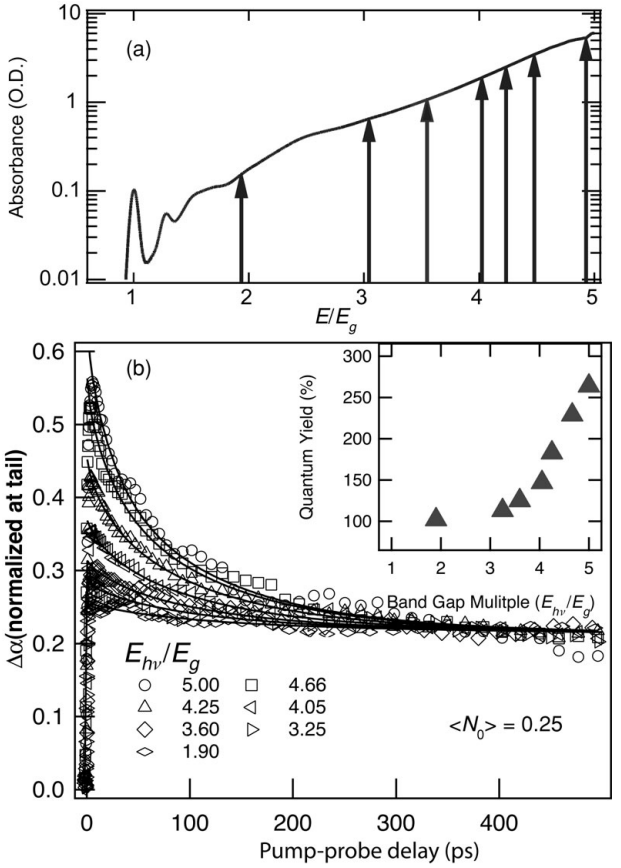


Figure 5.5 Typical MEG transient absorption experiment. (a) The linear absorption of PbSe QDs. The arrows show the excitation energies used to investigate MEG and correspond to the traces in (b). (b) The transients for a constant $\langle N_0 \rangle = 0.25$ but increasing the photon energy from $1.9E_g$ to $5E_g$. The amplitude of the fast component increases with increasing photon energy. The inset shows the extracted QYs for each trace. Adapted and reproduced with permission from ACS from [27].

is the photoexcited number density. At early times prior to any population relaxation $N_{ex}(\tau = 0) = J_0[1 - \exp(-\sigma_{pump} N_{QD} l)]/\beta$, where β is the absorption depth, σ_{pump} is the absorption cross section at the pump wavelength, N_{QD} is the density of QDs in solution and l is the cuvette pathlength. We consider two limiting cases: (1) high optical density (OD) at the pump wavelength and (2) low OD at the pump wavelength. Under these two conditions, we will have different values of $\beta : \beta = l$ at low OD and $\beta = 1/\alpha_{pump}$ at high OD. For pump–probe delay times much greater than the Auger decay time ($\tau > 3\tau_2$), any QDs with more than one exciton will undergo AR to yield one exciton per QD. We can calculate the number of excited QDs assuming Poisson statistics as $N_{ex}(\tau > 3\tau_2) = N_{QD}[1 - P_0]$. Finally we find R_{pop} is,

$$R_{pop} = \frac{J_0 \sigma_{pump} \delta \cdot QY}{[1 - \exp(-J_0 \sigma_{pump})]}, \tag{5.2}$$

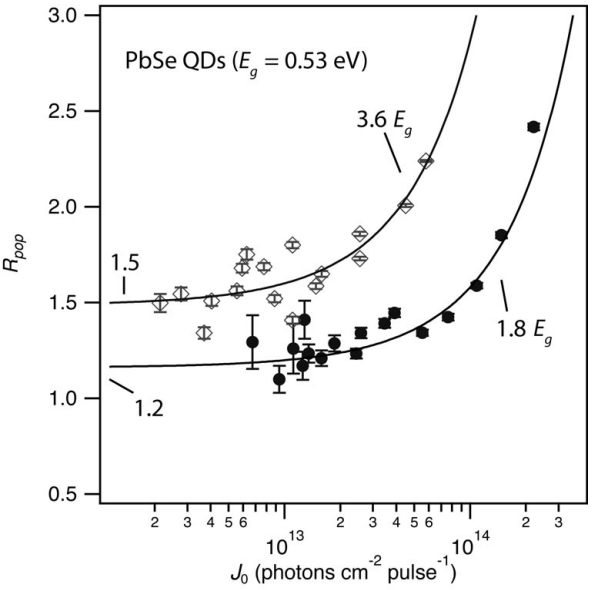


Figure 5.6 R_{pop} values derived from measuring TA traces for decreasing fluence (J_0). The open circles are for photoexcitation at $3.6E_g$ while the filled circles are for $1.8E_g$. Equation (5.2) is employed to model the $1.8E_g$ data set to determine δ (1.2) and then to model the $3.6E_g$ to extract the QY (1.5/1.2 = 1.25 ±.05).

where $\delta = \exp((t_{late} - t_{early}))/\tau_1$ accounts for any single exciton decay. We find that this ratio holds exactly in the low OD limit. In the high OD limit, the excitation volume is not uniform and Poisson statistics do not hold when considering the entire excitation volume. In this situation, (5.2) can still be employed to determine the QY, though σ_{pump} will be underestimated. We have treated this case in [55] and refer interested readers there for further and more detailed information. This method allows for the extraction of σ_{pump}. Using (5.2) is especially important when the measured optical density may not be linearly related to the absorption cross section, which occurs when measuring films of QDs where wavelength-dependent scattering may be important. In addition, for QD films that exhibit some degree of electronic coupling, σ may be modified due to a wavelength-dependent dielectric screening; therefore, σ_{pump} is not known a priori based on that of the isolated QDs. We illustrate this method in Figure 5.6 for a PbSe QD colloidal sample with $E_g = 0.53$ eV where the photoexcitation is at 0.95 eV ($1.8E_g$), and 1.9 eV ($3.6E_g$). Each of the points in Figure 5.6 is derived from a TA trace (not shown). Here the MEG yields show up as an offset in the R_{pop} values for lower fluences corresponding to low $\langle N_0 \rangle$. For this sample we see that R_{pop} approaches a value of 1.2 for the case of photoexciting below the MEG threshold (this corresponds a decay in the first exciton lifetime) and approaches a higher value of 1.5 for the case of $3.6E_g$ excitation. The data are modeled using (5.2) first to obtain δ and the QY. For this sample we determined the QY = 1.25 (± 0.05) when excited at $3.6E_g$.

It is important to rule out alternative processes that can additionally cause a fast decay component and corresponding offset in the R_{pop} analysis. Alternative processes must be consistent with the following experimentally determined observations: (1) the dynamics are the same as AR, showing the same decay rate and dependence on QD volume; (2) the fast component with time constant equal to that of AR steadily increases with photon energy with an onset greater than $2E_g$; and (3) the effect remains at low excitation fluences.

5.3.2 MEG controversy and role of photocharging

In 2007, Nair and Bawendi [49] reported that while investigating CdSe and CdTe QDs they did not observe a signature of MEG; the carrier dynamics was independent of excitation wavelength. In their study, they used a transient photoluminescence (TRPL) experiment rather than TA, but the general idea is the same: a biexciton has a faster decay than a single exciton. Their results were in contrast to a previous study from Schaller *et al*. that reported positive MEG results on CdSe QDs also using TRPL [31]. Nair and Bawendi followed their study on CdSe QDs with a TRPL study of PbS and PbSe QDs [48]. Here, they did observe MEG, but reported smaller QYs than previous papers. Subsequently, a study of InAs core/shell/shell QDs also reported a negative result for MEG [50], again contradicting a previous study by Schaller *et al*. [31]. A troubling report emerged from Pijpers *et al*. [51] when they could not reproduce their earlier results using similarly prepared InAs QDs. Beard *et al*. [54] reported a wide variation in the QYs of PbSe QD films, the variations depended on how the QDs were treated and the different surface chemistries used to produce conductive QD films. The situation began to clarify when McGuire and coworkers [52, 53] proposed that due to the repetitive nature of the pulsed laser experiments, a steady state population of charged QDs can be established, through a low probability photoionization event, if the lifetime of the photoionized state is longer than the time between excitation pulses (2 ms). The proposed scheme is illustrated in Figure 5.7. Unexcited QDs (labeled n_0) are excited to n^*, a hot-exciton state produced by absorption of a photon with $h\upsilon > E_g$. The hot exciton may cool to the band gap creating a single-exciton in its lowest energy state (labeled γ_{cool}), or the hot-exciton may undergo MEG to create two or more excitons. However, the hot-exciton state may also undergo photocharging with rate γ_g (labeled as n_T). QDs in the n_T state accumulate during the experiment because their lifetime exceeds that of the laser repetition rate, thereby, producing a measurable effect in the TA dynamics. If a QD in the n_T state absorbs another photon from the next laser pulse, a trion-like state (labeled n_{2T}) is produced that undergoes a non-radiative AR (γ_{trion}) process with similar dynamics to biexciton recombination. This photocharging pathway produces a similar dynamical signature that, if otherwise is ascribed solely to MEG, leads to an artificially high MEG yield [52, 53, 55]. This alternative pathway can be avoided by not exposing the QDs to multiple laser pulses either by stirring or by carefully flowing the QD solution, so that the small fraction of QDs that undergo photocharging are swept away and not allowed to accumulate.

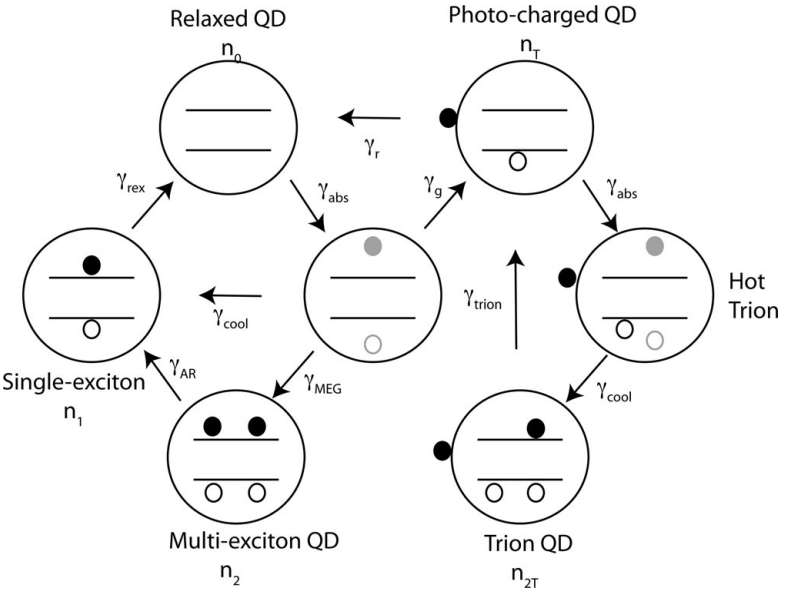


Figure 5.7 Relaxation pathways for excitons produced with high-energy photons. The photocharging pathway complicates the analysis of MEG yields and depends upon the photon energy, photon fluence, and QD surface quality. The effects of photocharging on MEG yields can be reduced by flowing or stirring the samples during the experiment. Reproduced with permission from ACS from [55].

Figure 5.8 shows a transient bleaching experiment on a 4.6 nm PbSe QD sample with a first exciton transition energy of $E_g = 0.84$ eV and 3.1 eV excitation light ($\sim 3.7E_g$). In Figure 5.8(a), the experiment was performed under static conditions, while in (b), the QDs dispersed in tetrachloroethylene were flowed at a volumetric flow rate of $Q = 150$ mL/min. The excitation fluences were such that the average occupation number, $\langle N_0 \rangle$, ranged from 0.04 to 0.58 and Figure 5.8(c) compares the $\Delta T/T$ at the highest fluence corresponding to $\langle N_0 \rangle = 0.58$. For static conditions, $\Delta T/T$ is smaller at longer pump-delay times because the fraction of QDs that are photocharged only contributes to $\Delta T/T$ at early delay times, $\tau < 3\tau_{2T}$. The difference in $\Delta T/T$ between static and flowing cases at long delay times is approximately equal to the degree of photocharging. At low $\langle N_0 \rangle$s (< 0.1) the difference between flowing and static conditions is greatly reduced. The degree of photocharging is also photon-energy-dependent (at $1.8E_g$ no differences between static and flowing conditions were observed) [55]. The results of the global fit described above are shown as the dotted lines for the flowing case. Midgett *et al*. [55] found that $\tau_{2T} = 217$ ps and this is consistent with the trion-decay pathway. They determined the lifetime of the photocharged state to be 10–30 s by measuring the degree of charging as a function of well-controlled flow rates.

Varying QD surface conditions, excitation fluence, and photon energy leads to variations in the degree of photocharging. Figure 5.9 compares the QYs obtained under static and flowing conditions. The static conditions produced results that differed between three

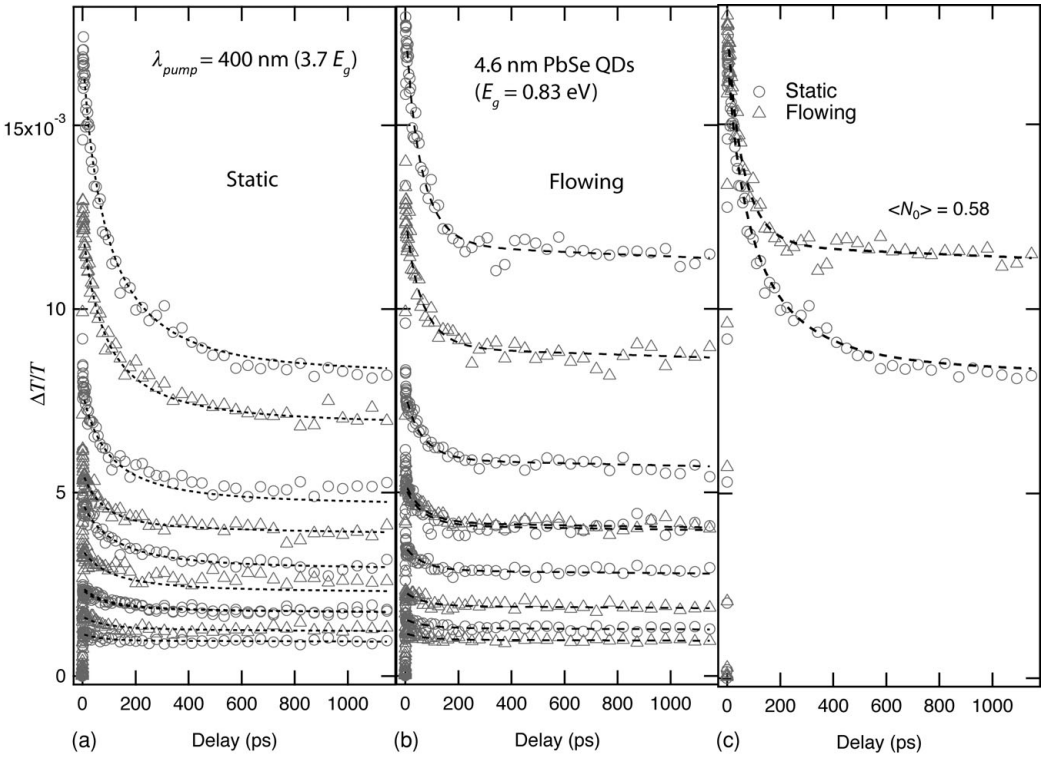


Figure 5.8 TA data for 4.6 nm PbSe QDs with a band gap of $E_g = 0.83$ eV excited at 400 nm ($3.7E_g$). The transient absorption signal ($\Delta T/T$) for (a) static conditions (b) flowing conditions; and (c) the data for the higher fluence from (a) and (b). The dotted lines in (a), (b), and (c) are for the model described in the text. Adapted and reproduced with permission from ACS from [55].

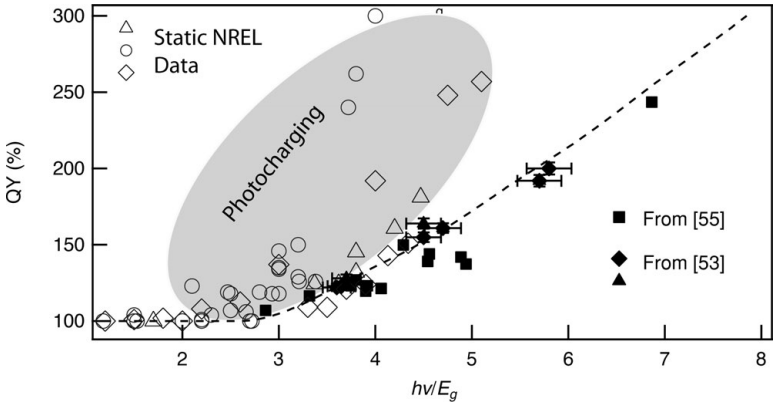


Figure 5.9 Comparison of the MEG QYs collected under stirring or flowing conditions (filled symbols) and those under static conditions. Under static conditions the uncontrolled charging produced results that varied widely and were artificially high. The static results are more reproducible, but yield lower QYs. The dashed line is drawn for clarity.

different samples, while the flowing conditions produced reproducible results. Accurate photon-to-exciton QYs can be obtained by not allowing the photocharged state to build up during the experiments. The flowing data compares well with an independent study of MEG in PbSe QDs where the samples were stirred [52, 53] rather than flowed. The proposed photocharging process that gives rise to the large variations in MEG QYs is similar to what is found in fluorescence intermittency experiments and it is tempting to assign them to the same mechanism, however, there are some striking differences that require further understanding. Fluorescence intermittency, or QD blinking, [85] refers to the observation that the photoluminescence of single QDs under continuous illumination does not exhibit a continuous emission intensity. The QD emits for some amount of time followed by no emission; the "on", and "off" times follow power law behavior (for a comprehensive review see [86, 87]). Despite numerous studies of QD blinking there is no clear agreement on the microscopic mechanism that can account for all observations. However, the "off", or dark, state is likely a photoionized or photocharged QD and quenches luminescence by providing a very efficient non-radiative decay pathway. The ionized carrier is trapped near the QD surface and has some probability of neutralizing the QD core and thereby turning "on" the emission [88, 89].

There are three factors that show blinking to be similar to photocharging. (1) Both processes can have similarly long lifetimes. (2) There is a clear dependence on surface passivation [85, 90–93]. (3) The Auger quenching mechanism, involving the trion and discussed above to explain blinking, can be used to interpret the difference between flowing and static conditions. There are also clear differences between blinking and photocharging. There is an energy dependence for the creation of photocharged QDs while in the blinking experiments, blinking is observed at all excitation wavelengths (due to material and detector sensitivity, this range has been limited to the visible 1.9–3.1 eV, or $< 2E_g$). The Auger ionization mechanism which is responsible for producing the off state was found not to be responsible for the creation of photocharged QDs in the transient absorption measurements.

5.3.3 MEG efficiency and comparison to impact ionization in bulk semiconductors

An important question that must be addressed with regard to MEG is whether the EHPM process is enhanced in QDs (MEG) relative to the equivalent process in a bulk semiconductor (II). To do that [12] consider the energy losses that occur with and without EHPM. For absorption of a photon with energy greater than E_g but in the absence of EHPM, all the excess energy is lost as heat, $E_{loss} = \Delta E_{tot} = (h\upsilon - E_g)$. When the EHPM efficiency, η_{EHPM}, is equal to 1 the amount of excess energy needed to produce an additional electron–hole pair is just the band-gap energy, E_g. In this case ($\eta_{EHPM} = 1$) the amount of energy lost at a photon energy $h\upsilon = xE_g$, where $x > 1$, is $E_{loss} = (x - m)\,E_g$, where $m = \lfloor h\upsilon/E_g \rfloor$ and the "floor" operator, $\lfloor \square \rfloor$, denotes rounding down to the nearest integer. The maximum QY exhibits a 'staircase' where $QY = 2$ at $2E_g$; 3 at $3E_g$; and so forth. This can be expressed as $QY = m = \lfloor h\upsilon/E_g \rfloor$, and is plotted as trace M_{max}, in Figure 5.10(b). When the EHPM efficiency is less than 1, the amount of energy required to produce an additional electron–hole pair defined as the

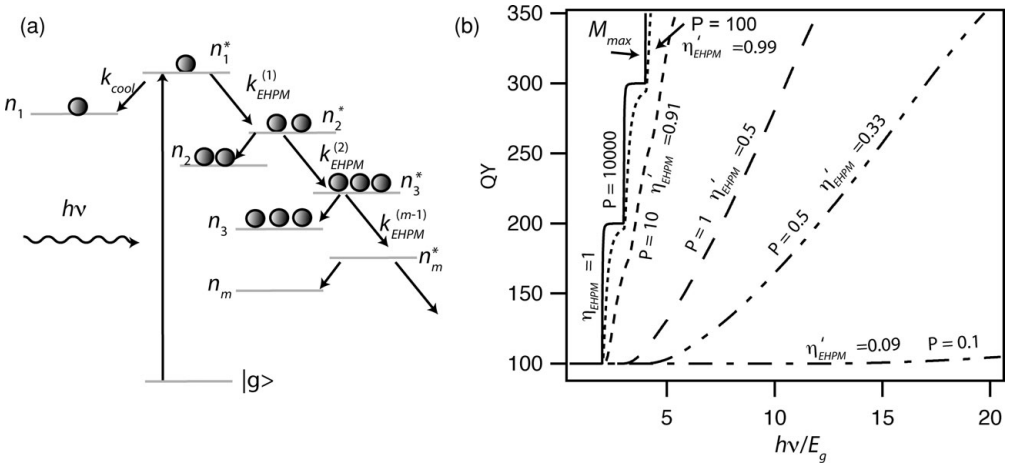


Figure 5.10 (a) Cascade scheme for EHPM discussed in the text. (b) Plots of (5.5)for different values of P. Reproduced with permission from ACS from [12].

electron–hole pair creation energy, ε_{EHPM} [94, 95], is greater than the band gap energy, $\varepsilon_{EHPM} \geq E_g$, Therefore, the EHPM efficiency is defined as the minimum amount of energy required to produce an electron–hole pair (i.e., the band gap), divided by the actual amount of energy required to produce an additional electron–hole pair after the MEG threshold is passed, $\eta_{EHPM} = E_g/\varepsilon_{EHPM}$. Experimentally, QYs begin to exceed 1 above an energy threshold, $h\upsilon_{th}$, and they increase linearly for $h\upsilon > h\upsilon_{th}$. In this non-ideal case, the amount of energy lost that is not used in creating additional electron–hole pairs is $E_{loss} = h\upsilon_{th} - E_g$ for photon energies greater than $E_g + \varepsilon_{EHPM}$, and the QY was found to be,

$$QY = \left(\frac{h\upsilon}{E_g} - 1\right)\eta_{EHPM} = \left(h\upsilon - E_g\right)\frac{1}{\varepsilon_{EHPM}}, \tag{5.3}$$

for $h\upsilon > h\upsilon_{th}$. The energy threshold, $h\upsilon_{th}$, is related to η_{EHPM}, and is,

$$h\upsilon_{th} = E_g + \frac{E_g}{\eta_{EHPM}}. \tag{5.4}$$

The total energy loss is $E_{loss} = h\upsilon_{th} - E_g = E_g/\eta_{EHPM}$; η_{EHPM} can be obtained from plotting the QY vs. $h\upsilon/E_g$, while $1/\varepsilon_{EHPM}$ is obtained from plotting QY vs. $h\upsilon$.

The competition between EHPM, k_{EHPM}, and alternative energy relaxation channels, such as cooling, has also been considered. Figure 5.10(a) shows a cascading kinetic scheme where the high-energy exciton either cools directly to the lowest state or produces a hot biexciton state, n_2^*. There it can either cool or undergo another EHPM event and so forth until the excited exciton eventually loses all of its excess energy. Solving the set of differential equations that describe the cascaded scheme [12] the QY can be expressed in terms of the rate of EHPM, k_{EHPM}, and the cooling rate k_{cool} :

$$QY = \sum_{f=1}^{m} f\frac{k_{cool}\Pi_{i=1}^{f}k_{EHPM}^{(t-1)}}{\Pi_{t=1}^{f}(k_{cool} + k_{EHPM}^{(t)})} \tag{5.5}$$

with EHPM rates denoted by $k_{EHPM}^{(m)}$, where m is an integer and is the maximum number of electron–hole pairs allowed by energy conservation and $k_{EHPM}^{(0)} = 1$. Equation (5.5) requires knowledge of how k_{EHPM} and k_{cool} vary with excess energy. Beard *et al.* [12] considered how the ratio of rates, k_{EHPM}/k_{phonon}, varies with excess energy by examining the ratio of the mean free path for phonon scattering, λ_{phonon} and the mean free path for EHPM, λ_{EHPM}, i.e., $k_{EHPM}/k_{phonon} \propto \lambda_{phonon}/\lambda_{EHPM}$. The length scales were considered for the case of bulk semiconductors. The average distance a charge carrier travels prior to phonon scattering is equal to the velocity of the carrier multiplied by the average time between collisions, $\lambda_{phonon} = \nu(\tau)$; λ_{phonon} is relatively independent of the kinetic energy of the charged carrier because the length scale for phonon scattering is determined by the properties of the lattice, so as ν increases it is offset by a shorter (τ). For bulk PbSe, $\lambda_{phonon} \sim 67$ nm, and is determined from the carrier mobility. In bulk semiconductors, λ_{EHPM} decreases with increasing carrier velocity (or excess kinetic energy) [96], corresponding to an increasing k_{EHPM}. For Si $\lambda_{EHPM} \sim 10$ nm [95] at a few electron volts above the bandedge, and for GaAs $\lambda_{EHPM} > 10$ nm for excess energies between 1 and 10 eV [96]. A Monte Carlo simulation of phonon cooling and impact ionization finds the phonon relaxation rate to be independent of excess energy, while the II rate increases with increasing excess energy [97]. The ratio k_{EHPM}/k_{cool} can be parameterized by the following expression [98]:

$$k_{EHPM} = k_{cool} P \left(\frac{h\upsilon - h\upsilon_{th}}{h\upsilon_{th}} \right)^{s}. \tag{5.6}$$

The exponent s can vary between 2 and 5. The EHPM efficiency, η'_{EHPM}, captures the competition between EHPM and cooling and is defined as $\eta'_{EHPM} = P/(1+P)$, where the prime is used to distinguish η'_{EHPM} from η_{EHPM} defined above in terms of ε_{EHPM}. The relationship between η'_{EHPM} and the energy threshold is given by, $h\upsilon_{th}^{(m)} = E_g(1 + m/\eta'_{EHPM})$, where $k_{EHPM}^{(m)}$ is zero below $h\upsilon_{th}$ and $k_{EHPM}^{(m)} = k_{cool} P[(h\upsilon - h\upsilon_{th})/h\upsilon_{th}]^s \Theta(h\upsilon - h\upsilon_{th}^{(m)})$, where θ is the Heaviside step function.

In Figure 5.10(b) plots of the QY calculated from (5.5) for various values of P (with $s = 2$) are shown. P is varied from 10 000 to 0.1. At $P = 10\,000$, $\eta'_{EHPM} = 1$, and EHPM dominates over cooling. At $P = 1$, $\eta'_{EHPM} = 0.5$, there is roughly a linear increase of the QY with $h\upsilon/E_g$, the onset, however, is not as sharp as that predicted from (5.5). For QY values less than ~150% and for $P < 10$, $k_{cool} > k_{EHPM}$, and QY increases approximately quadratically with $h\upsilon/E_g$.

Figure 5.11(a) displays QY data for three samples of different size PbSe QDs, where the samples are flowed at 150 ml/min during the transient absorption experiment, while data reported in [52] are for stirred samples. QYs for bulk PbSe (filled black squares) and bulk PbS (open circles) are plotted and reproduced from [26]. Equation (5.3) was fit to each data set with only one adjustable parameter, η_{EHPM}, to obtain both the slope and $h\upsilon_{\text{th}}$ and is shown as dotted lines. The solid lines are the best-fit lines using (5.6). The efficiency, η_{EHPM}, is clearly better for the PbSe QD samples (0.41) than for the bulk PbSe (0.19), while P increases from 0.45 to 1.5, $h\upsilon_{\text{th}}$ decreases from $4.2E_g$ to $2.7E_g$.

Solar cells produced from QDs can have much higher power conversion efficiencies than their bulk counterparts. A detailed balance calculation based on the SQ calculation

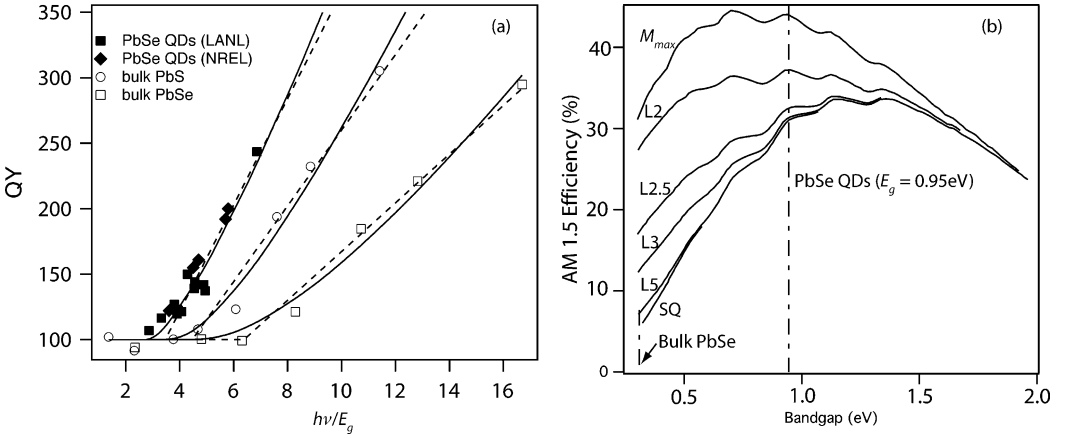


Figure 5.11 (a) The QYs for PbSe QDs measured under flowing conditions [55] and static conditions (Klimov group at LANL) compared to bulk PbS and bulk PbSe [26]. The solid lines are from (5.5)while the dashed lines use (5.3). (b) The detailed balanced efficiency calculations at AM 1.5 for conditions of no MEG (trace labeled SQ) theoretically highest efficiency MEG (M_{max}) and the various characteristics discussed in the text. Reproduced and adapted from ACS from [12].

but allowing for various MEG characteristics was performed and the results are shown in Figure 5.11(b). The conventional SQ result is labeled; curve M_{max} assumes the maximum multiplication. Curve L2, defined as the L2 characteristic, is when $h\upsilon_{th} = 2E_g$ and one extra exciton is created per additional increase in photon energy of E_g. Curve L2.5 is for a threshold of $2.5E_g$. The L3 characteristic is for a threshold of $3E_g$. Finally, the L5 characteristic is based on the measured EHPM for bulk PbSe and has a threshold of $4.5E_g$ with $\eta_{EHPM} = 0.19$. The maximum thermodynamic conversion efficiency for bulk PbSe (~5% – shown as the dotted line) is only marginally enhanced by the experimentally measured EHPM characteristics. In contrast, for PbSe QDs with $E_g = 0.95$ eV, the SQ efficiency is 31%, 37% for the L2 characteristic, and increases to 42% for the M_{max} characteristic. The calculated efficiencies demonstrate that the maximum possible efficiency assuming that the QDs achieved the measured EHPM characteristics (L3) is marginally enhanced compared to no MEG (32% vs. 31%, respectively). Therefore, $h\upsilon_{th}$ must be reduced to $2E_g$ (L2 characteristic) for the maximum efficiency to increase to 37%, and if the M_{max} could be reached the conversion efficiency would increase further to 42%. An M_{max} characteristic has been reported in individual SWCNTs [99]. The research challenge is to find materials and conditions that produce L2 and ultimately M_{max} characteristics.

5.4 QD solar cells

There are different approaches for incorporating QDs into solar cells so that they retain their useful quantum size effects. Several requirements must be satisfied: (1) the QDs

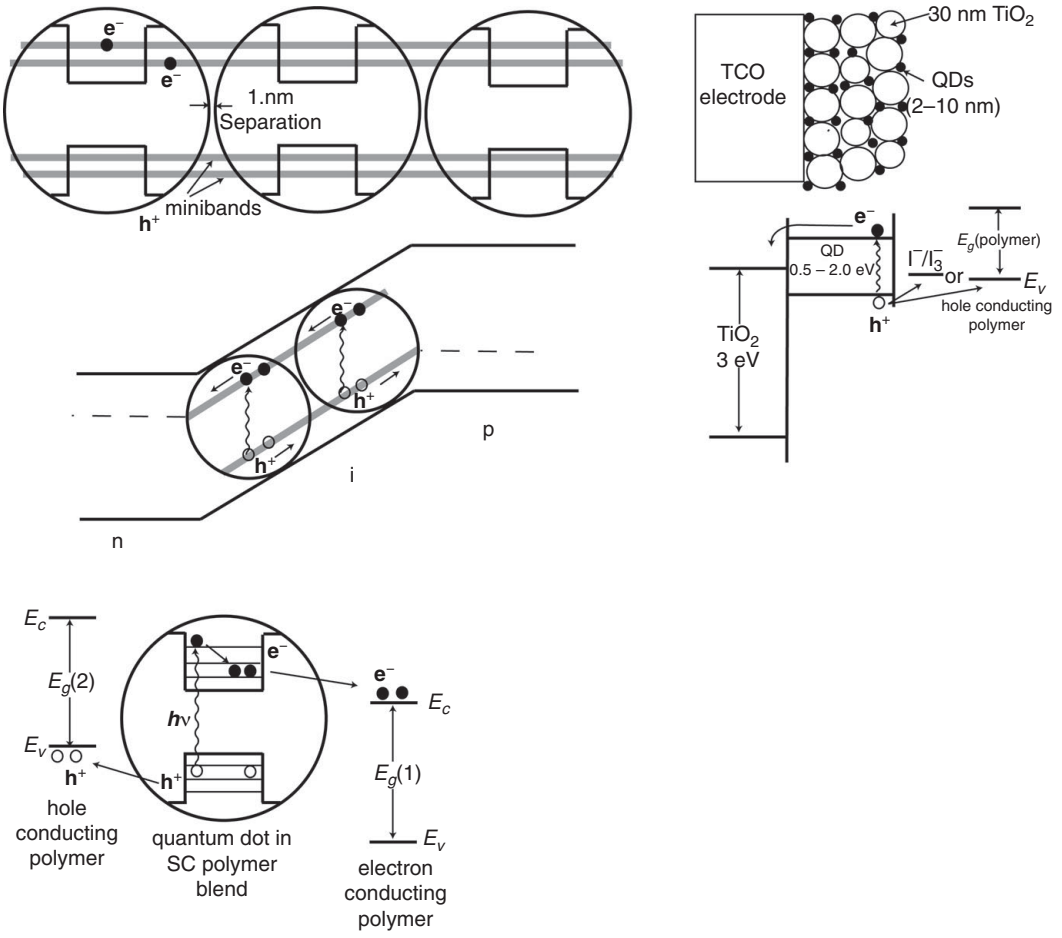


Figure 5.12 Three different generic QD solar cell configurations. Adapted and reproduced with permission from Elesevier [7].

must absorb at least the high energy photons; (2) the QDs must be coupled in some fashion to their environment so that excitons (electron–hole pairs) can be separated and then transported over macroscopic distances (an alternative approach involves transporting the excitons to a charge-separating interface); and (3) the coupling cannot eliminate quantum confinement. There are three basic approaches to incorporating QDs into PV devices and these are displayed schematically in Figure 5.12. If configured correctly, these approaches could meet the above requirements.

Arrays of quantum dots

In this configuration (Figure 5.12 top left), the QDs are formed into an ordered three-dimensional array with the inter-QD spacing sufficiently small that strong electronic coupling occurs to allow long-range electron transport. If the QDs have the same size and are positionally and orientationally aligned, then this system is a three-dimensional

analog of a one-dimensional superlattice and minibands form therein [100]. The moderately delocalized but still quantized three-dimensional states could be expected to produce MEG. Significant progress has been made in forming three-dimensional arrays of colloidal [101] QDs containing a reasonably uniform QD size distribution. Although the process can lead to close-packed QD films, they exhibit a significant degree of disorder. Major issues include the nature of the electronic states as a function of interdot distance, array order vs. disorder, QD orientation and shape, surface states, surface structure/passivation, and surface chemistry. We will discuss this case in more detail in the next section.

Quantum dot-sensitized nanocrystalline TiO_2 solar cells
This configuration (Figure 5.12 top right) is a variation of the dye sensitization of nanocrystalline TiO_2 cell [102–104]. Dye molecules are chemisorbed onto the surface of 10–30 nm TiO_2 particles that have been sintered into a highly porous nanocrystalline 10–20 μm TiO_2 film. Upon photoexcitation of the dye molecules, electrons are injected from the excited state of the dye into the conduction band of the TiO_2 producing a PV effect. For the QD-sensitized cell, QDs are substituted for the dye molecules [105, 106]. Successful PV effects in such cells have been reported for several semiconductor QDs including InP, InAs, CdSe, CdS, and PbS [105–108].

Quantum dots dispersed in organic semiconductor polymer matrices.
PV effects have been reported in structures consisting of QDs forming intimate junctions with organic semiconductor polymers. In one configuration, a disordered array of CdSe QDs is formed in a hole-conducting polymer – MEH-PPV [109]. Upon photoexcitation of the QDs, the photogenerated holes are injected into the MEH-PPV polymer phase, and are collected via an electrical contact to the polymer phase. The electrons remain in the CdSe QDs and are collected through diffusion and percolation in the nanocrystalline phase to an electrical contact to the QD network. Initial results show relatively low conversion efficiencies, but improvements have been reported with rod-like CdSe QD shapes [110] embedded in poly(3-hexylthiophene) (the rod-like shape enhances electron transport through the nanocrystalline QD phase) and with newer polymers that allow better electrical properties [111]. In another configuration [112], a polycrystalline TiO_2 layer is used as the electron conducting phase, and MEH-PPV is used to conduct the holes; the electron and holes are injected into their respective transport media upon photoexcitation of the QDs. A variation of these configurations is to disperse the QDs into a blend of electron- and hole-conducting polymers (Figure 5.12 bottom). This scheme is the inverse of the light emitting diode structures based on QDs [113–117].

5.4.1 MEG photocurrent and determination of the internal quantum efficiency (IQE) in QD solar cells

Establishing whether significant MEG photocurrent can be collected from a QD solar cell is very important, but is complicated by the poor external quantum efficiencies (EQEs) of existing QD devices [118–122]. Understanding the contribution from MEG can be

probed by determining the IQE of the layer with QDs. This has been accomplished in a very simple solar cell configuration that has the potential to harvest multiple excitons from individual QDs. An IQE substantially greater than 100% for high energy photons would indicate that MEG is occurring and a simple demonstration of this effect would further motivate the development of QD solar cells with subsequent improvements in EQE and power conversion efficiencies. The IQE of a solar cell is normally calculated from the ratio of its EQE and spectral absorptance as $IQE(\lambda) = EQE(\lambda)/[1 - \rho(\lambda) - \tau(\lambda)]$, where $\rho(\lambda)$ is the spectral reflectance and the device transmittance $\tau(\lambda)$ is usually zero. However, this approach can give an underestimated and misleading IQE spectrum if incident light is absorbed by the electrodes and other non-active layers of the device in addition to the active semiconductor layer(s). Further complicating the analysis, light absorption in a thin film solar cell can be affected by optical interference if the device is optically thin and has a highly reflective back electrode. Buildup of an optical mode structure will modify the apparent absorption spectrum of the active material relative to its absorption as a simple layer on a transparent substrate. Exponential, Beer's law type absorption/generation profiles cannot be assumed. Accurate values of the IQE of the device can be obtained only by determining the absorption spectrum as it exists within the device structure.

One of the more simple solar cell configurations is a Schottky-barrier solar cell where a Schottky junction forms at the junction of an active semiconductor layer and the metal electrode. An all-inorganic TCO/QD-layer/metal sandwich cell [43] has been shown to produce a reasonably large short-circuit photocurrent ($\sim$25 mA cm^{-2}). The PbSe QD-layer, deposited via layer-by-layer (LbL) dip coating, yields an EQE of 55–65% in the visible and up to 25% in the infrared region of the solar spectrum. Figure 5.13(a) is an illustration of the device structure and Figure 5.13(b) shows a cross-sectional scanning electron microscope (SEM) picture. The QD layer is deposited onto patterned indium tin oxide (ITO) coated glass using an LbL dip coating method and produces very smooth films that are essential for careful optical studies such as determining the IQE. Figure 5.13(c) is a representative current–voltage characteristic with the device parameters listed. Figure 5.13(f) displays an equilibrium band diagram showing the operation of the device.

Law *et al*. determined the IQE of a series of Schottky QD solar cells by combining EQE and total reflectance measurements with an optical model of the device stack [46]. The model is parameterized with the complex index of refraction of each layer in the stack as calculated from ellipsometry data. Figures 5.13(d) and (e) display the measured EQE and modeled absorbance of the QD layers. Good agreement between the experimental and modeled reflectance spectra permits a quantitative estimate of the fraction of incident light absorbed by the QD-layer at each wavelength. The IQE was obtained from the EQE and absorbance and is plotted in Figures 5.13(d) and (e). The QD solar cells achieve an IQE as high as 80 $\pm$ 7%. The mixed modeling/experimental approach is a rigorous and powerful way to determine if MEG photocurrent is collected by devices with EQE $<$ 100%. Based on the magnitudes and shapes of the IQE spectra, Law *et al*. concluded that the 1,2-ethanedithiol (EDT) treated QD solar cells do not produce appreciable MEG photocurrent in the wavelength range studied. The absence

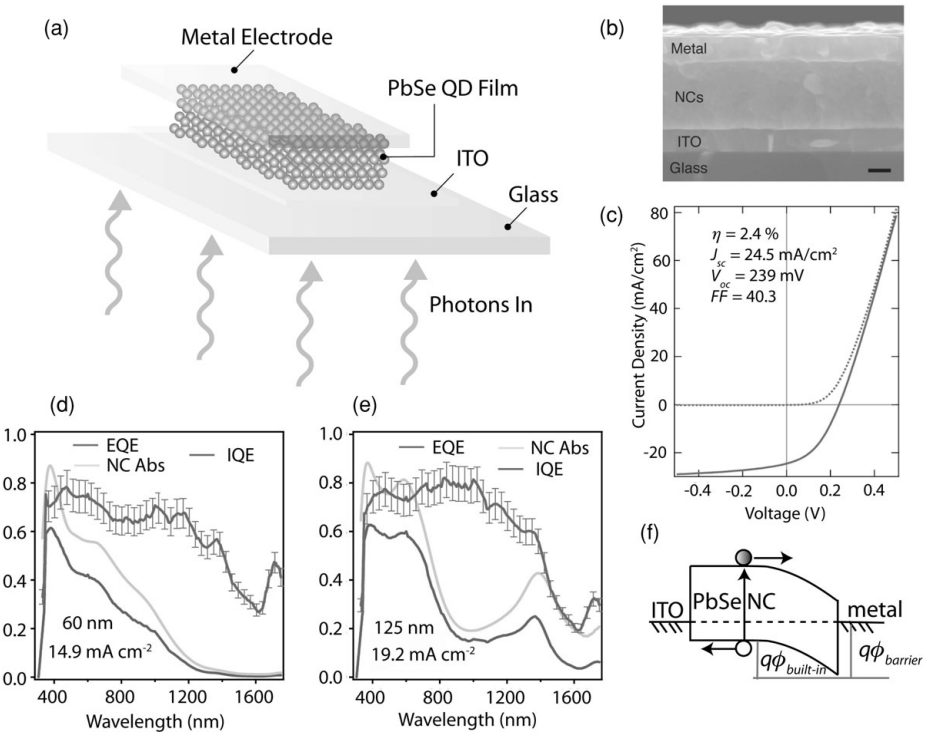


Figure 5.13 (a) Schematic representation of a simple Schottky-barrier QD solar cells: light enters through the glass/ITO layer where a thin layer (60–300 nm thickness) of QDs is deposited via an LbL approach. (b) A cross sectional scanning transmission electron microscopy (STEM) image of typical device; (c) the *I–V* characteristics, (d), (e) EQE, reflectance, and IQE spectra; (f) the proposed equilibrium band diagram. Adapted and reproduced with permission from ACS from [43] and [46].

of MEG in the IQE could result from several factors, such as: (1) the QD–QD coupling necessary to produce good charge-carrier mobility decreases the MEG effect; (2) the chemical treatments used to produce the QD solar cells could open up other carrier relaxation pathways that compete with MEG; and (3) MEG does occur in the QDs, but the multiple excitons decay via the very efficient Auger recombination prior to charge separation and are thus not collected.

In the simplest QD/TiO_2 cell configuration Sambur *et al*. observed an enhanced photocurrent that suggests that multiple excitons per absorbed photon can be collected in this configuration [123]. They attached a single layer of PbS QDs to an atomically flat TiO_2 (anatase) crystal. A short-chain 3-mercaptoproprionic acid linker molecule was used with one end (presumably the thiol) attached to the QD surface and the other (carboxylic acid) to the TiO_2. The device produced very small photocurrents because only a single layer of QDs was used (the OD was < 0.01). The IQE was determined by measuring the photocurrent with a series of LEDs and a lock-in amplifier followed by a careful determination of the OD of the device. Unfortunately, the OD was determined

on a rutile crystal, while the EQE was measured on the anatase crystal. They argue that the electronic coupling between the QD and metal oxide must be strong enough to induce very fast electron transfer from the conduction band of the QD to that of the TiO_2 (estimated here as ~ 50 fs). But it must be faster than the Auger recombination pathway (~ 50 ps). The IQE exceeds 100% in the blue region of the spectra suggesting that (1) MEG occurs very efficiently in the PbS QDs even with thiolate ligands and (2) the multiple excitons can be separated and collected in this system. If this result is confirmed and can be extended to the QD-sensitized solar cell configuration discussed above then it should be possible to construct a solar cell that exceeds the SQ limit.

5.5 QD arrays

As previously discussed, films composed of electronically coupled QDs can form the light-absorbing component of a QD PV device [40–45, 47]. The QDs must be electronically coupled in such a fashion that charge separation occurs on a timescale longer than MEG (~10^{-13} s) but shorter than the biexciton lifetime (~10^{-10} s). This requirement is necessary so that the system has enough time for MEG to redistribute the energy into multiple electron–hole pairs but excitons are spatially separated prior to Auger recombination. The separated charges must then drift and/or diffuse through the array to the electrodes prior to recombining. Significant challenges exist for producing highly ordered QD arrays that can exhibit large QD electronic coupling and the critical parameters to consider are: spacing between QDs; QD surface passivation; the electrical and optical properties of the composite matrix containing the QDs; QD orientation; size distribution; variations in surface states and defect sites; lability of surface atoms and ligand molecules; and the crystallinity of individual QDs. Ordered arrays may not be necessary, one theoretical study showed that the formation of delocalized states can occur for small inter-dot distances in *either* a perfect superlattice or in disordered arrays and that resonant coupling is not as important in the QD arrays. The randomly arranged QDs show both localized and delocalized states [124], where transitions between the two extremes are possible.

When the QD are capped with insulating organic ligands (to aid in solubility and surface passivation) a large potential barrier exists between the QDs and the electron–hole pairs remain confined to the QDs. A composite matrix of this type is termed a Mott insulator where the long range transport properties are hindered by spacing between the QDs. Exchanging the capping ligands that are used in the QD synthesis with shorter molecules can dramatically increase the carrier mobility in the QD films [125–129] by reducing the average inter-QD spacing [130] while retaining relatively highly-passivated surfaces. The ligands can be exchanged in solution, but often the ligands needed for conductive films are too short to retain the solubility of QDs and post-film-deposition ligand exchange is becoming popular [131, 132]. The strength of the electronic coupling increases with decreasing QD diameter and decreasing inter-dot distance. One study found that the mobility in PbS and PbSe films is determined by the capping ligand molecule length [133]; the mobility decreases exponentially

with increasing QD-separation. While high carrier mobilities are necessary for efficient extraction of carriers from a QD film, it is critical to determine if MEG is preserved in such QD films and to understand how the reduced quantum confinement modulates MEG. If multiexciton formation, dissociation, and charge collection are simultaneously efficient, the resulting enhanced photocurrent can increase solar energy conversion efficiencies.

5.5.1 MEG in PbSe QD arrays

The majority of PbSe and PbS QD based solar cells utilize a post-film-deposition procedure of treating the QD film with a dilute solution of 1,2-ethanedithiol (EDT) or similar thiols. The short thiol ligands replace the longer insulating carboxylic acid ligands bringing the QDs closer to allow efficient communication. The thiol soak tends to produce lightly conductive p-type QD films with modest carrier mobilities. As discussed above, the IQE of PV devices constructed using EDT is relatively high but no evidence has been found in the unbiased IQE spectra to suggest that multiple charge carriers are collected per absorbed photon. Other chemical soaks have also been explored and exhibit different optoelectronic effects depending on the precise nature of the chemical species used, but only the thiol treatments have shown reliable PV devices. To investigate the effects of chemical treatment on single and bi-exciton lifetimes and MEG, five chemical treatments that can produce conductive QD films have been studied. These treatments were: hydrazine (hy) in acetonitrile (CH_3CN); EDT in CH_3CN; hy in ethanol (EtOH); methylamine (me) in EtOH; and pure EtOH.

Enhanced QYs from MEG in arrays were studied using femtosecond transient absorption in the same fashion as for isolated QDs in colloidal solutions discussed above. The decay dynamics of single- and bi-excitons in the QD films were first determined by photoexciting the film below the threshold energy for MEG. Following characterization of the exciton dynamics, the films were photoexcited at higher photon energies to characterize their MEG behavior. Figure 5.14 shows the results of the single- and bi-exciton characterization for five different chemical treatments and characterization of an untreated QD film. The hy in EtOH film showed a dramatically reduced lifetime of the single exciton and was not further studied for its MEG properties. The study found that three important changes occur for the treated films: (1) the single-exciton lifetime decreases, reflecting an increased rate of surface recombination; (2) the bi-exciton lifetime increases for decreasing QD–QD distance; and (3) the absorption cross section per QD increases for films with longer bi-exciton lifetimes.

A wide variation in the enhanced QYs was observed for the different chemical treatments and the results are displayed in Figure 5.15(a). In agreement with the IQE measurements on Schottky cells above where the films are treated with EDT, MEG is nearly quenched for both QD sizes studied at $4E_g$ and $5E_g$. While for me and hy in CH_3CN the QY was found to be 1.5 at $4E_g$ and only increased to $\sim$1.6 at $5E_g$. It was found that the loss of oleate in itself was insufficient to determine the electrical behavior of the films, the carrier dynamics, or MEG. Therefore, other factors such as inter-QD separation or the chemical reactivity of the treatments are more important. The identity

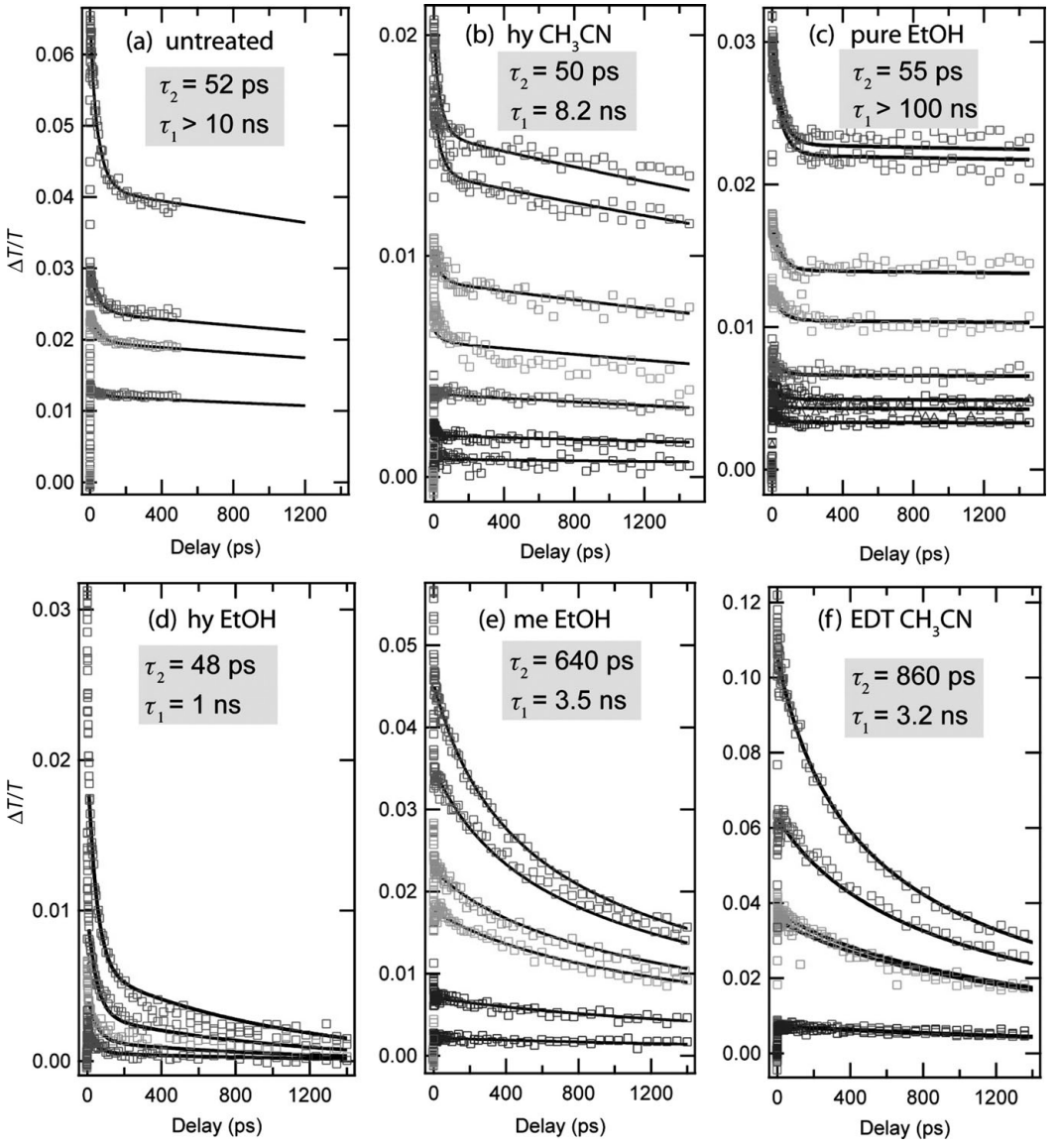


Figure 5.14 Single- and bi-exciton characterization of a series of PbSe QD solids all prepared from a solution of 3.7 nm PbSe QDs. The solids were exposed to various chemical treatments to modulate the electronic coupling in the QDs. Adapted and reproduced with permission from ACS from [54].

of the QD surface species after chemical treatment is difficult to ascertain and quantify, however, the precise nature of the resulting surface species may dictate many of the electrical properties and the carrier dynamics. A small defect concentration, corresponding to only one defect site in 10–100 nanocyrstals, could produce large changes in the measured conductivities. Three ways in which the various chemical treatments

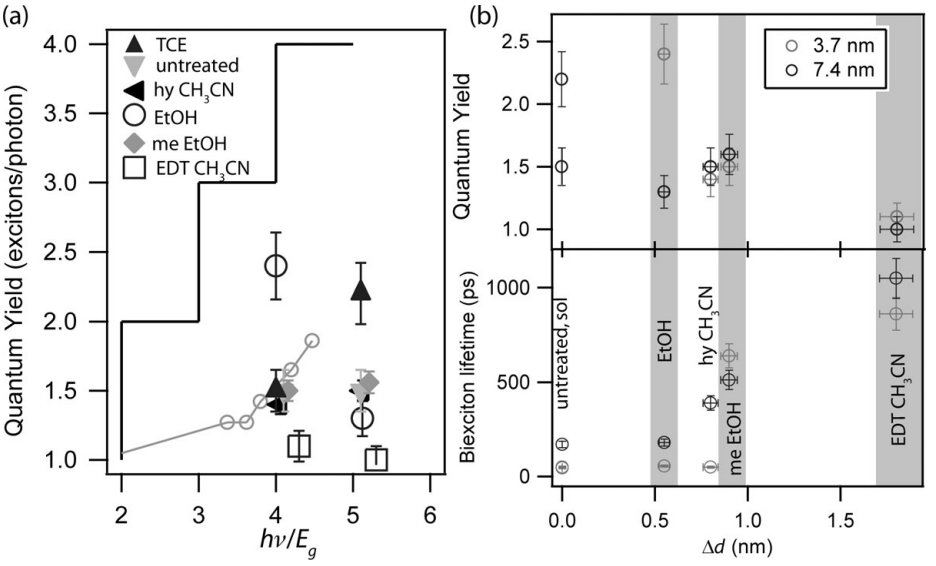


Figure 5.15 (a) The variations in the enhanced QYs that were observed for the various chemical treatments studied. The QY varied between 1 (no MEG) and ~2.4 at $4h\nu/E_g$ and from 1 to ~2.1 at ~ $5h\nu/E_g$. (b) The variations in QY with the increase in biexciton lifetime (τ_2) with the decrease in average QD–QD distance (here Δd is the change in average QD–QD distance). Adapted and reproduced with permission from ACS from [54].

can affect MEG were considered: (1) changes in the surface chemistry which affect QD–ligand interactions, and subsequently exciton relaxation rates, (2) doping of the QDs causing enhanced Auger recombination, and (3) an increase in inter-QD coupling producing diminished quantum confinement, and/or charge-transfer states with higher carrier mobilities and lower inter-QD charge-transfer barriers. The degree to which each of the above contributes to modulating MEG has not been determined and more work is needed to sort out how best to build a QD based PV device that preserves MEG.

The MEG efficiency was found to correlate with the change in inter-QD distance, with smaller QD separation coinciding with lower MEG yields. Figure 5.15(b) plots the QY versus the change in inter-QD distance. This correlation could arise due to an increase in inter-QD electronic coupling. As neighboring QDs couple more strongly to one another, quantum confinement could be reduced sufficiently to greatly decrease the Coulomb coupling necessary to drive the MEG process. Another possibility is that charge-transfer states, where the electron resides on one QD and the hole on an adjacent QD, could become lower in energy than highly excited single-exciton states isolated on single QDs. In a model that treats MEG, excitation at higher photon energies would result in a mixture of charge-transfer states, single-exciton states and multiexciton states and the interplay between these states could decrease MEG by rapid population of charge-transfer states. The final state of the system and hence any enhanced QYs would then be determined by the relative dephasing and carrier cooling rates within the different channels that include

the charge-transfer states. More work is needed to fully understand how surface states, QD–QD coupling, and other environmental factors can influence MEG.

An increase in bi-exciton lifetime, τ_2, was also found to correlate with the change in inter-QD distance indicating a reduced Auger recombination rate. This behavior was attributed to a delocalization of the excitons as inter-QD electronic coupling increased. The increased τ_2 is greatest for the EDT CH_3CN treated film, where τ_2 increases by an order of magnitude relative to untreated films. The degree of electronic coupling was found to be strongest in the EDT CH_3CN films, followed by me EtOH, hy CH_3CN, and finally the EtOH films and roughly correlates with the decreased MEG efficiency. The results for the EtOH treated films, while showing roughly the correlation with inter-QD distance, also demonstrate anomalous behavior. The MEG efficiency is greatly increased in the smaller QD films, while it decreases in the larger QD films.

Surprisingly QYs found for the untreated, hy CH_3CN, and me in EtOH treated films compare well with the results found for stirred or flowed PbSe QD solutions. For the film measurements, the samples are completely static and therefore any photocharging discussed above would seem to be more severe. However, only in the pure EtOH treated film was an apparent increase in the MEG yield observed, while all other films studied showed a decrease in MEG relative to that measured in static solutions. The photocharging discussed above results in an apparent increase of the QY and therefore it was concluded that photocharging in films must be of a different nature than that observed in the isolated QDs. In the heavily n-doped films of hy in EtOH it was estimated that dopant concentrations approaching 1 dopant per QD led to a drastic reduction in TA lifetime that could be assigned to a non-radiative recombination pathways, similar to the trion pathway discussed above. Photocharging in films may not occur as efficiently as in solutions for the following reasons: (1) the high mobility of carriers may allow faster regeneration of the photocharged state; and (2) differences in surface states induced by the different surface ligands as well as increased QD–QD coupling may reduce the density of acceptor sites. Future work will need to understand potential charging effects in QD films. Understanding exciton dynamics and MEG efficiency in electronically coupled QD films is essential for learning how to harness MEG to convert light into electricity with high efficiency.

5.6 Conclusions

MEG in QDs is potentially a very important process that if harnessed could lead to a new solar conversion efficiency limit. The parallel process of II in bulk semiconductors has been studied for many years as a means of bypassing the SQ limit. However, II is too inefficient to be of use for solar energy conversion but it does play a major role in enhancing the sensitivity of photodetectors. MEG in QDs is more efficient that II in bulk semiconductors; for the case of PbSe, MEG in PbSe QDs is $\sim 2\times$ more efficient than II in bulk PbSe. The onset photon energy is $\sim 2.8E_g$ in the QDs while it is $\sim 6E_g$ in bulk PbSe. To make the largest impact on solar energy technologies the MEG efficiency needs to be improved so that the onset for MEG occurs as close to $2E_g$ as possible. The

fact that MEG is enhanced in PbSe QDs is encouraging and a better understanding of the factors that influence MEG will lead to improvements in the MEG efficiency.

References

1 W. Shockley, H. J. Queisser, Detailed balance limit of efficiency of P–N junction solar cells. *Journal of Applied Physics*, **32** (1961), 510.
2 M. A. Green, K. Emery, Y. Hishikawa, W. Warta, Solar cell efficiency tables (version 36). *Progress in Photovoltaics*, **18** (2010), 346–352.
3 R. T. Ross, A. J. Nozik, Efficiency of hot-carrier solar-energy converters. *Journal of Applied Physics*, **53** (1982), 3813–3818.
4 M. A. Green, *Third Generation Photovoltaics*. Sydney: Bridge Printery, 2001.
5 J. M. Olsen, D. J. Friedman, S. Kurtz, High efficiency III–V multijunction solar cells. In: A. Luque, S. Hegedus, editors. *Handbook of Photovoltaic Science and Engineering*, p. 359. Hoboken: John Wiley & Sons LTd, 2003.
6 D. S. Boudreaux, F. Williams, A. J. Nozik, Hot carrier injection at semiconductor–electrolyte junctions. *Journal of Applied Physics*, **51** (1980), 2158–2163.
7 A. J. Nozik, Quantum Dot Solar Cells. *Physica E*, **14** (2002), 115–120-PII S1386–9477(02)00374–0.
8 S. Kolodinski, J. H. Werner, T. Wittchen, H. J. Queisser, Quantum efficiencies exceeding unity due to impact ionization in silicon solar-cells. *Applied Physics Letters*, **63** (1993), 2405–2407.
9 P. T. Landsberg, H. Nussbaumer, G. Willeke, Band–band impact ionization and solar-cell efficiency *Journal of Applied Physics*, **74** (1993), 1451–1452.
10 A. Luque, A. Marti, Increasing the efficiency of ideal solar cells by photon induced transitions at intermediate levels. *Physical Review Letters*, **78** (1997), 5014–5017.
11 R. D. Schaller, V. I. Klimov, High efficiency carrier multiplication in PbSe nanocrystals: implications for solar energy conversion. *Physical Review Letters*, **92** (2004), ARTN 186601.
12 M. C. Beard, A. G. Midgett, M. C. Hanna, *et al*., Comparing multiple exciton generation in quantum dots to impact ionization in bulk semiconductors: implications for enhancement of solar energy conversion. *Nano Letters*, **10** (2010), 3019–3027.
13 S. Koc, The quantum efficiency of the photo-electric effect in germanium for the 0.3–2 micron wavelength region. *Czech Journal of Physics*, **7** (1957), 91–95.
14 V. S. Vavilov, On photo-ionization by fast electrons in germanium and silicon. *Journal of the Physics and Chemistry of Solids*, **8** (1959), 223.
15 J. Tauc, Electron impact ionization in semiconductors. *Journal of the Physics and Chemistry of Solids*, **8** (1959), 219.
16 V. N. Ivakhno, Quantum yield of internal photoeffect and impact ionization in Pbs. *Fizika Tverdogo Tela*, **14** (1972), 578-&.
17 V. N. Ivakhno, Quantum efficiency of internal photoelectric effect and impact ionization in silicon. *Soviet Physics Semiconducturs*, **6** (1973), 1391–1392.
18 O. Christensen, Quantum efficiency of internal photoelectric effect in silicon and germanium. *Journal of Applied Physics*, **47** (1976), 689–695.
19 A. R. Beattie, Impact ionization and quatum efficiency in InSb. *Physics Status Solidi B*, **111** (1982), 141–153.

20 A. R. Beattie, Optically created hole multiplication in InSb. *Journal of Physics C Solid State Physics*, **16** (1983), L791–L795.

21 N. S. Baryshev, C. Shchetinmp, A. Kharionoys, Quantum efficiency and impact ionization in lead and lead–tin chalcogenides. *Soviet Physics–Semiconducturs*, **8** (1974), 192–194.

22 A. J. Nozik, Spectroscopy and hot electron relaxation dynamics in semiconductor quantum wells and quantum dots. *Annual Review of Physical Chemistry*, **52** (2001), 193–231.

23 A. Efros, *Auger Processes in Nanosize Semiconductor Crystals*. New York: Kluwer Academic/Plenum Publishers, 2003.

24 A. Shabaev, A. L. Efros, A. J. Nozik, Multiexciton generation by a single photon in nanocrystals. *Nano Letters*, **6** (2006), 2856–2863.

25 M. C. Beard, R. J. Ellingson, Multiple exciton generation in semiconductor nanocrystals: toward efficient solar energy conversion. *Laser Photonics Review*, **2** (2008), 377–399.

26 J. J. H. Pijpers, R. Ulbricht, K. J. Tielrooij *et al*., Assessment of carrier-multiplication efficiency in bulk PbSe and PbS. *Nature Physics*, **5** (2009), 811–814.

27 R. J. Ellingson, M. C. Beard, J. C. Johnson *et al*., Highly efficient multiple exciton generation in colloidal PbSe and PbS quantum dots. *Nano Letters*, **5** (2005), 865–871.

28 J. E. Murphy, M. C. Beard, A. G. Norman *et al*., PbTe colloidal nanocrystals: synthesis, characterization, and multiple exciton generation. *Journal of the American Chemical Society*, **128** (2006), 3241–3247.

29 M. T. Trinh, A. J. Houtepen, J. M. Schins, *et al*., In spite of recent doubts carrier multiplication does occur in PbSe nanocrystals. *Nano Letters*, **8** (2008), 1713–1718.

30 M. B. Ji, S. Park, S. T. Connor, *et al*., Efficient multiple exciton generation observed in colloidal PbSe quantum dots with temporally and spectrally resolved intraband excitation. *Nano Letters*, **9** (2009), 1217–1222.

31 R. D. Schaller, M. Sykora, S. Jeong, V. I. Klimov, High-efficiency carrier multiplication and ultrafast charge separation in semiconductor nanocrystals studied via time-resolved photoluminescence. *Journal of Physical Chemistry B*, **110** (2006), 25332–25338.

32 R. D. Schaller, M. A. Petruska, V. I. Klimov, Effect of electronic structure on carrier multiplication efficiency: comparative study of PbSe and CdSe nanocrystals. *Applied Physics Letters*, **87** (2005), ARTN 253102.

33 J. J. H. Pijpers, E. Hendry, M. T. W. Milder *et al*., Carrier multiplication and its reduction by photodoping in colloidal InAs quantum dots. *Journal of Physical Chemistry C*, **111** (2007), 4146–4152.

34 R. D. Schaller, J. M. Pietryga, V. I. Klimov, Carrier multiplication in InAs nanocrystal quantum dots with an onset defined by the energy conservation limit. *Nano Letters*, **7** (2007), 3469–3476.

35 M. C. Beard, K. P. Knutsen, P. R. Yu, *et al*., Multiple exciton generation in colloidal silicon nanocrystals. *Nano Letters*, **7** (2007), 2506–2512.

36 S. K. Stubbs, S. J. O. Hardman, D. M. Graham, *et al*., Efficient carrier multiplication in InP nanoparticles. *Physical Revies B*, **81** (2010), ARTN 081303.

37 Y. Kobayashi, T. Udagawa, N. Tamai, Carrier multiplication in CdTe quantum dots by single-photon timing spectroscopy. *Chemistry Letters*, **38** (2009), 830–831.

38 S. J. Wang, M. Khafizov, X. M. Tu, M. Zheng, T. D. Krauss, Multiple exciton generation in single-walled carbon nanotubes. *Nano Letters*, **10** (2010), 2381–2386.

39 D. Gachet, A. Avidan, I. Pinkas, D. Oron, An upper bound to carrier multiplication efficiency in type II colloidal quantum dots. *Nano Letters*, **10** (2010), 164–170.

40 E. H. Sargent, Infrared photovoltaics made by solution processing. *Nature Photonics*, **3** (2009), 325–331.
41 J. Tang, L. Brzozowski, D. A. R. Barkhouse, *et al*., Quantum dot photovoltaics in the extreme quantum confinement regime: the surface-chemical origins of exceptional air- and light-stability. *ACS Nano*, **4** (2010), 869–878.
42 J. M. Luther, J. B. Gao, M. T. Lloyd, *et al*., Stability assessment on a 3% bilayer PbS/ZnO quantum dot heterojunction solar cell. *Advanced Materials*, **22** (2010), 3704-+.
43 J. M. Luther, M. Law, M. C. Beard, *et al*., Schottky solar cells based on colloidal nanocrystal films. *Nano Letters*, **8** (2008), 3488–3492.
44 J. J. Choi, Y. F. Lim, M. B. Santiago-Berrios, *et al*., PbSe nanocrystal excitonic solar cells. *Nano Letters*, **9** (2009), 3749–3755.
45 K. S. Leschkies, T. J. Beatty, M. S. Kang, D. J. Norris, E. S. Aydil, Solar cells based on junctions between colloidal PbSe nanocrystals and thin ZnO films. *ACS Nano*, **3** (2009), 3638–3648.
46 M. Law, M. C. Beard, S. Choi, *et al*., Determining the internal quantum efficiency of PbSe nanocrystal solar cells with the aid of an optical model. *Nano Letters*, **8** (2008), 3904–3910.
47 A. G. Pattantyus-Abraham, I. J. Kramer, A. R. Barkhouse, *et al*., Depleted-heterojunction colloidal quantum dot solar cells. *ACS Nano*, **4** (2010), 3374–3380.
48 G. Nair, S. M. Geyer, L. Y. Chang, M. G. Bawendi, Carrier multiplication yields in PbS and PbSe nanocrystals measured by transient photoluminescence. *Physical Review B*, **78** (2008), ARTN 125325.
49 G. Nair, M. G. Bawendi, Carrier multiplication yields of CdSe and CdTe nanocrystals by transient photoluminescence spectroscopy. *Physical Review B*, **76** (2007), ARTN 081304.
50 M. Ben-Lulu, D. Mocatta, M. Bonn, U. Banin, S. Ruhman. On the absence of detectable carrier multiplication in a transient absorption study of InAs/CdSe/ZnSe core/shell1/shell2 quantum dots. Farkas Ctr Light Induced Proc, Inst Chem, IL-91904 Jerusalem, Israel sandy@fh.huji.ac.il: 2008:1207.
51 J. J. H. Pijpers, E. Hendry, M. T. W. Milder, *et al*., Carrier multiplication and its reduction by photodoping in colloidal InAs quantum dots. *Journal of Physical Chemistry C*, **111** (2007), 4146.
52 J. A. McGuire, J. Joo, J. M. Pietryga, R. D. Schaller, V. I. Klimov. New aspects of carrier multiplication in semiconductor nanocrystals. *Accounts of Chemical Research*, **41** (2008), 1810–1819.
53 J. A. McGuire, M. Sykora, J. Joo, J. M. Pietryga, V. I. Klimov, Apparent versus true carrier multiplication yields in semiconductor nanocrystals. *Nano Letters*, **10** (2010), 2049–2057.
54 M. C. Beard, A. G. Midgett, M. Law, *et al*., Variations in the quantum efficiency of multiple exciton generation for a series of chemically treated PbSe nanocrystal films. *Nano Letters*, **9** (2009), 836–845.
55 A. G. Midgett, H. W. Hillhouse, B. K. Huges, A. J. Nozik, M. C. Beard, Flowing versus static conditions for measuring multiple exciton generation in PbSe quantum dots. *Journal of Physical Chemistry C*, **114** (2010), 17486–17500.
56 O. E. Semonin, J. C. Johnson, J. M. Luther, *et al*., Absolute photoluminescence quantum yields of Ir-26 dye, PbS, and PbSe quantum dots. *Journal of Physical Chemistry Letters*, **1** (2010), 2445–2450.

57 P. Guyot-Sionnest, B. Wehrenberg, D. Yu, Intraband relaxation in CdSe nanocrystals and the strong influence of the surface ligands. *Journal of Chemical Physics*, **123** (2005), ARTN 074709.
58 A. Pandey, P. Guyot-Sionnest, Slow electron cooling in colloidal quantum dots. *Science*, **322** (2008), 929–932.
59 W. S. Pelouch, R. J. Ellingson, P. E. Powers, *et al*., Investigation of hot-carrier relaxation in quantum-well and bulk GaAs at high carrier densities. *Semicondor Science and Technology*, **7** (1992), B337-B339.
60 J. Ulstrup, J. Jortner, Effect of intramolecular quantum modes on free-energy relationships for electron-transfer reactions. *Journal of Chemical Physics*, **63** (1975), 4358–4368.
61 Y. Rosenwaks, M. C. Hanna, D. H. Levi, *et al*., Hot-carrier cooling in GaAs – quantum-wells versus bulk. *Physical Review B*, **48** (1993), 14675–14678.
62 W. S. Pelouch, R. J. Ellingson, P. E. Powers, *et al*., Comparison of hot-carrier relaxation in quantum-wells and bulk GaAs at high carrier densities. *Physical Review B*, **45** (1992), 1450–1453.
63 F. Williams, A. J. Nozik, Irreversibilities in mechanism of photoelectrolysis. *Nature*, **271** (1978), 137–139.
64 F. Williams, A. J. Nozik, Solid-state perspectives of the photoelectrochemistry of semiconductor electrolyte junctions. *Nature*, **312** (1984), 21–27.
65 H. Benisty, C. M. Soto-Mayor Torres, C. Weisbuch, Intrinsic mechanism for the poor luminescence properties of quantum-box systems. *Physical Review B*, **44** (1991), 10945–10948.
66 U. Bockelmann, G. Bastard, Phonon-scattering and energy relaxation in two-dimensional, one-dimensional, and zero-dimensional electron gases. *Physical Review B*, **42** (1990), 8947–8951.
67 J. L. Blackburn, R. J. Ellingson, O. I. Micic, A. J. Nozik, Electron relaxation in colloidal InP quantum dots with photogenerated excitons or chemically injected electrons. *Journal of Physical Chemistry B*, **107** (2003), 102–109.
68 R. J. Ellingson, J. L. Blackburn, P. R. Yu, *et al*., Excitation energy dependent efficiency of charge carrier relaxation and photoluminescence in colloidal InP quantum dots. *Journal of Physical Chemistry B*, **106** (2002), 7758–7765.
69 V. I. Klimov, Optical nonlinearities and ultrafast carrier dynamics in semiconductor nanocrystals. *Journal of Physical Chemistry B*, **104** (2000), 6112–6123.
70 U. Bockelmann, T. Egeler, Electron relaxation in quantum dots by means of Auger processes. *Physical Review B*, **46** (1992), 15574–15577.
71 H. Benisty, Reduced electron–phonon relaxation rates in quantum-box systems – theoretical analysis. *Physical Review B*, **51** (1995), 13281–13293.
72 A. L. Efros, V. A. Kharchenko, M. Rosen, Breaking the phonon bottleneck in nanometer quantum dots – role of Auger-like processes. *Solid State Communications*, **93** (1995), 281–284.
73 I. Vurgaftman, J. Singh, Effect of spectral broadening and electron-hole scattering on carrier relaxation in GaAs quantum dots. *Applied Physics Letters*, **64** (1994), 232–234.
74 P. C. Sercel, Multiphonon-assisted tunneling through deep levels – a rapid energy-relaxation mechanism nonideal quantum-dot heterostructures. *Physical Review B*, **51** (1995), 14532–14541.
75 T. Inoshita, H. Sakaki, Electron relaxation in a quantum dot – significance of multiphonon processes. *Physical Review B*, **46** (1992), 7260–7263.

76 T. Inoshita, H. Sakaki, Density of states and phonon-induced relaxation of electrons in semiconductor quantum dots. *Physical Review B*, **56** (1997), R4355–R4358.
77 V. I. Klimov, Spectral and dynamical properties of multilexcitons in semiconductor nanocrystals. *Annual Review of Physical Chemistry*, **58** (2007), 635–673.
78 V. I. Klimov, A. A. Mikhailovsky, D. W. McBranch, C. A. Leatherdale, M. G. Bawendi, Quantization of multiparticle Auger rates in semiconductor quantum dots. *Science*, **287** (2000), 1011–1013.
79 P. R. Yu, M. C. Beard, R. J. Ellingson, *et al*., Absorption cross-section and related optical properties of colloidal InAs quantum dots. *Journal of Physical Chemistry B*, **109** (2005), 7084–7087.
80 W. W. Yu, L. H. Qu, W. Z. Guo, X. G. Peng, Experimental determination of the extinction coefficient of CdTe, CdSe, and CdS nanocrystals. *Chemistry of Materials*, **15** (2003), 2854–2860.
81 C. A. Leatherdale, W. K. Woo, F. V. Mikulec, M. G. Bawendi, On the absorption cross section of CdSe nanocrystal quantum dots. *Journal of Physical Chemistry B*, **106** (2002), 7619–7622.
82 I. Moreels, K. Lambert, D. De Muynck, *et al*., Composition and size-dependent extinction coefficient of colloidal PbSe quantum dots. *Chemistry of Materials*, **19** (2007), 6101–6106.
83 I. Moreels, K. Lambert, D. Smeets, *et al*., Size-dependent optical properties of colloidal PbS quantum dots. *ACS Nano*, **3** (2009), 3023–3030.
84 I. Robel, R. Gresback, U. Kortshagen, R. D. Schaller, V. I. Klimov, Universal size-dependent trend in Auger recombination in direct-gap and indirect-gap semiconductor nanocrystals. *Physical Review Letters*, **102** (2009), 177404.
85 M. Nirmal, B. O. Dabbousi, M. G. Bawendi, *et al*., Fluorescence intermittency in single cadmium selenide nanocrystals. *Nature*, **383** (1996), 802–804.
86 D. E. Gomez, M. Califano, P. Mulvaney, Optical properties of single semiconductor nanocrystals. *Physical Chemistry Chemical Physics*, **8** (2006), 4989–5011.
87 F. Cichos, C. van Borczyskowski, M. Orrit, Power-law intermittency of single emitters. *Current Opinion in Colloid and Interface Science*, **12** (2007), 272–284.
88 A. L. Efros, M. Rosen, Random telegraph signal in the photoluminescence intensity of a single quantum dot. *Physical Review Letters*, **78** (1997), 1110–1113.
89 R. Verberk, A. M. van Orijen, M. Orrit, Simple model for the power-law blinking of single semiconductor nanocrystals. *Physical Revies B*, **66** (2002), ARTN 233202.
90 B. Mahler, P. Spinicelli, S. Buil, *et al*., Towards non-blinking colloidal quantum dots. *Nature Materials*, **7** (2008), 659–664.
91 S. Hohng, T. Ha, Near-complete suppression of quantum dot blinking in ambient conditions. *Journal of the American Chemical Society*, **126** (2004), 1324–1325.
92 X. Y. Wang, X. F. Ren, K. Kahen, *et al*., Non-blinking semiconductor nanocrystals. *Nature*, **459** (2009), 686–689.
93 K. T. Shimizu, R. G. Neuhauser, C. A. Leatherdale, *et al*., Blinking statistics in single semiconductor nanocrystal quantum dots. *Physical Review B*, **63** (2001), ARTN 205316.
94 R. C. Alig, S. Bloom, C. W. Sruck, Electron–hole-pair creation energies in semiconductors. *Bulletin of the American Physical Society*, **25** (1980), 175–175.
95 R. C. Alig, S. Bloom, Electron–hole-pair creation energies in semiconductors. *Physical Review Letters*, **35** (1975), 1522–1525.
96 B. Ziaja, R. A. London, J. Hajdu, Ionization by impact electrons in solids: Electron mean free path fitted over a wide energy range. *Journal of Applied Physics*, **99** (2006), ARTN 033514.

97 H. K. Jung, K. Taniguchi, C. Hamaguchi, Impact ionization model for full band Monte Carlo simulation in GaAs. *Journal of Applied Physics*, **79** (1996), 2473–2480.

98 B. K. Ridley, *Quantum Processes in Semiconductors*. New York, NY: Oxford University Press, 1988.

99 N. M. Gabor, Z. H. Zhong, K. Bosnick, J. Park, P. L. McEuen, Extremely efficient multiple electron–hole pair generation in carbon nanotube photodiodes. *Science*, **325** (2009), 1367–1371.

100 R. D. J. Miller, G. McLendon, A. J. Nozik, W. Schmickler, F. Willig. *Surface Electron Transfer Processes*. New York, NY: VCH Publishers, 1995.

101 C. B. Murray, C. R. Kagan, M. G. Bawendi, Synthesis and characterization of monodisperse nanocrystals and close-packed nanocrystal assemblies. *Annual Review Materials Science*, **30** (2000), 545–610.

102 A. Hagfeldt, M. Gratzel, Molecular photovoltaics. *Accounts of Chemical Research*, **33** (2000), 269–277.

103 J. E. Moser, P. Bonnote, M. Gratzel, Molecular photovoltaics. *Coordination Chemistry Reviews*, **171** (1998), 245–250.

104 M. Gratzel, Perspectives for dye-sensitized nanocrystalline solar cells. *Progress in Photovoltaics*, **8** (2000), 171–185.

105 R. Vogel, P. Hoyer, H. Weller, Quantum-sized PbS, CdS, Ag_2S, Sb_2S_3, and Bi_2S_3 particles as sensitizers for various nanopourous wide-bandgap semiconductors. *Journal of Physical Chemistry*, **98** (1994), 3183–3188.

106 D. Liu, P. V. Kamat, Photoelectrochemical behavior of thin CdSe and coupled TiO_2 CdSe semiconductor films, *Journal of Physical Chemistry*, **97** (1993), 10769–10773.

107 A. Zaban, O. I. Micic, B. A. Gregg, A. J. Nozik, Photosensitization of nanoporous TiO_2 electrodes with InP quantum dots. *Langmuir*, **14** (1998), 3153–3156.

108 P. R. Yu, K. Zhu, A. G. Norman, *et al*., Nanocrystalline TiO_2 solar cells sensitized with InAs quantum dots. *Journal of Physical Chemistry B*, **110** (2006), 25451–25454.

109 N. C. Greenham, X. G. Peng, A. P. Alivisatos, Charge separation and transport in conjugated-polymer/semiconductor–nanocrystal composites studied by photoluminescence quenching and photoconductivity. *Physical Review B*, **54** (1996), 17628–17637.

110 W. U. Huynh, X. G. Peng, A. P. Alivisatos, CdSe nanocrystal rods/poly(3-hexylthiophene) composite photovoltaic devices. *Advanced Materials*, **11** (1999), 923.

111 S. Dayal, N. Kopidakis, D. C. Olson, D. S. Ginley, G. Rumbles, Photovoltaic devices with a low band gap polymer and CdSe nanostructures exceeding 3% efficiency. *Nano Letters*, **10** (2010), 239–242.

112 A. C. Arango, S. A. Carter, P. J. Brock, Charge transfer in photovoltaics consisting of interpenetrating networks of conjugated polymer and TiO_2 nanoparticles. *Applied Physics Letters*, **74** (1999), 1698–1700.

113 B. O. Dabbousi, M. G. Bawendi, O. Onitsuka, M. F. Rubner, Electroluminescence from CdSe quantum-dot polymer composites. *Applied Physics Letters*, **66** (1995), 1316–1318.

114 V. L. Colvin, M. C. Schlamp, A. P. Alivisatos, Light-emitting-diodes made from cadmium selenide nanocrystals and a semiconductor polymer. *Nature*, **370** (1994), 354–357.

115 M. C. Schlamp, X. G. Peng, A. P. Alivisatos, Improved efficiencies in light emitting diodes made with CdSe(CdS) core/shell type nanocrystals and a semiconducting polymer. *Journal of Applied Physics*, **82** (1997), 5837–5842.

116 H. Mattoussi, L. H. Radzilowski, B. O. Dabbousi, *et al*., Composite thin films of CdSe nanocrystals and a surface passivating/electron transporting block copolymer: Correlations

between film microstructure by transmission electron microscopy and electroluminescence. *Journal of Applied Physics*, **86** (1999), 4390–4399.

117 H. Mattoussi, L. H. Radzilowski, B. O. Dabbousi, *et al*., Electroluminescence from heterostructures of poly(phenylene vinylene) and inorganic CdSe nanocrystals. *Journal of Applied Physics*, **83** (1998), 7965–7974.

118 X. M. Jiang, R. D. Schaller, S. B. Lee, *et al*., PbSe nanocrystal/conducting polymer solar cells with an infrared response to 2 micron. *J. Mater. Res.*, **22** (2007), 2204–2210.

119 D. H. Cui, J. Xu, T. Zhu, *et al*., Harvest of near infrared light in PbSe nanocrystal-polymer hybrid photovoltaic cells. *Applied Physics Letters*, **88** (2006), ARTN 183111.

120 K. P. Fritz, S. Guenes, J. Luther, *et al*., IV–VI nanocrystal-polymer solar cells. *Journal of Photochemistry and Photobiology A*, **195** (2008), 39–46.

121 S. A. McDonald, G. Konstantatos, S. G. Zhang, *et al*., Solution-processed PbS quantum dot infrared photodetectors and photovoltaics. *Nature Materials*, **4** (2005), 138-U14.

122 A. A. R. Watt, D. Blake, J. H. Warner, *et al*., Lead sulfide nanocrystal: conducting polymer solar cells. *Journal of Physics D: Applied Physics*, **38** (2005), 2006–2012.

123 J. B. Sambur, T. Novet, B. A. Parkinson, Multiple exciton collection in a sensitized photovoltaic system. *Science*, **330** (2010), 63–66.

124 B. B. Smith, A. J. Nozik, Theoretical studies of electronic state localization and wormholes in silicon quantum dot arrays. *Nano Letters*, **1** (2001), 36–41.

125 J. E. Murphy, M. C. Beard, A. J. Nozik, Time-resolved photoconductivity of PbSe nanocrystal arrays. *Journal of Physical Chemistry B*, **110** (2006), 25455–25461.

126 B. L. Wehrenberg, D. Yu, J. S. Ma, P. Guyot-Sionnest, Conduction in charged PbSe nanocrystal films. *Journal of Physical Chemistry B*, **109** (2005), 20192–20199.

127 R. M. Kraus, P. G. Lagoudakis, J. Muller, *et al*., Interplay between Auger and ionization processes in nanocrystal quantum dots. *Journal of Physical Chemistry B*, **109** (2005), 18214–18217.

128 B. L. Wehrenberg, P. Guyot-Sionnest, *Electron and Hole Injection In PbSe Quantum Dot Films*. Chicago, IL: University of Chicago, James Franck Inst, 2003, 7806.

129 D. Yu, C. J. Wang, P. Guyot-Sionnest, N-type conducting CdSe nanocrystal solids. *Science*, **300** (2003), 1277–1280.

130 J. J. Urban, D. V. Talapin, E. V. Shevchenko, C. B. Murray, Self-assembly of PbTe quantum dots into nanocrystal superlattices and glassy films. *Journal of the American Chemical Society*, **128** (2006), 3248–3255.

131 J. M. Luther, M. Law, Q. Song, *et al*., Structural, optical and electrical properties of self-assembled films of PbSe nanocrystals treated with 1,2-ethanedithiol. *ACS Nano*, **2** (2008), 271–280.

132 H. W. Hillhouse, M. C. Beard, Solar cells from colloidal nanocrystals: fundamentals, materials, devices, and economics. *Current Opinion in Colloid and Interface Science*, **14** (2009), 245–259.

133 Y. Liu, M. Gibbs, J. Puthussery, *et al*., Dependence of carrier mobility on nanocrystal size and ligand length in PbSe nanocrystal solids. *Nano Letters*, **10** (2010), 1960–1969.

6 Colloidal quantum dot light emitting devices

Vanessa Wood, Matthew Panzer, Seth-Coe Sullivan, and Vladimir Bulovic

6.1 Introduction

Colloidal quantum dot light emitting devices (QD-LEDs) have generated considerable interest for applications such as thin film displays with improved color saturation and white lighting with high color rendering index. In this chapter, we review the key advantages of using quantum dots (QDs) in display and lighting applications, including their color purity, solution processability, and stability. Section 6.2 provides an introduction to some of the photonic and electronic properties of QDs and QD thin films that must be considered when integrating QDs into LEDs. Section 6.3 reviews the standard methods for testing QD-LEDs. Sections 6.4–6.6 provide an overview of the primary QD-LED architectures to date and describe the three mechanisms for exciting QDs – optical excitation, Förster energy transfer, and direct charge injection – that have been leveraged to create QD-LEDs. We conclude by discussing some current directions in QD research that focus on achieving higher efficiency, cadmium free, and air stable QD-LEDs using electrical excitation of the luminescent QDs.

6.2 Why QDs for LEDs?

6.2.1 Saturated colors

Because the electronic structure of colloidal QDs is dominated by quantum size effects, colloidal QDs have narrow band emission that can be spectrally positioned by controlling the nanocrystal size during synthesis [1]. For example, CdSe QDs of different sizes provide emission from the blue through the red, while QDs made of a smaller band gap material such as PbS or CdTe offer spectral tunability in the near-infrared spectral region [1, 2]. Typical size distributions of colloidally synthesized QDs are $< 5\%$, leading to emission spectra of QD solutions with inhomogeneous line widths of 100 meV to 150 meV (or a full-width at half-maximum (FWHM) of 30–40 nm in the red wavelength regime).

To illustrate the benefit of this narrow spectrum of QD emitters, Figure 6.1 shows a Commission International de l'Eclairage (CIE) chromaticity diagram, which maps color

Colloidal Quantum Dot Optoelectronics and Photovoltaics, eds. G. Konstantatos and E. H. Sargent.
Published by Cambridge University Press. © Cambridge University Press, 2013.

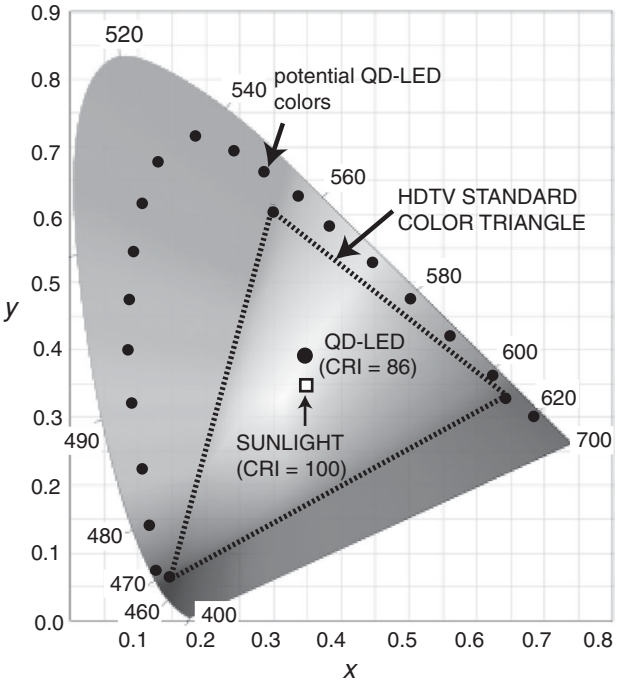


Figure 6.1 CIE chromaticity diagram showing the spectral purity of QDs enables a color gamut larger than the HDTV standard.

in terms of hue and saturation [3]. The boundary of the CIE diagram is defined by the different saturated hues that can be perceived by the human eye ranging in wavelength from $\lambda = 380$ nm to $\lambda = 780$ nm. The purer the color, the closer to the boundary of the CIE diagram it is mapped. The procedure for calculating the chromaticity coordinates, which define the location of an emitter on the CIE diagram, is discussed in Section 6.3. The color gamut enabled by a display with red, green, and blue pixels is the triangle defined by the coordinates of the individual pixels. The triangle that can be defined for a display using red, green, and blue emitting QDs (black circles) is larger than that of the International Telecommunication Union HDTV standard (dashed black line), highlighting the benefit of QD emitters.

Furthermore, QDs can be used to tune the quality of white lighting, which can be evaluated by color temperature and color rendering index (CRI) [3]. The color temperature of a light source is the temperature of an ideal black-body radiator that radiates light of the same hue (i.e., coordinate location on the CIE diagram). For solid state lighting applications, warmer white with a color temperature of 2700–4000 K is often preferred over bluish white (>5500 K). The CRI defines how well a particular artificial light source illuminates an object compared with illumination by natural light, with a CRI of 100 indicating that the artificial light source reproduces the lighting conditions achieved by a black-body light source (such as the sun) with the designated temperature. Most solid state lighting sources consist of a blue inorganic LED backlight coated

with a yellow phosphor (e.g., cerium-doped yttrium aluminum garnet (Ce^{3+}:YAG)). As discussed in Section 6.4, QD Vision Inc. has shown that by adding QD lumophores to the phosphor, it is possible to achieve white lighting with a color temperature of 2700 K and a CRI greater than 90 while maintaining over 90% of the efficiency in lumens per watt of the blue LED backlight. The ability to achieve high quality white lighting with QDs points to their potential use for large area lighting or as the backlight in liquid crystal display technology. An overview of QDs in white lighting applications can be found in Dai *et al*. [4].

6.2.2 Solution processable

QDs retain a passivating layer of surfactants ("ligands") after synthesis, which prevents their aggregation and makes them solution processable. Typically, the ligands have a polar group that coordinates with the surface of QDs and a hydrocarbon chain that provides the long-term stability of QDs in solution. After synthesis, the typical hydrophobic ligands such as oleic acid, trioctylphosphine, or trioctylphosphine, can be exchanged [5] or additional ligands can be added [6] to make the QDs compatible with aqueous solutions. The choice of ligand plays an important role in the conductivity of the QD solid. Metal chalcogenide complexes have been demonstrated to be suitable ligands for improving interparticle interaction in QD solids [7].

The wide range of possible QD surfaces facilitates a variety of low cost, large area deposition techniques, which have all been successfully applied to QD-LEDs. These include phase separation [8], layer-by-layer [9], inkjet printing [10], mist deposition [11], and microcontact printing [12, 13, 14]. Ligands can be selected to enable serial solution deposition of QD films of different colors by means of orthogonal solvents [15] or to permit post-deposition cross-linking for the creation of QD films that can withstand subsequent solvent-based deposition steps [16].

6.2.3 Stability

Because they are composed of inorganic semiconductors, QDs can be engineered to be more resistant to degradation than other excitonic materials for display and lighting applications such as the luminescent organic molecules used in organic LEDs. While CdSe core QDs exhibit photooxidation due to the formation of $CdSeO_x$ [17], overcoating of the QD core with a ZnS shell is shown to improve the photostability of the nanocrystal by offering a barrier to oxygen diffusion [18]. Common shell materials for CdSe cores are ZnS and CdS [19–22]. In general, a core–shell structure offers physical separation of the exciton from defect states on the surface of the QD that could contribute to non-radiative recombination. This is highlighted by thick-shell QDs [23, 24], which are reported to sustain a high degree of thermal stress and maintain their luminescence even when the passivating ligands are removed. Furthermore, these thick-shell QDs suppress blinking, which has been linked to suppressed Auger recombination [25] and which is considered to be a source of luminescence quenching. One concern for integration of

QDs into solid state devices has been the presence of organic ligands; however, work replacing organic aliphatic ligands on QDs with metal chalcogenide ligands has enabled QD films that are entirely inorganic and exhibit record electronic transport properties [7]. Other approaches for embedding the QDs in a stable inorganic matrix include atomic layer deposition [26, 27] and chemical bath deposition [28]. The ability to embed QDs within a robust, inorganic matrix with tunable electronic properties will likely be of great benefit for QD-LEDs.

6.3 QD and device physics influencing LED performance

The reported efficiencies of QD-LEDs remain relatively low; however, a complete physical understanding of QD-LEDs has yet to be achieved, indicating that substantial improvement in efficiency can be made by progressively optimizing QD selection and QD-LED architecture as insights into QD physics and QD-LED operation are made. This chapter highlights some effects occurring at the individual QD level and at the device level that are understood to have an impact on QD-LED performance. Some methods that can be used to arrive at a deeper understanding of these effects with the goal of facilitating next-generation QD-LED design are also presented.

6.3.1 Quantifying the luminescence efficiency

In LED applications, the luminescence efficiency of the QDs is clearly an important value as it places an upper limit on the external quantum efficiency of the LED. In this chapter, we use photoluminescence quantum yield (PLQY) in reference to solutions of QDs and photoluminescence (PL) efficiency in reference to QD thin films. Both values are defined as the ratio of the number of emitted photons to the number of absorbed photons. For reasons that are discussed in the following sections, it is critical to measure the PL efficiency of the QD thin film and the QD film within the device architecture in addition to the quantum yield (QY) of a QD solution.

While the QY of QD solutions can often be quickly determined by measuring relative to a reference solution of a dye that emits and absorbs at similar wavelengths, quantifying PL efficiency of QDs in a thin film and in a device can be difficult as the substrate can also absorb, scatter, or waveguide light at the wavelengths of interest. A preferred method for quantifying the luminescence efficiency uses an integrating sphere with ports for an excitation source (e.g., a laser diode) and a calibrated spectrometer. With the excitation kept constant, a sequence of measurements is performed: the wavelength-dependent photon count is determined (1) without a sample, (2) with a bare substrate, (3) with the substrate and QD film out of the beam, and (4) with the substrate and QD film inside the beam [29]. Collectively, these measurements provide readings of the total light power, the light scattering or absorption due to the substrate, the QD sample absorption, the QD sample self-absorption, and the QD sample emission. Systematic error is typically reduced using a large spot size with low incident power.

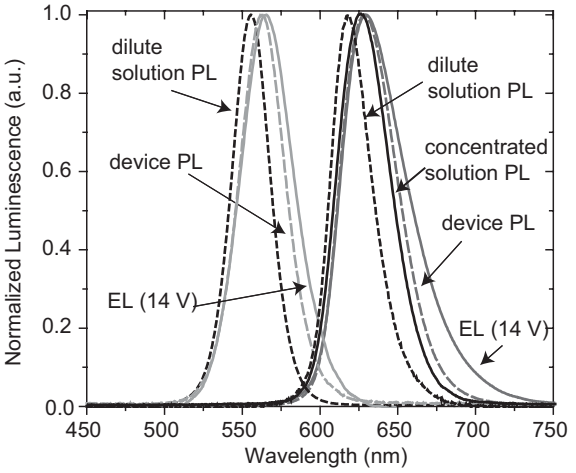


Figure 6.2 Spectra corresponding to PL of red and green QDs in a dilute solution (dashed black lines), PL of the QDs in the device structure (dashed gray lines), and electroluminescence (EL) from the QDs in an LED biased at 14 V (solid gray lines). The PL of a concentrated solution of red QDs is shown by a solid black line. Figure modified from [72].

6.3.2 QD surface states

A comparison of QD PLQY in solution and PL efficiency in thin film highlights the importance of developing a QD synthesis with an eye to the material that will be finally integrated into a device. While QDs suspended in solution routinely have PLQYs of greater than 50%, when the QDs are deposited in a close-packed thin film, their PL efficiency decreases by approximately an order of magnitude to 5% or 10%. One reason for this low efficiency is that dark or non-emitting surface states on QDs in a solid state film cannot be dynamically passivated by excess ligands as is possible in solution. Furthermore, when QDs are in a close-packed film, an exciton on one QD can Förster energy transfer to a dark (non-emitting) exciton state on any neighboring QD. Thus a single defect state can result in quenched luminescence of the five to ten surrounding QDs. This Förster energy transfer in the solid state can easily be seen by noting a red shift between the PL spectrum of a dilute solution and that of a close-packed thin film (Figure 6.2).

Embedding QDs in an insulating polymer matrix simulates the effect of a dilute solution and decreases the amount of QD luminescence quenching observed in closed-packed QD structures [30]. However, dc electrical conductivity through these QD-polymer composites is impeded by the low conductance of the wide-band-gap polymers, making them unsuitable for pn-junction-like QD-LED structures. In this case, the QD shell (which can spatially separate the excitons from the surface), or the selection of ligands that remain strongly bonded to the QD surface, plays an important role in preserving QD PL efficiency in the solid state. Alternatively, research has shown that field driven QD-LEDs enable electrical excitation of QD clusters embedded within insulating polymer composites [31].

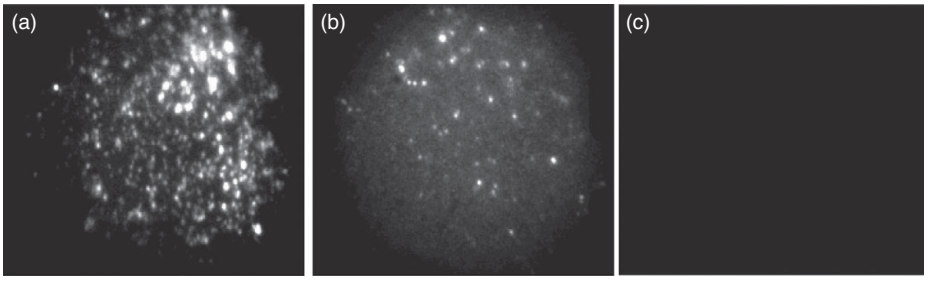


Figure 6.3 PL of QDs on (a) glass, (b) WO_3 with a resistivity of 10 Ω/cm, and (c) WO_3 with a resistivity of 0.2 Ω/cm. The concentration of QDs in the illuminated area is equivalent for each sample, and the excitation source is the same for each sample.

6.3.3 QD charging

Closely related to the issue of non-radiative recombination from surface states in QDs and variations in the fluorescence PL efficiency, is QD charging. In 1996 Nirmal *et al*. reported the observation of fluorescence intermittency (blinking) in single CdSe QDs [32]. To explain this phenomenon, it was proposed that the luminescence off-state of a QD corresponded to a charged QD core, which could result from a charge tunneling to or from the adjacent material. The extra carrier on the charged QD could then mediate an Auger non-radiative recombination event. An Auger process is a three-carrier effect, in which an electron–hole pair recombines non-radiatively, transferring the resultant energy to the third carrier (electron or hole), which then relaxes down to the band edge via phonon emission. Experimental work has deepened the understanding of the relation between QD charging and fluorescence intermittency by identifying two distinct sources of blinking [33]. In agreement with previous work, a charged QD core is observed to cause darkening of the QD. Additionally, it was found that blinking results from charge occupying unfilled surface states and then tunneling to the core. This work highlights the importance of selecting both QDs that suppress Auger non-radiative recombination and appropriate adjacent materials when designing QD-LEDs.

Auger processes are documented to be very efficient in colloidal QDs. While an exciton lifetime in a colloidal QD is 10 ns, multiexciton lifetimes are typically on the order of tens of picoseconds [34]. Theoretical work by Cragg and Efros [35] shows that softening the confinement potential in the QDs (e.g., through an alloyed core) reduces Auger non-radiative recombination and can be used to explain the results reporting suppression of blinking in ZnCdSe /ZnSe QDs even in the presence of charge [36]. Indeed, it is interesting to note that some of the early record reported efficiencies in QD-LEDs were achieved with alloyed QD materials such as ZnCdSe and ZnCdS [37–39].

The layers adjacent to the QD film also affect the QD luminescence. For example, if QDs are located next to a film with high carrier concentrations (e.g., a smooth gold film or conductive metal oxide) their luminescence will be quenched [39]. The photographs in Figure 6.3 demonstrate that progressively higher conductivity metal oxide films show increasing QD luminescence quenching. Luminescence quenching can be controlled to some extent by selecting the offset between the workfunction of the adjacent material

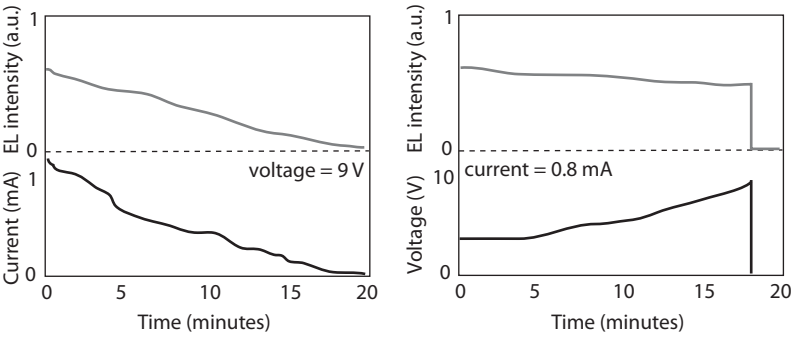


Figure 6.4 Schematic plots of the EL intensity of a QD-LED such as the one described in [72] as function of time at constant current or voltage.

and the QDs, e.g., by maximizing charge transfer away from the QDs [40]. However, in a QD-LED, we are most often not considering single, isolated QDs, but rather a thin film of QDs (or a QD solid). In a dc-driven QD-LED, for example, we must consider the additional complexities that arise from charge transport through the QD film, injection of charge into the QDs, and the presence of an electric field across the QD layer.

6.3.4 Charge transport in QD films

As a disordered solid, a film of QDs has relatively poor transport that is proposed to occur via hopping [41]. Certain QD solids, similar to those used in many QD-LEDs, have been shown to be effective Coulomb glasses [42]. If the active layer in an LED behaves as a Coulomb glass, the effect is dramatic. As charge is injected into the first layers of QDs, some charge becomes trapped in the QD film, creating a space charge layer that impedes additional injection of charge [43]. This is reflected in device operation as an increased difficulty in passing current through the device, which in turn results in a decrease in QD electroluminescence, as is shown schematically in Figure 6.4. In the case of constant current operation, higher and higher voltages are needed to maintain a constant current through the device. This eventually results in device breakdown. The time scales associated with QD charging range from minutes to days, making it challenging to obtain consistent luminescence from a QD film that experiences significant QD charging. While this effect is particularly pronounced in devices that use thick films of colloidal QDs (e.g., two or more layers), QD charging and the accompanying decrease in EL is observed in QD devices containing only a monolayer of QDs as well.

6.3.5 Field driven luminescence quenching

In addition to challenges in charge transport that can lead to reduction in QD luminescence due to charging, the effect of the applied electric field must also be taken into account. The QD layer in most QD-LEDs experiences an electric field greater than

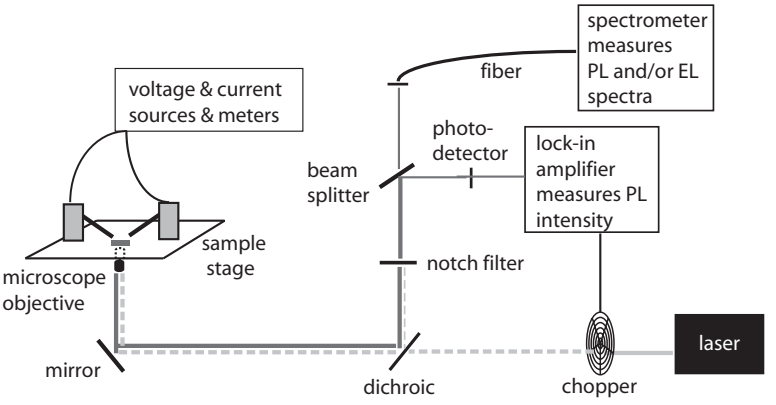


Figure 6.5 Experimental setup for measuring PL quenching and assessing key sources of inefficiencies in QD-LEDs.

1 MV/cm during device operation. It has recently been proposed that unlike organic small molecule thin films, exciton dissociation is not a primary mechanism for field-induced luminescence quenching [44]. Instead, the authors hypothesize that field-induced luminescence quenching results from a reduced optical transition matrix element, implying that QDs for LED applications should be specifically engineered to minimize the effect of an applied field on the optical matrix element [45]. Alternatively, field-induced luminescence quenching in QD-LEDs can be reduced by placing the QD active layer in a low field region of the device [46]. An example of such a QD-LED structure is discussed in Section 6.2.

6.3.6 Isolating the effects of charge and field

When seeking to understand the effects of charge and field-induced quenching, it is important to separate the effects of electric field and carriers. One can gain insight into the prevalence of field-driven and charge-carrier-driven non-radiative effects by recording the quenching of the PL response as a function of applied voltage and current. For example, in the experimental setup shown in Figure 6.5, a laser beam at a wavelength that excites the QDs is chopped or pulsed and focused onto the QD-LED, which can be electrically biased. The PL (and EL, if the QD-LED is biased above its turn on) response of the QDs is then split and collected by a photodetector and a spectrometer. If the photodetector is locked-in to the chopped or pulsed laser signal, it measures only the PL intensity. The spectrometer measures the combined PL and EL spectra, which, as discussed below, can be used to calculate the local fields within the QD film. Use of a streak camera instead of a spectrometer to record the time-resolved PL and EL can result in an even more detailed understanding of luminescence quenching.

To extract useful information from the PL quenching measurements and to accurately attribute the quenching to electric field or Auger effects, it is important to know the magnitude of the electric fields and carrier densities present in the QD film. Accurate

modeling of the potential profiles and current densities present in QD-LEDs is difficult, as many of the mechanisms at play are still not fully understood. One approach to understanding the electric field and charge carrier distributions in the device is to empirically extract information from the optical response of the QDs themselves. In response to an applied electric field, the bound state energies shift in what is known as the quantum confined Stark effect (QCSE). This shifting in energy levels causes a change in the effective band gap of the material, which can be observed optically as a change in the absorption spectrum or a shift in the position of the luminescence peak position as a function of applied field [47, 48]. If the interaction between the bound state energies and the electric field is assumed to be smaller than the energy difference between the excited states, the QCSE can be described with second-order perturbation theory. The shift in the effective band gap of a QD in the presence of an electric field, F, is given by

$$E_n^f - E_n = \left\langle \Psi_n \left| e\bar{r} \cdot \bar{F} \right| \Psi_n \right\rangle + \frac{\sum_{i \neq n} \left| \left\langle \Psi_n \left| e\bar{r} \cdot \bar{F} \right| \Psi_n \right\rangle \right|^2}{E_n - E_i} . \tag{6.1}$$

The first term on the right hand side is the dot product of the dipole moment of the QD and the electric field, which means that this term can range from negative to positive values depending on whether the dipole moment of the QD is anti-aligned or aligned with the electric field. The second term is related to the polarizability of the QD (the extent to which the electron cloud can move in response to an electric field). To see the dependence on field more clearly, (6.1) can be rewritten as

$$\Delta E = \mu F + \frac{1}{2}\alpha F^2, \tag{6.2}$$

where μ is the projection of the dipole moment in the direction of the electric field and α is the polarizability of QD in the direction of the electric field [48]. Empedocles and coworkers experimentally recorded the shift in the peak position of the luminescence spectrum of single QDs, and found a quadratic dependence of the shift with electric field and a superimposed linear dependence that can cause either a red shift in peak position (in the case where the QD dipole is aligned with electric field) or a blue shift in peak position (in the case where the QD dipole is anti-aligned with the electric field) [48]. In a QD ensemble, which is the case relevant to a thin film of QDs in a QD-LED, the dipoles of the different QDs will be randomly aligned [47, 48]. QDs with dipole contributions along the field and against the field will contribute to the broadening of the luminescence spectrum, but the shift in the spectral emission peak should be purely quadratic with field:

$$\Delta E = \frac{1}{2}aF^2. \tag{6.3}$$

Thus a purely optical measurement (recording of the shift in the QD emission) can provide an independent verification of the electrical field in the QD thin film in a specific LED architecture. In a QD-LED, a deviation from the quadratic dependence in the spectral peak as a function of applied field could suggest, for example, the presence of charge carriers that screen or augment the applied field.

6.4 Characterizing QD-LEDs

When characterizing QD-LEDs, there are three important data sets to report: the current–voltage characteristics, the external quantum efficiency (EQE), and the EL spectrum. We discuss the importance of each below. However, it is first important to note that QD-LEDs may have irregularities that can lead to non-uniform device operation on a micrometer or millimeter scale. Current–voltage, EQE, or EL measurements (and the human eye) will not necessarily be able to detect these irregularities. By taking a video of the devices through a microscope, for example, experimenters can assure themselves that pixels are turning on completely and uniformly. Non-uniform pixels can signal poor electrode quality or irregularities in the device thickness.

The current density vs. voltage (*J–V*) characteristics can easily be recorded with a LabView controlled current–voltage source-meter. As discussed in Section 6.2, electronic transport in QD solids is still a topic of ongoing research [41], and charge transport in QD-LEDs is even more complex due to the additional electron and hole transport layers. At this stage in QD-LED development, exploring the QDs separately from the transport layers in variety of device geometries (e.g., horizontal transistors or vertically stacked), the QD-LED structure without the QD layer, and the complete QD-LED under different biasing conditions can lead to important insights into the physics of the device operation and performance. It is also important to recognize that experimental procedure can have a significant effect on the observed *J–V* behavior. For example, because of QD charging dynamics, varying the speed of the voltage ramp by changing the wait time between voltage steps can have a dramatic impact on the type of current–voltage characteristics observed. Furthermore, "up" and "down" voltage sweeps may exhibit hysteretic behavior.

In some QD-LEDs, such as those with organic small molecule hole and electron transport layers, it is possible to gain some insight into the shape of the *J–V* curves using the theory for crystals with low mobility [49], which assumes a $J \sim V^n$ relation. A slope of 1 on a log–log *J–V* characteristic is characteristic of an ohmic conduction, while a slope of 2 signals space charge limited conduction, and steeper slopes indicate the presence of trap states. With this analysis, temperature dependent *J–V* measurements can provide a value for the energy of trap states, as demonstrated for organic LED (OLED) devices by Shen *et al.* [50].

EQE is defined as the ratio of the number of photons emitted per second to electrons injected into the device as a function of time. To calculate the EQE, the light intensity from the device is measured at the same time as the *J–V* curve. The emitted light can be collected by a Si photodetector (in the case of visible emission) or a Ge photodetector (in the case of infrared emission). The EQE is calculated using

$$\mathrm{EQE}(\%) = 100 \cdot g \cdot \frac{(I_p - I_d)}{R} \frac{\lambda}{hc} \cdot \frac{q}{i}, \tag{6.4}$$

where I_p is the photocurrent detected using a calibrated photodetector from the device EL, I_d is the dark current registered by the photodetector when the device is not operating, R is the wavelength dependent responsivity of the photodetector, i is the current through

the device, q is the electron charge, h is Planck's constant, and c is the speed of light. g is a configuration factor that accounts for the geometry of the light collection setup. It can be approximated as:

$$g = \left| \frac{a^2}{R^2 + a^2} \right|, \tag{6.5}$$

where R is the perpendicular distance between the photodetector and the LED, and a is the radius of the photodetector.

The luminescence spectra are key to understanding and characterizing QD-LED device operation. A comparison of different spectra (the PL of a diluted solution of the QDs used in the device, the PL of the QD solution used in the device, the PL of the QD layer within the QD-LED, and the EL of the device at different voltages) can be quite helpful in evaluating device fabrication and operation. Changes in the spectra between the PL of the QD solution and the QD thin film within the device can signal damage to the QD layer during device fabrication or a microcavity effect caused by the different indices of refraction in the thin film stack. For example, a blue shift of the luminescence peak of CdSe QDs can signal oxidation of Cd that may occur during device fabrication or operation. In Figure 6.2, comparing the PL of a diluted solution of the QDs with the PL of a concentrated QD solution and the PL of the QD layer within the QD-LED shows evidence of Förster energy transfer in close-packed conditions but no degradation of the QD film after deposition within the device. The further red shift in the EL is due to the Stark effect described in Section 6.2.6.

Extensive discussion of metrics for characterizing LEDs for display or white lighting application is provided in the comprehensive book *Light-Emitting Diodes* [3]; however, here we outline some of the more important metrics for QD-LEDs. Luminance can be determined from the EL spectrum. First, the luminous flux, Φ, is calculated using

$$\Phi = 683 \frac{lm}{W} \int_{\lambda} V(\lambda) P(\lambda) d\lambda. \tag{6.6}$$

where $V(\lambda)$ refers to the CIE sensitivity curve for the human eye and $P(\lambda)$ is the spectral power density of the QD-LED. Luminance (Cd/m^2) is then calculated by dividing the luminous flux by the active device area and the solid angle of emission. For simplicity, it is often assumed that thin film devices are Lambertian emitters, where the intensity of the emission as a function of angle varies as $I = I_0 \cos(\theta)$, such that the solid angle is π steradians.

To quantify the color purity of a QD-LED or the quality of white lighting, it is useful to calculate the CIE chromaticity coordinates (x and y) so that the emission color can be mapped on the chromaticity diagram as shown in Figure 6.1. The overlap of CIE color matching functions ($x(\lambda)$, $y(\lambda)$, and $z(\lambda)$) and the luminescence spectrum (EL(λ)) is used to find the tristimulus values X, Y, and Z:

$$X = \int \mathrm{EL}(\lambda)\bar{x}(\lambda)d\lambda, \qquad Y = \int \mathrm{EL}(\lambda)\bar{y}(\lambda)d\lambda, \qquad Z = \int \mathrm{EL}(\lambda)\bar{z}(\lambda)d\lambda. \tag{6.7}$$

The chromaticity coordinates (x, y) are then given by:

$$x = \frac{X}{X+Y+Z}, \quad y = \frac{Y}{X+Y+Z}. \tag{6.8}$$

A parameter related to the chromaticity coordinates that enables quick assessment of the quality of white light is the color temperature. Color temperature refers to the temperature (in kelvins) of a black body radiator that has the same chromaticity location as the white light source under consideration. The emission spectrum of a black body at a specific temperature as a function of wavelength that can be used to calculate the chromaticity coordinates is given by Planck's law:

$$I(\lambda) = \frac{2hc^2}{\lambda^5[\exp(hc/\lambda kT) - 1]} \tag{6.9}$$

QD-based solid state lighting is often designed to reproduce the color temperature of incandescent lighting (2000–3000 K) or sunlight (5000–6000 K).

The CRI indicates on a scale of 0 to 100 the ability of a lighting source to render colors of an object as compared to a Planckian black body source simulating daylight. To calculate the CRI, the white light is shone on a set of 15 colors and the reflected light is collected. The chromaticity coordinates of each sample of reflected light are calculated. Then, the Euclidan distances (ΔE_i) between these measured chromaticity coordinates and the chromaticity coordinates that would be obtained if the light source were an ideal Planckian black body are determined. The CRI is then calculated from these distances, using

$$\text{CRI} = (1/8)\sum_{\text{i}}^{8}(100 - 4.6(\Delta E_i)). \tag{6.10}$$

The CRI does not, however, provide information about the color of the light itself, so it is important for both chromaticity coordinates and the CRI to be reported.

A significant challenge in white lighting is achieving stable chromaticity coordinates and CRI as a function of operating voltage and current density. In standard crystalline semiconductors, changes in color often result from shifts in the energy band levels as a function of temperature. These spectral shifts are handled by developing better heat dissipation systems for the LEDs, and the problem is somewhat mitigated by the fact that the optical downconversion of phosphors plays a large role in the quality of the white lighting. In contrast to band transport semiconductors, the emission profiles of colloidal QDs are relatively stable with temperature, with the peak in emission red shifting approximately 1 ångstrom per degree C [51]. However, achieving stable spectral characteristics as a function of operating conditions in the case of electrically excited QDs is difficult. For example, in the case of a white QD-LED made from a monolayer of mixed blue, green, and red QDs, Anikeeva and coworkers demonstrated the complexity of achieving stable spectral characteristics, showing that the excitation efficiencies for the three types of QDs and the amounts of Förster energy transfer vary as a function of voltage [52]. Fortunately, much of the extensive research on achieving stable color in

white-emitting OLEDs can be applied directly to achieving color-stable QD-LEDs and should greatly shorten the development time for white-emitting QD-LEDs.

6.5 QD-LEDs based on optical downconversion

A unique combination of optical properties, namely, broadband absorption below the optical band gap combined with a small Stokes shift and highly narrowband emission, make colloidal QDs ideal candidates for the optical downconversion of high energy light. The basic concept of an optical downconversion QD-LED is simple: QDs with narrowband green, yellow, orange, or red emission spectra are placed between the viewer and a blue or ultraviolet photon source (such as a GaN LED); QDs absorb some fraction of the blue light and emit highly saturated, lower energy photons. QDs are generally strong absorbers, displaying absorption coefficients greater than 10^5 cm^{-1} (per QD) for wavelengths below 400 nm [53]. Using a single type of QD, saturated monochromatic devices can be fabricated, while a multicolor blend of QDs with different sizes and/or chemistries can produce white lighting.

Optical excitation circumvents many of the challenges associated with electrical QD excitation for light emission, including carrier injection, QD charging, and luminescence quenching. In order to realize an efficient optical downconversion QD-LED, however, high QD PLQY in the solid state is required. To date, this has been accomplished using composite films containing QDs in a transparent supporting matrix. The role of the transparent matrix is two-fold: to stabilize and encapsulate the QDs for prolonged operation in ambient conditions, and to isolate individual QDs from one another in order to preserve the high QY values observed for QDs in solution.

One of the first laboratory demonstrations of QD optical downconversion utilized a blue GaN LED to excite QDs embedded in a polylaurylmethacrylate matrix; saturated monochromatic as well as multicolor (including white) light emission was demonstrated [54–58]. Several groups have reported advances in the downconversion of blue light from GaN or InGaN LED point sources by QD/polymer composite films, with an emphasis on producing efficient white light sources. In 2010, Jang *et al.* demonstrated a white QD downconversion backlight array for a 46″ liquid crystal display (LCD) television panel that operated with an efficiency of 41 lm/W [57]. An inexpensive approach toward fabricating full color, flexible displays using inkjet-printed QD/polyisobutylene composite films and an AC power-driven blue electroluminescent paste was reported by Wood *et al.* [10]. Panzer *et al.* showed that the same simple device structure could be extended to create near-infrared displays using PbS/CdS core/shell QDs that strongly absorb blue photons and produce narrowband near-infrared emission peaks located between 1100–1550 nm [59].

The first commercial QD lighting products have been optical downconversion devices. In 2008, Evident Technologies, Inc. developed holiday lighting (Dotstrand™) that used blue LEDs to optically excite a QD-containing coating layer, producing a variety of unique colors (such as purple and aqua) as well as both warm and cool white lights. QD Vision, in partnership with Nexxus Lighting, introduced a warm white light

platform (Nexxus Lighting's Array Quantum LED R30 lamp) in 2010 as an energy-efficient replacement for incandescent light bulbs. A QD-containing composite (Quantum Light^{TM} Optic) is placed in front of a cool white LED to add a narrowband orange-red component to the lamp output, producing a CRI 91 and 475 lm (equivalent to a 40 W incandescent lamp) with a power consumption of only 7.8 W. In addition to solid state lighting, the next commercial application of QD-LED downconversion products will likely be white backlighting for LCD displays. The use of saturated red and green QD emitters with a blue LED should allow a trichromatic white light source that covers ~100% of the 1953 NTSC color gamut, compared with conventional white LED-based backlight units (~70% of the 1953 NTSC color gamut).

6.6 QD-LEDs based on organic charge transport layers

While optical downconversion QD-LEDs have the clear benefit of separating the emissive and electronic components, such that only the optical properties of the QDs must be considered and optimized, electrically driven QDs open a wider range of possible applications. Since the first reports of electrically driven QD-LEDs in the mid-1990s, significant progress has been made toward efficient electrical excitation of QDs. The first electrically driven QD-LEDs incorporated CdSe QDs and polymers between a transparent indium tin oxide (ITO) anode and a metal cathode. A layered CdSe QD and p-paraphenylene vinylene (PPV) architecture was used in the work of Colvin *et al*. [60], and QDs were dispersed in polyvinylcarbazole and an oxadiazole derivative in the work of Dabbousi *et al*. [61]. Both these initial efforts yielded QD-LEDs with low turn-on voltages and substantial EL from the polymers as well as the QDs. In this section, we describe the processing and fabrication advances that have enabled more efficient LEDs and a deeper understanding into the mechanisms behind the operation of QD-LEDs using organic transport materials.

6.6.1 Deposition of QDs: spin casting, phase separation, and microcontact printing

Since colloidal QDs are already in solution, a natural choice for QD deposition is drop- or spin-casting. Because of their outstanding monodispersity (typically < 5%), QDs that are deposited on a substrate directly from solution can form close-packed lattices over a large area [62]. However, the challenge facing solution-based deposition techniques becomes clear upon looking at the architecture followed by the majority of QD-LEDs (shown schematically in Figure 6.6). Historically, QD-LEDs were an extension of research on OLEDs and polymer LEDs (PLEDs), which have vertical architectures, such that the QD emissive layer is deposited onto the hole transport layer. Therefore, in the case of spin- or drop-casting, the solvent used must not dissolve or degrade the underlying transport layer. Many organics are soluble in standard solvents such as chloroform, hexane, toluene, and consequently, spin-casting QDs out of these solvents onto the organic charge transport layers is not possible. Development of QD and organic materials that are soluble in

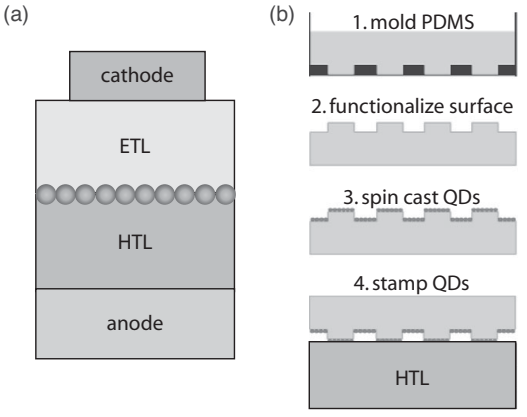


Figure 6.6 (a) Schematic of typical QD-LED architecture. (b) Steps involved in microcontact transfer printing of QDs.

orthogonal solvents or polymer charge transporting layers that can be crosslinked before the QD deposition step provide, a solution to these challenges. For example, Zhao *et al*. demonstrated a QD-LED incorporating a layer of QDs deposited from chloroform onto cross-linked polystyrene (PS) – N,N′-diphenyl-N,N′-bis(4-n-butylphenyl)-(1,1′-biphenyl)-4,4′-diamine (TPD) – perfluorocyclobutane (PFCB) [63].

In 2002, Coe *et al.* developed a phase separation technique that enabled formation of a close-packed monolayer of QDs on a molecular organic hole transport layer (TPD) from a single spin-cast step [8, 64]. Phase separation QD film formation takes advantage of the fact that an organic small molecule such as TPD has similar solubility in chloroform as colloidal QDs surrounded by hydrophobic organic ligands. At the same time, aliphatic ligands surrounding QDs (e.g., trioctylphosphine oxide (TOPO)) and aromatic organic molecules are immiscible. Therefore, once the QD and small molecule organic mixture is dropped onto the substrate and the solvent begins to evaporate during the spin process, the QDs segregate from the TPD molecules and float to the top, forming full or partial close-packed QDs layers on top of a TPD thin film. The initial device using a phase-separated QD thin film was completed with a thermally evaporated electron transporting organic molecule layer [64]. It exhibited minimal emission from the organic layers, a low turn-on voltage, and an EQE of 0.52%, which was a record at the time. The operating mechanism of QD-LEDs with organic charge transport layers is discussed extensively in Section 6.2; however, the efficiency improvement has been attributed to the use of a single monolayer of QDs, which improves the probability of non-radiative energy transfer of excitons formed in the organic transport layers to the QDs and decreases the amount of trapped charge [46]. While the phase-segregation method can be used to obtain QD monolayers, this technique cannot be applied to the patterning of QD monolayers. Additionally, it requires high solubility of organic charge transport layers in QD-carrying solvents, which restricts the choice of organic materials thereby compromising the design of efficient QD-LEDs.

Microcontact printing was developed in response to the challenges associated with spin-casting and phase separation and enables single monolayers of QDs to be transferred, solvent-free, from a functionalized poly(dimethylsiloxane) (PDMS) stamp onto an organic charge transport layer [13]. The work of Kim *et al.*, which used parylene-C coated PDMS stamps, shows the potential of this technique [13]. A display with side-by-side 25 μm by 25 μm RGB pixels was created in only two contact printing steps. First, lines of red QDs at 25 μm pitch were printed, followed by orthogonal lines of green QDs. The blue emission comes from the organic hole transport layer, TPD, onto which the QD stripes were stamped. Even for unpatterned QD films, microcontact printing shows the distinct benefit of being able to tune the emissive layer on the surface-functionalized stamp, independently of the QD-LED structure. For example, unlike most thin film white light sources that require stacking of different color pixels or downconversion schemes, the work of Anikeeva *et al.* demonstrates the ease in fabricating a white LED by mixing red, green, and blue QDs in solution, spin-casting this solution onto a functionalized PDMS stamp, and transferring the three colors simultaneously to the organic hole transport layer as a monolayer thin film [52]. This white QD-LED exhibited an EQE of 0.36% at 10 V applied bias and a CRI of 87.

With any deposition technique, removal of excess organic ligands from the growth solution is a key step in making QD films that are suitable for electrical excitation. Excess ligands can often be observed through atomic force microscopy of the QD film. For the work reported in [31, 37–39], for example, QDs were precipitated at least two times from their growth solution. For QDs with oleic acid capping ligands, for example, the QDs were precipitated from the growth solution using acetone, redispersed in hexane, precipitated a second time using methanol and butanol, and finally redispersed in chloroform. For QDs with trioctylphosphine (TOP) or TOPO ligands, the QDs were precipitated two times from hexane using methanol and butanol before being redispersed in chloroform. Prior to each precipitation step, the dispersion was passed through a 0.2 μm filter. Precipitation was accelerated by centrifuging the solution at 3500 RPM for 5 minutes.

6.6.2 Operation of colloidal QD-LEDs

QD-LEDs incorporating a monolayer of QDs between an organic electron transport layer (ETL) and an organic hole transport layer (HTL) have continuously held the efficiency records for electrically excited QD-LEDs, and numerous studies have been devoted to improving their performance and understanding the mechanisms behind their operation.

Experimental data and numerical modeling have confirmed that the high efficiency of these organic-based QD-LEDs can be attributed to the concomitant excitation of the luminescent QD film via Förster energy transfer and direct charge injection [46]. Förster energy transfer is a non-radiative (i.e., it does not involve the emission and reabsorption of a photon) dipole–dipole interaction between the electronic states of the donor and the acceptor. The first reports of Förster energy transfer in thin films of QDs were those of Kagan *et al*. [65], and studies have since shown evidence of Förster energy transfer between organics and QDs [66, 67].

The work of Anikeeva and coworkers was the first to both experimentally and numerically indicate the dominance of Förster energy transfer over direct charge injection in QD-LEDs using small molecule transport layers [46, 68]. In Förster energy transfer, an exciton from a wide-band-gap organic thin film can non-radiatively transfer to a QD, where it radiatively recombines. In direct charge injection, an electron and a hole are injected into the QD, form an exciton on the QD, and radiatively recombine. Anikeeva and coworkers compared the efficiency of device structures in which the monolayer of QDs was located at the HTL and ETL interface, was embedded into the HTL, or was embedded in the ETL. If direct charge injection were the dominant mechanism, the QD-LEDs with QDs located at the interface would be expected to have the highest efficiency. Instead, it was observed that structures in which QDs were embedded into the wide-band-gap HTL (but still within the Förster energy transfer radius of the interface) had the highest EQE. This suggests the excitons are first formed at the interface between the ETL and the HTL and then energy transfer to the QDs. Indeed, lower efficiencies and organic emission were observed in QD-LEDs where the QDs were embedded further than 10 nm from the ETL and HTL interface, a distance beyond which the probability of Förster energy transfer from an exciton created at the interface is lowered. Embedding the QDs in the ETL did not yield similar benefits to the EQE as embedding the QDs in the HTL because of the band structure of the constituent materials, which facilitates charging of the QDs with electrons when they are embedded in the ETL.

These experimental results were supported by numerical modeling of the electric fields, carrier densities, and exciton densities in the different QD-LED structures [68]. When Förster energy transfer was not included in the model, only organic emission is predicted from the device with QDs embedded in the HTL, which was not in agreement with the experimental results. In contrast, when Förster energy transfer was included in the model, pure QD emission was predicted, in agreement with the experimental results that show no EL from the organics.

This understanding of the roles of direct charge injection and Förster energy transfer made it possible to develop some design parameters crucial to the successful operation of QD-LEDs with organic hole and electron transport layers:

(1) The organic materials should have electronic structure that favors exciton transfer from the organic to the QDs.
(2) Only a monolayer of QDs should be used to decrease the amount of charge trapping.
(3) QDs should be located within a Förster radius of the charge transfer interface.
(4) QDs should be located away from high electric fields to minimize field-induced quenching.

With these guidelines in mind, for example, Anikeeva *et al*. showed EL from blue, cyan, green, orange, and red QD monolayers sandwiched between the same two organic layers (hole-transporting spiro-N,N′-diphenyl-N,N′-bis(3-methylphenyl)-(1,1′-biphenyl)-4,4′-diamine (spiroTPD) and electron-transporting 2,2′,2″-(1,3,5-benzenetriyl)-tris(L-phenyl-l-H-benzimidazole) (TPBi)) [38]. At the SPIE Meeting in January 2010, QD Vision, Inc. reported a red QD-LED with an EQE exceeding 8%.

While these results clearly illustrate the promise of electrically driven QDs for displays and large area lighting, one principal limitation of these QD-LEDs with organic transport layers is that, like OLEDs, they require environmental packaging to prevent degradation of the organic transport layers in the presence of atmospheric O_2 and water vapor.

6.7 QD-LEDs with inorganic charge transport layers

6.7.1 Reasons for inorganic charge transport layers

Historically, the integration of QDs into LEDs was built upon expertise from organic small molecule and polymer-based LEDs. However, since 2007, there has been interest in moving away from QD-LEDs with organic-based charge transport layers to QD-LEDs with inorganic charge transport layers. There are two main reasons for this shift. First, the need for environmental packaging of QD-LEDs using organic charge transport layers may unnecessarily increase the cost and complexity of device manufacturing. One of the benefits of using QD emitters is that, as inorganic particles, they are often more stable than many organic dyes. It is therefore rational to investigate whether replacing the organic charge transport layers with inorganic charge transport layers would enable air-stable devices that do not require packaging. Second, amorphous organic small molecule charge transport layers tend to have relatively low mobilities and limit the charge carrier densities. Now that higher mobility QD films have been achieved through inorganic ligands [7], transport in QD devices may no longer be limited by the QD layer and high current density devices could be feasible.

6.7.2 Fabrication of all inorganic QD-LEDs

One of the first promising efforts at building air-stable, colloidal QD-LEDs with p- and n-type, inorganic charge transport layers used doped GaN deposited by energy neutral atomic beam lithography/epitaxy (ENABLE) [69]. The EQE of the device ranged from 0.001% to 0.01%, although much of the observed EL was from the GaN. Subsequent work showed that it is possible to use metal oxide charge transport layers deposited at room temperature to build an air-stable QD-LED that exhibits pure QD emission and an efficiency of 0.1% [37]. The structure consisted of an ITO anode, a p-type NiO layer, a QD luminescent layer, an n-type zinc tin oxide layer, and a metal cathode.

In contrast to organic-based QD-LEDs, the use of inorganic layers means that the QDs can be directly spin-cast onto the inorganic hole transport material. While device efficiency in organic-based QD-LEDs was improved by using only a monolayer of QDs, inorganic QD-LED devices have thus far needed multilayer QD films. Material deposited directly on top of a QD monolayer through physical vapor, chemical vapor, or solution-based techniques fills voids in the monolayer and the space between the QDs, resulting at times in an interface between the n- and p-type layers of the device. In the QD-LEDs with organic charge transport layers, this interface enables the formation of an exciton on the organic film, which can then diffuse, energy transfer to an adjacent

QD, or recombine (perhaps emitting light characteristic of the organic material on which the exciton is formed). In contrast, if n- and p-type layers exhibiting band-like transport are in contact, no exciton is formed and the pn junction simply provides a favorable current pathway to circumvent the more resistive QD layer. The QD layer must therefore be complete. At the same time, if the QD layer is too thick, device resistivity and QD charging may increase as discussed in Section 6.2.

Another key consideration in the design of a QD-LED using inorganic charge transport layers is the choice of the deposition technique for the inorganic material on top of the QDs. For example, in the work of Mueller *et al.* the low temperature nature of ENABLE was key to maintaining luminescence from the QDs [69]. RF magnetron sputtering in argon was selected as the deposition method for the metal oxide transport layers in the work of Wood and coworkers, since it is a physical vapor deposition technique that can be performed at low power in an inert environment and at room temperature to minimize damage to the QD luminescence [37].

It is important to assess the extent to which deposition of the upper inorganic layer causes physical damage to the QDs and reduces their luminescent efficiency. One method for doing this is to compare the PL intensity from QDs (deposited on the bottom charge transport layers used in the device) before and after deposition of the upper charge transport layers. The PL intensity of (1) the QDs on glass and (2) the QDs on top of the upper charge transport layer deposited on glass should also be recorded. These two control samples can be used to determine whether a reduction in PL comes from luminescence quenching due the presence of the conductive charge transport layers (as discussed in Section 6.2) or from degradation due to the deposition of the top charge transport layer.

6.7.3 Operation of QD-LED with inorganic charge transport layers

QD-LED structures with inorganic charge transport layers have exhibited relatively low EQEs. Unlike QD-LEDs with organic-based charge transport layers, QD-LEDs with inorganic charge transport layers do not benefit from Förster energy transfer. While tightly bound Frenkel excitons form readily in organic thin films, they do not form on the inorganic thin films. Therefore, inorganic QD-LEDs operate solely via direct charge injection, requiring devices to be designed based largely on energy band alignment considerations. This hypothesis was verified in the work of Wood *et al*. by making systematic improvements to the efficiency of this structure through improvement in energy band alignment [39]. Ultraviolet photoelectron spectroscopy (to determine the valence band levels) and absorption spectroscopy (to determine the band gaps of the materials) were used to obtain a schematic picture of the energy band alignments between the charge transport layers and the QDs. In the structure under examination (ITO anode, NiO HTL, ZnCdSe QD multilayer, ZnO/SnO_2 ETL, and Cr/Au cathode), electron injection into the QD layer (no energy offset) was more energetically favorable than hole injection (0.4 eV offset). Upon device operation, QDs in this structure rapidly become charged with electrons. With the insertion of an electron blocking layer (ZnS) into the electron transport layer (ZnO/SnO_2) to balance the rate of electron and hole injection, device quantum efficiency was improved, which highlights the efficiency loss that accompanies

QD charging. The importance of energy band alignment was demonstrated with the following experiment. While hole injection from the NiO into red-emitting ZnCdSe QDs experiences a 0.4 eV energy barrier, injection from NiO into blue-emitting ZnCdS QD experiences a 0.7 eV energy barrier. Indeed, when the red-emitting QDs were exchanged with blue-emitting QDs, no more EL was observed. However, upon switching to a hole injection layer (WO_3), where again only a 0.4 eV barrier to hole injection is present, EL from blue-emitting ZnCdS QDs can be observed. The stringent energy band alignment requirements in a device operating entirely by direct charge injection makes multicolor EL from the same active layer a significant challenge.

6.7.4 Improving the efficiency of QD-LEDs with inorganic charge transport layers

Two main strategies have been used to improve the efficiency of inorganic QD-LED structures. One approach is to enable Förster energy transfer excitation of colloidal QDs within an inorganic structure. Work by Achermann *et al.* used InGaN/GaN quantum well structures in close proximity to the QD layer to enable both energy transfer and carrier injection as means for exciting QDs in an all-inorganic structure [70]. Other efforts have focused on hybrid QD-LEDs with both inorganic and organic transport layers. By retaining one organic layer, these devices benefit from the dual excitation mechanisms of Förster energy transfer and direct charge injection while gaining stability from the one ceramic transport layer. For example, red, green, and blue QD EL was achieved from a structure consisting of an ITO anode, PEDOT:PSS HTL, poly-(9-vinylcarbazole) HTL, QD emissive layer, solution-deposited ZnO nanocrystal-based ETL, and a metal cathode [15]. EQEs of 7.3%, 5.8%, and 1.7% have been reported from red, green, and blue QD-LEDs using a similar ZnO nanocrystal-based ETL [71]. The high efficiencies of this device can be attributed to its inverted structure, in which the ZnO layer was deposited prior to the QD layer, and the use of the small molecule 4,4′-bis(carbazole-9-yl)biphenyl (CBP) as HTL. Another group demonstrated high luminance ($> 10\ 000\ cd/m^2$) and EQE greater than 1% from a cross-linked layer of red-emitting QDs sandwiched between the polymer HTL, poly(9,9-dioctylfluorene-co-N-[4-(3-methylpropyl)]-diphenylamine) (TFB), and a spin-cast, sol-gel TiO_2 ETL [16].

A second approach is to investigate new mechanisms of QD excitation. For example, Wood and coworkers reported the development a field driven QD-LED architecture, which highlights the possibility for a paradigm shift away from direct charge injection into QDs as a means for EL in inorganic-based QD-LED structures [31, 72]. Field driven EL can be obtained with both DC and AC applied bias and these structures exhibit constant luminance over hours of continuous operation in air, unpackaged. Furthermore, this structure has also successfully been used to excite non-Cd containing QDs [73].

6.8 Future work

The field of QD optoelectronics has made tremendous strides since 2000, and the need for lower cost, higher efficiency devices with increased functionality will continue to

drive innovation. As the first colloidal QD-based products to see commercialization, QD-LEDs are playing a crucial role in demonstrating the potential for nanostructured materials in display and lighting technologies as well as other solid state devices such as solar cells, photodetectors, and imagers.

At the same time, the current challenges facing QD-LED performance highlight that further understanding and control of QD chemistry and physics and their interdependencies with QD-LED architecture are still needed. Reports on suppressed Auger recombination in QDs [23–25, 35, 36, 74] and enhanced mobility in QD thin films [7, 11] are particularly exciting, but their impact on lighting and display applications remains an open area for further research [75]. Furthermore, while LEDs incorporating $CuInSe_2$- and InP-based QDs have been demonstrated [76–78], much of our understanding of QD-LED performance is linked to Cd-containing QDs. While the percentage of cadmium in a QD-LED is small, demonstration of high-performing Cd-free QD-LEDs will likely be crucial to securing widespread industry and government support for QD-LEDs.

The open scientific questions surrounding QD chemistry, physics, and device engineering offer unique opportunities for both industry and basic research involvement in QD-LED development that will undoubtedly dramatically change the landscape of colloidally-synthesized QD usage in large-area optoelectronic nanotechnologies in the years to come.

References

1 C. B. Murray, D. J. Norris, M. G. Bawendi, Synthesis and characterization of nearly monodisperse CdE (E=S, Se, Te) semiconductor nanocrystallites. *Journal of the American Chemical Society*, **115**:4 (1993), 8706–8715.

2 M. A. Hines, G. D. Scholes, Colloidal PbS nanocrystals with size-tunable near-infrared emission: observation of post-synthesis self-narrowing of the particle size distribution. *Advanced Materials*, **15**:21 (2003), 1844–1849.

3 E. F. Schubert, *Light-Emitting Diodes*, second edition. Cambridge, UK: Cambridge University Press, 2006.

4 Q. Dai, C. E. Duty, M. Z. Hu, Semiconductor-nanocrystals-based white light-emitting diodes. *Small*, **6**:15 (2010), 1577–88.

5 W. C. Chan, Quantum dot bioconjugates for ultrasensitive nonisotopic detection. *Science*, **281**:5385 (1998), 2016–2018.

6 B. Dubertret, P. Skourides, D. J. Norris, *et al.*, In vivo imaging of quantum dots encapsulated in phospholipid micelles. *Science*, **298**:5599 (2002), 1759–62.

7 M. V. Kovalenko, M. Scheele, D. V. Talapin, Colloidal nanocrystals with molecular metal chalcogenide surface ligands. *Science*, **324**:5933 (2009), 1417–20.

8 S. Coe-Sullivan, J. S. Steckel, W.-K. Woo, M. G. Bawendi, V. Bulović, Large-area ordered quantum-dot monolayers via phase separation during spin-casting. *Advanced Functional Materials*, **15**:7 (2005), 1117–1124.

9 W. K. Bae, J. Kwak, J. Lim, *et al.*, Multicolored light-emitting diodes based on all-quantum-dot multilayer films using layer-by-layer assembly method. *Nano Letters*, **10**:7 (2010), 2368–73.

10 V. Wood, M. J. Panzer, J. Chen, *et al.*, Inkjet-printed quantum dot-polymer composites for full-color AC-driven displays. *Advanced Materials*, **21**:21 (2009), 2151–2155.
11 T. Zhu, K. Shanmugasundaram, S. C. Price, *et al.*, Mist fabrication of light emitting diodes with colloidal nanocrystal quantum dots. *Applied Physics Letters*, **92**:2 (2008), 023111.
12 A. Rizzo, M. Mazzeo, M. Palumbo, *et al.*, Hybrid light-emitting diodes from microcontact-printing double-transfer of colloidal semiconductor CdSe/ZnS quantum dots onto organic layers. *Advanced Materials*, **20**:10 (2008), 1886–1891.
13 L. Kim, P. O. Anikeeva, S. A. Coe-Sullivan, *et al*., Contact printing of quantum dot light-emitting devices. *Nano Letters*, **8**:12 (2008), 4513–7.
14 T.-H. Kim, K.-S. Cho, E. K. Lee, *et al.*, Full-colour quantum dot displays fabricated by transfer printing. *Nature Photonics*, **5**:3 (2011), 176–182.
15 J. W. Stouwdam, R. A. J. Janssen, Red, green, and blue quantum dot LEDs with solution processable ZnO nanocrystal electron injection layers. *Journal of Materials Chemistry*, **18**:16 (2008), 1889.
16 K.-S. Cho, E. K. Lee, W.-J. Joo, *et al.*, High-performance crosslinked colloidal quantum-dot light-emitting diodes. *Nature Photonics*, **3**:6 (2009), 341–345.
17 J. E. B. Katari, V. L. Colvin, A. P. Alivisatos, X-ray photoelectron spectroscopy of CdSe nanocrystals with applications to studies of the nanocrystal surface. *The Journal of Physical Chemistry*, **98**:15 (1994), 4109–4117.
18 W. van Sark, P. H. T. M. Frederix, D. J. Vanden Heuvel, H. C. Gerrit Sen, Photooxidation and photobleaching of single CdSe/ZnS quantum dots probed by room-temperature time-resolved spectroscopy. *The Journal of Physical Chemistry B*, **105**:35 (2001), 8281–8284.
19 M. A. Hines, P. Guyot-Sionnest, Synthesis and characterization of strongly luminescing ZnS-capped CdSe nanocrystals. *The Journal of Physical Chemistry*, **100**:2 (1996), 468–471.
20 B. O. Dabbousi, J. Rodriguez-Viejo, F. W. Mikulec, *et al.*, (CdSe)ZnS core−shell quantum dots: synthesis and characterization of a size series of highly luminescent nanocrystallites, *The Journal of Physical Chemistry B*, **101**:46 (1997), 9463–9475.
21 Y. Tian, T. Newton, N. A. Kotov, D. M. Guldi, J. H. Fendler, Coupled composite CdS−CdSe and core−shell types of (CdS)CdSe and (CdSe)CdS nanoparticles. *The Journal of Physical Chemistry* **100**:21 (1996), 8927–8939.
22 X. Peng, M. C. Schlamp, A. V. Kadavanich, A. P. Alivisatos, Epitaxial growth of highly luminescent CdSe/CdS core/shell nanocrystals with photostability and electronic accessibility. *Journal of the American Chemical Society*, **119**:30 (1997), 7019–7029.
23 Y. Chen, J. Vela, H. Htoon, *et al.*, "Giant" multishell CdSe nanocrystal quantum dots with suppressed blinking. *Journal of the American Chemical Society*, **130**:15 (2008), 5026–5027.
24 B. Mahler, P. Spinicelli, S. Buil, *et al.*, Towards non-blinking colloidal quantum dots. *Nature Materials*, **7**:8 (2008), 659–64.
25 F. García-Santamaría, Y. Chen, J. Vela, *et al.*, Suppressed Auger recombination in "giant" nanocrystals boosts optical gain performance. *Nano Letters* **9**:10 (2009), 3482–8.
26 A. Pourret, P. Guyot-Sionnest, J. W. Elam, Atomic layer deposition of ZnO in quantum dot thin films. *Advanced Materials*, **21**:2 (2009), 232–235.
27 Y. Liu, M. Gibbs, C. L. Perkins, *et al.*, Robust, functional nanocrystal solids by infilling with atomic layer deposition. *Nano Letters*, **11**:12 (2011), 5349–55.
28 E. Kinder, P. Moroz, G. Diederich, *et al.*, Fabrication of all-inorganic nanocrystal solids through matrix encapsulation of nanocrystal arrays. *Journal of the American Chemical Society*, **133**:50 (2011), 20488–99.

29 J. C. de Mello, H. F. Wittmann, R. H. Friend, An improved experimental determination of external photoluminescence quantum efficiency. *Advanced Materials*, **9**:3 (1997), 230–232.
30 J. Lee, V. C. Sundar, J. R. Heine, M. G. Bawendi, K. F. Jensen, Full color emission from II–VI semiconductor quantum dot-polymer composites. *Advanced Materials*, **12**:15 (2000), 1102–1105.
31 V. Wood, M. J. Panzer, D. Bozyigit, *et al.*, Electroluminescence from nanoscale materials via field-driven ionization. *Nano Letters*, **11**:7 (2011), 2927–32.
32 M. Nirmal, B. O. Dabbousi, M. G. Bawendi, *et al.*, Fluorescence intermittency in single cadmium selenide nanocrystals. *Nature*, **383**:6603 (1996), 802–804.
33 C. Galland, Y. Ghosh, A. Steinbrück, *et al.*, Two types of luminescence blinking revealed by spectroelectrochemistry of single quantum dots. *Nature*, **479**:7372 (2011), 203–7.
34 V. Klimov, A. Mikhailovsky, D. McBranch, C. Leatherdale, M. Bawendi, Quantization of multiparticle Auger rates in semiconductor quantum dots. *Science*, **287**:5455 (2000), 1011–3.
35 G. E. Cragg, A. L. Efros, Suppression of Auger processes in confined structures. *Nano Letters*, **10**:1 (2010), 313–7.
36 X. Wang, X. Ren, K. Kahen, *et al.*, Non-blinking semiconductor nanocrystals. *Nature*, **459**:7247 (2009), 686–9.
37 J. M. Caruge, J. E. Halpert, V. Wood, V. Bulović, M. G. Bawendi, Colloidal quantum-dot light-emitting diodes with metal-oxide charge transport layers. *Nature Photonics*, **2**:4 (2008), 247–250.
38 P. O. Anikeeva, J. E. Halpert, M. G. Bawendi, V. Bulović, Quantum dot light-emitting devices with electroluminescence tunable over the entire visible spectrum. *Nano Letters*, **9**:7 (2009), 2532–2536.
39 V. Wood, M. J. Panzer, J. E. Halpert, *et al.*, Selection of metal oxide charge transport layers for colloidal quantum dot LEDs. *ACS Nano*, **3**:11 (2009), 3581–3586.
40 S. Jin, N. Song, T. Lian, Suppressed blinking dynamics of single QDs on ITO. *ACS Nano*, **4**:3 (2010), 1545–1552.
41 P. Guyot-Sionnest, Electrical transport in colloidal quantum dot films. *The Journal of Physical Chemistry Letters*, **3**:9 (2012), 1169–1175.
42 N. Morgan, C. Leatherdale, M. Drndić, *et al.* Electronic transport in films of colloidal CdSe nanocrystals. *Physical Review B*, **66**:7 (2002), 1–9.
43 D. S. Ginger, N. C. Greenham, Charge injection and transport in films of CdSe nanocrystals. *Journal of Applied Physics*, **87**:3 (2000), 1361.
44 D. Bozyigit, V. Wood, Y. Shirasaki, V. Bulovic, Study of field driven electroluminescence in colloidal quantum dot solids. *Journal of Applied Physics*, **111**:11 (2012), 113701.
45 D. Bozyigit, O. Yarema, V. Wood. Origins of low quantum efficiencies in quantum dot LEDs. *Advanced Functional Materials*, DOI = 10.1002/adfm 20120319 (2013).
46 P. Anikeeva, C. Madigan, J. Halpert, M. Bawendi, V. Bulović, Electronic and excitonic processes in light-emitting devices based on organic materials and colloidal quantum dots. *Physical Review B*, **78**:8 (2008), 1–8.
47 A. Sacra, D. J. Norris, C. B. Murray, M. G. Bawendi, Stark spectroscopy of CdSe nanocrystallites:The significance of transition linewidths. *The Journal of Chemical Physics*, **103**:13 (1995), 5236.
48 S. A. Empedocles, Quantum-confined Stark effect in single CdSe nanocrystallite quantum dots. *Science*, **278**:5346 (1997), 2114–2117.
49 A. Rose, Space-charge-limited currents in solids. *Physical Review*, **97**:6 (1995), 1538–1544.

50 Z. Shen, P. E. Burrows, V. Bulovic, *et al.*, Temperature dependence of current transport and electroluminescence in vacuum deposited organic light emitting devices. *Japanese Journal of Applied Physics*, **35**(2):3B (1996), L401–L404.

51 T. Liptay, L. Marshall, P. Rao, R. Ram, M. Bawendi, Anomalous Stokes shift in CdSe nanocrystals. *Physical Review B*, **76**:15 (2007), 1–7.

52 P. O. Anikeeva, J. E. Halpert, M. G. Bawendi, V. Bulović, Electroluminescence from a mixed red-green-blue colloidal quantum dot monolayer. *Nano Letters*, **7**:8 (2007), 2196–200.

53 C. A. Leatherdale, W.-K. Woo, F. V. Mikulec, M. G. Bawendi, On the absorption cross section of CdSe nanocrystal quantum dots. *The Journal of Physical Chemistry B*, **106**:31 (2002), 7619–7622.

54 L. E. Shea Rohwer, Development of solid state light sources based on II–VI semiconductor quantum dots. *Proceedings of SPIE*, **5366** (2004), 66–74.

55 H. Song, S. Lee, Photoluminescent (CdSe)ZnS quantum dot–polymethylmethacrylate polymer composite thin films in the visible spectral range. *Nanotechnology*, **18**:5 (2007), 055402.

56 H. J. Yu, K. Park, W. Chung, J. Kim, S. H. Kim, White light emission from blue InGaN LED precoated with conjugated copolymer/quantum dots as hybrid phosphor. *Synthetic Metals*, **159**:23–24 (2009), 2474–2477.

57 E. Jang, S. Jun, H. Jang, J. Lim, B. Kim, Y. Kim, White-light-emitting diodes with quantum dot color converters for display backlights. *Advanced Materials*, **22**:28 (2010), 3076–80.

58 S. Nizamoglu, T. Erdem, X. W. Sun, H. V. Demir, Warm-white light-emitting diodes integrated with colloidal quantum dots for high luminous efficacy and color rendering. *Optics Letters*, **35**:20 (2010), 3372.

59 M. J. Panzer, V. Wood, S. M. Geyer, M. G. Bawendi, V. Bulović, Tunable infrared emission from printed colloidal quantum dot/polymer composite films on flexible substrates. *IEEE Journal of Display Technology*, **6** (2010), 90–93.

60 V. L. Colvin, M. C. Schlamp, A. P. Alivisatos, Light-emitting diodes made from cadmium selenide nanocrystals and a semiconducting polymer. *Nature*, **370**:6488 (1994), 354–357.

61 B. O. Dabbousi, M. G. Bawendi, O. Onitsuka, M. F. Rubner, Electroluminescence from CdSe quantum-dot/polymer composites. *Applied Physics Letters*, **66**:11 (1995), 1316.

62 D. V. Talapin, J.-S. Lee, M. V. Kovalenko, E. V. Shevchenko, Prospects of colloidal nanocrystals for electronic and optoelectronic applications. *Chemical Reviews*, **110**:1 (2010), 389–458.

63 J. Zhao, J. A. Bardecker, A. M. Munro, *et al.*, Efficient CdSe/CdS quantum dot light-emitting diodes using a thermally polymerized hole transport layer. *Nano Letters* **6**:3 (2006), 463–467.

64 S. Coe, W.-K. Woo, M. Bawendi, V. Bulović, Electroluminescence from single monolayers of nanocrystals in molecular organic devices. *Nature* **420**:6917 (2002), 800–803.

65 C. Kagan, C. Murray, M. Nirmal, M. Bawendi, Electronic energy transfer in CdSe quantum dot solids. *Physical Review Letters*, **76**:9 (1996), 1517–1520.

66 A. R. Clapp, I. L. Medintz, B. R. Fisher, G. P. Anderson, H. Mattoussi, Can luminescent quantum dots be efficient energy acceptors with organic dye donors? *Journal of the American Chemical Society*, **127**:4 (2005), 1242–50.

67 P. O. Anikeeva, C. F. Madigan, S. A. Coe-Sullivan, *et al.*, Photoluminescence of CdSe/ZnS core/shell quantum dots enhanced by energy transfer from a phosphorescent donor. *Chemical Physics Letters*, **424**:1–3 (2006), 120–125.

68 P. O. Anikeeva. Physical properties and design of light-emitting devices based on organic materials and nanoparticles. PhD Thesis. Massachusetts Institute of Technology (2009).

69 A. H. Mueller, M. A. Petrusta, M. Acherman, *et al.*, Multicolor light-emitting diodes based on semiconductor nanocrystals encapsulated in GaN charge injection layers. *Nano Letters*, **5**:6 (2005), 1039–1044.
70 M. Achermann, M. A. Petruska, D. D. Koleske, M. H. Crawford, V. I. Klimov, Nanocrystal-based light-emitting diodes utilizing high-efficiency nonradiative energy transfer for color conversion, *Nano Letters*, **6**:7 (2006), 1396–1400.
71 J. Kwak, W. K. Bae, D. Lee, *et al.*, Bright and efficient full-color colloidal quantum dot light-emitting diodes using an inverted device structure. Nano Letters (2012).
72 V. Wood, M. J. Panzer, J.-M. Caruge, *et al.*, Air-stable operation of transparent, colloidal quantum dot based LEDs with a unipolar device architecture. *Nano Letters*, **10**:1 (2010), 24–9.
73 V. Wood, J. E. Halpert, M. J. Panzer, M. G. Bawendi, V. Bulović, Alternating current driven electroluminescence from ZnSe/ZnS:Mn/ZnS nanocrystals. *Nano Letters*, **9**:6 (2009), 2367–71.
74 F. García-Santamaría, F. Brovelli, S. Viswanatha, *et al.*, Breakdown of volume scaling in Auger recombination in CdSe/CdS heteronanocrystals: the role of the core-shell interface. *Nano Letters*, **11**:2 (2011), 687–93.
75 B. N. Pal, *et al.*, "Giant" CdSe/CdS core/shell nanocrystal quantum dots as efficient electroluminescent materials: strong influence of shell thickness on light-emitting diode performance. *Nano Letters*, **12**:1 (2012), 331–6.
76 H. Zhong, Z. Wang, E. Bovero, *et al.*, Colloidal $CuInSe_2$ Nanocrystals in the quantum confinement regime: synthesis, optical properties, and electroluminescence. *The Journal of Physical Chemistry C*, **115**:25 (2011), 12396–12402.
77 Y. Zhang, C. Xie, H. Sw, *et al.*, Employing heavy metal-free colloidal quantum dots in solution-processed white light-emitting diodes. *Nano Letters*, **11**:2 (2011), 329–32.
78 S. Kim, T. Kim, M. Kang, *et al.*, Highly luminescent InP/GaP/ZnS nanocrystals and their application to white light-emitting diodes. *Journal of the American Chemical Society*, **134**:8 (2012), 3804–9.

7 Colloidal quantum dot photodetectors

Gerasimos Konstantatos

7.1 Introduction

7.1.1 Applications of top-surface photodetectors

Optical detection encompasses a vast number of applications, including optical communications, remote sensing, spectroscopy, and metrology. A major part of the sensor market is associated with imaging applications, hence image sensors have become ubiquitous. This has largely been due to the advent of digital imaging.

In an image sensor a photosensitive material is required to absorb optical signals in the visible range (i.e., wavelengths of 400–700 nm) and transform them into electronic signals. Visible imaging applications also include surveillance, machine vision, industrial inspection, spectroscopy, and fluorescent biomedical imaging.

Sensitive photodetection in the short wavelength infrared (SWIR), on the other hand, enables passive night vision [1, 2] from 1 μm to 1.7 μm and biomedical imaging for tumor detection [3] exploiting the tissue transparent windows around 900 and 1100 nm [4, 5]. Additional applications of SWIR imaging can be found in astrophysics [6], remote environmental sensing [7], quality control and product inspection [8] in the food and pharmaceutical industries, and identification [9].

Imaging in the visible is largely facilitated by silicon photodiodes. Early imaging arrays were based on charge-coupled devices (CCD). This approach involves a photoactive sensor array with several stages of photocharge transfer to the read-out circuit for electronic processing. CCD cameras offer a fill-factor – the ratio of the optically active area of the chip to its total area – that may vary from 100% to 50% depending on the chip design [10]. CCDs are prone to high fabrication and integration cost due to multiple chip interconnections and the incompatibility of CMOS with the process required for the CCD platform. In 1997, an integrated CMOS image sensor was reported on a single chip for optical sensing and signal processing [11]. Its fill-factor was limited to 30% due to the coexistence of photoactive elements and read-out circuitry on the same chip. Amorphous silicon photodetectors have been proposed as a top-surface photodetector with promise of a 100% fill-factor [12]. However, these suffer from long time constants [13] and material instabilities under illumination [14].

Colloidal Quantum Dot Optoelectronics and Photovoltaics, eds. G. Konstantatos and E. H. Sargent.
Published by Cambridge University Press. © Cambridge University Press, 2013.

Silicon photodiodes exhibit transient times in the nanosecond range, comfortably fulfilling, the requirements for imaging applications. Their photodiode mechanism of operation limits their internal quantum efficiency to 100% since at most one charge carrier is extracted for each absorbed photon. Their sensitivity is thus susceptible to the read-out circuit noise. In order to overcome this limit, Si avalanche photodiodes (APD) have been proposed for use in CMOS image sensors [15]. The required high applied bias, however, inhibits their integration in conventional CMOS circuits. Further design considerations are required to suppress the high leakage currents present in such structures [16].

For sensing and imaging applications in the SWIR, InGaAs photodiodes lead the market. An $In_{0.53}Ga_{0.47}As$ lattice matched with InP and with a bandgap of 0.73 eV addresses the SWIR spectrum and is suited for night vision applications. The molecular beam epitaxy (MBE) technique required for the growth of InGaAs imposes a high materials cost per unit area of sensor. Hybrid integration of the light-sensing InGaAs array requires bump-bonding techniques that increase the cost further and also limit the pixel resolution to a few hundred kilopixels. The complexity further increases in proposed hybrid solutions that enable visible and infrared imaging applications utilizing hybrid Si and InGaAs technologies, also known as VisGaAs [17].

The advent of self-assembled epitaxially grown quantum dots (QDs) has also led to dramatic progress in the development of QD infrared photodetectors. This technology has been employed to address the challenges of mid- and long-wavelength infrared detectors for sensing and imaging [18, 19]. QDs show promise for narrow spectral response, reduced dark current and thereby higher sensitivity with higher temperature operation compared with the quantum well counterparts [20, 21].

The development of a CMOS-compatible infrared detector has been undertaken by growing germanium on silicon. Even though these devices require costly epitaxial growth techniques, they show promise for monolithic integration of infrared detectors on CMOS. SiGe photodiodes have been reported with infrared sensitivity [22]. These detectors were developed with emphasis on high-speed performance for optical communications and exhibit bandwidths in excess of 1 GHz [23]; their responsivity, however, was reported to be ~0.1 A/W, resulting in insufficient sensitivity for imaging applications. Their integration onto CMOS focal plane arrays for imaging has also been reported [24]. Although this is promising, further research is required before sensitive imaging systems using SiGe can be fabricated.

7.1.2 Colloidal quantum dots (CQDs) for light detection

CQDs have attracted significant attention as a candidate material for a range of optoelectronic applications. Light emitting diodes [25, 26], lasers [27], optical modulators [28], solar cells [29, 30], and photodetectors [31] have all been reported. One major benefit of CQDs arises from their solution processibility: this facilitates ready integration with an almost limitless variety of substrates, including post-processing atop other integrated circuits. Additionally, optical absorption and emission spectra of QDs are widely tunable through the quantum size effect [32]. The impact of these traits on photodetector technology is discussed in the present section.

Device fabrication based on conventional single-crystalline semiconductors such as silicon and InGaAs requires high temperature processing and high vacuum conditions accompanied by high cost equipment. Monolithically integrated optoelectronics also mandates growth on crystalline substrates using lattice-matched semiconductors. Unlike electronic devices, low cost optoelectronic devices are therefore hard to achieve in view of material incompatibilities and highly customized deposition systems.

When it comes to practical implementation of an image sensor technology, the issue of convenient integration of light-sensitive materials with read-out electronics emerges as a great challenge. A photosensitive material should be readily monolithically integrated with a simple, low cost CMOS read-out integrated circuit, offering low fabrication cost, low complexity, and high pixel count.

Solution-synthesized CQDs can readily be deposited using spin-coating, spray-casting, or inkjet printing techniques on any substrate conducting or insulating, crystalline or amorphous, rigid or flexible, and large-area processing is facilitated by roll-to-roll processing onto flexible substrates. Colloidal nanocrystals are synthesized using wet chemistry techniques: reagents are injected into a flask and through control of reagent concentrations, ligand selection and temperature, nanocrystals of a desired size and shape can be delivered. Synthesis and growth of nanocrystals of the desired size is followed by isolation and redispersion in organic solvents for subsequent solution processing.

The facile control of the absorption spectrum in a semiconductor is also of paramount importance. In photodetectors, spectral tunability eliminates the need for optical filters to address the spectrum of interest, leading to lower implementation cost and avoiding the loss of signal that arises when filtering and sensing are implemented in series rather than within a single spectrally-selective sensing medium. Furthermore, the absorption onset of the detector can be selected to match the longer wavelength of the intended spectrum. This avoids absorption of longer wavelength photons that are not of interest in certain imaging applications but that do contribute to thermal noise.

Particularly, in the case of PbS CQDs, by varying the dot size from $\sim$10 nm to $\sim$2 nm in diameter, the whole SWIR and visible spectrum can be selectively addressed from 1800 nm to 700 nm. PbS QD photodetectors can thus address spectral windows of interest in a range of important applications: visible for video and photography; near-infrared for biomedical imaging; SWIR for night vision applications.

7.2 Fundamentals of photodetectors

7.2.1 Types of photodetectors

There are two main classes of photodetectors: the photoconductors and the photodiodes.

A photoconductor typically consists of a semiconducting material, single-crystalline, polycrystalline, or amorphous, and two ohmic metal contacts to form a two-port electrical device. Upon illumination, the conductivity of the material changes due to a variation in mobility or carrier density or both [33]. Conductivity increase upon illumination is most typically attributed to generation of electron–hole pairs resulting in a carrier density

increase. Photoconductors offer photoconductive gain, a greater-than-unity ratio of the number of circulated charge carriers per absorbed photon. The physical mechanism underlying photoconductive gain has been extensively studied [34, 35]. The trap states that contribute to photosensitization, also called sensitizing centres, favor the capture of one carrier (e.g., electrons) over the other (e.g., holes). Upon photoexcitation, electrons are captured by these centres whereas holes remain free to traverse the device. The low capture probability for holes prolongs their carrier lifetime. The holes, upon reaching one contact, can be replenished by the other contact. The number of passes of a hole across the device is then equal to the ratio of the carrier lifetime to its transit time, giving rise to photoconductive gain G equal to τ_p/τ_{trp}. A thorough investigation of the implications of this mechanism on the optoelectronic characteristics of such detectors is discussed by Rose, Bube and coworkers [36–38].

Photodiodes, on the other hand, are based on either the formation of a junction between two different semiconductors (heterojunctions), or a semiconductor with opposite doping (a homojunction), or a semiconductor and a rectifying metal contact (a Schottky junction). In each case the principle is separation of photogenerated electron–hole pairs by the action of the built-in electric field in the junction and transport of the carriers to the respective contacts for extraction. This principle ensures that photodiodes are limited in their quantum efficiency to one carrier extracted per absorbed photon. At the same time, since the temporal response of photodiodes is determined by the transit time of the carriers, and not their lifetime, photodiodes are often faster than photoconductors.

7.2.2 Figures of merit

A set of figures of merit has been formulated to evaluate various photodetector technologies for sensing applications [39].

Responsivity has been defined to quantify the electrical signal output of the detector per optical signal input. Responsivity R is the ratio of photocurrent to the incident optical power impinging on the detector and measured thus in amperes per watt. The general expression for responsivity is:

$$R = \frac{\eta q \lambda}{hc} \frac{1}{\sqrt{1+\omega^2\tau^2}} G, \tag{7.1}$$

where q is the electron charge, h Planck's constant, c the speed of light, ω the electrical modulation frequency, η the quantum efficiency, τ the time constant, and G the photoconductive gain.

The quantum efficiency is defined as the efficiency with which an incident photon results in the excitation of an electron that can be extracted from the device. It is a normalized value and is equal to the number of electrons excited divided by the number of photons incident on the detector's active area. Typically, quantum efficiency takes into account reflectance, absorbance, and scattering and in this case it may be also called external quantum efficiency (EQE). In photoconductive photodetectors, the time constant that determines the 3-dB bandwidth of responsivity is related to the carrier lifetimes introduced by the associated sensitizing trap states.

Another important parameter in the characterization of photodetector sensitivity is the noise current. There exist four major sources of noise in photoconductors: Johnson noise, shot noise, generation–recombination (G–R) noise, and $1/f$ noise [39].

By taking together the responsivity and the noise performance of the detector one can quantify the ultimate figure of merit of sensitivity. The minimum optical power level a detector can distinguish from noise depends on the responsivity and the noise level. The signal current produced by the input power must be above the noise level in order to be detected. The signal to noise ratio, SNR, is given by

$$\mathrm{SNR} = \frac{RP}{i_n}, \tag{7.2}$$

where R is responsivity, P the incident optical power, and i_n is the noise current. The optical power at which the SNR is equal to unity is the minimum optical power that the detector can discern; it is called the noise equivalent power, NEP, and is given by

$$\mathrm{NEP} = \frac{i_n}{R}. \tag{7.3}$$

The disadvantage of using NEP to describe detector performance is that it is specific to detectors having a particular surface area.

The figure of merit D^*, called the normalized or specific detectivity [40], is widely used as a descriptor of the detector's sensitivity that is insensitive to device area. This parameter allows comparison among detectors of different geometries, thus enabling the evaluation of sensitivity of photoconductive materials rather than specific devices. The expression for D^* is:

$$D* = \frac{\sqrt{A_d B}}{\mathrm{NEP}} = \frac{\sqrt{A_d B}\,R}{i_n}, \tag{7.4}$$

where A_d is the detector's area, B the electrical bandwidth, R the responsivity, i_n the noise current, and NEP the noise equivalent power. The units of D^* are cm $\mathrm{Hz}^{1/2}$ W^{-1} or Jones. It can be interpreted as the SNR produced by a detector of 1 cm^2 surface when 1 W of optical power impinges, measured with electrical bandwidth of 1 Hz. Similarly to responsivity, D^* is also a function of many parameters: applied bias, temperature, modulation frequency, wavelength; therefore measurement conditions should be included when giving D^* values.

7.3 Prior art in solution-processed photodetectors

The attractive features of solution processibility have been exploited to produce large-area, low cost, flexible, thin-film optoelectronic devices. Photodetectors have thus been reported from conjugated polymers and colloidal nanocrystals. We now present a review of the literature to demonstrate the progress in the field and also to establish the challenges that still need to be addressed.

The solution processibility of CQDs render them compatible with conjugated polymers and allow their integration to form nanocomposites with large interfaces. These

bulk heterojunctions provide high photon absorption and efficient exciton dissociation at the interfaces followed by charge separation due to the type II heterojunctions formed between polymers and QDs. Upon illumination, excitons dissociate and electrons and holes are transported to the contacts through separate paths within different physical media (polymer and nanocrystals), reducing recombination and thereby increasing quantum efficiency.

A polymer–nanocrystal composite photodetector was reported for the first time in 1996 [41]. It consisted of a blend of CdSe or CdS nanocrystals mixed with MEH-PPV. This material system exhibits a type-II heterostructure wherein electrons are energetically favored to stay in the nanocrystals, whereas holes are transferred to the polymer matrix. The mixture was spin-coated on an indium tin oxide (ITO) substrate, followed by metal evaporation to form the cathode. The efficiency of exciton dissociation was observed via the quenching of photoluminescence emitted by the nanocrystals. These devices were investigated as photovoltaic photodetectors and the reported quantum efficiency was ~12% at zero bias conditions while it reached ~60% at 3 V. The spectral sensitivity of the reported device was limited by the absorption of MEH-PPV and Cd(S, Se) nanocrystals to the visible up to 650 nm.

The use of PbS QDs in a polymer–nanocrystal bulk heterojunction device was reported in 2005 [42]; this was the first successful attempt to extend the polymer sensitivity into the infrared. This architecture is based on a photodiode principle of operation wherein photogenerated carriers are separated in two host media and transported to the respective contacts. The active layer consists of a nanocomposite film of PbS nanocrystals in MEH-PPV polymer, sandwiched between a thin PPV buffer layer and the metal contacts.

MEH-PPV was chosen due to the high hole mobility and the favorable band offset with the PbS nanocrystals that forms a type-II heterostructure. This means that electrons preferentially stay in the QDs, whereas it is energetically favorable for holes to transfer to the MEH-PPV. Upon photoexcitation therefore, electron–hole pairs created in the nanocrystals separate and electrons hop amongst nanocrystals to the anode, whereas holes are transported via the polymer towards the cathode. Under forward bias electrons are extracted through the Mg contact and holes through the PPV/ITO contact. Even though this was the first demonstration of a solution-processed photodetector with infrared sensitivity from 1 μm to 1.5 μm, the responsivity of the diode is estimated to be on the order of 3 mA/W, which is prohibitively low for practical sensing applications.

Photoconductivity in pure CQD solids was reported for the first time in 2000 [43]. Photoconductivity in CdSe QD solids was studied as a function of applied electric field and nanocrystal surface passivation. In this device, photogenerated excitons are ionized by the applied electric field and dissociate into electrons and holes that hop amongst nanocrystals either via QD bound states or surface trap states. In this approach, photocurrent competes with radiative and non-radiative recombination due to the fact that both types of carriers are transported via the same medium. The spectral sensitivity of this device was within the visible range but absolute responsivity values were not reported.

An orders of magnitude increase in photoconductivity was reported [44] from this material system, after post-deposition ligand exchange treatments on the nanocrystal

surface. It was found that shorter ligands improved carrier transport among nanocrystals by decreasing inter-nanoparticle spacing. The functionality of the ligand head group was also critical to passivating surface recombination states, enabling higher quantum efficiency. Increasing exciton ionization efficiencies were also reported as a result of the ligand modification. However, the absence of sensitizing centers in CdSe prevented the observation of photoconductive gain in this material system.

7.4 Solution-processed QD photoconductors

7.4.1 Photoconductive gain and noise in PbS QD photodetectors

Unlike Cd-based QDs, PbS QDs have demonstrated very large photoconductive gain and sensitivity due to the existence of sensitizing centers associated with the presence of oxide species on the surface of the QDs, similar to the case of bulk PbS [45]. We therefore now turn our attention to and review the progress made in the field of PbS CQD photoconductive detectors.

For sensitive photodetection, there are two prerequisite features: high photoconductive gain and low noise. Photoconductive gain expresses the number of electrical carriers circulated in the circuit per absorbed photon. This figure of merit determines the detector's ability to respond to light and is a crucial parameter for high sensitivity at a given noise level. The physical parameters that affect gain in a photoconductor are the minority carrier lifetime and the majority carrier transit time. For a sensitizing center characterized by a given carrier lifetime, therefore, increase in majority carrier mobility leads to higher photoconductive gains. Carrier transport in nanocrystal solids takes place via a thermally activated hopping mechanism [46]. A determining parameter for the transport in these materials is the inter-nanoparticle distance. The hopping probability depends exponentially on the inter-nanoparticle spacing. High mobility thus mandates nanocrystal close-packing [47].

Increase in carrier lifetime in a photoconductor, also called photosensitization, can be achieved by introducing sensitizing centers that trap one type of carrier but not the other. Previous studies in bulk PbS photoconductors have shown that photosensitization of PbS is followed by oxidation, and, in particular, formation of lead sulfates ($PbSO_4$) [48–51]. These oxide species act as sensitizing centers that prolong the minority (electron) carrier lifetime allowing holes to traverse the device within this carrier lifetime.

Oleate-capped as-synthesized nanocrystals yielded films with insulating properties. The ~2.5 nm long ligand – consisting of an eighteen-carbon-atom chain – inhibited carrier transport among the nanocrystals. To improve carrier mobility, a post-synthesis ligand exchange process was employed to replace oleic acid with a shorter ligand attachable to the nanocrystal Pb sites, leading to a decrease in the inter-nanoparticle spacing. N-butylamine, which consists of a four-carbon-atom chain of length ~0.6 nm, was therefore employed.

Photoconductive devices were fabricated by spin-coating butylamine exchanged nanocrystals to form a solid state film on a pre-patterned inter-digitated gold electrode

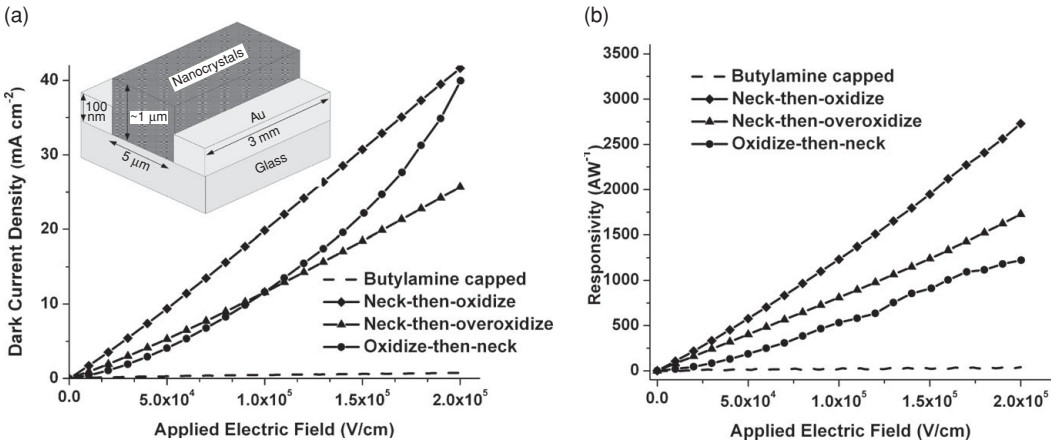


Figure 7.1 (a) Dark current density as a function of applied bias in PbS QD photoconductive devices. (b) Responsivity as a function of applied bias of photoconductive devices [45].

structure. The active area of the detector is determined by the 3mm length of the electrodes and their 5 μm gap spacing as shown in the inset of Figure 7.1(a).

Further reduction of nanocrystal spacing is desirable in order to further increase mobility in these films and therefore shorten the transit time of majority carriers. In order to eliminate any organic ligands from the nanocrystal surface and cause necking of the nanocrystals, the devices made of butylamine-capped nanocrystals, were dipped in a methanol solution.

Noise in photoconductors is determined by G–R and shot noise. There have been reports, however, of excess noise being observed in polycrystalline photoconductors [52, 53]. This excess noise is introduced by carrier transport along barriers formed at the interfaces of polycrystalline materials. These barriers, which are randomly modulated by G–R of thermal or photoexcited carriers, cause excess noise superimposed on the shot and G–R noise components.

Material processing routes have been developed to yield high carrier mobility and a long carrier lifetime in order to achieve high photoconductive gain. This, however, must be achieved without compromising the noise performance of the device. Konstantatos *et al.* [45] focused, therefore, on the effect of the sequence of the oxidation step on the noise current, in order to minimize the excessive noise. The following four classes of devices were investigated to concurrently optimize responsivity and noise:

(1) **Butylamine-capped:** devices made of butylamine exchanged nanocrystals.
(2) **Neck-then-oxidize:** devices made of butylamine exchanged nanocrystals followed by necking using methanol treatment.
(3) **Neck-then-over-oxidize:** devices made as neck-then-oxidize followed by further oxidation by annealing the devices in ambient atmosphere at 120 °C.
(4) **Oxidize-then-neck:** devices made of butylamine exchanged nanocrystals that had been exposed to ambient conditions during the final steps of the ligand exchange so that oxidation takes place at this stage. The devices were then treated with methanol for necking.

Films made of nanocrystals as-synthesized, capped with oleic acid, were insulating due to the suppression of carrier transport by the long oleate ligand. After ligand exchange, the film exhibited measurable conductivity and the carrier density reached 0.73mA/cm^2 at 100 V of bias. This is shown in Figure 7.1(a). The responsivity of this device was also measured as 27.7 A/W at 100 V, as shown in Figure 7.1(b).

Further reduction of inter-nanoparticle spacing via necking increased the dark current density to ~40 mA/cm^2 (a 57-fold increase) followed by an increase in responsivity of two orders of magnitude to 2700 A/W, pointing to an increase in the mobility. Similar effects of mobility increase have also been reported in CdSe nanocrystal films [54] using MeOH and NaOH treatments. To study the effect of the degree of oxidation on responsivity the device was oxidized further by annealing in ambient conditions (neck-then-overoxidize) which in turn led to a decrease in both responsivity and dark current density by a factor of ~1.6, which is suggestive of lower mobility.

The dark current–voltage characteristic indicates a field-activated transport mechanism when nanocrystals had been exposed to oxygen prior to film formation and necking (oxidize-then-neck). The superlinear behavior, shown in Figure 7.1(a), is believed to result from carrier transport limited by potential barriers formed by the oxides. When oxidation takes place prior to film formation and necking, it leads to oxide barriers being formed randomly on the nanocrystal surface. Upon necking, these potential barriers can be found at the points of nanocrystal necking affecting the energetics of carrier transport. In the case of neck-then-oxidize nanocrystals, however, oxidation takes place at the exposed nanocrystal surface sites. It should be noted that in the case of oxidize-then-neck nanocrystals, responsivity was as high as 10^3 A/W, lower by a factor of 3 compared to the neck-then-oxidize class of devices. The above findings suggest that the sequence of necking and oxidizing does not play a significant role in the responsivity performance of the photodetector.

A photodetector is ultimately characterized by its sensitivity. The noise current was therefore measured to investigate the effects of oxidation and barrier formation on the noise performance. The measured noise current density of the devices as a function of the dark current, which is the determining factor of noise in photoconductors, is illustrated in Figure 7.2(a). This representation allows comparison between devices with an eye to their deviation from the lower noise limit determined by the shot noise. Noise was measured at a modulation frequency of 30 Hz, which is relevant to imaging applications.

By comparing the noise of the butylamine capped, neck-then-overoxidize and oxidize-then-neck devices, it is evident that electronic barriers contribute high noise currents. The potential barriers in the butylamine-capped nanocrystal case are due to the ligands, whereas in the other two cases, barriers are formed by the surface oxides. The oxidation step in the fabrication process is thus of critical importance in the noise performance of the device.

In order to present the best performing photoconductive device, responsivity and noise current should be jointly taken into account to yield specific (or normalized) detectivity D^*. Figure 7.2(b) presents D^* of the devices described previously as a function of applied bias. The most sensitive device belongs to the neck-then-oxidize class of materials, whereas the least sensitive one is the device that had undergone oxidation

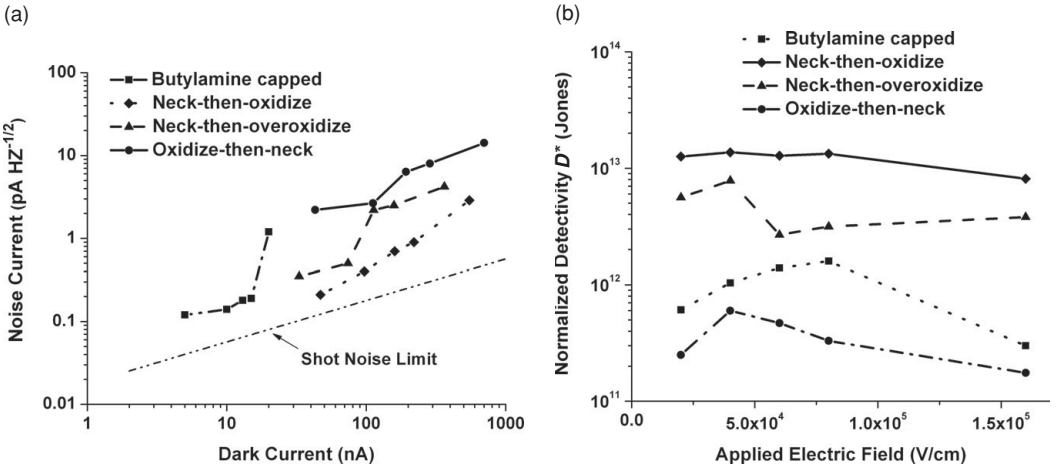


Figure 7.2 (a) Noise current dependence on the dark current level of the devices along with expected shot-noise-limited noise current. (b) The resultant normalized detectivity D^* as a function of applied bias for the various classes of devices investigated herein [45].

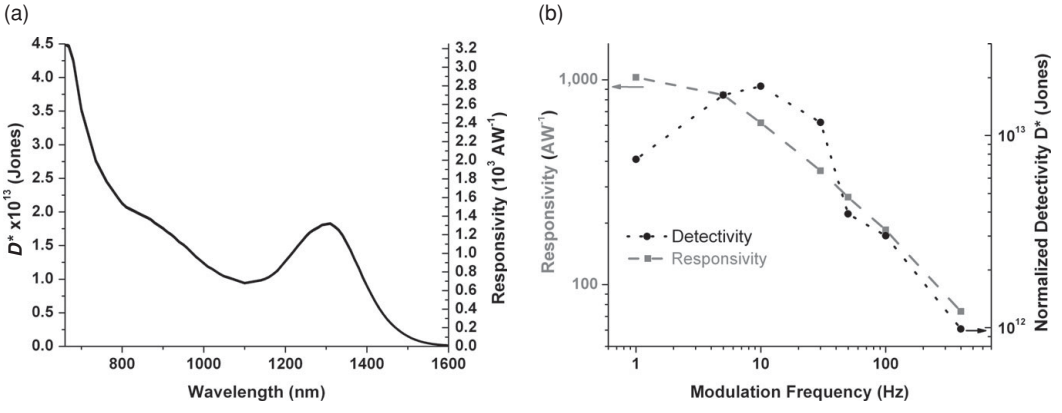


Figure 7.3 (a) Spectral responsivity and detectivity of a SWIR-sensitive PbS QD photodetector. (b) Responsivity and detectivity of the photodetector as a function of modulation frequency, showing a 3-dB bandwidth of ~18 Hz [45].

prior to necking (oxidize-then-neck). The best performing device demonstrates a D^* on the order of 10^{13} Jones.

The responsivity and resultant detectivity, as a function of wavelength, are illustrated in Figure 7.3(a). The photocurrent spectrum follows the absorption spectrum of nanocrystals covering a broad wavelength range from ~1.5 μm towards the visible. The spectral response of the device is suited for night vision and biomedical imaging applications addressing the 800–1400 nm spectrum with the high sensitivity of D^* greater than 10^{13} Jones. The responsivity and detectivity reported in Figure 7.3(a) were taken with an applied field of 8V/μm and a modulation frequency of 30 Hz, which are relevant to imaging applications. The modulation frequency response is shown in Figure 7.3(b),

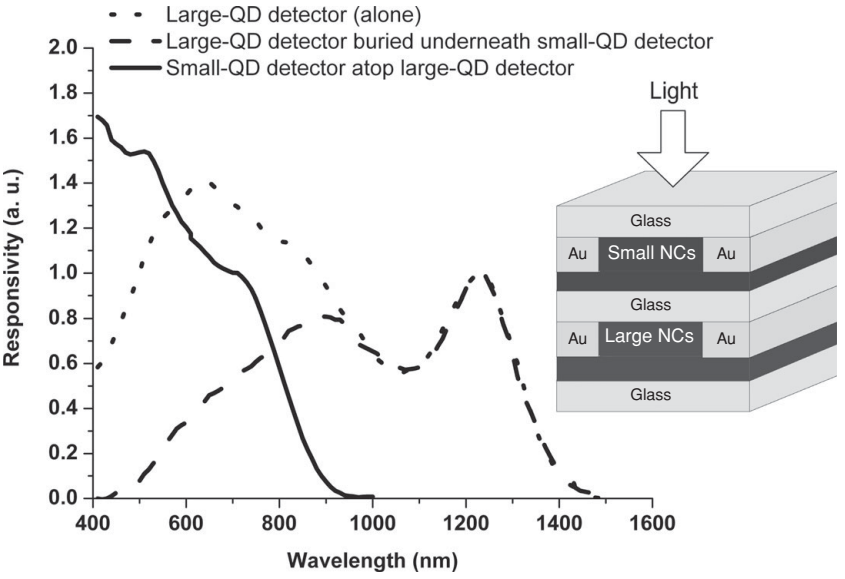


Figure 7.4 Spectral responsivity of the stacked device shown in the inset for dual-spectral detection. The small QD layer detects effectively the short wavelength light, whereas the longer wavelengths are detected from the large-QD layer. The responsivity of the large-QD device before the stacking is also shown to demonstrate the filtering functionality and spectral selectivity offered by the top photodetector.

where responsivity is plotted as a function of modulation frequency with a bias of 40 V and wavelength of 1300 nm. The device exhibits an effective 3-dB bandwidth of ~18 Hz. The temporal response of the device is limited by the lifetime of the minority carrier, which is dictated by the depth of the electron sensitizing trap states [35].

7.4.2 Visible-wavelength and multispectral photodetection

The promising performance of the SWIR photodetector motivated the work on visible wavelength photodetection; the quantum size effect offered by QDs was exploited to demonstrate a visible solution-processed PbS colloidal QD photoconductive detector [55]. The solution processibility combined with spectral tunability offered by CQDs was then exploited to demonstrate a multispectral photodetector promising for monolithic integration.

The expected benefits of solution-processed QD detectors can be seen from the facile tandem configuration of two photodetectors addressing complementary spectra of detection. This was achieved using the same semiconductor (PbS) in the form of QDs thereby enabling bandgap selectivity that is a priori determined by the size of the dots. The inset of Figure 7.4 shows the photodetector architecture that demonstrated dual-spectral detection. The device consists of two stacked PbS QD photodetectors of different nanocrystal size. The top detector is fabricated from small PbS QDs that detect effectively in the visible part of spectrum. The buried photodetector consists of larger PbS

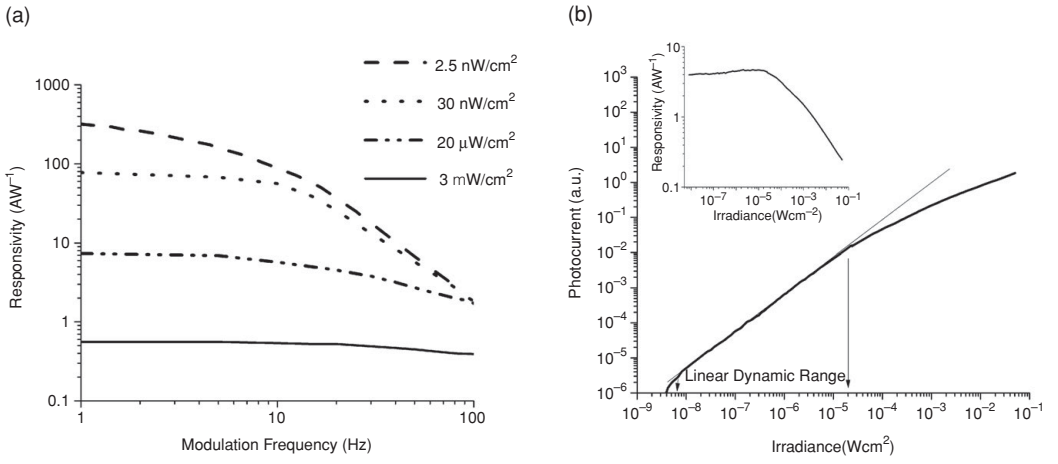


Figure 7.5 (a) Responsivity dependence on the modulation frequency at different illumination intensities. (b) The photocurrent versus optical illumination dependence reveals a dynamic range of 7.5 orders of magnitude (conventionally expressed as 150 dB) and a linear dynamic range in excess of 60 dB. The inset shows the responsivity as a function of optical intensity [55].

QDs to detect light in the SWIR and near-IR. This layer is prone to detecting light in the visible. The top layer, however, serves not only as a photosensitive layer of the visible but also as a longpass filter that prevents visible photons from reaching the buried detector. The sensitivity of the buried photodetector is thus suppressed in the visible part of spectrum.

The resultant responsivity spectra of the photodetectors are shown in Figure 7.4. The responsivities of the large-QD device in both cases have been normalized to their exciton peak value at 1230 nm. The large-QD photodetector in the stacked structure preserves responsivity at wavelengths longer than 900 nm, whereas it shows a significant decrease in responsivity at shorter wavelengths following the absorption onset of the small-QD photodetector.

The effect of the trap states in QD photodetectors on the optoelectronic characteristics of the device was further investigated. In particular, frequency response and responsivity, two features of practical interest, are measured at various optical intensities [55]. Figure 7.5(a) illustrates responsivity as a function of modulation frequency for a number of different optical intensities. The decrease of responsivity with increasing optical power originates from filling of the lowest-lying, longest-lived trap states that provide the highest photoconductive gain at low intensities. As intensity increases the effective responsivity drops as a result of the increasing contribution to photocurrent from the shorter-lifetime, shallower sensitizing centers. The 3-dB bandwidth increases from ~8 Hz at 5 nW/cm^{2}to ~17 Hz at 60 nW/cm^2 and beyond 300 Hz at 6 mW/cm^2. The 3-dB bandwidth increase is followed by a two-orders-of-magnitude decrease in responsivity, a mechanism potentially desirable as a self-limiting gain control.

Another significant property of photodetectors is their dynamic range, which is the intensity range within which the detector can distinguish between different optical

intensities. Dynamic range is typically given as $20\log(P_{max}/P_{min})$, where P_{max} is the maximum impinging power before saturation – a condition where photocurrent ceases to increase with increasing optical power; P_{min} is the minimum detectable optical power – or NEP.

In order to assess the impact of high-gain trap state filling on the dynamic range of the detector, the dependence of photocurrent on optical intensity at a modulation frequency of 30 Hz was measured. A monotonic, though at high intensities sublinear, dependence of photocurrent on intensity over more than 7.5 orders of magnitude in incident intensity corresponding to over 150 dB of intensity dynamic range (Figure 7.5(b)) was observed. The linear part of the curve extends for over 3 orders of magnitude corresponding to over 60 dB of intensity linear dynamic range, which is what is typically required for most imaging applications. At higher optical intensities, however, the detector exhibits an inherent sublinear transformation of the optical signal to electrical output desired for increased intra-scene dynamic range [56]. The inset of Figure 7.5(b) shows the onset of responsivity decrease, which is due to the filling of the high gain trap states at higher intensities.

7.4.3 Control of temporal response in photoconductive detectors via trap state engineering

Highly sensitive QD photodetectors have been achieved by sensitizing CQDs using surface trap states to prolong the carrier lifetime. The photoconductive gain, which is responsible for high sensitivity, is given by τ_c/τ_t, where τ_t is the time for the flowing carrier to transit the extent of the device, and τ_c is the carrier lifetime [34]. From a sensitivity point of view alone, this argues for longer trap state lifetimes.

Also important in photodetection is the temporal response of the device. In video frame rate imaging applications, for example, if the response of a photodetector to an optical transient exceeds the frame period, then lag, or ghosting, will be perceptible in the image. Temporal responses having time constants in the range of tens of milliseconds are thus typically required. The temporal response in photoconductive detectors is largely determined by the carrier lifetime. The challenge of practical photoconductive photodetector design is thus to establish a suitable balance between gain and temporal response; and to control material composition with care to implement the resultant design.

The energy levels associated with trap states in PbS CQD photodetectors that exhibit gains of the order of 100 A/W have been investigated using responsivity quenching and transient photocurrent spectroscopy [57]. Three sensitizing centers at 0.1, 0.2, and 0.34 eV from the conduction band resulted in carrier lifetimes of ~30 ms, 300 ms, and 2000 ms. Although the shortest lifetime of 30 ms is suitable for many imaging applications, the longer ones, which dominate at lower optical intensities in view of their deeper energy levels, introduce unacceptable lag.

In this section we consider the correlation between the oxide species on the QD surface and the resultant sensitizing centers with measured time constants and their related trap state energies [58]. This study led to a novel material processing methodology that facilitates suppression of the longest lived trap states, yet preserves sensitization only via

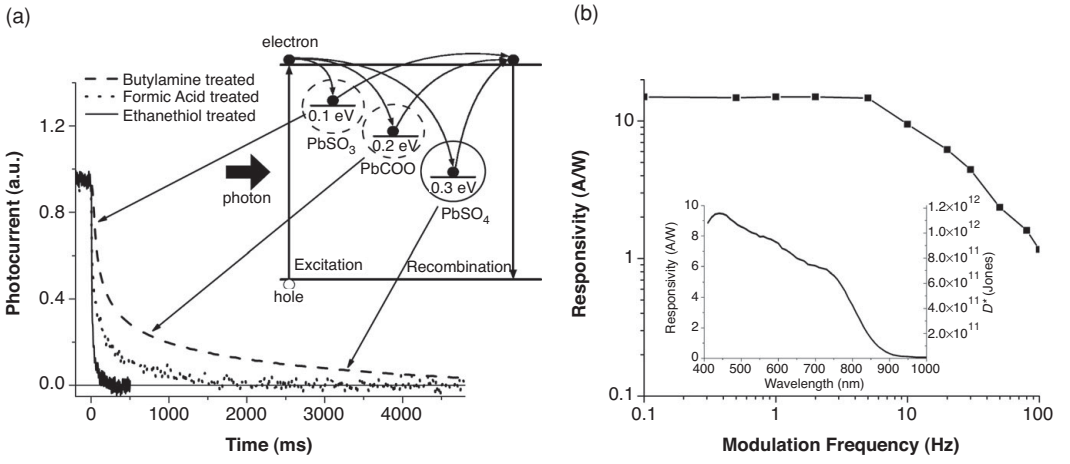


Figure 7.6 (a) Temporal response of the photocurrent in butylamine, formic acid and ethanethiol treated nanocrystal films. The inset shows the associated trap state levels responsible for the corresponding temporal components of the photocurrent [58]. (b) Frequency response of the ethanethiol treated PbS QD detector demonstrating a flat response up to ~10 Hz and 3-dB bandwidth of 30 Hz. The inset shows the spectral responsivity of this detector and the normalized D^* [58].

the shortest (temporally), thus the shallowest (energetically), trap state. For the purpose of this study, photoconductive devices made of nanocrystals with ligands of various head functional groups attached to the nanocrystal surface were investigated. Three types of ligands with different functional groups were employed: butylamine treated nanocrystals, formic acid treated nanocrystals, and ethanethiol treated nanocrystals.

We begin by looking at the correlation between nanocrystal surface species and the temporal response in butylamine treated nanocrystal devices. These devices exhibit multiple photocurrent decay time constants of ~60 ms, 300 ms, and 2000 ms, at room temperature (Figure 7.6(a)). X-ray photoelectron spectroscopy (XPS) analysis of nanocrystals treated using butylamine revealed the presence of lead sulfate ($PbSO_4$), lead sulfite ($PbSO_3$), and lead carboxylate attributable to oleic acid ligands attached to the nanoparticles' surfaces. The number of species found on the nanocrystal surface ($PbSO_4$, $PbSO_3$, and Pb carboxylate) is equal to the number of the photocurrent decay time constants; this suggests that each of the identified species may be responsible for a single time constant, associated with the energy depth of the trap.

We next consider the correlation between the lead carboxylate peak (due to the oleic acid–Pb bond) and a corresponding sensitizing trap state that has a specific temporal response. Nanocrystal films were treated with formic acid to exchange the long oleic acid ligand with a shorter one, preserving the carboxylic functionality to prevent sulfate formation. As a result, the internanoparticle spacing was reduced while preserving the carboxylate moiety bound to Pb atoms on the nanocrystal surface. Temporal measurements of photocurrent response revealed a main time constant of ~420 ms (Figure 7.6(a)) and also a faster component with time constant ~33 ms. XPS, in this case, revealed

the presence of Pb carboxylate group as well as $PbSO_3$. This evidence suggests that either Pb carboxylate or $PbSO_3$ serves as a sensitizing species having the (undesirably long-lived) time constant of ~420 ms.

Complete removal of the oleate ligands was sought, in order to elucidate which among the carboxylate/sulfite species is responsible for the ~420 ms time constant. A ligand that is short enough to promote transport and lacking carboxylate functionality was thus sought. Ethanethiol was chosen for its short length and its thiol moiety, which was expected to bind more strongly with Pb than the carboxylic group, therefore enabling effective ligand exchange. Photoconductive devices were fabricated from thiol-treated nanocrystals. XPS confirmed the complete removal of Pb carboxylate following ethanethiol treatment, leaving $PbSO_3$ as the sole oxidized species. Transient photocurrent measurements showed that ethanethiol treated nanocrystal films exhibited a single transient component having a ~27 ms time constant at room temperature (Figure 7.6(b)). These optimized devices demonstrated photoconductive gains on the order of 10 A/W under an electric field of 2V/μm and normalized detectivity of 10^{12} Jones across the visible as shown in Figure 7.6(b).

7.5 CQD based phototransistors

Central to any high performance photodetector is the carrier mobility of the semiconductor. There have been major improvements in carrier mobility of nanocrystal solids that have led to a photoconductive gain on the order of 10 A/W and a temporal response of ~2 ms [59]. Another important factor is the quantum efficiency, which indicates how efficiently photogenerated excitons dissociate and primary photocarriers are extracted from the device. Higher quantum efficiency necessitates surface passivation from midgap trap states and high carrier mobility. An alternative approach has been introduced in which the photon absorption takes place in the QD phase and the carrier circulation occurs in the graphene channel of a phototransistor architecture [60]. This makes it possible to combine passivated PbS QD films with exceptionally high carrier mobilities in excess of 1000 $cm^2/(V\ s)$ offered by the graphene channel. The QD film thus acts as a photogate layer of a graphene transistor to demonstrate a phototransistor with a gain in excess of 10^6 at an applied field of 0.1V/μm and a reported detectivity on the order of 7×10^{13} Jones.

QDs are deposited on top of a graphene channel as shown in Figure 7.7(a), which sits on top of a heavily doped Si substrate and a 300 nm thick SiO_2 layer to form the back-gate. Upon illumination photogenerated holes are transferred from the QD layer to the graphene channel as illustrated by the band alignment in Figure 7.7(b). This hole transfer has been monitored by a progressive shift of the Dirac peak in the graphene resistance towards higher back-gate potentials (Figure 7.7(c)), which in turn corroborates the photodoping of graphene with holes: illumination causes the Dirac point to shift to higher values of V_{BG}, and thus the resistance of the graphene channel decreases for $V_{BG} < V_D$, where the carrier transport is hole dominated, whereas it increases for $V_{BG} > V_D$, where carrier transport is electron dominated. For $V_{BG} > V_D$, illumination

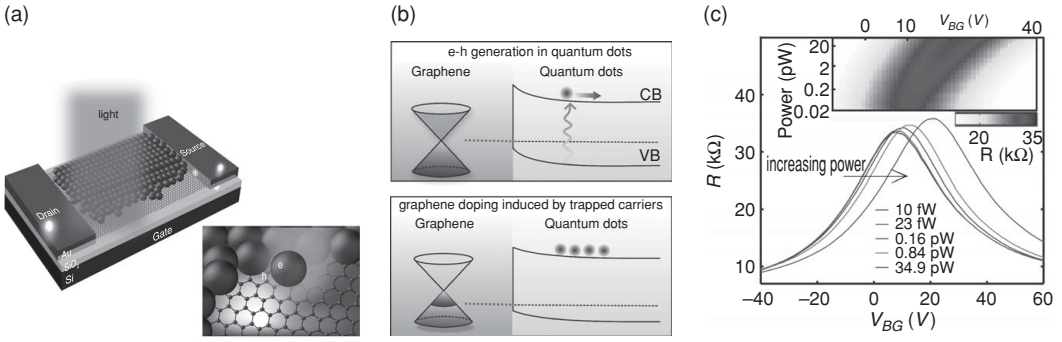


Figure 7.7 (a) Device structure of the graphene–QD phototransistor. (b) Band alignment at the graphene–PbS QD interface. (c) The shift in the Dirac peak of graphene upon increasing levels of illumination suggests transfer of photogenerated holes from the QD photogating layer to the graphene channel. Reprinted with permission from [60].

leads to resistance increase or current quenching, which is due to recombination that takes place between photogenerated holes transferred from the QDs to graphene and electrons induced by the backgate. As long as the photogenerated electrons remain trapped in the QD phase due to the existence of the sensitizing centers, as discussed in Section 7.4, the negatively charged QDs induce positive carriers in the graphene sheet through capacitive coupling, which explains the observed shift of the Dirac peak towards higher backgate voltages. These positive charges in the graphene can thus be recirculated in the graphene channel, provided Ohmic contacts in the source and the drain, leading to the observation of very high photoconductive gain. The photosensitivity of the device is demonstrated by the large shifts in the V_D of 20 V/pW, enabling the detection of incident power on the order of 10 fW.

Figure 7.8 illustrates the spectral responsivities of two devices that consist of PbS QDs which have their first exciton peaks at ~950 nm (upper panel) and at ~1450 nm (bottom panel). The photocurrent response follows the absorption of the PbS QDs as the sole source of photocarrier generation. These measurements therefore demonstrate the spectral selectivity of the graphene–QD phototransistors that is offered by the bandgap tunability of the QDs. At low excitation power, responsivity as high as $\sim 10^8$ AW^{-1} has been achieved, corresponding to a photoconductive gain of 5×10^7 at an excitation wavelength of 600 nm. This is in agreement with the short transit times that holes require to traverse the graphene channel ($\tau_{transit}$) with a mobility on the order of 10^3 $cm^2/(Vs)$ and the prolonged lifetime ($\tau_{lifetime}$) of the trapped in the PbS phase electrons which is on the order of 20 ms.

An additional feature that this device offers is the utilization of the back-gate as a control to tune the responsivity of the device electrically on demand. Graphene transistors offer gate-tunable carrier density and polarity which enables the sensitivity to be tuned and also to operate the detector with an electronic shuttering reset functionality, both of which are useful in imaging applications. Figure 7.9(a) plots the dependence of the responsivity on the applied back-gate voltage. By tuning the Fermi energy close to the Dirac point at $V_{BG} = 4$V, the responsivity completely vanishes, as in this condition the band alignment of the graphene and the QDs is such as to prevent

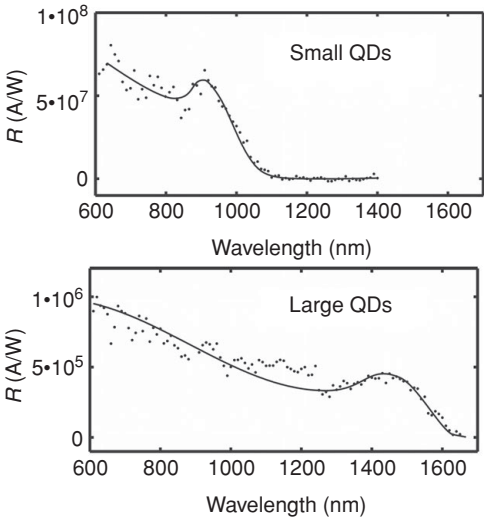


Figure 7.8 Spectral responsivity of graphene–QD phototransistors employing two different sizes of QDs to cover the vis–NIR (upper panel) and SWIR–vis (lower panel) parts of spectrum. The achieved responsivities are in both cases in excess of 10^6 A/W. Reprinted with permission from [60].

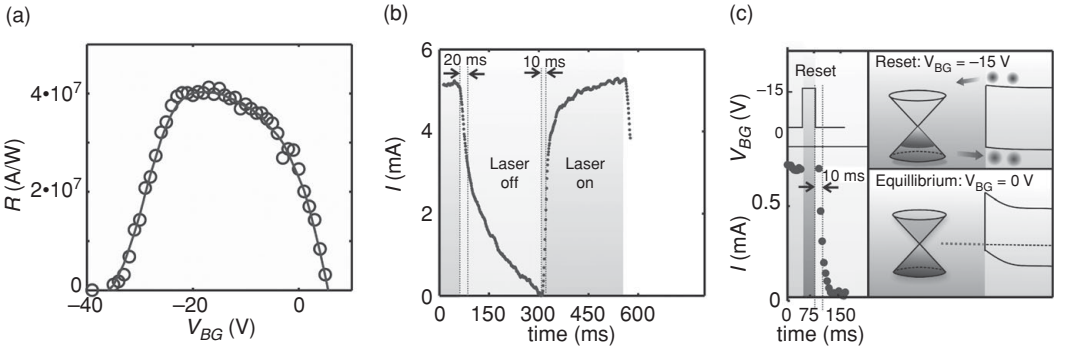


Figure 7.9 (a) Responsivity as a function of the back-gate bias of the graphene channel. (b) The temporal response of the photocurrent in pulsed illumination shows a relaxation time of hundreds of milliseconds. (c) The use of a reset pulse in the back-gate accelerates the temporal response of the detector to 10–20 ms. Reprinted with permission from [60].

transfer of photogenerated holes from the PbS to the graphene. This feature demonstrates the potential of this device as a back-gate-tunable ultrahigh-gain phototransistor.

The back-gate tunability of the graphene Fermi level can also be exploited to develop a reset functionality, similar to an electronic shutter, suited to video-frame-rate imaging applications. Figure 7.9(b) shows the temporal response of the photodetector which is dominated by two components: one with faster decay of about 10–20 ms (corresponding to 50% decay) and a slow component on the order of seconds. The latter, stems from trapped electrons in deep sensitizing trap states in the PbS QDs and it is unwanted for most imaging applications. The employment of a pulsed back-gate signal has been

found to act as a purging mechanism of these trapped electrons by flushing the device with excess of holes into the PbS layer to accelerate recombination; This, in turn leads to significantly accelerated decay of photocurrent (Figure 7.9(c)) with a relaxation time of 20 ms.

7.6 CQD photodiodes

The previous sections showed that CQD photoconductive photodetectors may yield sensitivities up to 10^{13} Jones. These remarkable sensitivities result from high photoconductive gain and low noise current. Photoconductive gain, however, requires carrier lifetimes that limit the temporal response of the devices to a few tens of milliseconds. Therefore, applications requiring high modulation frequencies, such as machine vision, high-speed process monitoring, and optical communications, are not generally addressed by this approach. Emerging classes of photodetectors for these applications must demonstrate both high sensitivity and high response speed if they are to compete in performance with photodetectors fabricated from traditional crystalline semiconductors.

An alternative to the photoconductor approach, the photodiode, is therefore explored in this section. Prior to the work of Clifford *et al.* [61], there were been no reports of CQD photodiodes that can achieve high speed and sensitivity simultaneously. The first report of a fast CQD detector (50 kHz bandwidth) demonstrated sensitivity in the visible with estimated $D^* \sim 10^8$ Jones [62]. This device, a diode formed by a junction between CdSe nanocrystals and a conductive polymer, had a zero-bias EQE of ~0.15% at the first excitonic wavelength of ~560 nm.

For a Schottky-barrier type photodiode formed between the nanocrystal film and a metal, efficient carrier transport and a metallurgical junction with a large built-in potential could potentially lead to the desired combination of sensitivity and speed. Nanocrystal films provide a number of chemically-tunable degrees of freedom which control their macroscopic electronic properties. The spacing between individual nanocrystals is controlled by the length of the organic ligands used to passivate their surfaces. This has been shown to be a determining factor of the carrier mobility. The consistency of surface passivation is also important, as it limits oxidation and other chemical modification of the nanocrystal surface. Oxidation provides a path to nanocrystal doping; however, uncontrolled surface variation leads to interface states and a reduction of the built-in potential. Noise performance in diodes is determined by the shunt resistance, which in turn depends on the energetic barrier associated with the metallurgical junction. Thus, this interfacial control is essential for fabricating high sensitivity photodiodes. Colloidal nanocrystals provide access and control of their surface properties via careful choice of the passivating ligands, yielding simultaneously high mobilities and a lack of surface states.

Photodiodes were formed between a PbS nanocrystal film and an aluminum contact (Figure 7.10(a)). A planar transparent ITO thin film formed the opposing ohmic contact. Light incident through the glass substrate generated electrons and holes in CQD film that were collected at the Al and ITO contacts, respectively. The energy band diagram in Figure 7.10(b) shows the Schottky barrier formed at the Al–PbS CQD interface and the built-in potential derived from the difference in work function between the nanocrystals

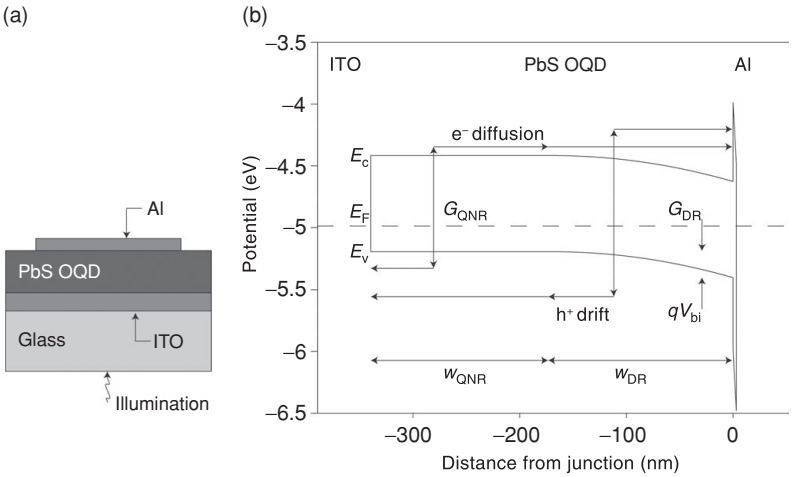


Figure 7.10 (a) The device structure in which a layer of PbS QDs is sandwiched between ITO and Al. (b) Band-diagram of the Schottky PbS QD photodetector. The detector consists of a depletion layer formed at the junction between PbS and Al, and a quasi-neutral region formed near the PbS–ITO ohmic contact. Reprinted with permission from [61].

and the metal contact [63]. Charge transfer between the semiconductor and the metal results in the formation of a wide depletion region in the nanocrystal film, while the remaining volume of the film is a quasi-neutral region of p-type semiconductor with no net charge or electric field. The formation of a Schottky barrier limits majority carrier (hole) injection from the Al contact, resulting in highly rectifying dark *I–V* characteristics [63].

Due to the insulating properties of oleic acid, the capping molecule of as-synthesized nanocrystals, a ligand exchange process was adopted to replace it with short butylamine ligands. The lack of stability of amines with respect to PbS nanocrystal forming a consistent Schottky barrier with Al imposed the employment of a bidendate linker molecule that would instead utilize a much stronger binding interaction with PbS nanocrystals providing higher stability and preserving at the same time the close-packing of nanocrystals. Benzenedithiol (BDT) was used for this purpose.

It was found, however, that BDT's thiol endgroup chemically reduces the surface of PbS nanocrystals by removing oxidation species that are known to act as p-type dopants. This reduction suppresses the effective doping and p-type semiconductor characteristics, and thus diminishes the built-in potential of the Schottky barrier from which the diode behavior originates. At the final stage, a reoxidation of the nanocrystal film was performed to restore the degree of effective doping required for creating Schottky barriers with a large built-in potential and energy barrier. This architecture achieved an EQE of 17% at 1450 nm and reaches a maximum of 52% at 580 nm. D^* was on the order of 10^{11} Jones at 1450 nm at room temperature, whereas it increased to order of 10^{12} Jones for temperatures below 255 K, which is reachable with thermoelectric cooling systems.

The modulation frequency response of the photocurrent is illustrated in Figure 7.11(a) to demonstrate the superior performance of the photodiode's temporal response. The

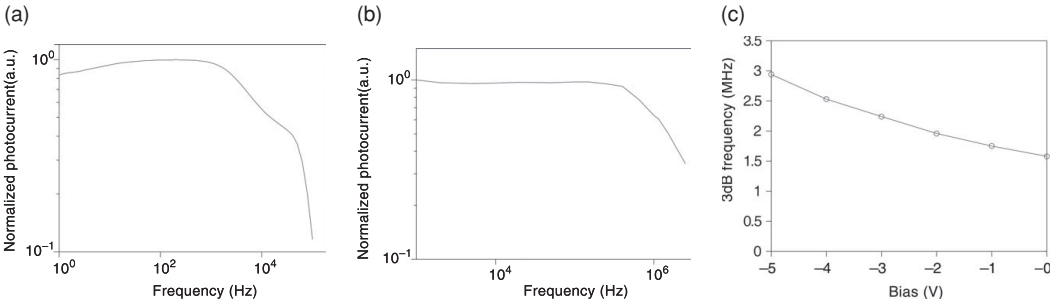


Figure 7.11 (a) Frequency response of the Schottky diode photodetector, demonstrating a 3-dB bandwidth in excess of 10 KHz. (b) Frequency response of the fully depleted Schottky diode photodetector, demonstrating a 3-dB bandwidth in excess of 1 MHz. (c) The dependence of the 3-dB bandwidth on the applied reverse bias shows a two-fold increase at –5 V of applied bias. Reprinted with permission from [61].

3-dB frequency is 10.7 kHz at zero bias and 1.95 μW/cm^2. At each bias, the transient response is composed of two distinct components: an initial, fast, component, linearly increasing with bias; and a slower component that exponentially settles to a steady state. These temporal components correspond to the time required to reach the steady state in the quasi-neutral region and the transit time of the depletion region, ~500 μs and ~10 μs, respectively. The fast photocurrent component is attributed to carriers generated in the depletion region and quickly swept out by a drift current proportional to the built-in electric field. The slower component is attributed to electrons generated in the quasi-neutral region which must diffuse to the depletion region before they are effectively swept out by the built-in electric field. The rise time of this component is the time required for generation, diffusion, and recombination processes in the quasi-neutral region to reach a steady state, and is dependent on the width of the quasi-neutral region (w_{QNR}) and inversely dependent on the electron diffusion coefficient (D_e).

These findings pointed towards the following hypothesis: an efficient and much faster photodiode could be developed if carrier transport relied solely on drift. In a fully-depleted photodiode all photogenerated electrons and holes are swept directly to the contacts by the electric field from the built-in potential of the junction and any externally applied bias. A fully-depleted photodiode could thus be developed by reducing the thickness of the film to match the depletion region width (180 nm). This would result in the demonstration of a single temporal component of photocurrent limited only by the drift transit time (~300 ns). The flatness of the frequency response of the fully-depleted photodiode extends beyond 100 kHz and the 3-dB frequency of this device ranges from 1.6 MHz at zero bias to >2.9 MHz at −5V bias, as shown in Figures 7.11(b) and 7.11(c). The increase in operating speed with applied bias is due to the reduction in carrier transit time with increasing electric field in the depletion region. By further optimization of the material for higher carrier mobility the ultimate normalized detectivity of the fast device was on the order of 10^{11} Jones at room temperature, representing the best performing solution-processed photodiode combining high sensitivity and MHz frequency response at that time.

It should be noted that since then, significant improvements in carrier collection efficiencies have been achieved in CQD photodiodes via further ligand engineering, which have dramatically increased the carrier mobilities and reduced the intrinsic doping of PbS QDs, which in turn yielded thicker depletion widths. The introduction of a CQD heterojunction relying on p-type PbS QDs and n-type TiO_2 electrodes has also led to a reduced recombination dark current in short-circuit conditions and lower reverse-bias dark currents, indicating that significantly better sensitivities can be achieved. Such structures are discussed in detail in Chapter 10 as they have found applications in CQD solar cells.

7.7 Conclusions – summary

Solution-processed optoelectronic materials such as CQDs offer dramatically lowered manufacturing cost and ease of large-area fabrication, including on flexible substrates. Significant further advantages in an imaging context include: high pixel count and small pixel size; outstanding sensitivity, including gain, reported herein; and access to new spectral regimes and multispectral capabilities outside silicon's realm.

Control over material definition on the nanoscale also enables device functionalities that are impossible to achieve with conventionally-grown semiconductors. Device physics and performance in colloidal nanocrystal devices, unlike those in bulk semiconductors, are determined by the nanocrystal surface and size. These two factors can be tuned via wet chemistry to tailor the material properties: the absorption and emission spectra can be tailored by choice of the nanocrystal size; mobility may be controlled using the new generation of capping ligands and QD packing [59]; carrier doping can be transformed between n-type and p-type by surface atomic modification [64]; carrier lifetime, which is determined by surface traps, can be tuned via selective passivation of the nanocrystal surface trap states.

Further progress has also been made in solution-processed nanocrystalline photodetectors towards expansion of spectral sensitivity in the mid-wavelength IR up to 3 μm using HgTe nanocrystals [65–67] and into the UV using visible-blind ZnO QD photodetectors [67]. Their facile integration into CMOS imaging sensor arrays has been demonstrated [68] and fulfills the expectations of this technology to revolutionalize the CMOS imaging market. Another emerging field of research is the exploration of candidate materials that do not contain heavy metals, for sensitive photodetection. Bi_2S_3 nanocrystalline sensitive photodetectors in the visible part of spectrum have been reported [69]. A successful demonstration of the multiple exciton generation (MEG) effect in PbS QD photodetectors showed an increase in the absorption-normalized responsivity in the near-UV part of spectrum at ~3 times the bandgap of the material, which was attributed to MEG assisted sensitization [70]. CQD photodetectors have also been reported as a candidates for near-field imaging applications [71].

CQD photodetectors are undoubtedly an extremely promising field of research and in Table 7.1 we summarize a concise, non-exhaustive list of achievements in the field.

Table 7.1. Summary of the progress in CQD photodetectors (*D** is inferred based on the shot noise limit)

Ref	Year	λ (nm)	EQE (%) / Responsivity (A/W)	*D** measured (Jones)	*D** inferred (Jones)	3 dB BW (Hz)	Mechanism	Material	Features
[62]	2005	400–700	0.2%		10^8	5×10^4	PD	CdSe QDs	Early QD photodiode
[45]	2006	Vis–1300	2700 A/W	2×10^{13}	5×10^{13}	2×10^1	PC	PbS QDs	Record sensitivity; pure QD device
[55]	2007	Vis–850	120 A/W	5×10^{12}	3×10^{13}	2×10^1	PC	PbS QDs	Visible-only device using ultra-confined dots
[65]	2007	Vis–3000	4.4 A/W	3×10^{10}		10^1	PC	HgTe QDs	Long wavelength operation
[72]	2008	350–650	50 A/W		5×10^{12}		PC	P3HT+PCBM+CdTe QDs	Sensitive heterojunction device
[73]	2008	Vis–950	10 A/W		1.3×10^{13}	5×10^1	PC	PbS QDs	High uniformity device
[58]	2008	Vis–950	12 A/W	10^{12}		3×10^1	PC	PbS QDs	Single trap timeconstant
[69]	2008	Vis –900	20 A/W	10^{11}		2×10^1	PC	Bi_2S_3Nanocrystals	Pb-free, single time constant
[67]	2008	370–395	61 A/W		1.3×10^{15}	10^0	PC	ZnO QDs	UV sensitivity
[70]	2009	250–930	18 A/W		1.5×10^{14}	3×10^1	PC	PbS QDs	Multiexciton-generation-enhanced
[61]	2009	Vis–1600	0.2 A/W	10^{12}		10^6	PD	PbS QDs	MHz response in fully depleted photodiode
[68]	2009	Vis–1300	51%	2×10^9		2×10^3	PD	PbS QDs + PCBM + P3HT	Integrated into an image array
[66]	2011	Vis–5000	10% 100 mA/W	10^9at 120 K			PC	HgTe QDs	Ultra-long wavelength operation
[59]	2011	Vis	~10 A/W	10^{13}		400	PC	CdSe QDs	High mobility – band-like carrier transport
[60]	2012	Vis–1600	$\sim10^7$ A/W	7 10^{13}		~30	PC	Graphene-QD phototransistor	Ultra-high gain and sensitivity

References

1 L. M. Vatsia, Atmospheric optical environment, *Research and Development Technical Report ECOM-7023* (1972).
2 M. Ettenberg, A little night vision, *Advanced Imaging*, **20** (2005), 29–32, 2005.
3 X. Gao, Y. Cui, R. M. Levenson, L. W. K. Chung, S. Nie, In vivo cancer targeting and imaging with semiconductor quantum dots, *Nature Biotechnology*, **22**:18 (2004), 969–976.
4 Y. T. Lim, S. Kim, A. Nakayama, *et al.*, Selection of quantum dot wavelengths for biomedical assays and imaging, *Molecular Imaging*, **2** (2003), 50–64, 2003.
5 S. Kim, Y. T. Lim, E. G. Soltesz, *et al.*, Near-infrared fluorescent type II quantum dots for sentinel lymph node mapping, *Nature Biotechnology*, **22** (2004), 93–97.
6 R. Schödel, T. Ott, R. Genzel, *et al.*, A star in a 15.2-year orbit around the supermassive black hole at the centre of the Milky Way, *Nature*, **419** (2002), 694–696.
7 W. Herrmann, M. Blake, M. Doyle, *et al.*, Short wavelength infrared (SWIR) spectral analysis of hydrothermal alteration zones associated with base metal sulfide deposits at Rosebery and Western Tharsis, Tasmania, and Highway-Reward, Queensland, *Economic Geology*, **96** (2001), 939–955.
8 M. Golic, K. Walsh, P. Lawson, Short-wavelength near-infrared spectra of sucrose, glucose, and fructose with respect to sugar concentration and temperature, *Applied Spectroscopy*, **57**(2) (2003), 64A-85A and 117–243.
9 J. Kang, A. Borkar, A. Yeung, *et al.*, Short wavelength infrared face recognition for personalization, *IEEE International Conference on Image Processing,* pp. 2757–2760, 8–11 Oct., 2006.
10 J. Nakamura, *Image Sensors and Signal Processing for Digital Still Cameras*. Boca Raton, FL: Taylor&Francis/CRC Press, 2006.
11 E. R. Fossum, CMOS image sensors: Electronic camera-on-a-chip, *IEEE Transactions on Electron Devices*, **44** (1997), 1689–1698.
12 J. A. Theil, a-Si:H photodiode technology for advanced CMOS active pixel sensor imagers, *Journal of Non-Crystalline Solids*, **299–302** (2002), 1234–1239, 2002.
13 Y. Vygranenko, J.H. Chang, A. Nathan, Two-dimensional a-Si:H n-i-p photodiode array for low-level light detection, *IEEE Journal of Quantum Electronics*, **41** (2005), 697–703, 2005.
14 D. L. Staebler, C. R. Wronski, Reversible conductivity changes in discharge-produced amorphous Si, *Applied Physics Letters*, **31** (1977), 292–294.
15 P. P. Web, R. J. McIntyre, J. Conradi, Properties of avalanche photodiodes, *RCA Reviews*, **35** (1974), 235–278.
16 A. Biber, P. Seitz, H. Jackel, Avalanche photodiode image sensor in standard BiCMOS technology, *IEEE Transactions on Electron Devices*, **47** (2000), 2241–2243.
17 T. Hoetler, Broad spectrum performance via VisGaAs. *Advanced Imaging*, **18** (2003), 14–19.
18 J. C. Campbell, A. Mdhukar, Quantum dot infrared photodetectors, *Proceedings of the IEEE*, **95**, No. 9 (2007), 1815–1827.
19 S. Krishna, S. D. Gunapala, S. V. Bandara, C. Hill, D. Z. Ting, Quantum dot based infrared focal Plane arrays, *Proceedings of the IEEE*, **95**:9 (2007), 1838–1852.
20 P. Bhattacharya, X. Su, G. Ariyawansa, G. U. Perera, High temperature tunneling quantum-dot intersublevel detectors for mid-infrared to terahertz frequencies, *Proceedings of the IEEE*, **95**, No. 9 (2007), 1828–1837.
21 P. Bhattacharya, Z. Mi, Quantum-dot optoelectronic devices, *Proceedings of the IEEE*, **95**, No. 9 (2007), 1723–1740.

22 S. B. Samavedam, M. T. Currie, T. A. Langdo, E. A. Fitzgerald, High-quality germanium photodiodes integrated on silicon substrates using optimized relaxed graded buffers, *Applied Physics Letters*, **73** (1998), 2125–2127.
23 O. Qasaimeh, Z. Ma, P. Bhattacharya, E. T. Croke, Monolithically integrated multichannel SiGe/Si p–i–n–HBT photoreceiver arrays, *Journal of Lightwave Technology*, **18** (2000), 1548–1553.
24 L. Colace, G. Masini, S. Cozza, *et al.*, Near-infrared camera in polycrystalline germanium integrated on complementary metal oxide semiconductor electronics, *Applied Physics Letters*, **90** (2007), 011103.
25 S. Coe, W. K. Woo, M. Bawendi, V. Bulovic., Electroluminescence from single monolayers of nanocrystals in molecular organic devices, *Nature*, **420** (2002), 800–803.
26 G. Konstantatos, C. Huang, L. Levina, Z. Lu, E. H. Sargent, Efficient infrared electroluminescent devices using solution-processed colloidal quantum dots, *Advanced Functional Materials*, **15** (2005), 1865–1869.
27 S. Hoogland, V. Sukhovatkin, I. Howard, *et al.*, A solution-processed 1.53 μm quantum dot laser with temperature-invariant emission wavelength, *Optics Express*, **14** (2006), 3273–3281.
28 E. J. D. Klem, L. Levina, E. H. Sargent, PbS quantum dot electroabsorption modulation across the extended communications band 1200–1700 nm, *Applied Physics Letters*, **87** (2005), 053101.
29 E. H. Sargent, Colloidal quantum dot solar cells, *Nature Photonics*, **6** (2012), 133–135, 2012.
30 I. Gur, N. A. Fromer, M. L. Geier, A. P. Alivisatos, Air-stable all-inorganic nanocrystal solar cells processed from solution, *Science*, **310** (2005), 462–465, 2005.
31 S. A. McDonald, P. W. Cyr, L. Levina, E. H. Sargent, Photoconductivity from PbS Nanocrystal / MEH-PPV composites for solution-processible, quantum-size tunable infrared photodetectors, *Applied Physics Letters*, **85** (2004), 2089–2091, 2004.
32 A. L. Efros, M. Rosen, The electronic structure of semiconductor nanocrystals, *Annual Reviews of Material Science* **30** (2000), 475–521.
33 R. L. Petritz, Theory of photoconductivity in semiconductor films, *Physical Review*, **104** (1956), 1508–1516, 1956.
34 R. Bube, *Photoconductivity of Solids*. New York, NY: John Wiley & Sons, 1960.
35 R. Bube, *Photoelectronic Properties of Semiconductors*. Cambridge, UK: Cambridge *University Press*, 1992.
36 A. Rose, *Concepts in Photoconductivity and Allied Problems*. New York, NY: Robert E. Krieger Publishing, 1972.
37 S. Espevik, C. Wu, R. H. Bube, Mechanism of photoconductivity in chemically deposited lead sulfide layers, *Journal of Applied Physics*, **42** (1971), 3513, 1971.
38 R. Bube, C. T. Ho, Laser saturation of photoconductivity and determination of imperfection parameters in sensitive photoconductors, *Journal of Applied Physics*, **37**(11) (1966), 4132–4138.
39 E. L. Dereniak, G. D. Boreman, *Infrared Detectors and Systems*. New York, NY: John Wiley & Sons, 1996.
40 R. C. Jones, A method of describing the detectivity of photoconductive cells, *Reviews of Scientific Instruments*, **24** (1953).
41 N. C. Greenham, X. Peng, A. P. Alivisatos, Charge separation and transport in conjugated-polymer/semiconductor-nanocrystal composites studied by photoluminescence quenching and photoconductivity, *Physical Review B*, **54** (1996), 17628.

42 S. A. McDonald, G. Konstantatos, S. Zhang, *et al.*, Solution-processed PbS quantum dot infrared photodetectors and photovoltaics, *Nature Materials*, **4** (2005), 138–142.

43 C. A. Leatherdale, C. R. Kagan, N. Y. Morgan, *et al.*, Photoconductivity in CdSe quantum dot solids, *Physical Review B*, **62** (2000), 2669.

44 M. V. Jarosz, V. J. Porter, B. R. Fisher, M. A. Kastner, M. G. Bawendi, Photoconductivity studies of treated CdSe quantum dot films exhibiting increased exciton ionization efficiency. *Physical Review B* **70**(19) (2004), 195327.

45 G. Konstantatos, I. Howard, A. Fischer, *et al.*, Ultrasensitive solution-cast quantum dot photodetectors, *Nature*, **442**(7099) (2006), 180–183.

46 D. Yu, C. Wang, B. L. Wehrenberg, P. Guyot-Sionnest, Variable range hopping conduction in semiconductor nanocrystal solids, *Physical Review Letters*, **92** (2004), 216802.

47 D. Talapin, C. B Murray, PbSe nanocrystal solids for n- and p-channel thin film field-effect transistors, *Science*, **310** (2005), 86–89.

48 R. H. Rahada, H. T. Minden, Photosensitization of PbS films, *Physical Review*, **102** (1956), 1258–1262.

49 G. W. Mahlman, Photoconductivity of lead sulfide films, *Physical Review*, **103** (1956), 1619–1630.

50 C. Naşcu, V. Vomir, I. Pop, V. Ionescu, R. Grecu,The study of lead sulphide films. VI. Influence of oxidants on the chemically deposited PbS thin films, *Materials Science and Engineering B*, **41** (1996), 235–240.

51 I. Pop, V. Ionescu, C. Nascu, *et al*., The study of lead sulfide films. The behaviour at low-temperature thermal treatment, *Thin Solid Films*, **283** (1996), 119–123.

52 A. Carbone, P. Mazzetti, Grain-boundary effects on photocurrent fluctuations in polycrystalline photoconductors, *Physical Review B*, **57** (1998), 2454.

53 A. Carbone, P. Mazzetti, F. Rossi, Low-frequency photocurrent noise in semiconductors: Effect of nonlinear current-voltage characteristics, *Applied Physics Letters*, **78** (2001), 2518–2520.

54 D. Yu, B. L. Wehrenberg, P. Jha, J. Ma, P. Guyot-Sionnest, Electronic transport of n-type CdSe quantum dot films: effect of film treatment, *Journal of Applied Physics*, **99** (2006), 104315.

55 G. Konstantatos, J. Clifford, L. Levina, E. H. Sargent, Sensitive solution-processed visible-wavelength photodetectors, *Nature Photonics*, **1** (2007), 531–534.

56 P. P. Suni, Gain compression photodetector array, US Patent 4967249, 1990.

57 G. Konstantatos, E. H. Sargent, PbS colloidal quantum dot photoconductive photodetectors: Transport, traps, and gain, *Applied Physics Letters*, **91**:17 (2007), 173505.

58 G. Konstantatos, L. Levina, A. Fischer, E. H. Sargent, Engineering the temporal rresponse of photoconductive photodetectors via selective introduction of surface trap states, *Nanoletters*, **8** (2008), 1446–1450.

59 J.-S. Lee, M. V. Kovalenko, J. Huang, D. S. Chung, D. V. Talapin, Band-like transport, high electron mobility and high photoconductivity in all-inorganic nanocrystal arrays, *Nature Nanotechnology*, **6** (2011), 348–352.

60 G. Konstantatos, M. Badioli, L. Gaudreau, *et al.*, Hybrid graphene quantum dot phototransistors with ultra-high gain, *Nature Nanotechnology*, **7** (2012), 363–368.

61 J. Clifford, G. Konstantatos, S. Hoogland, L. Levina, E. Sargent, Fast, sensitive, spectrally-tunable solution-processed photodiodes, *Nature Nanotechnology*, **4** (2009), 40–44.

62 D. C. Oertel, M. G. Bawendi, A. C. Arango, V. Bulovic, Photodetectors based on treated CdSe quantum-dot films, *Applied Physics Letters*, **87** (2005), 213505–213507.

63 J. P. Clifford, K. W. Johnston, L. Levina, E. H. Sargent, Schottky barriers to colloidal quantum dot films, *Applied Physics Letters*, **91**:25 (2007), 253117.

64 O. Voznyy, D. Zhitomirsky, P. Stadler, *et al.*, A charge-orbital balance picture of doping in colloidal quantum dot solids, *ACS Nano*, DOI: 10.1021/nn303364d, 2012.
65 M. Boberl, M. V. Kovalenko, S. Gamerith, E. J. W. List, W. Heiss, Inkjet-printed nanocrystal photodetectors operating up to 3 μm wavelengths, *Advanced Materials*, **19** (2007), 3574–3578.
66 S. Keuleuan, E. Luihller, V. Brajuskovic, P. G. Sionnest, Mid-infrared HgTe colloidal quantum dot photodetectors, *Nature Photonics*, **5** (2011), 489–493.
67 Y. Jin, J. Wang, B. Sun, J. C. Blakesley, N. C. Greenham, *Nano Letters*, **8** (2008), 1649–1653.
68 T. Rauch, M. Boberl, S. F. Tedde, *et al.*, Near-infrared imaging with quantum-dot-sensitized organic photodiodes, *Nature Photonics*, **3** (2009), 332–336.
69 G. Konstantatos, L. Levina, E. H. Sargent, Sensitive solution-processed Bi_2S_3 nanocrystalline photodetectors, *Nanoletters*, **8** (2008), 4002–4006.
70 V. Sukhovatkin, S. Hinds, L. Brzozowski, E. H. Sargent, Colloidal quantum-dot photodetectors exploiting multiexciton generation, *Science*, **324** (2009), 1542–1544.
71 M. Hegg, L. Y. Lin, Near-field photodetection with high spatial resolution by nanocrystal quantum dots, *Optics Express*, **15** (2007), 17163–17170.
72 H. Y. Chen, M. K. F. Lo, G. Yang, H. G. Monbouquette, Y. Yang, Nanoparticle-assisted high photoconductive gain in composites of polymer and fullerene, *Nature Nanotechnology*, **3** (2008), 543–547.
73 S. Hinds, L. Levina, E. J. D. Klem, *et al.*, Smooth-morphology ultrasensitive solution-processed photodetectors, *Advanced Materials*, **20** (2008), 4398–4402.

8 Optical gain and lasing in colloidal quantum dots

Sjoerd Hoogland

8.1 Introduction

Quantum dot materials utilize carrier confinement in all three dimensions. The properties associated with this provide superior lasing properties compared to the low dimensional semiconductor materials [1–2]. It has been identified that in strongly confined dots, allowed energy states are separated by energies far exceeding the thermal carrier energies, inhibiting thermal depopulation of the lowest allowed energy state with a low optical gain threshold, insensitivity of the gain threshold to the temperature together with a temperature stability of the emission wavelength, and ultra-narrow emission linewidths. These ideal laser operation properties triggered the development of quantum dot lasers. The first demonstration of a quantum dot laser was realized with relatively large CdSe nanoparticles inside a glass matrix, fabricated through high temperature precipitation processes [3]. With the advent of self-assembled epitaxially grown quantum dots the expected superior laser properties were demonstrated, including high differential gains [4], ultra-low lasing thresholds [5], and high characteristic temperatures [6] compared with the low dimensional semiconductor lasers. These epitaxial dots are highly asymmetric in shape and operate near the strong confinement limit. Both the success of the epitaxial quantum dot lasers and the short comings of the dots used as gain-providing material were a strong motivation for the development of lasers based on sub-10 nm particles synthesized through wet colloidal chemistry.

Colloidal quantum dots consist of nanometer-sized particles made from a semiconductor material whose surface is typically passivated by organic ligand molecules. Here, the semiconductor particle is the active part, while the ligands attached to the dot surface have three primary functions: (1) they keep the particles in a solution; (2) they prevent the particles aggregating together into some larger macro-sized polycrystalline particle; and (3) they passivate the unsatisfied bonds on the surface of the dots. The most widely used material systems to form colloidal quantum dots are based on cadmium and lead chalcogenides. One of the main reasons for this is that both these material systems have very large exciton Bohr radii. This has the consequence that the strong quantum confinement regime is attainable for relatively large particle sizes. Operation in this regime has the effect that the bandgap is tunable with the size of the particle. For

Colloidal Quantum Dot Optoelectronics and Photovoltaics, eds. G. Konstantatos and E. H. Sargent.
Published by Cambridge University Press. © Cambridge University Press, 2013.

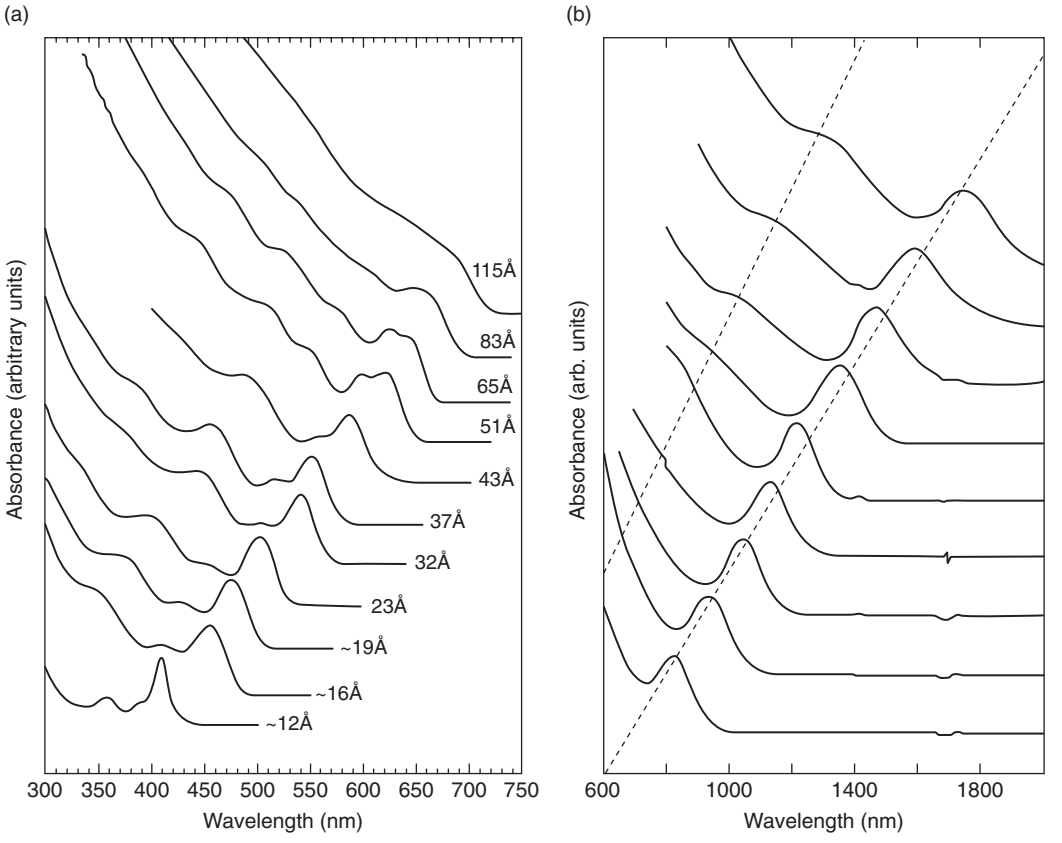


Figure 8.1 Size tunability of the absorption onset of (a) CdSe quantum dots [7], and (b) PbS quantum dots in solution [8]. The dashed lines indicate the position of the first and the second allowed absorption peak, showcasing that both transitions are size tunable.

the cadmium chalcogenides this results in tunability of the absorption onset wavelength from 400 nm to 800 nm by tuning the particle size from about 1 nm to 4 nm, while for the lead chalcogenides the bandgap can be changed from about 700 nm to more than 2000 nm for sizes ranging from about 2 nm to more than 7 nm (Figure 8.1). Therefore, between two material systems the emission wavelength can be changed from the blue to the mid-infrared. In this chapter the properties and results of colloidal quantum dots based on these two material systems will be discussed in the context of obtaining laser operation.

8.2 Optical properties of colloidal nanocrystal quantum dots

Colloidal quantum dots operating in the strong quantum confinement regime exhibit a delta-function-like density of states. Much like atomic energy transitions, the allowed energies are discrete and in the case of strong quantum confinement they are size tunable. During the synthesis of the colloidal quantum dots with wet chemistry, a very narrow size

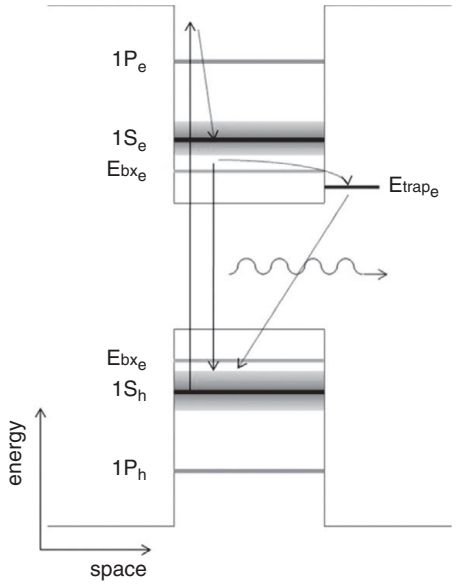


Figure 8.2 Energy diagram and carrier relaxation paths of a colloidal quantum dot overlayed on the cross section of the potential profile of the quantum dot. An electron excited at high energy thermalizes rapidly to the first excited state ($1S_e$). From there the electron can be captured by a trap state ($Etrap_e$), from where it nonradiatively recombines with the hole in the $1S_h$ level. Alternatively, the electron can recombine from the lowest energy state of the level (the state is homogenously broadened) with the hole in the $1S_h$ state. Also shown is the biexciton energy level, situated somewhat below/above the $1S_e/1S_h$ level due to the binding energy it takes to make this quasi-particle.

distribution is realized and control over the size is remarkably high with typical variances of less than one atomic monolayer [9]. The variance, however, results in a broadening of the allowed energies of the ensemble, which is apparent in Figure 8.1. Here not only can the first allowed transition, commonly denoted, in line with atomic orbital formalism, as the $1S_e–1S_h$ ($1S_{eh}$ in short) transition, be seen but also other allowed transitions are apparent as absorption peaks at higher energies.

Upon absorption of a photon with energies larger than the bandgap energy, an electron is excited to a state high in the conduction band. Due to the large degree of confinement, the generated electron and hole form a bound state, called an exciton. This quasi-particle can exist at room temperature within a strongly confining dot, since the binding energy cannot be overcome through thermal energy. An exciton is a neutral bound pair of an electron and hole. However, when two excitons are created within a dot, the strong confinement forces the excitons to interact with each other, resulting in a new quasi-particle called the biexciton. The binding energy to form this particle causes a small shift in the energy spectrum (Figure 8.2). In the presence of more excitons, exciton–exciton interactions can yield multi-excitonic quasi-particles with additional shifts in the energy spectrum as a result.

A high energy exciton loses its energy rapidly (Section 8.3) to the lowest excited state ($1S_{eh}$). The exciton has the chance to recombine radiatively emitting a photon at slightly

lower energy compared with the exciton absorption peak. This shift, called the Stokes shift, is to first order caused by the homogenous broadening of the allowed transition. Such broadening is affected by the quality of the dot, the surface, and the surrounding ligand, and can be as large as 100 meV [10]. The size distribution has the effect that the spontaneous emission spectrum is also broadened and can have spectral widths ranging from 20 meV for visible dots to 100 meV for infrared dots, depending on the material of the dots, the size of the dots, and the quality of the dots, including the surface and ligands.

Similar to any kind of semiconductor, on the surface of the dots dangling bonds are present due to the abrupt end of the crystal lattice. Such unsatisfied bonds form trap states in which excited carriers can become highly localized. In nanometer-sized quantum dots, the surface-to-volume ratio is very large and contributions from the surface to the properties of the dots are significant. Due to the large overlap of the excited carrier wavefunction with the surface of the dot, the probability of the exciton relaxing through surface states is large. Typically, these states are dark states, where a trapped carrier recombines nonradiatively, thus resulting in a lowering of the overall band edge radiative recombination efficiency. For light generation purposes, it is therefore very important that all surface states are passivated, which can be realized by choosing appropriate functional groups of the ligands that bind to the surface atoms of the dot. However, in the case of stimulated emission, if the carrier capture rate is much smaller than the stimulated emission rate, the surface traps do not constitute a great loss. Therefore, it is important to investigate the carrier dynamics within colloidal quantum dots.

8.3 Carrier dynamics in colloidal quantum dots

The most common technique for determining carrier dynamics in materials uses two-color pump–probe measurements. An ultra-fast pump laser with variable power is focussed onto the sample under investigation. A spectrally tunable pulsed probe laser is also focussed onto the sample overlapping the pump spot. The time delay between the arrivals of the pump pulse and the probe pulse can be varied so that the change in transmission can be probed at different times. In quantum dots the first excited state is the transition that will bleach first. Therefore, to gain insight into the population dynamics at the $1S_{eh}$ transition, the probe wavelength is tuned to around the exciton absorption wavelength. For different pump fluences, the time-dependent change in absorption is recorded, with curves like that shown in Figure 8.3 as a result. Calibration of the absolute change in absorption can be done by careful measurement of the linear absorption of the sample, e.g., with a spectrophotometer.

In transient absorption measurements with the aim of measuring the optical gain properties, the number of generated electron–hole pairs needs to be determined. Additionally, in order to determine the multi-exciton carrier dynamics behavior and functionality with the number of excitons, $\langle N_{eh} \rangle$, should be known. The average number of generated excitons per quantum dot can be computed as

$$\langle N_{eh} \rangle = J_{pump} \sigma_{NC}, \tag{8.1}$$

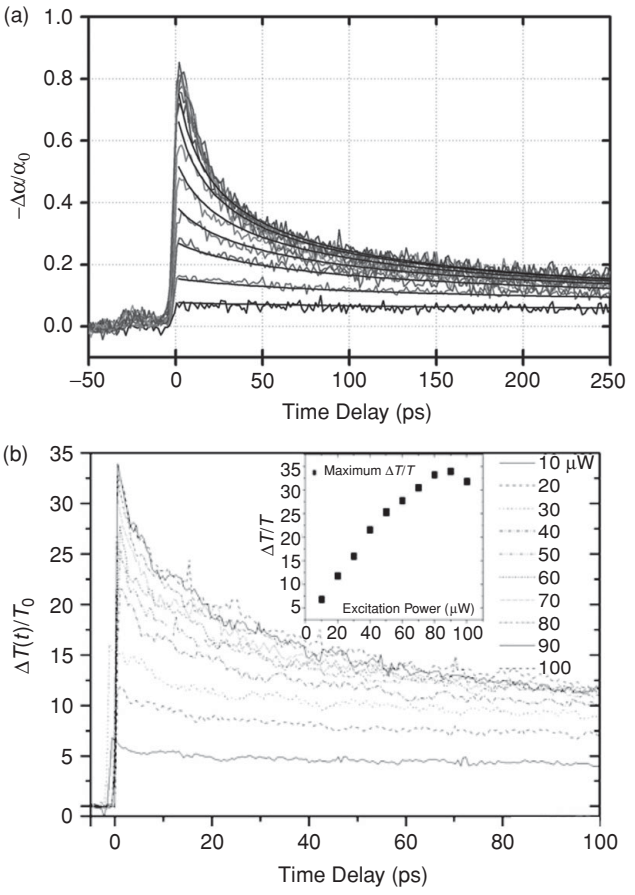


Figure 8.3 Ultra-fast pump–probe measurements, revealing the carrier dynamics at high pump fluences. (a) PbS dots in hexane, pumped at 800 nm and probed at the excitonic absorption peak at 1500 nm [13]. (b) CdSe dots in hexane, pumped and probed at the excitonic absorption peak around 2.1 eV [27].

where J_{pump} is the pump fluence presented in photons/cm^2 and σ_{NC} is the nanocrystal absorption cross section. Far away from the absorption edge, at high energies, the absorption cross section can be calculated using the relation

$$\sigma_{NC} = (4\pi/3)|f|^2 \alpha_b R^3 \tag{8.2}$$

Here, α_b is the bulk material absorption coefficient at the pump wavelength, R is the radius of the quantum dot, and f is a coefficient to account for the local field effects [11, 12]. It should be stressed that the dielectric screening is a function of the dielectric constants of the quantum dot material, the ligands, and the matrix material (e.g., the solvent). Therefore, the optical properties, including the optical gain of the colloidal quantum dots, will have a strong dependency on the surrounding media.

Table 8.1 shows the absorption cross section for different quantum dot systems. These numbers were obtained by using the absorption coefficient of the quantum dots at the

Table 8.1. Absorption cross section, σ_{NC}, for different nanocrystal material systems and sizes

	R (nm)	$\lambda_{abs\ xsection}$ (nm)	σ_{NC} (cm^{-2})	Note	Reference
PbS	2.75	800	2.5e-15	From absorption and quantum dot atomic weight	[13]
PbSe	2.45	800	3e-15	Calculated with (8.2)	[14]
	2.03	800	1e-15		
CdSe	1	413	2e-16	Calculated with (8.2)	[15, 16]
	4	413	1e-14		

pump wavelength and the atomic weight of one quantum dot (PbS). For other material systems, (8.2) is used. It should be noted here that the absorption cross sections of nanocrystals are vastly smaller than the cross sectional area of a dot, indicating weak light–matter interaction within the dot.

Colloidal quantum dots operating in quantum confinement result in the aforementioned size tunability of the bandgap. Additionally, the energies of higher energy allowed states are also size tunable (Figure 8.1). At first glance, this would mean that in small enough dots, only certain photon energies are absorbed, resulting in a discrete spectrum of absorbed wavelengths. For a single dot this is not the case since homogenous broadening of the allowed energy states results in a somewhat continuous absorption spectrum due to overlapping absorption peaks of all the allowed transitions. As mentioned above, in an ensemble the absorption spectrum is even more continuous due to the broadening of the allowed energies caused by the size distribution of the dots. One would also observe that there is a threshold of the particle size in which the energy spacing between allowed energies within a band is much larger than the phonon energy. In this case, carriers excited high in the band would not be able to thermalize to the ground state; this phenomenon is called the phonon bottleneck. However, such a regime has not been observed in regular quantum dots. The reason for this is thought to involve the interaction of the carriers, the ligands, and the surface atoms resulting in a spectrum of intermediate states through which carriers are allowed to thermalize to the lowest excited state [13]. In specially designed quantum dots, where neither electrons nor holes interact with surface states, intraband relaxation has been slowed down tremendously, which is indicative of the appearance of a phonon bottleneck [17].

Upon absorption of a photon with energies larger than the bandgap energy (Figure 8.2), a high energy exciton is created and relaxes quickly to the first excited state by thermalizing through the intermediate states. These thermalization times are measured to be on the order of a picosecond [13, 15]. The exciton lifetime in the first excited state can range from nanoseconds to microseconds depending on the quantum dot materials, the ligands, and the proximity of the dots to each other. Within this time, a carrier can be captured by a trap, where it is highly localized, with a decrease in wavefunction overlap between the electron and hole and a corresponding decrease in oscillator strength as a result. The carrier lifetime of a trapped carrier is therefore much

longer and ranges from microseconds to milliseconds [18, 19]. The photoluminescence quantum efficiency (PLQE) of dots in solution, where they are kept far apart from each other, is typically on the order of 40%, but depends on the surface ligands and passivation quality [20]. With the advent of core/shell quantum dots [21], where excitons can be more confined to the core so that they do not experience surface traps, PLQEs of more than 70% can be realized [22]. However, in close-packed films, the PLQE drops dramatically to below 10% which is caused by diffusion of excitons through efficient energy transfer between dots, therefore increasing the chance for the exciton to find a trap [23].

8.3.1 Auger recombination

In a semiconductor, excitation of an electron–hole pair reduces the number of possible upward transitions, diminishing the absorption. Excitation of more electron–hole pairs reduces the absorption further and for a certain population, optical transparency is realized when the absorption is zero. In quantum dots this occurs at exciton populations of half the excited state degeneracy number. In cadmium chalcogenides or silicon quantum dots the degeneracy number is 2 [24], while for lead chalcogenides the degeneracy number is 8 [25]. These numbers mean that on average the number of excitons per dot should be more than 1 for the cadmium chalcogenides and more than 4 for the lead chalcogenides to realize population inversion. The carrier concentration at which this transparency occurs is high, leading to nonlinear carrier relaxation processes. At such populations Auger recombination occurs. This recombination mechanism involves at least three particles, where the recombination energy from two particles is given to the third particle which is excited higher in the band. This carrier subsequently thermalizes back down to the first excited state, leading to a net loss of two carriers (i.e., one exciton) without the gain of a photon. Thus the Auger recombination mechanism is a parasitic process that competes with the build up of population inversion and thus with reaching optical gain.

In quantum dots Auger recombination is very efficient due to the abrupt potential profile occurring at the surface of the dots. At the dot surface carriers can scatter efficiently increasing the Auger recombination efficiency [26]. Since the Auger efficiency is very large in quantum dots, the exciton populations with $\langle N_{eh} \rangle > 1$ reduce very quickly to a population of $\langle N_{eh} \rangle = 1$. Figure 8.3(a) shows the evolution of the change in absorption of PbS colloidal quantum dots for different excitation levels. At low excitation levels the absorption is reduced a little and decays over a long period of time (order of nanoseconds). At increased excitation levels, absorption reduces more, but a faster decay component appears, reducing the absorption bleaching to the low level excitation absorption level, from where the decay constant is long again corresponding to the single exciton lifetime. Further increase in the excitation level shortens the decay constant even further, indicative of the Auger recombination mechanism. Figure 8.3(b) shows the same behavior for CdSe dots. For more than one exciton per dot the decay constant decreases quickly from about 0.2 ns to about 10 ps for multiple excitons per dot.

These results show that Auger recombination is very efficient and rapidly reduces multi-exciton populations, influencing the dynamics of carriers and the realization of

Table 8.2. Auger constant, C_A, for different NC material systems and sizes

	R (nm)	$\lambda_{exciton}$ (nm)	C_A ($cm^6\ s^{-1}$)	Note	Reference
CdSe	1.2 4.1		2e-30 7e-29	$C_A \sim R^3$	[28]
PbS	2.8	1550	4.5e-30		[13]
PbSe		~1350 ~1700	~1e-29 ~1e-30		[29]

optical gain. They indicate that for these types of dots, gain lifetimes can be only on the order of tens of picoseconds.

Since in bulk semiconductors, the Auger constant depends on the carrier concentration, it can be expected that the Auger recombination in quantum dots depends on the dot radius, R, as R^6. However, in quantum dots, it has been shown experimentally that the Auger constant follows a R^3 functionality for the particle size dependence, indicating the constant purely depends on the particle size (Table 8.2) [28]. In the same study it was shown that the Auger constant is not dependent on the surface passivation. These results indicate that the Auger process is to the first degree a property of the bulk part of the nanocrystal material.

8.3.2 Poisson statistics and state filling

High energy excitons follow Poisson statistics, since no state filling occurs at high energy states. The excitons decay rapidly to the first excited state, where they are distributed by the same Poisson statistics. In a perfect quantum confined system, excitons generated in number exceeding the degeneracy number of the first excited state would occupy the next excited state. However, Istrate *et al.* showed that some absorption bleaching of the second excited state occurs in PbS nanocrystals, but the bleaching recovers much more rapidly than the bleaching time in the $1S_{eh}$ state, indicating that the excess excitons must be able to access defect states, where they no longer contribute to the occupancy of the first excited state and the corresponding generation of optical gain [13].

In order to describe the population dynamics in the first excited state, Poisson statistics can be utilized, modified to limit the number of excitons in the level to the state degeneracy number. These statistics have been used in Figure 8.3(a) to fit the transient absorption data of PbS dots in solution. This procedure can yield the Auger coefficient, as it is one of the fitting parameters.

There is an important consequence of the Poisson statistics and state filling effect, namely that the threshold population to reach gain is increased. For the lead chalcogenide quantum dots with their eight-fold degeneracy of the first excited state these statistics show that: (a) at four absorbed photons, after Auger recombination, 98% of the dots contain one exciton; (b) at eight absorbed photons, after thermalization, 55% of the dots contain eight excitons in the first excited state; (c) at twelve absorbed photons,

Table 8.3. Summary of the optical gain and laser properties of colloidal nanocrystal materials

Property	Visible quantum dots	Infrared quantum dots	References
Gain value	15 cm^{-1} (CdSe/ZnS) 40–510 cm^{-1} (CdSe) 230 cm^{-1} (CdTe)	230 cm^{-1} (PbS)	[24, 39–42, 54]
Gain cross section	2e-17 cm^2 (CdSe)	~1e-16 cm^2 (PbS) 2e-15 cm^2 (PbSe)	[24, 42, 43]
Gain lifetime	10 ps (CdSe) 20 ps (CdS)	10 ps (PbSe)	[43, 45, 51, 71]
Gain threshold	0.8 mJ/cm^2 (CdSe) 0.7–2 mJ/cm^2 (CdS) $N_{eh} = 1.5$–2 (CdSe)	0.1–1 mJ/cm^2 (PbSe) 8 mJ/cm^2 (PbS)	[38, 43, 46, 51, 71]
ASE threshold	0.3–6 mJ/cm^2 (CdSe) 30 $\mu J/cm^2$ (ZnSe/CdSe)	2 mJ (PbSe) 1 mJ/cm^2 (PbS)	[42, 43, 46, 51, 68]
Waveguide losses	1 cm^{-1} (CdTe)	10 cm^{-1} (PbS)	[38, 39]
Laser Q factor	600 (DFB) 1e7 (microtorroid) >600 (microsphere) 400–1000 (microsphere) >600 (microcapillary)	500 (microcappilary)	[38, 54, 59, 64, 72, 73]
Laser threshold	1.3 mJ/cm^2 (CdSe)	160 $\mu J/cm^2$ (PbS)	[38, 40]
Refractive index	1.7–2.1 (CdSe/titania), 1.8 (CdSe)	1.7 (PbS)	[38, 40, 54]

after thermalization, nearly all dots contain eight excitons [13]. Therefore, to obtain maximum optical gain, the dots have to be pumped with fluences corresponding to twelve absorbed photons per dot for lead chalcogenide nanocrystals (or any other materials with a degeneracy of 8). For the cadmium chalcogenides (or other materials with two-fold degeneracies), the state filling effects together with the Poisson statistics do not have much effect on the exciton population required to reach transparency.

8.4 Gain in solid state nanocrystal quantum dot films

The gains observed in the quantum dots have lifetimes on the order of tens of picoseconds (Section 8.5), which is several orders of magnitude smaller than typical gain lifetimes observed in semiconductors. At such short gain lifetimes the question rises whether the gain lives long enough for stimulated emission to occur in quantum dots. To realize this, the stimulated emission build up time has to be shorter than the gain lifetime.

The stimulated emission build up time is given by $\tau_{SE} = n_r/Gc$, where n_r is the effective refractive index of the gain medium, G is the gain value, and c is the speed of light. As described later in this section and shown in Table 8.3, typical gain values for nanocrystal quantum dots are on the order of 100 cm^{-1}, while refractive indices are on order of 2, resulting in typical stimulated emission build up times on the order of 0.5 ps. The gain values, however, are dependent on the packing fraction of the dots inside the surrounding matrix. Therefore, instead of the gain coefficient, the gain cross section is a better measure for the gain parameter. The gain cross section, σ_g, is expressed in terms of the gain coefficient by $\sigma_g = G/n_0$, where n_0 is the quantum dot density, which can be

expressed in terms of the packing fraction, ξ, and the nanocrystal volume, V_{dot}, by $n_0 = \xi/V_{dot}$. Since τ_{SE} has to be smaller than the gain relaxation time τ_{gain}, this results in

$$\tau_{SE} = n_r V_{dot}/(\sigma_g c \xi) < \tau_g. \tag{8.3}$$

For a 5 nm diameter dot, a refractive index of 2, a typical gain cross section of 1e-17 cm^2 and a gain relaxation time of 10 ps, this puts a lower limit on the packing fraction of about 0.04. Such packing cannot be obtained when dots are in solution, where dots are typically so far apart that $\xi \ll$ 1e-3. With random packing of quantum dots in a solid film, the fraction can be on the order of 0.2. This shows that dots have to be in a closely packed solid to enable light amplification and only densely packed nanocrystal films can yield stimulated emission.

8.4.1 Amplified spontaneous emission (ASE)

Upon excitation of nanocrystals, spontaneous emission occurs at energies Stokes shifted with respect to the absorption edge. These photons are emitted in all directions with some of them coupled into the nanocrystal film. If this light is generated by nanocrystals in a solid thin film, some photons can be coupled into a waveguide mode, if (1) the film is sandwiched between media with smaller refractive indices than the nanocrystal film, and (2) the film thickness is larger than the critical film thickness to sustain a waveguide mode. The first criterion is fairly easily satisfied since nanocrystal films have a typical refractive index of around 2, making it possible to use any glass as the substrate and air as the covering cladding. The second criterion can be satisfied by adjusting the film thickness to ensure the waveguide modes are sustained by, for example, adjusting the film fabrication parameters; typically film thicknesses of 500 nm and up will sustain waveguide modes.

The spontaneously emitted photons coupled into a waveguide mode will be subjected to reabsorption due to the finite absorption tail from the nanocrystals, which typically partially overlaps with the emission profile. In addition, waveguide losses, for example, due to scattering from imperfections in the film, will reduce the waveguided light intensity with propagation distance. However, upon increased pumping intensities, the nanocrystal absorption bleaches and turns into optical gain. In the case that the waveguide losses are sufficiently small (see Section 8.4.3), the spontaneously emitted photons will be amplified and as a result an ASE spectral profile will appear in the emission spectrum. The ASE signal is strongest at the output of the waveguide, but due to some scattering inside the film some signal will be outcoupled from the waveguide, thus allowing ASE detection from the top surface of the waveguide.

ASE has several distinct features: (1) The ASE bandwidth is significantly narrower than the spontaneous emission spectrum, due to the relative narrow gain bandwidth. (2) The ASE signal has a distinct soft threshold with pump power, since amplification can occur only when sufficient optical gain is realized [30, 31]. (3) The ASE emission lifetime is much shorter than the spontaneous emission lifetime, since the stimulated

emission lifetime is inversely proportional to the flux of stimulating photons [31–33]. These features allow characterization of nanocrystal thin films for optical gain and amplification purposes without the need of stringent fabrication needs.

8.4.2 Variable strip length (VSL) for optical gain measurements

Nanocrystal films are fairly soft, making it very difficult to create perfectly cleaved edges. This prevents optical gain coefficient determination through conventional measurement techniques, which typically rely on Fabry–Perot effects in the emission spectrum, such as the Hakki–Paoli technique [34]. The VSL measurement technique overcomes this drawback, since it does not rely on perfectly cleaved film edges [35, 36]. Moreover, the data can be modeled with a simple one-dimensional amplifier model. Since the technique relies on waveguiding of light, parasitic waveguide losses should be minimized. Thin films made purely from nanocrystals fulfill the close packing requirement for stimulation build up, and can provide low waveguide losses (see Section 8.4.3). Therefore VSL is a very powerful technique for obtaining in-situ information on the amplification properties of the nanocrystals inside a pure film.

In a general VSL setup, a laser is focussed onto the sample surface into a narrow stripe by a cylindrical lens, where one end of the stripe overlaps the edge of the sample. The stripe length z is defined by a movable knife edge. The emitted light is collected at the edge of the sample at the position of the stripe and directed to a spectrometer where the emitted spectrum is recorded for different stripe lengths. Upon increase of the pump power, population inversion can be realized and ASE appears in the emission spectrum. Above the ASE threshold, the ASE intensity as function of the stripe length z is given by the one-dimensional amplifier model:

$$I_{ASE} = I_S/g * (e^{(gz)} - 1). \tag{8.4}$$

Here, I_S is a constant proportional to the spontaneous emission intensity, and g is the modal gain. Therefore, a fit with (8.4) of the ASE intensity versus the stripe length will yield the optical gain of the thin film. Note that this simple model only holds if three conditions are met: (1) the light collection efficiency does not depend on the pumping length z; (2) the gain and pump intensity are homogeneous over the whole pumping length z; and (3) the aspect ratio of the stripe is sufficiently large to ensure the one-dimensional amplifier is valid.

8.4.3 Experimental techniques for waveguide loss measurement in colloidal quantum dot films

The VSL technique yields the net modal gain, which can be greatly affected by the waveguide losses experienced by the (amplified) waveguided light. Additionally, typical semiconductor lasers are based on waveguided propagation of light in the amplifying

medium, during which parasitic losses can kill the amplification preventing the laser from oscillating. For these reason the waveguide losses should be characterized and minimized.

Nanocrystal films can be created by spin coating or dropcasting a solution containing the nanocrystals in a solvent. Such a film is generally highly uniform and its thickness can be modified by adjusting the concentration and spin speeds. Even though nanocrystal thin films appear smooth, they will exhibit some waveguide losses. Such losses originate from defects inside the film, caused by nonuniformities in packing of the dots, scattering by the quantum dots, and surface roughness of the nanocrystal film on the top and bottom side. For the same reasons brought up for the VSL technique, generated light inside the film can be utilized to characterize the waveguide losses. The shifting excitation spot (SES) technique utilizes this light to characterize the waveguide losses [37].

Luminescence coupled into the waveguide is subject to reabsorption due to the partial overlap of the emission spectrum and nanocrystal absorption. After propagation of waveguided luminescence over a certain distance, the spectral shape is greatly altered, appearing to be red-shifted compared to the nonwaveguided luminescence spectrum. The degree of the reshaping of the spectrum is determined by the Lambert–Beer law with the absorption coefficient determined by the nanocrystal absorption, $\alpha(\lambda)$, and the waveguide losses, K:

$$dI(x,\lambda)/dx = I_{sp}(\lambda)\exp(-[\alpha(\lambda) + K]x). \tag{8.5}$$

On the red side of the luminescence peak, where the nanocrystal absorption is negligible, the waveguide losses cause the luminescence to diminish.

For the SES technique, a thin film is deposited on a substrate with low optical losses in the spectral region of interest. The sample is then cleaved to create a fresh waveguide edge. An optical pump beam is focused into a small spot on the nanocrystal film. This pump generates photoluminescence, some of which is coupled into the nanocrystal waveguide. The waveguided luminescence is then collected at a cleaved edge of the waveguide for different positions of the excitation spot from the edge. Each part of the spectrum as a function of distance of the excitation spot from the edge can then be fitted by (8.5) to obtain the effective absorption coefficient.

Figure 8.4(a) shows an example of the evolution of the luminescence spectrum as a function of the distance of the excitation spot from the edge of the collection edge. The spectrum exhibits the expected red shift with the excitation position due to reabsorption in the nanocrystals. At longer wavelengths the spectrum exhibits very minor changes since there is no nanocrystal absorption in this part of the spectrum, which is confirmed by the absorption spectrum obtained from linear transmission measurements, and only waveguide losses cause the luminescence to decay. In this particular case the absorption spectrum on the red side of the luminescence peak reaches a wavelength independent value of 10 cm^{-1} (Figure 8.4(b)), corresponding to the parasitic waveguide losses.

The waveguide losses can be greatly improved when a layer-by-layer process is used to build up the film. Such a process can involve several types of treatment to ensure the dots do not redisperse on application of the next nanocrystal layers. Amongst these processes is the use of chemical linkers to bind dots to each other, solvent treatment to remove the original ligands, and heat treatment to fuse dots together. Using negatively charged

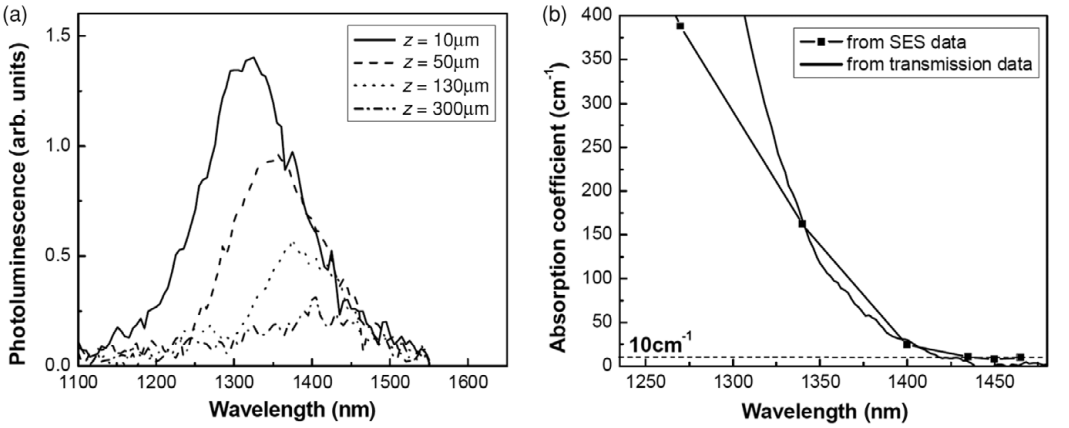


Figure 8.4 SES measurements on a 1 μm thick PbS nanocrystal solid film, excited at 800 nm. (a) Luminescence spectra of the waveguided luminescence for different positions of the excitation spot. (b) The resulting calculated absorption coefficient overlayed with the absorption obtained from transmission measurements, yielding a value of 10 cm^{-1} for the waveguide losses [38].

dots and positively charged molecules can yield ultra-smooth films with a roughness of less than 4 nm. Such films fabricated with CdTe dots have been used to characterize the waveguide losses with the SES technique leading to values of less than 1 cm^{-1} [39]. This shows that film fabrication techniques are very important for minimizing the waveguide losses.

8.4.4 Modal gain in visible colloidal quantum dots based on cadmium chalcogenides

CdSe dots were the first to be investigated with the VSL technique to determine the net optical gain [40]. For this a film was fabricated by dropcasting a solution onto a glass slide and allowing the solvent to evaporate, resulting in a 0.5–1 μm thick waveguide with a refractive index of ~1.8. Upon excitation in a stripe geometry, ASE occurred for a pump fluence of 1 mJ/cm^2 and had a clear dependence on the stripe length. Figure 8.5 shows the ASE intensity as function of the stripe length, clearly displaying the expected threshold behavior.

Relation (8.4) should describe the linear behavior of the emission intensity below the ASE threshold as well as the exponential dependence above threshold. In the case of nanocrystals, optical gain and therefore ASE is associated with multi-excitons. However, due to the efficient nonradiative Auger recombinations multi-exciton populations are reduced in a matter of picoseconds and therefore do not contribute to the spontaneous emission. Thus the waveguided emission originates from two sources: single excitons and multi-excitons; to take this into account (8.4) has to be modified:

$$I_{ASE} = I_{sx}z + I_{sxx}(e^{(gxxz)} - 1)/g_{xx}. \tag{8.6}$$

Here I_{sx} and I_{sxx} are proportionality constants for the single exciton and multi-exciton emission intensity, respectively, while g_{xx} is the biexciton modal gain value per unit stripe length and z is the stripe length. This relation yields a modal gain for the CdSe dots in

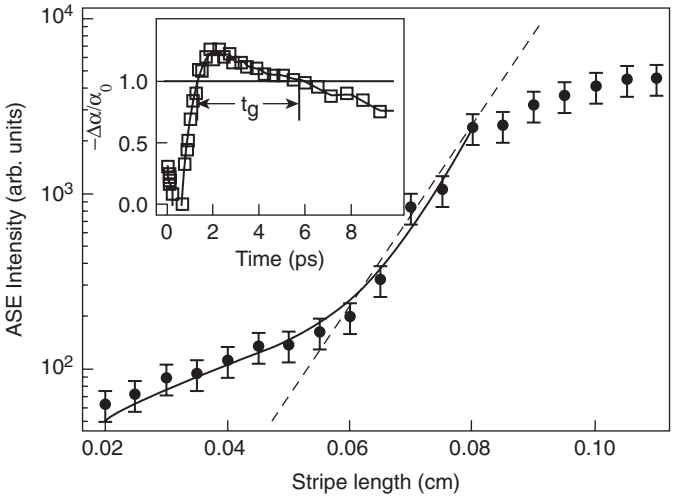


Figure 8.5 ASE intensity as function of stripe length to obtain the modal gain coefficient for CdSe quantum dots. The VSL signal is modeled using (8.4) (dashed line) and (8.6) (solid black line), yielding a modal gain of 120 cm^{-1} and 155 cm^{-1}, respectively. The inset shows the optical gain transient for the film, yielding a gain lifetime, τ_g, of about 5 ps [40].

Figure 8.5 of 155 cm^{-1}, with a good fit quality (solid line in Figure 8.5), compared to a modal gain of 120 cm^{-1} as obtained with (8.4) (dashed line in Figure 8.5).

In order to obtain the modal gain per unit propagation length without waveguide effects, it can be assumed that the ASE is dominated by the mode that corresponds to the critical angle of total internal reflection. In that case, the modal gain value has to be adjusted by a correction factor $n_{glass}/n_{NC} \sim 0.83$, which yields a net gain, time averaged over the gain lifetime, of about 130 cm^{-1}.

CdSe dots in titania sol–gel matrices have been used to fabricate films in which the photoluminescence quantum efficiency remained high (>10%), the fill factor was high (nearly 20%), while the polydispersity of the dots remained low (<7%). Films with thickness of 1–2 μm were fabricated on glass and pumped with a variable stripe length. ASE appeared on the red side of the luminescence peak, associated with the biexciton energy level, whose intensity as function of stripe length exhibited a clear threshold behaviour. Fitting the data with (8.6) resulted in a net gain of 130 cm^{-1}, very close to the gain values of films made out of just nanocrystals. The gain bandwidth in both CdSe and CdSe/ZnS was measured with the VSL method to be about 70 nm for both material systems [41].

Increasing the packing fraction of the dots inside the film influences the modal gain [39]. A high packing fraction of CdTe was accomplished by using a layer-by-layer deposition method with positively charged small molecules and negatively charged CdTe nanocrystals, resulting in 60% dot packing fraction by volume. These films, with thicknesses on order of 170 nm yielded gain values of 230 cm^{-1}, which is about 2× higher than the lower packing fraction CdSe nanocrystal films. This indicates that the packing fraction inside a nanocrystal film is important when optimizing the optical gain values.

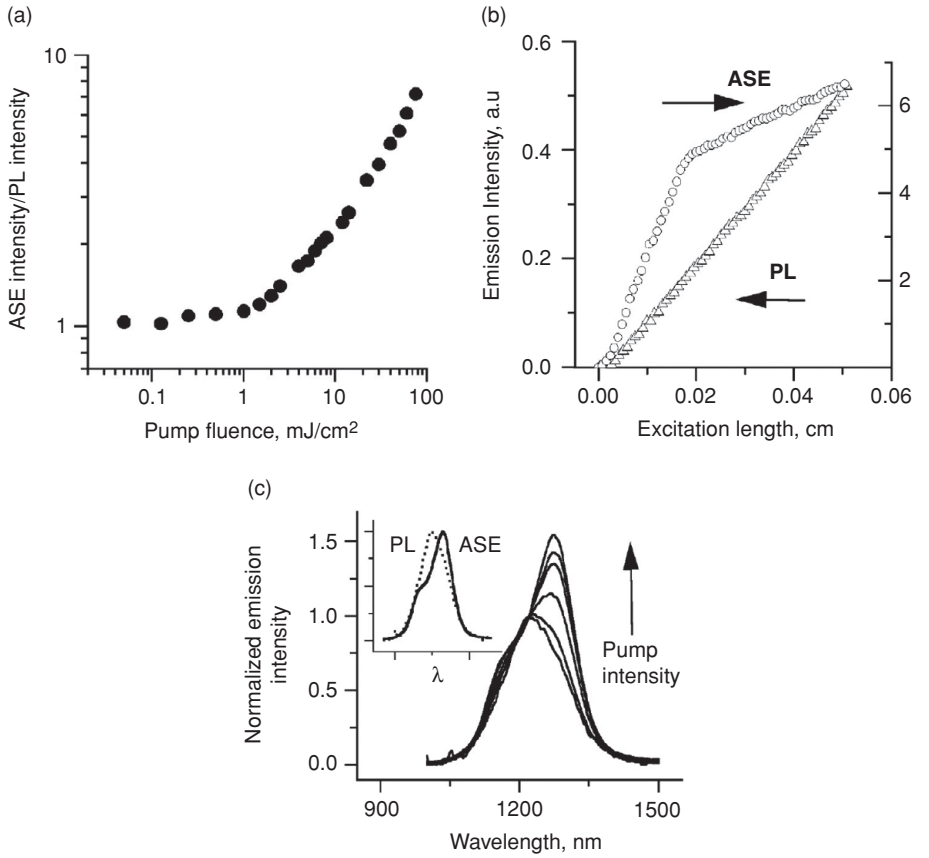


Figure 8.6 VSL and pump fluence dependence of PbS nanocrystal thin films. (a) ASE intensity as function of pump fluence, revealing a threshold of 1 mJ/cm^2. (b) Emission intensity at the luminescence peak and ASE peak spectral positions as a function of stripe length, revealing a modal gain coefficient of 230 cm^{-1} [42]. (c) Emission spectrum evolution for increasing pump powers. Inset: Emission spectra below (dashed) and above (solid) the ASE threshold.

8.4.5 Modal gain in infrared colloidal quantum dots based on lead chalcogenides

In the lead chalcogenide family, both lead sulfide and lead selenide colloidal quantum dots exhibit amplified spontaneous emission [42, 43]. Gain values for PbS quantum dots have been obtained using the VSL method. For this, an important part of the film fabrication was the preparation of the individual dots to ensure a large packing fraction. To accomplish this, short thioglycerol based ligands were used resulting in packing fractions of about 30%, enough to fulfill the required packing fraction limit as determined by (8.3) for gain lifetimes of several picoseconds. The resulting spin-coated film was optically pumped with photon energies higher than the bandgap and had an emission maximum at about 1.2 μm.

Upon excitation of the film with increasing pump fluence ASE appeared with a threshold of about 1 mJ/cm^2 (Figure 8.6(a)), accompanied by a narrow spectral feature

to the red side (1.3 μm) of the low pump fluence luminescence peak corresponding to the multi-exciton energy level (Figure 8.6(b)). Setting the fluence to a value above the ASE threshold and varying the pump stripe length revealed a near-linear dependence of the ASE luminescence signal with a steeper slope compared to the linear dependence of the luminescence signal at the position of the peak at low pump fluence (Figure 8.6(c)). The resulting linear dependence of the ASE signal strength with stripe length was fitted with the one-dimensional amplifier model described by (8.4), yielding a modal gain value of 230 cm^{-1}. These threshold and gain values are close to those obtained for the low degeneracy cadmium chalcogenides, mostly due to the increased absorption and gain cross sections for the lead chalcogenides [43].

8.5 Spectral and temporal characteristics of optical gain in nanocrystal quantum dots

8.5.1 Visible colloidal quantum dots based on cadmium chalcogenides

The first demonstration of size-tunable gain in strong quantum confined colloidal quantum dots was published by Klimov and coworkers [24, 44]. Here, transient absorption measurements were used with a wavelength-tunable probe to investigate transient absorption around the excitonic absorption peak and the spontaneous emission peak. Visible emitting CdSe nanocrystals with radii of 1.2–1.3 nm were used embedded in different matrix materials.

Figure 8.7(a) shows the linear absorption and continuous wave photoluminescence (PL) of CdSe dots with a radius of about 2.3 nm in a solution of trioctylphosphine. The first exciton absorption peak is situated at 2.1 eV, and extends to the red with a small amount of absorption present at the peak emission energy of about 2.05 eV. Upon increasing the pump laser intensity, the $1S_{eh}$ exciton absorption peak diminishes in magnitude due to state filling. The rate of the relative absorption change with the exciton population is shown in Figure 8.7(b) for probe photon energies corresponding to the $1S_{eh}$ exciton absorption peak and the red side of the luminescence peak. The absorption bleaches quickly for both parts of the spectrum, but for the $1S_{eh}$ absorption peak, the absorption change saturates to a value well below the optical transparency number. On the other hand, the relative absorption change keeps increasing at the red side of the luminescence peak and reaches transparency at $\langle N_{eh} \rangle \sim 1.5$, closely matching the expected one exciton per dot as predicted in a two-level system with a degeneracy of 2. The change in absorption saturates at an exciton population of just over 2, confirming the two-level system.

There are several reasons for the optical gain to occur at the red side of the luminescence peak rather than at the exciton absorption peak. Holes in the first excited state are liable to be captured in intrinsic hole traps [45], independent of the surface properties of the dots. Electrons, on the other hand, can be captured very rapidly in surface traps, which are highly dependent on the quality of the dot surface passivation [15]. Additionally, multi-carrier dynamics causes carriers to be lost preventing the nanocrystals yielding optical gain.

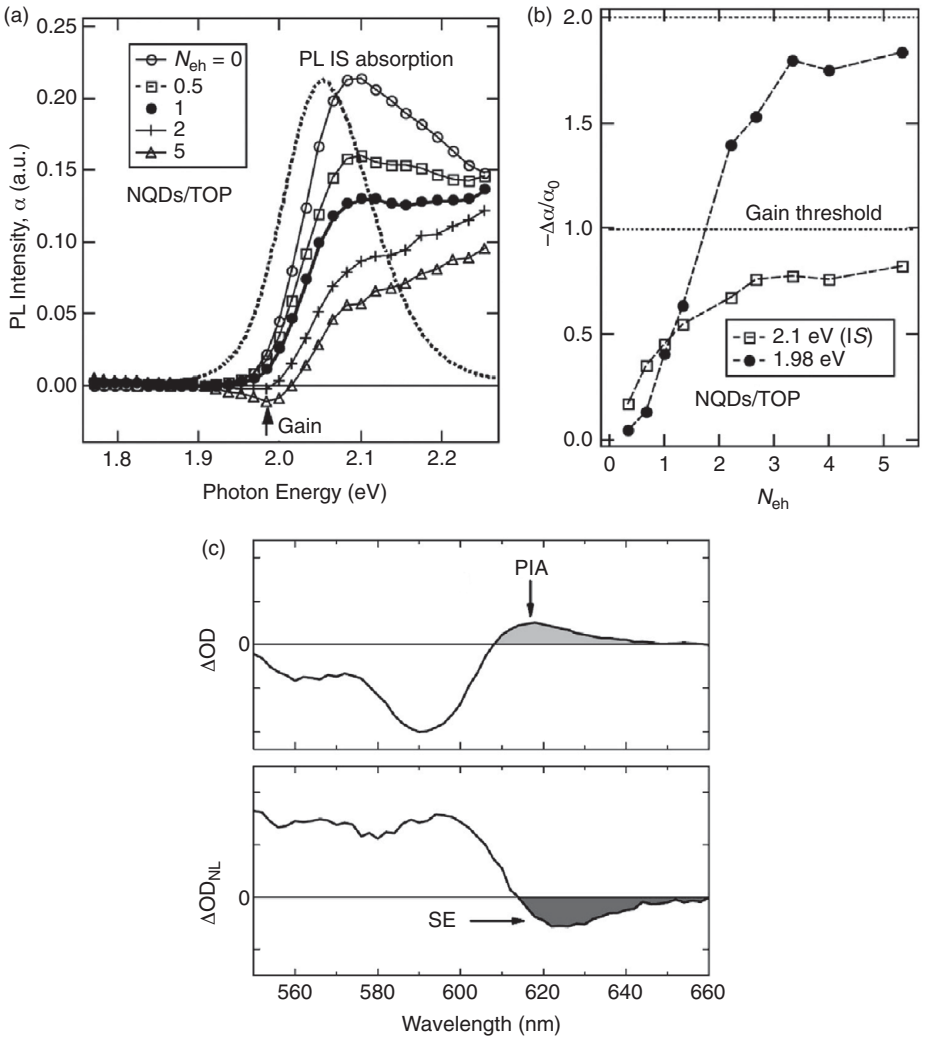


Figure 8.7 Optical gain in 2.3 nm CdSe nanocrystals in trioctylphosphine solution. (a) Linear absorption and spontaneous emission spectra with superimposed bleached absorption spectra for different number of excitons per dot. (b) Dependence of the change in absorption strength on the number of excitons per dot when probed at the first excited state absorption maximum (1S) and the red side of the maximum luminescence energy [44]. (c) Change in optical absorption (OD) for 2.1 nm radius CdSe dots in toluene at different pump levels. (top) Change in absorption under low pump fluences. Photo-induced absorption (PIA) appears around 615 nm, where the peak luminescence occurs. (bottom) Nonlinear change in absorption under high pump fluence. Optical gain ($OD_{NL} < 0$) appears at the same spectral position where PIA occurred at low pump fluences [46].

The absorption dependence on the number of electron–hole pairs per dot in Figure 8.7(b), was obtained at a constant probe delay time of about 2 ps. Changing the delay time with the probe energy tuned to a certain spectral position reveals the carrier dynamics in the nanocrystals. For nanocrystals in a solid thin film, at early times there is an induced absorption, which recovers well within a picosecond, and turns into absorption bleaching. The reduction in absorption recovers within tens of picoseconds due to the efficient Auger recombination mechanism.

For nanocrystals in hexane a vastly different absorption dynamics can be observed. At very small delay times induced absorption occurs much like in solid thin films. However, instead of this induced absorption turning into absorption bleaching, it remains and recovers within tens of picoseconds. This behavior was found to be more pronounced when the dots were dispersed in solvents, compared to solid thin films, and prevented the dots from exhibiting gain.

At population densities of more than 1 exciton per dot, multi-exciton interactions occur and biexcitons can form. These interactions result in a red-shift of the absorption edge and can be substantial enough to move the absorption edge into the spectral region where photoluminescence (luminescence) occurs (Figure 8.7(c)). This is the cause of the observed photo-induced absorption (PIA), in which photons are absorbed by excited electron–hole pairs. PIA is an undesired parasitic effect that reduces optical gain values or even prevents a material from exhibiting optical gain. It was found that PIA efficiency was closely related to the matrix material in which the dots are embedded. Notably the PIA spectral region was red-shifted beyond the emission spectrum in close-packed films and optical gain was observed with dots in polyvinyl butyral dispersions as well as in later studies in sol–gel titania waveguides [47]. Since PIA is eliminated in solid thin films, this indicates that the final state is directly related to the solvent/matrix material. Since the wavefunction overlaps well with the surface, the initial state of the PIA signal is probably associated with surface states like dangling bonds. This is in agreement with the fact that for smaller dots, where the surface-to-volume ratio is large, the PIA threshold is decreased. Moreover, the PIA cross section is not sensitive to the nanocrystal size, indicating that the quantum size effect is not at play and therefore other states are the origin of the PIA signal [48].

The nature of the multi-excitonic interactions depends strongly on the energetic properties of the excitons. The energy of the initially generated excitons influences the dynamics and magnitude of the PIA signal, and thus the optical gain. Excitons with larger energies result in larger PIA signals, while resonant transition excitation minimizes the PIA interference and thus increases the measured optical gain. This behavior is attributed to exciton energy dependent binding energies of multi-excitons as well as exciton energy dependent capture efficiencies of carriers into interface or surface states [46, 49, 50]. Much like the dielectric screening that affects the absorption cross section of the nanocrystals, these results show that the surrounding matrix has a very great influence on the carrier dynamics and interaction efficiencies of multi-excitons and therefore needs to be carefully chosen in order to design a nanocrystal laser.

At the same time that optical gain in colloidal quantum dots was demonstrated, ASE was realized in thin films [24, 44]. Solid state films were fabricated by drop-casting

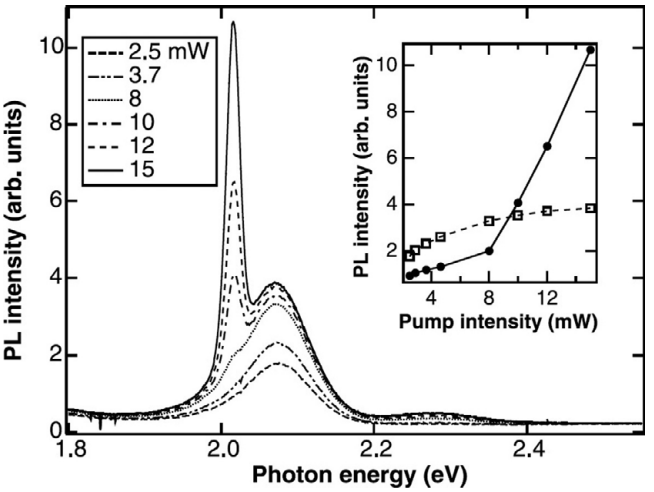


Figure 8.8 Emission spectra for 2.1 nm CdSe colloidal quantum dots in a solid thin film, measured at 80 K for different pump fluences. A clear threshold behavior is present above which a narrow low energy emission peak appears, which grows much faster with pump power (inset, solid circles) than the spontaneous emission (inset, squares) [44].

a solution of CdSe dots onto a transparent substrate. With the measured optical gain lifetime on the order of 10 ps, these solid films made from about 2 nm sized dots yielded a sufficiently high packing fraction to allow stimulated emission to occur. Similar to the transient absorption measurement results, the amplified spontaneous emission occurred to the red side of the low pump level spontaneous emission spectrum associated with the biexciton energy level (Figure 8.8). These results could only be obtained at cryogenic temperatures, thought to be a result of increased damage threshold at these temperatures.

ASE in visible quantum dots at room temperature was observed with threshold pump fluences of about 1 mJ/cm^2 with the ASE peak also occurring on the red side of the low intensity luminescence peak, corresponding to the biexciton energy level [51]. In order to increase the optical damage threshold, nanocrystals were incorporated in a titania sol–gel matrix [52]. The resulting film contained CdSe nanocrystals at a volume fraction of more than 10%, which is sufficient for ASE to be generated. Tunable ASE was observed at room temperature over a range from 560 to 650 nm for different nanocrystal sizes.

ASE spectral dependence on the incident pump power was used to investigate properties of higher excited states [53, 54]. Photoluminescence transients were recorded for CdSe dots of different sizes as a function of pump power. At short detection times (order of 100 ps), biexciton luminescence at low energy was observed, while at longer times (order of 1 ns) all the luminescence originated from the single exciton $1S_{eh}$ transition. CdSe in a sol–gel titania matrix also exhibited ASE, with a threshold for the biexciton ASE occurring at a population of $\langle N_{eh} \rangle \sim 1.5$. Upon increasing the pump power, the biexciton ASE intensity saturated at a population of about 4.2 excitons per dot, after which a second ASE peak at higher emission energy appeared. This second peak

corresponds to the next allowed transition involving more than three electron–hole pairs. Multi-excitonic interactions lift the expected six-fold degeneracy of this state leading to the relative low ASE threshold.

Utilizing the VSL method the modal gain coefficients were obtained for both these energy transitions. Both the low and high energy ASE peaks exhibited the same threshold stripe length and nearly the same above-threshold intensity dependence on the stripe length. The resulting modal gains for the low energy and high energy ASE peaks were about 40 and 70 cm^{-1}, respectively. Although the lowest allowed energy states have comparable oscillator strengths [55], multi-excitonic interactions can increase the absorption cross section for the higher energy state and therefore cause the larger gain values compared to the lowest allowed energy state.

Auger recombination increases the threshold to realize optical gain, and therefore ASE, and ultimately increases the laser threshold. Additionally, the absorption cross section of individual dots is relatively small, also resulting in increased optical thresholds. Having a large shell on a small core allows some inter-diffusion of the core and shell atoms resulting in a gradual potential profile, thus decreasing the potential carrier scattering at the nanocrystal interface [56]. Regularly sized CdSe cores coated with up to 19 monolayers of CdS result in confinement of the holes in the core, while the electrons are situated more in the shell. Such quasi- type-II heterostructure dots exhibit highly suppressed Auger recombination rates, with biexciton lifetimes on order of 10 ns, several orders of magnitude longer than regular dots. As a result of the highly increased dot diameter, the absorption cross section is also increased. These properties lead to an ASE threshold reduction by more than one order of magnitude.

In addition to the highly reduced threshold and the increased gain lifetime, the reduced Auger recombination efficiency has the effect that at large population levels ($\langle N_{eh} \rangle \gg 1$), higher energy levels can be easily populated. Just above threshold the ASE peak is concentrated on the blue side of the low pump intensity luminescence peak. Upon increasing pump intensity, second and third ASE peaks appear at higher photon energies corresponding to multi-excitonic states (Figure 8.9). The thresholds of $\sim$100 $\mu J/cm^2$ and 200 $\mu J/cm^2$ for the second and third ASE peaks are remarkably lower for the biexcitonic ASE threshold of regular core-only dots. These results show that, with control over the Auger recombination rates, amplification over more than 500 meV can be achieved within one device.

8.5.2 Infrared colloidal quantum dots based on lead chalcogenides

Lead chalcogenides have a complex electronic band structure. Instead of having the minima at the Γ-point like the cadmium chalcogenides, they exhibit a multi-valley structure with four band minima at the L-points of the Brillouin zone (see Figure 8.10(a)(inset) for the case of PbSe). This leads to the aforementioned eight-fold degeneracy of the emitting states in the nanocrystal, when the two-fold spin degeneracy in each valley is taken into account [25]. As a consequence, the population densities needed to reach transparency in these material systems involve a large number of excitons per dot. It can thus be expected that multi-exciton interactions are very predominant.

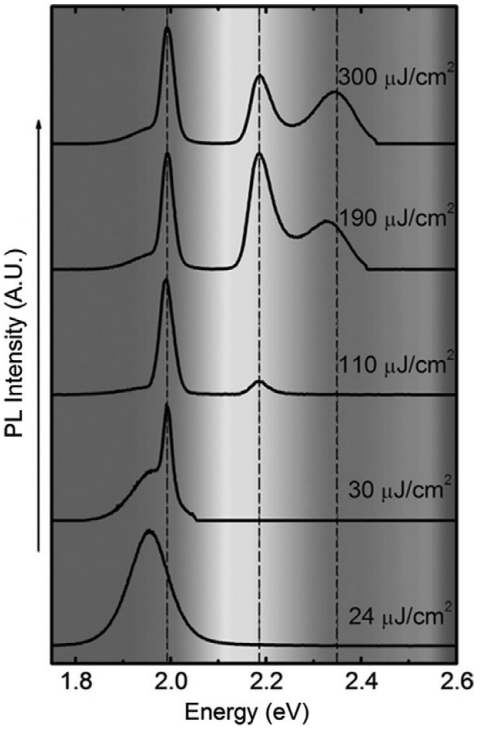


Figure 8.9 Emission spectra of solid thin films made from giant core/shell CdSe/CdS nanocrystals. Upon increase of the pump intensity, ASE features appear at 1.99, 2.19 and 2.34 eV corresponding to biexciton, and multi-excitonic states. The corresponding thresholds were about 30, 100 and 200 μJ/cm^2, respectively [56].

In bulk semiconductors the Auger recombination rate becomes more efficient with decreasing bandgap. Therefore, it is expected that, compared to the large bandgap cadmium chalcogenides, the lifetime of multi-excitons in lead chalcogenide quantum dots is highly reduced due not only to the necessary large exciton populations, but also to the bandgap dependence of the Auger recombination constant. This expected highly reduced multi-exciton lifetime could therefore potentially lead to a failure to reach optical gain in these nanocrystals. Schaller *et al*. demonstrated that despite these unfavorable conditions, gain can be realized in this type of dots under conditions similar to the two-fold degenerate Cd-based nanocrystals [43].

For PbSe dots in hexane solution, Figure 8.10(a) shows the dependence of the nonlinear absorption bleaching as function of the exciton population, when the probe wavelength was tuned to the spectral positions of the exciton absorption peak (open squares) and luminescence peak (solid circles). Compared with two-fold degenerate materials, the absorption bleaching with increasing N_{eh} is much weaker. Fitting the absorption bleaching below transparency at relatively low exciton levels using state filling and Poisson statistics, the state degeneracy (D) is confirmed to be 8. Much like the cadmium-based materials presented in Figure 8.7, the dots do not reach transparency at the exciton

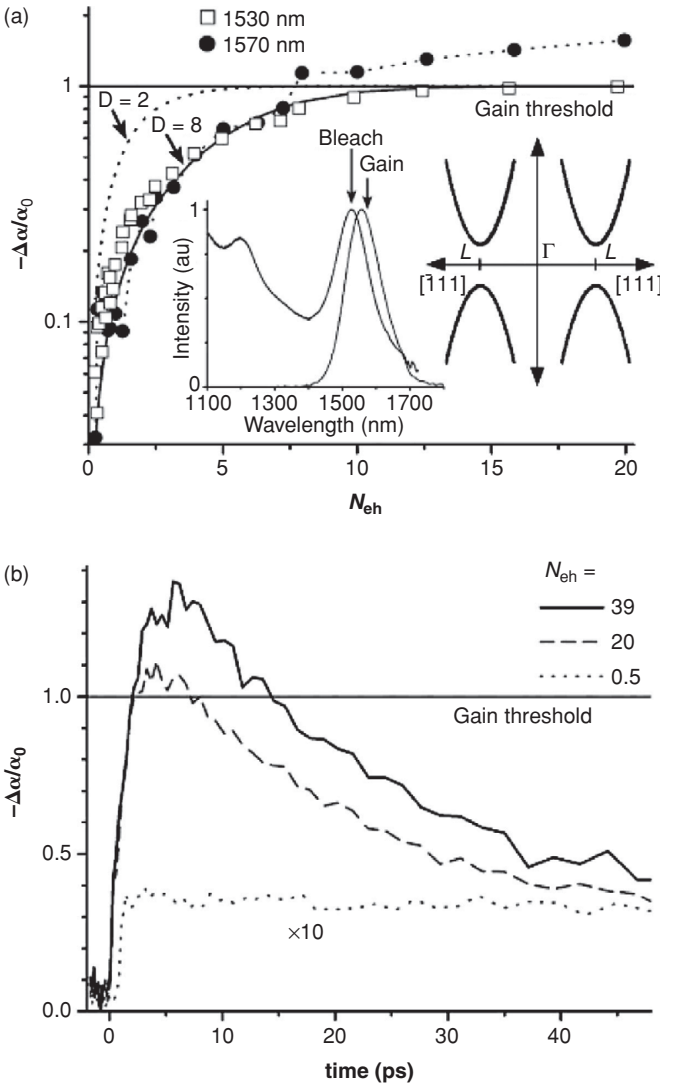


Figure 8.10 Optical gain in PbSe quantum dots. (a) Relative absorption bleaching as a function of exciton population for probe wavelengths at the absorption maximum and the luminescence peak. Fitting the change in absorption with Poisson statistics reveals a degeneracy of $D = 8$. The insets show the absorption and luminescence spectra and a schematic of the electronic band structure of bulk PbSe. (b) Absorption bleaching dynamics at the luminescence peak for different exciton population levels, revealing a gain lifetime on the order of up to 10 ps [43].

absorption peak. At the luminescence peak the absorption bleaching turns into optical gain at an exciton population of about 8. This is twice the theoretically predicted population, and is caused by state filling effects as well as contributions from PIA. Although the transparency exciton population is high, the effective pump energy to reach this

is similar to that for cadmium-based nanocrystals (order of 0.1–1 mJ/cm^2) due to the increased absorption cross section of the infrared dots.

The transient absorption dynamics for these dots at the luminescence peak spectral position is revealed in Figure 8.10(b). For low exciton densities resulting in some mild bleaching, the absorption change is long lived. For very large exciton populations optical gain is detected for 5–10 ps. The decay time of the absorption bleaching at these high population levels is fairly constant with characteristic times of several tens of picoseconds. These times are very similar to those for cadmium-based nanocrystals, even though the multi-exciton population is much higher, indicating that in the PbSe nanocrystals the multi-exciton dynamics is much less efficient.

PbSe dots in close-packed films were found to degrade rapidly under intense optical illumination. In analogy with the visible cadmium chalcogenides, PbSe dots in a titania sol–gel matrix did not exhibit this degradation [43]. At sufficiently high pump fluences films with a filling fraction of about 15% exhibited an ASE peak at 1555 nm, situated on the red side of the low pump power luminescence peak.

Remarkably similarly to PbSe, PbS in hexane operating around 1.55 μm wavelengths exhibited gain around the luminescence peak [38]. Maximum gain occurred at the minimum of the absorption spectrum of hexane (Figure 8.11(a)), giving evidence for the influence of the surrounding matrix on the gain spectrum. At this wavelength of 1570 nm, the gain threshold was about 8 mJ/cm^2 (Figure 8.11(b)), almost 1 order of magnitude larger than the gain threshold for PbSe dots, which is thought to be caused by PIA possibly induced by the finite absorption of the hexane matrix.

8.6 Colloidal nanocrystal lasers

Optical gain, amplification of photoluminescence, and the ability to make waveguides with low propagation losses are necessary ingredients for building a laser. For nanocrystal quantum dots, factors that have to be considered in cavity design include: (1) the gain on order of 100 cm^{-1} requires ultra-high quality factor cavities (2) the gain lifetime, τ_{gain}, of several tens of picoseconds requires the cavity length to be smaller than $\tau_{gain}c_{light}/n$, where n is the refractive index. Cavity lengths typically less than 100 μm are required. Several cavity designs have been considered that could satisfy these requirements. Most of these designs are based on whispering gallery mode operation.

In circular cavities, light inside a high refractive index material can bounce around the circumference through total internal reflection. These optical propagation modes are called whispering gallery modes [57]. The quality factor, or Q factor, describes the degree of feedback the cavity can attain. This factor is affected by any losses and imperfections inside the waveguide as well as absorption in any of the materials used to form the cavity. Q factors can be calculated by $\lambda/\Delta\lambda$, where λ and $\Delta\lambda$ are the laser wavelength and the laser emission full width half maximum, respectively. Whispering gallery mode cavities can yield Q factors of more than 1e9 due to near lossless total internal reflection propagation, while the best Fabry–Perot cavities have yielded Q factors on order of 1e6,

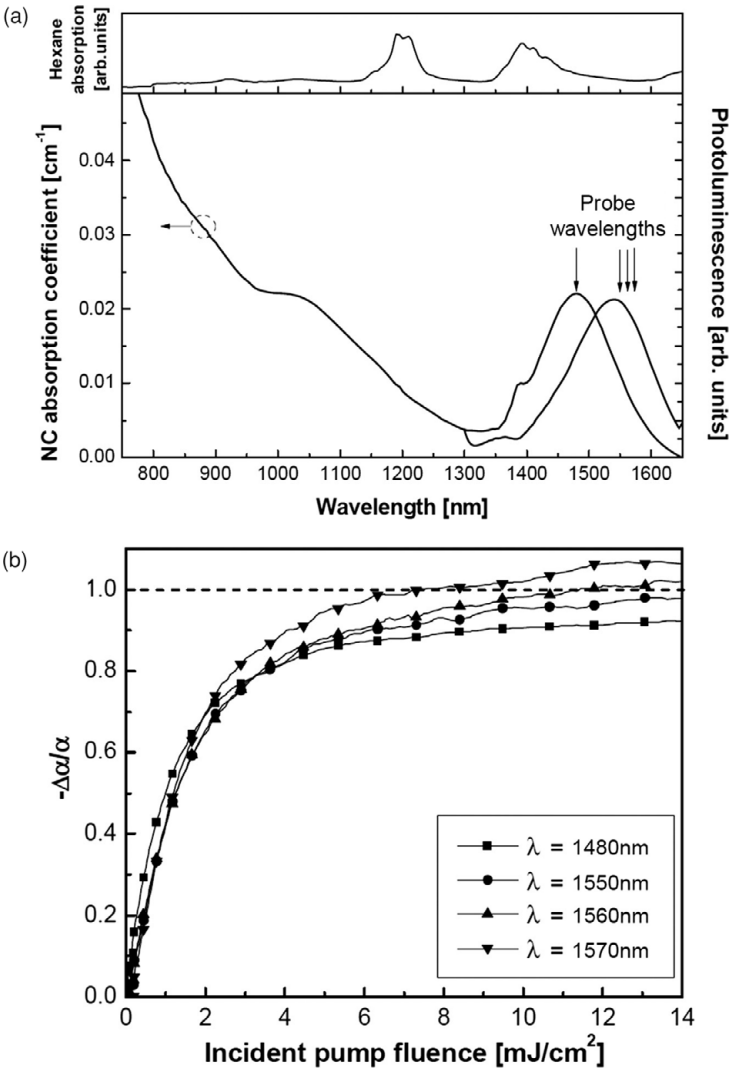


Figure 8.11 Gain in PbS nanocrystals in hexane solution. (a) Absorption and emission spectra of 5.5 nm diameter nanocrystals in hexane solution. The graph on the top depicts the absorption spectrum of hexane, showing a minimum absorption value around the peak luminescence wavelength. (b) Nonlinear absorption change as a function of the incident pump fluence for different spectral positions around the absorption edge, revealing optical gain at 1570 nm at a threshold fluence of 8 mJ/cm^2 [38].

thus making whispering gallery mode cavities ideal candidates for lasers made from low gain materials, such as nanocrystals [58]. Moreover, incorporation of gain material poses difficulties for most material systems, while solution processable nanocrystals can be functionalized to adhere to the required surface. For example, nanocrystals can be coated on the outer surface of microspheres, on the inside of a microcapillary tube, or on the surface of micro-torroids.

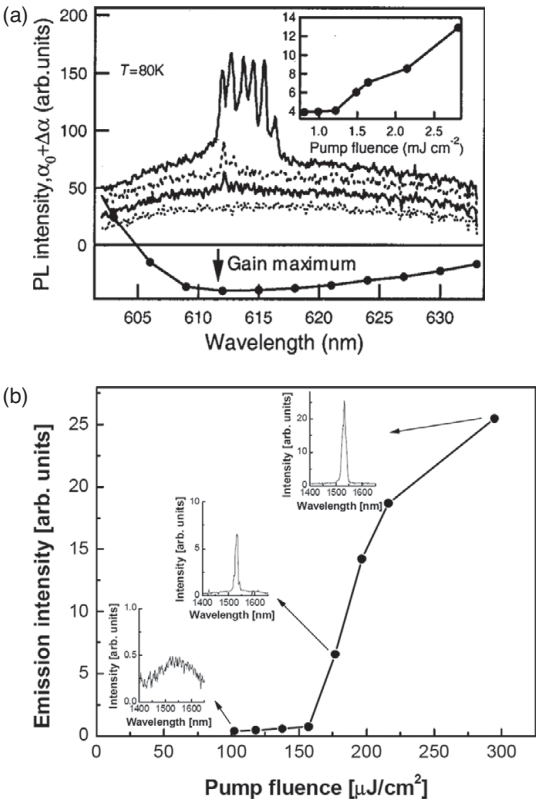


Figure 8.12 (a) Whispering gallery mode emission spectrum for CdSe dots in an 80 μm inner-diameter microcapillary tube for pump powers of 1, 1.4, 1.6, and 2.8 mJ/cm^2 (lines) and different optical gain (symbols). Inset: Emission intensity dependence of the 612 nm whispering gallery mode as function of incident pump fluence [40]. (b) Pump fluence dependence of the emission intensity at the laser wavelength of 1532 nm for a film made from PbS dots applied on the inner circumference of a glass microcapillary tube. The insets show the appearance of a narrow laser line above a threshold pump fluence of about 160 μJ/cm^2 [38].

8.6.1 Microcapillary resonators

The first demonstration of lasing operation of colloidal quantum dots was based on CdSe dots coating the inner circumference of a microcapillary glass tube with an inner diameter of 80 μm [40]. In this configuration, several modes are possible: waveguide modes along the length of the tube, nonfeedback whispering gallery modes, where light propagates through total internal reflection around the inner circumference of the tube, and whispering gallery modes experiencing optical feedback. At a temperature of 80 K, the laser structure exhibited a threshold behavior of the emission at a pump fluence of about 1.2 mJ/cm^2, coinciding with the appearance of distinct laser emission peaks at the peak gain spectral position of 615 nm (Figure 8.12(a)). The spacing between the multiple whispering gallery modes that appear above lasing threshold yields a modal refractive index of 1.8, closely matching typical refractive index values of CdSe dots in thin

film, thus indicating that the laser modes are primarily situated inside the nanocrystal film. Very similar results were obtained with CdSe in a titania matrix applied to the inside of a microcapillary tube. Much like the ASE results, the improved thermal and optical stability of the nanocrystals in such a matrix has led to lasing operation at room temperature [59].

In similar fashion to visible quantum dot whispering gallery mode lasers, infrared colloidal quantum dots have been used to realize lasing operation [38]. The short gain lifetimes for the PbS dots required the packing fraction of the dots inside a solid film to be very high. In order to fulfill this requirement bulky oleic acid ligands were replaced with much shorter butylamine ligands. A concentrated solution of these dots in chloroform was drawn up inside the capillary tube through capillary action and a film was created by carefully flowing nitrogen gas through the tube, causing the liquid to propagate through the tube. During propagation, the solvent evaporated leaving a thin film behind on the inner wall of the capillary tube. When pumped at 80 K the emission spectrum exhibited a sharp narrow peak at 1532 nm at a pump fluence of about 180 $\mu J/cm^2$ (Figure 8.12(b)). This threshold is very similar to that of the cadmium chalcogenide dots, even though the transparency population is 4 times higher for the PbS dots.

Investigation of the mode profile revealed an effective modal refractive index of 1.7, closely matching the refractive index of a solid thin film, indicating that for this structure as well, the whispering gallery mode is closely confined within the nanocrystal film. The threshold pump fluence was found to be highly temperature dependent, which was caused by the temperature dependent Auger recombination efficiency, resulting in a maximum operation temperature of 250 K.

For quantum dots it is expected that the emission wavelength is nearly temperature independent, which was confirmed with a 0.03 nm/K red shift of the emission wavelength as a function of temperature. This rate is 2 times lower than the best values observed with self-assembled epitaxial quantum dots [60], confirming the high quality of the colloidal nanocrystals and operation in the true strong quantum confinement.

8.6.2 Microsphere resonators

Microspheres can be mixed with materials in solution and deposited on a substrate. When coated with gain material, each sphere can provide a whispering gallery mode cavity in which the generated light is tightly confined within the gain material applied on the outside surface of the sphere. Uniform coating is essential in this case to ensure low propagation losses. Sol–gel solutions mixed with nanocrystals can provide physical wetting when microspheres are mixed with the viscous sol–gel solution so that shape of the spheres is preserved. Coating CdSe–titania sol–gel solutions on 5–20 μm silica spheres yielded smooth films, preserving the spherical template and minimal coating build up at the base. Laser operation was observed at room temperature with a threshold of about 40 mJ/cm^2. By adjusting the CdSe/ZnS core/shell emission wavelength, to overlap with the whispering gallery resonance and the pump power, single mode operation can be realized. Analysis of the laser spectrum revealed a modal Q factor of 400–1000. Surface roughness from the titania matrix, scattering inside the active film, non-uniformity of

the spherical template and PIA are thought to be the cause of this somewhat lower Q factor.

This technique is more versatile than the microcapillary tube, since the laser is placed directly on top of a substrate, allowing, for example, direct coupling of the generated laser light into on-chip waveguides. The technique is also universal and can be applied to any nanocrystal material systems. For example, a blue laser has been made with silica spheres and small core CdS/ZnS nanocrystals in a titania matrix. Similar operating conditions as for the red emitting laser were obtained, with a Q factor of >600 and a threshold power of about 4 mJ/cm^2. The modal refractive index also confirmed the high confinement of the optical mode inside the nanocrystal film.

8.6.3 Distributed feedback resonators

Distributed feedback lasers have the advantage that the output can be directly coupled into on-chip waveguides. These lasers consist of a grating structure embossed in-plane with the substrate, which interacts with the waveguide modes. In these structures the active waveguide parameters, such as thickness and refractive index, as well as the grating properties, such as the pitch and shape, determine the wavelength at which the optical feedback maximizes and overlaps with the maximum gain [61]. Gratings that operate in the second-order diffraction regime provide feedback at the desired wavelength λ, when the grating pitch Λ is given by $\Lambda = \lambda/n_{eff}$, where n_{eff} is the effective refractive index of the waveguide mode. Typical numbers for n_{eff} are on the order of 1.8, meaning that for red luminescent nanocrystal films, the grating pitch should be about 300 nm. Such features are easily attainable with standard lithography processes.

Pre-patterned substrates with etched gratings can be used as the substrate on which the nanocrystal films is deposited [47]. Pre-patterning of the substrate is a very involved process; instead the grating structure can be embossed in the nanocrystal film using elastometric grating stamps [54, 62]. For both cases the Q factor was found to be on the order of 500, demonstrating the high quality that can be obtained from these feedback structures.

8.6.4 Microtoroid resonators

Microtoroidal resonators can be pre-fabricated through lithography on top of a substrate. These resonators have the ability to provide Q factors of more than 1e8, while silica torroidal microcavities have yielded longer photon storage times as well as better spatial confinement than microcapillary tube or microsphere resonators [63]. CdSe/ZnS core/shell dots applied at very low packing fractions on a silica microtoroid yielded near ideal Q factors of about 1e7, limited by scattering processes [64]. The torroid was pumped through evanescent coupling of the pump light from a tapered fiber to the outer part of the toroid. Single mode lasing was observed at pump energies as low as 10 fJ for about 2000 dots applied to the torroid. At higher pump energies multi-mode lasing was observed. For higher dot numbers, the threshold pump energy increased accordingly due to lowering of the Q factor at the pump wavelength. These ultra-low thresholds obtained

at room temperature indicate that careful design of the laser cavity is very important for real applications of these lasers.

8.6.5 Other resonators

Other laser cavity designs have also been used to realize colloidal quantum dot lasers. Notably, microdrops, which contained nanocrystals and which were suspended in air, yielded whispering gallery mode lasing operation when pumped with nanosecond pulses [65]. In this configuration, lasing operation was observed at nanocrystal volume fractions of 0.006%, much lower than the predicted lower-bound fractions of 0.2%. It was thought that the nanocrystal distribution was not uniform throughout the microdroplet, and therefore most of the nanocrystals would be on the outer surface due to increased surface tensions, thus increasing the local concentration.

Photonic crystal structures have shown to yield very high Q factors and therefore would be interesting candidates as resonators for nanocrystals. Nonuniform coating of the photonic bandgap structures decreases the Q factor rapidly and only ASE has been observed from these structures [66, 67].

8.7 Future prospects

For everyday applications of nanocrystal lasers, it is highly advantageous to drive the laser electrically. However, currently, with the given optical properties of colloidal nanocrystals related to lasing and ASE (Table 8.3), the optical pump fluences needed to realize optical transparency in these materials are not compatible with such a pumping scheme. To demonstrate this, assume a structure containing a monolayer of nanocrystals with a degeneracy of 2 and a diameter of 5 nm in which enough carriers need to be injected to active transparency. The corresponding current density is on the order of 10 kA/cm^2, assuming a gain lifetime of 10 ps. Such current densities are not compatible with soft nanocrystal thin films.

The main contributor to such high current densities is the ultra-short gain lifetime occurring in nanocrystals. To lower the necessary current densities to attainable values, the Auger recombination time needs to be increased dramatically with an increased gain lifetime as a result. In the following a design scheme of core/shell nanocrystals is discussed in which the transparency population is lowered to below 1 exciton per dot, avoiding any multi-exciton interactions and thus Auger recombination.

8.7.1 Single exciton gain

The multi-exciton interactions not only cause PIA, which could influence the magnitude of the optical gain, but also reduce the lifetime of the gain through the ultra-fast Auger recombination process. These unfavorable processes should be avoided through careful engineering of the colloidal quantum dots to realize optical gain at a population of a single exciton per dot. This was first realized by forming core/shell dots in which the exciton is spatially separated, with the electron residing predominantly in the shell and the hole

delocalized over the entire dot [68]. In this inverted core/shell system of ZnSe/CdSe dots, the Auger recombination time is increased by about a factor of 3, demonstrating that spatial separation of the electrons and holes can yield favourable properties for low threshold lasing.

An improvement in the above system would be for the electron and hole to be truly spatially separated. A type II heterostructure made with materials in which the bandgaps are offset for both the conduction and the valence band could accomplish this: e.g., a core whose material has a larger electron affinity and ionization energy than the shell material will confine the excited electron to the core and the hole to the shell. Compared with the inverted core/shell structure this type of core/shell dot has the benefit that there are fewer restrictions on the shell thickness: the thickness needs to be large enough for an allowed state to exist, but there is no limit on the maximum thickness.

With the electron and hole separated, positive and negative charges are spatially separated, which induces a strong local electric field. This field leads to effective splitting of the degeneracy of the allowed energy states through the Stark effect and effectively alters the allowed energy spectrum of singly excited nanocrystal. If the magnitude of the Stark shift (Δ_{Stark}) is comparable to or greater than the transition linewidth (Γ), absorption losses at the emission wavelength can be completely eliminated. In the presence of the induced field, the population threshold to achieve optical transparency is therefore altered and is given by $\langle N\rangle = 2/(3 - \exp(-\Delta_{Stark}{}^2/\Gamma^2))$ [69]. This relation shows that for a large enough Stark shift, optical transparency is achieved at $\langle N\rangle = 2/3$ and therefore optical gain does not require multi excitons.

CdS/ZnSe material systems do exhibit this type of band alignment (Figure 8.13(a)). Klimov and coworkers [69, 70] showed that in this material system at a shell thickness of more than ~0.8 nm and a core radius of more than 1.2 nm the structures would exhibit the desired type II structure, in which the spatial separation of electrons and holes is realized (Figure 8.13(b)). Additionally, the Stark shift due to the presence of a separated exciton in the dot has the desired repulsive nature making the shift positive; the magnitude of the shift can be fine tuned by adjusting the radius of the dot with the shell thickness (Figure 8.13(c)).

Dots with these type II architectures should exhibit gain thresholds at exciton populations of less than 1 per dot. Ultra-fast pump probe measurements at the single exciton peak reveal a linear dependence of the absorption bleaching with the exciton population showing an optical gain threshold of $\langle N_{eh}\rangle \sim 0.7$ (Figure 8.14) in close agreement with the theoretical predicted exciton population. In contrast, at the biexciton energy level type I nanocrystals exhibit a quadratic dependence of the absorption bleaching on the exciton population and yield an optical gain threshold of $\langle N_{eh}\rangle \sim 2$. Transient absorption dynamics with the probe at the ASE peak wavelengths reveal that the Auger recombination is highly reduced resulting in a 50-fold increase of the absorption bleaching decay time to a value of 1.7 ns. This increase of the absorption decay time is a direct result of the electron–hole spatial separation. Additionally, it was shown that ASE occurs just above threshold for type II nanocrystals at the single exciton peak (X), since at this pumping level the population is less than 1 exciton per dot. For type I nanocrystals the threshold is at more than 1 exciton per dot and therefore the ASE signal occurs at the biexciton energy level.

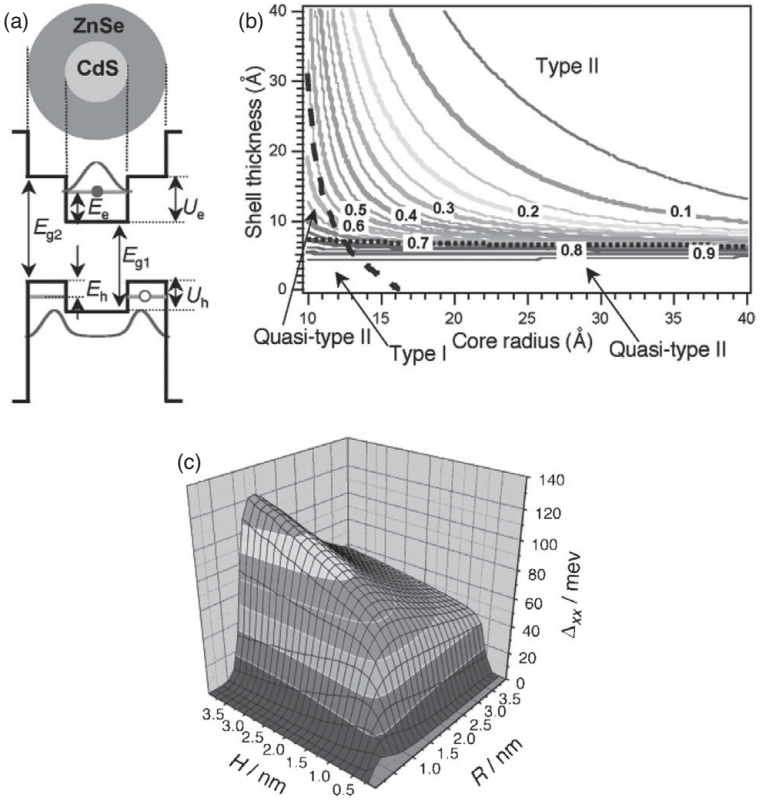


Figure 8.13 (a) Band alignment of a CdS/ZnSe core/shell design for single exciton optical gain realization. (b) Dependence of the CdS/ZnSe core/shell structure type on the core radius, *R*, and shell thickness, *H*. Type II heterostructure with electrons confined to the core and holes confined to the shell can be realized at dimensions larger than the threshold values indicated by the black lines. (c) Exciton–exciton interaction energy, corresponding to the shift in the $1S_{eh}$ transition energy as function of ZnSe shell thickness (*H*) and CdS core radii (*R*) [70].

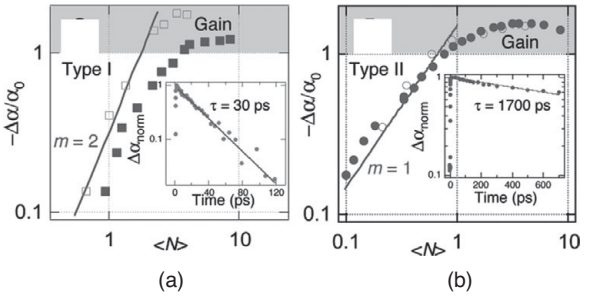


Figure 8.14 Nonlinear change in absorption for type I and type II heterostructure CdSe nanocrystals. (a) Type I heterostructure nanocrystals in TOP solution (open squares) and solid state film as measured at the biexciton ASE peak wavelength. The straight line indicates a quadratic growth. (b) Type II heterostructure nanocrystals for two different samples as measured at the exciton ASE peak wavelength. The straight line indicates a linear growth [70].

These results show that careful design of type II nanocrystals can yield single exciton lasing action. Together with the greatly increased gain lifetime this could pave the way towards attainable electrical pumping schemes. Such schemes could make colloidal nanocrystal lasers a new type of efficient lasers with operating wavelengths tunable from the blue to beyond the short-wavelength-infrared.

References

1 M. Asada, Y. Miyamoto, Y. Suematsu, Gain and the threshold of 3-dimensional quantum-box lasers. *IEEE Journal of Quantum Electronics*, **22**(9) (1986), 1915–1921.

2 Y. Arakawa, H. Sakaki, Multidimensional quantum well laser and temperature-dependence of its threshold current. *Applied Physics Letters*, **40**(11) (1982), 939–941.

3 Y. V. Vandyshev, V. S. Dneprovskii, V. I. Klimov, D. K. Okorokov, Lasing on a transition between quantum-well levels in a quantum dot. *JETP Letters*, **54**(8) (1991), 442–445.

4 P. G. Eliseev, H. Li, A. Stintz, *et al*., Transition dipole moment of InAs/InGaAs quantum dots from experiments on ultralow-threshold laser diodes. *Applied Physics Letters*, **77**(2) (2000), 262–264.

5 G. Park, O. B. Shchekin, D. L. Huffaker, D. G. Deppe, Low-threshold oxide-confined 1.3-μm quantum-dot laser. *Photonics Technology Letters, IEEE*, **12**(3) (2000), 230–232.

6 D. Bimberg, M. Grundman, N. N. Ledentsov, *et al*., Novel infrared quantum dot lasers: Theory and reality. *Physica Status Solidi B–Basic Solid State Physics*, **224**(3) (2001) 787–796.

7 C. B. Murray, D. J. Norris, M. G. Bawendi, Synthesis and characterization of nearly monodisperse CdE (E = S, Se, Te) semiconductor nanocrystallites. *Journal of the American Chemical Society*, **115**(19) (1993), 8706–8715.

8 E. H. Sargent, Infrared quantum dots. *Advanced Materials*, **17**(5) (2005), 515–522.

9 M. A. Hines, G. D. Scholes, Colloidal PbS nanocrystals with size-tunable near-infrared emission: Observation of post-synthesis self-narrowing of the particle size distribution. *Advanced Materials*, **15**(21) (2003), 1844–1849.

10 M. J. Fernee, P. Jensen, H. Rubinsztein-Dunlop, Origin of the large homogeneous line widths obtained from strongly quantum confined PbS nanocrystals at room temperature. *Journal of Physical Chemistry C*, **111**(13) (2007), 4984–4989.

11 D. Ricard, M. Ghanassi, M. C. Schanneklein, Dielectric confinement and the linear and nonlinear-optical properties of semiconductor-doped glasses. *Optics Communications*, **108**(4–6) (1994), 311–318.

12 P. R. Yu, M. C. Beard, R. J. Ellingson, *et al*., Absorption cross-section and related optical properties of colloidal InAs quantum dots. *Journal of Physical Chemistry B*, **109**(15) (2005), 7084–7087.

13 E. Istrate, S. Hoogland, V. Sukhovatkin, *et al*., Carrier relaxation dynamics in lead sulfide colloidal quantum dots. *Journal of Physical Chemistry B*, **112**(10) (2008), 2757–2760.

14 J. M. Luther, M. C. Beard, Q. Song, *et al*., Multiple exciton generation in films of electronically coupled PbSe quantum dots. *Nano Letters*, **7**(6) (2007), 1779–1784.

15 V. I. Klimov, C. J. Schwarz, D. W. McBranch, C. A. Leatherdale, M. G. Bawendi, Ultrafast dynamics of inter- and intraband transitions in semiconductor nanocrystals: Implications for quantum-dot lasers. *Physical Review B*, **60**(4) (1999), R2177–R2180.

16 C. A. Leatherdale, W.-K. Woo, F. V. Mikulec, M. G. Bawendi, On the absorption cross section of CdSe nanocrystal quantum dots. *Journal of Physical Chemistry B*, **106**(31) (2002), 7619–7622.

17 A. Pandey, P. Guyot-Sionnest, Slow electron cooling in colloidal quantum dots. *Science*, **322**(5903) (2008), 929–932.

18 J. Tang, L. Brzozowski, D. Aaron, *et al*., Quantum dot photovoltaics in the extreme quantum confinement regime: the surface-chemical origins of exceptional air- and light-stability. *ACS Nano*, **4**(2) (2010), 869–878.

19 G. Konstantatos, L. Levina, A. Fischer, E. H. Sargent, Engineering the temporal response of photoconductive photodetectors via selective introduction of surface trap states. *Nano Letters*, **8**(5) (2008), 1446–1450.

20 T. W. F. Chang, A. Maria, P. W. Cye, *et al*., High near-infrared photoluminescence quantum efficiency from PbS nanocrystals in polymer films. *Synthetic Metals*, **148**(3) (2005), 257–261.

21 B. O. Dabbousi, J. Rodriguez-Viejo, F. V. Mikulec, *et al*., (CdSe)ZnS core-shell quantum dots: Synthesis and characterization of a size series of highly luminescent nanocrystallites. *Journal of Physical Chemistry B*, **101**(46) (1997), 9463–9475.

22 P. J. Reiss, J. Bleuse, A. Pron, Highly luminescent CdSe/ZnSe core/shell nanocrystals of low size dispersion. *Nano Letters*, **2**(7) (2002), 781–784.

23 C. R. Kagan, C. B. Murray, M. G. Bawendi, Long-range resonance transfer of electronic excitations in close-packed CdSe quantum-dot solids. *Physical Review B*, **54**(12) (1996), 8633–8643.

24 V. I. Klimov, A. A. Mikhailovsky, S. Xu, *et al*., Optical gain and stimulated emission in nanocrystal quantum dots. *Science*, **290**(5490) (2000), 314–317.

25 I. Kang, F. W. Wise, Electronic structure and optical properties of PbS and PbSe quantum dots. *Journal of the Optical Society of America B–Optical Physics*, **14**(7) (1997), 1632–1646.

26 G. E. Cragg, A. L. Efros, Suppression of Auger processes in confined structures. *Nano Letters*, **10**(1) (2010), 313–317.

27 K. Kyhm, J. H. Kim, S. M. Kim, H.-S. Yang, Gain dynamics and excitonic transition in CdSe colloidal quantum dots. *Optical Materials*, **30**(1) (2007), 158–160.

28 V. I. Klimov, A. A. Mikhailovsky, D. W. McBranch, C. A. Leatherdale, M. G. Bawendi, Quantization of multiparticle Auger rates in semiconductor quantum dots. *Science*, **287**(5455) (2000), 1011–1013.

29 M. C. Beard, R. J. Ellingson, Multiple exciton generation in semiconductor nanocrystals: Toward efficient solar energy conversion. *Laser & Photonics Reviews*, **2**(5) (2008), 377–399.

30 O. Svelto, S. Taccheo, C. Svelto, Analysis of amplified spontaneous emission: some corrections to the Linford formula. *Optics Communications*, **149**(4–6) (1998), 277–282.

31 L. Dal Negro, M. Cazzanelli, N. Daldosso, *et al*., Stimulated emission in plasma-enhanced chemical vapour deposited silicon nanocrystals. *Physica E–Low-Dimensional Systems & Nanostructures*, **16**(3–4) (2003), 297–308.

32 L. Dal Negro, M. Cazzanelli, L. Pavesi, *et al*., Dynamics of stimulated emission in silicon nanocrystals. *Applied Physics Letters*, **82**(26) (2003), 4636–4638.

33 L. Khriachtchev, M. Räsänen, S. Novikov, J. Sinkkonen, Optical gain in Si/SiO_2 lattice: Experimental evidence with nanosecond pulses. *Applied Physics Letters*, **79**(9) (2001), 1249–1251.

34 B. W. Hakki, T. L. Paoli, Gain spectra in GaAs double-heterostructure injection lasers. *Journal of Applied Physics*, **46**(3) (1975), 1299–1306.

35 L. Dal Negro, *et al*., Applicability conditions and experimental analysis of the variable stripe length method for gain measurements. *Optics Communications*, **229**(1–6) (2004), 337–348.

36 K. L. Shaklee, R. E. Nahory, R. F. Leheny, Optical gain in semiconductors. *Journal of Luminescence*, **7** (1973), 284–309.

37 J. Valenta, I. Pelant, J. Linnros, Waveguiding effects in the measurement of optical gain in a layer of Si nanocrystals. *Applied Physics Letters*, **81**(8) (2002), 1396–1398.
38 S. Hoogland, V. Sukhovatkin, I. Howard, *et al*., A solution-processed 1.53 μm quantum dot laser with temperature-invariant emission wavelength. *Optics Express*, **14**(8) (2006), 3273–3281.
39 J. Roither, S. Pichler, M. V. Kovalenko, *et al*., Two- and one-dimensional light propagations and gain in layer-by-layer-deposited colloidal nanocrystal waveguides. *Applied Physics Letters*, **89**(11) (2006), 111120.
40 A. V. Malko, A. A. Mikhailovsty, M. A. Petruska, *et al*., From amplified spontaneous emission to microring lasing using nanocrystal quantum dot solids. *Applied Physics Letters*, **81**(7) (2002), 1303–1305.
41 K. Kyhm, S. M. Kim, J. M. Kim, *et al*., Optical gain in CdSe nanocrystals. *Journal of Luminescence*, **122** (2007), 808–811.
42 V. Sukhovatkin, S. Musikhin, I. Gorelikov, *et al*., Room-temperature amplified spontaneous emission at 1300 nm in solution-processed PbS quantum-dot films. *Optics Letters*, **30**(2) (2005), 171–173.
43 R. D. Schaller, M. A. Petruska, V. I. Klimov, Tunable near-infrared optical gain and amplified spontaneous emission using PbSe nanocrystals. *Journal of Physical Chemistry B*, **107**(50) (2003), 13765–13768.
44 V. I. Klimov, M. G. Bawendi, Ultrafast carrier dynamics, optical amplification, and lasing in nanocrystal quantum dots. *MRS Bulletin*, **26**(12) (2001), 998–1004.
45 A. A. Mikhailovsky, A. V. Malko, J. A. Hollingsworth, M. G. Bawendi, V. I. Klimov, Multiparticle interactions and stimulated emission in chemically synthesized quantum dots. *Applied Physics Letters*, **80**(13) (2002), 2380–2382.
46 R. R. Cooney, S. L. Sewall, D. M. Sagar, P. Kambhampati, State-resolved manipulations of optical gain in semiconductor quantum dots: Size universality, gain tailoring, and surface effects. *Journal of Chemical Physics*, **131**(16) (2009), 164706.
47 H. J. Eisler, V. C. Sundar, M. G. Bawendi, *et al*., Color-selective semiconductor nanocrystal laser. *Applied Physics Letters*, **80**(24) (2002), 4614–4616.
48 A. V. Malko, A. A. Mikhailovsky, M. A. Petruska, J. A. Hollingsworth, V. I. Klimov, Interplay between optical gain and photoinduced absorption in CdSe nanocrystals. *Journal of Physical Chemistry B*, **108**(17) (2004), 5250–5255.
49 S. L. Sewall, R. C. Cooney, K. E. H. Anderson, E. A. Dias, P. Kambhampati, State-to-state exciton dynamics in semiconductor quantum dots. *Physical Review B*, **74**(23) 2006.
50 S. L. Sewall, R. R. Cooney, K. E. Anderon, *et al*., State-resolved studies of biexcitons and surface trapping dynamics in semiconductor quantum dots. *Journal of Chemical Physics*, **129**(8) (2008), 084701.
51 H. Htoon, J. A. Hollingsworth, A. V. Malko, R. Dickerson, V. I. Klimov, Light amplification in semiconductor nanocrystals: Quantum rods versus quantum dots. *Applied Physics Letters*, **82**(26) (2003), 4776–4778.
52 V. C. Sundar, H. J. Eisler, M. G. Bawendi, Room-temperature, tunable gain media from novel II–VI nanocrystal-titania composite matrices. *Advanced Materials*, **14**(10) (2002), 739-+.
53 J. M. Caruge, Y. Chan, V. Sundar, H. J. Eisler, M. G. Bawendi, Transient photoluminescence and simultaneous amplified spontaneous emission from multiexciton states in CdSe quantum dots. *Physical Review B*, **70**(8) (2004), 085316.
54 Y. Chan, J.-M. Caruge, P. T. Snee, M. G. Bawendi, Multiexcitonic two-state lasing in a CdSe nanocrystal laser. *Applied Physics Letters*, **85**(13) (2004), 2460–2462.

55 D. J. Norris, M. G. Bawendi, Measurement and assignment of the size-dependent optical spectrum in CdSe quantum dots. *Physical Review B*, **53**(24) (1996), 16338–16346.

56 F. Garcia-Santamaria, Y. Chen, J. Vela, *et al*., Suppressed Auger recombination in "giant" nanocrystals boosts optical gain performance. *Nano Letters*, **9**(10) (2009), 3482–3488.

57 A. N. Oraevsky, Whispering-gallery waves. *Quantum Electronics*, **32**(5) (2002), 377–400.

58 C. G. Garrett, W. Kaiser, W. L. Bond, Stimulated emission into optical whispering modes of spheres. *Physical Review*, **124**(6) (1961), 1807-&.

59 M. A. Petruska, A. V. Malko, P. M. Voyles, V. I. Klimov, High-performance, quantum dot nanocomposites for nonlinear optical and optical gain applications. *Advanced Materials*, **15**(7–8) (2003), 610–613.

60 J. D. Thomson, H. D. Summers, P. M. Smowton, *et al*., Temperature dependence of the lasing wavelength of InGaAs quantum dot lasers. *Journal of Applied Physics*, **90**(9) (2001), 4859–4861.

61 H. Kogelnik, C. V. Shank, Stimulated emission in a periodic structure. *Applied Physics Letters*, **18**(4) (1971), 152.

62 V. C. Sundar, H. J. Eisler, T. Dany, *et al*., Soft-lithographically embossed, multilayered distributed-feedback nanocrystal lasers. *Advanced Materials*, **16**(23–24) (2004), 2137.

63 D. K. Armani, T. J. Kippenberg, S. M. Spillane, K. J. Vatiala, Ultra-high-Q toroid microcavity on a chip. *Nature*, **421**(6926) (2003), 925–928.

64 B. Min, S. Kim, K. Okamoto, *et al*., Ultralow threshold on-chip microcavity nanocrystal quantum dot lasers. *Applied Physics Letters*, **89**(19) 2006, 191124.

65 J. Schafer, J. P. Mondia, R. Sharma, *et al*., Quantum dot microdrop laser. *Nano Letters*, **8**(6) (2008), 1709–1712.

66 Z. Wu, Z. Mi, P. Bhattacharya, T. Zhu, J. Xu, Enhanced spontaneous emission at 1.55 μm from colloidal PbSe quantum dots in a Si photonic crystal microcavity. *Applied Physics Letters*, **90**(17) (2007), 171105.

67 G. R. Maskaly, M. A. Petruska, J. Nanda, *et al*., Amplified spontaneous emission in semiconductor-nanocrystal/synthetic-opal composites: Optical-gain enhancement via a photonic crystal pseudogap. *Advanced Materials*, **18**(3) (2006), 343–347.

68 S. A. Ivanov, J. Nanda, A. Piryatinski, *et al*., Light amplification using inverted core/shell nanocrystals: Towards lasing in the single-exciton regime. *Journal of Physical Chemistry B*, **108**(30) (2004), 10625–10630.

69 V. I. Klimov, S. A. Ivanov, J. Nanda, *et al*., Single-exciton optical gain in semiconductor nanocrystals. *Nature*, **447**(7143) (2007), 441–446.

70 J. Nanda, S. A. Ivanov, M. Achermann, *et al*., Light amplification in the single-exciton regime using exciton–exciton repulsion in type-II nanocrystal quantum dots. *Journal of Physical Chemistry C*, **111**(42) (2007), 15382–15390.

71 Q. Darugar, W. Qian, M. A. El-Sayed, Observation of optical gain in solutions of CdS quantum dots at room temperature in the blue region. *Applied Physics Letters*, **88**(26) (2006), 261108.

72 P. T. Snee, Y. Chan, D. G. Nocera, M. G. Mawendi, Whispering-gallery-mode lasing from a semiconductor nanocrystal/microsphere resonator composite. *Advanced Materials*, **17**(9) (2005), 1131–1136.

73 Y. Chan, J. S. Steckel, P. T. Snee, *et al*., Blue semiconductor nanocrystal laser. *Applied Physics Letters*, **86**(7) (2005), 073102.

9 Heterojunction solar cells based on colloidal quantum dots

Jeffrey J. Urban and Delia J. Milliron

9.1 Introduction

Solar cells based on inorganic semiconductor nanocrystals or colloidal quantum dots (CQDs) aim to capture the benefits of inorganic materials, the advantages of solution processing, and the unique size-dependent properties of these materials. Inorganic semiconductors are ideal for fabricating highly efficient solar cells as they absorb a broad range of light and transport charge effectively. However, bulk and traditional thin film inorganic semiconductors require expensive processing, historically limiting the cost effectiveness of these cells. This has motivated extensive research on organic photovoltaic cells since small molecule and especially polymer semiconductors can be inexpensively processed into flexible, thin film photovoltaics. CQDs combine many advantageous characteristics of bulk inorganic materials with the solution processability and low temperature chemical synthesis of polymers. Additionally, the optical gap of CQDs can be tuned by material selection and quantum confinement, and advances in synthesis techniques allow control over nanocrystal size and shape to optimize photovoltaic performance.

A number of strategies have been explored for the integration of CQDs into solar cells. CQDs have been explored as substitutes for organic dyes in dye-sensitized solar cells (see Chapter 11). Monolithic films of CQDs have been employed as the active semiconductor (SC) material in metal–semiconductor Schottky junction based solar cells (see Chapter 10). Another class of CQD solar cells, which are the focus of this chapter, incorporate a heterojunction between two distinct semiconductors, across which electrons and holes are separated. The first semiconductor consists of the CQDs, while the second can be, variously, a bulk inorganic material [1], CQDs of a distinct composition [2, 3], or a semiconducting polymer [4–6].

The operating principles of these CQD heterojunction solar cells lie on a spectrum between a conventional thin film solar cell on the one hand, and an organic solar cell on the other. This is because a CQD is in some ways a very large molecule, and the photoexcited excitonic state can be understood as analogous to the excitonic state of a conjugated organic molecule [7]. However, as will be elaborated below, adjacent CQDs in a solar cell device are electronically coupled to facilitate charge transport. In the

Colloidal Quantum Dot Optoelectronics and Photovoltaics, eds. G. Konstantatos and E. H. Sargent.
Published by Cambridge University Press. © Cambridge University Press, 2013.

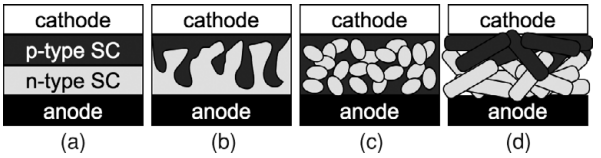


Figure 9.1 Schematic of : (a) a planar heterojunction and (b) a large area heterojunction solar cell. Schematic realization of a large area heterojunction by (c) blending CQDs (light) with a polymer (dark) or (d) layering two nanorod CQD films.

extreme of extensive coupling, a CQD solar cell can be better understood by analogy to a thin film inorganic cell. In every case, carrier transport is poorer than in high efficiency thin film solar cells, which leads to the common architecture for most of this class of solar cells – a large area heterojunction (Figure 9.1). Such a configuration reduces the distance photoexcited charge carriers must travel to reach the heterojunction compared with the planar configuration employed in conventional thin film cells, thus reducing the number of carriers lost to recombination before charge separation can occur at the interface. However, this gain is traded off against the enhanced opportunity for recombination *across* the heterojunction interface during transport of electrons and holes to their respective charge collecting contacts. In practice, large area heterojunctions (or bulk heterojunctions, BHJ) have been created in CQD solar cells by various methods including blending CQDs and polymers into a single casting solution [4, 5] or layering two CQD films with a high roughness interface [2]. Innovative integration strategies to incorporate CQDs into large area heterojunction cells continue to emerge and additional approaches will be highlighted throughout this chapter.

9.2 Chemistry of CQDs for solar cells

Colloidal synthesis strategies have afforded high quality semiconductor nanocrystals of varying compositions with exceptional control over size and morphology. Some of the resulting quantum dots (QDs) have already been put to use in solar cells, while other, cutting-edge, synthetic triumphs hold promise for the optoelectronic devices of the future. A wide range of synthetic approaches have been investigated, including the use of soft templates, such as inverse micelles or rod-shaped viruses, and crystallization from aqueous salt solutions. However, surfactant-mediated growth in organic media has afforded the greatest morphological and compositional control and generally results in high electronic quality crystals and surfaces.

Beginning with CdSe nanocrystals [8], the chemistry of synthesizing QDs in organic media has matured since its inception in the early 1990s, and this material still serves as a prototype for developing new synthetic methods. Now, CdSe QDs can be synthesized in nearly monodisperse (typically $\sigma < 5\%$) batches with diameters of between 2 and 8 nm (about the diameter of the bulk exciton) from organometallic precursors or organic salts of cadmium and trialkylphosphine selenides, with the growing particles stabilized by a wide selection of surfactants [9]. By adjusting reaction conditions, high quality

QDs of other II–VI semiconductors, such as CdTe, ZnSe, etc., have been synthesized, though the synthetic methods have been less thoroughly optimized [10, 11].

Owing in part to the early establishment of synthetic control, CdSe QDs formed the basis for the first CQD solar cells, in which the active layer was a blend of CdSe QDs and a semiconducting polymer [4]. This material has also been at the forefront of shape-controlled QD synthesis, with the direct implications for improving QD solar cell performance. CdSe commonly occurs in the hexagonal wurtzite structure, which contains a crystallographically unique *c*-axis, unlike the cubic symmetry of the closely related zinc blende structure. Alivisatos and coworkers leveraged this reduced symmetry to synthesize elongated nanorod QDs from CdSe whose long axis corresponds with the *c*-axis of the wurtzite structure [12]. The [0001] and [000–1] end facets of the rod are polar (Cd- or Se-terminated) and are of higher energy than the neutral facets which form the sides of the rod. Chemical control of the aspect ratio is possible by tuning the concentration and nature of alkylphosphonate surfactants, which can be understood as arising from preferential adsorption of these to the side facets during growth, heightening the difference in surface energy [13, 14]. High growth rates also favor elongated morphologies [15], highlighting the complex parameter space of reaction conditions which must be explored to control and optimize colloidal synthesis reactions.

A further development in shape control of CQDs was realized by leveraging the zinc blende–wurtzite polytypism of II–VI semiconductors to create branched tetrapod nanocrystals. These crystal structures contain nearly identical, four-coordinate first coordination spheres, differing in the spatial relationship of the second nearest neighbors. Because this difference is subtle, the two phases differ only slightly in energy, with wurtzite increasingly favored in more ionic materials owing to the closer proximity of the second nearest anion–cation neighbors. Tetrapods can be formed from a zinc blende core from which four wurtzite arms project at tetrahedral angles. Initially, CdSe tetrapods were observed as a minority product when using surfactant variations to tune nanorod shape [16]. Later, high yield tetrapods with arms of tunable length and diameter were achieved in CdTe (and subsequently in CdSe), with the alkylphosphonate surfactant again playing a critical role in varying the aspect ratio of the arms [17].

Branched QDs are attractive for solar cells since they have the potential to substantially improve electron collection compared with a network of isolated QDs. With this goal, Greenham and coworkers used CdSe tetrapods in place of CdSe nanorods in a QD–polymer solar cell [18]. Meanwhile, Alivisatos and coworkers explored new integration strategies made possible by the tetrapod geometry, first depositing a layer of CdTe tetrapods to create an open network of nanoscale semiconducting pathways, then backfilling with semiconducting polymer [19]. A natural extension of this approach was to incorporate hyperbranched CdSe QDs, which allowed a higher volumetric density of semiconducting material [6].

Additional complexity has been introduced to colloidal QDs by including multiple semiconductor materials in each nanocrystal, i.e., by making nanoscale heterostructures (Figure 9.2). The first QD heterostructures were radially symmetric core/shell structures in which a higher bandgap shell material reduces the interaction of the quantum confined

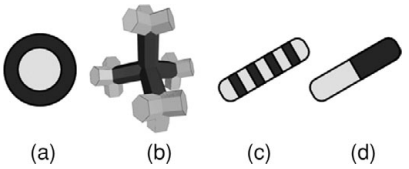


Figure 9.2 Schematics of various CQD heterostructures: (a) core/shell, (b) branched, (c) superlattice, and (d) linear nanorod heterostructures.

exciton with the nanocrystal surface [20, 21]. These Type I core/shells are advantageous for luminescence applications, but the isolation of the charge carriers is not ideal for electronic applications, including their use in solar cell active layers. Axial heterostructures with branched or linear topology were prepared from cadmium chalcogenides by sequential injection of different chalcogen precursors under high growth rate conditions [22]. These include material combinations expected to yield either Type I or Type II energy level alignment. Some of these have the potential to create long-lived charge separated states following photoexcitation, e.g., confining the hole to the core of a branched tetrapod and the electron to the arm's end, 50 nm or more distant. Even if such a state were realized with high yield, however, it remains a substantial integration challenge to collect these carriers efficiently in a solar cell. Type II core/shell QDs, whose synthesis and optical characterization have advanced markedly [23], may be applicable to solar cells in the shorter term. These structures induce a radial separation of electrons and holes, and both carriers might feasibly be collected, especially if well-controlled Type II core/shell nanorods or other elongated structures emerge.

In another approach to synthesizing nanocrystal heterostructures, Alivisatos and coworkers reported that post-synthetic exchange of some Cd^{2+} in CdS nanorods for Ag^{+} results in the formation of superlattice nanorods containing alternating CdS and Ag_2S domains [24]. These structures are also intriguing for solar cell applications since a regular QD superlattice is one potential route to realizing an intermediate band solar cell whose theoretically achievable efficiency lies well above the single bandgap Shockley–Queisser limit. However, the integration challenges to achieve such a result from these heterostructured nanocrystals are daunting indeed. Also intriguing for solar cells, a similar partial exchange of Cd^{2+} for Cu^{+} resulted not in an alternating superlattice, but rather in simpler A–B–A or A–B nanorod heterostructures with A = Cu_2S and B = CdS [25]. This Type II material pair has been applied in thin film heterostructure solar cells for decades, and there is some potential for leveraging these QDs in prototype solar energy conversion devices in the near future.

Cu_2S QDs have themselves been directly synthesized and incorporated into solar cells [3]. While the extinction coefficient of this material is far lower than those of other colloidal QDs considered for solar cell applications, this represents an important step toward efficient QD solar cells based on materials with high natural abundance and availability, and low inherent toxicity. Further targeted synthetic development efforts have been aimed at achieving this goal. For instance, pyrite (FeS_2) has a far higher extinction coefficient and its elemental components are among the most abundant in

the earth's crust [26]. The synthesis of pyrite QDs under solvothermal conditions has been reported [27], though improved control over size, composition, dispersability, and morphology will be needed to optimize pyrite QD solar cells.

Synthetic control of lead chalcogenide QDs (PbX, X = S, Se, Te), which have bulk bandgaps in the near infrared (NIR), has become well established [28–30] and, as for the cadmium chalcogenides, these have been effectively employed in a new generation of NIR solar cells (see Chapter 10). Being more ionic in character, the lead chalcogenides always occur in the six-coordinate, cubic rock salt structure. Hence, the strategies for shape control developed for four-coordinate II–VI semiconductors cannot be applied. However, very elongated nanowires of PbSe and other complex shapes – apparently resulting from crystallographically oriented attachment of more symmetric nanocrystals – have been reported [31], so some analogous shapes may eventually be achievable. In addition, lead chalcogenides have already been incorporated into heterostructures by the cation exchange approach [32]. Some of the cadmium ions are first replaced with Cu^{+} to create a heterostructure, then a second cation exchange reaction selectively replaces the Cu^{+} with Pb^{2+}, resulting in Pb–Cd chalcogenide heterostructures. Heterostructures containing two lead chalcogenide materials have likewise been synthesized by combining direct synthesis and ion exchange strategies [33].

Incorporating further compositional complexity into colloidal QDs is still an emerging science. Various ternary or quaternary compounds and alloys related to the more established binary semiconductors are clearly of interest for solar cell applications, and controlled colloidal approaches to their syntheses have begun to emerge. For instance, CdS/Se alloy QDs have been synthesized that are brightly luminescent at the blue edge of the visible spectrum [34]. The analogous PbS/Se alloy QDs have improved the performance of Schottky junction solar cells compared to that of pure PbSe [35]. Thin film solar cells based on $Cu(In,Ga)Se_2$ (CIGS) are emerging on the commercial market. Meanwhile, the synthesis of $CuInSe_2$ CQDs (and related ternary and quaternary compositions) has been reported [36, 37]. However, in all of these examples, the pursuit of such complex materials involves an even more expansive parameter space for synthetic optimization. Thus, controlling the stoichiometry of the product selectively while also manipulating its size and shape is at the limit (or, in many cases, surpasses the limit) of what is achievable by available synthetic methods. High throughput, automated synthesis workstations like that developed by Milliron and coworkers [38] may enable more efficient discovery of synthetic pathways to optimal QDs with complex compositions.

Finally, the inorganic core of a CQD is necessarily capped by a layer of surfactant, and the chemistry of this, too, must be considered for effective solar cell integration. Surfactants used to control the size and shape of the QDs are retained on their surfaces after synthesis. While these usefully impart solvent dispersibility, their long hydrocarbon tails electronically isolate the QDs from their environment, making charge carrier extraction difficult. In one integration strategy, these insulating surfactants are displaced with the more weakly adsorbing, volatile ligand pyridine, which can be removed in a later processing step by moderate thermal annealing [4, 5]. While effective, this strategy can introduce challenges for reproducibility, particularly when QDs are blended with

polymers to form the active layer. Another strategy involves exchanging the native surfactants for electronically active ones specifically designed to mediate charge transfer to/from the QDs. For instance, Alivisatos and coworkers reported a series of CdSe QD–oligothiophene complexes where the oligothiophene was decorated with alkyl chains to simultaneously mediate QD dispersion and electron transfer [39]. Extending this concept to solar cell integration, Frechet and coworkers used similarly end-functionalized polythiophenes to make polymer–QD solar cells with reliable QD dispersion characteristics [40]. While these early demonstrations illustrate the potential impact of specifically addressing QD surface chemistry, far greater opportunity exists to apply these concepts to evolving QD solar cell designs. In parallel, surface chemical control over QDs is rapidly gaining sophistication and new approaches, such as chemical reaction-driven organic ligand exchange [41, 42] and using anionic inorganic clusters as ligands [43, 44], have yet to be applied to QD solar cells.

9.3 Physics of CQDs for solar cells

As introduced previously, the intriguing promise of using CQDs for photovoltaic applications relies on unique physical phenomena arising from the intermediate size of these materials between molecules and bulk semiconductors. Through variations in size and shape, one can modify the bandgap energy (E_g), absolute energy of the absorption onset (a), and the electronic density of states (DOS) in one homogeneous material [45]. The ability to manipulate these fundamental parameters, all of which are immutable for bulk semiconductors, derives from the fundamental physics of quantum mechanical confinement of charge carriers in these nanoscale systems. This section will present an introduction to the electronic structure of CQDs and how light–matter interactions are modified by quantum confinement, and will discuss the consequent implications for optoelectronic devices while highlighting outstanding questions in the field.

9.3.1 Electronic structure evolution in low dimensional systems

In nanostructuring of bulk materials, one or more of the critical spatial dimensions is reduced to on the order of nanometers. Bulk energy level schemes for electronic structure are inadequate for crystallites of sufficiently small dimension, specifically when the region of space available for a charge carrier becomes comparable to its de Broglie wavelength. In this circumstance, the electron and hole interactions with the surface dominate the energetics and prevent the formation of extended Bloch states and the familiar parabolic bands, bandgaps, and energetics of bulk semiconductors [46]. Here, the spectrum of energies much more closely resembles a discrete “molecular” ladder of states. The standard convention in optoelectronics is to parameterize the dimensionality of a system by comparing the extent of the 1S exciton with the physical dimensions of the system [47]. This naturally leads to the familiar situations two-dimensional (quantum wells), one-dimensional (quantum wires), and zero-dimensional (quantum dots). In this chapter, we will primarily focus on the physics of QDs.

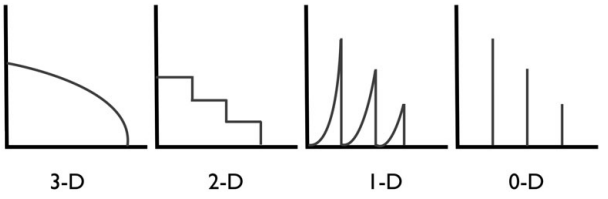


Figure 9.3 DOS vs. k in three-, two-, one-, and zero-dimensional cases.

To recapitulate, the solution of the Schrödinger equation for electrons freely propagating in a cube of dimension L is

$$\psi = e^{ikr} \tag{9.1}$$

for which each component of the wavevector satisfies the following conditions:

$$k_x = 2\pi/L_x, \qquad k_y = 2\pi/L_y, \qquad k_z = 2\pi/L_z \tag{9.2}$$

from which the overall energy of the system may be expressed as

$$E_n = \left(\frac{h}{2\pi}\right)^2 \frac{k^2}{2m} = \left(\frac{h}{2\pi}\right)^2 \left(\frac{k_x^2 + k_y^2 + k_z^2}{2m}\right). \tag{9.3}$$

Note that this treatment assumes that the available energetic states are distributed (energetically) equally in all three dimensions of k-space. Thus, the DOS available per volume at a given energy is

$$D_{3d} = \left(\frac{dN}{dE}\frac{1}{L^3}\right) = CE^{\frac{1}{2}} \quad \text{and} \quad k = \left(\frac{h}{2\pi}\right)\left(2m\,E^{\frac{1}{2}}\right) \tag{9.4}$$

Thus, in three dimensions we observe that a plot of DOS vs. k yields the familiar $E^{1/2}$ relationship (Figure 9.3). This is simply understood by noting that each energy interval in this three-dimensional space is a shell of the Fermi sphere whose energy (E) and volume (proportional to DOS and L^3) scale as $\sim k^2$ in all three directions of k. Thus, for any component k, it is true that $k \sim E^{1/2}$. Thus the DOS available also scales as $E^{1/2}$.

In two-dimensional systems, the scaling is k vs. L^2 in two dimensions and discrete in the "confined" direction, with the discrete DOS described by the Heaviside step function. In one-dimensional systems, two of the dimensions are confined and in zero-dimensional quantum dots, the energetic spectrum for the carriers in the quantum dots is described by a series of delta functions, leading to the familiar discrete set of states (Figure 9.3). So, each reduction in dimensionality renders the contribution of one of the k components a constant. Thus the energetic relationships step down by $E^{1/2}$ progressively from DOS $\sim E^{1/2}$, to E, to $E^{-1/2}$, finally to a fully discrete spectrum in all three dimensions. The DOSs in semiconducting systems critically impact the potential performance of photovoltaic devices, as they determine the absorption coefficient and how many carriers can be excited across the gap for a given energy of illumination. In particular, we note that QD photovoltaics have the potential to thus harness the energetic tunability and selectivity of molecules with the mature transport physics of semiconductors [48]. The use of

CQDs in place of dye molecules in sensitized solar cells (see Chapter 11) highlights this molecular limit of QD physics and its utility for solar conversion.

9.3.2 Fundamentals of light–matter interactions in QDs

As mentioned above, the electronic structure of a semiconductor is one of the key determinants of how it will absorb radiant energy. The simplest quantum mechanical model which describes how light couples to electronic transitions is called Fermi's Golden Rule (FGR). This simple model provides a framework for understanding how the individual QDs in a CQD photovoltaic absorb light and convert that energy into charge carriers. The remaining details of what happens to those carriers (relaxation, charge separation, recombination, scattering, transport, etc.) will be left to the later sections of this chapter. Here, we concern ourselves only with the question of understanding the physical basis for how light absorption in quantum mechanics operates and how this may be used to optimally engineer QD photovoltaics.

FGR is an approximation culled from the full quantum mechanical treatment of time-dependent perturbation theory [49]. While it makes several critical assumptions, it generally does an adequate job of describing the energy dependence of the rate for a transition to occur between some pair of initial (filled) and final (empty) states. The expression describing the probability of carrier transition from an filled, initial state $|i\rangle$ to a final state $|f\rangle$ is

$$\left(\frac{4\pi^2}{h}\right)|\langle i|H|f\rangle|^2\delta(E_f - E_i \pm E). \tag{9.5}$$

The term in angle brackets outlines a set of matrix elements that describe the coupling between the initial and final states; the probability of connecting these two states is determined by the Hamiltonian (H), which in this case represents the action of illumination. The delta function ensures that conservation of energy is maintained. Thus, we note that the ability to excite carriers in a semiconductor QD critically depends on the nature of the exciting electromagnetic field, the energy gap between the initial and final states, and the symmetry of the two states being "connected" by the Hamiltonian. We also note that this is, again, a first-order simplification of the full expression and that multi-photon, multi-carrier, etc. effects are not correctly accounted for in this framework.

Building on this simple framework, understanding the elementary photophysics of thin-film photovoltaics (which may emerge in the strong-coupling limit for QCD photovoltaic films) is straightforward. We only need to modify this basic equation by the particle-counting statistics relevant for fermions (electrons and holes). For example, the net absorption of light in a two-level (conduction band and valence band, Figure 9.4) model semiconductor is

$$R_{abs} = \left(\frac{4\pi^2}{h}\right)|H_{cv}|^2\,(f_0(f_v - f_c)), \tag{9.6}$$

where f_0 is the probability of a photon with sufficient energy arriving, and f_v and f_c define the joint DOS, i.e. the population of electronic states in the valence and conduction

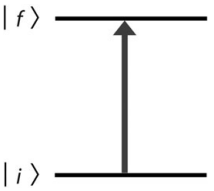


Figure 9.4 Two-level systems and light absorption.

bands separated by this energy. This net action of absorption of light and promotion of carriers into unoccupied states is the first key step in photovoltaic operation.

9.3.3 Selection rules and the complications of *H*

Above, we briefly mentioned that the Hamiltonian in the FGR rate expression had important information about the symmetry of the system. Understanding the energy expression in FGR is trivial, as photons with insufficient energy will not (acting alone) have enough energy to promote electrons into the conduction band, but the role of symmetry is more nuanced. To understand this, we observe that, in addition to conservation of energy, conservation of momentum also underpins the fundamental physics of light absorption and carrier generation. Selection rules emerge naturally from the requirements of momentum conservation in semiconductors. To see this, a greatly simplified version of the $\langle i|H|f\rangle$ matrix element for a two-level system excited by light (an electric dipole operator, formally) is

$$M_{if} = C \int \left[e^{i(k'-k)r} u_i^*(r) \nabla u_f(r) + ik' e^{i(k'-k)r} u_i^*(r) u_f(r) \right] d^3r. \tag{9.7}$$

As you might recall from basic quantum mechanics, the motion of an electron in a semiconductor is captured as the product of a slowly varying plane wave (e^{ikr}) and a rapidly varying periodic atomic portion (u_{ik}). Here we let $\psi(k, r) = u_{ik}\, e^{ikr}$. While even the simplified expression (some important constants are bundled into the generic constant, C) is intricate, the key point is that $M_{if} = 0$ whenever k is not equal to k'. That is, there can only be a chance for photogeneration of carriers in this case when the momentum of the initial state (e.g., electron in the valence band) is equal to the momentum of the final state (e.g., electron in the conduction band). This is the standard selection rule for optical transitions and the fundamental reason why light absorption and photogeneration in indirect semiconductors, such as Si and Cu_2S, is orders of magnitude weaker than it is in direct semiconductors, including CIGS, CdSe, CdTe, and pyrite (Figure 9.5).

9.4 Optical and electronic properties of CQD films for solar cells

Carrier transport in QD devices differs fundamentally from band transport in bulk semiconductors. The granularity of the system introduces several new physical parameters

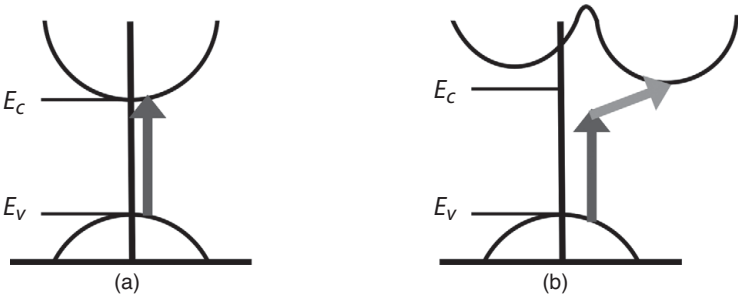


Figure 9.5 (a) Direct and (b) indirect semiconductors and momentum conservation.

that must be considered, the most important of which are the capacitance of individual QDs and the coupling of one dot to another [50]. These concepts enable one to leverage the basic chemical and physical properties of QDs to achieve many different modes of transport, from field-activated hopping to Bloch-like delocalized transport, in these systems.

The specifics of how carriers move through QD films and which energy levels they sample depends upon the competition between three energy scales that are often of similar magnitude: (1) the energy level spacing (δ), (2) the Coulomb charging energy (E_c), and (3) the dot–dot tunnel coupling (β). Thus, simple models for considering these parameters will be discussed here, as they provide a systematic basis for understanding and optimizing transport in CQD based solar cells.

As discussed in the previous section, the quantum confinement of carriers in CQDs leads to a discrete energy level spectrum. To ascertain how many of these levels participate in transport, we first consider the level spacing, δ. To a first approximation, δ scales inversely with the volume of the QD, leading us to the expression

$$\delta = \left(\frac{1}{\upsilon V}\right), \tag{9.8}$$

where υ is the DOS at the Fermi level of the dot and V is the volume of the grain. In the absence of intradot tunneling (we are discussing room-temperature CQD based devices where the tunneling conductance is much less than the hopping conductance), we can easily develop a portrait of granular transport. The geometric consideration in (9.8) sets natural length and energy scales for the states available for carrier transport at a given temperature. If $T > \delta$ then there is sufficient thermal energy that the next highest unoccupied level will participate in transport, but if $\delta > T$, then carrier motion will be restricted to the lowest levels on each QD, barring the input of sufficient additional energy from electric fields, photons, multiple phonons, etc. The same considerations can be applied to understand the impact of energy level offsets between adjacent QDs. Such energetic disorder inevitably results from even minor size and shape variations. In either case, it will be necessary to thermally promote carriers to higher energy levels to facilitate transport which will yield Arrhenius-like transport behavior whose conductivity scales as $\sim e^{-\sqrt{T}}$.

The ability of a given QD to hold charge is also of critical importance. This self-capacitance of a QD leads to a natural energy scale, called the Coulomb charging energy, which may be approximated as follows:

$$E_c = \left(\frac{e^2}{2C}\right) = \left(\frac{e^2}{4\pi\varepsilon_m\varepsilon_0 r}\right), \tag{9.9}$$

where C is the self-capacitance of a sphere, expressed in terms of ε_0 (the permittivity of vacuum), ε_m (the static dielectric constant of the medium), and r (the radius of the sphere). This is the electrostatic cost that must be paid to move an electron from one dot to another, and a fundamentally new consideration in transport through QD films. This emerges from the fact individual electrons and holes carry charges which, while electrostatically irrelevant in a sea of carriers in a doped bulk semiconductor, matter greatly on QD semiconductor "islands" each of which will typically contain zero to one mobile carriers. Thus, motion of electrons from one QD to another can be thought to represent "oxidation-" and "reduction-" like events with an associated energy consideration that depends on the energy levels and dielectric properties of the material. So, it is now easy to see that if E_c is large, then even if there are unoccupied states available, the Coulomb charging energy effectively makes these states higher in energy and unavailable, rendering the system insulating. However, basic electrostatics states that $C = Q/V$, so the application of an appropriate "gate" voltage to the system can reduce this charging energy and overcome this penalty [51]. As discussed below, light can act as such a "gate" in a CQD solar cell.

Lastly, the particle-to-particle coupling parameter, β, expresses the degree of quantum mechanical coupling between the individual energy levels of neighboring QDs. Here again we can see the connection between the physics of CQDs and that of organic semiconductors since the same parameter plays a central role in describing carrier transport through films of the latter. Modeled semiclassically [52], β is related to the tunneling rate (Γ) of an electron between two states (the energy levels of the adjacent QDs) separated by a tunneling barrier (the ligand shells and/or gap between dots) as follows:

$$\beta = \left(\frac{h}{2\pi}\right)\Gamma \tag{9.10}$$

where

$$\Gamma = \exp\left[-2\left\{2m^*\Delta E\left(\frac{h}{2\pi}\right)^2\right\}^{\frac{1}{2}}\Delta x\right] \tag{9.11}$$

where m^* is the effective mass of the electron and ΔE and Δx are the height and width, respectively, of the tunneling barrier. Thus, as β becomes large (small barriers; strong dot–dot coupling), electrons and holes become more delocalized over the array and, in the strong coupling limit, experience band-type transport. In the limit of small β, $\beta \ll kT$, carriers are localized and require either field- or temperature-assisted mechanisms to enable transport across the array.

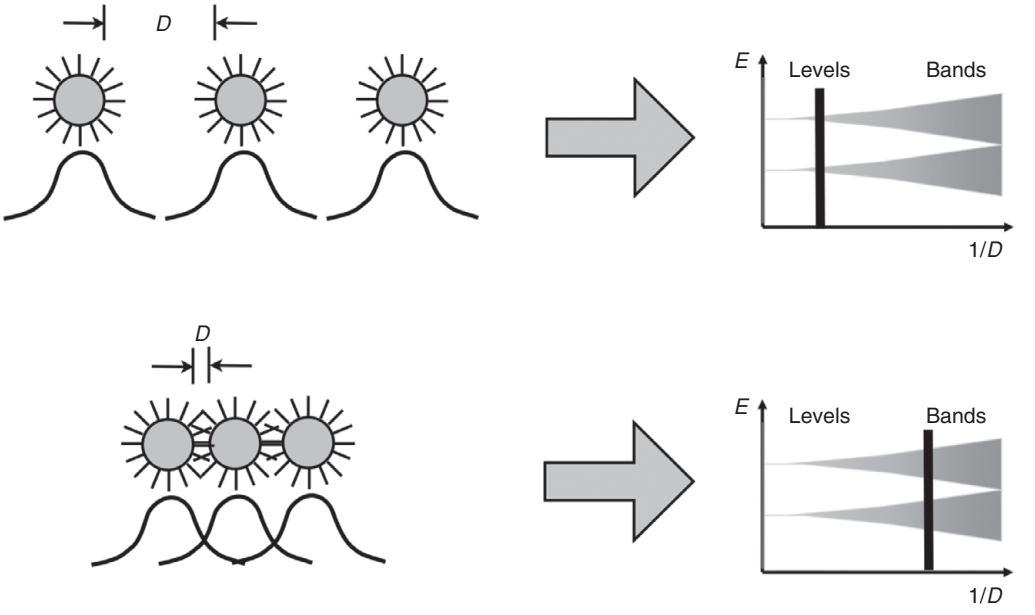


Figure 9.6 Interplay of electronic structure and interparticle interactions in a QD solid. This figure shows how dot–dot coupling and Coulomb charging energies allow one to transition from hopping behavior to fully delocalized behavior.

The integration of all of these parameters into a framework for engineering transport in QD arrays is shown in Figure 9.6.

As we will discuss later, a photovoltaic device may be simply modeled as a load (resistor) and transistor with illumination-dependent values wired up in parallel. And while the physics of a resistor is straightforward to grasp, the modulation of a photovoltaic device is derived from the transistor properties. Indeed, one can conceptualize a photovoltaic device as a photon-gated transistor. First, we will briefly review the physical properties of QD transistors, and how they may be improved and modified for photovoltaic cells.

Following the early reports on CQD synthesis, their unique optical properties were quickly and effectively harnessed for luminescence applications. While there were also early efforts to leverage CQD in electronic devices, truly impactful device results have taken longer to emerge. A major hurdle has been coping with the insulating ligand shells that surround the QD after synthesis, which, if left in place, makes the β parameter for interdot coupling very low. Early demonstrations of CQD based solar cells and electrochemical studies of CQD films [53] hinted at the use of ligand replacement to reduce this barrier and provided some indication of the potential for efficient injection and extraction of charges from quantum dots. However, reports of electronic properties in nanocrystal transistors that qualitatively reproduced those of conventional semiconductors did not come until much later [54]. These hinged on further advances in manipulating the ligand shell, not covered here, and the results have shed light on the physics governing transport through CQDs incorporated into solar cells.

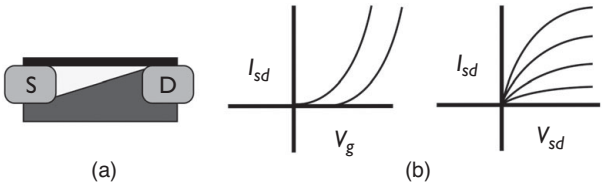


Figure 9.7 (a) Cartoon of a TFT device with the source (S) and drain (D) electrodes. The gate voltage, V_g, applied through the top gate (black) can deplete the channel and "pinch off" the device (decreasing width in white), precluding the transport of carriers by closing the channel. (b) Standard transfer and output curves for a TFT. The output curve clearly depicts both linear (low-V_{sd}) and saturation (high V_{sd}) regimes.

Fundamentally, the transistor is a three-terminal device for which either the current or the voltage between two terminals (the source and drain electrodes) can be modified by applying a voltage to the third terminal (the gate). While there are many different instantiations of this physics, here we will only discuss the thin-film transistor (TFT) geometry, shown in Figure 9.7. This figure depicts not only the architecture of these devices, but also a cartoon of operation, and output (I_{sd} vs. V_{sd}) and transfer (I_{sd} vs. V_g) curves. These are the two standard types of measurements that are used to characterize TFT devices and provide information on the carrier type and mobility [55]. The mobility is extracted from the transfer curve using the following equation:

$$I_{d,sat} = \frac{WC_i\mu_{sat}}{2L}(V_G - V_T)^2, \tag{9.12}$$

typically in the saturation regime, although occasionally linear-regime field-effect mobilities are reported. In (9.12), W and L are the width and length of the channel, respectively, and C is the gate capacitance. One must exercise caution in interpreting these reported mobilities, particularly in cases where granular systems or films whose contact resistances are dominant.

As you can see, the physics of a transistor provides a mechanism to bias the flow of carriers. This is a critical requirement for photovoltaic action – the holes must be driven to one electrode, and electrons to the other electrode, selectively and consistently. It is therefore not surprising that the most common materials science choice used to create transistor action in semiconductors, the p–n junction, forms the basis of the vast majority of photovoltaic cells, although, both metal–insulator–metal and Schottky cells can also provide similar physics [56]. In many cases, the chief advantage of QDs is simply a practical one – easy and cheap production of materials that reproduce the physics of the most exquisitely crafted, expensively produced crystalline devices.

Ultimately, in order to understand the operation of a solar cell, we must model what happens to the fundamental charge carriers as they are displaced from equilibrium due to the absorption of light. This is commonly introduced using the Boltzmann transport equation (BTE) under the relaxation time approximation. This formalism describes the induced motion of electrons and holes due to gradients in electrical potential (drift) and chemical potential (diffusion) at a p–n junction. In order to remain tractable, the key assumption of quasi-thermal equilibrium is made – this assumption provides for

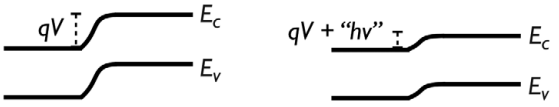


Figure 9.8 A p–n junction at equilibrium (left) and under illumination (right). Thus, illumination of a p–n junction acts analogously to a forward bias on a gate, lowering the potential barrier for carrier transport.

local disturbances in electrochemical potential to exist, which allows for discussions of local populations of electrons (in the conduction band) and holes (in the valence band) separately, each with its own equilibrium statistical mechanics. While the basic principles of the p–n junction are beyond the scope of this chapter, the drift-diffusion equation for electrons and holes in this system is

$$J_p(r) = -q\,D_p\,\nabla p + \mu_p p(qF - \nabla\chi - \nabla E_g + kT\,\nabla ln\,N_\upsilon), \tag{9.13}$$

or, if one substitutes the Einstein relations which relate carrier mobilities to diffusion constants ($\mu_p = q\,Dp/kT$), one obtains a simplified form of this expression:

$$J_p(r) = -q\,D_p\nabla p + q\mu_p Fp \tag{9.14}$$

See also Figure 9.8. Gradients in electron affinity (χ), bandgap (E_g), and DOSs (N_v) thus can provide an extra motive force for carriers in addition to applied electric fields (F). Note that these equations are written for holes (p subscripts), but take a similar form for electrons.

Equation (9.14) is the celebrated drift-diffusion equation, and it demonstrates that gradients in *either* carrier concentration *or* electric field can drive a current. Bear in mind that the assumptions made here may not necessarily hold for transport in all QD solar cells [57]. This is, in part, a reason to enthusiastically explore these materials for potential "next-generation" thin-film photovoltaics that provide higher efficiencies as they are not governed by the traditional rules of semiconductor physics. For example, the "quasi-thermal" equilibrium assumption may be invalid for the so-called "hot carrier" cells where energetic carriers are collected before they scatter off of phonons and relax. As shown by the Sargent group [58], this is one potential unique use of QDs as photovoltaic materials which can provide a route to higher performance materials by reliance on physics not accessible in bulk semiconductors.

9.5 Device physics and design of CQD heterojunction solar cells

Having discussed the physics and materials science underlying the principal acts of light absorption, charge generation, and transport, it is now time to widen our view to the macroscale aspects of photovoltaic operation. In this section, a basic engineering view of a photovoltaic cell will be described, along with the most common sources of nonideality and how they impact the operation of the device. The emphasis here is on applying the basic physics to understand performance characteristics of CQD solar cells.

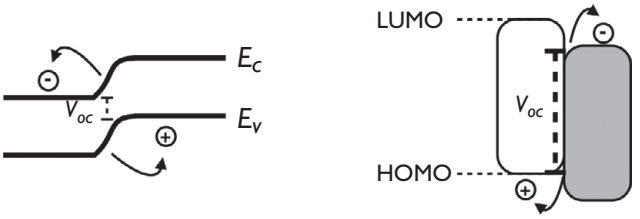


Figure 9.9 Comparison of charge generation, separation, and transport in p–n and excitonic solar cells. There is a correspondence between the valence and conduction bands and the HOMO–LUMO offset between donor–acceptor junctions in excitonic solar cells (HOMO: highest occupied molecular orbital; LUMO: lowest unoccupied molecular orbital). Moreover, the origin of open circuit voltages and transport and separation of photogenerated carriers is denoted by the arrows.

While this section will go into detail principally on the CQD correlates of standard p–n heterojunction thin-film devices, analogies with excitonic cells (e.g., dye-sensitized and polymer BHJ cells) will also be highlighted. While the microscopic details of charge generation, separation, and transport are different in excitonic cells, many of the approaches to quantifying and understanding the behavior of these cells remain similar to all-inorganic p–n type devices.

This comparison is summarized in Figure 9.9, which demonstrates the microscopic differences and macroscopic similarities between p–n and excitonic cells. At the most basic level, the principal difference is the mechanism for photogeneration of carriers. In excitonic cells, photoexcited intermolecular charge transfer across an energetically asymmetric interface between "donor" and "acceptor" species, this potential offset is the driving force for photovoltaic action. Spontaneous separation of photogenerated excitons is negligible due to an exciton binding energy well in excess of the available thermal energy, k_BT. Furthermore, there is a substantial barrier to dissociation of interfacial excitons into free carriers. Once dissociated, the free carriers are transported to the anode and cathode. In a p–n cell, the exciton binding energy is sufficiently small that dissociation between the electron and hole occurs spontaneously, even away from the asymmetric interface which arises in this case from either doping of a homogeneous semiconductor or from a heterojunction between chemically distinct n- and p-type materials. The transport is, in this case, understood as introduced above and can be mapped onto the drift-diffusion equation.

On the other hand, the device physics of BHJ solar cells consisting of intermixed polymer and CQD semiconductors can be anticipated to resemble, in many ways, those of (excitonic) all-organic BHJ cells. Blom *et al*. [59] have suggested that the dissociation of geminate pairs from a bound interfacial state into free carriers can be a key limiting step in such cells, and recombination of these bound pairs is a major loss mechanism. Based on the higher dielectric constant of inorganic CQDs and the greater delocalization of a carrier in a CQD compared to a typical organic polaron, we can anticipate that this problem may be relieved to some extent in CQD-based BHJ cells. On the other hand, all-organic BHJ cells have been successfully modeled considering trap-free hopping

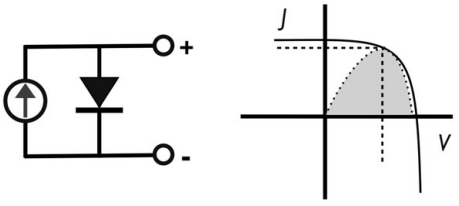


Figure 9.10 Basic electrical engineering diagram of an ideal photovoltaic cell and a standard *J–V* plot (here *J* denotes J_{sc} and *V* denotes V_{oc}). The maximum power output (denoted by the peak of the gray curve and intersecting dashed lines) occurs at intermediate values of *J* and *V*.

transport of photogenerated carriers and Langevin recombination of non-geminate pairs [60]. Langevin recombination describes the statistical "bimolecular" intersection of mobile electrons and holes and it is applicable when the mean free path is short compared with the Coulombic trapping distance. These processes are critical to understanding the limitations on device efficiency; for instance, a ten-fold enhancement in mobility substantially suppresses recombination of mobile charge carriers and doubles device efficiency under the conditions considered by Marsh *et al*. [61]. It is still unclear under which conditions such a model can describe transport through networks of CQDs and when trapping may play a significant role (besides considering the transition to band-like transport in the limit of strong coupling). Very likely, the extent of trapping and its role in determining device behavior is strongly dependent on the surface chemistry of the CQDs which, as discussed in Section 9.2, is emerging as a systematic science. Clear relationships between surface chemistry and transport behavior can be expected to emerge and understanding of CQD device physics will certainly deepen following such advances.

A great deal of insight can be gained by considering even basic device level models for operation of photovoltaic cells (Figure 9.10). Here the photovoltaic cell is modeled as a set of parallel elements – a diode and a load (resistor), both of these elements have values that depend sensitively on light illumination. To characterize the limiting values of operation, two quantities, the open circuit voltage (V_{oc}) and short circuit current (J_{sc}) are used. These may be thought of as the limits of zero (J_{sc}) and infinite (V_{oc}) parallel resistances. In the simple circuit in Figure 9.10, if the cell is illuminated and generates a voltage with no current flow then the maximum possible voltage for that device, the V_{oc}, is obtained with no measured current. With no resistance in the connected circuit, all of the current flows freely and the maximum current, the J_{sc}, is obtained and no measurable voltage is maintained across the leads.

This model is simple, and effective, as illumination of the cell is understood simply as follows. For a photovoltaic-active material, light absorption will generate a voltage bias across the thickness of the cell. This voltage can be considered as the voltage applied across the diode. In the dark, $V \sim 0$ and no current flows. When illuminated, a photovoltage develops across the active material and it acts as though it is putting the diode under reverse bias and current begins to flow and power is produced. The power produced is then a product of the photocurrent and photovoltage, and this value

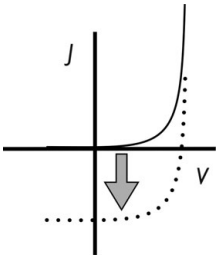


Figure 9.11 Basic *J–V* curve in the dark (solid) and bright (dotted) state.

determines the power conversion efficiency that device designers aim to maximize. To further understand the device physics, we look to Figure 9.11 and the following equations:

$$J(V) = J_{sc} - J_{dark}(V) = J_{sc} - J_0\left[\exp\left(\frac{qV}{kT}\right) - 1\right], \tag{9.15}$$

$$V_{oc} = \left(\frac{kT}{q}\right)\ln\left(\frac{J_{sc}}{J_0} + 1\right). \tag{9.16}$$

These equations show that J and V are inextricably linked, that they cannot simultaneously take their maximum values, and that the measured V scales with the natural log of the illumination intensity. It is now clear that the maximum power is obtained for intermediate values of V and J. Comparing this to the product of the individually maximized current and voltage (V_{oc} * J_{sc}), we arrive at a figure of merit called the fill factor (FF = $V_m J_m / V_{oc} J_{sc}$), which is always less than 1 for given values of the voltage and current density of a cell at maximum power, V_m and J_m, respectively. In practice, commercially viable cells typically have FFs which range from 0.75 to 0.9. Together, J_{sc}, V_{oc}, and FF are the quantities to be optimized in solar cell engineering since they combine to establish the power conversion efficiency (i.e., conversion of the incident power into generated power by the photovoltaic cell), which is simply:

$$\eta = \frac{P_{max}}{P_{in}} = \frac{J_m V_m}{P_{in}} = \frac{J_{sc} V_{oc} FF}{P_{in}}. \tag{9.17}$$

While the basic circuit model introduced above is a useful starting point, in order to grasp the operation of real devices, some deviations from ideal behavior need to be introduced. As shown in Figure 9.12, this can be effectively captured by adding in two new resistances – the series resistance (which acts to model the contact resistances for the electrodes which touch the active material) and the shunt resistance (which acts to model the leakage currents which develop through and around the sides of the device). Needless to say, these two parasitic resistances act to decrease the FF and performance of the photovoltaic devices, as shown in Figure 9.12. The full diode equation with parasitics is:

$$J = J_{sc} - J_0\left(e^{q(V+JAR_s/kT)} - 1\right) - \frac{V + JAR_s}{R_{sh}} \tag{9.18}$$

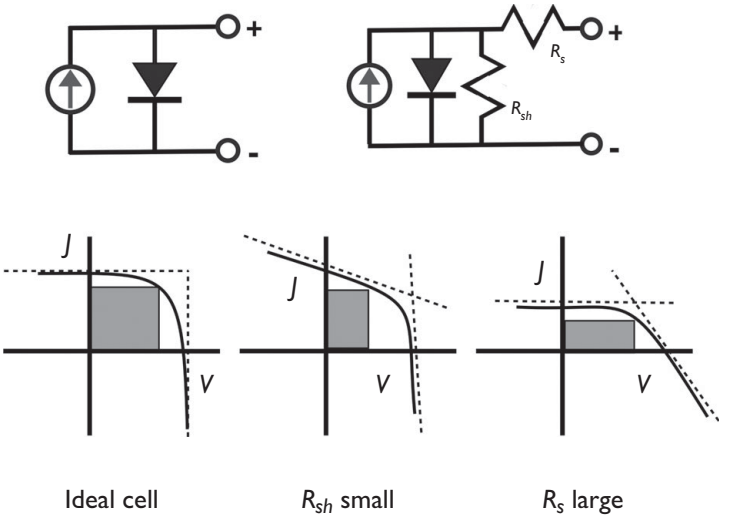


Figure 9.12 Standard circuit diagrams and *J–V* curves of ideal and non-ideal photovoltaic cells. The FFs are denoted by the gray area under the curve. Limits of small shunt resistance (current lost) or large sheet resistances (voltage lost) are individually shown in independent *J–V* curves. It should be noted that the sheet and shunt resistances are found by taking the reciprocal of the slope through J_{sc} and V_{oc}, respectively.

While the effects of R_{sh} and R_s are now obvious, surmounting and defeating these challenges is one of the primary objectives of the materials physicist in this field. There are unique "recipes" developed over thousands of trial-and-error runs which have emerged to develop the most ohmic contacts (decrease R_s) and best processing conditions (increase R_{sh}). The solutions to these challenges may be (and often are) quite different in CQD photovoltaic systems, as the physics and materials science are so different. For instance, problematic recombination across the large area junction can appear as a contribution to R_{sh} since it effectively introduces a leakage current which opposes the positive photocurrent. Developing further methods to transfer or utilize some of the knowledge gleaned from thin-film photovoltaics will be of critical value.

9.6 Technology and scientific outlook

At present, the most efficient CQD heterostructured solar cells reported are those which most resemble thin film solar cells in their design and operational principles. This is not surprising given the massive effort devoted to understanding and optimizing thin film photovoltaics over the past several decades. Thus, it is likely that the greatest short-term success for CQD solar cells will follow this model. There is already much to be gained if durable, high efficiency, thin film modules can be manufactured using a low-cost solution process and CQDs represent one intriguing option in this regard. Indeed, since 2000 there have already been significant advances made in the performance of QD-based

Table 9.1. Progress in performance of CQD-based photovoltaic devices. References for the colloidal QD [62, 63], bulk heterojunction [64, 65], polymer-QD [5, 66] and dye-sensitized QD [67, 68] systems are included as representative publications demonstrating the status and progress of the different approaches to photovoltaics, rather as than a comprehensive list of work

Material	2000 efficiency	2010 efficiency
Colloidal QDs	1–2%	3–4%
BHJ	2–3%	5–6%
Polymer QD	1–2%	3–4%
Dye-sensitized QD	9–10%	11–12%

cells of varying types which are summarized in Table 9.1. For this purpose, the well-known chemistry of synthesizing CQDs from CdTe and CdSe and the rapidly advancing chemistry for various CIGS materials provide a solid starting point for development. However, no CQD materials are currently manufactured on a large scale and this is a critical need to enable development of any CQD based solar cell technology. In the case of widespread adoption of solar photovoltaics, the abundance and availability of the semiconductor material itself will become critical. Though this need will only arise in the long term, the current activity aimed at preparing CQDs and CQD solar cells from materials with high natural abundance and ready availability is justified since technological development will also be a lengthy process.

The intriguing heterostructured CQDs described in Section 6.2 present new challenges and opportunities for device integration schemes. Significant innovation in device design will be required to take advantage of intra-QD charge separation occurring in Type II heterostructures and even more inventive approaches would be required to leverage the potential of nanorod superlattices. As such, it will only be in the long term that any potential solar cell technology based on these advanced CQDs could have a real-world impact. Nonetheless, such potential devices are tantalizing and any successes are likely to also suggest new ways to exploit these materials for related applications, such as photoelectrochemical fuel production.

The coming years will therefore bring parallel development of first-generation, CQD based, solar cell technologies and innovative demonstrations of solar cells based on sophisticated nanocrystal heterostructures. Combined, these approaches have the potential to yield cost-competitive technologies in the short term and high-efficiency (while still low cost) technologies based on distinctive CQD physics in the long term.

References

1 E. J. D. Klem, D. D. MacNeil, P. W. Cyr, L. Levina, E. H. Sargent, Efficient solution-processed infrared photovoltaic cells: Planarized all-inorganic bulk heterojunction devices via inter-quantum-dot bridging during growth from solution, *Appl. Phys. Lett.* **90** (2007), 183113.

2 I. Gur, N. A. Fromer, M. L. Geier, A. P. Alivisatos, Air-stable all-inorganic nanocrystal solar cells processed from solution, *Science* **310** (2005), 462–5.
3 Y. Wu, C. Wadia, W. Ma, B. Sadtler, A. P. Alivisatos, Synthesis and photovoltaic application of copper(I) sulfide nanocrystals, *Nano Lett.* **8** (2008), 2551–2555.
4 N. C. Greenham, X. Peng, A. P. Alivisatos, Charge separation and transport in conjugated-polymer/semiconductor-nanocrystal composites studied by photoluminescence quenching and photoconductivity, *Phys. Rev. B* **54** (1996), 17628–17637.
5 W. U. Huynh, J. J. Dittmer, A. P. Alivisatos, Hybrid nanorod-polymer solar cells, *Science* **295** (2002), 2425–2427.
6 I. Gur, N. A. Fromer, C. P. Chen, A. G. Kanaras, A. P. Alivisatos, Hybrid solar cells with prescribed nanoscale morphologies based on hyperbranched semiconductor nanocrystals, *Nano Lett.* **7** (2007), 409–414.
7 G. D. Scholes, G. Rumbles, Excitons in nanoscale systems, *Nat. Mater.* **5** (2006), 683–696.
8 C. B. Murray, D. J. Norris, M. G. Bawendi, Synthesis and characterization of nearly monodisperse CdE (E = S, Se, Te) semiconductor nanocrystallites, *J. Am. Chem. Soc.* **115** (1993), 8706–8715.
9 L. H. Qu, Z. A. Peng, X. G. Peng, Alternative routes toward high quality CdSe nanocrystals, *Nano Lett.* **1** (2001), 333–337.
10 D. V. Talapin, S. Haubold, A. L. Rogach, *et al*., A novel organometallic synthesis of highly luminescent CdTe nanocrystals, *J. Phys. Chem. B* **105** (2001), 2260–2263.
11 D. J. Norris, N. Yao, F. T. Charnock, T. A. Kennedy, High-quality manganese-doped ZnSe nanocrystals, *Nano Lett.* **1** (2001), 3–7.
12 X. G. Peng, L. Manna, W. D. Yang, *et al.*, Shape control of CdSe nanocrystals, *Nature* **404** (2000), 59–61.
13 L. S. Li, J. T. Hu, W. D. Yang, A. P. Alivisatos, Band gap variation of size- and shape-controlled colloidal CdSe quantum rods, *Nano Lett.* **1** (2001), 349–351.
14 L. Manna, L. W. Wang, R. Cingolani, A. P. Alivisatos, First-principles modeling of unpassivated and surfactant-passivated bulk facets of wurtzite CdSe: A model system for studying the anisotropic growth of CdSe nanocrystals, *J. Phys. Chem. B* **109** (2005), 6183–6192.
15 Z. A. Peng, X. G. Peng, Mechanisms of the shape evolution of CdSe nanocrystals, *J. Am. Chem. Soc.* **123** (2001), 1389–1395.
16 L. Manna, E. C. Scher, A. P. Alivisatos, Synthesis of soluble and processable rod-, arrow-, teardrop-, and tetrapod-shaped CdSe nanocrystals, *J. Am. Chem. Soc.* **122** (2000), 12700–12706.
17 L. Manna, D. J. Milliron, A. Meisel, E. C. Scher, A. P. Alivisatos, Controlled growth of tetrapod-branched inorganic nanocrystals, *Nat. Mater.* **2** (2003), 382–385.
18 B. Q. Sun, E. Marx, N. C. Greenham, Photovoltaic devices using blends of branched CdSe nanoparticles and conjugated polymers, *Nano Lett.* **3** (2003), 961–963.
19 I. Gur, N. A. Fromer, A. P. Alivisatos, Controlled assembly of hybrid bulk-heterojunction solar cells by sequential deposition, *J. Phys. Chem. B* **110** (2006), 25543–25546.
20 X. G. Peng, M. C. Schlamp, A. V. Kadavanich, A. P. Alivisatos, Epitaxial growth of highly luminescent CdSe/CdS core/shell nanocrystals with photostability and electronic accessibility, *J. Am. Chem. Soc.* **119** (1997), 7019–7029.
21 B. O. Davvousi, J. Rodriguez-Veijo, F. V. Mikulec, *et al.*, (CdSe)ZnS core–shell quantum dots: Synthesis and characterization of a size series of highly luminescent nanocrysatllites, *J. Phys. Chem. B* **101** (1997), 9463–9475.

22 D. J. Milliron, S. M. Hughes, Y. Cui, *et al.*, Colloidal nanocrystal heterostructures with linear and branched topology, *Nature* **430** (2004), 190–195.
23 A. M. Smith, A. M. Mohs, S. Nie, Tuning the optical and electronic properties of colloidal nanocrystals by lattice strain, *Nat. Nano*., **4** (2009), 56–63.
24 R. D. Robinson, B. Sadtler, D. O. Demchenko, *et al.*, Spontaneous superlattice formation in nanorods through partial cation exchange, *Science* **317** (2007), 355–358.
25 B. Sadler, D. O. Demchenko, H. Zheng, *et al.*, Selective facet reactivity during cation exchange in cadmium sulfide nanorods, *J. Am. Chem. Soc.* **131** (2009), 5285–5293.
26 C. Wadia, A. P. Alivisatos, D. M. Kammen, Materials availability expands the opportunity for large-scale photovoltaics deployment, *Envir. Sci. Tech.* **43** (2009), 2072–2077.
27 C. Wadia, Y. Wu, S. Gul, *et al.*, Surfactant-assisted hydrothermal synthesis of single phase pyrite FeS_2 nanocrystals, *Chem. Mater.* **21** (2009), 2568–2570.
28 C. B. Murray, S. H. Sun, W. Gaschler, *et al.*, Colloidal synthesis of nanocrystals and nanocrystal superlattices, *IBM J. Res. Dev.* **45** (2001), 47–56.
29 A. Sashcuiek, L. Langof, R. Chaim, E. Lifshitz, Synthesis and characterization of PbSe and PbSe/PbS core–shell colloidal nanocrystals, *J. Cryst. Growth* **240** (2002), 431–438.
30 J. J. Urban, D. V. Talapin, E. V. Shevchenko, C. B. Murray, Self-assembly of PbTe quantum dots into nanocrystal superlattices and glassy films, *J. Am. Chem. Soc.* **128** (2006), 3248–3255.
31 K. S. Cho, D. V. Talapin, W. Gaschler, C. B. Murray, Designing PbSe nanowires and nanorings through oriented attachment of nanoparticles, *J. Am. Chem. Soc.* **127** (2005), 7140–7147.
32 J. M. Luther, H. Zheng, B. Sadtler, A. P. Alivisatos, Synthesis of PbS nanorods and other ionic nanocrystals of complex morphology by sequential cation exchange reactions, *J. Am. Chem. Soc.* **131** (2009), 16851–16857.
33 P. K. Jain, L. Amirav, S. Aloni, A. P. Alivisatos, Nanoheterostructure cation exchange: Anionic framework conservation, *J. Am. Chem. Soc.* **132** (2010), 9997–9999.
34 R. E. Bailey, S. M. Nie, Alloyed semiconductor quantum dots: Tuning the optical properties without changing the particle size, *J. Am. Chem. Soc.* **125** (2003), 7100–7106.
35 W. Ma, J. M. Luther, H. Zheng, Y. Wu, A. P. Alivisatos, Photovoltaic devices employing ternary PbS_xSe_{1-x} nanocrystals, *Nano Lett.* **9** (2009), 1699–1703.
36 P. M. Allen, M. G. Bawendi, Ternary I–III–VI quantum dots luminescent in the red to near-infrared, *J. Am. Chem. Soc.* **130** (2008), 9240–9241.
37 M. G. Panthani, V. Akhavan, B. Goodfellow, *et al.*, Synthesis of $CuInS_2$, $CuInSe_2$, and $Cu(In_xGa_{1-x})Se_2$ (CIGS) nanocrystal "inks" for printable photovoltaics, *J. Am. Chem. Soc.* **130** (2008), 16770–16777.
38 E. M. Chan, C. M. Xu, A. W. Mao, *et al.*, Reproducible, high-throughput synthesis of colloidal nanocrystals for optimization in multidimensional parameter space, *J. Am. Chem. Soc.* **10** (2010), 1874–1885.
39 D. J. Milliron, A. P. Alivisatos, C. Pitois, C. Edder, J. M. J. Frechet, Electroactive surfactant designed to mediate electron transfer between CdSe nanocrystals and organic semiconductors, *Adv. Mater.* **15** (2003), 58–60.
40 J. S. Liu, T. Tanaka, K. Sivula, A. P. Alivisatos, J. M. J. Frechet, Employing end-functional polythiophene to control the morphology of nanocrystal–polymer composites in hybrid solar cells, *J. Am. Chem. Soc.* **126** (2004), 6550–6551.
41 J. S. Owen, J. Park, P. E. Trudeau, A. P. Alivisatos, Reaction chemistry and ligand exchange at cadmium-selenide nanocrystal surfaces, *J. Am. Chem. Soc.* **130** (2008), 12279–12281.

42 M. A. Caldwell, A. E. Albers, S. C. Levy, *et al.*, Driving oxygen coordinated ligand exchange at nanocrystal surfaces using trialkylsilylated chalcogenides, *Chem. Commun.* **47** (2011), 556–558.

43 M. V. Kovalenko, M. Scheele, D. V. Talapin, Colloidal nanocrystals with molecular metal chalcogenide surface ligands, *Science* **324** (2009), 1417–1420.

44 R. Tangirala, J. L. Baker, A. P. Alivisatos, D. J. Milliron, Modular inorganic nanocomposites by conversion of nanocrystal superlattices, *Angew. Chem. Int. Ed.* **49** (2010), 2878–2882.

45 A. P. Alivisatos, Semiconductor clusters, nanocrystals, and quantum dots, *Science* **271** (1996), 933–937.

46 M. G. Bawendi, M. L. Steigerwald, L. E. Brus, The quantum mechanics of larger semiconductor clusters (quantum dots), *Annu. Rev. Phys. Chem.* **41** (1990), 477–496.

47 L. E. Brus, Electron–electron and electron–hole interactions in small semiconductor crystallites: the size dependence of the lowest excited electronic state, *J. Chem. Phys.* **80** (1984), 4403–4409.

48 A. J. Nozik, Nanoscience and nanostructures for photovoltaics and solar fuels, *Nano Lett.* **10** (2010), 2735–2741.

49 R. Shankar, *Principles of Quantum Mechanics*, New York: Springer, second edition (1994).

50 I. S. Beloborodov, *et al.*, Granular Electronic Systems, *Rev. Mod. Phys.* **79** (2007), 469–518.

51 S. M. Reimann, M. Manninen, *Rev. Mod. Phys.* **74** (2002), 1283–1342.

52 A. Zabet-Khosousi, A.-A. Dhirani, Charge transport in nanoparticle assemblies, *Chem. Rev.* **108** (2008), 4072–4124.

53 C. Wang, M. Shim, P. Guyot-Sionnest, Electrochromic nanocrystal quantum dots, *Science* **291** (2001), 2390–2392.

54 D. V. Talapin, C. B. Murray, PbSe nanocrystal solids for n- and p-channel thin film field-effect transistors, *Science* **310** (2005), 86–89.

55 D. V. Talapin, J. S. Lee, M. V. Kovalenko, *et al.*, Prospects of colloidal nanocrystals for electronic and optoelectronic applications, *Chem. Rev.* **110** (2010), 389–458.

56 E. H. Sargent, Infrared photovoltaics made by solution processing, *Nat. Photonics* **3** (2009), 325–331.

57 J. Nelson, *The Physics of Solar Cells*. London: Imperial College Press (2008).

58 V. Sukhovatkin, S. Hinds, L. Brzozowski, E. H. Sargent, Colloidal quantum-dot photodetectors exploiting multiexciton generation, *Science* **324** (2009), 1542–1544.

59 V. D. Mihailetchi, L. J. A. Koster, J. C. Hummelen, P. W. M. Blom, Photocurrent generation in polymer–fullerene bulk heterojunctions, *Phys. Rev. Lett.* **93** (2004), 216601.

60 L. J. A. Koster, E. C. P. Smits, V. D. Mihailetchi, P. W. M. Blom, Device model for the operation of polymer/fullerene bulk heterojunction solar cells, *Phys. Rev. B* **72** (2005), 085205.

61 R. A. Marsh, C. Groves, N. C. Greenham, A microscopic model for the behavior of nanostructured organic photovoltaic devices, *J. Appl. Phys.* **101** (2007), 083509.

62 J. M. Luther, M. Law, M. C. Beard, *et al.*, Schottky solar cells based on colloidal nanocrystal films, *Nano Lett.* **8** (2008), 3488.

63 W. Ma, J. M. Luther, H. Zheng, Y. Wu, A. P. Alivisatos, Photovoltaic devices employing ternary PbS_xSe_{1-x} nanocrystals, *Nano Lett.* **9** (2009), 1699.

64 S. H. Park, A. Roy, S. Beaupré, *et al.*, Bulk heterojunction solar cells with internal quantum efficiency approaching 100%, *Nat. Photonics* **3** (2009), 297.

65 S. E. Shaheen, C. J. Brabec, N. S. Sariciftci, *et al.*, 2.5% efficient organic plastic solar cells, *Appl. Phys. Lett.* **78** (2001), 841.

66 J. Liu, E. N. Kadnikova, Y. Liu, M. D. McGehee, J. M. Fréiher, Polythiophene containing thermally removable solubilizing groups enhances the interface and the performance of polymer–titania hybrid solar cells, *J. Am. Chem. Soc.* **126** (2004), 9486.
67 M. Graetzel, Solar energy conversion by dye-sensitized photovoltaic cells, *Inorg. Chem.* **44** (2005), 6841.
68 P. V. Kamat, Quantum dot solar cells. semiconductor nanocrystals as light harvesters, *J. Phys. Chem. C* **112** (2008), 18737.

10 Solution-processed infrared quantum dot solar cells

Jiang Tang and Edward H. Sargent

Colloidal quantum dots (CQDs) are solution-processed semiconductors of interest in low-cost photovoltaics. Tuning of the bandgap of CQD films via the quantum size effect enables customization of solar cell's absorption profile to match the sun's broad visible- and infrared-containing spectrum reaching the earth. Here we review progress in the realization of low-cost, efficient solar cells based on CQDs. We focus in particular on CQD materials and approaches that provide both infrared and visible-wavelength solar power conversion. CQD photovoltaics now exceed 5% solar power conversion efficiency, which has been achieved by the introduction of a new architecture, the depleted-heterojunction CQD solar cell, that jointly maximizes current, voltage, and fill factor. CQD solar cells have also seen major progress in materials processing for stability, achieving extended operating lifetimes in an air ambient. We summarize progress both in device operation and also in gaining new insights into materials properties and processing – including new electrical contact materials and deposition techniques, as well as CQD synthesis, surface treatments, film-forming technologies – that underpin these rapid advances.

10.1 Introduction

Single-crystal materials such as silicon and epitaxial III–V compound semiconductors have led to remarkable solar photovoltaic power conversion efficiencies in the range of 20–41.4% [1, 2]. For their high efficiencies, these devices rely on the efficient matching of the light absorption spectrum to that of the sun's power reaching the earth, combined with the excellent electronic transport properties of crystalline semiconductors.

In parallel, low-cost, low-energy-consumption means of producing solar cells – often using solution-processing and roll-to-roll fabrication [3] – have emerged. Organic and polymer photovoltaics represent a particularly promising example of these low-cost devices. The organics have reached certified AM1.5 power conversion efficiencies of 6.8% [4] – a particularly impressive achievement in view of the constraints on these devices' maximum theoretical efficiencies due to their limited spectral absorption and considerable exciton dissociation energy [5].

Colloidal Quantum Dot Optoelectronics and Photovoltaics, eds. G. Konstantatos and E. H. Sargent.
Published by Cambridge University Press. © Cambridge University Press, 2013.

There is considerable interest in photovoltaic technologies that suffer no compromise between the desired high efficiency and equally important low cost.

The present review focuses on emerging solar cell technologies that are:

(1) solution-processed;
(2) fabricated at 200 °C and below;
(3) capable of absorbing the sun's entire visible, near infrared, and short-wavelength infrared;
(4) significantly spectrally tuned via the quantum size effect, empowering a single material strategy to create the different-bandgap layers required to produce stacked multi-junction solar cells.

CQDs, synthesized in the solution phase and possibly coated on substrates (including flexible ones) using drop-casting [6], spin-coating [7], and ink-jet printing [8, 10], have demonstrated many potential applications such as light emitting diodes [11–13]. In this research progress report, we focus in particular on infrared CQDs for photovoltaic applications. The materials that have seen the most intensive recent investigation – PbS and PbSe CQDs – possess bulk bandgaps that lie to the red of even the longest-wavelength junction required in multi-junction cells. Their large Bohr exciton radius allows wide tunability, even producing bandgaps that cut off at the red edge of the visible. As a consequence, these materials offer a single, binary-composition strategy to produce any and all of the junctions needed in triple-junction photovoltaics.

We begin with a discussion of material selection in CQD photovoltaics. We proceed to review briefly the fundamentals of p–n junctions and solar cell operation. We then introduce the experimental tools used to characterize the electrical properties of CQD films. We follow with a review of the understanding of carrier transport, surface passivation, doping, and dielectric constant in CQD films. We close with a detailed account of the research progress in performance, materials processing, and stability of CQD solar cells and a perspective on some of the many key questions and opportunities remaining open in the field.

10.2 Infrared CQDs for the full absorption of solar spectrum

10.2.1 Bandgap engineering for the broadband solar spectrum match

Before it reaches the earth's surface, the black body radiation ($T = 5762$ K) from sun is attenuated by the ozone, moisture, carbon dioxide, dust and other components in the atmosphere. AM1.5G (air mass 1.5 global includes both direct and diffusive radiation) is thus adopted as the standard spectrum for testing. The integrated power density of AM1.5G is 100 mW/cm^2 with the spectral intensity distribution matching that of sunlight at the earth's surface at an incident angle of 48.2°. As shown in Figure 10.1(a), AM1.5G is a broadband spectrum spanning ~280 nm in the ultraviolet to ~4000 nm in mid-infrared region. Half of the integrated power resides in the infrared spectral region.

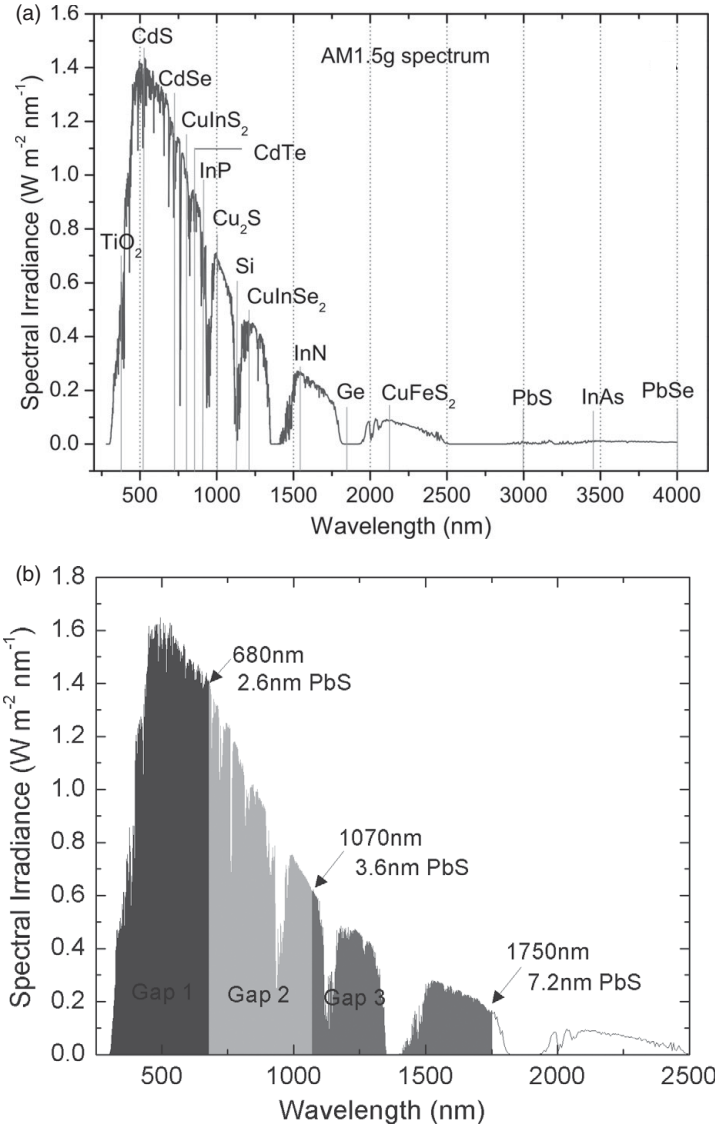


Figure 10.1 (a) AM1.5G solar spectrum from ASTM G173–03 reference spectra. The bandgaps for some common bulk semiconductors are: TiO_2 3.3 eV; CdS 2.5 eV; CdSe 1.7 eV; $CuInS_2$ 1.54 eV; CdTe 1.5 eV; InP 1.34 eV; Cu_2S 1.21 eV; Si 1.12 eV; $CuInSe_2$ 1.0 eV; InN 0.8 eV; Ge 0.66 eV; $CuFeS_2$ 0.6 eV; PbS 0.41 eV; InAs 0.35 eV and PbSe 0.28 eV. (b) Concept of using PbS CQDs of different sizes to build a triple-junction tandem solar cell.

Figure 10.1(a) includes the absorption onset of 15 typical bulk semiconductors with respect to the AM1.5G spectrum. In inorganic semiconductors, the absorption coefficient generally increases as the photon energy is increased starting from the semiconductor's band edge, in contrast with many organics whose absorption spectra peak as a result of the well-defined highest occupied to lowest unoccupied molecular orbital

(HOMO–LUMO) transition [14]. Low-bandgap materials absorb more light and produce large current at the cost of a low voltage; in contrast, large-bandgap materials output high voltage but low current due to their limited absorption. As a consequence, the balance between voltage and current necessitates an optimal choice of bandgap in the range 1.1–1.4 eV in order to yield the best power conversion efficiency in a single-junction solar cell. Bulk Si, InP and $CuInSe_2$ have the optimal bandgaps, while bulk PbS, InAs and PbSe are not suitable for photovoltaic application.

One way to tune the bandgap of a semiconductor is to manipulate its composition. According to Vegard's law [15], the bandgap of an alloyed semiconductor is approximately equal to the compositionally-weighted average of the bandgaps of the constituent semiconductors. Ternary and quaternary compounds such as InGaP, $Cu(InGa)Se_2$, and Cu_2ZnSnS_4, provide stoichiometry-tuned absorber materials for efficient photovoltaics.

Quantum confinement provides a promising alternative for bandgap engineering without relying on ternary and quaternary stoichiometric tuning. Decreasing the size of particles to less than their Bohr radius results in confinement of electron and hole wavefunctions and a significant increase in bandgap [16, 17]. This strategy enables the use of low-bandgap binary compound semiconductors such as PbS and PbSe for photovoltaic application.

We illustrate the quantitative aspects of quantum size effect tuning for the case of PbS (the numbers are similar for the case of PbSe). The Bohr radius of excitons in PbS is 18 nm. By controlling the size of PbS CQDs in synthesis, the absorption onset can be tuned from 3000 nm to $\sim$ 600 nm [18]. In the case of a single-junction device having optimal bandgap circa $E_g = 1.1$ eV, PbS CQDs of diameter $\sim$3.5 nm are desired. A triple-junction solar cell may also be achieved within a single material system [19]:

- the first (top) layer is composed of smallest PbS CQDs with diameters of 2.6 nm and absorption onset 680 nm;
- the second layer is composed of PbS CQDs with diameters of 3.6 nm and absorption onset 1070 nm;
- the bottom layer is composed of PbS CQDs with diameters of 7.2 nm and absorption onset 1750 nm.

The resultant distribution of spectral absorbance is illustrated schematically in Figure 10.1(b).

The desire for solution-processing, combined with the need for absorption of the majority of the sun's broad solar spectrum, motivates interest in infrared colloidal nanoparticles. Since InP, CdSe, CdTe have bulk bandgaps in the near infrared, quantum confinement generally tunes them into the visible. They may be of interest in one junction in a multi-junction cell, but are not materials that offer to span the entire multi-junction stack [19]. Si, Cu_2S, $CuInS_2$, $Cu(InGa)Se_2$, and Cu_2ZnSnS_4, having small Bohr exciton radii, generally preserve their bulk properties. Here we focus therefore on photovoltaics based on infrared CQDs that offer wide tuning across the solar spectrum based on a dramatic range of quantum confinement. These materials hold great potential for low-cost, high-efficiency photovoltaics. Intensive effort with these materials in the

since 2008 has also raised a number of important fundamental and applied questions that merit review.

10.2.2 Light absorption in CQD film

Light absorption may be described using the Beer–Lambert law:

$$I = I_0 e^{-\alpha(h\upsilon)l}, \tag{10.1}$$

where I, I_0, $\alpha(h\upsilon)$, and l are the transmitted light intensity, incident light intensity, absorption coefficient, and film thickness, respectively. Indirect-bandgap semiconductors offer weak absorption coefficients because their absorption relies on a multi-particle interaction that includes a phonon. Direct-bandgap semiconductors offer much stronger absorption coefficients, providing α of 10^4 cm^{-1} and above. Such a strong absorption enables reduced material consumption and enables the realization of efficient devices based on materials having modest transport lengths.

The absorption coefficient of CQDs is of crucial importance in engineering films of suitable thicknesses to enable efficient photovoltaics. Studies on CQDs dispersed in solution provide a basis for interpreting film-based results [20, 21]. The refractive index n and extinction coefficient k for typical PbSe CQD films have been studied and reported in the literature [22]. PbSe CQDs having an excitonic peak at 1686 nm were treated using 1,2-ethanedithiol (EDT). At short wavelengths, the absorption coefficient was ~5 times lower than that of bulk PbSe, suggestive of 20% by volume of CQDs within the film [21]. Optical penetration depths were estimated to be ~20 nm for 400 nm wavelength photons and ~500 nm for 1700 nm wavelength photons. Similar optical penetration depths have been obtained for PbS CQD films having a similar quantum-confined bandgap [23].

Many CQD photovoltaics employ a reflective back contact. To achieve 90% absorption of incident photons in a double-pass fashion, and use the absorption coefficient for photons with bandgap wavelength (most weakly absorbed), simple calculation suggests that the CQD film needs to be about 1 μm thick, which is much thinner than in indirect-gap devices using Si (where typically a thickness of 180 μm is required).

10.3 Semiconductor solar cell fundamentals

10.3.1 Fundamentals of p–n junction

To provide a framework for investigation and optimization of CQD materials and devices summarized herein, we begin with an introduction to the operation of p–n junction devices. We first point out evident deviations of CQD films from the homogeneous bulk film described by the canonical semiconductor theory and justify our pursuit of this first-order, highly simplified model notwithstanding:

(1) Strong electron interactions in bulk semiconductor solids and periodic crystal structures result in the formation of bands of delocalized carriers, whereas in semiconductor CQD films, CQDs are surrounded by an insulating matrix material, typically

organic ligands, and hence carriers are largely confined to the CQDs. Transport in these films occurs mainly through tunneling or hopping. Carrier transport can be described in both cases by an average velocity – thus a time to transit a depletion region or a quasi-neutral region – and this simple consideration underpins many general concepts such as characteristic drift and diffusion length scales of major importance to understanding the performance of junction-based devices.

(2) CQD films incorporate quantum dots, which results in a large internal surface area and may also produce fluctuations in doping and trap state distributions across the film. Spatially-averaged doping and defect densities may nonetheless be applied over macroscopic (many tens of quantum dots) volumes. Such volumes correspond to the measured length scales of depletion regions, diffusion lengths, and drift lengths in these films, justifying their judicious use as helpful simplifying approximations.

When a p-type and an n-type semiconductor are brought together, diffusion of majority carriers leads to the establishment of a depletion region. The width of this region, W, is

$$W = \left[\frac{2\varepsilon kT}{q^2}\ln\left(\frac{N_A N_D}{n_i^2}\right)\left(\frac{1}{N_A}+\frac{1}{N_D}\right)\right]^{1/2}, \tag{10.2}$$

where ε, k, T, q, n_i, N_A, and N_D are the permittivity, Boltzmann's constant, temperature, elementary charge, intrinsic carrier density, acceptor density, and donor density, respectively. Permittivity ε is the product of dielectric constant (or relative permittivity) ε_m and the permittivity of vacuum ε_0. The depletion region is not equally distributed on both sides, but is rather spread wider on the relatively less doped region based on

$$x_{p0} = \frac{W}{1+N_A/N_D} \text{ and } x_{n0} = \frac{W}{1+N_D/N_A}, \tag{10.3}$$

where x_{p0} and x_{n0} are the depletion region widths an the p-side and the n-side, respectively.

The built-in potential, V_0, reflects the potential change within the depletion region. It is dependent on the doping density:

$$V_0 = \frac{kT}{q}\ln\left(\frac{N_A N_D}{n_i^2}\right). \tag{10.4}$$

Carrier transport relies on drift in the depletion region and diffusion in the quasi-neutral region, as indicated in Figure 10.2(a). The drift length l_{drift} depends on the built-in field E, carrier mobility μ and carrier lifetime τ:

$$l_{drift} = \mu E \tau. \tag{10.5}$$

The carrier diffusion length $l_{diffusion}$ is calculated as

$$l_{diffusion} = \sqrt{D\tau}. \tag{10.6}$$

The diffusion coefficient D and carrier mobility μ are related by the Einstein relation:

$$\frac{D}{\mu} = \frac{kT}{q}. \tag{10.7}$$

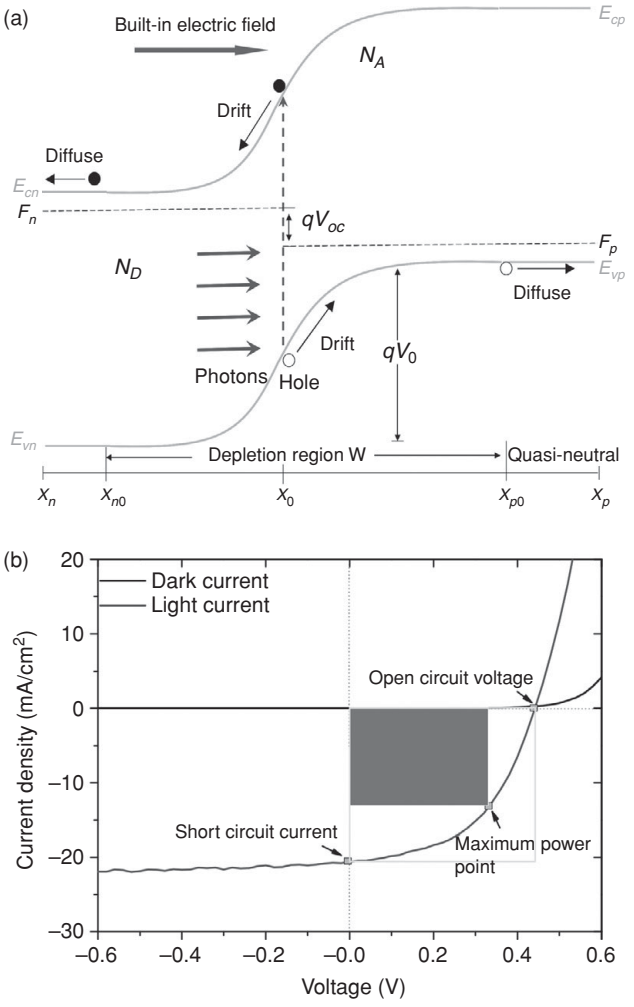


Figure 10.2 (a) Schematic diagram of a p–n junction. qV_{oc} is the difference between the quasi-Fermi level F_n of electrons in the n-type material and quasi-Fermi level F_p of holes in the p-type material under illumination. Mid-gap states and shallow traps are present in both the p- and the n-type materials. Shallow traps capture and/or release free carriers to the valence/conduction band through thermal activation. (b) *J–V* characteristic of a solar cell in the dark and under 1-sun illumination. The area of the gray rectangle represents the maximum power output, the product of the optimally chosen operating current and voltage.

Under illumination, photogenerated carriers in the depletion region are swept by the built-in field to the edge of the depletion region. These carriers, as well as carriers generated in the quasi-neutral region, are required to diffuse across the quasi-neutral region to their respective collecting electrodes. Mid-gap states, also known as recombination centers, provide undesired nonradiative pathways for the loss of carriers prior to their successful extraction (Figure 10.2(a)). Shallow traps play a much less deleterious role, extending

the excited state lifetime at the price of lowered mobility, typically keeping the mobility and lifetime product unchanged compared to the trap-free case.

While the preceding discussion ostensibly focused on homojunctions, Schottky (metal–semiconductor) contacts and heterojunction (p–n) junctions function similarly. For Schottky contacts, band-bending occurs at the metal–semiconductor interface. The metal contact can be viewed as heavily doped ($N > 10^{21}$ cm^{-3}) semiconductor which indicates that the entire depletion region falls on the semiconductor side of the junction. Schottky devices are thus sometimes referred to as single-sided p–n junctions. In the case of heterojunctions, the difference in the Fermi energies across the semiconductor–semiconductor junction produces a depletion region and thus a driving force for the separation of photogenerated carriers as described above. Differences in electron affinity and ionization potential provide additional discontinuities in conduction and valence bands across the interface that – ideally – should promote the donation of one carrier (e.g., electrons) to the acceptor side, and block the egress of the other type of charge carrier (e.g., holes).

10.3.2 Fundamentals of solar cells

Figure 10.2(b) shows the current density as a function of voltage (J–V) characteristic of a solar cell in the dark and under illumination. The dark current shows rectification, characteristic of the diode nature of a solar cell. Under illumination, photogenerated carriers shift the J–V curve downward into the fourth quadrant. The power conversion efficiency η is given by

$$\eta = \frac{V_{max} J_{max}}{P_{inc}} = \frac{V_{oc} J_{sc} FF}{P_{inc}}, \tag{10.8}$$

where V_{max} and J_{max} are the voltage and current density at the maximum power point, P_{inc} is the incident light intensity, V_{oc} is the open-circuit voltage, J_{sc} is the short-circuit current density, and FF is the fill factor.

The short-circuit current density J_{sc} is the maximum number of photogenerated carriers per unit area that are extracted from the solar cell. J_{sc} depends on the illumination intensity, the total absorbance of the solar cell and its match to the solar spectrum, and the recombination losses prior to extraction. J_{sc} can also be obtained by integrating the external quantum efficiency (EQE) or incident-photon-to-electron conversion efficiency (IPCE) with the standard AM1.5G spectrum.

The open-circuit voltage V_{oc} is the maximum voltage that a solar cell can generate. V_{oc} reflects the difference between the quasi-Fermi level of electrons F_n in the n-type material and the quasi-Fermi level of holes F_p in the p-type material. V_{oc} and J_{sc} are related to one another, and to the reverse saturation current density $J_{0,}$ as follows:

$$V_{oc} = \frac{kT}{q} \ln \frac{J_{sc} + J_0}{J_0} \approx \frac{kT}{q} \ln \frac{J_{sc}}{J_0}. \tag{10.9}$$

This mandates a low reverse saturation current density J_0, requiring low recombination in the quasi-neutral region and a highly rectifying diode.

In real photovoltaic devices, the parasitic series resistance R_s the shunt resistance R_{sh} also need to be considered. The following equation describes the *J–V* characteristics of a solar cell:

$$J = J_{sc} - J_0 \left[\exp\left(\frac{q(V + \mathrm{J}R_s)}{A_0 kT} \right) - 1 \right] - \frac{V + \mathrm{J}R_s}{R_{sh}}, \tag{10.10}$$

where J_{sc} is the short-circuit current density when series resistance is zero and the shunt resistance is infinite; A_0 is the diode ideality factor and it typically has a value between 1and 2. As can be seen in (10.10), series resistance R_s reduces J_{sc} but has no effect on V_{oc}, while shunt resistance R_{sh} has no effect on J_{sc} but reduces the V_{oc}. The series resistance is the sum of film resistance, electrode resistance and the contact resistance between the film and the electrode. The shunt resistance is mainly associated with carrier recombination loss. In addition, *FF* is also related to R_s and R_{sh}: large R_{sh} and small R_s leads to device with good *FF*. In short, maximized R_{sh} and minimized R_s all maximize V_{oc}, J_{sc}, and *FF* and thus power conversion efficiency η.

10.3.3 Implications for CQD solar cell optimization

The above discussions lead to some useful broad guidelines for CQD solar cell optimization:

(1) Since efficient carrier extraction mandates all photogenerated carriers transit to the electrodes within their lifetime, a simple planar device will require l_{drift} for each carrier that exceeds the depletion region width, and $l_{diffusion}$ greater than the quasi-neutral-region thickness.
(2) Since V_{oc} is determined by the quasi-Fermi level difference across the junction, high doping levels are generally desired (Equation (10.1)). However, high doping density results in thinning of the depletion region (Equation (10.2)), which in turn requires charge carriers to diffuse greater distances through quasi-neutral regions.
(3) Since typical carrier lifetimes in CQD films are on the order of microseconds in the best cases [24], and since minority carriers need to be extracted over distances on the order of hundreds of nanometers, mobilities of 1E-2 cm^2/V s and well above are desired.
(4) The preceding choice of bimolecular lifetime assumes that radiative recombination limits carrier lifetime; the inclusion of mid-gap states, even at very low density, can dramatically lower lifetime into the nanosecond regime and below. Excellent passivation of nanoparticle surfaces, eliminating the defect states that lead to mid-gap centers, is thus urgently required.
(5) More limited mobilities may be tolerated, yet complete absorption achieved, when architectures inspired by organics' bulk heterojunctions [25] and dye-sensitized solar cells' nanoporous electrodes [26] are employed. Majority carrier mobilities in the donor and acceptor phases must nonetheless be maximized (ideally 1E-2 cm^2/V s and above) to minimize the series resistance term in the fill factor.

(6) Strategies to increase absorption per unit length, such as in plasmonics where metal nanoparticles are employed [27], are also of considerable interest for the same reason.

10.4 Electrical properties of CQD films

10.4.1 Measurements of electrical properties of CQD films

As discussed in Section 10.3, carrier mobilities, doping density, and carrier lifetime as well as dielectric constant are crucial to modeling photovoltaic device operation. In this section we briefly review the experimental tools that are frequently applied in the field to obtain such physical parameters.

Time of flight (TOF) is used to measure the drift mobility of electrons and holes. It involves photogeneration of a pocket of charge carriers via illumination of a semiconductor sample of interest addressed with rectifying electrical contacts [28]. Under an external bias, the photogenerated carriers drift to the collection electrode, leading to the time-dependent current that is monitored across an external load resistor. The choice of bias polarity determines which carrier mobility is measured. Illumination at a short wavelength that ensures substantial absorption of light within a small fraction of the sample thickness ensures that the dimension of the initially-created carrier pocket is small compared with the sample thickness in which drift is then observed.

Carrier mobility can be calculated from the transit time t_T, film thickness d and the external bias V:

$$\mu = \frac{d^2}{t_T V}. \tag{10.11}$$

The transit time t_T can be extracted from the intersection point of the asympotes to the double-logarithmic current plotted against time (Figure 10.3(a)). The absence of a constant-current plateau after the initial current spike indicates dispersive transport.

Successful application of TOF for mobility measurement necessitates that the dielectric relaxation time t_σ exceed the transit time (t_T) of photogenerated carriers:

$$t_\sigma = \frac{\varepsilon_m \varepsilon_0}{\sigma} > t_T = \frac{d^2}{\mu V}, \tag{10.12}$$

where σ is the conductivity. If $t_\sigma < t_T$, the drifting pocket of photogenerated carrier will be incapable of reaching the collecting electrode [29]. In addition, TOF measurement also requires t_σ be longer than the delay time between the application of voltage and the light pulse (t_D).

Carrier extraction by linearly increasing voltage (CELIV) – a purely electronic technique by contrast – follows the transient current induced by the change in the width of the depletion layer in response to a pulsed electrical bias [29]. CELIV enables extraction of the majority carrier mobility. It relies on devices having strong rectification. The

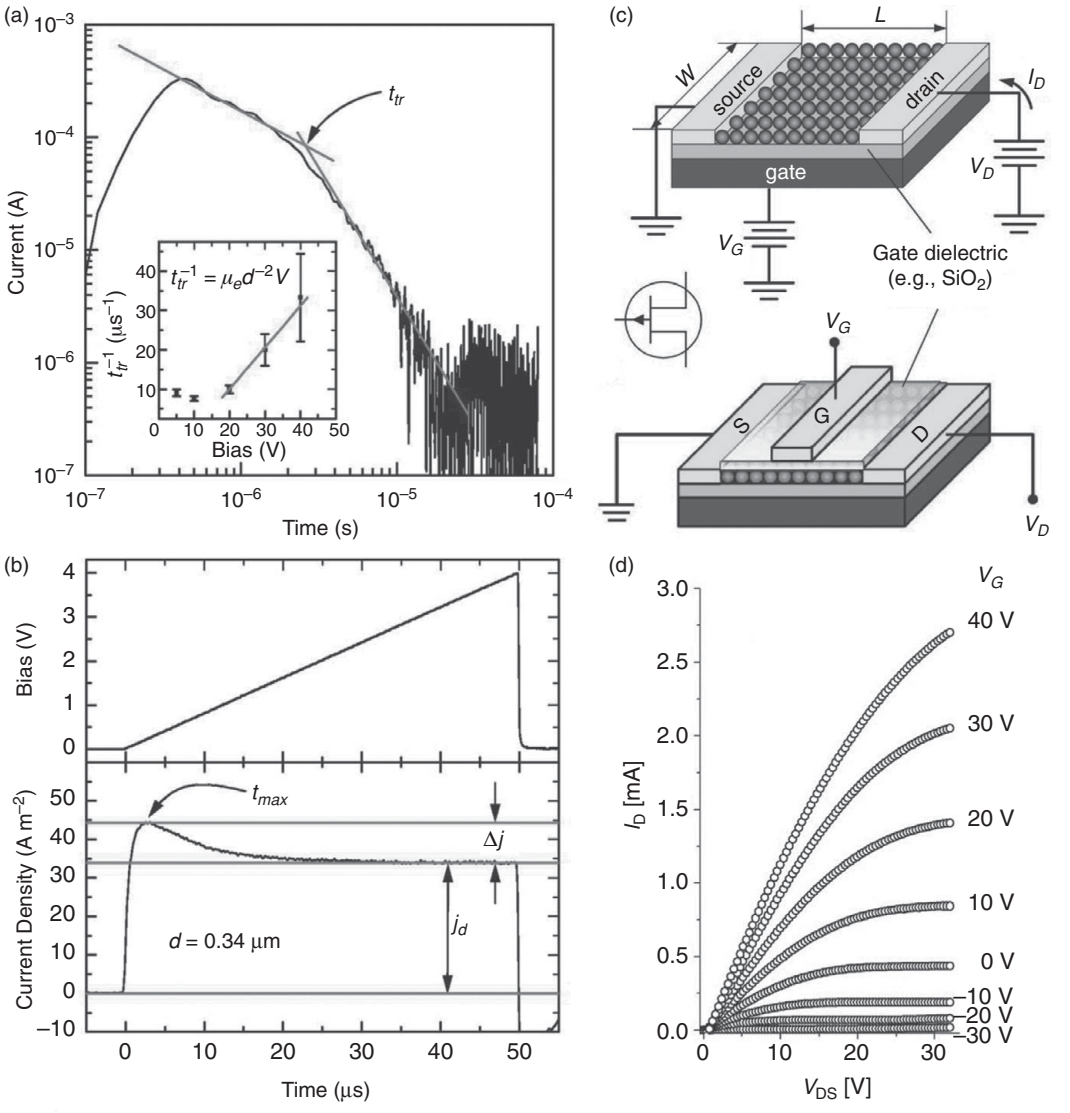


Figure 10.3 Characterization of carrier mobility. (a) TOF and (b) CELIV measurements of an ITO/PbS/Al device. Reproduced with permission from [24]. Copyright 2008 American Institute of Physics. (c) Schematic diagram of FET configuration. Reprinted from [30] Copyright 2010, American Chemical Society. (d) I_D–V_{DS} plot under different V_G. Reproduced with permission from [31]. Copyright 2005 American Association for the Advancement of Science.

linearly increasing voltage is applied through a function generator and the transient current is monitored through a load resistor. Figure 10.3(b) shows a representative CELIV transient, from which the hole mobility μ_h may be extracted:

$$\mu_h = \frac{2d^2}{3At_{max}^2\left(1 + 0.36\frac{\Delta J}{J_d}\right)}, \tag{10.13}$$

where d is device thickness, A is ramp rate, t_{max} is the time for the transient current signal to reach its maximum value, ΔJ is the maximum drift current, and J_d is the displacement current. CELIV also allows determination of the dielectric constant ε_m of the film:

$$\varepsilon_m = \frac{J_d d}{A\varepsilon_0}. \tag{10.14}$$

The construction and characterization of field-effect transistors (FETs) enables the determination of carrier type and carrier mobility within a semiconductor that serves as the channel of the FET [30]. The gate electrode is isolated electrically from the source and drain through the use of a thin oxide, typically thermally-grown SiO_2 atop a heavily-doped silicon substrate (Figure 10.3(c)). Drain and source electrodes desirably form low-resistance contacts to the CQD film. The free carrier density available in the channel, and thus the current flowing between the source and drain upon application of a source–drain bias, is modulated by the gate voltage. For an n-type film, a negative gate voltage depletes the transistor channel, increasing its resistance, while a positive gate voltage enhances the density of free carriers, decreasing its resistance (Figure 10.3(d)). The linear regime field-effect mobility μ_{lin} of the film can be extracted from the linear regime of drain–source I_D vs. gate voltage V_G plot [31]:

$$\mu_{lin} = \frac{L\left(\frac{\partial I_D}{\partial V_G}\right)}{WC_i V_D}, \tag{10.15}$$

where L is channel length, W is channel width, V_D is drain–source voltage and C_i is the unit capacitance of the dielectric layer:

$$C_i = \varepsilon_{\mathrm{m}}\varepsilon_0/\mathrm{d}. \tag{10.16}$$

ε_m is the dielectric constant (3.9 for SiO_2) and d is the thickness of the dielectric layer.

Another mobility from FET measurement, μ_{sat}, the saturation regime field-effect mobility, can be calculated from the $[I_D]^{1/2}$ vs. V_G plot:

$$\mu_{sat} = \frac{2L\left(\frac{\partial I_D^{1/2}}{\partial V_G}\right)^2}{WC_i}. \tag{10.17}$$

The measured μ_{sat} is often higher than μ_{lin}, because the trapping of charge carriers degrades the linear mobility, but these traps are filled by the time the saturation regime is entered. Knowledge of the mobility and measured conductance can then be used to estimate the free carrier density.

The activated doping density of a semiconductor film can also be ascertained from Mott–Schottky capacitance–voltage (C–V) analysis [32]. The doping density can be calculated from the C^{-2} vs. V plot:

$$N = \frac{2}{A^2 q\varepsilon_m\varepsilon_0 \frac{dC^{-2}}{dV}} \tag{10.18}$$

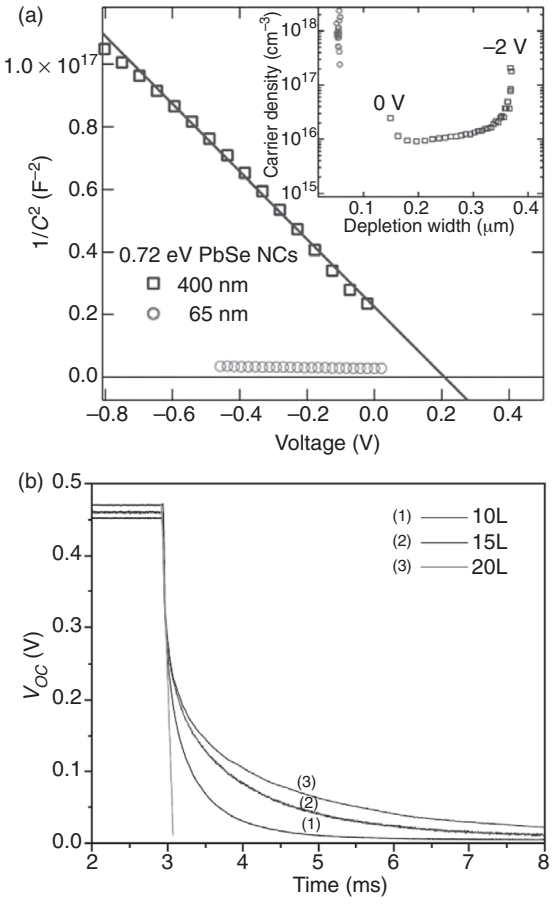


Figure 10.4 Measurement of doping density and carrier lifetime: (a) *C–V* analysis of an ITO/PbSe/Al device. Reproduced with permission from [45]. Copyright 2008 American Chemical Society. (b) V_{oc} decay analysis of an ITO/PbS/LiF/Al device. The straight line is the linear fitting of voltage decay. Reproduced with permission from [33] Copyright 2010 American Chemical Society.

where A is the device area and C is the measured capacitance. Figure 10.4(a) shows a linear fit of C^{-2} vs. V whose slope allows determination of the doping density. When the device is fully depleted, the capacitance is constant during the voltage scan, and dielectric constant ε_m can be obtained from this measurement.

The carrier lifetime may be determined in operating photovoltaic diodes from measurement of the open-circuit decay characteristic (Figure 10.4(b)) [24, 33]. Devices are illuminated with a transient pulse that establishes the initial open-circuit voltage V_{oc}. Once illumination is turned off, V_{oc} decays at a rate used to estimate the carrier lifetime τ:

$$\tau = -\frac{\kappa T}{q}\frac{F_I}{\frac{dV_{oc}}{dt}}. \tag{10.19}$$

Here κ is the Boltzmann constant, F_I is a factor ranging between 1 at low injection and 2 at high injection, and dV_{oc}/dt is the measured initial slope of V_{oc} degradation. Study of the intensity dependence of open-circuit voltage decay allows the recombination behavior of a semiconductor device to be explored in detail at light intensities both above and below 1 sun.

10.4.2 Transport in CQD film

As argued above, improved charge transport in CQD films, ideally reaching well above 10^{-2} cm^2 V^{-1} s^{-1}, is prized in realizing high-performance CQD photovoltaics. Transport mechanisms explored include resonant energy transfer [34], variable range hopping (VRH), and tunneling between adjacent CQDs. We summarize briefly the fundamentals of VRH and the tunneling mechanism.

Mott variable range hopping (Mott-VRH) describes low-temperature conduction in strongly disordered systems with localized states [35, 36]. Charges localized to have energy E_i may acquire sufficient energy to hop thermally to a nearby site where the energy difference is $\Delta E_{ij} = E_j - E_i$. The spatial distance r_{ij} and energy difference ΔE_{ij} together determine the hopping probability: small r_{ij} and large ΔE_{ij} facilitate the hopping. As shown in Figure 10.5, when the hopping between nearest-neighbor sites (path I) dominates, the dependence of conductivity on temperature is given by

$$\sigma = \sigma_0 \exp[-(T_0/T)^1]. \tag{10.20}$$

When hopping not between nearest neighbors (path II) also makes a large contribution to the conductivity, the dependence of conductivity on temperature is

$$\sigma = \sigma_0 \exp[-(T_0/T)^{1/4}], \tag{10.21}$$

where $T_0 = e^2/\varepsilon\alpha$, α is the localization length, and ε is the dielectric constant of the material.

In Efros–Shklovskii variable range hopping (ES-VRH) [37, 38], the quantum localization length is assumed to be much smaller than the spatial distance between centers and the overlap between the wavefunctions is neglected. In this case the relationship between temperature and conductivity is given by

$$\sigma \propto \exp[-(T_0/T)^{1/2}]. \tag{10.22}$$

The conduction mechanism changes from ES- to Mott-VRH when the energy difference of hopping sites (ΔE_{ij}) equals to the Coulomb gap Δ [39]. In an array of weakly coupled CQDs, the Coulomb gap is

$$\Delta \approx 2E_c, \tag{10.23}$$

where E_c is the energy required to add one charge to or remove one charge from the particle [30]. For a spherical CQD it can be approximately calculated as

$$E_c = \frac{e^2}{4\pi\varepsilon r}, \tag{10.24}$$

where r is the radius of the CQD.

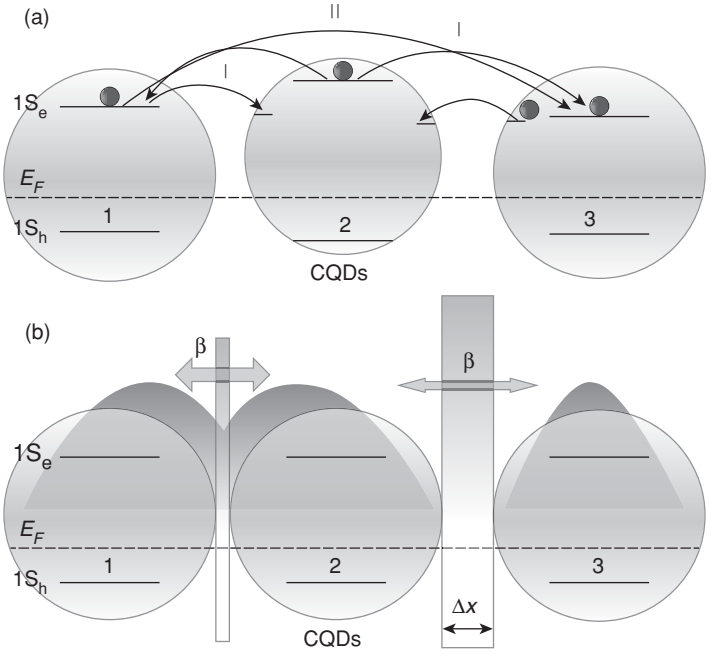


Figure 10.5 Charge transport in CQD films. Fermi level (dashed lines) and the lowest CQD states ($1S_h$ for holes and $1S_e$ for electrons) are depicted. (a) Nearest-neighbor hopping (I) and VRH (I + II) occur between CQD states and surface trap states. Variations in CQD size distribution can produce an energy misalignment between the states among which transport is desired. (b) Tunneling between adjacent CQDs allows charge carriers to cross the inter-particle barrier (rectangular bar) of width Δx. Exciton delocalization (wavefunction overlap) and coupling energy β are stronger between CQDs 1 and 2 (narrower barrier) than between CQDs 2 and 3. While not depicted here, similar pathways for carrier hopping and tunneling also occur within the valance band.

These concepts have been applied in the study of transport in films consisting of ~5.5 nm diameter PbSe CQDs capped with oleic acid [40]. When the as-produced film was annealed at 373 K, Coulomb blockade dominated because the ~36 meV charging energy E_c for the PbSe CQDs exceeded kT, thus rendering the PbSe CQD film essentially insulating. Annealing at 473 K and higher temperatures decreased inter-particle spacing and made the film much more conductive through VRH. Fitting the conductivity as a function of temperature (T) through the following equation (G_0 and T_0 are constants):

$$G = G_0 \exp[-(T_0/T)^p]. \tag{10.25}$$

led to $p \sim 0.95$–1.05 in the high-temperature region and ~0.48–0.55 in the low-temperature region, as shown in Figure 10.6. These values closely approach the unity value characteristic of Mott-VRH and the ~0.5 value characteristic of ES-VRH [40].

While transport based on hopping is temperature-dependent, transport based on tunneling is temperature-independent. For a general model, the quantum mechanical

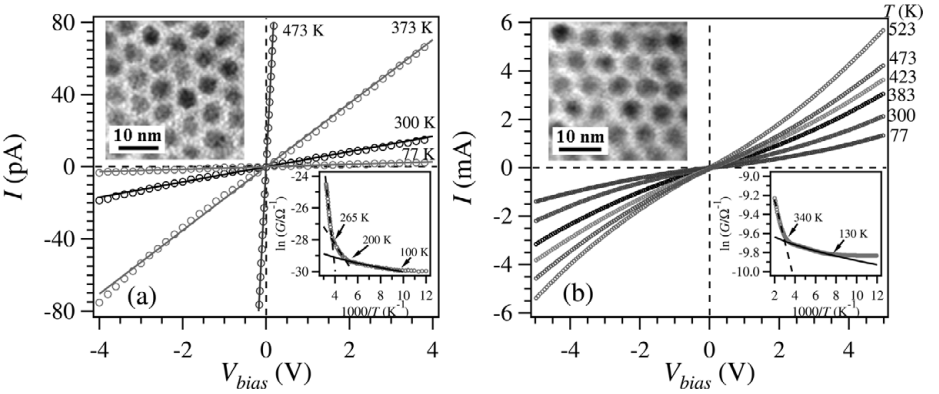


Figure 10.6 I–V_{bias} characteristics versus T for PbSe CQD film vacuum annealed at (a) 473 and (b) 523 K. The lower insets show G (in log scale) vs. the inverse of T. The upper insets are TEM images of PbSe CQDs arrays after vacuum annealing. Reproduced with permission from [40]. Copyright 2005 American Physical Society.

coupling between two adjacent CQDs can be expressed in terms of coupling energy β:

$$\beta \approx h\Gamma, \tag{10.26}$$

where h is Planck's constant and Γ is the tunneling rate, which can be approximated as [41]:

$$\Gamma \approx \exp\left(-2\pi\,\Delta x\sqrt{\frac{8m^*\Delta E}{h^2}}\right), \tag{10.27}$$

where m^* is the carrier effective mass and ΔE and Δx are the height and width of the tunneling barrier. The tunneling rate Γ and also the coupling energy β thus drop exponentially with increasing inter-particle distance Δx. The dependence on the barrier height ΔE and carrier effective mass m^* is weaker [30]. As shown in Figure 10.6(b), a larger barrier between CQD 2 and 3 leads to less wavefunction overlap compared with the wavefunction overlap between CQD 1 and 2. As in the case of hopping, efficient electron transport requires a coupling energy β that exceeds the Coulomb gap Δ.

Exchanging long original ligands with shorter ligands before film formation is one practice used to decrease the inter-particle distance r_{ij} [42]. Following the ligand exchange, smooth and dense film can be directly fabricated using spin-coating or spray deposition. In one study, solution-phase butylamine ligand exchange was used to remove long oleate ligands capping PbS CQDs [24, 43]. In a similar vein, molecular metal chalcogenides have been employed in solution ligand exchange, producing close packing among $Sn_2S_6^{4-}$ capped CdSe CQDs and $\mu_e \sim 3 \times 10^{-2}$ cm^2 V^{-1} s^{-1} [44].

Another way to reduce inter-particle distance is to treat the CQD films in the solid phase using short, often bidentate, ligands that substitute for the original long ligands. Ligands of interest include methylamine [45], hydrazine [31], pyridine [46], and dithiols such as EDT [47, 48] and benzenedithiol (BDT) [49]. The deposition of multiple layers is often used to infill cracks resulting from volume contraction. This

layer-by-layer strategy has been applied to build films from 8-nm PbSe CQDs treated using 1.0 M hydrazine. An impressive $\mu_e \sim 0.7$ cm^2 V^{-1} s^{-1} for as-treated films and μ_h of 0.12–0.18 cm^2 V^{-1} s^{-1} for films exposed to air have been obtained [31]. Similar solid-state treatments of PbSe CQD film using alternative ligands and linkers have been reported [50, 51].

Methods that combine solution-phase and solid-state treatments may be beneficial. Koleilat *et al.* reported that PbSe CQDs were first exchanged from oleate to octylamine in solution, after which films were fabricated using layer-by-layer processing. These films were further treated with BDT and $\mu_e \sim 1.4 \times 10^{-3}$ cm^2 V^{-1} s^{-1} and $\mu_h \sim 2.4 \times 10^{-3}$ cm^2 V^{-1} s^{-1} were obtained [49]. A similar strategy was applied in the case of PbS CQD films [23]. The use of BDT was advanced as a means to promote electron delocalization by virtue of the conjugated benzene ring, a means to decreasing barrier height ΔE and increasing coupling energy β.

Table 10.1 summarizes the electron and hole mobilities reported for different CQD films. The range of reported mobility values is expected to arise due to differences in inter-particle spacing resulting from the various treatments. As seen in (10.27), a small variation in Δx may lead to a large change in the coupling energy and measured mobility. Different methods of mobility characterization are also expected to produce discrepancies in reported mobilities. In FET mobility measurements, the applied gate bias results in filling of the deeper traps, and the modulation of the current flowing through the channel reveals the high mobilities associated with shallow traps and subbands [19]. In CELIV and TOF measurements, traps are more prone to dominate mobility measurements, leading to smaller extracted mobility values.

It should be emphasized that quantum confinement in CQDs should be substantially preserved in order to maintain high V_{oc}. Hence, it is important to monitor the preservation of an excitonic peak in absorption [48] and/or quantum efficiency spectra in films and devices following ligand exchanges and film fabrication.

10.4.3 CQD passivation

As discussed in Section 10.3.1, mid-gap defects in devices act as recombination centers. They reduce the number of extractable photogenerated carriers, leading to suboptimal internal quantum efficiency and thus J_{sc}. They also suppress quasi-Fermi level splitting under illumination, decreasing the available V_{oc}. Passivation of these mid-gap defects is therefore crucial to achieve efficient solar cells. In solution-based studies of CQD luminescence, there is no limit on the ligand length that can be used to enhance passivation [52, 53]; however, in optoelectronic applications such as photovoltaics, good carrier transport mandates a small inter-particle spacing requiring the use of short – yet still strongly passivating – ligands.

Experiments have established lead chalcogenide CQDs as composed of a stoichiometric core surrounded by a Pb-rich cation layer [20, 21]. This nonstoichiometric nature has been found to simplify the implementation of complete passivation. Ligands that bind strongly only to surface cations may substantially passivate surface defects.

Table 10.1. Reported electron and hole mobilities for various CQD films

Material	Film preparation	Ligand	CQDs size	μ_e ($cm^2\ V^{-1}\ s^{-1}$)	Measurement technique	μ_h ($cm^2\ V^{-1}\ s^{-1}$)	Measurement technique	Reference
PbS	solution exchange	butylamine	6 nm	$(2 \pm 1) \times 10^{-4}$	TOF	$(1.5 \pm 0.1) \times 10^{-3}$	CELIV	[24]
CdSe		$Sn_2S_6^{4-}$ +heat treatment	4.5 nm	3×10^{-2}				[44]
PbSe	solid state treatment	hydrazine	8 nm	0.7		0.12–0.18	FET	[31]
			7.4 nm	0.5–1.2				[50]
			5.6 nm	0.4		0.02		[89]
		EDT	3.1 nm	0.006	FET	0.0002		[41]
			4.1 nm	0.016		0.0023		
			4.8 nm	0.032		0.0056		
			5.6 nm	0.057		0.015		
			6.5 nm	0.056		0.017		
			8.6 nm	0.025		0.039		
		formic acid	6.0 nm			0.02		[70]
		acetic acid				0.006		
		oxalic acid				0.0025		
PbS		formic acid	8.8 nm			0.0024		
		acetic acid				0.00038		
		oxalic acid				0.00015		
PbS	mixed[a]	butylamine +1,4-BDT	6 nm	$(1–6) \times 10^{-4}$	transient photocurrent			[23]
PbSe	mixed	octylamine +1,4-BDT	4 nm	1.4×10^{-3}	FET	2.4×10^{-3}	CELIV	[49]

[a] The third strategy: first solvent exchange then solid-state treatment.

Pb-rich nanoparticles passivated using short thiols – ligands that are minimal in volume and high in affinity to surface Pb^{2+} – have therefore attracted considerable attention.

The nature of the defects – whether they produce deep mid-gap recombination centers or more innocuous shallow traps – depends on chemical treatment. Related work on the temporal response of PbS CQD photoconductive photodetectors showed that both amine and carboxylic acid-terminate ligand treatments resulted in long-lived defects having >2s time constants. These long-lived – hence energetically deep – traps were associated chemically with the presence of $PbSO_4$ on the surface of the nanoparticles. Once treated with thiol-terminated ligands, these films exhibited only the presence of $PbSO_3$ and evinced a much shorter-timescale temporal response consistent with shallow traps [54].

The choice of ligand end functional group has a correspondingly dramatic influence on photovoltaic device performance. Vapor treatment using ethanethiol improved PbS CQD photovoltaic device performance [55]. Following the passivation of mid-gap recombination centers on the PbS CQD surface, V_{oc} increased from 0.28 V to 0.43 V and EQE increased from 5% to 22%, leading to a 10-fold improvement in device efficiency. Another study revealed that EDT treatment not only removed all oleate ligands from PbSe CQDs, but also effectively passivated the CQDs and produced photovoltaic devices with an internal quantum efficiency greater than 80% [48].

Whereas short-thiol-based ligands have shown great success in CQD passivation for photovoltaic devices, they suffer from two major limitations:

(1) Due to their small molecular weight, many of these ligands are volatile and may be readily removed under thermal annealing [56, 57]. Relatedly, metal–sulfur moieties are susceptible to oxygen attack, leading to devices having poor air stability.
(2) Most thiol-based ligands explored to date passivate surface cations, leaving the surface anions incompletely passivated [58]. These unpassivated anions may yield mid-gap recombination centers and deteriorate device performance [59].

The epitaxial growth of a thin wide-bandgap semiconductor shell around the CQD core offers one potential solution to overcome these limitations. In the solution phase, this approach has been found to improve the photoluminescence yield of CdSe CQDs by the growth of a ZnS shell [60]. Even when the shell is not epitaxial to all facets of the core, such as in the PbS/CdS core/shell system, photoluminescence emission intensity has been seen to improve appreciably [61, 62]. Related systems such as PbSe/PbS and $PbSe/PbSe_xS_{1-x}$ core/shell CQDs [63, 64], as well as PbSe/PbS core/shell nanowires [65], have seen similar study.

Only air stability and photoluminescence yield [66, 67] – and not absolute device performance – have been reported for lead chalcogenide core/shell CQDs. Shell growth, while reducing surface defects, is expected to come at a cost to carrier transport. Core/shell CQDs generally confine one (type II core/shell) or two (type I core/shell) carrier wavefunction inside the core, militating against delocalization of either both or one charge carrier. A delicate balance between surface passivation and carrier transport necessitates the careful engineering of ultrathin shell growth.

10.4.4 CQD film doping

Both doping type and doping density are important for the operation of photovoltaic devices. A p-type CQD film is required for Schottky devices that employ shallow work function metals. Doping density is a crucial variable in device operation: increasing doping density (N_A and N_D) will increase contact potential V_0 (Equation (10.4)) but decrease the depletion region thickness W (Equation (10.2)).

Doping CQD films based on the deliberate introduction of specific impurity ions into the core remains a challenge. Self-purification – wherein dopants segregate out from the core to the surface – results because the formation energy of defects increases as the size of the nanocrystal decreases [67, 69]. Experimental observations by several groups have nonetheless confirmed the doping of CQD film. In one report, a hydrazine-treated PbSe CQD film was originally n-type. After vacuum treatment or mild heating, the film switched to p-type [31]. Similarly, butylamine-capped PbS CQD film has been shown to exhibit p-type behavior based on Mott–Schottky analysis [24].

Successful doping of CQD film can be explained with reference to the formation of traps at the CQD surface. Unpassivated surface atoms – either cations or anions – can, by trapping free carriers, act equivalently to donors if they trap holes, or to acceptors if they trap electrons. The net doping density is the difference between the number of electron-capture defects and the number of hole-capture defects. Treatments applied to CQD films will naturally influence the number of each type of surface defect and thus change net doping type and density. Hole density has been observed to equal 3×10^{16} cm^{-3} for untreated PbS CQD films and to vary from 2×10^{16} cm^{-3} to 1×10^{17} cm^{-3} following EDT treatment and air annealing, respectively [47]. These findings may be explained by noting that EDT passivates surface defects and thus reduces film doping density, whereas air annealing removes EDT and re-exposes surface defects, leading to an increased doping density. Another example is the short chain carboxylic acid (formic, acetic and oxalic acids) treated PbS and PbSe CQD films, all of which showed p-type doping with a doping density of $\sim 10^{18}$ cm^{-3} due to the formation of Pb–O bonds on the surface [70].

The density of the quantum dots themselves in CQD films lies in the vicinity of 10^{19} cm^{-3} for the case of ~3 nm dots. For measured N_A of order 10^{17} cm^{-3} [33], this corresponds to only one acceptor per >100 nanocrystals. This is low considering the abundant surface area of the materials, and is suggestive that thiols are indeed highly effective in passivation.

An alternative means of doping CQD film involves combining two types of nanoparticles. A 1:1 composite of PbTe : Ag_2Te nanocrystals was found to exhibit a 100-fold increase in conductivity compared to pure-phase PbTe and Ag_2Te films [71]. Because of the staggered band diagram between PbTe and Ag_2Te nanoparticles, electrons move from Ag_2Te nanoparticles to fill the trap states of neighboring PbTe nanoparticles, leaving mobile holes in Ag_2Te nanoparticles that increase the conductivity of this p-type film [72]. This finding suggests that CQD mixtures may be used to tune the net doping of CQD film.

10.4.5 Dielectric constant of CQD film

The dielectric constant ε_m of CQD films is relevant to the depletion region width (Equation (10.2.2)). The dielectric constant of CQD films is expected and observed to be lower than that of their bulk counterparts [73] from volume fraction considerations [33]. In Maxwell–Garnett effective medium theory, this can be explained quantitatively as

$$\varepsilon_m = \varepsilon_1 \frac{\varepsilon_2(1+2\delta) - \varepsilon_1(2\delta - 2)}{\varepsilon_1(2+\delta) + \varepsilon_2(1-\delta)}, \tag{10.28}$$

where ε_1 and ε_2 are the dielectric constants of the matrix and embedded material and δ is the volume fraction of the embedded material. As one example, taking a volume fraction δ of 0.5 and ε_2 of 50 for the quantum dot phase, and ε_1 of 4 for the remaining volume occupied by ligands, results in a predicted dielectric constant of 12 for a typical PbSe CQD film. This is in good agreement with capacitance–voltage results that allow extraction of the effective dielectric constant of the film [45]. Both CELIV and *C–V* measurements also indicate the typical PbS CQD film effective dielectric constants are in the range 15–20.

10.5 Progress in CQD solar cell performance

Ever since the first observation of the photovoltaic effect from PbS CQDs in 2005 [42], rapid progress has been achieved in this field. The AM1.5G efficiency has now reached 5.1%. Various device architectures, including metal/CQD film, oxide/CQD film, organic layer (polymer or small molecules)/CQD film, and CQD film/CQD film, have been explored. The nature of photovoltaic device operation – excitonic solar [74] vs. p–n heterojunction mechanisms [43, 45] – remains a lively topic within the published literature.

10.5.1 Schottky solar cells

The junction between a p-type semiconductor and a low work function metal (Al, Ca, Mg etc.) or between an n-type semiconductor and a deep work function metal (Au, Pt, etc.) forms a Schottky contact. Because Pb chalcogenide CQD films are generally p-type, the preponderance of published Schottky barrier photovoltaic work employs shallow work function metals. In these devices, band bending occurs only inside the CQD film. A depletion region is established and the resultant internal field separates electron–hole pairs. Electrons flow into the metal, and holes to a transparent deep-work-function ohmic contact such as indium tin oxide (ITO) and fluorine tin oxide (FTO).

The first CQD solar cells to exceed 1% AM1.5 PCE were reported in 2008 [43] and employed a Schottky architecture. PbS CQDs underwent a solution-phase ligand exchange to replace original oleate ligands (~2.5 nm) with much shorter (~0.5 nm) butylamine ones. Spin-coating of these nanocrystals from octane solution led to smooth, densely packed arrays, as shown in Figure 10.7. A Schottky barrier was formed at the

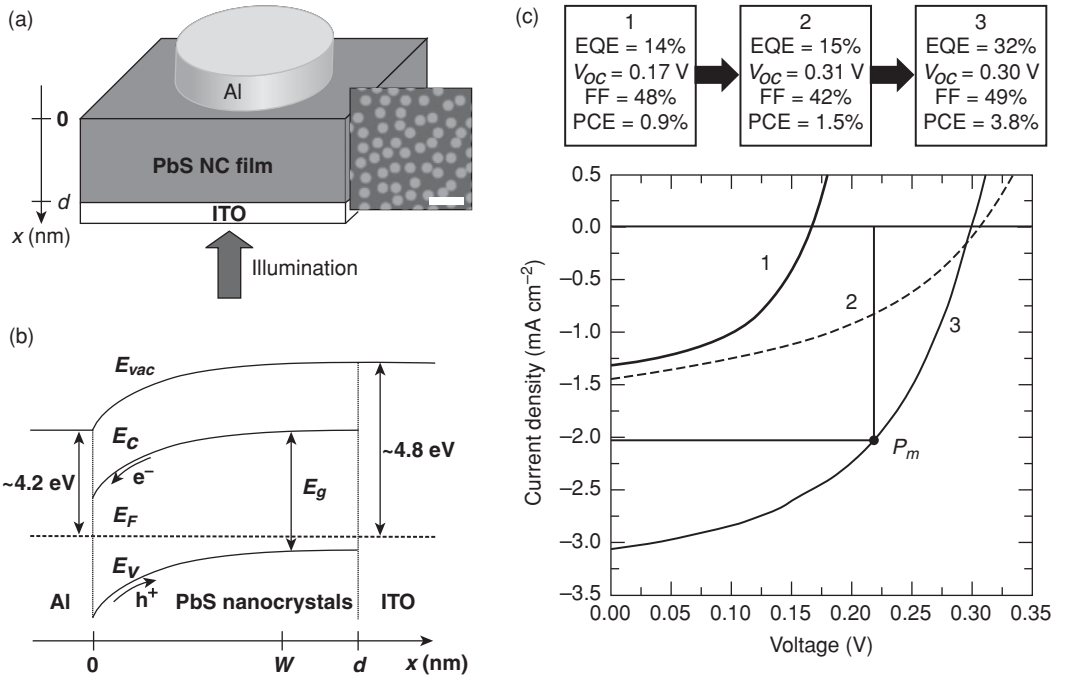


Figure 10.7 (a) Depiction of the architecture of a typical CQD-Schottky device. The inset shows an SEM image of the nanocrystal film (scale bar is 20 nm). (b) The energy band model. (c) The *J–V* curve and photovoltaic performance (under 975 nm, 12 mW cm^{-2} illumination) for the baseline device (1), the device produced using the fast cooling PbS CQDs (2) and the device produced using fast cooling CQDs and butylamine ligand exchang (3). Reproduced with permission from [43]. Copyright 2008 American Physical Society.

junction between Al and the PbS CQD film. The device showed an AM1.5G efficiency of 1.8% with a V_{oc} of 0.33 V and a J_{sc} of 12.3 mA cm^{-2}. The PbS CQD film had a μ_h of (1.5±0.1) ×10^{-3} cm^2 V^{-1} s^{-1} and μ_e of (2±1) ×10^{-4} cm^2 V^{-1} s^{-1}. The drift lengths l_{drift} for holes and electrons in the depletion region were found to be 10 μm and 1 μm, respectively. The diffusion length $l_{diffusion}$ for minority carriers (electrons) in the quasi-neutral region was estimated to be 0.1 μm. The majority of collected photocarriers were generated and effectively separated in the depletion region, and the efficiency of the device was limited by the rate of carrier diffusion through the quasi-neutral region [43].

Soon thereafter, a Schottky device was reported that employed PbSe CQDs that were brought together and passivated using treatment with 1,4-benzenedithiol [49]. It is believed that some of these bidentate thiols bind to the surface of the same nanocrystal, while others may bridge nearby particles. These devices showed an AM1.5G efficiency of 1.1% and offered a significant improvement in air stability over the butylamine-based devices.

In 2008, a Schottky device using PbSe CQDs and having an AM1.5G efficiency of 2.1% was reported (Figure 10.8) [45]. EDT was used to treat the film. It served both to remove the long oleate ligand and passivate the PbSe CQDs. A layer-by-layer dip-coating

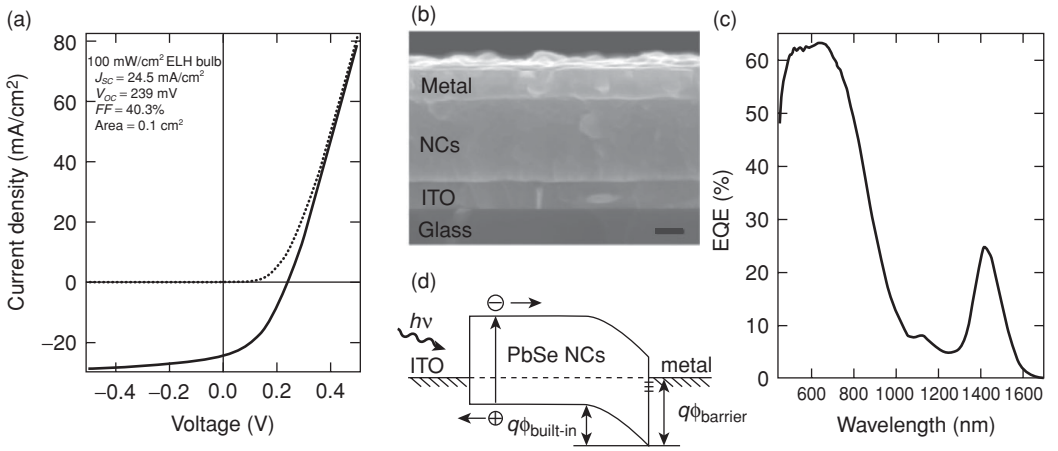


Figure 10.8 Structure, performance, and schematic diagram of the ITO/PbSe/Ca Schottky device. (a) *J–V* characteristics of a representative device in the dark and under simulated AM1.5G illumination. (b) SEM cross-section of the device stack. (c) EQE spectrum of a 140 nm-thick device (PbSe CQDs $E_g = 0.95$ eV). (d) Proposed equilibrium band diagram. Reproduced with permission from [45]. Copyright 2008 American Chemical Society.

strategy was again applied such that any cracks and pinholes from the EDT treatment were filled in using the next layer. An impressive short-circuit current density J_{sc} of 24 mA/cm^{-2} was obtained; the low V_{oc} of 0.239 V and *FF* of 40.3% account for the overall efficiency. The EQE spectrum reached 55–65% at wavelengths shorter than 800 nm, photon frequencies for which absorption of light was substantially complete. The ~80% internal quantum efficiency estimated in this part of the spectrum indicates minimal recombination loss and efficient carrier extraction. By building devices having different bandgaps, it was found that the open-circuit voltage V_{oc} of the device depended on E_g according to $V_{oc} \approx 0.49\,(E_g/q) - 0.253$ V. This pinning relative to the half-bandgap of the semiconductor is often seen in Schottky devices [75]. V_{oc} was observed to decrease with increasing work function of the top metal contact, as expected for a Schottky solar cell.

In 2009, the efficiency of a CQD Schottky device was further improved to 3.3% by employing ternary PbS_xSe_{1-x} CQDs. Devices attained a V_{oc} of 0.45 V and a J_{sc} of 14.8 mA cm^{-2}. The higher efficiency was ascribed to the synergetic effect of the alloyed PbS_xSe_{1-x} CQDs [76]. In 2010, the efficiency of a PbS CQD Schottky device was further improved to 3.6%. Small and conjugated molecules *N*-2,4,6-trimethylphenyl-*N*-methyldithiocarbamate (TMPMDTC) were used as ligands and benzenethiol was applied to treat the film during layer-by-layer coating. LiF/Al was used as the Schottky contact and the devices showed a record V_{oc} of 0.51 V, J_{sc} of 14.0 mA cm^{-2} and *FF* of 51% [77].

While Schottky devices benefit from straightforward fabrication, their efficiency is limited by three factors:

(1) Light absorption begins at the transparent conductive oxide side, requiring that the highest density of photogenerated electrons travel through much of the film

thickness before reaching the electron-collecting Schottky contact. These carriers are vulnerable to loss via recombination.

(2) For an ideal Schottky junction, the barrier height is typically limited to $\sim 0.67E_g$, while in practical devices the V_{oc} is often lower because of the Fermi-level pinning by defect states at the metal-semiconductor interface.

(3) A minimal barrier to hole injection is present at the electron-extracting electrode of the Schottky device, limiting shunt resistance and inviting back-recombination.

10.5.2 Heterojunction solar cells

Heterojunction solar cells have been shown to overcome each of the key limitations of the Schottky architecture [78]. In the highest-efficiency CQD photovoltaics reported by 2013, a p–n heterojunction was formed by bringing together two semiconductors of opposite doping type and generally different composition and bandgap. For efficient dissociation of photogenerated carriers, the donor and acceptor materials should form a type II heterojunction: the (electron) acceptor – the n-type material – should have a lower conduction band level while the (electron) donor – the p-type material – should attract holes. Quantum size-effect tuning provides an added degree of freedom, beyond material composition alone, in the manipulation of the band position of CQDs. Consequently, the restriction on the material selection for appropriate band offset is significantly relaxed and more materials are available for CQD heterojunction solar cells.

Sensitizing nanocrystal TiO_2 solar cells using InAs CQDs [79] has been found to lead to efficient charge transfer from InAs CQDs to TiO_2 particles without deliberate modification of the quantum dot capping layer. For the InAs CQD sensitized solar cell using a Co^{2+}/Co^{3+} electrolyte, devices showed $\sim$1.7% efficiency under 5 mW cm^{-2} illumination but decreased to 0.3% under 1 sun illumination. HgTe CQDs have also been used to sensitize nanoporous TiO_2 electrodes and extend the photon-harvesting spectral regime to 1500 nm [80]. HgTe CQDs, either aqueous soluble or organic solvent soluble, were mixed with nanoporous TiO_2 electrodes and a poly(3-hexylthiophene) (P3HT) matrix to combine the concepts of nanocrystal/polymer-blend solar cells and a solid-state nanocrystal-sensitized solar cell. The devices showed improved J_{sc} compared with a control device without HgTe CQDs, suggesting a role for HgTe CQDs in infrared light absorption.

Polymers and small organic molecules have also been applied when building CQD heterojunction solar cells [81]. Hybrid heterojunction photovoltaic cells using 1,3-BDT crosslinked PbS CQDs and a vacuum-deposited C_{60} layer achieved an AM1.5G efficiency of 2.2%, compared with 1.6% in the corresponding Schottky device [82]. The increase in efficiency arose largely from the V_{oc} and FF improvement due to the reduced recombination current and higher carrier collection efficiency at the PbS CQDs/C_{60} interface, an intrinsic advantage associated with a well-engineered heterojunction device.

A photovoltaic device based on PbS CQDs and amorphous silicon (a-Si) was reported in 2009 [83]. The device showed a V_{oc} of 0.2 eV, a J_{sc} of 4.13 mA cm^{-2}, a FF of 0.39, corresponding to an efficiency of 0.9% under 36.5 mW cm^{-2} xenon lamp illumination. EQE reached 50% at $\sim$500 nm in the device and both a-Si and PbS CQDs contributed

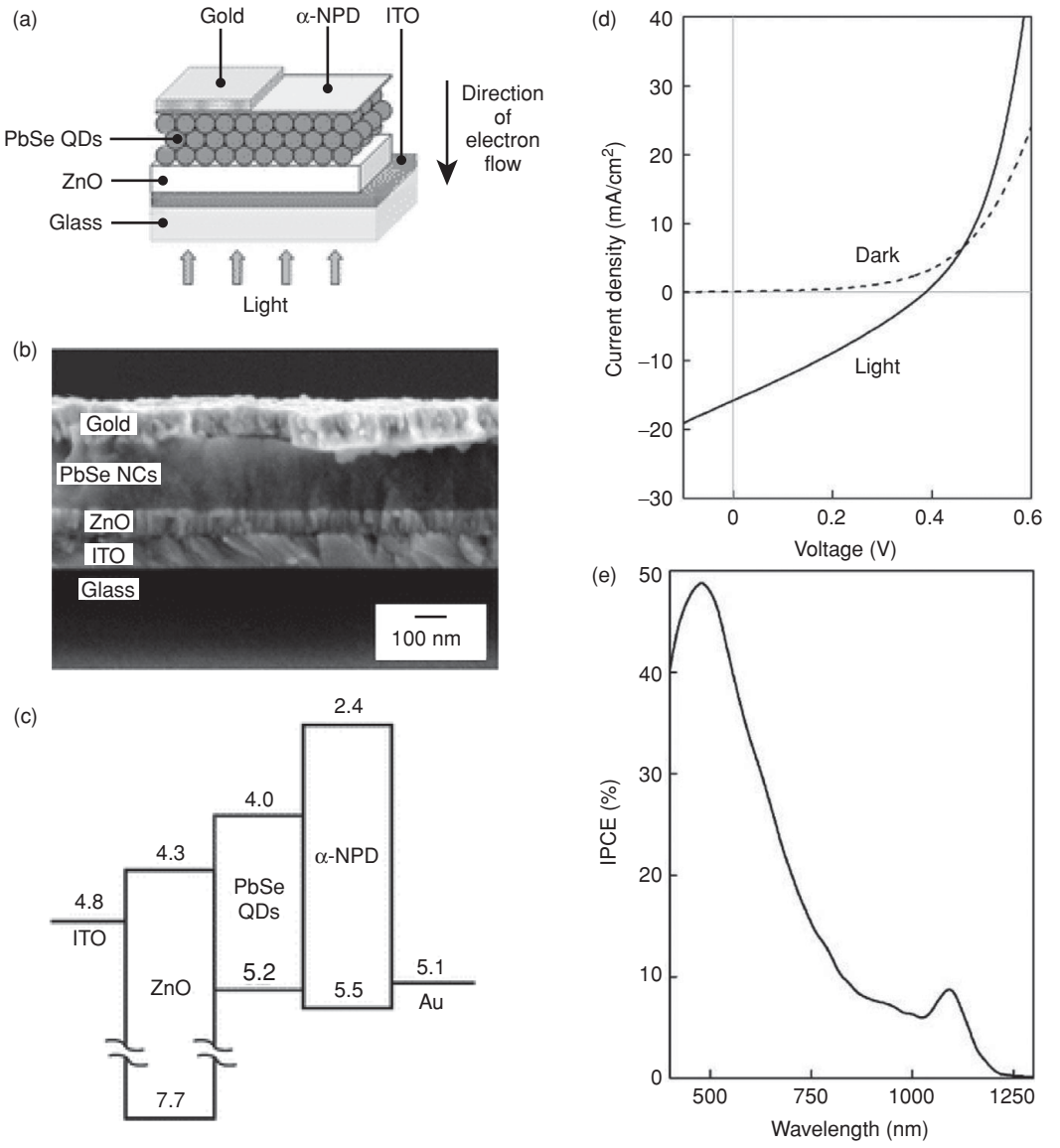


Figure 10.9 (a) Schematic, (b) cross-sectional SEM image, and (c) energy band diagram of the ITO/ZnO/PbSe CQDs/α-NPD/gold heterojunction solar cell. (d) *J–V* characteristics of the cell recorded in the dark and under simulated AM1.5G illumination and (e) its corresponding EQE spectrum. Reproduced with permission from [84]. Copyright 2009 American Chemical Society.

to the photocurrent. During operation, photogenerated electrons flowed to a-Si and were collected using an Al electrode, and holes flowed from a-Si through PbS CQDs to ITO, corresponding to a p(PbS)–n(a-Si) junction device.

Heterojunction devices based on PbSe CQDs and ZnO film have been reported with an AM1.5G efficiency of 1.6% [84]. As shown in Figure 10.9, the device was composed of a ZnO film made using rf magnetron sputtering, a layer-by-layer dip-coated PbSe CQD film

treated using EDT, an electron-blocking layer α-NPD [*N, N*′-bis(1-naphthalenyl)-*N*, *N*′-bis(1-phenylbenzidine))], and an ohmic gold contact deposited via thermal evaporation. Electrons were injected from the PbSe layer into the ZnO as seen in Figure 10.9(c). The device showed a J_{sc} of 15.7 mA cm^{-2} under simulated AM1.5G illumination. The optimal thickness for the PbSe film was determined to be ~100 nm, a balance between absorption and carrier transport; and the optimal thickness for α-NPD layer was determined to be ~30 nm, a balance between shunt resistance gain (improved V_{oc}) and series resistance loss (decreased J_{sc}).

The record-setting CQD solar cells reported in 2010 reached above 5% AM1.5 solar power conversion efficiencies for the first time (Figure 10.10) [78]. These devices – known as depleted-heterojunction colloidal quantum dot (DH-QCD) solar cells – took advantage of an N–p heterojunction between a transparent n-type TiO_2 electrode and an active layer consisting of PbS CQDs. The 1S electron excited state of the CQD lies well above (>0.3 eV) the TiO_2 conduction band level: photoexcited electron injection was favored therefore into TiO_2 due to both the band offset and the built-in potential from the N–p diode junction. The 1P hole level exhibits a large (>1.5 eV) discontinuity with the TiO_2 valence band, providing a sizeable barrier against the undesired passage of majority holes from the p-type CQD layer into the TiO_2 electrode. Holes were conducted away using a top ohmic Au contact to the p-type PbS CQD layer.

DH-CQD photovoltaics successfully overcame the limitations of prior work on Schottky barrier CQD devices in three principal ways. First, the DH design employed a transparent electron-accepting TiO_2 contact, thereby benefiting more efficiently from minority carrier separation due to the placement of the junction on the illuminated side. Second, whereas the Schottky device's open-circuit voltage is limited by Fermi-level pinning due to defect states at the metal–semiconductor interface, the TiO_2–CQD interface benefited from passivation during the solution-phase deposition of the quantum dots. Third, a large discontinuity in the valence band of the DH device, combined with the minimization of electron density in the electron acceptor near the junction, maximized shunt resistance to enhance fill factor and minimized back-recombination to improve one-sun performance.

Under 1 sun illumination, the best devices showed a V_{oc} of 0.51 V, a J_{sc} of 16.2 mA cm^{-2}, and *FF* of 58%, corresponding to an efficiency of 5.1%. The improvement in performance over previous reports derives principally from improved V_{oc} and *FF*, both traceable to the improved device architecture. The shape of the EQE spectrum of the device resembled its absorption spectrum and reached a maximum value of 60%.

For the PbS CQDs used in these devices, simple calculation suggests that Förster energy transfer should allow the transport of excitons over distances corresponding to at most a few quantum dots; however, efficient carrier extraction occurred in this 200–250 nm thick PbS CQD film. Additionally, the V_{oc} in devices made using CQDs with different size-tuned bandgaps was found to correlate closely with the Fermi level difference. These observations lend additional support to the p–n junction picture of device operation presented herein.

Heterojunction solar cells from EDT-treated PbS on top of mesoporous TiO_2 yielded an AM1.5G efficiency of 3.13% (V_{oc} = 0.456 V, J_{sc} = 20.7 mA cm^{-2}, and

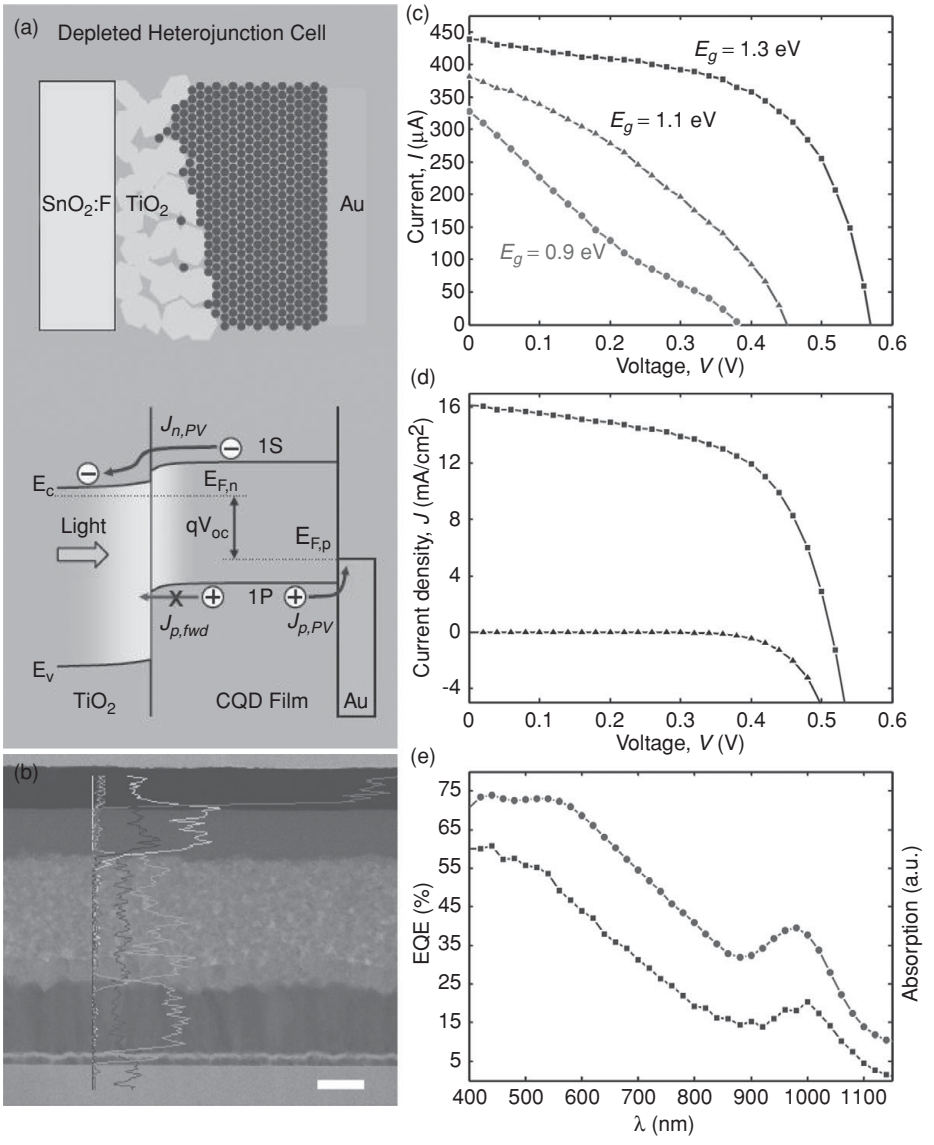


Figure 10.10 Device architecture and performance of TiO_2/PbS heterojunction solar cells. (a) Schematic demonstration of FTO/TiO_2/PbS/Au and its band diagram. (b) Cross-sectional TEM as well as elemental distribution plot of a photovoltaic device. The scale bar is 200 nm. (c) *I–V* response of devices using three different size CQDs. (d) *J–V* curves for the champion device recorded with and without sun illumination. (e) EQE and absorption spectra of the champion device. Reproduced with permission from [78]. Copyright 2010 American Chemical Society.

FF = 33.2%) at room temperature [85]. Surprisingly, when the device was cooled down to 170 K, the efficiency improved to 8.0% (V_{oc} = 0.66 V, J_{sc} = 28.6 mA cm^{-2} and *FF* = 42.4%). This was tentatively assigned to the 10-fold improvement in carrier mobility with decreasing temperature. This result is very encouraging for the community to target 10% AM1.5G efficiency at room temperature.

Table 10.2. Summary of device performance based on infrared CQDs

CQDs material	Device architecture	V_{oc} (V)	J_{sc} (mA cm^{-2})	*FF*	AM1.5G efficiency	Reference
PbS	Au/P3HT/PbS/ITO[a]	0.4	0.13	0.38	0.02%	[90]
	ITO/SnS/PbS/Al	0.35	7.22	0.32	0.37	[91]
	ITO/PbS/a-Si/Al	0.2	8.99	0.39	0.7%	[83]
	ITO/PbS/Al	0.33	12.3	0.44	1.8%	[43]
	ITO/PbS/LiF/Al	0.46	8.57	0.545	2.15%	[33]
	ITO/PbS/C60/LiF/Al	0.40	10.5	0.52	2.2%	[82]
	ITO/PbS/LiF/Al	0.51	14.0	0.51	3.6%	[77]
	ITO/PEDOT:PSS/PbS/PDTPQ$_X$/Al[b]	0.38	4.2	0.34	0.55%	[92]
	FTO/TiO_2/PbS/Au	0.51	16.2	0.58	5.1%	[78]
	ITO/PbS/PC_{61}BM/LiF/Al	0.59	10.0	0.63	3.7%	[93]
	ITO/PbS/PCBM/Mg/Ag	0.24	14.0	0.50	1.68%	[94]
	ITO/TiO_2/PbS/Au	0.456	20.7	0.332	3.13%	[85]
		0.66	28.6	0.424	8.00%[c]	
PbSe	ITO/PEDOT/(BP:PbSe)/PbSe/Al[d]	0.65	0.0258	0.22	0.003%	[95]
	ITO/PEDOT/P3HT/P3HT:PbSe/Al	0.41	1.01	0.46	0.19%	[96]
	ITO/MOPphotovoltaic-MWNT:PCBM/PbSe/Al[e]	0.406	1.71	0.35	0.40%	[97]
	ITO/PbSe/Al	0.24	12	0.38	1.1%	[49]
	ITO/PbSe/PEDOT:PSS/P3HT:PCBM/Al[f]	0.57	6.38	0.32	1.17%	[98]
	ITO/ZnO/PbSe/α-NPD/Au[g]	0.39	15.7	0.27	1.6%	[84]
	ITO/PEDOT:PSS/PbSe/Ca/Al	0.24	20.7	0.455	2.4%	[99]
	ITO/PbS_xSe_{1-x}/Al	0.45	14.8	0.50	3.3%	[76]
	ITO/PEDOT:PSS/PbSe/ZnO/Al	0.44	24	0.32	3.4%	[76]
InAs	FTO/TiO_2/InAs/electrolyte/Pt	0.35	1.8	0.48	0.3%	[79]
HgTe	ITO/TiO_2/(HgTe:TiO_2)/(HgTe:P3HT)/Au	0.40	2	0.5	0.4%	[80]

[a] P3HT: poly(3-hexylthiophene).
[b] PDTPQx poly(2,3-didecyl-quinoxaline-5,8-diyl-alt-N-octyldithieno [3,2-b:2′,3′-d]pyrrole).
[c] same device but measured at 170 K.
[d] PEDOT: poly(3,4-ethylenedioxythiophene), BP: tetrabenzoporphyrin.
[e] MOPphotovoltaic-MWNT: poly[(2-methoxy,5-octoxy)-1,4-phenylenevinylene]-multiwalled carbon nanotubes.
[f] PSS: poly(styrene-sulfonate), PCBM phenyl-C61-butyric acid methyl ester.
[g] A-NPD [N,N'-bis(1-naphthalenyl)-N,N'-bis(phenylbenzidine)].

In all the reported CQD devices, the EQE spectrum has yet to approach its potential. High-efficiency solar cells with an EQE exceeding 90% above the bandedge would lead to $J_{sc} > 35$ mA cm^{-2}. Efforts to minimize recombination loss and maximize film absorption are thus of great importance to improve device efficiency.

We summarize some reports on photovoltaic device performance from various infrared CQDs in Table 10.2.

10.6 Device stability

Solar cells based on infrared CQDs were initially reported to suffer from poor stability. Stored in air, butylamine-capped PbS CQD devices degraded within minutes [43].

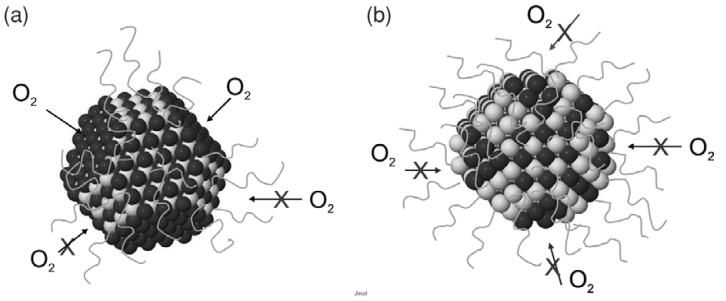


Figure 10.11 Schematic illustration of oxidation for (a) large and (b) small PbS CQDs. Large PbS CQDs are faceted and small ones are spherical. Small PbS CQDs have a denser oleate ligand shell, leading to the better resistivity to oxidation. In the figure, surface ligands are shown passivating lead atoms on the surface of PbS CQDs. Reprinted from [33]. Copyright 2010 American Chemical Society.

Significant progress was made when 1,4-BDT treated PbSe CQD devices were found to be stable in a glove box over weeks and in air over a few hours [49]. In contrast, EDT-treated PbSe devices lost performance completely even within a few minutes' air exposure [45, 83].

The mechanisms underlying device degradation have been investigated systematically [86]. Two key and independent mechanisms have now been pinpointed. First, degradation of the metal–semiconductor interface has been identified and successfully addressed. Second, the loss of passivation within the film, leading to the development of mid-gap recombination centers, has also been identified and remedied.

Ultimately these new insights have enabled processing of devices entirely within an air ambient instead of requiring glovebox processing. The best stability results reported >60 hours of continuous and simultaneous 100 mW cm^{-2} AM1.5G illumination and current–voltage scanning in an air ambient. The unencapsulated devices exhibited an AM1.5G efficiency of 2.1% and retained ~87% of their initial power conversion efficiency. This dramatic improvement in device stability originated from two factors:

(1) The distinctive surface-chemical properties of small PbS CQDs (~3 nm) (Figure 10.11(b)). Small PbS CQDs have been reported to be more spherical than larger particles, and also have a higher Pb:S ratio compared with the more faceted large PbS CQDs. Ligands binding to surface Pb cations form a dense ligand shell, blocking oxygen access and protecting CQD films from oxidation. In contrast, large PbS CQDs include exposed {111} facets consisting of sulfur anions not protected by thiol-terminated ligands. Oxygen can easily attack these unprotected {111} surfaces (as shown in Figure 10.11(a)). X-ray photon spectroscopy studies reveal that the main oxidation product of small PbS CQDs is $PbSO_3$, a shallow trap state with a trap depth of 0.1 eV [54, 87]. In contrast, the main oxidation product of large PbS CQDs is $PbSO_4$, a deeper mid-gap state. Thus, oxidation of small PbS CQDs is impeded, and the oxidation products are more inoccuous shallow traps; oxidation of large PbS CQDs occurs more readily and the oxidation products are recombination

centers. These findings account for the improved air stability of the PbS CQD films themselves [33].

(2) A Schottky contact engineered for air stability. Initial Schottky devices employed Al metal in direct contact with CQD films. Subsequent control experiments revealed that using Ag instead led to enhanced air stability, though inferior absolute initial performance. These initial findings suggested that a component of photovoltaic device degradation was occurring at the metal–semiconductor interface. Sandwiching a very thin (nominally 0.8 nm) layer of LiF between the Al electrode and the CQD film suppressed the interfacial reaction and dramatically improved air stability. The LiF:Al electrode also benefited from improved open-circuit voltage, leading to a device with improved overall AM1.5 power conversion efficiency [86].

In 2010, the stability of a PbS CQD photovoltaic device was further improved by applying the PbS/ZnO heterojuction device architecture [88]. Employment of the same PbS CQD fabrication procedure as previously discussed, but using ZnO instead of the unstable Al contact, the device showed an NREL certified efficiency of 2.94%. More importantly, the unencapsulated device showed less than a 10% decrease in efficiency after 1000 h light soaking in air, a remarkable improvement over previous stability record.

10.7 Perspectives and conclusions

Infrared CQDs are promising functional materials that hold great potential for low-cost and/or high-efficiency solar cells. Since the first report of a photovoltaic effect from PbS CQDs in 2005, rapid progress has been achieved, with the latest AM1.5G efficiencies reaching 5.1%, a value approaching that of polymer solar cells that have seen two decades' investigation, conceptual advances, and optimization. The size-tunable bandgap, long carrier lifetime, and solution-processing are the three intrinsic advantages associated with lead chalcogenide CQD solar cells.

We summarize in Table 10.3 the electronic materials properties that will be required to advance CQD photovoltaics beyond 10% AM1.5G efficiency.

The key advances required are as follows [100]:

(1) Improve CQD surface engineering for enhanced electronic transport. The carrier mobility in the best CQD photovoltaic devices has been of the order of 10^{-5}–10^{-3} $cm^2\ V^{-1}\ s^{-1}$. An improvement of mobility to 10^{-2} $cm^2\ V^{-1}\ s^{-1}$ and above will break the absorption–extraction tradeoff and lead to much improved J_{sc}. Previously-reported devices have had doping densities $>10^{16}$ cm^{-3} and a further reduction in doping density to $\sim 10^{15}$ cm^{-3} will increase the width of the high-internal-quantum-enery depletion region and promote carrier extraction. At a materials processing level, these advances require new strategies that simultaneously achieve excellent surface passivation and minimal interparticle spacing.

(2) Improve device architectures. The move from Schottky to p–n heterojunctions led to a doubling in solar efficiency, reinforcing the major impact of architecture on performance. n–i–p architectures exploiting wide-bandgap materials such as CdS, TiO_2,

Table 10.3. Approximate estimation of device parameters to achieve the targeted efficiency for PbS CQD photovoltaic device[a]

Device efficiency	Device architecture	Mobility ($cm^2\ V^{-1}\ s^{-1}$)	N_A (cm^{-3})	$W_{depletion}$ (nm)	τ (μs)	$L_{diffusion}$ (nm)	V_{oc} (V)	J_{sc} (mA cm^{-2})	FF
~2%[b]	Schottky	10^{-5}–10^{-4}	~10^{17}	~100	~15	< 20	0.4	10	0.5
~5%[c]	p–n	10^{-4}–10^{-3}	~10^{16}	~200	~15	20–50	0.5	18	0.55
~10%[d]	p–n	10^{-3}–10^{-2}	~10^{15}	~800	~15	50–200	0.55	28	0.65

[a] All calculations are based on PbS CQDs with $E_g \sim 1.3$ eV.
[b] Representative Schottky device performance based on PbS CQDs.
[c] N_D in the n-type material is assumed to be ~10^{16} cm^{-3}.
[d] N_D in the N-type material is assumed to be ~10^{18} cm^{-3}.
Abbreviations: N_A acceptor density of CQD film; $W_{depletion}$ depletion region width in the CQD film; τ carrier lifetime; $L_{diffusion}$ carrier diffusion length.

ZnO, SnO_2, and a-Si may offer further advances. Bulk heterojunctions, nanoporous electrodes, and nanorod arrays offer to overcome, in part, limitations in carrier mobility.

(3) Improve CQD photovoltaic device stability further. Although the report in [88] of air stability of a device is encouraging, further improvements in thermal stability require effort. Core/shell dots and progress in all-inorganic CQD films from molecular metal chalcogenide ligands may provide a path towards robustly passivated quantum dot films exhibiting further-improved long-term stability.

References

1 M. A. Green, K. Emery, Y. Hishikawa, W. Warta, Solar cell efficiency tables (version 35). *Progress in Photovoltaics*, **18**:2 (2010), 144–150.

2 W. Guter, J. Schone, S. P. Philipps, *et al.*, Current-matched triple-junction solar cell reaching 41.1% conversion efficiency under concentrated sunlight. *Applied Physics Letters*, **94** (2009), 223504.

3 S. E. Shaheen, R. Radspinner, N. Peyghambarian, G. E. Jabbour, Fabrication of bulk heterojunction plastic solar cells by screen printing. *Applied Physics Letters*, **79**:18 (2001), 2996–2998.

4 H. Y. Chen, J. H. Hou, S. Q. Zhang, *et al.*, Polymer solar cells with enhanced open-circuit voltage and efficiency. *Nature Photonics*, **3**:11 (2009), 649–653.

5 M. C. Scharber, D. Wuhlbacher, M. Koppe, *et al.*, Design rules for donors in bulk-heterojunction solar cells – towards 10% energy-conversion efficiency. *Advanced Materials*, **18**:6 (2006), 789-+.

6 J. Tang, G. Konstantatos, S. Hinds, *et al.*, Heavy-metal-free solution-processed nanoparticle-based photodetectors: Doping of intrinsic vacancies enables engineering of sensitivity and speed. *ACS Nano*, **3**:2 (2009), 331–338.

7 S. Maenosono, T. Okubo, Y. Yamaguchi, Overview of nanoparticle array formation by wet coating. *Journal of Nanoparticle Research*, **5**:1–2 (2003), 5–15.

8 H. M. Haverinen, R. A. Myllyla, G. E. Jabbour, Inkjet printing of light emitting quantum dots. *Applied Physics Letters*, **94** (2009), 073108.

9 M. Singh, H. M. Haverinen, P. Dhagat, G. E. Jabbour, Inkjet printing-process and its applications. *Advanced Materials*, **22**:6 (2010), 673–685.

10 H. M. Haverinen, R. A. Myllyla, G. E. Jabbour, Inkjet printed rgb quantum dot-hybrid led. *Journal of Display Technology* **6**:3 (2010), 87–89.

11 S. Coe-Sullivan, W. K. Woo, J. S. Steckel, M. Bawendi, V. Bulovic, Tuning the performance of hybrid organic/inorganic quantum dot light-emitting devices. *Organic Electronics* **4**:2–3 (2003), 123–130.

12 S. Coe, W. K. Woo, M. Bawendi, V. Bulovic, Electroluminescence from single monolayers of nanocrystals in molecular organic devices. *Nature*, **420**:6917 (2002), 800–803.

13 J. L. Zhao, J. A. Bardecker, A. M. Munro, *et al.*, Efficient CdSe/CdS quantum dot light-emitting diodes using a thermally polymerized hole transport layer. *Nano Letters*, **6**:3 (2006), 463–467.

14 H. Hoppe, N. Arnold, N. S. Sariciftci, D. Meissner, Modeling the optical absorption within conjugated polymer/fullerene-based bulk-heterojunction organic solar cells. *Solar Energy Materials and Solar Cells*, **80**:1 (2003), 105–113.

15 A. R. Denton, N. W. Ashcroft, Vegard law. *Physical Review A*, **43**:6 (1991), 3161–3164.

16 L. E. Brus, A simple-model for the ionization-potential, electron-affinity, and aqueous redox potentials of small semiconductor crystallites. *Journal of Chemical Physics*, **79**:11 (1983), 5566–5571.

17 L. E. Brus, Electron–electron and electron–hole interactions in small semiconductor crystallites – the size dependence of the lowest excited electronic state. *Journal of Chemical Physics*, **80**:9 (1984), 4403–4409.

18 M. A. Hines, G. D. Scholes, Colloidal PbS nanocrystals with size-tunable near-infrared emission: Observation of post-synthesis self-narrowing of the particle size distribution. *Advanced Materials*, **15**:21 (2003), 1844–1849.

19 E. H. Sargent, Infrared photovoltaics made by solution processing. *Nature Photonics*, **3**:6 (2009), 325–331.

20 Q. Q. Dai, Y. N. Wang, X. B. Li, *et al.*, Size-dependent composition and molar extinction coefficient of PbSe semiconductor nanocrystals. *ACS Nano*, **3**:6 (2009), 1518–1524.

21 I. Moreels, K. Lambert, D. Smeets, *et al.*, Size-dependent optical properties of colloidal PbS quantum dots. *ACS Nano*, **3**:10 (2009), 3023–3030.

22 M. Law, M. C. Beard, S. Choi, *et al.*, Determining the internal quantum efficiency of PbSe nanocrystal solar cells with the aid of an optical model. *Nano Letters* **8**:11 (2008), 3904–3910.

23 J. P. Clifford, G. Konstantatos, K. W. Johnston, *et al.*, Fast, sensitive and spectrally tuneable colloidal quantum-dot photodetectors. *Nature Nanotechndogy*, **4**:1 (2009), 40–44.

24 K. W. Johnston, A. G. Pattantyus-Abraham, J. P. Clifford, *et al.*, Efficient Schottky-quantum-dot photovoltaics: The roles of depletion, drift, and diffusion. *Applied Physics Letters* **92** (2008), 122111.

25 K. M. Coakley, M. D. McGehee, Conjugated polymer photovoltaic cells. *Chemistry of Materials*, **16**:23 (2004), 4533–4542.

26 B. Oregan, M. Gratzel, A low-cost, high-efficiency solar-cell based on dye-sensitized colloidal tio2films. *Nature*, **353**:6346 (1991), 737–740.

27 W. J. Yoon, K. Y. Jung, J. W. Liu, *et al.*, Plasmon-enhanced optical absorption and photocurrent in organic bulk heterojunction photovoltaic devices using self-assembled layer of silver nanoparticles. *Solar Energy Materials and Solar Cells* **94**:2 (2010), 128–132.

28 M. Redecker, D. D. C. Bradley, M. Inbasekaran, E. P. Woo, Nondispersive hole transport in an electroluminescent polyfluorene. *Applied Physics Letters* **73**:11 (1998), 1565–1567.

29 G. Juska, M. Viliunas, K. Arlauskas, *et al.*, Hole drift mobility in mu c-Si : H. *Journal of Applied Physics*, **89**:9 (2001), 4971–4974.

30 D. V. Talapin, J. S. Lee, M. V. Kovalenko, E. V. Shevchenko, Prospects of colloidal nanocrystals for electronic and optoelectronic applications. *Chemical Reviews*, **110**:1 (2010), 389–458.

31 D. V. Talapin, C. B. Murray, PbSe nanocrystal solids for n- and p-channel thin film field-effect transistors. *Science*, **310**:5745 (2005), 86–89.

32 J. P. Clifford, K. W. Johnston, L. Levina, E. H. Sargent, Schottky barriers to colloidal quantum dot films. *Applied Physics Letters*, **91**:25 (2007).

33 J. Tang, L. Brzozowski, D. A. R. Barkhouse, *et al.*, Quantum dot photovoltaics in the extreme quantum confinement regime: The surface-chemical origins of exceptional air- and light-stability. *ACS Nano*, **4**:2 (2010), 869–878.

34 R. Bose, J. F. McMillan, J. Gao, *et al.*, Temperature-tuning of near-infrared monodisperse quantum dot solids at 1.5 μm for controllable forster energy transfer. *Nano Letters* **8**:7 (2008), 2006–2011.

35 N. F. Mott, Electrons in disordered structures. *Advanced Physics*, **16**:61 (1967), 49-&.

36 N. F. Mott, Conduction in non-crystalline materials. 3. Localized states in a pseudogap and near extremities of conduction and valence bands. *Philosophical Magazine*, **19**:160 (1969), 835–852.

37 A. L. Efros, B. I. Shklovskii, Coulomb gap and low-temperature conductivity of disordered systems. *Journal of Physics C: Solid State Physics*, **8**:4 (1975), L49–L51.

38 A. L. Efros, B. I. Shklovskii, Critical behavior of conductivity and dielectric-constant near metal-non-metal transition threshold. *Physics Stat Solidi B*, **76**:2 (1976), 475–485.

39 A. Zabet-Khosousi, A. A. Dhirani, Charge transport in nanoparticle assemblies. *Chemical Reviews*, **108**:10 (2008), 4072–4124.

40 H. E. Romero, M. Drndic, Coulomb blockade and hopping conduction in PbSe quantum dots. *Physicsl Review Letters*, **95**:15 (2005), 156801.

41 Y. Liu, M. Gibbs, J. Puthussery, *et al.*, Dependence of carrier mobility on nanocrystal size and ligand length in PbSe nanocrystal solids. *Nano Letters* **10**:5 (2010), 1960–1969.

42 S. A. McDonald, G. Konstantatos, S. G. Zhang, *et al.*, Solution-processed PbS quantum dot infrared photodetectors and photovoltaics. *Nature Materials*, **4**:2 (2005), 138-U14.

43 K. W. Johnston, A. G. Pattantyus-Abraham, J. P. Clifford, *et al.*, Schottky-quantum-dot photovoltaics for efficient infrared power conversion. *Applied Physics Letters*, **92**:15 (2008).

44 M. V. Kovalenko, M. Scheele, D. V. Talapin, Colloidal nanocrystals with molecular metal chalcogenide surface ligands. *Science*, **324**:5933 (2009), 1417–1420.

45 J. M. Luther, M. Law, M. C. Beard, *et al.*, Schottky solar cells based on colloidal nanocrystal films. *Nano Letters*, **8**:10 (2008), 3488–3492.

46 M. Law, J. M. Luther, O. Song, *et al.*, Structural, optical, and electrical properties of PbSe nanocrystal solids treated thermally or with simple amines. *Journal of the American Chemical Society*, **130**:18 (2008), 5974–5985.

47 E. J. D. Klem, H. Shukla, S. Hinds, *et al.*, Impact of dithiol treatment and air annealing on the conductivity, mobility, and hole density in PbS colloidal quantum dot solids. *Applied Physics Letters*, **92**:21 (2008).

48 J. M. Luther, M. Law, Q. Song, *et al.*, Structural, optical and electrical properties of self-assembled films of PbSe nanocrystals treated with 1,2-ethanedithiol. *ACS Nano*, **2**:2 (2008), 271–280.

49 G. I. Koleilat, L. Levina, H. Shukla, *et al.*, Efficient, stable infrared photovoltaics based on solution-cast colloidal quantum dots. *ACS Nano*, **2**:5 (2008), 833–840.

50 J. E. Murphy, M. C. Beard, A. J. Nozik, Time-resolved photoconductivity of PbSe nanocrystal arrays. *Journa of Physical Chemistry B*, **110**:50 (2006), 25455–25461.

51 M. C. Beard, A. G. Midgett, M. Law, *et al.*, Variations in the quantum efficiency of multiple exciton generation for a series of chemically treated PbSe nanocrystal films. *Nano Letters* **9**:2 (2009), 836–845.

52 J. W. Stouwdam, F. van Veggel, Improvement in the luminescence properties and processability of LaF_3/ln and $LaPO_4$/ln nanoparticles by surface modification. *Langmuir* **20**:26 (2004), 11763–11771.

53 A. J. Morris-Cohen, M. D. Donakowski, K. E. Knowles, E. A. Weiss, The effect of a common purification procedure on the chemical composition of the surfaces of CdSe quantum dots synthesized with trioctylphosphine oxide. *Journal of Physical Chemistry C*, **114**:2 (2010), 897–906.

54 G. Konstantatos, L. Levina, A. Fischer, E. H. Sargent, Engineering the temporal response of photoconductive photodetectors via selective introduction of surface trap states. *Nano Letters*, **8**:5 (2008), 1446–1450.

55 D. A. R. Barkhouse, A. G. Pattantyus-Abraham, L. Levina, E. H. Sargent, Thiols passivate recombination centers in colloidal quantum dots leading to enhanced photovoltaic device efficiency. *ACS Nano*, **2**:11 (2008), 2356–2362.

56 L. Turyanska, U. Elfurawi, M. Li, *et al.*, Tailoring the physical properties of thiol-capped PbS quantum dots by thermal annealing. *Nanotechnology*, **20**:31 (2009).

57 J. Aldana, Y. A. Wang, X. G. Peng, Photochemical instability of cdse nanocrystals coated by hydrophilic thiols. *Journal of the American Chemical Society*, **123**:36 (2001), 8844–8850.

58 I. Moreels, B. Fritzinger, J. C. Martins, Z. Hens, Surface chemistry of colloidal PbSe nanocrystals. *Journal of the American Chemical Society*, **130**:45 (2008), 15081–15086.

59 N. B. Pendyala, K. Rao, Identification of surface states in PbS quantum dots by temperature dependent photoluminescence. *Journal of Luminescence*, **128**:11 (2008), 1826–1830.

60 M. A. Hines, P. Guyot-Sionnest, Synthesis and characterization of strongly luminescing ZnS-capped cdse nanocrystals. *Journal of Physical Chemistry*, **100**:2 (1996), 468–471.

61 M. Fernee, A. Watt, J. Warner, *et al.*, Investigation of the role of cadmium sulfide in the surface passivation of lead sulfide quantum dots. *Journal of Crystal Growth*, **270**:3–4 (2004), 380–383.

62 M. J. Fernee, A. Watt, J. Warner, *et al.*, Inorganic surface passivation of PbS nanocrystals resulting in strong photoluminescent emission. *Nanotechnology*, **14**:9 (2003), 991–997.

63 A. C. Bartnik, F. W. Wise, A. Kigel, E. Lifshitz, Electronic structure of PbSe/PbS core-shell quantum dots. *Physical Review B*, **75**:24 (2007).

64 M. Brumer, A. Kigel, L. Amirav, *et al.*, PbSe/PbS and PbSe/$PbSe_xS_{1-x}$ core/shell nanoparticles. *Advanced Functional Materials*, **15**:7 (2005), 1111–1116.

65 D. V. Talapin, H. Yu, E. V. Shevchenko, A. Lobo, C. B. Murray, Synthesis of colloidal PbSe/PbS core-shell nanowires and PbS/au nanowire-nanocrystal heterostructures. *Journal of Physical Chemistry C*, **111** (2007), 14049–14054.

66 J. M. Pietryga, D. J. Werder, D. J. Williams, *et al.*, Utilizing the lability of lead selenide to produce heterostructured nanocrystals with bright, stable infrared emission. *Journal of the American Chemical Society*, **130**:14 (2008), 4879–4885.
67 E. Lifshitz, M. Brumer, A. Kigel, *et al.*, Stable PbSe/PbS and PbSe/$PbSe_xS_{1-x}$ core-shell nanocrystal quantum dots and their applications. *Journal of Physical Chemistry B*, **110**:50 (2006), 25356–25365.
68 G. M. Dalpian, J. R. Chelikowsky, Self-purification in semiconductor nanocrystals. *Physical Review Letters*, **96**:22 (2006).
69 S. C. Erwin, L. J. Zu, M. I. Haftel, *et al.*, Doping semiconductor nanocrystals. *Nature*, **436**:7047 (2005), 91–94.
70 M. H. Zarghami, Y. Liu, M. Gibbs, *et al.*, P-type PbSe and PbS quantum dot solids prepared with short-chain acids and diacids. *ACS Nano*, **4**:4 (2010), 2475–2485.
71 J. J. Urban, D. V. Talapin, E. V. Shevchenko, C. R. Kagan, C. B. Murray, Synergism in binary nanocrystal superlattices leads to enhanced p-type conductivity in self-assembled PbTe/Ag_2te thin films. *Nature Materials*, **6**:2 (2007), 115–121.
72 D. K. Ko, J. J. Urban, C. B. Murray, Carrier distribution and dynamics of nanocrystal solids doped with artificial atoms. *Nano Letters*, **10**:5 (2010), 1842–1847.
73 A. C. Sharma, Size-dependent energy band gap and dielectric constant within the generalized penn model applied to a semiconductor nanocrystallite. *Journal of Applied Physics,* **100** (2006).
74 J. J. Choi, Y. F. Lim, M. B. Santiago-Berrios, *et al.*, PbSe nanocrystal excitonic solar cells. *Nano Letters*, **9**:11 (2009), 3749–3755.
75 J. Nelson, *The Physics of Solar Cells*. World Scientific Pub. Co. Inc; 2003.
76 W. Ma, J. M. Luther, H. M. Zheng, Y. Wu, A. P. Alivisatos, Photovoltaic devices employing ternary PbS_xSe_{1-x} nanocrystals. *Nano Letters*, **9**:4 (2009), 1699–1703.
77 R. Debnath, J. Tang, D. A. Barkhouse, *et al.*, Ambient-processed colloidal quantum dot solar cells via individual pre-encapsulation of nanoparticles. *Journal of the American Chemical Society*, **132**:17 (2010), 5952–5953.
78 A. G. Pattantyus-Abraham, I. Kramer, A. R. Barkhouse, *et al.*, Depleted-Heterojunction colloidal quantum dot solar cells. *ACS Nano*, **4**:6 (2010), 3374–3380.
79 P. R. Yu, K. Zhu, A. G. Norman, *et al.*, Nanocrystalline TiO_2 solar cells sensitized with inas quantum dots. *Journal of Physical Chemistry B*, **110** (2006), 25451–25454.
80 S. Gunes, H. Neugebauer, N. S. Sariciftci, *et al.*, Hybrid solar cells using HgTe nanocrystals and nanoporous TiO_2 electrodes. *Advanced Functional Materials*, **16**:8 (2006), 1095–1099.
81 D. Dissanayake, R. A. Hatton, T. Lutz, R. J. Curry, S. R. P. Silva, The fabrication and analysis of a PbS nanocrystal:C-60 bilayer hybrid photovoltaic system. *Nanotechnology*, **20**:24 (2009), 5.
82 S. W. Tsang, H. Fu, R. Wang, J. Lu, K. Yu, Y. Tao, Highly efficient cross-linked PbS nanocrystal/C-60hybrid heterojunction photovoltaic cells. *Applied Physics Letters*, **95**:18 (2009).
83 B. Sun, A. T. Findikoglu, M. Sykora, D. J. Werder, V. I. Klimov, Hybrid photovoltaics based on semiconductor nanocrystals and amorphous silicon. *Nano Letters*, **9**:3 (2009), 1235–1241.
84 K. S. Leschkies, T. J. Beatty, M. S. Kang, D. J. Norris, E. S. Aydil, Solar cells based on junctions between colloidal PbSe nanocrystals and thin ZnO films. *ACS Nano*, **3**:11 (2009), 3638–3648.
85 T. Ju, R. L. Graham, G. M. Zhai, *et al.*, High efficiency mesoporous titanium oxide PbS quantum dot solar cells at low temperature. *Applied Physics Letters*, **97** (2010), 043106.

86 J. Tang, X. H. Wang, L. Brzozowski, *et al.*, Schottky quantum dot solar cells stable in air under solar illumination. *Advanced Materials*, **22**:12 (2010), 1398–1402.
87 G. Konstantatos, E. H. Sargent, PbS colloidal quantum dot photoconductive photodetectors: Transport, traps, and gain. *Applied Physics Letters*, **91** (2007).
88 J. M. Luther, J. B. Gao, M. T. Lloyd, *et al.*, Stability assessment on a 3% bilayer PbS/ZnO quantum dot heterojunction solar cell. *Advanced Materials*, **22**:33 (2010), 3704-+.
89 M. S. Kang, J. Lee, D. J. Norris, C. D. Frisbie, High carrier densities achieved at low voltages in ambipolar PbSe nanocrystal thin-film transistors. *Nano Letters*, **9**:11 (2009), 3848–3852.
90 K. P. Fritz, S. Guenes, J. Luther, *et al.*, IV–VI nanocrystal-polymer solar cells. *Journal of Photochemistry and Photobiology A: Chemistry*, **195**:1 (2008), 39–46.
91 A. Stavrinadis, J. M. Smith, C. A. Cattley, *et al.*, SnS/PbS nanocrystal heterojunction photovoltaics. *Nanotechnology*, **21**:18 (2010), 185202.
92 K. M. Noone, E. Strein, N. C. Anderson, *et al.*, Broadband absorbing bulk heterojunction photovoltaics using low-bandgap solution-processed quantum dots. *Nano Letters*, **10**:7 (2010), 2635–2639.
93 S. W. Tsang, H. Y. Fu, J. Y. Ouyang, *et al.*, Self-organized phase segregation between inorganic nanocrystals and $PC_{61}BM$ for hybrid high-efficiency bulk heterojunction photovoltaic cells. *Applied Physics Letters*, **96**:24 (2010).
94 N. Zhao, T. P. Osedach, L. Y. Chang, *et al.*, Colloidal PbS quantum dot solar cells with high fill factor. *ACS Nano*, **4**:7 (2010), 3743–3752.
95 S. Kitada, E. Kikuchi, A. Ohno, S. Aramaki, S. Maenosono, Effect of diamine treatment on the conversion efficiency of PbSe colloidal quantum dot solar cells. *Solid State Communications*, **149**:41–42 (2009), 1853–1855.
96 Z. N. Tan, T. Zhu, M. Thein, *et al.*, Integration of planar and bulk heterojunctions in polymer/nanocrystal hybrid photovoltaic cells. *Applied Physics Letters* **95**:6 (2009), 063510.
97 Y. Y. Feng, D. Q. Yun, X. Q. Zhang, W. Feng, Solution-processed bulk heterojunction photovoltaic devices based on poly(2-methoxy,5-octoxy)-1,4-phenylenevinylene-multiwalled carbon nanotubes/PbSe quantum dots bilayer. *Applied Physics Letters*, **96** (2010), 093301.
98 S. J. Kim, W. J. Kim, A. N. Cartwright, P. N. Prasad, Self-passivating hybrid (organic/inorganic) tandem solar cell. *Solar Energy Materials and Solar Cells*, **93**:5 (2009), 657–661.
99 C. Y. Kuo, M. S. Su, Y. C. Hsu, H. N. Lin, K. H. Wei, An organic hole transport layer enhances the performance of colloidal PbSe quantum dot photovoltaic devices. *Advanced Functional Materials*, **20**:20 (2010), 3555–3560.
100 J. Tang, E. H. Sargent, Infrared colloidal quantum dots for photovoltaics: fundementals and recent progress. *Advanced Materials*, **23**: 1 (2011), 12–29.

11 Semiconductor quantum dot sensitized TiO_2 mesoporous solar cells

Lioz Etgar, Hyo Joong Lee, Sang Il Seok, Md. K. Nazeeruddin, and Michael Grätzel

11.1 Introduction

Dye-sensitized solar cells (DSSCs) have attracted significant attention throughout the world from both academic and industrial fields as a promising alternative to conventional solid-state photovoltaic devices since a report by O'Regan and Grätzel in 1991 [1]. To improve the overall efficiency and long-term stability of DSSCs, several groups have investigated various sensitizers, photoanode materials, counterelectrodes, and redox systems. Light absorbers, such as transition metal complexes and organic molecules, have been designed and tested in DSSCs. In these cells the photoexcited dye injects electrons into the conduction band of TiO_2, then the oxidized dye cations are regenerated by electron donation from the electrolyte or, alternatively, by hole injection into an organic hole transporting material for the solid-state counterpart [2, 3]. Although the results obtained so far are very impressive, further improvements in both efficiency and stability by introducing new materials and engineering their interfaces are anticipated.

Inorganic semiconducting materials "quantum dots (QDs)" are attracting increasing attention because of their technological importance in solar energy conversion, light emitting diodes, and sensor applications [4]. The attractive properties of QDs, i.e., their size dependent optical, electronic, and mechanical properties, coupled with the available synthetic protocols allow these materials to be integrated into various types of solar cell. In this chapter we focus mainly on incorporating the QDs into mesoscopic TiO_2 based solar cells.

Semiconductor QDs possess unique properties, not encountered in their corresponding bulk materials [5–7]. In a bulk crystal, the properties of the material are independent of the crystal size but depend on the chemical composition. As the size of a crystal decreases to the nanometer regime, the nano-scale QDs begin to exhibit modified crystal properties. The electronic structure is altered from continuous electronic bands to discrete or quantized electronic levels. Decreasing the size of a crystal to the nanometer regime results in observation of the so-called quantum size effect (QSE). The bound

Colloidal Quantum Dot Optoelectronics and Photovoltaics, eds. G. Konstantatos and E. H. Sargent.
Published by Cambridge University Press. © Cambridge University Press, 2013.

electron–hole (e–h) state (Wannier exciton) has slightly less energy than the band gap. The Bohr radius of the exciton (a_B) is given by

$$a_B = \frac{4\pi\varepsilon_0\varepsilon_\infty\hbar^2}{m_0e^2}\left(\frac{1}{m_e^*}+\frac{1}{m_h^*}\right) \tag{11.1}$$

where ε_∞ is the high frequency relative dielectric constant of the medium, m_e^* and m_h^* are the effective masses of the electron and hole, respectively (both in units of m_0), and m_0 is the electron rest mass. When the radius of a QD approaches a_B, the motion of the electrons and holes becomes confined. A created e–h pair can only fit into the QDs when the charge carriers are in a higher energy state. As a result, the band gap increases with decreasing particle size. In this regime of special confinement of the charge carriers (particle in a box), the kinetic energy becomes quantized and the allowed energy bands split into discrete levels. Due to the QSE both the absorption spectrum and the emission spectrum of semiconductors shift to higher energies (blue shift) with decreasing particle size. As a result of the large optical cross section and tunability of their band gap, QDs have potential for use in several applications including telecommunications, eye-safe lasers, solar cells, and electroluminescence devices [5, 6].

In particular, PbS and PbSe QDs are the focus of extensive attention due to some unique intrinsic properties [7, 8]. They have high dielectric constants and a small electron and hole effective mass, corresponding to excitons with a relatively large effective Bohr radius (18 nm and 46 nm, respectively) [7–11]. Inter-band optical studies of PbS and PbSe QDs reveal band-edge excitonic transitions tuned between 0.3 and 2 eV (meaning they are good absorbers in the visible and in the near IR regime), relatively large ground state cross sections of absorption ($\sim 10^{-15}$ cm^{-2}), long excitonic lifetimes ($\sim$200–800 ns), and exceptionally high quantum efficiencies of the luminescence (80%) [12].

QDs have been intensively investigated in a variety of photovoltaic device architectures, including nanocrystal(NC)–polymer hybrid solar cells, NC–Schottky solar cells, NC–sensitized titanium dioxide (TiO_2) solar cells, and NC hybrid bilayer solar cells [13–24].

Reports of PbS and PbSe QD Schottky solar cells suggest that PbS and PbSe QD films exhibit p-type semiconductor behavior after thiol treatment and form Schottky junctions when contacted with metals [13, 14, 25]. While QD Schottky solar cells reach high short circuit current densities (J_{sc}), their open-circuit voltage (V_{oc}) remains low.

Another type of QD has been used in order to improve V_{oc} and J_{sc}, i.e. PbS_xSe_{1-x} ternary QDs. These ternary Schottky solar cells yield power conversion efficiencies (PCEs) of 3.3% under AM 1.5 illumination [15]. In addition there have been reports of devices with a heterojunction architecture in which a thin layer of NC oxide is used as a spacer between the QDs and the fluorine-doped tin oxide (FTO) [26, 27].

In this chapter two main types of QD/TiO_2 mesoporous solar cell are discussed:

(1) Cells in which the synthesized QDs are attached to the TiO_2 film using linker molecules.

(2) Cells in which the QDs are synthesized directly on the mesoporous film by chemical bath deposition (CBD) or by the successive ionic layer adsorption and reaction (SILAR) process.

The discussion starts by describing a new type of mesoscopic PbS quantum dot/TiO_2 heterojunction solar cell. The PbS QDs are synthesized separately and are attached through a linker molecule to the TiO_2 mesoscopic film. The discussion continues by describing the SILAR process used in the QD/TiO_2 mesoporous solar cell. Here the QDs are synthesized directly on the TiO_2 mesoscopic film. Finally the possibility of using a new type of electrolyte, a cobalt complex-based one, in the QD/TiO_2 mesoporous solar cell is discussed.

11.2 Mesoscopic PbS quantum dot/TiO_2 heterojunction solar cells

The idea behind the solid-state QD solar cell is to avoid using a liquid electrolyte, which can corrode the QDs. The PbS QDs act as the sensitizer and at the same time as the hole conductor.

The architecture of the mesoscopic PbS QD/TiO_2 hetrojunction solar cell consists of several layers (see Figure 11.1(a)):

(1) FTO glass;
(2) TiO_2 NC layer (which consists of a compact TiO_2 layer overcoated with a mesoporous NC TiO_2 layer);
(3) QDs layer;
(4) metal electrode (gold or silver).

The bottom layer of the semiconducting device is composed of a compact and mesocopic TiO_2 layer, which acts as the electron collector as well as a blocking layer. Light is absorbed by the PbS QD layer, which acts as the hole conductor, so there is no need to incorporate another p-type material to transport the positive charge carriers. The top contact is a layer of Au or Ag without additional electron blocking layers.

A schematic energy level diagram of the mesoscopic PbS QDs/TiO_2 hetrojunction solar cell is shown in Figure 11.1(b); the conduction and valence bands of the PbS QDs permit electron injection and hole transportation to the TiO_2 and the metal respectively. Figure 11.1(c) shows a cross section of the device where the different layers can be observed. In this device the metal contact was gold.

The performance of such mesoscopic PbS QDs/TiO_2 heterojunction solar cells can be affected by several factors such as: (i) the thickness of the QD overlayer (number of QD layers), (ii) QD size (which affects the QD band gap), (iii) the TiO_2 film, (iv) the linkers that connect the QDs to the TiO_2 film and the QDs themselves.

(i) The number of QD layers

The number of QD layers deposited on the TiO_2 plays an important role in the photovoltaic performance. If the QD layer is too thick, collection of photogenerated charge

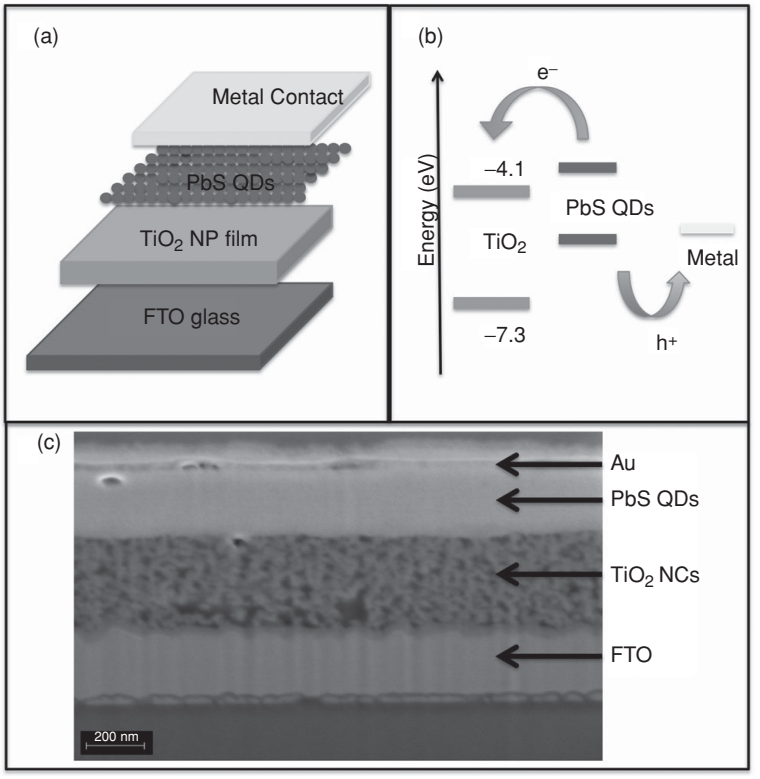


Figure 11.1 (a) The architecture of the PbS(QD)/mesocopic TiO_2 photovoltaic device, the light is incident through the glass (NP = nanoparticle). (b) Energy level diagram of the solar cell for PbS quantum dots. (c) Cross-sectional high resolution scanning electron microscope image of the photovoltaic device. It can be seen that the PbS QDs form a nanocrystalline layer on top of the TiO_2 film, very few of the QDs penetrating into the porous network of the TiO_2 film. The scale bar is 200 nm.

carriers will be incomplete, while too thin a layer of QDs leads to poor light harvesting. It appears that depositing 12 layers of QDs (concentration of 50 mg/ml) is a reasonable compromise to satisfy both the light absorption and carrier collection criteria (see Figure 11.2).

(ii) The size of the QDs

The open-circuit voltage, fill factor, and photocurrent decrease with increasing QD size, however, inter-particle electron transfer is facilitated in films made of the larger QDs because for a given film thickness there are fewer particle boundaries to cross before the electrons arrive at the TiO_2. According to Matt Law and coworkers [28], the mobility of electrons and holes increases by 1–2 orders of magnitude with increasing QD diameter. The size–mobility trends seem to be driven primarily by the smaller number of hops required for transport through arrays of larger QDs but may also reflect a systematic decrease in the depth of trap states with decreasing QD band gap. These authors also observed that the carrier mobility is independent of the polydispersity of

Table 11.1. Comparison of the photovoltaic characteristics using TiO_2, 1% Ga–TiO_2, and 1% Y–TiO_2 photoanodes in PbS/Au solid-state QD solar cells. Reprinted with permission from [29]. Copyright 2011 American Chemical Society

Sample	TiO_2	1% Y–TiO_2	1% Ga–TiO_2
V_{OC} (mV)	507	502	485
J_{SC} (mA/cm^2)	5.2	6.5	11.1
ff (%)	25	32	35
η *(%)*	0.7	1.0	1.9

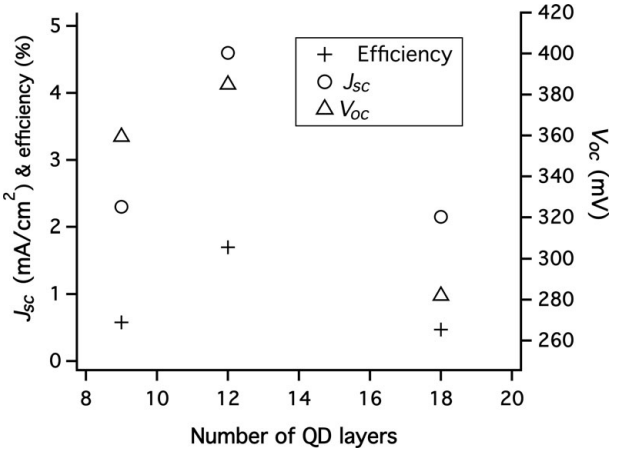


Figure 11.2 The influence of the number of the QDs layers on the short-circuit current, efficiency, and open-circuit voltage (V_{oc}). The cells used for this figure were not optimized; they were made for studying the effect of changing the number of layers of QDs.

the QD samples. This fact is rationalized in terms of the smaller band gap, i.e., larger diameter QDs carrying most of the current in these QD solids, if they can form a percolation network.

(iii) Ga^{3+} and Y^{3+} cationic substitution in TiO_2 photoanode

The cationic substitution of gallium and yittrium in the TiO_2 photoanode increases the power conversion efficiency of DSSC from 7.0% to 8.0% for gallium and even to 9.0% in the case of yttrium. The beneficial effect of gallium and yttrium on the photovoltaic characteristics is attributed to a lower electrical resistance and longer electron lifetime enhancing the charge collection efficiency in the transparent layer. The potential of this approach was also confirmed for solid-state PbS QD solar cells [29]. The photovoltaic properties of cell with the PbS/Au architecture have been measured using standard 20 nm based TiO_2 particles and compared with 1% Ga–TiO_2 and 1% Y–TiO_2 nanoparticles.

Table 11.1 shows all the photovoltaic characteristics of the photoanodes used. The photovoltaic properties of both the gallium–TiO_2 and yttrium–TiO_2 electrodes are better than

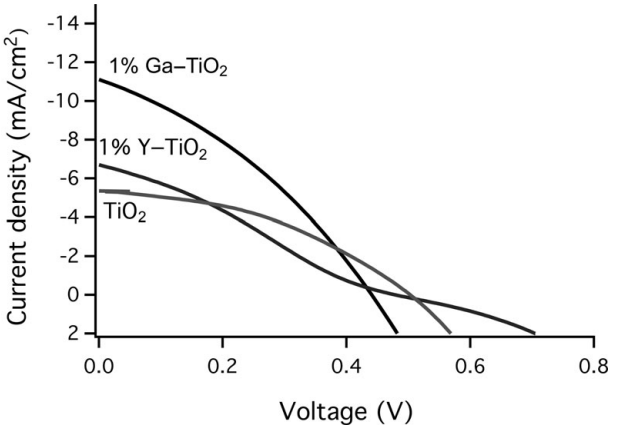


Figure 11.3 *J–V* curve measured under 100 mW/cm^2 illumination (air mass 1.5 G conditions) for TiO_2 / PbS / Au, 1% Ga–TiO_2 / PbS / Au and 1% Y–TiO_2 / PbS / Au heterojunction solar cells. Reprinted with permission from [29]. Copyright 2011 American Chemical Society.

those of TiO_2 electrodes. The most striking result comes from 1% Ga–TiO_2 where the short-circuit current density is significantly improved from 5.2 mA/cm^2 to 11.1 mA/cm^2, although at the expense of the photovoltage which decreases from 507 mV to 485 mV (Figure 11.3). Note that the fill factor was also substantially increased from 0.25 to 0.35. These characteristics bring the PCE to 1.9% compared with 0.7% when TiO_2 was used. The incorporation of yttrium-doped TiO_2 nanoparticles was also beneficial in increasing the short-circuit current density ($J_{sc} = 6.5$ mA/cm^2) and the fill factor ($ff = 0.32$) leading to a PCE of 1.0%. We could speculate that a higher electron lifetime and hence most likely more efficient collection of the charges is the result of such short-circuit current density enhancement. The cationic substitution of yttrium or gallium in TiO_2 is presented here as an additional factor which can influence dramatically the performance of the solid-state QD solar cell.

(iv) The QDs' linker

One of the important parameters for determining the performance of the solid state QD solar cell is the organic molecule attached to the QD surface and to the TiO_2 nanoparticle (NP) surface. The linker molecule should have bi-functional groups that can be attached to the QDs and to the TiO_2 NP film. In addition, the conductivity of the linker can enhance the electron transport through the QD film. A variety of linkers have been used in QD solar cells, such as mercaptopropionic acid, ethane-dithiol, thioglycolic acid, cysteine, thiolacetic acid, mercaptohexadecanoic acid, and benzenethiol derivatives [30–32]. However, no tailored linker molecules have been reported in the literature.

Bis(4-mercaptophenyl)phospinic acid (BMPA, see Figure 11.4) is a bifunctional linker molecule which was specifically designed for the photovoltaic PbS QD/TiO_2 mesoporous solar cell. The phosphinic acid functional group anchors to the TiO_2 mesoporous film and the two thiol groups to the PbS QDs. The short aromatic ring bridge provides better conductivity for electrons injected from the QDs to the TiO_2 conduction band.

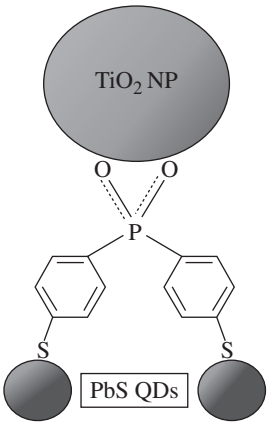


Figure 11.4 The way the BMPA molecule is linked between the TiO_2 NP and the PbS QDs. Reprinted with permission from [34]. Copyright 2011 American Chemical Society.

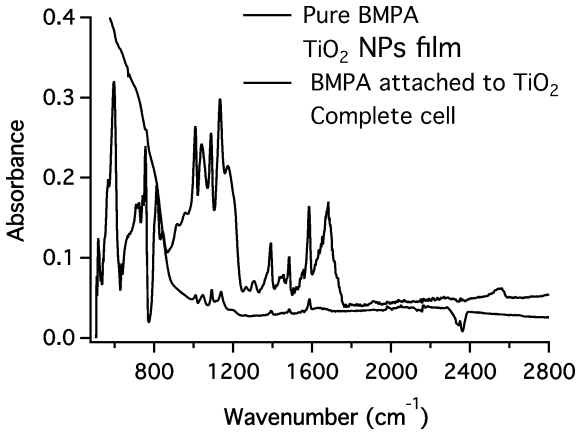


Figure 11.5 FTIR spectra of the pure BMPA, TiO_2 NP film without BMPA treatment, with BMPA attached to TiO_2 NP film and of the complete cell. Reprinted with permission from [34]. Copyright 2011 American Chemical Society.

To confirm the chemical attachment of the BMPA to the TiO_2 surface, Fourier transform infrared (FTIR) spectra were recorded (Figure 11.5) for pure BMPA, TiO_2 NP film without the treatment with BMPA, with BMPA attached to TiO_2 NP film and the complete PbS QD solar cell using the BMPA as a linker.

The stretching, bending, and contraction of the aromatic rings are assigned to the frequency range 900–1100 cm^{-1}. In addition, the phosphorus aromatic ring mode is assigned to the band at 1092 cm^{-1} [33]. These modes can be recognized for all the spectra except the TiO_2 NP film without the BMPA treatment spectrum. This observation is evidence that the BMPA is attached to the TiO_2 surface.

Moreover, the P = O mode of the phospinic acid appears at 1200 cm^{-1} for the pure BMPA, but it disappears once the BMPA is attached to the TiO_2 surface. The absence of

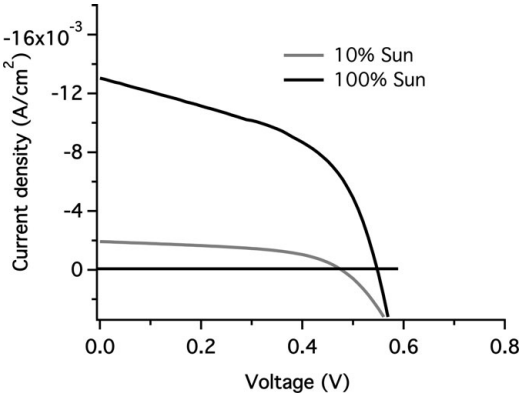


Figure 11.6 Measured *J–V* characteristics for the solid-state PbS QD device. An aperture of 0.12 cm^2 was placed over the device. The horizontal line parallel to the voltage axis is a guiding for the eye.

this peak is additional proof of the chemical attachment of the BMPA to the TiO_2 surface through the phosphinic acid. According to the literature the possible bonding modes of the phosphoryl oxygens to the TiO_2 surface are tridentate or bidentate [33]. In our case the BMPA molecule has two aromatic rings and as a result the tridenate bonding of the phosphoryl oxygens to the TiO_2 surface cannot occur because it requires three oxygen atoms connected to the TiO_2 surface. As a result bidentate bonding is the preferred attachment of the phosphoryl oxygens to the TiO_2 surface (see Figure 11.4).

The pure BMPA spectrum exhibits hydrogen vibrations related to the aromatic rings in the range 1300–1500 cm^{-1} [33]. The S–H stretching band at 2560 cm^{-1} appears in the BMPA spectrum and in the BMPA attached to the TiO_2 surface spectrum. The S–H stretching band disappears once the BMPA is associated with the PbS QDs.

The preliminary photovoltaic results using BMPA as a linker between the PbS QDs and the TiO_2 NPs showed an open-circuit voltage (V_{oc}) of 0.58 V, a short-circuit current density (J_{sc}) of 1.55 mA/cm^2 and a fill factor of 37% corresponding to a PCE of 0.33% under AM1.5. There are still solubility problems regarding the BMPA molecule which cause the low photovoltaic performance. It is assumed that not all the oleic acid that previously capped the PbS QDs is exchanged by the BMPA linker, hence the current density of the device is still low. However, the high V_{oc} compared to that obtained for QD solar cells is promising, and it may be possible to achieve high PCE using this new linker.

11.2.1 Solid-state PbS/TiO_2 heterojunction solar cell

The best performance for mesoscopic PbS/TiO_2 heterojunction solar cells was achieved when taking into consideration all the factors mentioned above. Figure 11.6 presents the photovoltaic results obtained for 1.39 eV PbS QDs. The best performance was obtained with QDs with a diameter of about 3.2 nm (first excitonic peak at 895 nm, $E_g = 1.39$ eV). These PbS produce an open-circuit voltage (V_{oc}) of 0.548 V, a short-circuit current

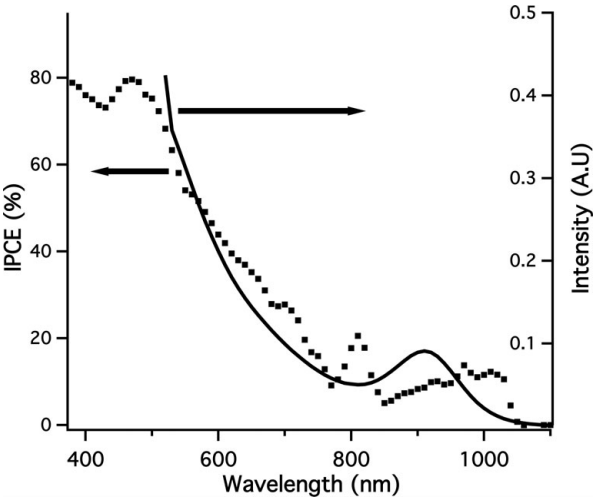


Figure 11.7 Spectral response curves of the photocurrent for the solid-state PbS QD device. The external quantum efficiency, or IPCE, is plotted as a function of the wavelength of the incident light, together with the absorbance spectrum of the PbS QDs measured in a solution of tetrachloroethylene at a low concentration of approximately 3 mg/ml.

density (J_{sc}) of 13.04 mA/cm^2 and a fill factor of 49% corresponding to a PCE of 3.5% under AM1.5. The PCE at a light intensity of 10 mW/cm^2 was 4.4% with a V_{oc} of 0.47 V, a fill factor of 49.5% and a J_{sc} of 1.9 mA/cm^2. The photocurrent density at full sun is significantly lower than the extrapolated value of 19 mA/cm^2 expected for a device with linear response to light intensity. This is due to the charge carrier collection problem [34].

The incident photon to current conversion efficiency (IPCE), or external quantum efficiency, specifies the ratio of extracted electrons to incident photons at a given wavelength. The IPCE spectrum and the PbS QDs absorption spectrum (Figure 11.7) are plotted as a function of the wavelength of the light. The solid-state QD cell shows a good response from the visible through the near infra-red (NIR), with the IPCE reaching its maximum of 80% at 470 nm. Photons of these wavelengths are converted most efficiently as they are absorbed by PbS particles located close to the TiO_2 interface. A wide size distribution of the QDs can be seen in the IPCE spectrum. The excitonic peak of the PbS QDs was blue or red shifted as a result of the device preparation. The excitonic peaks can be observed at 810 nm and 970 nm corresponding to IPCEs of 20% and 14% respectively. Integration of the IPCE spectrum over AM1.5 solar emission yields a photocurrent density of 15 mA/cm^2 in reasonable agreement with the measured value.

To conclude, the structure of a mesoscopic PbS QD/ TiO_2 hetrojunction solar cell has been described. The factors which most influence its performance such as number of QD layers, QD size, the substitution of cations in the TiO_2 film, and the role of the linker have been discussed. Finally, based on those factors, the best cell performance reaching a PCE of 3.5% under 1.5AM has been presented [34].

11.3 QD/TiO_2 mesoporous solar cell using the SILAR process

QDs are attractive candidates for sensitization of a TiO_2 semiconductor because of the facile tunability of their effective band gaps using proper precursor combinations. For in-situ deposition of PbS QDs by the SILAR process from their precursor solutions, four different vessels are prepared: one contains 0.02 M $Pb(NO_3)_2$ in methanol, a second contains 0.02 M Na_2S in methanol, and the other two contain pure methanol to rinse the samples from the excess of each precursor solution. The TiO_2-modified electrode is dipped into the Pb^{2+} solution and then rinsed in pure methanol (and dried in air), then dipped in the S^{2-}solution, followed again by dipping in pure methanol (and again dried in air), successively for 1 minute each. Such an immersion cycle is repeated several times (five or six times). The electrode becomes darker as the number of SILAR cycles increases. For CdS QDs, the SILAR process is the same as for PbS QDs except for minor differences in the concentrations of the precursors and number of cycles; 0.05 or 0.4 M $Cd(NO_3)_2$ dissolved in ethanol and 0.05 or 0.1 M Na_2S dissolved in methanol, respectively. When 0.4 M Cd^{2+} solution is used, four SILAR cycles are performed, whereas nine cycles are performed when the 0.05M solution was used [35].

Assembly of QD-sensitized cells

The photoelectrodes consist of a TiO_2 film with a double or triple layer structure. A compact blocking underlayer of spray-pyrolyzed TiO_2 (ca. 80 nm thick) is deposited onto a clean conducting glass substrate (NSG, F-doped SnO_2, sheet resistance 8 Ω sq^{-1}). A solution of titanium diisopropoxide bis(acetylacetonate) in ethanol (0.02 M) is sprayed 16 times over the conducting glass surface, which is maintained at 450 °C. The treated glass plates are fired at 450 °C for 30 minutes to remove remaining organic traces. Successive depositions of a 2.8 μm thick transparent layer and a 5.6 μm thick 60 nm light-scattering layer by screen-printing, and final post-treatment with an aqueous solution of $TiCl_4$ are then carried out according to usual procedures for dye-cells [36]. After preparing the QD-sensitized electrode by the SILAR process described above, the cell is assembled using a transparent hot-melt 25 μm thick Surlyn ring (DuPont) as a spacer between the QD-sensitized electrode and the counterelectrode (Pt on FTO glass, chemical deposition of 0.05 M hexachloroplatinic acid in 2-propanol at 400 °C for 20 min). The electrolyte is injected into the interelectrode space from the counterelectrode side through a predrilled hole, and the hole is then heat-sealed with a Bynel sheet and a thin glass slide cover. All of the procedures used to prepare electrodes and assembling cells are the same as for typical dye-sensitized cells [36] except for the QD deposition onto the TiO_2 films. The active area is defined with a mask in the same way that typical dye-cells are tested.

A simplified schematic diagram of the SILAR process for preparing PbS- and CdS-sensitized electrodes is presented in the inset of Figure 11.8.

This SILAR process looks facile and straightforward for depositing the wanted QDs and any additional coatings over the mesoporous metal oxide films if the appropriate precursors are available. After a few cycles of SILAR from precursor solutions of Pb^{2+}

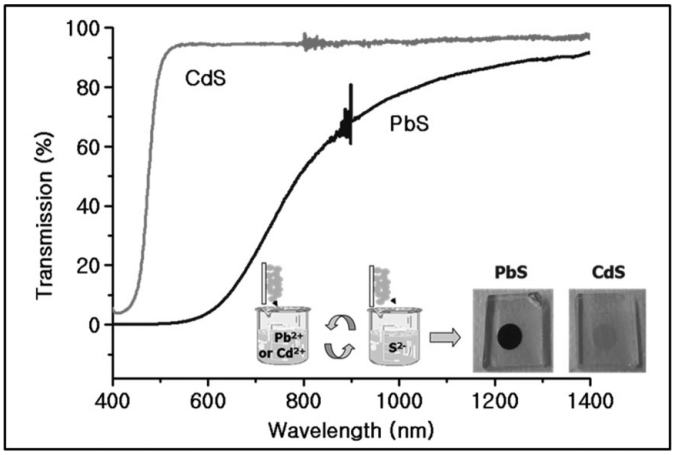


Figure 11.8 Transmission (%) spectra of PbS- and CdS-sensitized electrodes obtained by applying the SILAR process as described in the text. Inset: A schematic diagram of the SILAR process, and pictures of the QD-sensitized photoelectrodes. Reprinted with permission from [35]. Copyright 2011 American Chemical Society.

(or Cd^{2+}) and S^{2-}, the color changes of the electrodes are clear, as shown in the inset of Figure 11.8. Based on such observations, the SILAR process has been used for a long time to make photoactive layers over various substrates, and it is considered a very effective way to prepare QDs inside the mesopores of metal oxide films [17, 18, 37]. As confirmed in [17, 38], alcohol-based SILAR gave more reproducible and better results in QD photoelectrochemical cells than the classical aqueous solvent-based SILAR procedure used so far because alcohols have better wetting and faster drying characteristics than water, which could lead to the formation of better-defined QDs on mesoporous metal oxides. Therefore, Pb^{2+} and S^{2-} precursors were dissolved in methanol, while Cd^{2+} precursors were dissolved in ethanol owing to its different solubility. The concentrations were adjusted to reach optimal photovoltaic performance.

Transmission spectra of typical PbS- and CdS-sensitized electrodes are shown in Figure 11.8. As expected, the transmission of the CdS–TiO_2 film decreases at wavelengths shorter than about 510 nm due to absorption by the deposited CdS (bulk energy gap = 2.5 eV). The PbS-sensitized film shows a very broad feature throughout the visible spectrum that tails of at least down to 1000 nm (bulk energy gap ~ 0.4 eV). These transmission spectra of PbS- and CdS-sensitized films agree well with the IPCE curves obtained from the corresponding solar cells. For better performance, a thin transparent layer (2–3 μm) has been combined with a ~5 μm backscattering layer. For the SILAR PbS deposition, a low concentration precursor solution in methanol (20 mM) was found to be better than the higher concentration aqueous solutions (>1 M or saturated) described more typically in the literature. It has been demonstrated that the SILAR process in an alcoholic medium with precursors of low concentration produces better-defined QDs on mesoporous TiO_2 films, thus resulting in better photovoltaic performances [17, 38, 39]. These new findings imply that the solvent in which SILAR is carried out and the

Table 11.2. Summary of short-circuit currents, open-circuit voltages, fill factors, and overall conversion efficiencies obtained from the data shown in Figure 11.9(b)

	J_{sc} (mA/cm^2)	V_{oc} (V)	*FF*	Efficiency (%)
9.4% sun	0.82	0.34	0.69	2.01
29.8% sun	2.06	0.38	0.55	1.43
99.7% sun	2.64	0.41	0.57	0.62

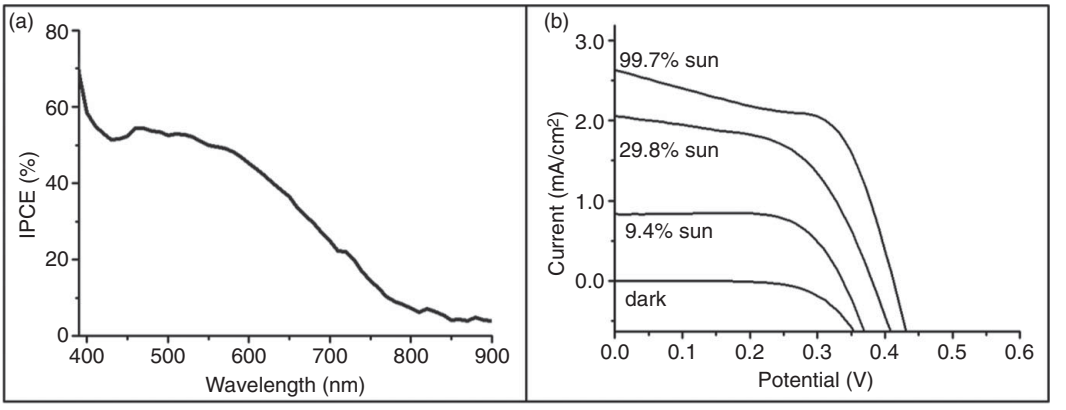


Figure 11.9 (a) Photocurrent action spectra of the best PbS QD-sensitized cell working with a regenerative cobalt complex, $[Co(o\text{-phen})_3^{2+/3+}]$, and (b) photocurrent density–voltage curves of the same device under the various light intensities indicated. Reprinted with permission from [35]. Copyright 2011 American Chemical Society.

concentration of precursors are both important parameters in the preparation of superior QD sensitizers within mesoporous films of small pore size. A reliable delivery of the Pb^{2+} and S^{2-} precursors to the surface of TiO_2 particles deep within the film and then fast elimination of solvent during the drying process could help the sequential growth of homogeneous particles or thin layers. Clogging of the mesopores as the number of SILAR layers is increased can thus be avoided. Using these improved procedures in the SILAR process, a PbS-sensitized solar cell showing about 2% overall efficiency in a *regenerative mode* with the cobalt redox couple, $[Co(o\text{-phen})_3]^{2+/3+}$ can be constructed. As can be seen in Figure 11.9(a), the obtained IPCE value is over 50% throughout a large part of the visible range, and the IPCE curve tails out to more than 900 nm. The shape of the IPCE curve reflects the pattern of non-transmitted light of the same film very well (Figure 11.8), indicating that most of the non-transmitted light is ultimately absorbed by the PbS.

The integrated photocurrent from the IPCE curve was calculated to be about 8–9 mA/cm^2, which agrees well with the short-circuit current measured at low intensity (Table 11.2) and demonstrates the effectiveness of the charge generation and extraction from the interfaces between TiO_2/PbS and $[Co(o\text{-phen})_3]^{2+/3+}$ at low intensity. The

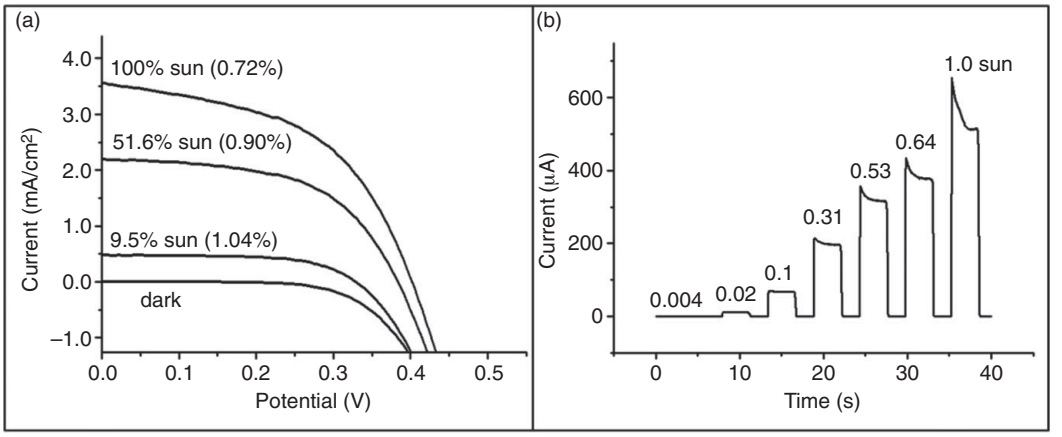


Figure 11.10 (a) Photocurrent density–voltage curves of PbS-sensitized TiO_2 film composed of 60 nm scattering particles only under the various light intensities indicated, and (b) the current dynamics of the same device measured over the course of light-on and light-off (3.5 seconds) at various light intensities. Reprinted with permission from [35]. Copyright 2011 American Chemical Society.

overall efficiency of 2.01% at 9.4% sun intensity comes mostly from the high short-circuit current (I_{sc}) despite a rather low open-circuit voltage of ca. 0.3V. Based on the optical band gap of the deposited PbS (E_g = 1.2–1.5 eV), this result suggests that gaining an understanding of the overpotential for charge transfer at the interfaces may lead to further increases in V_{oc}. Whilst the QD regeneration efficiency leads to a high photocurrent with the regenerative cobalt complex redox couple [40, 41] particularly at low intensity, the short-circuit current does not increase proportionally with increasing light intensity as can be seen in Figure 11.9(b). This results in a substantial reduction of overall efficiency from 2.01% at 9.4% sun intensity to 0.64% at full-sun intensity (Table 11.2).

The difference in the short-circuit current density with light illumination and the abnormal evolution of the current in the *J–V* curves observed with higher light intensities appears thus to arise from diffusion difficulties of the cobalt complex within small mesopores with an average pore size of ~20 nm. The pore size of the photoanode should thus be a parameter of importance, while an increase in pore size would significantly increase the mobility of the redox mediator and consequently improve the photovoltaic characteristics. This is illustrated in Figure 11.10(a), which shows the *J–V* curve under different light intensities when using PbS-sensitized TiO_2 film composed of 60 nm scattering particles only. The increase in the particle size increases the average pore size to 49 nm. Figure 11.9 shows that when this electrode was sensitized by SILAR deposition of PbS QDs and the resulting solar cell was tested under the same conditions as in Figure 11.9, the difference in overall efficiency between 10% and 100% sun was significantly smaller than in Figure 11.9, dropping 30% over this range. This ~20–30% decrease at full sun was still observed as previously [40]. The current dynamics shown in Figure 11.10(b) clearly stress again the diffusion control of the cell. At light intensities

Table 11.3. A summarized data set of short-circuit currents, open-circuit voltages, fill factors, and overall conversion efficiencies obtained under 9.4% sun, from the PbS- and CdS-sensitized electrodes prepared by the SILAR process with different numbers of turns and different last turns (the number appearing after PbS and CdS is the number of repeated cycles of the SILAR process while (+) after the number indicates that SILAR process finished after the electrode dipped in a bath containing the cationic precursor)

	J_{sc} (mA/cm^2)	V_{oc} (V)	FF	Efficiency (%)
PbS5(+)	0.79	0.34	0.69	1.93
PbS5	0.57	0.38	0.68	1.57
PbS6(+)	0.82	0.34	0.69	2.01
CdS9(+)	0.24	0.37	0.68	0.64
CdS9	0.27	0.43	0.72	0.91
CdS10(+)	0.26	0.37	0.66	0.67

greater than 0.3 sun, the initial value was not maintained but just decayed during the light pulse as is similarly observed when solvent-free ionic liquids are used as electrolytes in dye-sensitized solar cells, indicating the mass-transport limitations of photocurrents [42]. To mitigate the diffusion problems of cobalt complexes, irradiating the cell from the counter electrode side and reducing the distance between working and counter electrodes while also taking into account the best compromise between particle size, Brunauer–Emmett–Teller surface area, and pore size could be considered [43]. The present results demonstrate that the cobalt complexes are promising first-generation redox mediators for this purpose, which could lead to better redox couples for regenerative QD-sensitized solar cells in the near future.

The TiO_2/SILAR-PbS/cobalt complex redox couple shows that the efficiency is highly dependent on whether Pb^{2+} or S^{2-} is deposited last. Contrary to general expectations, PbS-sensitized electrodes always give a higher efficiency when the SILAR deposition process terminates with Pb^{2+} deposition, rather than S^{2-} deposition. As seen in Table 11.3, Pb^{2+}-terminated electrodes give about 30% higher short circuit photocurrents than S^{2-} terminated ones, while their open-circuit voltages are about 10% smaller. In contrast, in the case of CdS sensitizers, exactly the opposite trend is observed: S^{2-} termination always leads to better cell performance, with small improvements in V_{oc}, I_{sc}, and FF.

11.4 Cobalt complex-based redox couples in CQD–TiO_2 mesoporous solar cells

The well-known and most efficient I^-/I_3^- redox couple is not compatible with low band gap semiconducting materials leading to a rapid corrosion process of the semiconductor. Therefore, efficient regenerative redox couples appropriate for QD or thin absorber sensitized solar cells have to be tailored and developed. Alternative redox couples based on polypyridyl cobalt complexes [40, 41] appear to work quite well.

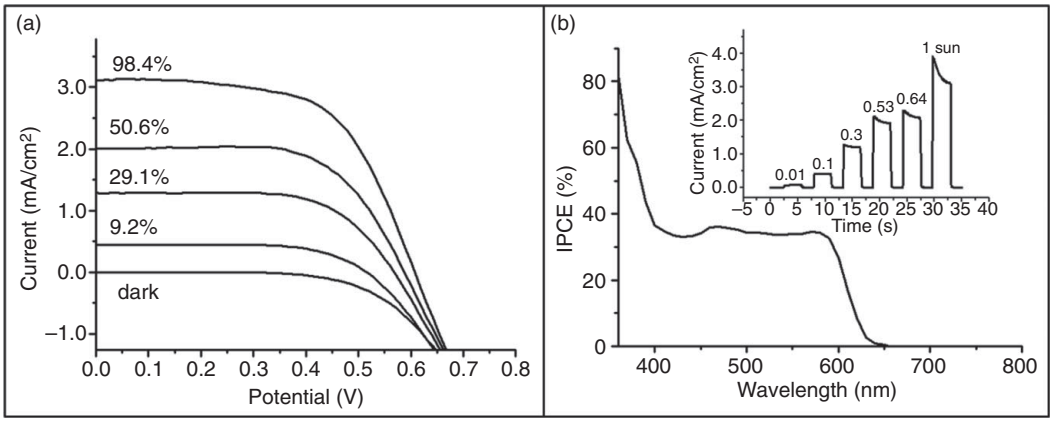


Figure 11.11 (a) Photocurrent density–voltage curves of the best CdSe QD-sensitized cell under various light intensities and (b) the photocurrent action spectra of the same device. Inset: The current dynamics transient spectra of the same device under various light intensities. Reprinted with permission from [40]. Copyright 2011 American Chemical Society.

A new redox system based on cobalt complexes has been identified as a promising hole carrier for testing liquid type QD-sensitized cells. The $[Co(O\text{-phen})_3]^{2+/3+}$ has shown efficient hole carrier properties, giving overall efficiencies of over 1% at full-sun intensity and a high IPCE value (over 35% at broad ranges) as well as reasonable stability for QD sensitized solar cells prepared from CdSe colloids [40]. Using this redox relay, it was possible to characterize interfacial charge transfer kinetics in a regenerative QD-sensitized solar cell successfully.

Among various cobalt complexes, doubly positively charged cobalt complexes have been tested such as the $Co(dbbip)_2$ complex, which was shown to be superior to all other cobalt redox mediators containing polypyridyl ligands [43]. However, for CdSe QD sensitized cells, the $Co(O\text{-phen})_3$ redox system seems to be more efficient than the $Co(dbbip)_2$ complex with an overall incident photon to electron conversion efficiency larger by 30%. The standard redox potential of the $Co(O\text{-phen})_3$ complex is only 30 mV less positive than that of the $Co(dbbip)_2$ complex, and also the valence band position of the CdSe QDs used lies at a sufficiently low energy to transfer holes efficiently. The significant enhancement of the overall conversion efficiency seen with the use of the $Co(O\text{-phen})_3$ complex is due to the small size of the O-phen ligand compared to that of dbbip.

When the concentration of cobalt electrolytes is increased from 0.1 M to 0.5 M, the photocurrent increases to over 3 mA/cm^2 and the efficiency was seen to reach about 1.2% at full-sun intensity [43]. The best efficiency is obtained using relatively thin electrodes (2 and 4 μm) and highly concentrated (0.5 M) pure cobalt complexes with (O-phen) ligands. As can be seen in Figure 11.11(a), well-defined current-density–voltage curves were obtained using various light intensities. At low intensity, the overall efficiency was found to be 1.7–1.8% and it decreased by about 30% at full-sun intensity (Table 11.4). This nonlinear behavior is evident in the transient-current-density curve shown in the

Table 11.4. A summarized data set of short-circuit currents, open-circuit voltages, fill factors, and overall conversion efficiencies from the *I–V* curves in Figure 11.12

	I_{sc} (mA/cm^2)	V_{oc} (V)	*FF*	Efficiency (%)
9.2% sun	0.46	0.52	0.67	1.67
29.1% sun	1.35	0.57	0.65	1.64
50.6% sun	2.10	0.59	0.65	1.50
98.4% sun	3.15	0.61	0.61	1.17

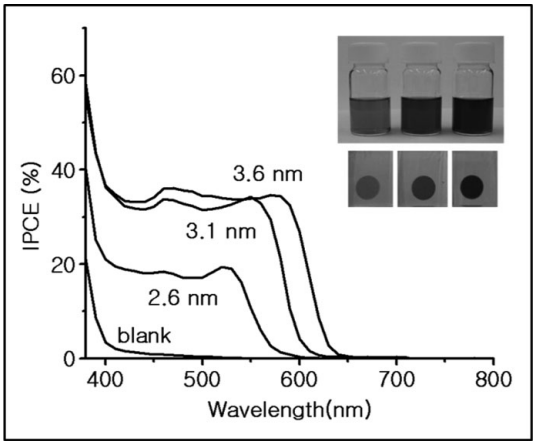


Figure 11.12 Photocurrent action spectra of CdSe QDs sensitized cells in which three different sizes of CdSe QDs were used as a sensitizer, and of a blank cell where CdSe QDs were not included. Inset: Pictures showing different sizes of CdSe QDs dissolved in toluene and their adsorption onto the TiO_2 electrodes used in this experiment. Reprinted with permission from [40]. Copyright 2011 American Chemical Society.

inset of Figure 11.11(b). There are no problems in maintaining a constant current from initial to final illumination times until 0.1 sun, but the current is seen to decrease slightly under 0.3 sun intensity and about 30% loss in current is observed at full-sun intensity. This diffusion-related problem was also seen in our dye cell [43], and in previously reported QDs cells [32, 41]. The IPCE data of Figure 11.11(b) were unprecedently high, ~36% at maximum peak and the integrated value is well matched by the short-circuit current value obtained in current–voltage curves. This relatively good IPCE value indicates the immense promise of this type of colloidal QD cell.

To illustrate the generality of this concept, different size CdSe QDs were prepared and tested under identical conditions. There were no significant differences in terms of the overall efficiencies (1.0–1.2%) obtained from CdSe QDs sensitizers having first excitonic peaks between ~550 nm and ~580 nm. The onset and first maximum positions of the photocurrents are well matched with those of the corresponding absorption spectra. The electron injection rate from the CdSe QDs to the TiO_2 conduction band was reported to be dependent on the size of CdSe QDs and appeared accelerated for smaller sizes of

CdSe QDs [44]. But, when smaller QDs were used, the range of photocurrent narrowed, resulting in lower photocurrents and overall efficiencies as can be seen in Figure 11.12. Therefore, small QDs, with a first excitonic peak lower than about 550 nm, are less appropriate as sensitizers even though the rate of electron transfer is higher than for larger ones. The different colors (orange, red, and light brown) from different sizes of CdSe QDs in solution were transferred exactly to sensitized-TiO_2 films by attachment as can clearly be seen in the inset of Figure 11.12.

References

1 B. O'Regan, M. Grätzel, *Nature*, **353** (1991), 737.
2 N. Robertson, *Angewandte Chemie* International Edition, **45** (2006), 2338.
3 A. Hägfelt, L. Boschloo, L. Sun, L. Kloo, H. Patterson, *Chemical Reviews*, **110** (2010), 6596.
4 M. S. Skolnick, D. J. Mowbray, *Annual Review of Materials Research*, **34** (2004), 181.
5 A. P. Alivisatos, *Journal of Physical Chemistry*, **100** (1996), 13226.
6 C. R. Kagan, C. B. Murray, M. G. Bawendi, *Physical Review B*, **54** (1996), 8633.
7 F. W. Wise, *Accounts of Chemicals Research*, **33** (2000), 773.
8 M. A. Hines, G. D. Scholes, *Advanced Materials*, **15** (2003), 1844.
9 C. M. Evans, L. Guo, J. J. Peterson, S. Maccagnano-Zacher, T. D. Krauss, *Nano Letters*, **8** (2008), 2896.
10 J. M. Pietryga, R. D. Schaller, D. Werder, *et al.*, *Journal of the American Chemical Society*, **126** (2004), 11752.
11 M. V. Kovalenko, D. V. Talapin, M. A. Loi, *et al.*, *Angewandte Chemie International Edition*, **47** (2008), 3029.
12 R. D. Schaller, V. I. Klimov, *Physical Review Letters*, **92** (2004), 186601.
13 K. W. Jonhston, A. G. Pattantyus-Abraham, J. P. Clifford, *et al*., *Applied Physics Letters*, **92** (2008), 151115.
14 J. M. Luther, M. Law, M. C. Beard, *et al*., *Nano Letters*, **8** (2008), 3488.
15 W. Ma, J. M. Luther, H. Zheng, Y. Wu, A. P. Alivisatos, *Nano Letters*, **9** (2009), 1699.
16 B.-R. Hyun, Y.-W. Zhong, A. C. Bartnik, *et al*., *ACS Nano*, **2** (2008), 2206.
17 H. Lee, H. C. Leventis, S.-J. Moon, *et al*., *Advanced Functional Materials*, **19** (2009), 2735.
18 R. Plass, S. Pelet, J. Krueger, M. Grätzel, U. Bach, *Journal of Physical Chemistry B*, **106** (2002), 7578.
19 B. Sun, A. T. Findikoglu, M. Sykora, D. J. Werder, V. I. Klimov, *Nano Letters*, **9** (2009), 1235.
20 J. M. Luther, M. Law, Q. Song, *et al*., *ACS Nano*, **2** (2008), 271.
21 S. Zhang, P. W. Cyr, S. A. McDonald, G. Konstantatos, E. H. Sargent, *Applied Physics Letters*, **87** (2005), 233101.
22 D. Cui, J. Xu, T. Zhu, *et al*., *Applied Physics Letters*, **88** (2006), 138111.
23 J. Seo, S. J. Kim, W. J. Kim, *et al*., *Nanotechnology*, **20** (2009), 95202.
24 V. Sholin, A. J. Breeze, I. E. Anderson, D. Reddy, S. A. Carter, *Solar Energy Materials and Solar Cells*, **92** (2008), 1706.
25 G. I. Koleilat, L. Levina, H. Shukla, *et al*., *ACS Nano*, **2** (2008), 833.
26 J. M. Luther, J. Gao, M. T. Lloyd, *et al*., *Advanced Materials*, **22** (2010), 3704.
27 A. G. Pattantyus-Abraham, I. J. Kramer, A. R. Barkhouse, *et al*., *ACS Nano*, **4** (2010), 3374.
28 Y. Liu, M. Gibbs, J. Puthussery, *et al*., *Nano Letters*, **10** (2010), 1960.

29 A. K. Chandiran, F. Sauvage, L. Etgar, M. Graetzel, *Journal of Physical Chemistry C*, **115** (2011), 9232.
30 S. Menny, R. Sven, H. Idan, S. Yahav, A. Zaban., *Journal of the American Chemical Society*, **131** (2009), 9876.
31 I. Mora-Sero, S. Gimenez, T. Moehl, *et al*., *Nanotechnology*, **19**, 424007.
32 I. Robel, V. Subramanian, M. Kuno, P. V. Kamat, *Journal of the American Chemical Society*, **128** (2006), 2385.
33 G. Guerrero, P. H. Mutin, A. Vioux A., *Chemistry of Materials*, **13** (2001), 4367.
34 L. Etgar, T. Moehl, S. Tscharntke, *et al*., Submitted to *Journal of the American Chemical Society* (2011).
35 H. J. Lee, P. Chen, S.-J. Moon, *et al*., *Langmuir*, **25** (2009), 7602.
36 D. Kuang, S. Ito, B. Wenger, *et al*., *Journal of the American Chemical Society*, **128** (2006), 4146.
37 H. M. Pathan, C. D. Lokhande, *Bulletin of Material Science*, **27** (2004), 85.
38 C.-H. Chang, Y.-L. Lee, *Applied Physics Letters*, **91** (2007), 053503.
39 G. Larramona, C. Choné, A. Jacob, *et al*., *Chemistry of Materials*, **18** (2006), 1688.
40 H. J. Lee, J.-H. Yum, H. C. Leventis, *et al*., *Journal of Physical Chemistry C*, **112** (2008), 11600.
41 P. Yu, K. Zhu, A. G. Norman, *et al*., *Journal of Physical Chemistry B*, **110** (2006), 25451.
42 S. Ito, S. M. Zakeeruddin, R. Humphry-Baker, *et al*., *Advanced Materials*, **18** (2006), 1202.
43 H. Nusbaumer, S. M. Zakeeruddin, J.-E. Moser, M. Grätzel, *Chemistry – A European Journal*, **9** (2003), 3756.
44 I. Robel, M. Kuno, P. V. Kamat, *Journal of the American Chemical Society*, **129** (2007), 4136.

Index

1/*f* noise, 177

ab initio, 78
absorption cross section, 203
absorption spectroscopy, 67
aerogels, 50
aggregation, 48
alkylation, 20
alloy, 34, 237
Alq_3, 99
AM1.5G, 257
amphiphilic, 36
amplified spontaneous emission, 208
anchoring, 16
anisotropic shape, 7
aqueous, 30
arrays, 136
artificial solids, 8
assemblies, 41
atomistic, 76
Auger recombination, 113, 120, 205, 219

backlighting, 161
band alignment, 166
band gap, 61
band gap engineering, 38
band-like transport, 20
bandwidth, 176
beads, 46
Beer's law, 134
Beer–Lambert law, 260
biexciton, 201
biexciton lifetime, 121
binary NC superlattices, 9
binding mode, 17
biolabelling, 32
black body, 159
bleach, 117
blinking, 128, 150
Bloch function, 66
Bloch's theorem, 66
Bohr radius, 63, 199, 259, 293
Boltzmann transport equation, 245
bottom-up, 1, 61
branched QDs, 235
Brillouin zone, 75
built-in field, 262
built-in potential, 190
bulk heterojunction, 91

capacitance-voltage, 267
capping ligands, 117
carboxylic, 4
carrier dynamics, 202
carrier extraction by linearly increasing voltage, 265
carrier lifetime, 176, 264, 268
carrier mobility, 136
carrier transport, 241, 261
cation exchange, 7, 237
cationic substitution, 296
cavity, 221
CdS, 5
CdSe, 5, 39, 234
CdTe, 5, 35
charge transfer, 97
charging, 99, 153
chromaticity, 158
chromaticity diagram, 148
CIE, 149
colloidal quantum dots, 257
color gamut, 149
color rendering index, 149, 159
color temperature, 149, 159
Commission International de l'Eclairage, 148
conduction band, 61
conductivity, 18
conversion efficiency, 131
cooling rate, 116
coordinating solvent, 4
core/shell, 6, 30, 71, 205, 235
Coulomb charging energy, 243
Coulomb glass, 154
Coulombic attraction, 63
coupling energy, 271
covalent coupling, 47
covalent linking, 35
CRI, 159

cross-linking, 18
crystal momentum, 113
cubic rock salt, 237
cubic superlattice, 15

dangling bond, 16, 202
dark exciton, 74
dark states, 202
defects, 274
degradation, 284
density of states, 239
dephasing, 78
depleted heterojunction, 281
depletion region, 100, 261
destabilization, 9
detection, 173
detectivity, 177
detector, 174
DFT, 78
dielectric constant, 276
dielectric screening, 203
differential transmission, 122
diffusion, 245
diffusion coefficient, 261
diffusion length, 100, 261
diode equation, 249
dipole, 156
dipole moment, 97, 156
dipole–dipole interaction, 163
Dirac peak, 187
discrete energy levels, 63
disorder, 133, 242
dispersion curve, 62
dissociation, 247
distributed feedback laser, 225
donor–acceptor, 97
doping, 261, 264, 275
downconversion, 160
drift, 192, 245, 261
dye-sensitized solar cells, 292
dynamic range, 184

effective mass, 62
effective medium theory, 276
Efros–Shklovskii variable range hopping, 269
eigenfunctions, 67
Einstein relation, 261
electric dipole approximation, 74
electroluminescence, 154, 157
electron acceptors, 96
electron donors, 96
electron mobility, 20
electron–hole pair multiplication, 128
electron–hole pair multiplication process, 113
electronic structure, 59
electron–phonon scattering, 112
electrostatic assembly, 45
emission linewidth, 199
energy states, 61
energy transfer, 205
energy transport, 48
ensemble, 204
enthalpy, 10
entropy, 10
Euclidan distance, 159
exciton, 63, 201
exciton binding energy, 247
exciton diffusion length, 101
exciton lifetime, 119, 153
exciton multiplication, 114
external quantum efficiency, 91, 134, 157, 263

Fabry–Perot, 221
faceting, 10
facets, 7
Fermi level, 242
Fermi's Golden Rule, 240
field driven electroluminescence, 167
field driven QD-LED, 167
field-effect transistor, 267
field-induced luminescence quenching, 155
fill factor, 249, 263
fluence, 203
fluorescence, 60
fluorescence intermittency, 128, 153
fluorescence line narrowing spectroscopy, 69
fluorophores, 79
Förster energy transfer, 90, 152, 163
Frenkel, 166
FRET, 45, 99

gain cross section, 207
gain lifetime, 206
gate-tunable, 188
gelation, 50
gels, 49
generation–recombination, 177
Gibbs free energy, 10
graphene, 187
grating, 225
growth, 3, 30
growth kinetics, 7

Hamiltonian, 73, 240
hard-sphere approximation, 8
heterojunction, 176, 234, 279
HgTe, 37, 39
hollow structures, 7
homogenous broadening, 204
homojunction, 176
hopping, 154, 179, 242
hot carrier, 115

hot carrier relaxation, 113
hot carrier solar cells, 113
hot phonon bottleneck, 116
hot exciton, 125
hot-injection technique, 3
hybrid, 88
Hyo, 307

ideality factor, 264
image sensor, 173
imaging, 94
impact ionization, 113
InAs, 5, 97
incident-photon-to-electron conversion efficiency, 263
incorporation method, 38
infrared, 213
inorganic capping ligands, 19
inorganic charge transport layer, 165
InP, 5
integrating sphere, 151
interference, 134
intermediate confinement, 64
internal quantum efficiency, 100, 133
interstate transitions, 116
intraband absorption, 119
intraband relaxation, 204
intrastate transitions, 116
ionic liquid, 305

Johnson noise, 177

k • *p* theory, 73
Kane Hamiltonian, 73
Kirkendall effect, 7

Lambert–Beer law, 210
Lambertian, 158
Langevin recombination, 248
laser, 199
layer-by-layer assembly, 43
lead chalcogenides, 218
LED, 40
ligand, 4, 16, 78, 96, 150
ligand exchange, 16, 17, 179, 238, 271
light emitting devices, 148
light emitting diodes, 88
linear regime field effect mobility, 267
linker, 297
luminance, 158
luminescence, 151
luminescence quenching, 153
luminous flux, 158
Luttinger Hamiltonian, 73

magic sized clusters, 78
magnetic, 13
majority carrier mobility, 265
MDMO-PPV, 103
MEG, 59
MEH-PPV, 92
metal chalcogenide complexes, 19
metal-to-insulator transition, 18
microcapillary, 223
microcontact printing, 163
microsphere resonator, 224
microtorroidal resonator, 225
microwave irradiation, 36
mid-gap states, 262
Minkowski lattice, 15
mobility, 265, 272
modal gain, 209, 212
molecular clusters, 79
momentum, 62
monomer, 2
multiband, 73, 113
multiband envelope function, 73
multicomponent superlattices, 13
multiple exciton generation, 193
multiple exciton generation, 113
multispectral, 183

nanocrystal, 1, 30
nanocubes, 15
nanoparticle, 2
nanorod, 7, 15, 31, 235
nanorod superlattices, 15
nanowire, 7, 49
necking, 181
noise, 180
noise current, 177
noise equivalent power, 177
nonradiative recombination, 33
normalized detectivity, 93
nucleation, 2, 3, 30

open-circuit voltage, 248, 263
optical bowing effect, 38
optical gain, 199
optical microsensors, 48
optical transition, 68
organic capping ligands, 16
organic semiconductors, 88
organometallic, 30
Ostwald ripening, 2
overpotential, 304
oxidation, 284

P3HT, 92
packaging, 165
packing, 8

passivation, 264, 272
PbS, 5, 39, 257
PbSe, 5
PbTe, 5
PCBM, 94, 96
PCP-DTBT, 92
PDTPQx, 103
percolation, 133
phase separation, 162
phase transfer, 18
phonon bottleneck, 78, 116, 204
phonon relaxation, 112
phosphor, 150
photocharging, 115, 125
photochemical treatment, 33
photoconductive gain, 95, 176
photoconductivity, 18, 178
photoconductor, 175
photocurrent, 306
photodetectors, 93
photodiode, 94, 176, 190
photogate, 187
photoinduced absorption, 216
photoinduced absorption spectroscopy, 102
photoionization, 125
photoluminescence, 68, 151
photoluminescence excitation, 69
photoluminescence quantum yield, 32, 151
photonic crystal, 226
photosensitization, 176
photostability, 150
phototransistor, 187
photovoltaic, 90, 244
plasmonics, 265
p–n junction, 246, 260
Poisson statistics, 123, 206
polarizability, 156
polarons, 102
polymer, 152, 233
polymer photovoltaics, 256
polymer-nanocrystal, 178
polymorphism, 10
power conversion efficiency, 91, 112, 263
primary photocarriers, 187
protonation, 20
pseudopotential, 76
pump-probe, 202
PVK, 94
pyrite, 236

QD-sensitized cell, 133
quality factor, 221
quantization, 63
quantum confined Stark effect, 156
quantum confinement, 64
quantum dot, 1, 2, 30, 59, 174, 292
quantum efficiency, 176
quantum size effect, 1, 259, 292
quasicrystalline, 12
quasi-Fermi level splitting, 272
quasi-neutral region, 100, 191, 261

radiative recombination, 264
redox couple, 303, 305
reflectance, 134
regenerative mode, 303
responsivity, 176
responsivity quenching, 185
rod, 7

saturation regime field-effect mobility, 267
Schottky junction, 176
Schottky barrier, 190
Schrödinger equation, 65, 239
selection rule, 241
self-assembly, 8, 13
self-capacitance, 243
self-organization, 10
self-purification, 275
sensitivity, 177
sensitizing centers, 176, 179
series resistance, 249, 264
shallow traps, 262
sheets, 49
shell, 274
shifting excitation spot, 210
short-circuit current, 248
short-circuit current density, 263
short wavelength infrared, 173
shot noise, 177
shunt resistance, 249, 264
shuttering, 188
signal to noise ratio, 177
SILAR, 37, 301
single exciton gain, 226
single exciton lasing, 229
size-tunability, 60
solar cells, 131
solar concentration, 112
solar spectrum, 257
spontaneous emission, 202, 208
stability, 283
stabilizer, 3, 30
stabilizer exchange, 36
Stark effect, 119
Stark shift, 227
stimulated emission, 202, 207
stimulated emission lifetime, 209
Stokes shift, 74, 202
strong confinement, 64
successive ionic layer adsorption and reaction, 301
supercrystals, 9

superlattice, 7, 43, 236
supersaturation, 4
surface states, 152
surfactants, 3

temporal response, 185
tetrapod, 7, 235
thermalization, 204
thermophotovoltaic, 113
thin-film transistor, 245
thiols, 35
third-generation, 113
tight binding, 76
time constant, 176
time of flight, 265
time-resolved spectroscopy, 117
top-down, 1, 61
top-surface photodetector, 173
transient absorption, 202
transient absorption spectroscopy, 117
transient bleaching, 126
transient photocurrent spectroscopy, 185
transient photoluminescence, 117, 125
transient THz spectroscopy, 117
transistor, 245
transit time, 176
transmittance, 134
trap, 16, 274
trap states, 157, 184
trion decay, 126
triple-junction solar cell, 259
tunneling, 269
tunneling rate, 243, 271
twinning, 10
type I, 71, 98, 236
type II, 71, 98, 178, 236
type-III, 98

ultrasonic treatment, 37

valence band, 61
van der Waals force, 15
variable range hopping, 269
variable stripe length, 209
Vegard's law, 259
visible spectrum, 183, 211

wavefunction, 63, 66
waveguide losses, 210
weak confinement, 64
whispering gallery mode, 47, 221
wurtzite, 235

Zn chalcogenides, 32